

Lecture Notes in Mechanical Engineering

Nasrul Hadi Johari

Wan Azmi Wan Hamzah

Mohd Fairusham Ghazali

Herma Dina Setiabudi

Sudhakar Kumarasamy *Editors*


Proceedings of the 2nd Energy Security and Chemical Engineering Congress

Selected Articles from ESChE 2021,
Malaysia

 Springer

Lecture Notes in Mechanical Engineering

Editorial Board

Francisco Cavas-Martínez , Departamento de Estructuras, Construcción y Expresión Gráfica Universidad Politécnica de Cartagena, Cartagena, Murcia, Spain

Francesca di Mare, Institute of Energy Technology, Ruhr-Universität Bochum, Bochum, Nordrhein-Westfalen, Germany


Mohamed Haddar, National School of Engineers of Sfax (ENIS), Sfax, Tunisia

Young W. Kwon, Department of Manufacturing Engineering and Aerospace Engineering, Graduate School of Engineering and Applied Science, Monterey, CA, USA

Justyna Trojanowska, Poznan University of Technology, Poznan, Poland

Series Editors

Fakher Chaari, National School of Engineers, University of Sfax, Sfax, Tunisia

Francesco Gherardini , Dipartimento di Ingegneria “Enzo Ferrari”, Università di Modena e Reggio Emilia, Modena, Italy

Vitalii Ivanov, Department of Manufacturing Engineering, Machines and Tools, Sumy State University, Sumy, Ukraine

Lecture Notes in Mechanical Engineering (LNME) publishes the latest developments in Mechanical Engineering—quickly, informally and with high quality. Original research reported in proceedings and post-proceedings represents the core of LNME. Volumes published in LNME embrace all aspects, subfields and new challenges of mechanical engineering. Topics in the series include:

- Engineering Design
- Machinery and Machine Elements
- Mechanical Structures and Stress Analysis
- Automotive Engineering
- Engine Technology
- Aerospace Technology and Astronautics
- Nanotechnology and Microengineering
- Control, Robotics, Mechatronics
- MEMS
- Theoretical and Applied Mechanics
- Dynamical Systems, Control
- Fluid Mechanics
- Engineering Thermodynamics, Heat and Mass Transfer
- Manufacturing
- Precision Engineering, Instrumentation, Measurement
- Materials Engineering
- Tribology and Surface Technology

To submit a proposal or request further information, please contact the Springer Editor of your location:

China: Ms. Ella Zhang at ella.zhang@springer.com

India: Priya Vyas at priya.vyas@springer.com

Rest of Asia, Australia, New Zealand: Swati Meherishi at swati.meherishi@springer.com

All other countries: Dr. Leontina Di Cecco at Leontina.dicecco@springer.com

To submit a proposal for a monograph, please check our Springer Tracts in Mechanical Engineering at <https://link.springer.com/bookseries/11693> or contact Leontina.dicecco@springer.com

Indexed by SCOPUS. All books published in the series are submitted for consideration in Web of Science.

Nasrul Hadi Johari · Wan Azmi Wan Hamzah ·
Mohd Fairusham Ghazali · Herma Dina Setiabudi ·
Sudhakar Kumarasamy
Editors

Proceedings of the 2nd Energy Security and Chemical Engineering Congress

Selected Articles from ESChE 2021, Malaysia

Editors

Nasrul Hadi Johari
Faculty of Mechanical and Automotive
Engineering Technology
Universiti Malaysia Pahang
Pekan, Pahang, Malaysia

Mohd Fairusham Ghazali
Universiti Malaysia Pahang
Pekan, Pahang, Malaysia

Sudhakar Kumarasamy
Universiti Malaysia Pahang
Pekan, Pahang, Malaysia

Wan Azmi Wan Hamzah
Universiti Malaysia Pahang
Pekan, Pahang, Malaysia

Herma Dina Setiabudi
Universiti Malaysia Pahang
Pekan, Pahang, Malaysia

ISSN 2195-4356

ISSN 2195-4364 (electronic)

Lecture Notes in Mechanical Engineering

ISBN 978-981-19-4424-6

ISBN 978-981-19-4425-3 (eBook)

<https://doi.org/10.1007/978-981-19-4425-3>

© The Editor(s) (if applicable) and The Author(s), under exclusive license to Springer Nature Singapore Pte Ltd. 2023

This work is subject to copyright. All rights are solely and exclusively licensed by the Publisher, whether the whole or part of the material is concerned, specifically the rights of translation, reprinting, reuse of illustrations, recitation, broadcasting, reproduction on microfilms or in any other physical way, and transmission or information storage and retrieval, electronic adaptation, computer software, or by similar or dissimilar methodology now known or hereafter developed.

The use of general descriptive names, registered names, trademarks, service marks, etc. in this publication does not imply, even in the absence of a specific statement, that such names are exempt from the relevant protective laws and regulations and therefore free for general use.

The publisher, the authors, and the editors are safe to assume that the advice and information in this book are believed to be true and accurate at the date of publication. Neither the publisher nor the authors or the editors give a warranty, expressed or implied, with respect to the material contained herein or for any errors or omissions that may have been made. The publisher remains neutral with regard to jurisdictional claims in published maps and institutional affiliations.

This Springer imprint is published by the registered company Springer Nature Singapore Pte Ltd.

The registered company address is: 152 Beach Road, #21-01/04 Gateway East, Singapore 189721, Singapore

*To the new generations of engineers working
for a sustainable world...*

Preface

The 2nd Energy Security and Chemical Engineering Congress (ESChE 2021) was organized by Center for Research in Advanced Fluid and Processes (Fluid Centre), Universiti Malaysia Pahang (UMP) in partnership with Nguyen Tat Thanh University, University of Stavanger and Ton Duc Thang University during November 3–5, 2021.

The objective of ESChE'21 Congress is to provide a platform to discuss ideas and latest research findings especially in energy, environment, chemical and thermal engineering fields. With the theme “**Sustainable Technological Solution for a Better World**”, ESChE 2021 is meant to offer a scientific platform for researchers from all around the globe to present their research. The papers submitted to ESChE'21 Congress were single-blind peer-reviewed, at least by two independent referees. A brief overview on the ESChE'21 Congress reveals the following: 102 presented papers in the conference, 3 invited keynote speeches, 1 plenary presentation, 5 conference sections in which the papers were distributed, 126 participants from 4 countries (Malaysia, Thailand, Vietnam and Indonesia). Professors and notable specialists in the fields of mechanical and chemical engineering from Universiti Putra Malaysia, University of Stavanger, Norway and PETRONAS Malaysia were invited as keynote speakers. The technical session presentations were allocated 15 minutes for the presentation and 5 minutes for comments, questions and answers, for a total of 20 minutes for each paper (both presentation and Q&A). During each technical session, the best papers were chosen and honored based on technical, quality and presentation.

We would like to thank the Organizing Committee for their significant contribution to the success of ESChE 2021. We also like to convey our heartfelt gratitude to everyone who assisted with the review process and contributed to improve the scientific value and quality of the proceedings. We also appreciate the participation of the authors, as well as the presenters and attendees of the ESChE 2021. We wish to welcome them, as well as new attendees, to the ESChE 2023 event. We also want

to thank Springer Publisher for publishing the conference proceedings as a book (Lecture Notes in Mechanical Engineering).

Pekan, Pahang, Malaysia

Dr. Nasrul Hadi Johari
Editor, ESChE'21

About This Book

Mechanical engineering is a field that is continuously evolving as a profession to provide sustainable design, products and technologies for society. Mechanical engineering products, in conjunction with technological advances in other sectors, contribute to noise, water and air pollution, and the degradation of land and landscape. The rate of production, both energy and products, is increasing at such a rapid rate that natural regeneration can no longer sustain. Emission control is a fast-growing topic for mechanical engineers and others, encompassing the development of machines and processes that produce fewer pollutants as well as new materials and processes that can decrease or eliminate pollution that has already been generated. And, in an increasingly environmentally conscious world, the concept of sustainability is also intrinsically important to the success or failure of any engineering product or processes. Mechanical engineers thus play a central role in applying a truly modern approach for enabling the global transition to green energy and sustainable practices. To address climate change, researchers are progressively looking into a wide range of novel solutions for energy conversion, engine efficiency, alternative fuels, nature-inspired materials, enhanced manufacturing processes and so on.

In this context, this book presents part of the proceedings of the Mechanical and Materials track of the 2nd Energy Security and Chemical Engineering Congress (ESChE 2021) as presented by the academics, researchers and postgraduate students. The book provides insights into different aspects of mechanical processes, nanomaterials and alternate fuels that set the stage for development of sustainable technological solutions. The content of this book will be useful for students, researchers and professionals working in the areas of mechanical engineering, materials, energy technologies, optimization and allied fields.

Highlights

- Discusses the energy recovery issues, alternative fuels and nanolubricants.
- Provides a snapshot of advanced technology in automobiles and manufacturing processes.
- Covers design, simulation and finite element modeling of equipment and processes.

Contents

Prospects of Energy Recovery in Offshore Oil and Gas Operations	1
Qi Yun Koh, Srithar Rajoo, and Kuan Yew Wong	
An Overview of Organic Rankine Cycle for Waste Heat Recovery on Offshore Oil and Gas Platform	9
Qi Yun Koh, Srithar Rajoo, and Kuan Yew Wong	
Numerical Simulation of Heat Transfer Performance of Water: Ethylene Glycol Mixture (W:EG) Through Turbine-Like Decaying Flow Swirler	19
At-Tasneem Mohd Amin, Wan Azmi Wan Hamzah, and Mohd Azmi Ismail	
Pareto Solution of Autocatalytic Esterification in Semi-batch Reactor Using Control Vector Parameterization (CVP) and ϵ-Constraint	31
F. S. Rohman, K. A. Zahan, and N. Aziz	
Control Analysis of Biomass Gasification with Combined Heat and Power System	41
Y. H. Kok, N. Kamarulzaman, Z. F. Mohd Shadzalli, N. Abdul Manaf, Ku Nur Afrina Ku Azman Shah, Mohd Zamri Mohd Yusop, Jafri Mohd Rohani, Budi Hartono, and Nguyen Duc Tuyen	
Effects of Pineapple Leaf Fibre as Reinforcement in Oil Palm Shell Lightweight Concrete	51
Siew Choo Chin, Mun Lin Tang, Norliana Bakar, Jia Ling Che, and Shu Ing Doh	
Pedal Error Naturalistic Driving Study Among Malaysian Drivers	61
Mohamad Zairi Baharom, Zulkifli Ahmad Manap, Nursya Mimie Ayuny Ismail, Mohd Hasnun Arif Hassan, Juffrizal Karjanto, and Khairil Anwar Abu Kassim	

Copper Coated Electrode by Fused Deposition Modelling (FDM) Process 77
Nicolas Ng Yang Zu, Reazul Haq Abdul Haq, Mohd Fahrul Hassan, Mohd Nasrull Abdol Rahman, Said Ahmad, and Haslina Abdullah

FTIR Analysis of Plant-Based Cellulose as Adsorbents for Water Remediation 89
Arjun Asogan, Norazlianie Sazali, Wan Norharyati Wan Salleh, Haziqatulhanis Ibrahim, and Rishen Nair Krishnan

A Study on the Wear Resistance and Lubrication Properties of Mixed Engine Oils 95
Khairulafizal Sultan Ali, Mohd Nadzeri Omar, Nasrul Hadi Johari, and Mohd Hasnun Arif Hassan

Effect of Hot Cylinder Materials on Gamma-Type Stirling Engine Performance Using Solar Dish Concentrator 109
Purbo Suwandono, Gigih Priyandono, Kushendarsyah Saptaji, and Akhmad Rizal Fanani

The Analysis of Risk Factor Repetitive Motion in Manufacturing Activities Based on Ergonomics 119
Nur Ezzatul Balqis Binti Mohd Zahari, Norazlianie Sazali, Zawati Harun, and Norsuhailizah Sazali

The Development of Quick Response Manufacturing in Supply Chains Activities Based on Product Planning Control 127
Siti Nursuhailah Md Suhaidin, Norazlianie Sazali, and Wan Norharyati Wan Salleh

Rheological Characteristics and Optimization of Novel TiO₂-POE Nanolubricant Using Response Surface Method (RSM) for Air Conditioning System Compressor Application 133
Agus Nugroho, Rizalman Mamat, Zhang Bo, Wan Azmi Wan Hamzah, Mohd Fairusham Ghazali, and Talal Yusaf

A Comprehensive Investigation of Low Proportion TiO₂-POE Nanolubricant Stability for Residential Air Conditioning System Application 147
Agus Nugroho, Rizalman Mamat, Zhang Bo, Wan Azmi Wan Hamzah, Talal Yusaf, Mohd Fairusham Ghazali, and Fitri Khoerunnisa

OFAT Adoption on FAI₂O₃-POE Nanolubricant Absorbance Ratio Optimization Based on Spectrophotometric Method 165
Agus Nugroho, Rizalman Mamat, Zhang Bo, Wan Azmi Wan Hamzah, Mohd Fairusham Ghazali, and Talal Yusaf

Surface Modification for Dispersion Stability of Novel FAI_2O_3 -POE Nanolubricant Using Functional SiO_2 179
 Agus Nugroho, Rizalman Mamat, Zhang Bo, Wan Azmi Wan Hamzah, Mohd Fairusham Ghazali, and Talal Yusaf

Absorbance Ratio Optimization as a Function of TiO_2 -POE Nanolubricant Spectrophotometric Wavelength Using the Quadratic Design on One Factor at a Time 193
 Agus Nugroho, Rizalman Mamat, Zhang Bo, Wan Azmi Wan Hamzah, Talal Yusaf, Mohd Fairusham Ghazali, and Fitri Khoerunnisa

Multiscale Modelling of 3-Dimensional Brain Tissue Using Ideal Capillary Model 205
 Abbas Shabudin, Mohd Jamil Mohamed Mokhtarudin, Stephen Payne, Wan Naimah Wan Ab Naim, and Nik Abdullah Nik Mohamed

Tribological Performance Effect of SiO_2 and TiO_2 Nanoparticles as Lubricating Oil Additives 223
 M. F. Ismail and Wan Azmi Wan Hamzah

Comparison of Thermal Efficiency and Heat Transfer Rate on the Fluidized-Bed Combustor Using Oil Palm Fuel 233
 Muhammad Faisal, Erdiwansyah, Muhtadin, Mahidin, Asri Gani, Mahyuddin, Rizalman Mamat, Mohd Fairusham Ghazali, and Bukhari Manshoor

Performance Optimization of Low Proportion Biodiesel Blend on Marine Diesel Engine Using Response Surface Method 243
 C. W. Mohd Noor, Rizalman Mamat, Mohd Fairusham Ghazali, S. M. Rosdi, Husni Husin, and Bukhari Manshoor

Performance Investigation of R32 and R410a Refrigerants with Different Compressor Lubricants 259
 M. F. Ismail and Wan Azmi Wan Hamzah

Micromechanical Modeling of Glass Filled Epoxy Using the Variational Asymptotic Method for Unit Cell Homogenization 271
 Izzuddin Zaman, Nurul Jannah Mohammad, Bukhari Manshoor, and Amir Khalid

Finite Element Analysis of Tuned Mass Damper 281
 Izzuddin Zaman, Bukhari Manshoor, Amir Khalid, and Shiau Wei Chan

Comparison of Frequency Levels in Internal Combustion Engines Using a Gasoline-Methanol Fuel Blend 291
 Erdiwansyah, Husni Husin, Fitri Khoerunnisa, Asri Gani, R. E. Sarjono, Rizalman Mamat, Mohd Fairusham Ghazali, S. M. Rosdi, and Bukhari Manshoor

Corrosion Performance of Nanopaint for Automotive Application 299
 S. Z. A. Sakinah, Wan Azmi Wan Hamzah, and J. Alias

Laser Processing of $La_{61.4}Al_{15.9}Ni_{11.35}Cu_{11.35}$ Based Functionally Graded Material Bulk Metallic Glass 309
 Qayyum Halim, Nik Abdullah Nik Mohamed, Mohd Ruzaimi Mat Rejab, Mohd Kamal Kamarulzaman, Sakinah Hisham, and A. M. Aizzuddin

Prediction and Optimization of Thermophysical Properties of Hybrid Cellulose Nanocrystal-Copper (II) Oxide Nanolubricant for Tribology Application 325
 Sakinah Hisham, K. Kadirgama, D. Ramasamy, M. Samykan, N. W. Awang, and Mohd Kamal Kamarulzaman

Fabrication of Superhydrophobic on Ti6Al4V by Using the Hybrid Process of Nanosecond Laser Texturing 341
 M. H. Zul, M. Ishak, M. H. Aiman, and M. M. Quazi

Statistical Approach to the Cellulose Nanocrystal Tribological Behavior on the Piston Liner Contact Using Full Factorial Design (FFD) 351
 N. W. Awang, Sakinah Hisham, D. Ramasamy, K. Kadirgama, and Mohd Kamal Kamarulzaman

Covid-19 Embedded with Aerosol Particles Travel Simulation Inside a Mosque 365
 Mohd Rezan Hamji Ajirun, Syifak Izhar Hisham, Mohd Nadzeri Omar, and Nasrul Hadi Johari

A Review on Automotive Tires Significant Characteristic Identification for General Consumers 375
 Ahmad Noor Syukri Zainal Abidin, Arief Hakimi Azmi, Khairil Anwar Abu Kassim, Ahmad Shahir Jamaludin, and Mohd Nizar Mhd Razali

Evaluation of Palm Oil Leaves Extracts as a Potential Environment Friendly Corrosion Inhibitor for Metals 387
 Arman Abdullah, Euodia Banius, Azizul Helmi Sofian, and Lum Wai Bin

Editors and Contributors

About the Editors

Dr. Nasrul Hadi Johari obtained his Ph.D. in Biofluid Mechanics from Imperial College London, UK. He is currently a senior lecturer at the Faculty of Mechanical and Automotive Engineering Technology, Universiti Malaysia Pahang. Dr. Johari's research activities include computational modeling of blood flow, tissue mechanics and mass transport in the cardiovascular system, with applications ranging from evaluating the hemodynamic performance of medical devices to predict the outcome of endovascular interventional procedures. He is also interested in computational and experimental modeling of the interaction between human and sports equipment particularly in improving training aid systems and injury prevention.

Dr. Wan Azmi Wan Hamzah is a Professor at the College of Engineering, Universiti Malaysia Pahang. His research activities include the topics of heat transfer, thermo-fluid engineering, automotive, nanotechnology, cooling system, lubrication, air-conditioning system, solar system, tribology and many more. His specialization area was related to nanoparticle dispersion technology (Nano-DisTec). He was awarded a remarkable total of 100 awards from national and international bodies for the research outcome. Recently, he is listed among the top 2% best scientists in the world according to the recent data from Stanford University.

Dr. Mohd Fairusham Ghazali is an associate professor and director of Center for Research in Advanced Fluid and Processes (CARIFF), Universiti Malaysia Pahang. He graduated from The University of Sheffield, UK with a Ph.D. in Mechanical Engineering in 2012. He has shown vast interest in the signal analysis and vibration control research areas. At present, he is actively involved in vibration control, automatic control engineering, advanced signal processing and computational fluid dynamics (CFD) research activities. He is a Professional Engineer under BEM and also registered as a corporate member of IEM.

Dr. Herma Dina Setiabudi is an Associate Professor at the Faculty of Chemical and Process Engineering Technology, Universiti Malaysia Pahang, Malaysia. She has considerable expertise in the areas of advanced materials, heterogeneous catalysis and environmental engineering. She has served as Guest Editor for several special issues in high-impact journals, namely *Catalysis Today* (Elsevier), *Industrial and Engineering Chemistry Research* (American Chemical Society), *Chemical Engineering and Processing: Process Intensification* (Elsevier), *International Journal of Hydrogen Energy* (Elsevier), *Chemical Engineering and Technology* (Wiley), etc. She is also an active reviewer for many international journals published by ACS, Elsevier, RCS, Wiley and Springer.

Dr. Sudhakar Kumarasamy is currently a Senior Lecturer at the Faculty of Mechanical and Automotive Engineering Technology, Universiti Malaysia Pahang. He is also a Visiting Faculty/Researcher at several universities in India, Russia and Vietnam. He obtained his Ph.D. from the National Institute of Technology, Tiruchirapalli, India in 2013. He is also serving as Associate Editor, *Frontiers in Energy Research* (Solar section) and Editorial Board of *Energy Engineering* (Scopus indexed). He has been actively involved in teaching and research in the area of renewable energy. His primary research areas include heat transfer in energy applications, exergy analysis, energy conservation, carbon sequestration, biofuel, solar thermal and PV systems, hybrid electric vehicle, energy modeling, food–water–energy nexus. He has published around 150 research papers in both SCI/Scopus indexed international journals and conference proceedings. He has authored more than ten technical books. He is a Certified Energy Manager and Auditor by Bureau of Energy Efficiency, Ministry of Power, Government of India. Dr. Kumarasamy is also recognized by the Stanford University database as the top 2% best scientists in the world.

Contributors

Abdul Manaf N. Department of Chemical and Environmental Engineering, Malaysia-Japan International Institute of Technology (MJIT), Universiti Teknologi Malaysia, Kuala Lumpur, Malaysia

Abdullah Arman Faculty of Chemical and Process Engineering Technology, Universiti Malaysia Pahang, Gambang, Kuantan, Pahang, Malaysia

Abdullah Haslina Faculty of Mechanical and Manufacturing Engineering, Universiti Tun Hussein Onn Malaysia, Batu Pahat, Johor, Malaysia

Abidin Ahmad Noor Syukri Zainal Malaysian Institute of Road Safety Research (MIROS), Kajang, Selangor, Malaysia;
Faculty of Manufacturing & Mechatronic Engineering Technology, University Malaysia Pahang (UMP), Pekan, Pahang, Malaysia

Ahmad Said Faculty of Mechanical and Manufacturing Engineering, Universiti Tun Hussein Onn Malaysia, Batu Pahat, Johor, Malaysia

Aiman M. H. Faculty of Mechanical and Automotive Engineering Technology, Universiti Malaysia Pahang, Pekan, Pahang, Malaysia

Aizzuddin A. M. College of Engineering, Universiti Malaysia Pahang, Pekan, Pahang Darul Makmur, Malaysia

Ajirun Mohd Rezan Hamji Centre for Advanced Industrial Technology, Universiti Malaysia Pahang, Pekan, Pahang, Malaysia;
Faculty of Mechanical and Automotive Engineering Technology, Universiti Malaysia Pahang, Pekan, Pahang, Malaysia

Ali Khairulafizal Sultan Faculty of Mechanical and Automotive Engineering Technology, Universiti Malaysia Pahang, Pekan, Pahang, Malaysia

Alias J. Department of Mechanical Engineering, College of Engineering, Universiti Malaysia Pahang, Gambang, Kuantan, Pahang, Malaysia;
Faculty of Mechanical and Automotive Engineering Technology, Universiti Malaysia Pahang, Pekan, Pahang, Malaysia

Asogan Arjun Centre of Excellence for Advanced Research in Fluid Flow (CARIFF), Universiti Malaysia Pahang, Pekan, Pahang, Malaysia

Awang N. W. Faculty of Mechanical and Automotive Engineering Technology, Universiti Malaysia Pahang, Pekan, Pahang, Malaysia;
Politeknik Sultan Mizan Zainal Abidin, Dungun, Terengganu, Malaysia;
College of Engineering, Universiti Malaysia Pahang, Gambang, Pahang, Malaysia

Aziz N. School of Chemical Engineering, Engineering Campus, Universiti Sains Malaysia, Seri Ampangan, Nibong Tebal, Seberang Perai Selatan, Penang, Malaysia

Azmi Arief Hakimi Malaysian Institute of Road Safety Research (MIROS), Kajang, Selangor, Malaysia

Wan Hamzah Wan Azmi Department of Mechanical Engineering, College of Engineering, Universiti Malaysia Pahang, Gambang, Kuantan, Pahang, Malaysia;
Centre of Excellence for Advanced Research in Fluid Flow, Gambang, Kuantan, Pahang, Malaysia;
College of Engineering, Universiti Malaysia Pahang, Gambang, Pahang, Malaysia;
Centre for Research in Advanced Fluid & Processes, Universiti Malaysia Pahang, Gambang, Kuantan, Pahang, Malaysia;
College of Engineering, Universiti Malaysia Pahang, Pekan, Pahang, Malaysia

Baharom Mohamad Zairi Faculty of Mechanical and Automotive Engineering Technology, Universiti Malaysia Pahang, Pekan, Pahang, Malaysia

Bakar Norliana Department of Civil Engineering, College of Engineering, Universiti Malaysia Pahang, Gambang, Pahang, Malaysia

Banius Euodia Faculty of Chemical and Process Engineering Technology, Universiti Malaysia Pahang, Gambang, Kuantan, Pahang, Malaysia

Bin Lum Wai Faculty of Chemical and Process Engineering Technology, Universiti Malaysia Pahang, Gambang, Kuantan, Pahang, Malaysia

Bo Zhang School of Mechanical Engineering, Ningxia University, Yinchuan, China

Chan Shiau Wei Faculty of Technology Management and Business, Universiti Tun Hussein Onn Malaysia, Batu Pahat, Johor, Malaysia

Che Jia Ling School of Civil and Hydraulic Engineering, Ningxia University, Ningxia, China

Chin Siew Choo Department of Civil Engineering, College of Engineering, Universiti Malaysia Pahang, Gambang, Pahang, Malaysia;
Centre for Research in Advanced Fluid and Processes (Fluid Centre), Universiti Malaysia Pahang, Gambang, Pahang, Malaysia

Doh Shu Ing Department of Civil Engineering, College of Engineering, Universiti Malaysia Pahang, Gambang, Pahang, Malaysia

Erdiwansyah Faculty of Engineering, Universitas Serambi Mekkah, Banda, Aceh, Indonesia

Faisal Muhammad Department of Mechanical Engineering, Universitas Abulyatama Aceh, Besar Aceh, Indonesia

Fanani Akhmad Rizal Universitas Widyagama, Kota Malang, Indonesia

Gani Asri Department of Chemical Engineering, Universitas Syiah Kuala, Banda Aceh, Indonesia

Ghazali Mohd Fairusham Centre for Research in Advanced Fluid & Processes, Universiti Malaysia Pahang, Gambang, Kuantan, Pahang, Malaysia

Halim Qayyum Faculty of Mechanical and Automotive Engineering Technology, Universiti Malaysia Pahang, Pekan, Pahang Darul Makmur, Malaysia

Haq Reazul Haq Abdul Faculty of Mechanical and Manufacturing Engineering, Universiti Tun Hussein Onn Malaysia, Batu Pahat, Johor, Malaysia;
Precision Manufacturing Research Center, UTHM, Batu Pahat, Johor, Malaysia

Hartono Budi Mechanical and Industrial Engineering Department, Gadjah Mada University, Yogyakarta, Indonesia

Harun Zawati Advanced Materials and Manufacturing Centre (AMMC), Faculty of Mechanical and Manufacturing Engineering, Universiti Tun Hussein Onn, Batu Pahat, Johor, Malaysia

Hassan Mohd Fahrul Faculty of Mechanical and Manufacturing Engineering, Universiti Tun Hussein Onn Malaysia, Batu Pahat, Johor, Malaysia

Hassan Mohd Hasnun Arif Faculty of Mechanical and Automotive Engineering Technology, Universiti Malaysia Pahang, Pekan, Pahang, Malaysia

Hisham Sakinah Faculty of Mechanical and Automotive Engineering Technology, Universiti Malaysia Pahang, Pekan, Pahang Darul Makmur, Malaysia;
Advanced Nano Coolant-Lubricant (ANCL) Lab, Automotive Engineering Centre, Universiti Malaysia Pahang, Pekan, Pahang, Malaysia

Hisham Syifak Izhar Faculty of Computing, Universiti Malaysia Pahang, Pekan, Pahang, Malaysia

Husin Husni Department of Chemical Engineering, Universitas Syiah Kuala, Banda Aceh, Indonesia

Ibrahim Haziqatulhanis Centre of Excellence for Advanced Research in Fluid Flow (CARIFF), Universiti Malaysia Pahang, Pekan, Pahang, Malaysia

Ishak M. Faculty of Mechanical and Automotive Engineering Technology, Universiti Malaysia Pahang, Pekan, Pahang, Malaysia

Ismail M. F. Department of Mechanical Engineering, College of Engineering, Universiti Malaysia Pahang, Gambang, Kuantan, Pahang, Malaysia;
Faculty of Mechanical and Manufacturing Engineering Technology, Universiti Teknikal Malaysia Melaka, Durian Tunggal, Melaka, Malaysia

Ismail Mohd Azmi School of Mechanical Engineering, Universiti Sains Malaysia Engineering Campus, Nibong Tebal, Penang, Malaysia

Ismail Nursya Mimie Ayuny Faculty of Mechanical and Automotive Engineering Technology, Universiti Malaysia Pahang, Pekan, Pahang, Malaysia

Jamaludin Ahmad Shahir Faculty of Manufacturing & Mechatronic Engineering Technology, University Malaysia Pahang (UMP), Pekan, Pahang, Malaysia

Johari Nasrul Hadi Faculty of Mechanical and Automotive Engineering Technology, Universiti Malaysia Pahang, Pekan, Pahang, Malaysia;
Centre for Advanced Industrial Technology, Universiti Malaysia Pahang, Pekan, Pahang, Malaysia

Kadrigama K. Faculty of Mechanical and Automotive Engineering Technology, Universiti Malaysia Pahang, Pekan, Pahang, Malaysia;
Advanced Nano Coolant-Lubricant (ANCL) Lab, Automotive Engineering Centre, Universiti Malaysia Pahang, Pekan, Pahang, Malaysia

Kamarulzaman Mohd Kamal Advanced Nano Coolant-Lubricant (ANCL) Lab, Automotive Engineering Centre, Universiti Malaysia Pahang, Pekan, Pahang Darul Makmur, Malaysia

Kamarulzaman N. Department of Chemical and Environmental Engineering, Malaysia-Japan International Institute of Technology (MJIT), Universiti Teknologi Malaysia, Kuala Lumpur, Malaysia

Karjanto Juffrizal Faculty of Mechanical Engineering, Universiti Teknikal Malaysia Melaka, Melaka, Malaysia

Kassim Khairil Anwar Abu Malaysian Institute of Road Safety Research (MIROS), Kajang, Selangor, Malaysia

Khalid Amir Faculty of Engineering Technology, Universiti Tun Hussein Onn Malaysia, Batu Pahat, Johor, Malaysia

Khoerunnisa Fitri Department of Chemistry, Faculty of Mathematics and Science, Indonesia University of Education, Bandung, Indonesia

Koh Qi Yun School of Mechanical Engineering, Universiti Teknologi Malaysia, Skudai, Malaysia;
Institute for Vehicle Systems and Engineering (IVESE), UTM, Skudai, Malaysia

Kok Y. H. Department of Chemical and Environmental Engineering, Malaysia-Japan International Institute of Technology (MJIT), Universiti Teknologi Malaysia, Kuala Lumpur, Malaysia

Krishnan Rishen Nair Centre of Excellence for Advanced Research in Fluid Flow (CARIFF), Universiti Malaysia Pahang, Pekan, Pahang, Malaysia

Mahidin Department of Chemical Engineering, Universitas Syiah Kuala, Banda, Aceh, Indonesia

Mahyuddin Department of Mechanical Engineering, Universitas Abulyatama Aceh, Besar, Aceh, Indonesia

Mamat Rizalman Centre for Research in Advanced Fluid & Processes, Universiti Malaysia Pahang, Gambang, Kuantan, Pahang, Malaysia;
School of Mechanical Engineering, Ningxia University, Yinchuan, China;
College of Engineering, Universiti Malaysia Pahang, Gambang, Malaysia;
College of Engineering, Universiti Malaysia Pahang, Pekan, Pahang, Malaysia

Manap Zulkifli Ahmad Faculty of Mechanical and Automotive Engineering Technology, Universiti Malaysia Pahang, Pekan, Pahang, Malaysia

Manshoor Bukhari Faculty of Mechanical and Manufacturing Engineering, University Tun Hussein Onn Malaysia, Parit Raja, Batu Pahat, Johor, Malaysia

Mohamed Nik Abdullah Nik Faculty of Mechanical and Automotive Engineering Technology, Universiti Malaysia Pahang, Pekan, Pahang Darul Makmur, Malaysia

Mohammad Nurul Jannah Mega Label (Malaysia) Sdn. Bhd, Shah Alam, Selangor, Malaysia

Mohd Amin At-Tasneem Faculty of Mechanical and Automotive Engineering Technology, Universiti Malaysia Pahang, Pekan, Pahang, Malaysia

Mohd Noor C. W. Faculty of Ocean Engineering Technology and Informatics, Universiti Malaysia Terengganu, Kuala, Terengganu, Malaysia

Mohd Shadzalli Z. F. Department of Chemical and Environmental Engineering, Malaysia-Japan International Institute of Technology (MJIT), Universiti Teknologi Malaysia, Kuala Lumpur, Malaysia

Mokhtarudin Mohd Jamil Mohamed College of Engineering, Universiti Malaysia Pahang, Gambang, Malaysia

Muhtadin Department of Mechanical Engineering, Universitas Abulyatama Aceh, Besar, Aceh, Indonesia

Naim Wan Naimah Wan Ab Faculty of Mechanical and Automotive Engineering Technology, Universiti Malaysia Pahang, Pekan, Pahang, Malaysia

Nugroho Agus School of Mechanical Engineering, Ningxia University, Yinchuan, China;
College of Engineering, Universiti Malaysia Pahang, Gambang, Pahang, Malaysia;
College of Engineering, Universiti Malaysia Pahang, Pekan, Pahang, Malaysia

Omar Mohd Nadzeri Faculty of Mechanical and Automotive Engineering Technology, Universiti Malaysia Pahang, Pekan, Pahang, Malaysia;
Centre for Advanced Industrial Technology, Universiti Malaysia Pahang, Pekan, Pahang, Malaysia

Payne Stephen Institute of Applied Mechanics, National Taiwan University, Taipei, Taiwan

Priyandono Gigih Universitas Widyagama, Kota Malang, Indonesia

Quazi M. M. Faculty of Mechanical and Automotive Engineering Technology, Universiti Malaysia Pahang, Pekan, Pahang, Malaysia

Rahman Mohd Nasrull Abdol Faculty of Mechanical and Manufacturing Engineering, Universiti Tun Hussein Onn Malaysia, Batu Pahat, Johor, Malaysia

Rajoo Srithar School of Mechanical Engineering, Universiti Teknologi Malaysia, Skudai, Malaysia;
Institute for Vehicle Systems and Engineering (IVESE), UTM, Skudai, Malaysia

Ramasamy D. Advanced Nano Coolant-Lubricant (ANCL) Lab, Automotive Engineering Centre, Universiti Malaysia Pahang, Pekan, Pahang, Malaysia;
College of Engineering, Universiti Malaysia Pahang, Gambang, Pahang, Malaysia

Razali Mohd Nizar Mhd Faculty of Manufacturing & Mechatronic Engineering Technology, University Malaysia Pahang (UMP), Pekan, Pahang, Malaysia

Rejab Mohd Ruzaimi Mat Faculty of Mechanical and Automotive Engineering Technology, Universiti Malaysia Pahang, Pekan, Pahang Darul Makmur, Malaysia

Rohani Jafri Mohd School of Mechanical Engineering, Faculty of Engineering, Universiti Teknologi Malaysia, Johor, Malaysia

Rohman F. S. School of Chemical Engineering, Engineering Campus, Universiti Sains Malaysia, Seri Ampangan, Nibong Tebal, Seberang Perai Selatan, Penang, Malaysia;

Department of Chemical Engineering, Universitas Brawijaya, Malang, Indonesia

Rosdi S. M. Politeknik Sultan Mizan Zainal Abidin, Dungun, Terengganu, Malaysia

Sakinah S. Z. A. Department of Mechanical Engineering, College of Engineering, Universiti Malaysia Pahang, Gambang, Kuantan, Pahang, Malaysia;
Centre of Excellence for Advanced Research in Fluid Flow, Gambang, Kuantan, Pahang, Malaysia

Salleh Wan Norharyati Wan Advanced Membrane Technology Research Centre (AMTEC), School of Chemical and Energy, Faculty of Engineering, Universiti Teknologi Malaysia, Skudai, Johor Bahru, Johor, Malaysia

Samykan M. College of Engineering, Universiti Malaysia Pahang, Gambang, Pahang, Malaysia

Saptaji Kushendarsyah Sampoerna University, Jakarta, Indonesia

Sarjono R. E. Department of Chemistry, Faculty of Mathematics and Science, Indonesia University of Education, Bandung, Indonesia

Sazali Norazlianie Centre of Excellence for Advanced Research in Fluid Flow (CARIFF), Universiti Malaysia Pahang, Pekan, Pahang, Malaysia

Sazali Norsuhailizah Advanced Materials and Manufacturing Centre (AMMC), Faculty of Mechanical and Manufacturing Engineering, Universiti Tun Hussein Onn, Batu Pahat, Johor, Malaysia

Shabudin Abbas College of Engineering, Universiti Malaysia Pahang, Gambang, Malaysia

Shah Ku Nur Afrina Ku Azman School of Mechanical Engineering, Faculty of Engineering, Universiti Teknologi Malaysia, Johor, Malaysia

Sofian Azizul Helmi Faculty of Chemical and Process Engineering Technology, Universiti Malaysia Pahang, Gambang, Kuantan, Pahang, Malaysia

Suhaidin Siti Nursuhailah Md Centre of Excellence for Advanced Research in Fluid Flow (CARIFF), Universiti Malaysia Pahang, Pekan, Pahang, Malaysia

Suwandono Purbo Universitas Widyagama, Kota Malang, Indonesia

Tang Mun Lin Department of Civil Engineering, College of Engineering, Universiti Malaysia Pahang, Gambang, Pahang, Malaysia

Tuyen Nguyen Duc School of Electrical Engineering, Hanoi University of Science and Technology, Hanoi, Vietnam

Wong Kuan Yew School of Mechanical Engineering, Universiti Teknologi Malaysia, Skudai, Malaysia;
Institute for Vehicle Systems and Engineering (IVESE), UTM, Skudai, Malaysia

Yusaf Talal School of Engineering and Technology, Central Queensland University, Rockhampton, Australia

Yusop Mohd Zamri Mohd School of Mechanical Engineering, Faculty of Engineering, Universiti Teknologi Malaysia, Johor, Malaysia

Zahan K. A. Department of Systems Science, Graduate School of Informatics, Kyoto University, Kyoto, Japan;
Faculty of Engineering Technology, Universiti Tun Hussein Onn Malaysia, Batu Pahat, Johor, Malaysia

Zahari Nur Ezzatul Balqis Binti Mohd Centre of Excellence for Advanced Research in Fluid Flow (CARIFF), Universiti Malaysia Pahang, Pekan, Pahang, Malaysia

Zaman Izzuddin Mechanical Failure Prevention and Reliability Research Centre, Universiti Tun Hussein Onn Malaysia, Batu Pahat, Johor, Malaysia

Zu Nicolas Ng Yang Faculty of Mechanical and Manufacturing Engineering, Universiti Tun Hussein Onn Malaysia, Batu Pahat, Johor, Malaysia

Zul M. H. Faculty of Mechanical and Automotive Engineering Technology, Universiti Malaysia Pahang, Pekan, Pahang, Malaysia

Prospects of Energy Recovery in Offshore Oil and Gas Operations



Qi Yun Koh, Srithar Rajoo, and Kuan Yew Wong

Abstract Offshore oil and gas platforms are one of the energy industries that generate huge amount of waste heat and CO₂ emission that cause environmental impacts. This paper performed an investigation on the potential source of waste heat on the offshore oil and gas operation. Brief explanation on the standard operating strategy of the offshore platform was given and the processes that released huge amount of recoverable waste were emphasized. The waste heat recovery (WHR) is a method of capturing and transferring the waste heat from a process with gas or liquid to the system as an additional energy source. Technologies that were utilized by previous researchers were reviewed and the future direction on the waste heat recovery of offshore operation was described. The oil extraction and processing platform which is also known as the “Central Power Platform” was discovered to be the main source of waste heat and the processes involved were the potential candidates for waste heat recovery. Although there have been studies utilizing different technologies on the waste heat recovery of offshore oil and gas sector, more improvement could be made in the future to the efficiency of the power system by applying other WHR technologies such as turbo compound or combination of several WHR technologies to recover more waste heat, hence reducing environmental impacts.

Keywords Oil and gas · Waste heat recovery · Offshore platform

1 Introduction

A country’s long-term economic growth critically depends on a safe and reliable energy supply. Nevertheless, environmental issues such as air pollution, ozone layer depletion and climate changes are continuing to happen nowadays due to non-stop industrialization that leads to increase in the global consumption and the growing of

Q. Y. Koh (✉) · S. Rajoo · K. Y. Wong
School of Mechanical Engineering, Universiti Teknologi Malaysia, 81310 Skudai, Malaysia
e-mail: qiyoungkoh@utm.my

Institute for Vehicle Systems and Engineering (IVESE), UTM, Skudai, Malaysia

© The Author(s), under exclusive license to Springer Nature Singapore Pte Ltd. 2023
N. H. Johari et al. (eds.), *Proceedings of the 2nd Energy Security and Chemical Engineering Congress*, Lecture Notes in Mechanical Engineering,
https://doi.org/10.1007/978-981-19-4425-3_1

CO₂ concentration level. According to the forecast made by the experts, if the CO₂ concentration level continue to increase from 440 to 450 ppm, the global temperature will raise by 2 °C and the environmental problems will becoming more serious [1]. Without new policies to confine the energy consumption, the CO₂ emission produced by the energy industries will continue to grow at a rate of 130% by 2050 [2]. Hence, actions should be taken to reduce the Greenhouse Gases (GHG) or CO₂ concentration to an acceptable level.

There are several energy industries that contribute to these global problems and offshore oil and gas platform is one of the major contributors. Nguyen et al. [3] had stated that in 2011, the total GHG emissions of Norway coming from the oil and gas extraction sector reached 26% which is quite a big portion from the overall emission. Besides, 55 and 39% from the overall CO₂ emission in Malaysia in 2015 and 2020 respectively are related to energy industries as stated in the Malaysia Biennial Update Report to the United Nations Framework Convention on Climate Change (UNFCCC) [4]. Although there is a clear dropping of CO₂ emission coming from the energy industries, effort still needs to be made to reduce it further for mitigating climate change impacts. The offshore oil platform is also one of the energy industries that generates large quantity of waste heat to the atmosphere which contributes to a significant amount of carbon dioxide.

Recently, as the environmental awareness has increased, more attention has been paid to reduce the GHG emissions and energy demand for offshore oil platform. Since 2013, the National Corporate GHG had launched the carbon and Environmental Reporting Program in Malaysia which targeted to minimize the emission by stimulating private companies to measure and disclose their GHG emissions so that actions could be made wisely. Thus, from the economic and environmental aspects, improving the performance and efficiency of power systems in offshore oil and gas sectors have become an area of focus. There are several studies conducted to discover techniques to enhance the power generation efficiency by utilizing the potential and accessible source of waste heat energy. This paper discussed the main areas or processes to be focused as the potential sources of energy recovery on the offshore oil and gas operation and the future direction of the WHR in this field. The basic operating manner of an existing offshore oil and gas platform and type of waste heat produced are explained in the sections below.

2 Overview of Offshore Oil and Gas Platform

An oil and gas platform usually works by firstly extracting petroleum from a reservoir, then the gas, water and oil phases will be separated. The oil will be treated to the saleable product specifications before exporting it onshore, the gas will be purified for injection, export or lift uses and the water will be cleaned before discharged into the sea or reinjection into the reservoir [5]. In a standard offshore oil project, it usually comprises four offshore platforms. These are the oil extraction and processing platform, the oil storage platform, the support and maintenance platform and the

mooring platform. The oil extraction and processing platform or it is also called the central power platform as it provides power for others through sea cables [6]. In the oil extraction and processing platform, there are processing plant that purifies and separates raw gases into different chemicals and other processes that support the operation of the platform as shown Fig. 1. The power and heat generation and other utilities systems are named as Auxiliary systems [5]. In the processing plant, there are several stages in oil and gas extraction such as production separation, CO₂ removal system, flare system, sales gas compression.

All these stages produce waste heat that could be recovered as energy instead of wasting to the environment. According to the Malaysia Energy Statistics Handbook 2018 prepared by the Energy Commission [7], from 2005 to 2016, the natural gas is concluded to be the primary energy supply in Malaysia, followed by crude oil and petroleum as shown in Fig. 2. According to this statistic, the offshore oil and gas platform can be seen to play a vital role in Malaysia to generate and provide energy to different sectors or people. Nevertheless, with the increase of energy demands

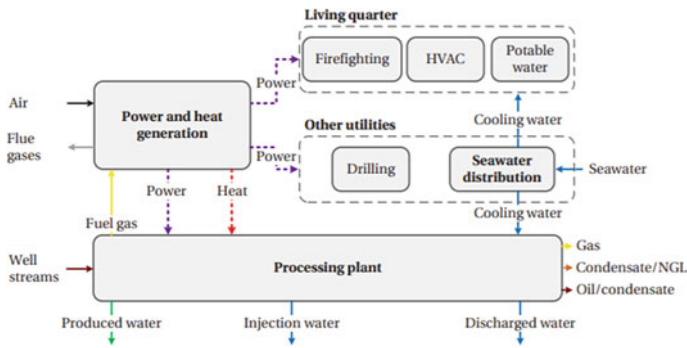


Fig. 1 Overview of a typical oil and gas extraction and processing platform [5]

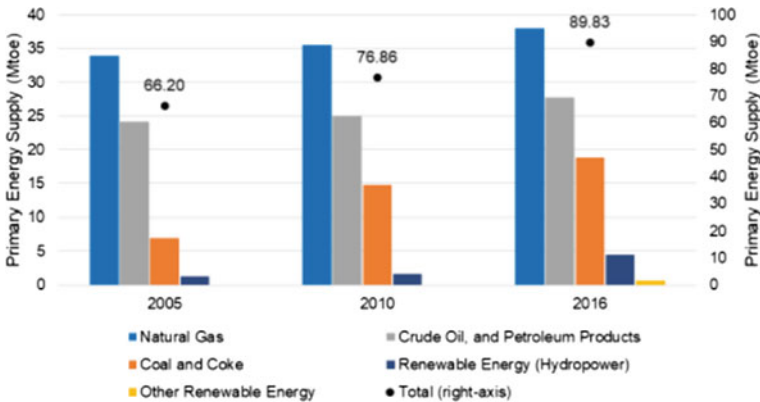


Fig. 2 Primary energy supply breakdown for 2005, 2010 and 2016 in Malaysia [7]

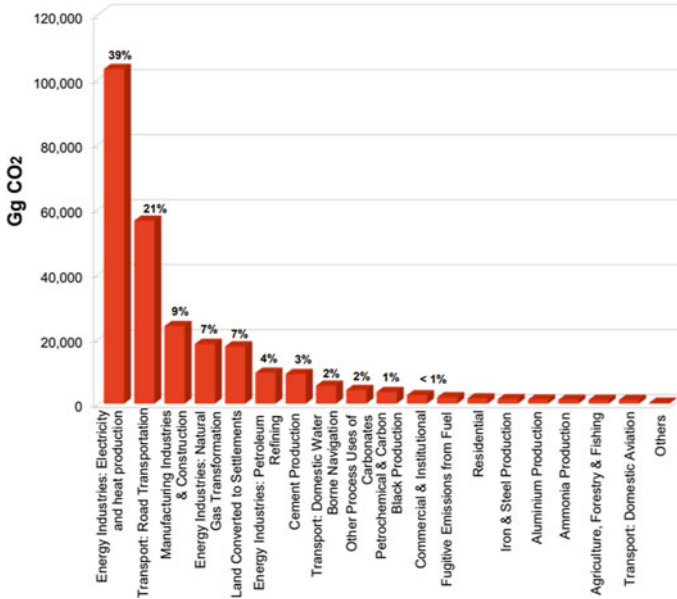


Fig. 3 Major sources of carbon dioxide emission in Malaysia in 2016 [8]

and global consumption, this has caused many environmental issues. Ministry of Environment and Water Malaysia had stated in the Malaysia Biennial Update Report to the UNFCCC 2020 that the energy industries had contribute to the most CO₂ emission in 2016 with a total of 39% of the overall emission and this amount of CO₂ emission comes from the waste heat released by combustion of fuel as shown in Fig. 3 [8].

Offshore oil and gas platforms are considered as one of the energy industries that produce huge amount of heat. Therefore, to resolve the environmental problems, one of the methods could be reducing and recovering waste heat produced in the offshore application.

3 Waste Heat

Waste heat is the energy that is produced in-process, and it has not been utilized wisely and is simply dumped and dissipated into the environment. In majority of the literature, waste heat is also being mentioned as secondary heat [9] and as more general inefficiencies or conversion losses. The waste heat is normally created when there are losses of heat transferred via convection, radiation and conduction from processes, products and machinery. Besides, it can also be heat discharged from combustion processes. There are several types of waste heat too which include low, medium and high temperature grades. According to a survey conducted by Colonna,

high temperature waste heat is with temperature higher than 400 °C, medium temperature waste heat is 100–400 °C and low temperature waste heat is less than 100 °C and energy capacity may range from small to large values which are 3 MW–15 kW [10]. Using the heat generated from one end to the other end to reduce the net-work input of the system is not considered as waste heat. Waste heat should be the heat wasted or released to the atmosphere, which could cause environmental problems.

4 Waste Heat Recovery

The waste heat recovery (WHR) system is a method of capturing and transferring the waste heat from a process with gas or liquid to the system as an additional energy source. Additional heat can be created, or electrical and mechanical power can be generated with the energy source obtained. Waste heat can be released to the environment at any temperature, typically, the optimization of WHR process will be easier with high temperature waste heat, the easier the optimization of WHR process. Therefore, it is crucial to investigate the highest potential amount of recoverable heat from a process to obtain the maximum efficiency of WHR system [11].

5 Prospects

Normally, there will be on-site generators to supply and provide electrical power to the offshore oil and gas facilities. Additionally, compression machines will be operated by high powered gas turbines which is important for extraction and transportation of oil and gas. With all the machines stated above, large amount of waste heat will be generated and most of them are wasted into the environment. Only part of it has been utilized inside the internal process of the platform. Moreover, on a standard operated offshore platform, there will be three engines needed for it to work smoothly. Two engines will operate by sharing the loads and the other one will be on stand-by or maintenance mode. The two gas turbines of the machines will be running in low loads to lower the risk of system failure which lead to high economic loss. Nonetheless, with this type of strategy, the system performance will reduce seriously and generate even more waste heat to the environment [11]. As a result, the potential for energy recovery on the offshore platform will be its power system as it is the major contributor of overall emissions and major source of energy wastage.

From all the platforms in an offshore oil and gas project, the oil exploitation and processing, the central processing and power platform could be the focus to potentially recover waste heat. As this platform generates power and supply to all the other platform, it could be the primary source of waste heat for an offshore oil and gas project. In the oil extraction and processing platform, there are processing plant that purifies and separates raw gases into different chemicals and other processes that support the operation of the platform. The power and heat generation and other

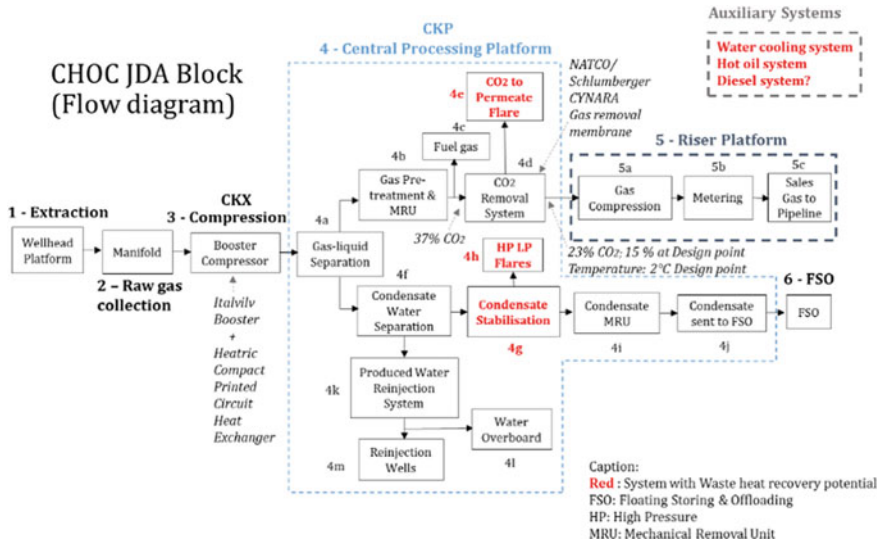


Fig. 4 Flow diagram of the Malaysia-Thailand Joint Authority Carigali Hess operating company production facility

utilities systems are named as Auxiliary systems. In the processing plant, there are several stages on oil and gas extraction and all the stages could be a potential for WHR. By taking the Cakerawala offshore platform located approximately 150 km northeast of Kota Bahru, Kelantan as an example, the process flow diagram of Carigali Hess Operating Company is presented in Fig. 4.

6 Future Research

The best way to reduce the waste heat produced by the offshore oil and gas operation is by recovering the waste heat with WHR technologies. Several previous studies had been carried out on the application of WHR technologies for the offshore platform. Kolahi et al. [12] has carried out a comparative analysis on simple Organic Rankine Cycles (ORCs) and ORCs with Internal Heat Exchanger (IHE) as the WHR system for the 425 °C high temperature waste heat of large diesel engines using pure and zeotropic mixtures in phase 12 of South Pars Gas on Persian Gulf offshore platform. The analysis was carried out by choosing the arrangement of ORCs and working fluid for the best exergy efficiency, energy efficiency, specific investment cost and payback period. The results showed that both the ORC with IHE thermal and exergy efficiencies are higher when compared to the simple ORC with working fluid R236ea/Cyclohexane (0.6/0.4). By adding IHE, the energy efficiency is increased from 14.57% to 16.81%. In terms of economic aspect, ORC with IHE also have better results.

Furthermore, Pierobon et al. [10] also aimed to find the most suitable WHR technology that can be used on the Draugen offshore oil and gas platform power system to recover the medium temperature waste heat produced at 379 °C by the Siemens SGT500 twin-spool gas turbine. Comparison analysis was conducted among three technologies which are single pressure Steam Rankine Cycle (SRC), Air Bottoming Cycle (ABC) without intercooler and ORC. Multi-objective optimization based on genetic algorithm was used to investigate the best system designs for each of the technologies. The results showed that ABC units are not convenient for the offshore platform from the performance and economic aspects. ORC and SRC are competing when aiming to have a highly efficient offshore platform, although the investment cost must be lower to have better economic return. However, in terms of system performance and applicability range, combination of ORC with turbo generators is the best but with the same disadvantage of low economic return.

Moreover, Walnum et al. [13] also found that transcritical CO₂ power cycle could be suitable for the WHR system of the Norwegian Continental Shelf offshore oil and gas platform. A double stage transcritical CO₂ cycle system and a single stage recuperated simple transcritical cycle are analyzed with topping cycle of the G4 DLE + GE LM2500 gas turbine having high temperature waste heat of 532 °C. With the transcritical CO₂ cycle with recuperator, the energy efficiency and the net power output of the plant were improved by 27.6% and 10.6% respectively. For the double stage transcritical CO₂ cycle, it can further enhance outputs when compared with the single stage system.

From all the previous studies, ORC, SRC, ABC and transcritical CO₂ power cycle had been utilized on the offshore oil and gas operation as WHR system. However, they were just analysis and were not put into practical use on the offshore oil and gas operation. Besides, many other WHR technologies have not been analyzed for this application. Aghaali and Ångström [14] have stated that the internal combustion engine coupled with turbo compound can recover up to two-thirds of waste and thermoelectric generator (TEG) is also a good WHR technology in some of the applications. Moreover, Pierobon et al. [11] also showed that with the combination of ORC and turbo generator, the system performance could be greatly improved. Therefore, more studies could be made in the future on the application of other WHR technologies or combination of WHR technologies on the power system of offshore oil and gas sector which could further improve the efficiency of the power system and recover more waste heat.

7 Conclusions

Offshore oil and gas sectors are one of the energy industries that generate huge amount of waste heat and CO₂ emission to the environment through power generation process which happened in the oil production and processing platform. Processing plant and other processes which include the power and heat generation, and other utilities systems are named as Auxiliary systems, and they support the operation of the

oil extraction and processing platform. Processes involved in the central processing platform can be the potential sources of energy recovery. Although there have been studies conducted utilizing different technologies on the WHR of offshore oil and gas operation, more improvement could be made in the future to the efficiency of the power system with other WHR technologies or combination of WHR technologies to recover more waste heat released by the offshore oil and gas platform.

Acknowledgements The authors are grateful to Malaysia-Thailand Joint Authority (MTJA), UTM LoCARtic and IVESE UTM for supporting in publishing this work.

References

1. Omara A, Saghaififar M, Mohammadi K, Alashkar A, Gadalla M (2018) A review of unconventional bottoming cycles for waste heat recovery: part II—applications. *Energy Convers Manage* 180(1):559–583
2. Oh TH (2010) Carbon capture and storage potential in coal-fired plant in Malaysia—a review. *Renew Sustain Energy Rev* 14(9):2697–2709
3. Nguyen T-V, Pierobon L, Elmegaard B, Haglind F, Breuhaus P, Voldsund M (2013) Exergetic assessment of energy systems on north sea oil and gas platforms. *Energy* 62(1):23–36
4. Malaysia Biennail Update Report to the UNFCCC (2016) Ministry of Environment and Water Malaysia, Putrajaya
5. Nguyen T-V, Elmegaard B, Breuhaus P, Haglind F (2014) Modelling, analysis and optimisation of energy systems on offshore platforms, Phd thesis, Technical University of Denmark
6. Zhang A, Zhang H, Qadrdan M, Yang W, Jin X (2019) Optimal planning of integrated energy systems for offshore oil extraction and processing platforms. *Energies* 12(4):756
7. Malaysia Energy Statistics Handbook 2018 (2019) Energy Commission, Putrajaya
8. Malaysia Biennail Update Report to the UNFCCC 2020 (2020) Ministry of Environment and Water Malaysia, Putrajaya
9. Hnat JG, Coles WF (1985) A feasibility assessment of cogeneration from a regenerative glass furnace. *IEEE Trans Ind Appl IA-21(4)*:1064–1069
10. Pierobon L, Nguyen T-V, Larsen U, Haglind F, Elmegaard B (2013) Multi-objective optimization of organic Rankine cycles for waste heat recovery: application in an offshore platform. *Energy* 58(1):538–549
11. Pierobon L, Benato A, Scolari E, Haglind F, Stoppato A (2014) Waste heat recovery technologies for offshore platforms. *Appl Energy* 136(1):228–241
12. Kolahi M, Yari M, Mahmoudi SMS, Mohammadkhani F (2016) Thermodynamic and economic performance improvement of ORCs through using zeotropic mixtures: case of waste heat recovery in an offshore platform. *Case Stud Thermal Eng* 8:51–70
13. Walnum HT, Neksa P, Nord LO, Andresen T (2013) Modelling and simulation of carbon dioxide bottoming cycles for offshore oil and gas installations at design and off-design conditions. *Energy* 59:513–520
14. Aghaali H, Ångström H-E (2015) A review of turbo compounding as a waste heat recovery system for internal combustion engines. *Renew Sustain Energy Rev* 49(1):813–824

An Overview of Organic Rankine Cycle for Waste Heat Recovery on Offshore Oil and Gas Platform



Qi Yun Koh, Srithar Rajoo, and Kuan Yew Wong

Abstract Researchers have analyzed Organic Rankine Cycle (ORC) recently on its potential for waste heat recovery (WHR) on offshore oil and gas platform. However, there is still no practical application of ORC on this sector currently. An extensive overview of the ORC for offshore oil and gas platform has been performed in this paper. The discussion investigates the capability of this technology as the WHR for offshore oil and gas platform application. In this study, a brief explanation of the process that happened on the offshore platform which is the potential source of waste heat to be recovered will be given. The studies conducted by previous researcher on the offshore application were reviewed and the benefits of ORC were emphasized and some information on the configuration of the ORC on offshore oil and gas platform were described. ORC was found to be able to adapt to low or medium grade which is between 150–400 °C heat source with different type of configurations. The flexibility of ORC makes it easier to be used on offshore oil and gas platform with different configuration and contribute to many advantages. The electricity generated can increased up to 20.3%, 11.3% increase in the overall system efficiency and 18.3% in the utilization factor. Furthermore, an average reduction of 22% in the fuel consumption and CO₂ emissions could be achieved over the platform operating years. Dry and isentropic fluids are more suitable to be the working fluid of ORC system on offshore application which could lead to better system performance and efficiency. Cyclopentane had been widely used as it is thermally stable in the temperature range between 220 and 350 °C. From the economic aspects, although involving ORC could increase the initial investment cost up to 46%, it also increases the net present value, leading to a discount rate up to 10%.

Keywords Oil and gas · Waste heat recovery · Offshore platform · Organic Rankine cycle

Q. Y. Koh (✉) · S. Rajoo · K. Y. Wong

School of Mechanical Engineering, Universiti Teknologi Malaysia, 81310 Skudai, Malaysia
e-mail: qiyunkoh@utm.my

Institute for Vehicle Systems and Engineering (IVESE), UTM, Skudai, Malaysia

© The Author(s), under exclusive license to Springer Nature Singapore Pte Ltd. 2023
N. H. Johari et al. (eds.), *Proceedings of the 2nd Energy Security and Chemical Engineering Congress*, Lecture Notes in Mechanical Engineering,
https://doi.org/10.1007/978-981-19-4425-3_2

1 Introduction

Recently, the environmental awareness has been on the rise, hence more attention is given to the serious environmental issues, especially due to the fossil fuel usage. The issues are mainly due to the rapid industrialization over many decades that leads to the growth of global consumption and CO₂ concentration level. The CO₂ concentration level now had reached 440 ppm and as forecasted, the global temperature will rise by 2 °C if the level continues to increase and achieves 450 ppm [1]. According to Nguyen et al. [2], the oil and gas facilities in Norway had contribute 26% from the total greenhouse gas emission in 2011. Furthermore, in Malaysia, 55% from the overall CO₂ emission came from the energy industries in 2015 [3]. Although the CO₂ emission had reduced to a percentage of 39% in 2020 [4], energy industries are still the biggest contributor and oil and gas exploitation sector is one of the energy industries which release vast amount of waste heat and carbon dioxide to the atmosphere.

Oh [5] had predicted that the CO₂ emission released by the energy industries will increase in a rate of 130% by 2050 if there is no actions or policies identified to control these problems. Therefore, in Malaysia, the National Corporate Greenhouse gas had launched a program called the carbon and Environmental Reporting Program to resolve this problem by promoting private enterprises to report their Greenhouse Gases (GHG) emissions for proper actions identification could be made. Hence, this has made the boosting of power system's efficiency and performance to be a focus area in the offshore application. Several numbers of studies have been carried out by researchers to find out methods to enhance the performance of power generation by making use of the potential source of wasted energy. WHR system is one of the methods used and Organic Rankine cycle (ORC) had been widely used recently in many sectors, but there is no practical case on offshore oil and gas operation. Therefore, this paper provides an overview of the ORC for the WHR on the offshore oil and gas operation to investigate the capability of this technology for future offshore application. In the first few sections of the paper, an overview of offshore oil and gas platform, waste heat and the ORC were explained. Furthermore, previous studies on the utilizing of ORC as the WHR in the offshore application were reviewed with analysis.

2 Overview of Offshore Oil and Gas Platform

An oil and gas platform work on a purpose to extract petroleum from reservoir and separate it into water, gas and oil phases. The oil and gas will be treated and purified respectively before exporting it onshore while the water will be cleaned and released back to the sea [6]. A typical offshore oil project normally consists of four offshore platform which include the oil extraction and processing platform, the mooring platform, the support and maintenance platform and the oil storage platform.

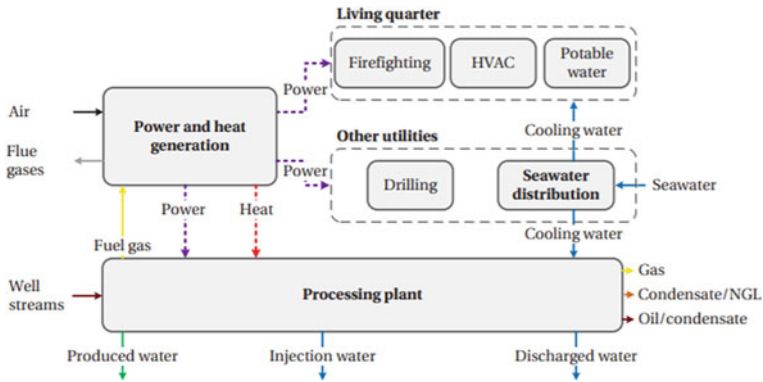


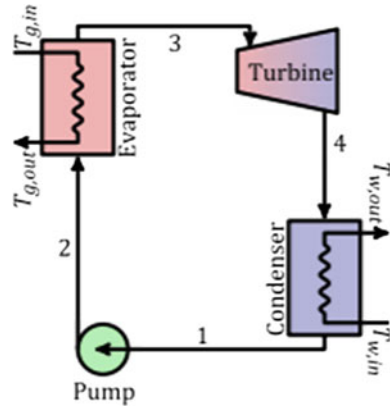
Fig. 1 Overview of a standard oil and gas extraction and processing platform [6]

Among all the platform, one of the platforms provide power supply to all the other platform via sea cables which is the oil exploitation and processing platform or it is also known as the central power platform [7]. As shown in Fig. 1, there are several systems inside the oil and gas extraction platform. The processing plant is a process where purification and separation of raw gases happened while the Auxiliary system comprises the power and heat generation and other utilities [6]. Several stages and processes are included for the oil and gas extraction in the processing plant such as production separation, CO₂ removal system, flare system, sales gas compression, etc. Due to the oil extraction and processing platform supplies power for all the platform, it is the focus to potentially recover waste heat.

3 Waste Heat

Waste heat is energy generated in process and it is simply dumped or wasted into the atmosphere without making good use of it. From the previous studies, some of them mentioned waste heat as the secondary heat [8] and as general inefficiencies or conversion losses as well. Heat loss transferred through radiation, conduction and convection from process, product or equipment are typically the sources of waste heat. Furthermore, the heat discharged from the combustion process is cause of producing waste heat to the environment. Waste heat can be categorized into three groups, which are the low grade, medium grade and high-grade heat. The high grade heat is heat with temperature higher than 400 °C, medium grade heat is between 100–400 °C and low grade heat is less than 100 °C and power capacity could be around 15 MW–3 kW which is scale from large to small [9]. Waste heat should be heat or energy wasted or dissipated to the environment, but not using it from one end to the other end to reduce the net-work input of the system.

Fig. 2 Simple organic Rankine cycle [10]



4 Organic Rankine Cycle

As presented in Fig. 2, a typical Rankine cycle is made up of a condenser, a turbine, a pump and an evaporator. The working principle of a Rankine cycle is first having fuel to burn in the evaporator which makes the working fluid performing phase changes from liquid phase into superheated vapor phase. The power is produced with the turbine by directing the working fluid in superheated vapor state into it. Then, at the turbine outlet, the fluid will flow to the condenser, and it will undergo the process of losing the heat and change back into liquid form. Lastly, the fluid is pumped into the evaporator again and the cycle repeats. To generate electrical power instead of mechanical power, a generator is connected to the turbine's shaft. There are several types of Rankine cycle, such as Steam Rankine Cycle (SRC), ORC, Rankine cycle with Internal Heat Exchanger (IHE) and many more. Looking at the ORC, it has the same working principle and system layout as a simple Rankine cycle but with organic substance with low boiling points and high vapor pressures as the working fluid to generate power instead of water or steam [10].

5 ORC Application for the Waste Heat Recovery on Offshore Oil and Gas Platform

There are several previous studies related to this subject. Kolahi et al. [11] has conducted a comparative analysis on ORC with IHE and simple ORC as the WHR system for the 425 °C high grade heat of large diesel engines using pure and zeotropic mixtures in phase 12 of South Pars Gas on Persian Gulf offshore platform. Results showed that in term of economic and thermodynamic aspect, ORC with IHE has better results than the simple ORC. Both the energy and exergy efficiencies of the

ORC with IHE are higher with working fluid R236ea/Cyclohexane (0.6/0.4). The energy efficiency is increased from 14.57 to 16.81% with IHE included.

Moreover, on power system of the Draugen offshore oil and gas platform, the most suitable WHR unit to recover the medium temperature waste heat produced at 379 °C by the Siemens SGT500 twin-spool gas turbine was done by Pierobon et al. [9]. Three technologies which are ORC, single pressure SRC and air bottoming cycle (ABC) were compared and optimized using the multi-objective genetic algorithm (MOGA) to discover the optimal system designs. It was found that ABC units are not suitable for the offshore platform from the economic and performance aspects. ORC and SRC are appropriate to be used when a highly efficient offshore platform are desired, but the cost needs to be lower for better economic return. From the aspect of applicability range and system performance, the combination of ORC with turbo generators stands out but with poor economic return too.

Besides the Draugen offshore oil and gas platform, ORC had been utilized on a Brazilian floating oil platform by Barrera et al. [12] to conduct an exergetic analysis related to 2nd law of thermodynamic. The working fluid selected was Cyclopentane and ORC with optimal configuration was discovered according to the vapor saturation curve. The results showed that the exhaust gas exergy could be considered to improve the output power and ORC can save the fuel consumption up to 15–20%. Apart from that, the basic and recuperated ORCs were analyzed by Khatita et al. [13] which aim to apply a WHR system on an existing oil and gas facilities in Egypt. The reaction of decision parameters to the systems efficiency and net output power were investigated by conducting simulation with several working fluids. The results shown that an ORC with recuperator with either cyclohexane or benzene as working fluids are the best choice for the current case.

Furthermore, Bhargava et al. [14] also conducted an overall investigation of ORC with different types of gas turbines that are normally used by offshore platform with different power ratings as the bottoming cycle for WHR. Thermal connections with the presence or absence of secondary heat transfer fluid between the ORC and gas turbine exhaust gas are both considered in this analysis. Dowtherm-A was used as the thermal fluid while cyclopentane used as the ORC working fluid. The results shown that although having secondary thermal fluid had several feasible advantages than the direct evaporation, it led to poor thermodynamic performance. Evely et al. [15] had proposed and analyzed a cogeneration system which targeted to produce heat, power and clean water from the waste heat released from a Persian Gulf offshore sector. A reverse osmosis desalination system applied in the ORC was used in their research to recover the heat content of the exhaust gas. Additionally, heat dissipated from the process of condensation in ORC was utilized in the process of heating. The results showed that by using working fluid Octamethyltrisiloxane for the ORC, the cogeneration system boosted the exergetic efficiency of gas turbine by 6%.

Apart from that, Reis et al. [16] had developed an off-design model to check the viability of ORC under different operating conditions when aiming to maximize the energy recovery of exhaust gas from the General Electric LM 2500 gas turbine in an offshore oil and gas platform. Simple ORC and regenerative ORC had been utilized in the system to conduct a comparative analysis. Medium grade heat source

with temperature of 329.6 and 299.2 °C were one of the design conditions used on the simple ORC and regenerative ORC respectively. Energy, exergy and economic analysis was made, and the results showed that with simple ORC applied to the gas turbine, the electricity generated can increased up to 19, 5.2% increase in the overall system efficiency and 17.3% in the utilization factor. Furthermore, an average reduction of 23% in the fuel consumption and CO₂ emissions could be achieved over the platform operating years. For the regenerative ORC, up to 20.3% increase of electricity generation, 26% in the overall system efficiency and 18.3% in the utilization factor. For both simple and regenerative ORC, the heat recovery devices contribute up to 68.0% of the destroyed exergy. For the economic analysis, the total initial investment cost increased due to the involvement of ORC, but with a much higher net present value produced, a discount rate up to 10.0%.

6 Analysis

According to the previous studies, there are several types of ORC system that were used and analyzed on the offshore oil and gas operation from different countries, but they were not put into practical use for the WHR system. By considering the thermodynamic performance of the central power system, a boost on the efficiency is achievable through enhancing the performance of the processing plant and the efficiency of the Auxiliary system [17]. ORC has the advantages of low operating pressure, low maintenance cost and can be adapted to low or medium grade heat source which is between 150–400 °C with different type of configurations. Furthermore, due to the variety choices of organic working fluids have provided ORC system more flexibility in the application of offshore oil and gas platform. The available heat source and the platform size are two main components that decides the best working fluid that suits the ORC in offshore application. Working fluid with good thermal stability results in higher performance and better turbomachinery efficiency [12]. Based on the studies conducted by researchers, dry and isentropic fluids are more suitable to be the working fluid of ORC system to prevent the presence of liquid droplets that could damage the turbo expander [13]. Cyclopentane had been utilized as the working fluid of ORC in most of the previous studies when taking into account of different aspect such as thermal efficiency and volume of ORC component. This working fluid has a good thermal stability in temperature range between 220 and 350 °C [9, 18, 19], which is quite suitable for the application of WHR on offshore oil and gas platform.

Furthermore, the parameters of the ORC systems must be in their optimal condition to enhance the performance and efficiency. The ORC turbine inlet temperature and pressure has found out to be the most effective parameters on the net power output, energy and exergy efficiency and the costs too [9, 20]. When the pressure and temperature at the turbine inlet increased, the net power output increased. By using Cyclopentane as the working fluid, the optimum turbine inlet temperature was found to be around 320 °C to obtain better performance and efficiency [21, 22]. There was

also reaction on the system created for other parameters which includes proximity temperature difference at the heat exchanger and the pinch temperature difference at the condenser, but when comparing to former, the influence of it is lower.

With the large source of waste heat produced by the offshore oil and gas platform, this allows ORC to possess a great potential for electricity generation from energy recovery to reduced irreversibility and cost of process, and increase the energy and exergy efficiencies, as it reduced the original fuel consumption needed to achieve the electricity demands. According to the research done by previous studies, with ORC in this application, the electricity generated can increased up to 20.3, 11.3% increase in the overall system efficiency and 18.3% in the utilization factor. Furthermore, an average reduction of 22% in the fuel consumption and CO₂ emissions could be achieved over the platform operating years. From the economic aspects, although involving ORC could increase the initial investment cost up to 46%, it also increases the net present value, leading to a discount rate up to 10%, which make it economic acceptable [16].

With simple ORC, having a low exhaust gases temperature after the gas turbine has limited the implementation in the offshore oil and gas platform as acid component could be formed in the condensation by chance and lead to equipment damage and growth of maintenance cost. Hence, a simple ORC is suggested to be in a configuration where the temperature of exhaust gases is consistently higher than the dew point temperature of the water contained in the exhaust gases. Besides, ORC could contribute to higher exergy destruction. Regenerative ORC can improve this problem as it has higher exergy efficiency. Generally, ORC is a good technology to be added as the WHR from productive process, even for typical operating conditions as oil exploitation in the offshore oil and gas platform is a very great example.

7 Conclusion

Although the actual application of ORC as a WHR on offshore oil and gas platform is almost non-existent now, ORC has some considerable advantages on the offshore oil and gas platform that can be observed from the previous studies when compared to SRC and ABC. ORC can better minimize the CO₂ emission and fuel consumption and exhibits the highest system performance; however, it comes with high cost. It also has low operating pressure, low maintenance cost and can better adapt when recovering low and medium grade heat, which is between which 150–400 °C make it a potential WHR system on the offshore oil and gas sector. From most of the previous research, dry fluid such as Cyclopentane has been stated to be the most suitable ORC working fluid for WHR on the offshore oil and gas application. Nevertheless, the working fluids should still be chosen according to the available heat source and platform size. Turbine inlet temperature and pressure of ORC has found out to be the most effective parameters on the net power output, energy and exergy efficiency and cost.

Acknowledgements The authors are grateful to Malaysia-Thailand Joint Authority (MTJA), UTM-LoCARTic and IVESE UTM for the support in publishing this work.

References

1. Omara A, Saghafifar M, Mohammadi K, Alashkar A, Gadalla M (2018) A review of unconventional bottoming cycles for waste heat recovery: part II—applications. *Energy Convers Manage* 180(1):559–583
2. Nguyen T-V, Pierobon L, Elmegaard B, Haglind F, Breuhaus P, Voldsund M (2013) Exergetic assessment of energy systems on north sea oil and gas platforms. *Energy* 62(1):23–36
3. Malaysia Biennial Update Report to the UNFCCC 2016 (2016) Ministry of Environment and Water Malaysia, Putrajaya
4. Malaysia Biennial Update Report to the UNFCCC 2020 (2020) Ministry of Environment and Water Malaysia, Putrajaya
5. Oh TH (2010) Carbon capture and storage potential in coal-fired plant in Malaysia—a review. *Renew Sustain Energy Rev* 14(9):2697–2709
6. Nguyen T-V, Elmegaard B, Breuhaus P, Haglind F (2014) Modelling, analysis and optimisation of energy systems on offshore platforms, Phd thesis, Technical University of Denmark
7. Zhang A, Zhang H, Qadrdan M, Yang W, Jin X (2019) Optimal planning of integrated energy systems for offshore oil extraction and processing platforms. *Energies* 12(4):756
8. Hnat JG, Coles WF (1985) A feasibility assessment of cogeneration from a regenerative glass furnace. *IEEE Trans Ind Appl IA-21(4)*:1064–1069
9. Pierobon L, Nguyen T-V, Larsen U, Haglind F, Elmegaard B (2013) Multi-objective optimization of organic rankine cycles for waste heat recovery: application in an offshore platform. *Energy* 58(1):538–549
10. Jouhara H, Khordehghah N, Almahmoud S, Delpech B, Chauhan A, Tassou SA (2018) Waste heat recovery technologies and applications. *Therm Sci Eng Prog* 6(1):268–289
11. Kolahi M, Yari M, Mahmoudi SMS, Mohammadkhani F (2016) Thermodynamic and economic performance improvement of ORCs through using zeotropic mixtures: case of waste heat recovery in an offshore platform. *Case Stud Therm Eng* 8:51–70
12. Barrera JE, Bazzo E, Kami E (2015) Exergy analysis and energy improvement of a Brazilian floating oil platform using organic Rankine cycles. *Energy* 88:67–79
13. Khatita MA, Ahmed TS, Ashour FH, Ismail IM (2014) Power generation using waste heat recovery by organic Rankine cycle in oil and gas sector in Egypt: a case study. *Energy* 64:462–472
14. Bhargava RK, Bianchi M, Branchini L, De Pascale A, Orlandini V (2015) Organic Rankine cycle system for effective energy recovery in offshore applications: a parametric investigation with different power rating gas turbines. *Turbo expo: power for land, sea, and air*, vol 3. American Society of Mechanical Engineers, Montreal, Canada, pp 1–13
15. Eveloy V, Rodgers P, Qiu L (2016) Performance investigation of a power, heating and seawater desalination poly-generation scheme in an off-shore oil field. *Energy* 98:26–39
16. Reis MML, Guillen JAV, Gallo WLR (2019) Off-design performance analysis and optimization of the power production by an organic Rankine cycle coupled with a gas turbine in an offshore oil platform. *Energy Convers Manage* 196:1037–1050
17. Nami H, Ertesvåg IS, Agromayor R, Riboldi L, Nord LO (2018) Gas turbine exhaust gas heat recovery by organic Rankine cycles (ORC) for offshore combined heat and power applications—energy and exergy analysis. *Energy* 165:1060–1071
18. Lai NA, Wendland M, Fischer J (2011) Working fluids for high-temperature organic Rankine cycles. *Energy* 36(1):199–211

19. Pasetti M, Invernizzi CM, Iora P (2014) Thermal stability of working fluids for organic Rankine cycles: an improved survey method and experimental results for cyclopentane, Isopentane n-butane. *Appl Therm Eng* 73(1):764–774
20. Roy J, Mishra M, Misra A (2010) Parametric optimization and performance analysis of a waste heat recovery system using organic Rankine cycle. *Energy* 35(12):5049–5062
21. Baik Y-J, Kim M, Chang K-C, Lee Y-S, Yoon H-K (2013) A comparative study of power optimization in low-temperature geothermal heat source driven R125 transcritical cycle and HFC organic rankine cycles. *Renew Energy* 54:78–84
22. Dai Y, Wang J, Gao L (2009) Parametric optimization and comparative study of organic Rankine cycle (ORC) for low grade waste heat recovery. *Energy Convers Manage* 50(3):576–582

Numerical Simulation of Heat Transfer Performance of Water: Ethylene Glycol Mixture (W:EG) Through Turbine-Like Decaying Flow Swirler



At-Tasneem Mohd Amin, Wan Azmi Wan Hamzah, and Mohd Azmi Ismail

Abstract The propeller-type swirler has been mentioned several times in the literature as one of the decaying flow swirlers designed to improve heat transfer performance while maintaining a low friction factor. However, the distance travelled by swirling flow varies according to the swirler's design configuration. As a result, the purpose of this paper is to investigate the heat transfer performance and friction factor of a new turbine-like decaying flow swirler (TDS). The distance traversed and decays downstream the tube by the created swirling flow will then be determined. The TDS is a rigid turbine or compressor consist of four twisted blades at 172.2° set at the entrance of a fully developed 1.5 m tube with a dimensionless length (L/D) of 93.75. A 60:40% water and ethylene glycol mixture was employed as a working fluid for the turbulent flow with Reynolds numbers ranging from 4583 to 35,000. The results indicate that the maximum relative heat transfer is 1.16 and the highest relative friction factor is 1.47 at the lowest Reynolds number tested. For Reynolds numbers less than and equal to 10,136, the thermal hydraulic performance achieved unity. The obtained relative heat transfer is deemed to be poor in comparison to several publications. The swirl flow finally entirely decays after $L/D = 70.32$ after being visualised through the vortex core and cross-sectional plane of the tube, contributing to a reduced heat transfer performance. In conclusion, TDS performance can be optimised for a lower dimensionless length using the same design configuration, or the design configuration should be modified to increase the generated swirl flow intensity.

A.-T. Mohd Amin (✉)

Faculty of Mechanical and Automotive Engineering Technology, Universiti Malaysia Pahang, 26600 Pekan, Pahang, Malaysia
e-mail: tasneem@ump.edu.my

W. A. Wan Hamzah

Department of Mechanical Engineering, College of Engineering, Universiti Malaysia Pahang, Lebuhraya Tun Razak, 26300 Gambang, Kuantan, Pahang, Malaysia

M. A. Ismail

School of Mechanical Engineering, Universiti Sains Malaysia Engineering Campus, 14300 Nibong Tebal, Penang, Malaysia

Keywords Passive method · Heat transfer enhancement · Propeller-type swirler · Friction factor

1 Introduction

Passive approaches, such as the insertion of a swirler in a circular heated tube, have received more attention in the operation of an efficient heat exchanger than various heat transfer enhancement techniques (HTET) due to their obvious superiority in terms of lower energy, material, cost, and ease of maintenance because they do not require extra power supply [1, 2]. Swirling flow inside the tube of a heat exchanger improves heat transfer efficiency by thinning the thermal boundary layers near the tube wall. Swirlers are classified into two types: continuous flow swirlers and decaying flow swirlers. A continuous flow swirler was installed along the tube to constantly create swirl flow [3–9]. It sparked a lot of interest in HTET research since it increased heat transfer by up to 1466% when compared to plain tube heat transfer [8]. However, the presence of the swirler along the tube, which continuously blocked the incoming flow, resulted in a high friction factor of up to 5122% along the tube. This consequence may go against the fundamental goal of the passive approach, which is to save energy, materials, and money while also making heat exchanger maintenance easier. As a result, a decaying flow swirler was placed at the tube's inlet to induce a swirl flow downstream and allow the swirl flow to flow freely downstream the tube. The flow disturbance that contributed to the high friction factor will be minimised using this technique. Numerous decaying flow swirlers have been introduced to create a high intensity of swirling flow along the tube. Alhendal and Gomaa [10], Gorman et al. [11], Indurain et al. [12], Nikoozadeh et al. [13], and Ahmadvand et al. [14] examined numerically how a propeller-type swirler can change uniform incoming flow to swirl flow along the tube. The swirlers were placed at the inlet or before the fully developed region of the flow, altering the uniform incoming flow by using different propeller designs to generate the swirling flow. They used several parameter configurations such as the number of blades, angle of attack, blade thickness, diameter, and length of the propeller to achieve maximal heat transfer with the least amount of friction.

Alhendal and Gomaa [10] fitted a swirler consisting of six blades parallel to the incoming flow 0.2 after the tube's inlet. The heat transfer increased by 20% but the friction factor rose by only 28%. Nikoozadeh et al. [13] also inserted a propeller-type swirler with six blades and an attach angle of 45° at $L/D = 9$ in a tube with $L/D = 34.7$. Heat transfer increased by 28% with a skin friction factor of 68% as compared to a simple tube with the same working fluid specification. Even though the swirlers did not improve heat transfer as much as continuous flow swirlers, the increase in friction factor is acceptable when the same amount of pumping power is utilised to drive the flow. Indurain et al. [12] employed no supporting device, instead attaching the profiling blade to the tube wall, to reduce the possibility of secondary flow and avoid reverse flow, which contributed to a greater friction factor. The profiled blade

has eight blades and a 40° angle of attack. The heat transfer increased by 57%, while the friction factor increased by 290%. Ahmadvand et al. [14] attached axial guiding vanes with profiling blades at three different attach angles, 30° , 45° , and 60° , at the annular duct inlet. The simulation demonstrated an increase in heat transfer of 50–110%, as well as an increase in friction factor of 90–500%. As the angle of attack increases, so do the Nusselt number and friction factor. In contrast to the findings of Bali and Sarac [15], the highest heat transfer rate of 163% was obtained at the lowest analysed angle of attach, 15° , and a higher number of blades, 6. Despite this, the friction factor increased by 2050% with the same configuration. The lowest friction is obtained with the smallest number of blades and the highest angle of attack investigated.

Even though the decaying flow swirler shown the ability to increase heat transfer with a lower friction factor, the investigations were carried out with a variety of design configurations and experimental setups. These factors provide heat transfer and friction factor results that are not comparable amongst the literatures. The reason for this is that, unlike a continuous flow swirler, the swirl flow that was formed uniquely based on the swirler's design will provide varied turbulence strength downstream the tube flow. The swirl flow will then progressively decay as it flows downstream the tube due to friction between the fluid particles and the wall. After a certain distance downstream the tube, the flow will return to a uniform flow. As a result, the location of the swirler is critical in determining the starting point of where the swirl flow was formed and how long the generated swirl flow will survive and fade. The longer the tube, the lower the heat transfer enhancement and the greater the friction factor. Gorman et al. [11] verified these results using a rotary fan generated swirler. When the data is measured until $L/D = 5$, the heat transmission increases by 95%, but drops to 51% when the data is measured until $L/D = 20$.

As a result, the aim of the present work is to investigate numerically the heat transfer and friction factor performance of a new design of turbine-like decaying flow swirler (TDS). The survival of the generated swirl flow will be visualised along the tube, as well as the point where the generated swirl flow decays and eventually returns to uniform flow.

2 Numerical Modeling

This research investigates the turbine-like decaying flow swirler (TDS). TDS was inspired by Beaubert et al.'s design of an eight-bladed swirler [16]. Figure 1 shows how the TDS was designed.

It is composed of four blades that twist 172.2° from leading to trailing edge. The blade has an axial chord length of 27.01 mm and a flow inlet angle of 0° . The swirler's diameter is 15.15 mm, and the blade thickness is 0.81 mm. The swirler blades were secured in the centre of the oval holed hub. The oval hub measures 16.01 mm in length and 4 mm in width, with a diameter of 2 mm cut through the oval. For future experimental investigation, the thermo-physical properties of TDS

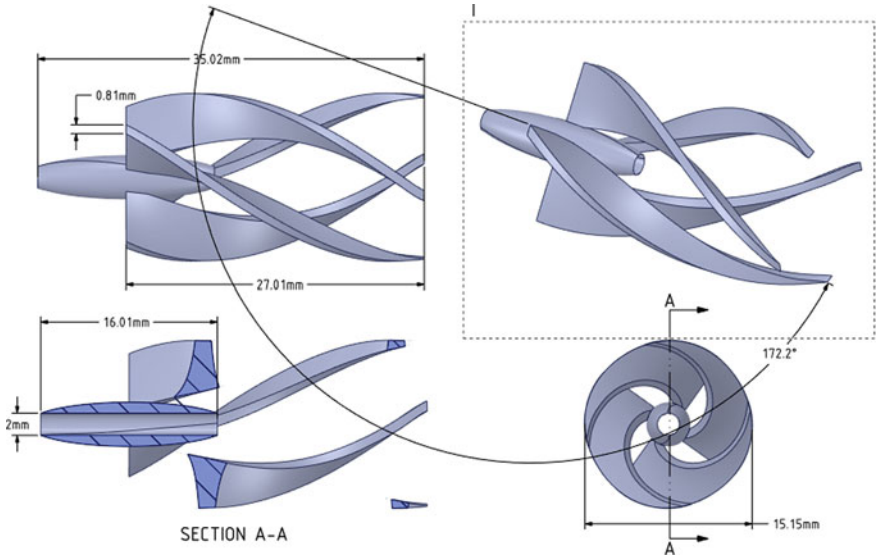


Fig. 1 Turbine-like swirler geometry

were set to be resin material. As a result, the thermo-physical properties of the resin were established for TDS, as displayed in Table 1.

The computational domain of a three-dimensional straight tube in horizontal orientation was adopted from the experimental setup of force convection for heat transfer exchanger in Abdul Hamid et al. [20]. Figure 2 shows a copper tube with a

Table 1 Thermophysical properties

Descriptions	Resin [17]	Copper [18]	W:EG 60:40% [19]
Thermal conductivity, k (W/mK)	0.681	387.6	0.4112
Density, ρ (kg/m ³)	–	8978	1055.832
Specific heat, C_p (J/kg K)	–	–	0.002322
Dynamic Viscosity, μ (Pa s)	–	381.0	3498.6

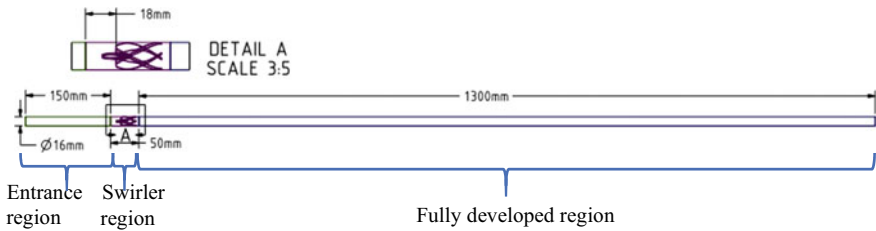


Fig. 2 Computational domain geometry

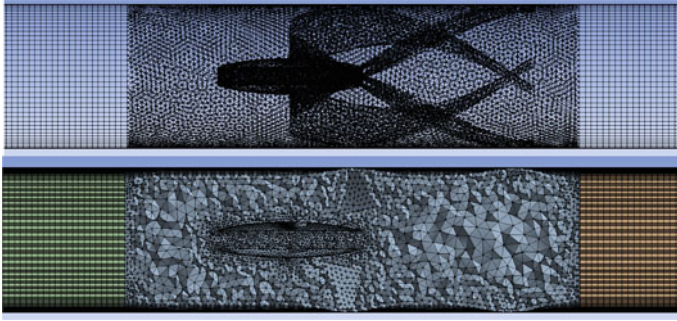


Fig. 3 Mesh generation

constant diameter of 0.016 m and a length of 1.5 m ($L/D = 93.75$). Table 1 displays the thermophysical characteristics of copper tube. The tube domain was divided into three areas labelled entrance, swirler, and fully developed region to differentiate the mesh generation for analysis purposes. The entrance region was fixed at 0.15 m ($L/D = 9.4$) before TDS was inserted into the flow at swirler region. The length of the swirler zone, where the turbine-like swirl generator was positioned, is 0.05 m. The fully developed region where the analysis will be performed is 1.34 m long and begins at the leading edge of TDS at $L/D = 10$.

Figure 3 shows a multi-block mesh of structured and unstructured mesh that was generated using ANSYS MESH to discretize the geometry domain. At the swirler insert region, a tetrahedral cell was employed. The hexahedral cell was used at the tube domain’s inlet and downstream flow of the swirler.

The working fluid is a 60:40% mixture of water and ethylene glycol (W:EG). Azmi et al. [21] employed W:EG 60:40% as a working fluid to increase heat transfer convection of a cooling system by dispersing Al_2O_3 nanoparticles at different Reynolds numbers. The mixture of W:EG 60:40% improved by 24.6% when compared to the other mixtures of W:EG 50:50% and 40:60%. Thermophysical properties of W:EG 60:40% displays in Table 1.

The simulation is carried out for three-dimensional, incompressible, and steady flow in the turbulence regime with Reynolds numbers ranging from 4583 to 35,000. To evaluate the swirl flow induced by inserting TDS in a straight horizontal tube, the simulation for a set of governing equations of continuity, Reynolds Averaged Navier–Stokes (RANS), and energy equations are carried out using ANSYS Fluent. Turbulence is represented by the Reynolds Stress Model (RSM). The boundary condition employed in this simulation is illustrated in Fig. 4.

A relative friction factor, f_{rel} and relative Nusselt number, Nu_{rel} are calculated as

$$f_{rel} = \frac{f_{TDS}}{f_{PT}} \tag{1}$$

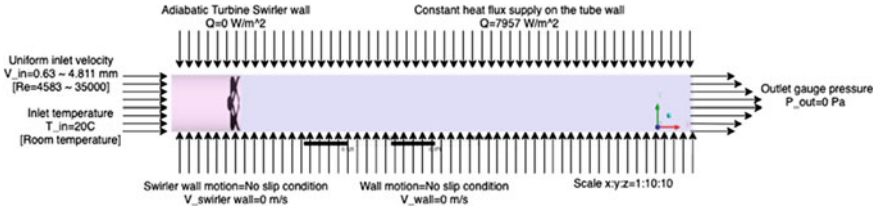


Fig. 4 Boundary condition

$$Nu_{rel} = \frac{Nu_{TDS}}{Nu_{PT}} \quad (2)$$

where f_{TDS} and Nu_{TDS} are the friction factor and Nusselt number of the flow when the TDS was inserted in the tube, and f_{PT} and Nu_{PT} are the friction factor and Nusselt number of the plain tube flow. Thermal Hydraulic Performance (THP) is measured the ratio of heat transfer enhancement over a friction factor drawback with the same pumping power.

$$THP = \frac{Nu_{rel}}{(f_{rel})^{\frac{1}{3}}} \quad (3)$$

3 Result and Discussion

The numerical investigation of the heat transfer performance and friction factor obtained by inserting the turbine-like decaying flow swirler (TDS) in a heated circular tube. The heat transfer performance TDS was measured by taking the average of the surface temperature at the tube wall and the bulk temperature of the working fluid along the tube. Then, Nusselt number was computed after obtaining the convective heat transfer coefficient. On the other hand, the pressure differential between the tube's inlet and outlet flow was used to calculate the friction factor. The data was collected for both with and without the TDS insert along the tube, and the relative Nusselt number and friction factor were determined.

The friction factor and Nusselt number are shown in Fig. 5 for both the plain tube and the plain tube with TDS insert. The plain tube's friction factor and Nusselt number are represented by the solid line plot, whereas the plain tube with TDS insert is represented by the dashed line plot. For both plots, the friction factor decreases and the Nusselt number increases as the Reynolds number increases. Both the Nusselt number and the friction factor are clearly increased with the TDS insert when compared to the plain tube. Nonetheless, the friction factor increment is greater than the Nusselt number. As a result, Fig. 6 shows that the relative friction factor ranges from 1.45 to 1.47 and the relative Nusselt number ranges from 1.09 to 1.16, with larger values

Fig. 5 Friction factor

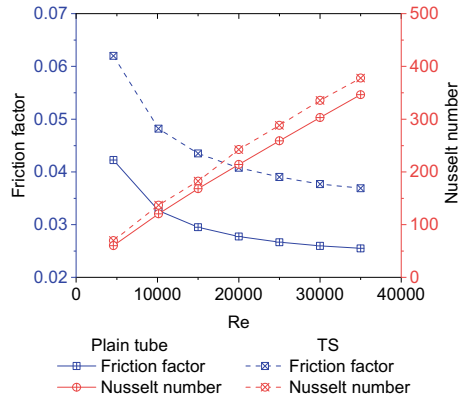
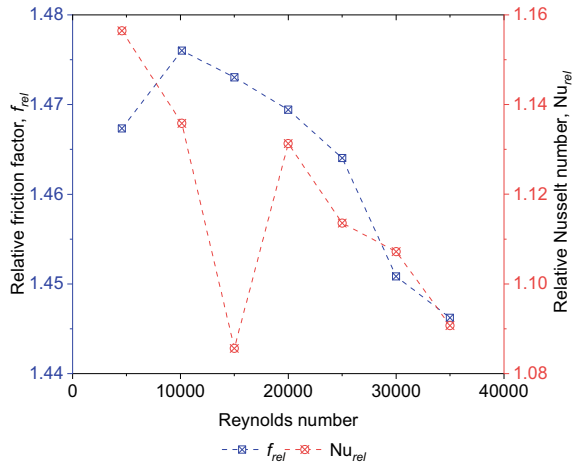


Fig. 6 Relative friction factor



at lower Reynolds numbers and lower values at higher Reynolds numbers. This data shows that, amidst the disadvantage of the friction factor, TDS can improve heat transfer at all examined Re for the tube length with a dimensionless length of $L/D = 93.75$. For some reason, the relative friction factor fluctuated abruptly at $Re = 15,000$ before returning to its normal trend with other Reynolds numbers. However, the TDS is only worthwhile to implement when the THP is greater than one to ensure that the heat transfer performance is superior enough to overcome the friction drawback by using the same amount of pumping power. Thermal hydraulic performance (THP) attained unity for $Re = 4583$ and $10,136$, as illustrated in Fig. 7. Because the THP is less than anticipated, the induced swirl flow structure inside the tube is visualised.

The vortex core and cross-sectional plane of velocity circumferential formed as the incoming flow passed through the TDS are illustrated in Fig. 8.

The illustration was obtained for the flow at $Re = 4583$, where the THP is maximum for the range of Re studied. The blue and red contours represent the

Fig. 7 Thermal–hydraulic performance (THP)

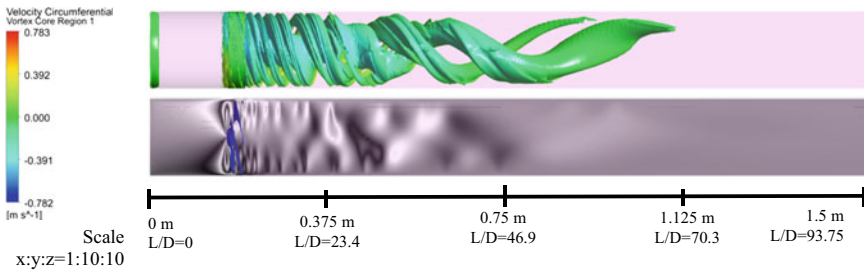
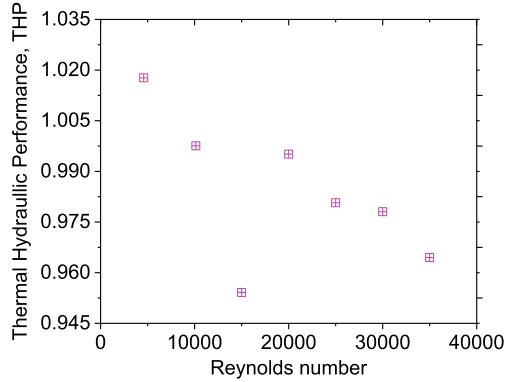


Fig. 8 Vortex core (top) and cross sectional plane (bottom) of velocity circumferential

lowest and highest circumferential velocity, respectively. The cross-sectional plane tube was shown in zebra colour to clearly show the contrasting intensity of turbulence structure downstream of the TDS. This visual clearly indicates that the swirling flow generated a larger intensity in the first half of the tube and then vanished in the second half of the tube. The most intense swirling flow was produced as the inlet flow passed the trailing edge of the TDS. The intensity of the swirling flow steadily decays as it travels downstream until it reaches $L/D = 70.32$ before the swirling flow entirely decays and the flow returns to a uniform flow with the same velocity as the input flow.

The heat transfer performance may be efficient before $L/D = 46.88$ because the swirling flow structure swipes the tube wall, thinning the thermal boundary condition and enhancing convective heat transfer at the swirling flow structure—wall contact point. As a result, for the TDS that is positioned in the same location, it is more effective to utilise a tube length of less than $L/D = 46.88$ or 0.75 m with a diameter of 0.016 m. The shorter the tube length, the better the heat transfer performance. Gorman et al. [11] agreed on this statement for a rotating fan generated swirler. When heat transfer performance is measured at $L/D = 5$, the enhancement is 1.95 , and it decreases to 1.51 when the tube length is extended to $L/D = 20$. To compare TDS’s performance to that of the literature, Table 2 summarises the performance of

Table 2 Data comparison with the literatures

Authors	Name of swirler	Working fluid	L/D	Nu_{rel}	f_{rel}
Present work	Turbine-like swirler	W:EG 60:40%	93.75	1.16	1.47
Indurain et al. [12]	Axial guide vane swirler with profiling blades	Air	45.56	1.57	2.9
Nikoozadeh et al. [13]	Propeller-type swirler	Al ₂ O ₃ nanofluid	34.7	1.28	1.68
Alhendal and Gomaa [10]	Swirler vane blades	Air	40	1.2	1.38
Gorman et al. [11]	Rotating fan generated swirl	Air	20	1.51	-

four other propeller-type swirlers at various dimensionless lengths. In comparison to the literature, the present data employed the longest dimensionless length. The results also revealed that the heat transfer increase is the smallest when compared to other literatures because the swirl flow completely decays after half of the tube. As a result, the performance of the TDS heat transfer is less than expected. Heat transfer can thus be improved by utilising a shorter tube, or the TDS design configuration, such as the number of blades, twist angle, or TDS dimensions, should be modified to boost the swirl flow intensity.

4 Conclusion

The heat transfer performance and friction factor of a new turbine-like decaying flow swirler (TDS) design were explored. Then, the survival of swirl flow was revealed by visualising the vortex flow and cross-sectional velocity plane circumferential along the tube. The following statements are the conclusion that can be made from this research:

- The relative range of Nusselt number is 1.09 to 1.16 with the highest Nusselt number obtained at the lowest investigated Re of 4583.
- The relative range of friction factor is 1.45 to 1.47 with the highest friction factor obtained at Re of 10,000.
- The thermal hydraulic performance (THP) attained unity at lower investigated Re of 4583 and 10,000.
- The generated swirling flow using TDS decayed downstream the tube until it completely disappear at $L/D = 70.32$.

The heat transfer performance was lower than intended, and the friction factor was indeed low. The reason for this is that the distance travelled by the swirling flow entirely decays before it reaches the end of the tube, reducing its contribution to heat transfer enhancement. The TDS performance can be maximised for a dimensionless length of less than $L/D = 46.88$, or the TDS design configuration should be improved

by exploring the modifications the TDS dimensions, number, and twist angle of the blades.

Acknowledgements The authors would like to thank the Center of Excellence for Advanced Research in Fluid Flow (CARIFF) for funding assistance under RDU190385 for inventory and the Advance Automotive Liquids Laboratory (A2LL) for providing full access to a high-performance computer. The authors are also grateful to UMP Research and Innovation and Universiti Malaysia Pahang for their financial support through UMP Tabung Persidangan Dalam Negara (TPDN).

References

1. Firoozi AO, Majidi S, Ameri M (2020) A numerical assessment on heat transfer and flow characteristics of nanofluid in tubes enhanced with a variety of dimple configurations. *Therm Sci Eng Prog* 19
2. Zhang K, Sun Z, Zheng N, Chen Q (2020) Effects of the configuration of winglet vortex generators on turbulent heat transfer enhancement in circular tubes. *Int J Heat Mass Transf* 157
3. Alimoradi A, Fatahi M, Rehman S, Khoshvaght-Aliabadi M, Hassani SM (2020) Effects of transversely twisted-turbulators on heat transfer and pressure drop of a channel with uniform wall heat flux. *Chem Eng Process Process Intensification* 154
4. Ahmad S, Abdullah S, Sopian K (2020) A review on the thermal performance of nanofluid inside circular tube with twisted tape inserts. *Adv Mech Eng* 12(6)
5. Maghrabie HM, Attalla M, Mohsen AAA (2021) Performance assessment of a shell and helically coiled tube heat exchanger with variable orientations utilizing different nanofluids. *Appl Therm Eng* 182:116013
6. Chaurasia SR, Sarviya RM (2020) Thermal performance analysis of CuO/water nanofluid flow in a pipe with single and double strip helical screw tape. *Appl Therm Eng* 166:114631
7. Azmi WH, Abdul Hamid K, Ramadhan AI, Shaiful AIM (2021) Thermal hydraulic performance for hybrid composition ratio of TiO₂-SiO₂ nanofluids in a tube with wire coil inserts. *Case Stud Thermal Eng* 25
8. Pourramezan M, Ajam H, Raoufi MA, Abadeh A (2020) Performance evaluation and optimization of design parameters for twisted conical strip inserts in tubular laminar flow using Taguchi approach. *Int J Therm Sci* 152:106324
9. Mashayekhi R, Arasteh H, Toghraie D, Motaharpour SH, Keshmiri A, Afrand M (2020) Heat transfer enhancement of water-Al₂O₃ nanofluid in an oval channel equipped with two rows of twisted conical strip inserts in various directions: a two-phase approach. *Comput Math Appl* 79(8):2203–2215
10. Alhendal Y, Gomaa A (2017) Three dimensional CFD modeling of turbulent flow through circular tube using swirl generator vanes I. *Introduction* 6:106–111
11. Gorman JM, Sparrow EM, Ilamparuthi S, Minkowycz WJ (2016) Effect of fan-generated swirl on turbulent heat transfer and fluid flow in a pipe. *Int J Heat Mass Transf* 95:1019–1025
12. Indurain B, Beaubert F, Lalot S, Uystepuyt D (2020) Computational fluid dynamics investigation of the thermal performances of a swirler with profiled blades. *Heat Transfer Eng* 7632
13. Nikoozadeh A, Behzadmehr A, Payan S (2020) Numerical investigation of turbulent heat transfer enhancement using combined propeller-type turbulator and nanofluid in a circular tube. *J Therm Anal Calorim* 140(3):1029–1044
14. Ahmadvand M, Najafi AF, Shahidinejad S (2010) An experimental study and CFD analysis towards heat transfer and fluid flow characteristics of decaying swirl pipe flow generated by axial vanes. *Meccanica* 45(1):111–129

15. Bali T, Sarac BA (2014) Experimental investigation of decaying swirl flow through a circular pipe for binary combination of vortex generators. *Int Commun Heat Mass Transfer* 53:174–179
16. Beaubert F, Pálsson H, Lalot S, Choquet I, Bauduin H (2015) Design of a device to induce swirling flow in pipes: a rational approach. *Comptes Rendus Mecanique* 343(1):1–12
17. Hu G, Cao Z, Hopkins M, Lyons JG, Brennan-Fournet M, Devine DM (2019) Nanofillers can be used to enhance the thermal conductivity of commercially available SLA resins. *Procedia Manuf* 38(2019):1236–1243
18. Perry RH (1997) *Perry's chemical engineers' handbook*. McGraw-Hill
19. ASHRAE Handbook—Fundamental (SI Edition) (2009) American Society of Heating, Refrigerating and Air-Conditioning Engineers Inc. Atlanta, GA
20. Abdul Hamid K, Azmi WH, Rizalman M, Sharma KV (2019) Heat transfer performance of $\text{TiO}_2\text{-SiO}_2$ nanofluids in a tube with wire coil inserts. *Appl Therm Eng* 152:275–286
21. Azmi WH, Usri NA, Mamat R, Sharma KV, Noor MM (2017) Force convection heat transfer of Al_2O_3 nanofluids for different based ratio of water: ethylene glycol mixture. *Appl Therm Eng* 112:707–719

Pareto Solution of Autocatalytic Esterification in Semi-batch Reactor Using Control Vector Parameterization (CVP) and ϵ -Constraint



F. S. Rohman, K. A. Zahan, and N. Aziz

Abstract In this research, the optimal feed flowrate trajectories, and reaction temperature for autocatalytic esterification of sec-butyl propionate in the semi-batch reactor had been determined using dynamic-nonlinear programming (NLP) based optimization. The dynamic multi-objective optimization (DMOO) problem yielded from this autocatalytic esterification due to contrary objective functions. The DMOO problem was characterized by multiple solutions, which are non-dominated or Pareto solutions. In this work, to generate the Pareto solutions for the chosen objective functions, which maximize conversion and minimize process time, the ϵ -constraint approach and control vector parameterization (CVP) has been applied. Here, various combinations of conversion and process time were obtained as a result of different optimal temperatures and feed flowrates in each point of Pareto solutions. Finally, these solution methods could benefit industries in evaluating and selecting the trade-offs and operating policies.

Keywords Dynamic optimization · Multi-objective optimization · Autocatalytic esterification

F. S. Rohman · N. Aziz (✉)

School of Chemical Engineering, Engineering Campus, Universiti Sains Malaysia, Seri Ampangan, 14300 Nibong Tebal, Seberang Perai Selatan, Penang, Malaysia
e-mail: chnaziz@usm.my

F. S. Rohman

Department of Chemical Engineering, Universitas Brawijaya, Jalan Mayjen Haryono 167, Malang 65145, Indonesia

K. A. Zahan

Department of Systems Science, Graduate School of Informatics, Kyoto University, Kyoto 606-8501, Japan

Faculty of Engineering Technology, Universiti Tun Hussein Onn Malaysia, Parit Raja, 86400 Batu Pahat, Johor, Malaysia

1 Introduction

Esterification has been recognized as one of the most reliable and effective reactions for synthesizing organic products. Ester could be found in natural and synthetic forms, essential for flavours and fragrance components [1, 2]. The esterification in a batch reactor is the most common industrial process used due to the well-known technical and engineering knowledge. However, on the other point of view, batch reactors also present disadvantages [3]. To enhance the conversion, the semi-batch reactor had gained increased attention among industrialists due to the better temperature control and potential to minimize the unwanted side reactions. This research has studied the autocatalytic esterification of an ester, namely *sec*-butyl propionate, in a semi-batch reactor. *Sec*-butyl propionate is a colourless liquid with a fruity odour that has been widely used for flavourings and perfumes. This ester can be produced in a catalyzed reaction of propionic anhydride with 2-butanol [4, 5]. The optimum operating parameters for a semi-batch reactor are critical in producing high quality and high quantity of ester. Here, the model-based optimization strategy could be beneficial for the decision-makers in industries to obtain the optimal solution with least experimental works and cost [3, 6]. However, considering various technical constraints involved in the autocatalytic esterification is a must. In this *sec*-butyl ester production, the reaction was operating under transient conditions comprises mixed systems of differential algebraic equations (DAE) and ordinary differential equations (ODE). Applying the dynamic optimization would suggest the best feed flowrate trajectories and operating temperature which finally maximize the conversion and efficiency [7].

To date, almost all available literature for optimizing autocatalytic esterification between propionic anhydride with 2-butanol was solved by a single-objective function [8]. Due to the presence of contradictory objective functions (maximum conversion and minimum process time) in this reaction, single-objective optimization could not be the best option. The results generated could not explain the relationship between the contradicting objective functions thus failed to suggest a combination set of optimal solutions. To solve this, multi-objective optimization (MOO) strategy has been employed to determine the optimal solution for all objective functions. MOO will generate various combinations of optimal parameters and could also offer an alternative for the trade-offs performance prediction resulting from the opposite actions of various objective functions involved. Additionally, this work would fill the gap that had been unexplored in the optimization study of *sec*-butyl propionate autocatalytic esterification in a semi-batch reactor.

Thus, this study was intended to solve the MOO problem for autocatalytic esterification of *sec*-butyl propionate in a semi-batch reactor. The MOO aims to obtain the optimal feed flowrate and operating temperature profiles in order to optimize the objective functions (maximize conversion and minimize process time).

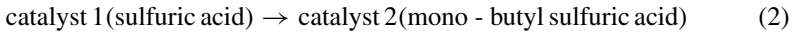
2 Process Modeling

The autocatalytic esterification of anhydride and 2-butanol will produce sec-butyl propionate and propionic acid, presented by Eq. 1 [5]. When sulfuric acid (catalyst) presence, the rate of reaction will be proportionally affected by the catalyst concentration, which results in different trends of autocatalytic behaviors [5]. Here, two catalysts have existed as a representation of the reaction mechanism, and the acidity function expressed the catalyst transformation as shown in Eq. 2 [5].

Main reaction:



Catalyst transformation:



The reaction rate constants were computed using Arrhenius law and the approximation of the acidity function was modeled as in Eq. 3 [5]:

$$H = -(p_1 C_{cat1} + p_2 C_c) \left(p_3 + \frac{p_4}{T} \right) \quad (3)$$

The mass balances for the semi-batch autocatalytic esterification reactor were included in the dynamic optimization work to observe the concentrations trend and represented by Eqs. (4–8) [9].

$$\frac{dC_A}{dt} = -((k_1 + k_2 C_{cat1}) C_A C_B + k_3 C_{cat2} C_B) - \frac{F_0 C_A}{V} \quad (4)$$

$$\frac{dC_B}{dt} = -((k_1 + k_2 C_{cat1}) C_A C_B + k_3 C_{cat2} C_B) + \frac{F_0}{V} (C_{B0} - C_B) \quad (5)$$

$$\frac{dC_B}{dt} = -((k_1 + k_2 C_{cat1}) C_A C_B + k_3 C_{cat2} C_B) + \frac{F_0}{V} (C_{B0} - C_B) \quad (6)$$

$$\frac{dC_{cat1}}{dt} = -\frac{dC_{cat2}}{dt} = -(k_4 10^{-H} C_{cat1} C_A) - \frac{F_0 C_{cat1}}{V} \quad (7)$$

$$\frac{dV}{dt} = F_0 \quad (8)$$

where C_A , C_B , C_c , C_{cat1} , and C_{cat2} are the concentration of 2-butanol, propionic anhydride, propionic acid, sulfuric acid, and mono-butyl sulphuric acid, respectively. F_0 , V and T are the feed flowrate, volume of solution and temperature within reactor.

Table 1 Kinetic parameter equations [5]

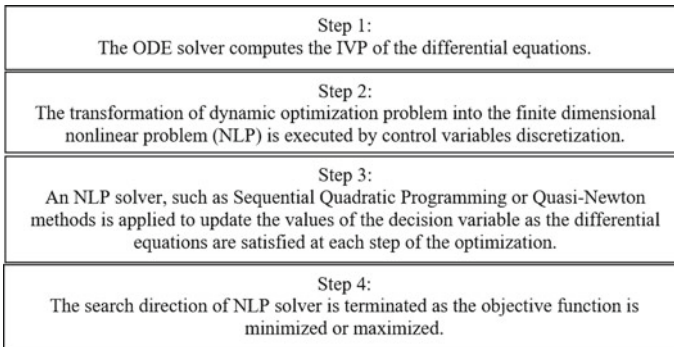
Subscript i	k_{0i}	E_{ai} (J mol ⁻¹)	Parameter p_i
1	$5.36178 \times 10^7 \text{ L mol}^{-1} \text{ s}^{-1}$	80,478.64	2.002×10^{-1}
2	$2.8074 \times 10^{10} \text{ L}^2 \text{ mol}^{-2} \text{ s}^{-1}$	79,159.5	3.205×10^{-2}
3	$3.9480 \times 10^{10} \text{ L mol}^{-1} \text{ s}^{-1}$	69,974.6	-21.3754
4	$1.4031 \times 10^8 \text{ L mol}^{-1} \text{ s}^{-1}$	76,6172.2	12,706

The initial value of C_A , C_B , C_C , C_D , C_{cat1} , C_{cat2} and V_j is 3.4 M, 0 M, 0 M, 0 M, 1.02×10^{-2} M, 0 M and 1L, respectively.

The kinetic parameters of autocatalytic esterification were adopted from Zaldivar et al. [5] as summarized in Table 1.

3 Dynamic Multi-objective Optimization

The control vector parameterization (CVP) had been applied for the dynamic multi-objective optimization (MOO) of autocatalytic esterification. The CVP used was the AMIGO2 package in the MATLAB environment developed by Balsa-Canto et al. [10], while the AMIGO2's algorithm of CVP was adopted from Vassiliadis et al. [11]. The basic steps of CVP are shown in Fig. 1.

**Fig. 1** Basic steps of CVP method

3.1 Multi-objective Optimization (MOO) Technique

The optimal solution for MOOs expressed as multiple optimal solutions produce a set of solutions known as a Pareto-optimal set. Pareto-optimal set refers to a set of optimal solutions that are not dominated by any other solution that belongs to the same set. If the improvement of a given objective is absent and no degenerating amount of another objective, the Pareto-optimal set could be the best optimal solution for all objective functions.

The ϵ -constraint method was used to recompose the multi-objective function into a unified objective optimization problem. In this method, accumulation in single objective was eliminated in which the first objective was optimized while the second objective was served as constraint using threshold values ϵ . Thus, the problem:

$$\text{Min}_{x,u(t),z(t)} \mu_1[d, U(t), V(t)]$$

Subject to

$$\begin{aligned} \mu_2[d, U(t), V(t)] &\leq \epsilon \\ F[x, U(t), V(t), t] &\in S \end{aligned} \quad (9)$$

In these techniques, the dynamic multi-objective optimization problem (DMOOP) was resolved at every iteration to determine the Pareto-optimal set. By sampling discrete points and applying non-dominated points produced from multiple runs, the Pareto-front and the possible trade-off between objectives will be generated. The optimal points on the Pareto-front were updated by progressively changing the ϵ values for multiple runs [12].

3.2 Problem Optimization Formulation

In this work, the control or decision variables are feed flowrate and operating temperature. The states variables are reactant, catalyst, and product concentrations which expressed as a mass balance (Eqs. 4–8) and imposed as a shortcut-process model for the autocatalytic esterification. This model is employed to attain the desired reactor performances.

Then, the lower and upper limits applied are the minimum and maximum capacity of the reactor temperature (303–343 K) and the pumps flowrate ($0\text{--}5 \times 10^{-4}$ L/s). Additionally, the overall process time consisted of six intervals of time (Δt), served as a free final time. Here, the Δt was optimized between 10–30 min.

The bi-objective functions aimed to maximize the conversion and minimize the process time. The objective function is assumed in the form of min. function. For the maximization of $\frac{C_{A0}V_0 - C_A V}{C_{A0}V}$, the max function is presented as $\min - \left(\frac{C_{A0}V_0 - C_A V}{C_{A0}V} \right)$,

while the inequality constraint is the volume solution accumulated at the final process time, 2L. Finally, the dynamic optimization problem is expressed mathematically as:

$$\begin{aligned} \min_{T(t), F_o(t)} \mathcal{P}_1 &= -\left(\frac{C_{A0}V_0 - C_A V}{C_{A0} V}\right) \\ \min_{T(t), F_o(t), \Delta t} \mathcal{P}_2 &= t_f \end{aligned}$$

Subject to:

$$Mdx/dt = f(x(t), u(t), p, t) \quad (\text{Model equation})$$

$$0 \leq F_0 \leq 5 \times 10^{-4} \text{ L/s}$$

$$303 \text{ K} \leq T \leq 343 \text{ K}$$

$$10 \text{ min} \leq \Delta t \leq 30 \text{ min} \quad (\text{Lower and upper limits})$$

$$V \leq 2L \quad (\text{Final inequality constraint})$$

4 Results and Discussion

Figure 2 shows the Pareto-optimal front (for example, the ϵ -constraint). The Pareto-optimal front consist of three zones; Zone 1: the lower end of the Pareto-optimal front, which is indicated by relatively short process time and low conversion; Zone 2: upper end of the Pareto-optimal front, which is indicated by relatively long process

Fig. 2 Pareto-front

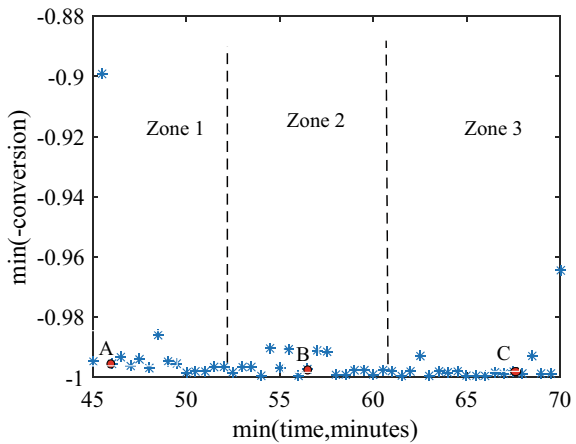
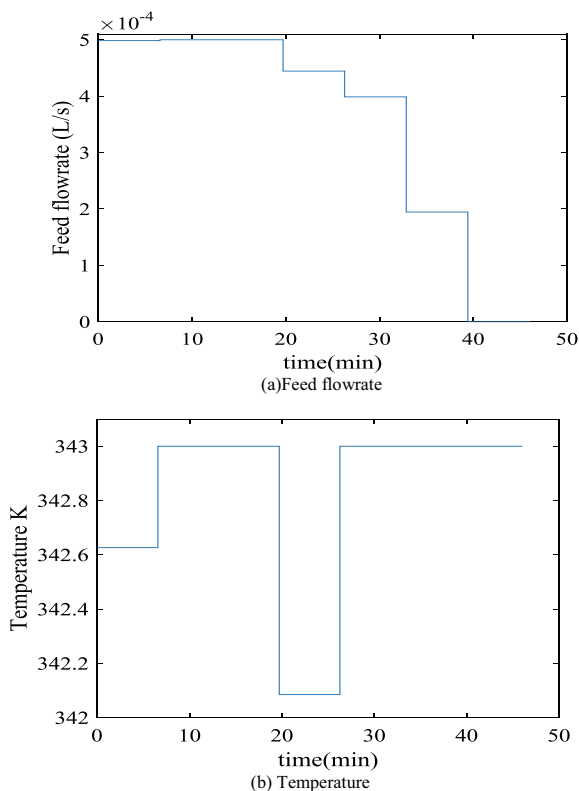


Fig. 3 Optimal trajectories in point A

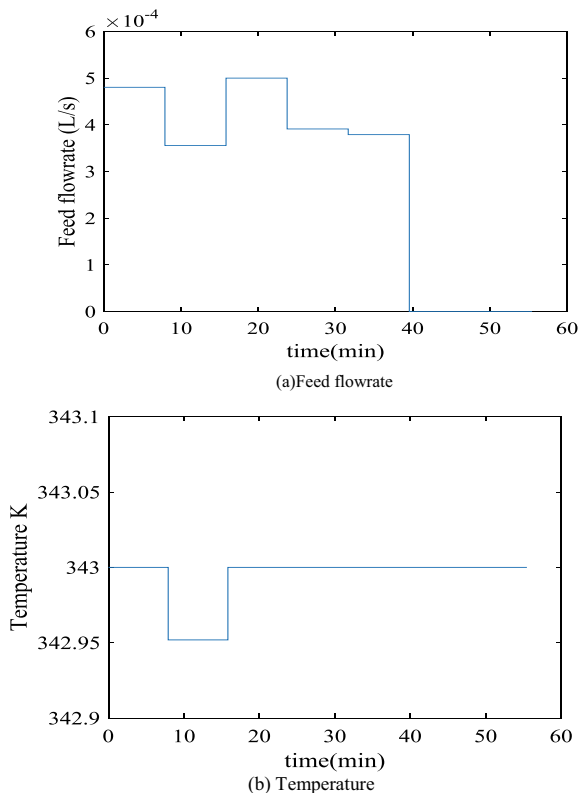


time and high conversion; Zone 3: intermediate zone which signified as moderate process time and conversion.

Figure 3 depicts the correlation between each point of the Pareto-optimal front with various operating temperatures and feed flowrates. The non-dominated points (A, B, and C) found at Zone 1, 2, and 3, respectively, gave non-identical trend trajectories, as presented in Figs. 3, 4 and 5. Table 2 summarizes the dynamic optimization results for non-dominated points A, B, and C.

From Table 2, the process time for non-dominated points A, B, and C are 46 min, 55.39 min and 66.88 min, while the conversion achieved for each point are 0.993, 0.998 and 0.999, respectively. Temperature had been determined as the most significant control variable that affect the process time and conversion for the autocatalytic esterification of sec-butyl propionate. This result agreed with [9] who stated that the rates of reaction for reactant, catalyst, and product rise significantly when the temperature rise. Thus, non-identical temperature profiles offer variety amount of process time and conversion of ester as depicted in Figs. 3b, 4b and 5b. Here, because of the lowest amount of optimal temperature trajectory at point A, the process time and conversion obtained was smallest as compared to point B and C.

Fig. 4 Optimal trajectories in point B



The optimal feed flowrate (Figs. 3a, 4a and 5a) and operating temperature (Figs. 3b, 4b and 5b) shows an oppose trend. However, both variables present a complementary effect to support the reaction rate. As the operating temperature profile located at the lower value, the trajectory of the feed flowrate will equilibrate (increase the flowrate) so that the reaction rate will be stable and maintain. In a semi-batch reactor, higher reactant (propionic anhydride) feed flowrate will stimulate the autocatalytic mechanism which also enhance the rate of conversion. Additionally, longer process time is required if the feed flowrate is low.

The use of the Pareto-optimal front determined is aligned with the decision-maker's capacity. The non-identical optimal trajectories along the Pareto-optimal front will help the decision-maker to choose the best trade-off and select the best operational parameters for the autocatalytic esterification of sec-butyl propionate. The Pareto-optimal front of ϵ -constraint determined will prepares a lot of possible alternatives for the decision-maker to use the optimal trajectories based on the feasibility and practicality thought of the process.

Fig. 5 Optimal trajectories in point C

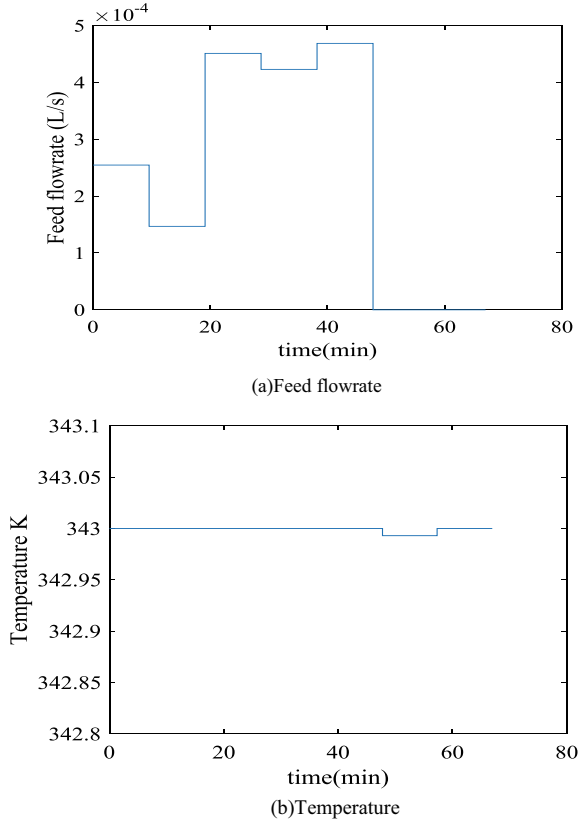


Table 2 Process time and conversion in point A, B and C

Non-dominated point	Point A	Point B	Point C
Process time, min	46.00	55.39	66.88
Conversion	0.993	0.998	0.999

5 Conclusion

Due to various performance objectives with contradictory effects between each other in the autocatalytic esterification, single-objective optimization will not be suitable. In this study, the dynamic multi-objective optimization method was applied. The control vector parameterization and ϵ -constraint were utilized to determine the Pareto-optimal solution for operating temperature and process time. The correlation obtained between multiple objective functions could help decision-makers to select the trade-offs and choose the best operational conditions for the process. Finally, the optimal temperature trajectory from the selected trade-off becomes

the pre-determined set point. It is tracked afterward by the controller in the online application.

References

1. Zulkeflee SA, Sata SA, Rohman FS, Aziz N (2020) Modelling of immobilized *Candida Rugosa* lipase catalysed esterification process in batch reactor equipped with temperature and water activity control system. *Biochem Eng J* 161:107669
2. Khan Z, Javed F, Shamair Z, Hafeez A, Fazal T, Aslam A, Zimmerman WB, Rehman F (2021) Current developments in esterification reaction: a review on process and parameters. *J Ind Eng Chem* 103:80–101
3. Zahan KA, Kano M (2019) Technological progress in biodiesel production: an overview on different types of reactors. *Energy Procedia* 156:452–457
4. Chang J, Chen K (2004) An integrated strategy for early detection of hazardous states in chemical reactors. *Chem Eng J* 98:199–211
5. Zaldivar JM, Hernandez H, Molga E, Galvan IM, Panetos F (1993) The use of neural networks for the identification of kinetic functions of complex reactions. In *Proceedings of the third European symposium on computer aided process engineering. ESCAPE 3*
6. De R, Bhartiya S, Shastri Y (2019) Multi-objective optimization of integrated biodiesel production and separation system. *Fuel* 243:519–532
7. Faust JMM, Hamzehlou S, Leiza JR, Asua JM, Mitsos A (2019) Dynamic optimization of a two-stage emulsion polymerization to obtain desired particle morphologies. *Chem Eng J* 359:1035–1045
8. Rohman FS, Sata SA, Othman MR, Aziz N (2021) Dynamic optimization of autocatalytic esterification in semi-batch reactor. *Chem Eng Technol* 44:648–660
9. Ubrich O, Improving Safety and Productivity of isothermal semi batch reactor by modulating feed rate, PhD thesis, Écolepolytechnique fédérale de Lausanne
10. Balsa-Canto E, Henriques D, Gábor A, Banga JR (2000) 2016 AMIGO2, a toolbox for dynamic modeling, optimization and control in systems biology *Bioinformatics* 32:3357–3359
11. Vassiliadis VS, Sargent RWH, Pantelides CC (1994) Solution of a class of multistage dynamic optimization problems. 1. Problems without path constraints, 2. Problems with path constraints. *Ind Eng Chem Res* 33:2111–2122, 2123–2133
12. Maiti SK, Lantz AE, Bhushan MB, Wangikar PP (2011) Multi-objective optimization of glycopeptide antibiotic production in batch and fed batch processes. *Bioresour Technol* 102:6951–6958

Control Analysis of Biomass Gasification with Combined Heat and Power System



Y. H. Kok, N. Kamarulzaman, Z. F. Mohd Shadzalli, N. Abdul Manaf, Ku Nur Afrina Ku Azman Shah, Mohd Zamri Mohd Yusop, Jafri Mohd Rohani, Budi Hartono, and Nguyen Duc Tuyen

Abstract A reduction of anthropogenic CO₂ emissions and extensive demand for electricity has motivated cleaner power production. Renewable energy source from biomass features an alternative option for sustainable energy generation. Innovation in biomass gasification with combined heat and power (BG-CHP) system emerges as a potential technology to achieve and stimulate the Sustainable Development Goal 11 (SDG 11: Climate Change). Nevertheless, a major problem of BG-CHP is its bulkiness and inconvenient form of biomass along with the multifaceted process behavior. All these feature non-linearities as well as high process interactions, and therefore require a control advancement to ensure feasible and flexible operation. Two different types of controllers [viz; proportional, integral, and derivative controller (PID) and Model Predictive Controller (MPC)] are designed and evaluated to identify the best control system via set point tracking scenario. Embedment of MPC into palm kernel shell BG-CHP plant outperformed the performance of PID controller with minimal overshoot and precise set-point tracking. The findings obtained from this study are valuable in identifying the practicability of BG-CHP system as a sustainable and clean waste to energy (WtE) technology.

Keywords MPC · PID · Biomass gasification

Y. H. Kok · N. Kamarulzaman · Z. F. Mohd Shadzalli · N. Abdul Manaf (✉)
Department of Chemical and Environmental Engineering, Malaysia-Japan International Institute of Technology (MJIT), Universiti Teknologi Malaysia, Kuala Lumpur, Malaysia
e-mail: norhuda.kl@utm.my

K. N. A. K. A. Shah · M. Z. M. Yusop · J. M. Rohani
School of Mechanical Engineering, Faculty of Engineering, Universiti Teknologi Malaysia, Johor, Malaysia

B. Hartono
Mechanical and Industrial Engineering Department, Gadjah Mada University, Yogyakarta, Indonesia

N. D. Tuyen
School of Electrical Engineering, Hanoi University of Science and Technology, Hanoi, Vietnam

1 Introduction

Aligning with the country's economic growth and urbanization, energy is a vital role in supporting the activity of industrial, agricultural as well as daily human lives. The main sources of energy supply in Malaysia are crude oil and petroleum products (46.8%), natural gas (41.3%), coal and coke (9.1%), and hydro (2.8%) [8]. Recently, World Energy Markets Observatory (WEMO) reported that Malaysia's energy usage is projected to increase by 4.8% right up to 2030. This scenario may subsequently increase the emission of greenhouse gas (GHG) since Malaysia is heavily relied on the fossil fuel energy generation. On contrary, raising of oil price and challenges in supplies of fossil fuel as well as awareness about reduction of GHG emission have created a demand for clean energy from renewable to overcome this issue [10]. Comparing to fossil fuels, a renewable resource such as biomass is considered as carbon neutral because the GHG produced during gasification process can be reutilized through the process [15]. Furthermore, the emission of NO_x and SO_x is lower, hence, acid rain formation could be avoided [12].

Oil palm waste, among other biomass forms, has the greatest potential for energy production in Malaysia, as Malaysia is the world's second-largest producer and exporter of palm oil after Indonesia [2]. In palm oil mills, the conversion of fresh fruit bunches (FFB) into crude palm oil (CPO) will produce several types of wastes such as empty fruit bunch (EFB), mesocarp fiber, palm kernel shell (PKS) and palm oil mills effluent (POME). In the conversion of palm oil, 90% of them is in the form of waste while only 10% palm oil is produced [3]. Among the waste, PKS has lower moisture content and high calorific value which make it exhibits excellence biomass feedstock for energy generation.

Biomass gasification combined heat and power (BG-CHP) system is a promising renewable technology that has potential to be commercially installed in Malaysia. Nevertheless, the major problem of BG-CHP system is its bulkiness and inconvenient form of biomass along with the multifaceted process behavior. All these feature nonlinearities as well as high process interactions thus require implementation of an advance and robust control strategy to ensure stable and feasible operation under the unprecedented plant perturbation.

At present, application of control system has proven to provide positive impact to the industrial plants in achieving optimal operation and economic feasibility. Employment of simple modelling approach usually required for the control analysis study to reduce the complexity of the evaluation but still able to mimic the actual plant operation. Several studies have used conventional feedback control system (i.e., proportional, integral, derivative, PID) to control the performance of gasifier process. For instance, Vijay Daniel and Sanjeevi Gandhi [16] employed PID controller to control reaction temperature of downdraft biomass gasification system by manipulating the air flowrate. In their work, a second order-plus-time-delay model was derived to mimic the system. Their result showed that installation of PID controller was able to improve the process settling time at approximately 80% subjected to set point tracking and regulatory changes. Huang and Shen [11] carried out a study on the maximum

hydrogen production of coal gasification plant by manipulating the water flowrate using different control configurations. A mathematical modelling and control analysis was built and simulated in Simulink Matlab. It was observed that employment of multiple adaptive neural fuzzy inference system (MANFIS)-particle swarm optimization (PSO)-PID was able to improve the hydrogen production efficiency by 25.43% and reduction of slag formation of the gasifier by 36.8%, compared to other control configurations.

An advanced and intelligent control approach features significant element in the modern and high-end industrial plant due to its capability to accommodate robust operation subsequently generate feasible income and provide plant safety. Böhler et al. [6] and Elmaz and Yücel [9] indicated that model predicted based algorithm exhibited excellent control performance compared to conventional feedback controller. A fuzzy model predictive control (FMPC) and linear model predictive control (LMPC) outperformed the PI controller two times better stationary performance based on the calculated root mean square error (RMSE). Whereas, both controllers were able to optimally control water supply temperature of biomass furnace, oxygen concentration of the flue gas and freeboard temperature [6]. Similarly, MPC was successfully controlled the syngas composition and high heating value (HHV) at set point of 10 MJ/kg to maximize the power output. Based on the aforementioned work, data driven identification model has been employed to reflect the biomass gasification process in Simulink, Matlab [9]. Table 1 summarizes the existing studies related to control analysis of gasification process.

Based on the existing studies, there is scarce work has been done on the control analysis of BG-CHP system with target variable, power output. Thus, this work presents a control analysis (closed loop analysis) of BG-CHP system to assess the performance of plant subjected to intermittent power output (reflect as plant control objective). The objective here is to evaluate the plant's feasibility and capability while considering the embedment of control system. Two control schemes (viz; PID and MPC) are designed and evaluated to identify the best control system via servo problem (intermittent power output). The structure of this paper is as follows: Sect. 2 presents the development of BG-CHP dynamic model and BG-CHP control design. Finally, result and conclusions from this study are presented in Sect. 3.

2 Modelling of BG-CHP System

2.1 *A Dynamic BG-CHP Flowsheet Model in Aspen Plus Software*

In this work, Aspen Plus (Aspen Technology, Inc.) software is used to develop a BG-CHP dynamic flowsheet model. A steady state BG-CHP system is initially developed using Aspen Plus software based on the actual unit operation of 20 kW pilot scale manufactured by APL Power Pallets [1]. This steady state PKS BG-CHP model was

Table 1 Summary of existing studies related to control analysis of different type of gasification plants

Reference	Modelling approach	Control system	Plant type	Control Objective	Manipulated variable	Output/finding
Elmaz and Yücel [9]	NARXNN	MPC	Downdraft gasifier	Syngas composition HHV	Equilibrium ratio	MPC can stabilize the output at desired level in all cases
Böhler et al. [6]	Grey box model	MPC FMPC PI	Biomass combustion furnaces	Supply water temperature Oxygen concentration of the flue gas Freeboard temperature	Fuel mass flow of wet biomass The primary air from below the grate and additional air inlet	FMPC controller shows the best result in the considered categories
Huang and Shen [11]	Mathematical model	PID MANFIS-PID PSO-PID MANFIS-PSO PID	Counter-current gasifier	H ₂ production	Water flow rate	Gasifier under the MANFIS- PSO-PID control not only obtains the maximum hydrogen production but also reduce slag formation
Vijay Daniel and Sanjeevi Gandhi [16]	Empirical model	PID	Downdraft biomass gasifier	Temperature	Air flow	PID shows a better result than manual controller
Seepersad, Ghouse, and Adams (2015)	Mathematical model	PI	Co-current, and counter-current gasifier	Tube gas exit temperature CH ₄ slip	Flow rate into the SMR tube Steam-to-carbon ratio (RS/C)	The control system of counter-current system is better than co-current

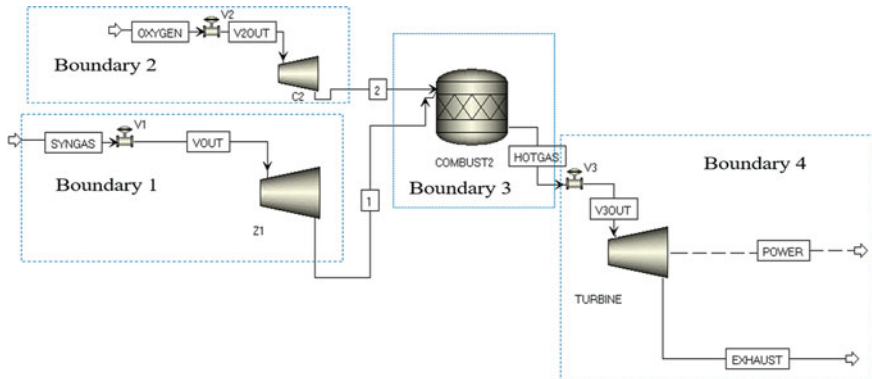


Fig. 1 A dynamic BG-CHP flowsheet model in Aspen Plus workspace and the model boundaries

directly adopted from the study conducted by [4]. Valves are added to the steady-state flowsheet to provide pressure drop for material flow with selection of pressure-driven dynamic simulation. The gasification process (in steady state flow sheet) is represented by the syngas stream in Aspen Dynamic Simulation to reduce the complexity of simulation process as illustrated in Fig. 1. A 21,601 data with 6 min interval time is generated from the Aspen Dynamic simulation and data is exported to the Matlab workspace.

2.2 An Empirical Model of BG-CHP System in Simulink, Matlab Software

From the dataset obtained in Aspen Dynamics, an empirical model (data-driven model) based on non-linear autoregressive with exogenous input (NLARX) technique is developed using System Identification Toolbox, in Matlab environment. Four process boundaries (as shown in Fig. 1) are individually modelled using NLARX approach before being integrated to represent a complete BG-CHP system, as increasing the number of boundaries is able to obtain a higher accuracy of model [5]. A developed NLARX-BG-CHP illustrated in Fig. 2 has priorly undergone validation process with averaged 85% best-fit via five-step-ahead prediction output at 95% confidence level. The NLARX-BG-CHP model built in Simulink, Matlab consisted of 6 inputs and 1 output as shown in Fig. 2.

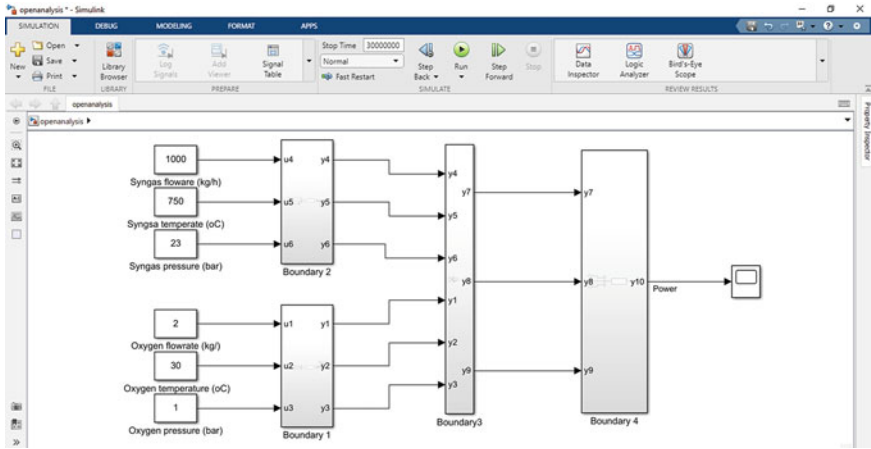


Fig. 2 An empirical model of NLARX-BG-CHP model in Simulink, Matlab

2.3 Control Design of BG-CHP System

This work uses Simulink environment as the control analysis platform due to its computational efficiency in evaluating and simulating the controller performance with more realistic plant dynamics [7]. Two different types of controllers which are conventional feedback PID controller and MPC are designed and evaluated to identify the best control system via set point tracking scenario. A control pairing for PID controller and MPC is syngas flowrate (as the manipulated variable) and power output (as the control variable). Intermittent power output in a range of 12–20 kW for 10-h operation is simulated to reflect hypothetical operation of large-scale BG-CHP plant at peak and off load. In this analysis, ready to use PID and MPC toolbox are used and embedded into the BG-CHP model.

3 Modelling of BG-CHP System

3.1 A Control Scenario

Control analysis is conducted around nominal operating condition based on the actual operation of biomass gasification pilot plant. One can refer to Annuar et al. [4] and Rasid et al. [13] on the detail operation of pilot plant. Table 2 shows the control algorithm and parameters set in the PID and MPC toolbox in Simulink workspace. An auto-tuning set-up was selected for both controllers.

An intermittent set point trajectories at 15–18–12–15–20 kW is simulated based on 10-h operation as illustrated in Fig. 3. Based on this in-depth analysis, MPC

Table 2 Control parameter setting in PID and MPC toolbox in Simulink, Matlab

Parameter setting	PID	Parameter setting	MPC
P	0.809	Prediction horizon	10
I	0.453	Control horizon	2
D	-0.214		

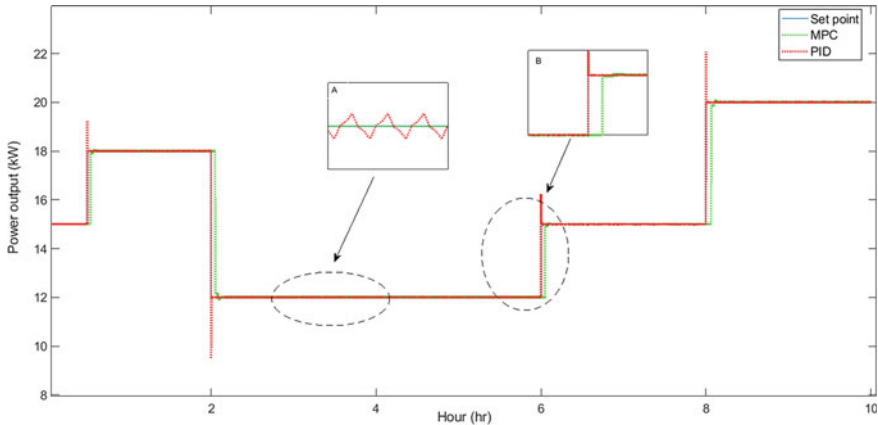


Fig. 3 Control performance analysis of power output (set point trajectories) for PID controller and MPC

outperformed the PID controller performance in meeting the set points of power output in BG-CHP system. This can be highlighted during the constant power output (constant set point), where PID unable to stabilize/maintain the power output where minor oscillation was exhibited throughout those period as shown in block A. While MPC was efficiently tracked the power output’s set point without any fluctuation. This outcome evident that MPC is able to explicitly predict the future behavior of the plant as well as capable to optimally reduce the process variance.

On the hand, during the set point transitions/changes, MPC is successfully minimize the overshoot with minimal delay at approximately 5 min as shown in block B. Whilst, significant overshoot is exhibited under the sudden change of power output (block B) which evident that PID controller unable to provide efficient control performance under the multifaceted condition (reflected by the intermittent power output). Diminutive control error (root means square error) was demonstrated for PID and MPC controllers at approximately 0.02. Nevertheless, in this case, MPC is technically preferable to be embedded with BG-CHP system due to it robustness and capability to work under the complex process and unprecedented disturbances. This verdict can be explained as follows: According to the control profile, it can be seen that at the on-set of power transition (increment and decrement), MPC requires only minimum ramp up/ramp down if compared to the PID controller. Where, similar performance was found in the study conducted by Seyab and Cao [14].

4 Conclusion

This paper used a previously developed steady-state BG-CHP flowsheet model before converted to the dynamic flowsheet in Aspen Dynamic. A dynamic data obtained from Aspen Dynamic was used to develop a data driven NLARX model for control analysis in Simulink, Matlab. Application of PID controller has contributed to large overshoot with consistent oscillation throughout the set-point (power output). Contrariwise, MPC was able to efficiently track the power output's set point with minimal delay during the transition or changes of power output. Results obtained in this study indicated the robustness of the developed MPC thus enhance the dynamic performance and provide good process controllability.

This preliminary control study of BG-CHP system is able to provide insight for the feasible and optimal operation of large-scale BG-CHP plant subsequently contribute to reduction in costs of the plant.

References

1. ALL Power Labs (2020) ALL Power Labs: about us. <http://www.allpowerlabs.com>
2. International Trade Administration. www.trade.gov, last accessed 2021/6/20
3. Abdullah N, Sulaiman F, Aliasak Z (2013) A case study of pyrolysis of oil palm wastes in Malaysia. AIP conference proceedings. American Institute of Physics, pp 331–336
4. Annuar NN, Kamarulzaman N, Shadzalli Z, Abdullah I, Liew P, Manaf N (2021) Simulation of Palm Kernel Shell gasification for small scale power generation using Aspen Plus Software. IOP conference series: materials science and engineering. IOP Publishing, p 012054
5. Ashok S, Siby J (2010) Application of model predictive controller in gasifier power plant. International conference on system modelling, optimisation and advanced process automation
6. Böhler L, Krail J, Görtler G, Kozek M (2020) Fuzzy model predictive control for small-scale biomass combustion furnaces. Appl Energy 276:115339
7. Chinpravit J, Panjapornpon C (2020) Model predictive control of vinyl chloride monomer process by Aspen Plus dynamics and MATLAB/simulink co-simulation approach. IOP conference series: materials science and engineering. IOP Publishing, p 012080
8. Chua SC, Oh TH (2010) Malaysia's national energy developments: key policies, agencies, programmes and international involvements. Renew Sustain Energy Rev 2916–2925
9. Elmaz F, Yücel Ö (2020) Data-driven identification and model predictive control of biomass gasification process for maximum energy production. Energy 195:117037
10. Esmaeili A, Shokoohi Z (2011) Assessing the effect of oil price on world food prices: application of principal component analysis. Energy Policy 1022–1025
11. Huang C-N, Shen H-T (2019) Maximum hydrogen production by using a gasifier based on the adaptive control design. Int J Hydrogen Energy 44:26248–26260
12. Rahman FA, Aziz MMA, Saidur R, Bakar WAWA, Hainin MR, Putrajaya R, Hassan NA (2017) Pollution to solution: Capture and sequestration of carbon dioxide (CO₂) and its utilization as a renewable energy source for a sustainable future. Renew Sustain Energy Rev 71:112–126
13. Rasid A, Abdullah I, Siaw C, Zani M, Shadzalli ZM, Abbas A, Manaf NA (2020) Sensitivity analysis of small scale biomass gasification-based CHP system: a way forward for sustainable urban waste to energy technology. IOP conference series: materials science and engineering. IOP Publishing, p 012123
14. Seyab RKA, Cao Y (2005) Nonlinear model predictive control for the Alstom gasifier benchmark problem IFAC Proceedings Volumes 38:69–74

15. Shen Y, Li X, Yao Z, Cui X, Wang C-H (2019) CO₂ gasification of woody biomass: experimental study from a lab-scale reactor to a small-scale autothermal gasifier. *Energy* 170:497–506
16. Vijay Daniel P, Sanjeevi Gandhi A (2017) Design of mathematical modelling and control of downdraft biomass gasifier. *Int J Control Autom* 10:175

Effects of Pineapple Leaf Fibre as Reinforcement in Oil Palm Shell Lightweight Concrete



Siew Choo Chin , Mun Lin Tang, Norliana Bakar, Jia Ling Che, and Shu Ing Doh

Abstract This paper presents the mechanical behaviour of pineapple leaf fibre (PALF) in oil palm shell (OPS) lightweight concrete (LWC). Various fibre volume fractions were considered which include 0.5%, 1.0%, 1.5% and 2.0% of PALF. In this study, the PALF was extracted and treated with sodium hydroxide solution with a 10% concentration. The length of the PALF was made constant as 40 mm based on the optimum fibre length obtained from previous work. The experimental testing in this work includes slump test, compressive strength test, splitting tensile test and four-point bending test. Results showed that the compressive strength decreased at all ages with an increase in PALF volume fraction, whereas improvement in strength was observed in both splitting tensile strength and flexural strength. The inclusion of PALF increases the tensile and flexural strength up to 3.28 MPa and 6.55 MPa respectively. The findings revealed that 1.0% PALF is the optimum fibre volume ratio for tensile and flexural strength. The oven-dry density and demoulded density of all OPS concrete mixes fall within the range of 1526–1731 kg/m³ and 1787–1853 kg/m³ which are in the range of structural lightweight concrete. The splitting tensile strength of OPS and PALF reinforced OPS-LWC in this study falls in the range to that of conventional concretes. Flexural strength to compressive strength ratio showed that all PALF reinforced OPS concretes had ratios ranging 12–22% which were greater than the usual range for lightweight aggregate concrete. Hence, this indicates that PALF fibre can improve significantly the flexural strength of OPS lightweight concrete.

Keywords Fibre · Lightweight concrete · Pineapple leaf · Reinforcement

S. C. Chin (✉) · M. L. Tang · N. Bakar · S. I. Doh
Department of Civil Engineering, College of Engineering, Universiti Malaysia Pahang, 26300
Gambang, Pahang, Malaysia
e-mail: scchin@ump.edu.my

S. C. Chin
Centre for Research in Advanced Fluid and Processes (Fluid Centre), Universiti Malaysia Pahang,
26300 Gambang, Pahang, Malaysia

J. L. Che
School of Civil and Hydraulic Engineering, Ningxia University, Ningxia 750021, China

© The Author(s), under exclusive license to Springer Nature Singapore Pte Ltd. 2023
N. H. Johari et al. (eds.), *Proceedings of the 2nd Energy Security and Chemical
Engineering Congress*, Lecture Notes in Mechanical Engineering,
https://doi.org/10.1007/978-981-19-4425-3_6

51

1 Introduction

Conventional concrete which is generally made of Ordinary Portland Cement, water, coarse and fine aggregates has a density that lies within the range of 2200–2600 kg/m³ [1]. Cement functions as the binding property of concrete. In this case, a chemical reaction between the water and cement occurred which is known as the hydration process where concrete changes from a plastic to a solid-state [2]. Several factors could affect the density and compressive strength of concrete cement paste such as water cementitious materials ratio, supplementary cementitious materials, use of admixtures, curing condition, cement type and so on [3]. Hydration of cement takes place through curing which usually consists of control of temperature and moisture movement from and into the concrete. Suitable curing application gives a significant impact on density and compressive strength [4].

Lightweight concrete is better known as a type of concrete that consists of expanding agent that can increase the volume of the mixture at the same time reduce the deadweight [5]. Lightweight coarse aggregates such as clay, slate, shale are the main ingredients towards lightweight concrete which possess low-density characteristics. According to BS EN 206-1, lightweight concrete is defined as having an oven-dry density of not less than 800 kg/m³ and not greater than 2000 kg/m³ when dense natural aggregates were replaced either wholly or partially with lightweight aggregates [6].

Concrete which is brittle in nature is strong in compression but weak in tension has the minimal capability to take tensile loads and strain capacity [7, 8]. Despite as a brittle material, concrete is still widely used as a construction material. Brittle material has weaknesses such as sudden failure without warning due to low deformation compared to ductile materials [8]. Cracking is one of the common issues in concrete which is mainly due to plastic shrinkage cracking or externally imposed loading. This can cause a reduction in the mechanical properties of concrete structures that may be harmful to the occupants and structures nearby.

To overcome the weakness and enable concrete to cater more tensile loads, fibres are introduced into the concrete. Fibres when incorporated into the concrete can change their mechanical properties, hence making them different from the conventional concrete [7]. Thus, concrete needs to be reinforced so that it can be utilized widely as construction materials. Conventional method of reinforcing is by placing steel bars in the concrete structure at suitable locations to withstand the imposed shear and tension loads. Fibres incorporated into concrete are typically short, discontinuous, being randomly dispersed throughout the concrete produces a composite construction material known as fibre reinforced concrete (FRC).

FRC has been a common solution nowadays towards a better property of tensile strength in concrete. It is also capable to reduce crack growth, increasing ductility and durability as well as impact strength. The matrix in this composite material contains a random distribution or dispersion of small fibres, either natural or artificial giving high tensile strength [9]. The fibres being dispersed uniformly in concrete gives higher cracking strength of concrete and act as crack arrestors [10].

Researchers have focused on studying various types of fibres either natural or synthetic as reinforcing material in concrete. Omar and Hamid [8] studied the stress-strain behaviour of normal concrete containing polypropylene fibre. There were investigations on the behaviour of reinforced concrete [7] and high strength concrete [11] with glass fibre. Zhou et al. [12] focused on the engineering properties of treated natural hemp fibre reinforced concrete. Mechanical properties of FRC made with basalt filament fibres [13], sisal fibre reinforced concrete (SFRC), steel and glass fibre reinforced concrete (SGFRC) [14] as well as mineral fibres and nano-silica [15]. This review shows that recent investigations have focused mainly on natural, mineral and synthetic fibres as the reinforcing material in FRC.

There were investigations to determine the performance of fibre in lightweight concrete. This includes the study of coconut fibre in super lightweight concrete [16], flexural behaviour of steel and glass fibre in lightweight concrete [17, 18], mechanical properties of structural lightweight concrete reinforced with waste steel wires [19], low volume steel fibre [20] as well as carbon and/or polypropylene fibres [21]. Most of the previous investigations focused on using synthetic fibre in lightweight concrete. Investigations on lightweight concrete incorporating natural fibres are still limited, thus further research using this material is in need.

Pineapple leaf fibre (PALF) is one of the fast-growing plants and is available abundantly in Malaysia as compared to other types of natural fibre plants [22]. This fast-growing plant can be an alternative raw material to the industries. It can be a potential replacement for synthetic fibres which are expensive and non-renewable. In this research, the experimental work was carried out to study the effect on lightweight concrete when it is reinforced with PALF fibres at various volume fractions and to determine the optimum percentage of PALF fibres.

2 Experimental Program

2.1 Materials

Raw materials. The raw materials used in this study were ASTM Type I ordinary Portland cement (OPC); silica fume (SF) named Greco SF-90D of 5% of the cement weight was included in this study; river sand with a maximum grain size of 4.75 mm and OPS in a saturated surface dry (SSD) condition, with size less than 9.5 mm. The OPS was obtained from one of the local palm oil mills in Pahang. The OPS collected was rinsed with clean water to remove the impurities and oil coatings from their surface. After rinsing, the OPS was placed outside the laboratory to allow the fibre contents to wither. A water-cement ratio of 0.3 was used for all mixes. Superplasticizer (SP) was kept constant at 1.2% of the cement weight.

Pineapple Leaf Fibre. The pineapple leaf fibre (PALF) was extracted from its leaves through a conventional decorticator machine. Dry PALF was soaked into a 10 wt%

Table 1 Mix proportions for all mixes

Cement	Coarse aggregate (OPS)	Fine aggregate (Sand)	W/C	Superplasticizer (% of cement weight)	Silica Fume (% of cement weight)
520 kg/m ³	330 kg/m ³	960 kg/m ³	0.3	1.2%	5%
			156 kg/m ³	6.24 kg/m ³	261 g/m ³

NaOH solution at 30 °C, maintaining a liquor ratio of 1:10. Fibres were kept immersed for 2 h into the alkali solution before washing it with fresh water several times to remove the alkaline solution. After washing, the fibres were dried in an oven at 80 °C for 24 h to remove the moisture content and lignin. The treated fibres were dried under the sun for several days. The fibres were then cut into pieces approximately 40 mm in length.

2.2 Mix Proportions

The mix proportions for all mixes are summarized in Table 1. The water-cement ratio used in this concrete mix design was 0.30. A dosage of 1.2% of Superplasticizer known as Sika ViscoCrete-2199, by cement weight was added.

2.3 Test Methods

Fibre volume fractions of PALF considered in this study include 0.5%, 1%, 1.5% and 2.0% percentage by weight of cement. Firstly, cement, sand and OPS were weighed and mixed for two minutes by using a concrete drum mixer. After that, the prepared cut-in-size PALF was spread evenly into the concrete drum mixer and mixed for two minutes. Finally, water and superplasticizer were mixed thoroughly for approximately 30 s before adding into the mixer and mixed for three minutes. After 24 h, the concrete specimens were demolded and cured in water. The dimension of the concrete cube considered in this study was 100 mm × 100 mm × 100 mm. Beam specimens were cast into the size of 100 mm width × 100 mm height with a total length of 500 mm whereas cylinder specimens were 100 mm in diameter with 200 mm height in size. The targeted concrete strength in this study was 30 MPa. All the concrete specimens were tested at curing ages of 3, 7, 14 and 28 days. A compressive strength test was conducted at 28 days according to the BS 1881: Part 116. Concrete specimens for splitting tensile strength and flexural strength were tested at 28 days according to ASTM C496 and ASTM 78, respectively.

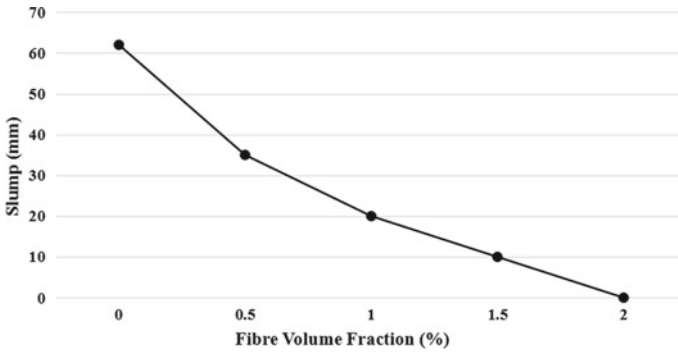


Fig. 1 Effect of PALF volume fraction on a concrete slump

3 Results and Discussion

3.1 Workability

Figure 1 shows the effect of slump versus fibre volume fractions of PALF in the lightweight concrete mix. A decreased exponential curve was observed whereby the slump was reduced concerning the increase of PALF. This resulted in the low workability of concrete. The inclusion of PALF from 0%, 0.5%, 1.0%, 1.5% and 2.0% decrease the workability. The slump result showed that adding PALF from 0%, 0.5%, 1.0%, 1.5% and 2.0% decreased the workability to approximately 43.55%, 67.74%, 83.87% and 100% as compared to the control mix. The control mix has the highest slump value which is 62 mm whereas the addition of 2.0% PALF volume fraction gives the lowest slump value. The decrease in workability could be due to the bonding of fibre-matrix in the concrete which restrained the flow of the concrete mix.

3.2 Density

Figure 2 shows the comparison of the relationship between the PALF volume fraction versus hardened density at the oven-dried condition and demoulded density. According to ASTM C 567, LWC has an air-dry density not exceeding 2000 kg/m^3 . In this study, the oven-dry density and demoulded density of all OPS concrete mixes fall within the range of $1526\text{--}1731 \text{ kg/m}^3$ and $1787\text{--}1853 \text{ kg/m}^3$ respectively. Hence, this signifies that the concrete mixes can be considered as structural lightweight concrete. Normal weight concrete will have a density in the range of $2240\text{--}2400 \text{ kg/m}^3$. The oven-dry density and demoulded density for all lightweight mixes are approximately 29% and 21% lower than normal-weight concrete taken as 2300 kg/m^3 . Hence, there

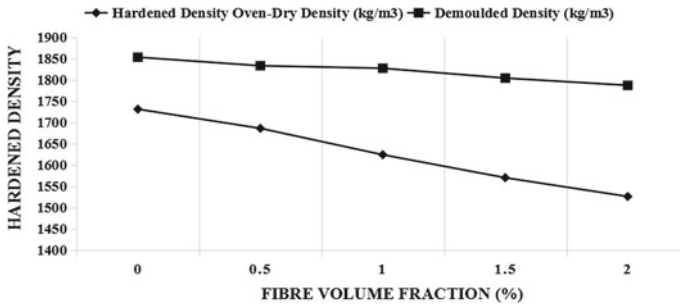


Fig. 2 Effect of PALF volume fraction on concrete hardened density

are substantial cost savings by providing less dead load for lightweight concrete in this study.

3.3 Compressive Strength

Compressive strength results at 3, 7, 14 and 28 days are summarized in Table 2. The control concrete had a 28-day compressive strength of 41.7 MPa. It is noticeable that the compressive strength of OPS-LWC decreased at all ages with an increase in PALF volume fraction as shown in Fig. 3. The mixes from 0.50 to 2.00% fibre volume fraction decrease the compressive strength by 19.48%, 7.35% and 7.18% at 3 days, 9.78%, 8.45% and 9.88% at 7 days, 10.53%, 6.07% and 9.92% at 14 days, 10.58%, 6.22% and 6.39% at 28 days, respectively. Holm et al. [23] reported that the 7 days strength to 28 days strength ratio for high strength lightweight concrete normally is between 86 and 92%. Many researchers have proved that the use of fibre has a relatively low effect on the enhancement of compressive strength and may even decrease further [20]. In this study, the addition of PALF does not give significant improvement to the compressive strength. This may be due to the high water absorption of OPS and fibres. Water content may also affect the development of concrete strength as cement needs to react with water during the hydration process.

Table 2 Development compressive strength of OPS concrete in continuously moist curing

No	Description	Compressive strength (MPa)			
		3rd day	7th day	14th day	28th day
1	Control	29.60 (71.0%)	33.80 (81.1%)	38.50 (92.3%)	41.70
2	0.50% fibre	22.95 (67.8%)	25.97 (76.7%)	30.49 (90.1%)	33.84
3	1.00% fibre	18.48 (61.1%)	23.43 (77.4%)	27.28 (90.2%)	30.26
4	1.50% fibre	17.12 (60.3%)	21.45 (75.6%)	25.62 (90.3%)	28.38
5	2.00% fibre	15.89 (59.8%)	19.33 (72.8%)	23.08 (86.9%)	26.57

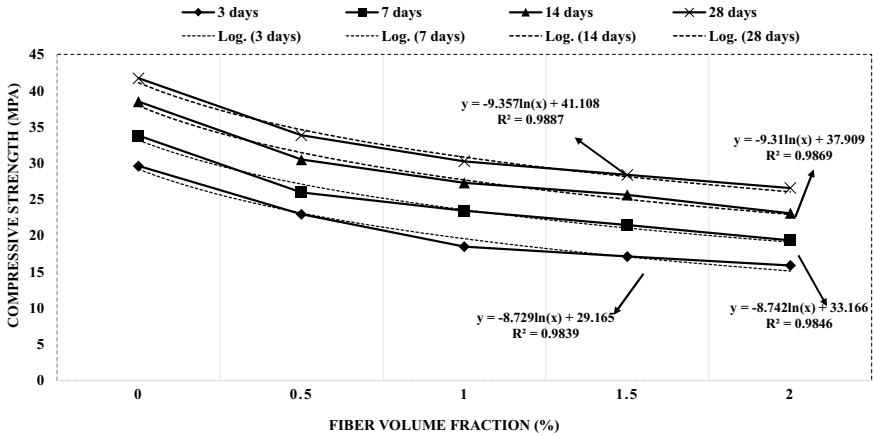


Fig. 3 Effect of fibre volume fraction on compressive strength

Furthermore, high fibre content increases the probability of fibre agglomeration, the uneven distribution of fibre in cement paste will affect concrete strength significantly [24].

3.4 Splitting Tensile Strength

Figure 4 shows the correlation between the effects of fibre volume fraction and splitting tensile strength. In this study, the control concrete showed a splitting tensile strength of 3.12 MPa. The OPS concrete added with 1% PALF exhibited the highest strength of 3.28 MPa. The development of tensile strength could be due to the crack arresting ability of fibres, whereby the tensile stress was transferred across the fibres and inhibited the crack extension, giving rise to the splitting tensile strength of concrete [25]. Similar to the trend reported in the work of [25] that a decrease in

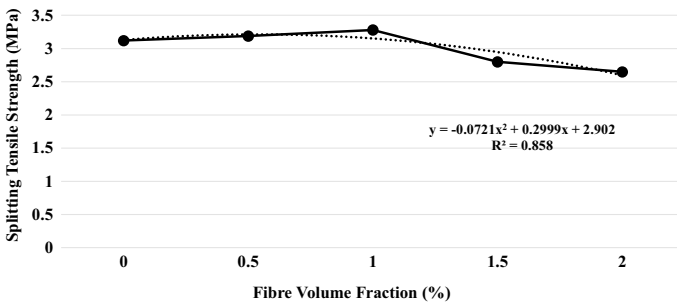


Fig. 4 Effect of fibre volume fraction on splitting tensile strength

splitting tensile strength was observed even lower than control concrete when the fibre was added beyond 1%. The reduction in strength is because of the balling effect. As the surface area of fibres increased, a larger amount of cement mortar was required to coat the fibres. As a result, the strength was reduced due to the large growth of porosity.

The splitting tensile strength of OPS concrete (control) and PALF fibre OPS concrete at 28 days was 3.12 and 3.28 MPa, respectively which is about 7.6% and 10.84% of the compressive strength. This shows that the PALF fibre enhanced the splitting tensile to compressive strength ratio. In general, the splitting tensile strength of conventional concrete is about 8 to 14% of the compressive strength [26]. The splitting tensile strength of OPS and PALF reinforced OPS-LWC in this study falls in the range to that of conventional concretes. Normally, LWAC possesses a lower splitting tensile strength to compressive strength ratio than the conventional concrete at the same compressive strength, even with the addition of fibre [25, 27]. It can be regarded that the PALF reinforced OPS concretes had similar or even higher splitting tensile strength than normal concrete of the equivalent compressive strength.

3.5 Flexural Strength

Figure 5 plots the results of flexural strength versus fibre volume fraction. A linear increasing trend was observed from 0% up to 1% at 28 days curing, 4.805 MPa to 6.55 MPa. A decrease in trend was observed at 1.5% and 2% with a flexural strength of 5.65 MPa and 5.317, respectively. The OPS concrete incorporating PALF with fibre volume fraction from 0.5% up to 2% showed flexural strength higher than the control mix, in the range of 6% up to 20%. Hence, it is evident that the improvement of flexural strength was governed by PALF. It was reported that the flexural strength of lightweight aggregate concrete is about 9–11% of 28-day compressive strength [23]. In this study, all PALF reinforced OPS concretes had ratios ranging 12–22%

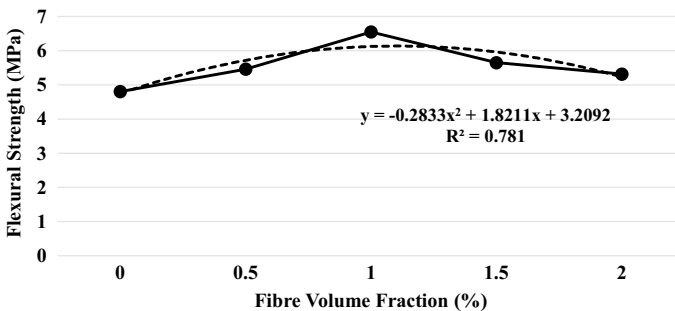


Fig. 5 Effect of fibre volume fraction on flexural strength

which were greater than the usual range for lightweight aggregate concrete. This indicates that PALF can improve considerably the flexural strength of OPS concrete.

4 Conclusions

In this study, the oven-dry density and demoulded density of all OPS concrete mixes fall within the range of 1526–1731 kg/m³ and 1787–1853 kg/m³ which are in the range of structural lightweight concrete. The splitting tensile strength of OPS and PALF reinforced OPS-LWC in this study falls in the range to that of conventional concretes. Flexural strength to compressive strength ratio showed that all PALF reinforced OPS concretes had ratios ranging 12–22% which were greater than the usual range for lightweight aggregate concrete. Hence, this indicates that PALF fibre can improve significantly the flexural strength of OPS lightweight concrete.

Acknowledgements This research is supported by the internal grant of Universiti Malaysia Pahang PGRS 200375. The authors would like to acknowledge the Centre for Research in Advanced Fluid and Processes (Fluid Centre) and the Faculty of Civil Engineering Technology, Universiti Malaysia Pahang for the equipment and facilities provided.

References

1. Neville AM (2000) Properties of concrete, 4th edn. Longman, England
2. Neville AM (1996) Properties of concrete, 4th edn. Wiley, USA, New York
3. Rasa E, Ketabchi H, Afshar MH (2009) Predicting density and compressive strength of concrete cement paste containing silica fume using artificial neural networks. *Trans A Civil Eng* 16(1):33–42
4. Raheem AA, Soyingbe AA, Emenike AJ (2013) Effect of curing methods on density and compressive strength of concrete. *Int J Appl Sci Technol* 3(4)
5. Ismail KM., Fathi MS, Manaf N (2004) Study of lightweight concrete behaviour. Universiti Teknologi Malaysia
6. Owens PL, Newman JB (2003) Lightweight aggregate. *Advanced concrete technology 1: constituent materials*
7. Alsadey S, Abdallateef M, Mohamed M, Milad A (2021) Investigating behaviour of reinforced concrete with glass fibre. *Jurnal Kejuruteraan* 33(3):551–557
8. Omar SMA, Hamid HA, Stress-strain behavior of normal concrete containing polypropylene fibre
9. Sonule SJ, Deshmukh GP (2017) Study of conventional concrete, fiber reinforced concrete and self curing concrete. *Int J Res Trends Innov* 2(8):74–82
10. Parra-Montesinos GJ (2005) High-performance fiber-reinforced cement composites: an alternative for seismic design of structures. *ACI Struct J* 102(5):668
11. Hilles MM, Ziara MM (2019) Mechanical behavior of high strength concrete reinforced with glass fiber. *Eng Sci Technol Int J* 22(3):920–928
12. Zhou X, Saini H, Kastiukas G (2017) Engineering properties of treated natural hemp fiber-reinforced concrete. *Front Built Environ* 3:33

13. Iyer P, Kenno SY, Das S (2015) Mechanical properties of fiber-reinforced concrete made with basalt filament fibers. *J Mater Civ Eng* 27(11):04015015
14. Chaichannawatik B, Sirisonthi A, Hussain Q, Joyklad P (2018) Mechanical properties of fiber reinforced concrete. *Appl Mech Mater* 875:174–178
15. Larisa U, Solbon L, Sergei B (2017) Fiber-reinforced concrete with mineral fibers and nanosilica. *Procedia Eng* 195:147–154
16. Hardjasaputra H, Ng G, Urgessa G, Lesmana G, Sidharta S (2017) Performance of lightweight natural-fiber reinforced concrete. In: *MATEC web of conferences*, vol 138. EDP Sciences, p 01009
17. Infant Alex X, Arunachalam K (2019) Flexural behavior of fiber reinforced lightweight concrete. *Revista de la construcción* 18(3):536–544
18. Kumar JDC, Arunakanthi E (2018) Experimental analysis of light weight concrete and fiber reinforced concrete. *Int J Civil Eng Technol* 9:59–69
19. Aghae K, Yazdi MA, Tsavdaridis KD (2014) Mechanical properties of structural lightweight concrete reinforced with waste steel wires. *Mag Concr Res* 66(1):1–9. ISSN 0024-9831
20. Hassanpour M, Shafigh P, Mahmud HB (2014) Mechanical properties of structural lightweight aggregate concrete containing low volume steel fiber. *Arab J Sci Eng* 39(5):3579–3590
21. Wei H, Wu T, Yang X (2020) Properties of lightweight aggregate concrete reinforced with carbon and/or polypropylene fibers. *Materials* 13(3):640
22. Asim M, Abdan K, Jawaid M, Nasir M, Dashtizadeh Z, Ishak MR, Hoque ME (2015) A review on pineapple leaves fibre and its composites. *Int J Polym Sci*
23. Holm TA, Bremner TW (2000) State-of-the-art report on high-strength, high-durability structural low-density concrete for applications in severe marine environments. US Army Corps of Engineers, Engineer Research and Development Center. Technical Report. 00-2. ERDC/SL TR-00-3
24. Pickering KL, Efendy MGA, Le TM (2016) Composites : Part A. A review of recent developments in natural fibre composites and their mechanical performance 83:98–112
25. Chin SC, Wong QHR, Lim KS, Doh SI (2021) Performance of oil palm shell lightweight concrete incorporated with bamboo fiber. In: *Proceedings of the international conference on civil, offshore and environmental engineering*. Springer, Singapore, pp 405–412
26. Kosmatka SH, Kerkhoff B, Panarese WC (2003) Design and control of concrete mixtures. Portland Cem Assoti, USA
27. Rossignolo JA, Agnesini MVC, Morais JA (2003) Properties of high-performance LWAC for precast structures with Brazilian lightweight aggregates. *Cement Concr Compos* 25(1):77–82

Pedal Error Naturalistic Driving Study Among Malaysian Drivers



Mohamad Zairi Baharom, Zulkifli Ahmad Manap, Nursya Mimie Ayuny Ismail, Mohd Hasnun Arif Hassan, Juffrizal Karjanto, and Khairil Anwar Abu Kassim

Abstract The article discussed about pedal misapplication or pedal error among Malaysian drivers. The variability of driver's foot movement could result in an error in foot placement. The farther the foot from the intended pedal, the larger the potential errors to occur while hitting the pedal. The goals of this research are to conduct a study to determine the Malaysian driver's foot placement on pedal and the total emergency braking response during the normal driving and emergency braking situation, and also to define the sources of foot placement errors and factors which contributing to the wrong pedal placement among Malaysian drivers. The scopes of this research are to develop a test setup to determine the foot placement on pedal by using video observation and measure the total emergency braking response by using force sensor, to determine the source of foot placement errors and to define the factors contributing to the wrong pedal placement. The study is limited to automatic transmission car, Malaysian drivers aged from 20 to 65 years old. In order to conduct the naturalistic driving test, an instrumented car is prepared and equipped with some important instruments such as cameras, force pressure sensor, light cue device, audio cue device and Arduino hardware. A study has been successfully conducted to determine the Malaysian driver's foot placement on the pedal during the emergency braking. According to our research, 10% of the participants from the driving study conducted use both legs while driving and press the brake pedal using their left foot during emergency braking. It is dangerous for other drivers because the brake light can turn on at any time, causing other drivers to become distracted.

M. Z. Baharom (✉) · Z. A. Manap · N. M. A. Ismail · M. H. A. Hassan
Faculty of Mechanical and Automotive Engineering Technology, Universiti Malaysia Pahang,
26600 Pekan, Pahang, Malaysia
e-mail: mohamadzairi@ump.edu.my

J. Karjanto
Faculty of Mechanical Engineering, Universiti Teknikal Malaysia Melaka, Hang Tuah Jaya,
Durian Tunggal, 76100 Melaka, Malaysia

K. A. A. Kassim
Malaysian Institute of Road Safety Research (MIROS), 43000 Kajang, Selangor, Malaysia

Keywords Pedal error · Pedal misapplication · Sudden unintended acceleration (SUA) · Foot pedals · Naturalistic driving study

1 Introduction

One of the most common causes of death, disability, and hospitalization is from the road accidents. According to a research from Malaysia's Department of Road Safety, there are about 30.2 million vehicles registered in the country over the last 10 years [1]. A total of 9355 deaths in Malaysian road accidents are reported between January 2018 and December 2019, which motorcycle and passenger vehicle users account for the majority of deaths, accounting for 84% of all deaths [1]. Malaysian Institute of Road Safety (MIROS) has conducted a research and found that 80.6% of road accidents were caused by human error, 13.2% by road conditions, and only 6.2% were caused by vehicles [1].

One of the factors that lead to road accidents is when there are too many construction projects going on at the same time, the designs of urban infrastructure can be regarded barriers [2]. It can cause confusion to the drivers as they are unfamiliar with the route and it is possible for an accident to occur. Other than that, distracted driving is another factor that contributes to road accidents. It can happen in a variety of ways, including using and talking on a cell phone, which can cause mental distraction [3]. Also in Malaysian road accidents, overtaking, driving in the other lane, and tailgating are all contributory factors [4]. In Malaysia, speeding, running red lights, and drunken driving are all factors that lead to traffic accidents in Malaysia [5].

However, sudden unintended acceleration (SUA) is one of the serious issues, which causes injuries and deaths every year on the road. SUA is defined as an unintentional, unexpected, and high-powered acceleration from a stationary or moving position that is accompanied by a loss of apparent braking effectiveness [6]. The unintended acceleration could also happened when a driver intends to press his/her right foot on the brake while shifting from Park (P) to a drive gear [drive (D) or reverse (R)] but ended up step on the accelerator pedal (full-throttle acceleration and cause a crash) [7]. Pedal error has been identified as a prominent factor in these types of accidents by a number of publications [7, 8]. Pedal misapplication events that resulting in crashed have been a matter of discussion for decades [9]. The designers have attempted to build various mixed brake-accelerator pedals in order to reduce the chance of the operator's risk of pressing the wrong pedal [10]. There are several research areas that related to the pedal error study. A research in [11] in the United States of America (USA) aims to examine the factors, which might cause the pedal errors. In their study, they look into how do the pedal application types related with the foot placement on the pedal and investigates whether the error is related to the previous foot locations or not. Meanwhile, a study explored the effect of phone conversations and other potential interference on reaction time (RT) in a braking response [12]. A questionnaire survey was conducted among the elderly

aged 65 years and above to explore key issues with the driving experiences of older compared with younger drivers [13].

The correlation between pedal operations (foot manoeuvres) and drivers' workload by using the mechanism of workload on sloped segments of mountainous roads have been studied in [14]. The study performed naturalistic driving tests on two-lane mountainous roads in China. Another study looked at two types of accidents and their relative frequencies in order to figure out the fundamentals of pedal misapplications [7]. Besides, [9] use police-reported crash data (year 1994–2009) to find out about the crash characteristics and other circumstances that contributed to the pedal misapplication events. Another study compared the braking responses of active human emergency braking (control condition), cruise control (CC), and adaptive cruise control in the event of a vehicle collision (ACC) [15]. There is also a study where the researchers in [16] looked into the reasons behind an apparent increase in single-vehicle run-off-road crashes and a decrease in multi-vehicle on-road crashes as vehicles transitioned from conventional to ABS brakes. A publication that concentrate on the ergonomics topic (sitting position) is also found where the researchers conducted a research to see if the driver's seating height affects the distance between the pedals [17]. The study looks into whether sitting lower or higher affects the accuracy of stepping on the pedals from the gas pedal to the brake pedal or not.

Numerous studied have attempted to explain the construction of their test set up and apparatus. Two multi-modal driving testbeds (including both a real-world vehicle and a driving simulator) were introduced by describing two novel joint audio-visual driving experiments and databases [18]. It was built to investigate the driver pedal misapplication error. Some researchers has discussed the creation of a basic device that includes a laptop computer and a three-pedal foot mouse for measuring response time (RT), accuracy, and flexibility of pedal application to visual stimuli [19]. Meanwhile, a research was conducted to obtain if simulators accurately depict real-world driving and how different parts of driving relate to each other [20]. Other than that, there is a study that investigated the trajectories of elderly drivers' pedal movements while driving on the road in response to changing traffic signal conditions [21].

The common research approach that most of the researchers have done in their study to investigate the pedal error is by naturalistic driving method. Naturalistic driving study is a study that records details about the driver, the vehicle, and the surroundings using unobtrusive data collection and without the use of experimental controls in order to gain insight into driver behavior during normal excursions [22].

In this project, a naturalistic driving study was conducted to determine the Malaysia driver's foot placement on pedal and the total emergency braking response during the normal driving and emergency braking situation. Other than that, this paper also emphasizes the sources of foot placement errors and factors which contributing to the wrong pedal placement among Malaysian drivers.

2 Methods

2.1 Participants

Malaysian drivers with a valid driver's license whom aged from 20 to 65 years old were invited to participate in this study. All of them are able to drive an automatic car transmission. There were 28 drivers who participated in this study and all of them have completed the study. There were 14 males and 14 females, which contribute to 50% for both male and female respectively. The participants are grouped into few groups of ages such as 20–29 years old (89.29%), 30–39 years old (7.14%), and 40 years old and above (3.57%).

2.2 Apparatus

The test car that is used to conduct this study is a 2015 Mazda 3. The car is equipped with important tools such as cameras, force sensor and lights cue device. However, the audio cue is produced by connecting the Bluetooth from a cellphone to the car audio system.

Figure 1 shows the location of the cameras and force sensor that were placed inside the test car cabin. Two action cameras (1) were placed inside the car cabin. One of the cameras was placed under the car steering wheel to capture the movement of the driver's foot from the top view. Another camera was placed on the car windshield in front of the driver to capture their face while they are driving. Force sensors (2) were attached on the brake pedal and accelerator pedal to measure the force then driver pressed the pedals. The data was processed by the data acquisition (3) that was connected to both of the sensors on the brake pedal and accelerator pedal. The light cue device (4) was placed on top of the car meter in front of the driver. The complete instrumented test car that was used in this study is as shown in Fig. 2.

Fig. 1 Location of cameras (1), force sensors (2), data acquisition (3), and light braking cue device (4) that are equipped inside the test car cabin

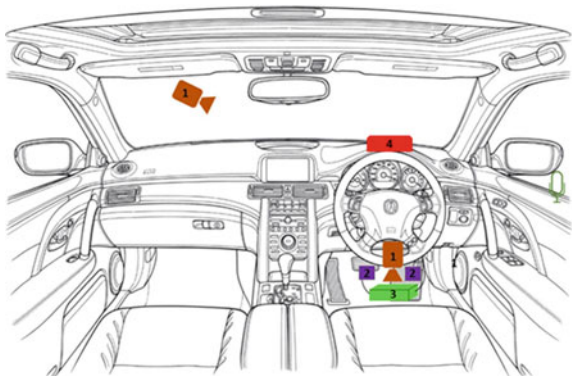




Fig. 2 Test car setup

2.3 *Naturalistic Driving Study Flow*

After arriving at the test track (Pekan Speedway Circuit, Pekan), ID number was assigned and completion of a consent form, the participants were briefed and guided to the test car to begin the test. The first round is a trial lap, which has no braking cues as its purpose was only for the drivers to suit themselves with the car and the track before proceeding to the actual test. The second lap was called Lap 1: Light Cue and third lap was Lap 2: Audio Cue. The participants were required to drive around 50–70 km/h due to safety reason. They were asked to press on the brake pedal every time they received a signal from the braking cue devices such as light cue device and audio cue. They did not need to brake until the car was completely stop instead, they only required to brake until the car speed dropped around 30–40 km/h and continued driving as usual by pressing the accelerator pedal.

The light braking cue device produced red lights as an indicator for the driver to press on the brake pedal while driving. However, for Lap 2, the braking cue was produced by the audio that came from the car audio system. They were required to press on the brake pedal once they heard a signal sounded “BERHENTI” means to stop. After finishing all the laps, every participant was required to fill in and answer a set of questionnaire. It only required about 5–10 min to answer all of the questions which are regarding to the driving experience, pedal error experience, factors of accident and also feedback about the naturalistic driving test that they have completed.

3 Result and Discussion

3.1 Naturalistic Driving Test

The questionnaire was distributed only for participants who participated in the naturalistic driving test. They filled in the form and answered the questionnaire after they finished all the laps during the driving test. The total number of participants for naturalistic driving test is 28 participants. There were 14 males and 14 females, which contribute to 50% for both male and female respectively. The participants are grouped into few groups of ages such as 20–29 years old (89.29%), 30–39 years old (7.14%), and 40 years old and above (3.57%).

Another characteristics that are taken into account is driving experience. Based on the total 28 participants, 17.86% of them have less than 2 years of driving experience, while 71.43% have 3–10 years, 7.14% with 11–20 years of driving experience, and only 3.57% have experience in driving for 21–30 years. In term of driving period in a day, 32.14% out of the total of participants drive for less than 1 h in a day, while 50% drive for around 2–3 h, and 17.86% drive for about 4–5 h per day. It can be concluded that most of the participants drive for around 2–3 h per day.

3.2 Driving Experience

Figure 3 shows the statistics for driving experience by the participants for naturalistic driving test. It can be observed that only 53.57% from the total of 28 participants have experienced pedal error while driving. Based on the data, there are 14 participants (87.5%) out of 16 have experienced pedal error, have accidentally pressed on

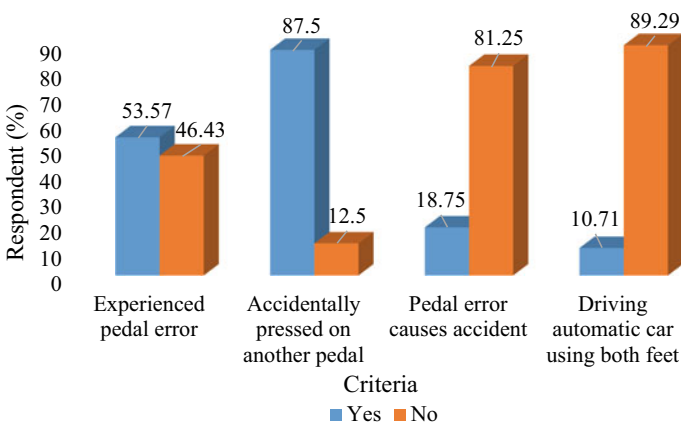


Fig. 3 Percentage of respondent response

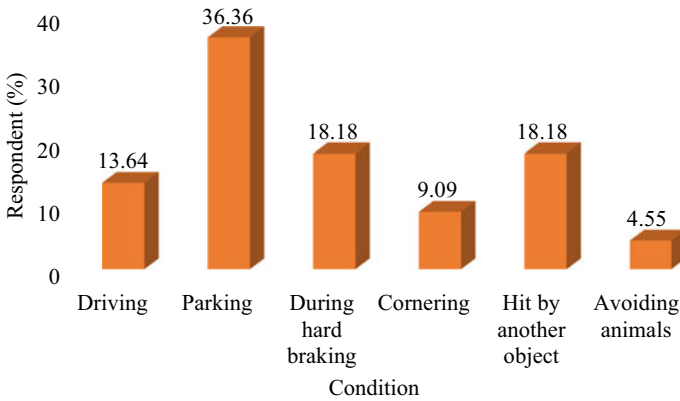


Fig. 4 Percentage of respondent response for condition of pedal error

accelerator pedal instead of brake pedal. Meanwhile, the remaining 2 participants who contributes 12.5% never mistakenly pressed the accelerator pedal while wanted to press on brake pedal. However, 18.75% of the participants who have ever accidentally pressed on accelerator pedal instead of brake pedal has caused road accident. Among 28 participants, 10.71% or 3 participants drive the automatic transmission car using both feet, while another 89.29% only use right leg to drive the automatic transmission car.

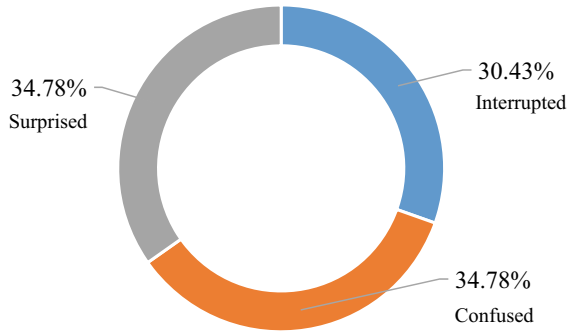
3.3 Pedal Error Condition

Figure 4 shows the pedal error conditions that were experienced by 15 participants. Most of them have ever experienced pedal error during parking (36.36%), followed by during hard braking (18.18%), and after they got hit by another object (18.18%). Only 13.64% of them experienced pedal error during driving, cornering (9.09%), and the least condition of pedal error to occur is while avoiding animals (4.55%).

3.4 Pedal Error Factors

Based on Fig. 5, 30.43% of 15 participants are disturbed while driving and that has caused them to accidentally pressed on another pedal instead of the pedal which they wanted to press. However, some of the participants pressed on the wrong pedal because they were confused (34.78%) and surprised (34.78%). It can be concluded that the main factors of their pedal misapplication are because of confusion and shocked, therefore they accidentally pressed on the wrong pedal of their car.

Fig. 5 Pedal error factors while driving



3.5 Factors of Road Accidents

Figure 6 shows the boxplot for the factors of road accident based on the questionnaire that were answered by the participants. Dangerous driving, changing lane dangerously and driving under influence have the highest mean of Likert scale score which were answered by 27 participants. Those factors are strongly agreed that they contribute to the factors of road accidents. However, the most disagree factors are safe driving and using turning indicator correctly. It can be seen that those factors do not contribute to road accidents.

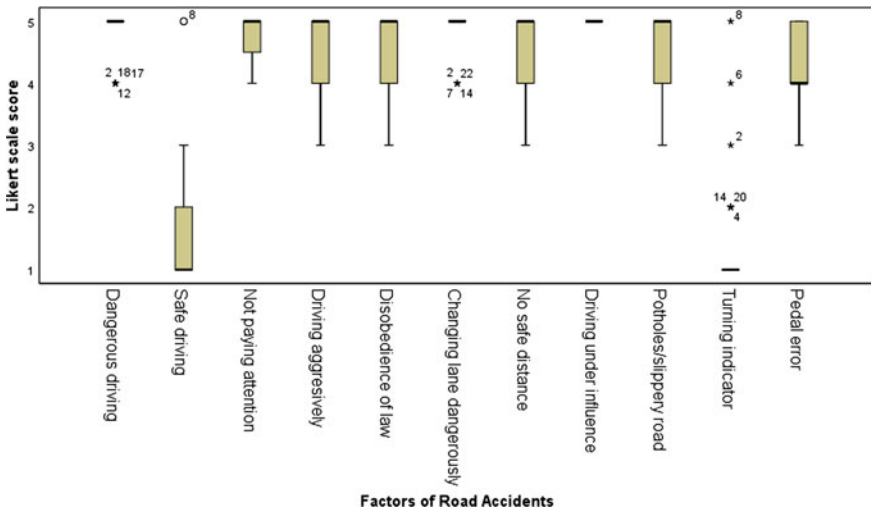


Fig. 6 Boxplot for road accident factors

3.6 Participants' Feedback for the Naturalistic Driving Study

Figure 7 shows the percentage of participants' feedback for the naturalistic driving test. The total participants of the test is 28 participants and all of them have answered all of these questions. Based on the data, 10.71% of the participants could not clearly see and understand the light cue during the test. However, there was a remark regarding to it, the difficulties to see the lights from the device was because of the LEDs were not too bright. In addition, the weather during the test was very sunny and the lights could not be seen clearly by the participants even the device was right in front of them.

However, all of the participants clearly heard and understood the audio braking cue. Since the audio that was played by the audio system was in high volume and unavoidable to not to hear. Some of the participants (7.14%) felt pressured and stressed out while running the test. Some of them also were shocked by the cues given, for light braking cue, only 17.86% were surprised by the signal and 57.14% were surprised by the audio cue. The possible reason of feeling shocked during audio braking cues is because the volume of the audio was quite high. However, there was a remark by the participant to use the audio in lower volume and different tone of voice. It might be because after the second time hearing the cue, they did not feel shocked anymore to brake the car immediately.

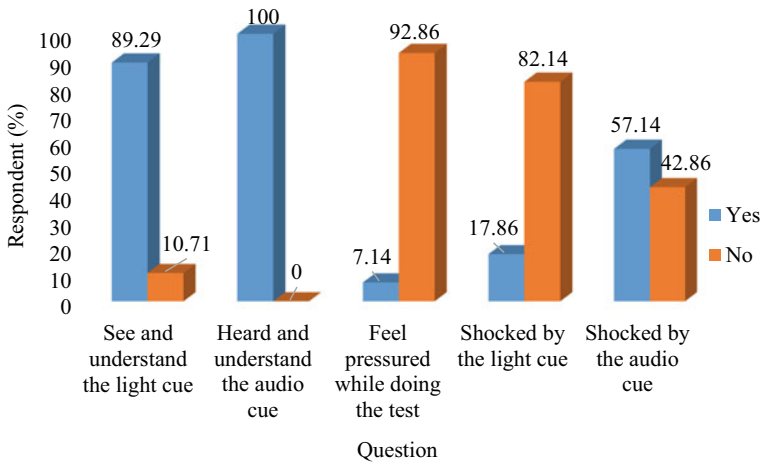


Fig. 7 Participants' feedback of naturalistic driving test

3.7 Pedal Force Comparison

The pedal force that are obtained from the force sensor used during naturalistic driving test will be discussed and compared. Based on the test that have been done, it is obtained that there are 3 participants whom drive using both legs. The force on the pedals that was recorded by the force sensor between one-legged driving behavior and two-legged driving behavior will be discussed.

Comparison between one-legged and two-legged driving behavior. A participant with one-legged driving behavior and two-legged driving behavior are chosen respectively in order to make a comparison regarding to the force applied during braking and accelerating in the study.

Figure 8a shows the graph of analog reading versus time for one-legged driving behavior by participant 22 while Fig. 8b is the analog graph reading versus time for two-legged driving behavior by participant 6. According to the graphs, one-legged driving behavior shoes the reading for accelerate and brake are always contradict to each other. Meanwhile, for two-legged driving behavior, the reading for accelerator pedal and brake pedal are almost in similar trend except during braking. For two-legged driving behavior, when the accelerator pedal is pressed, the brake pedal is also pressed.

From the observation during the test, participants who drive by using both legs always place their feet on brake and accelerator pedal all the time. Based on the graphs, the force applied when the driver put their left foot on the brake pedal while right foot pressing the accelerator pedal is quite high. It is completely different compared to one-legged driving behavior because driver who uses one leg only place their right foot on the accelerator pedal and their left foot is on the footrest or on the floor. Hence, the analog reading for the brake pedal is null since there are no forces applied on the brake pedal while accelerating.

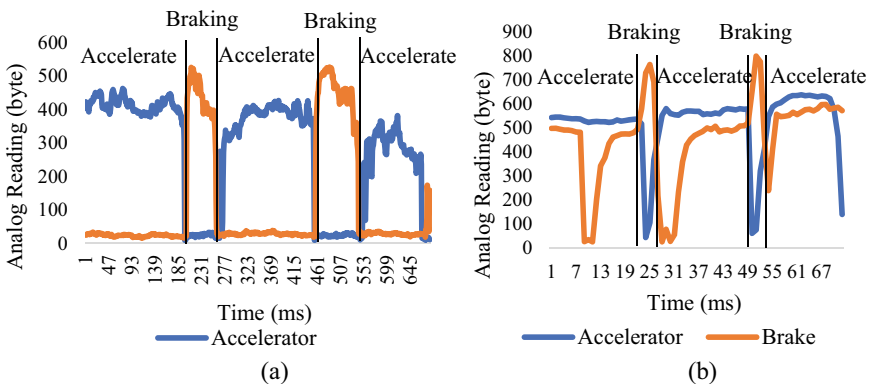


Fig. 8 Driving behavior. a One-legged (P22); b two-legged (P06)

Comparison among one-legged driving behavior. In terms of the force applied during braking and accelerating, three participants with one-legged driving behavior are compared to one another.

Figure 9 shows the graphs of analog reading versus time for 3 different participants in the naturalistic driving test. Based on the graphs shown, there are no obvious differences between those 3 participants. Since they used only one leg during driving, only one foot was on the pedal and another foot was either on the floor or on the footrest. Hence, the force for accelerator and brake pedal will always contradict to each other. For instance, when force is applied on the accelerator pedal, which means the driver only pressed on one pedal only, the brake pedal will have zero force value, and vice-versa. Therefore, it can be concluded that the driving behavior for all participants with one-legged driving behavior are similar to each other.

Comparison among two-legged driving behavior. The force applied during braking and accelerating of all the naturalistic driving study participants who drive the automatic transmission car by using both feet are compared to one another.

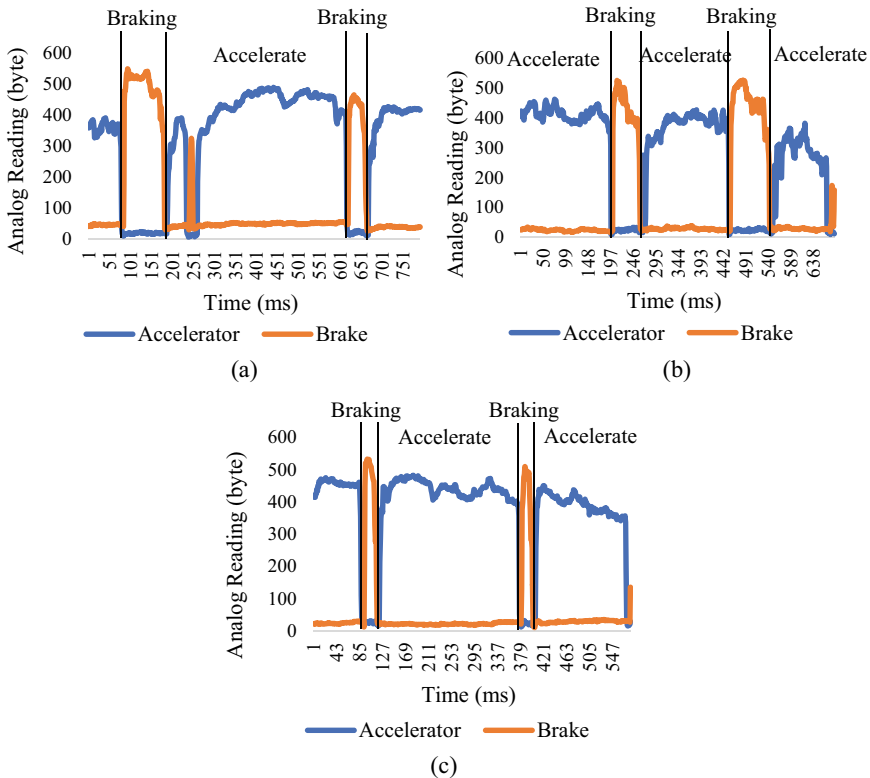
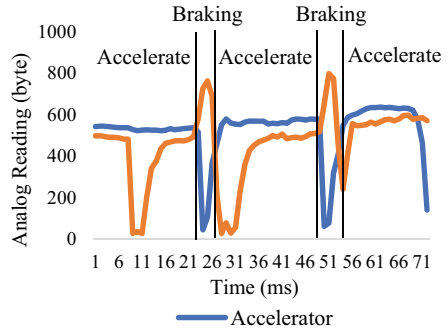


Fig. 9 One-legged driving behavior. **a** Participant 18; **b** Participant 22; **c** Participant 25



(a)

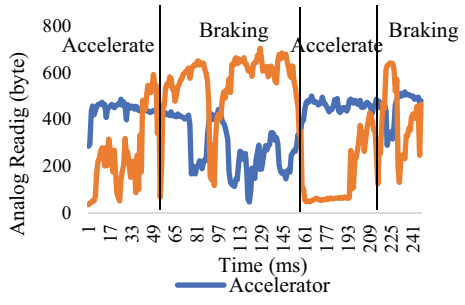


(b)

Fig. 10 Participant 6. a Driving footage; b two-legged force applied



(a)

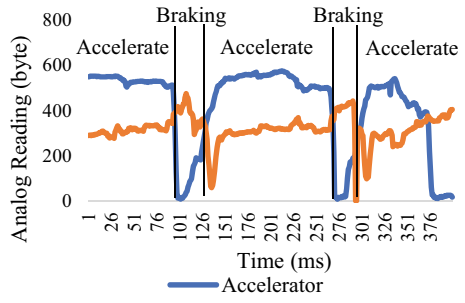


(b)

Fig. 11 Participant 10. a Driving footage; b two-legged force applied



(a)



(b)

Fig. 12 Participant 17. a Driving footage; b two-legged force applied

Figures 10a, 11a, and 12a show the footage of the participants who used both legs while driving during the naturalistic driving test. Figures 10b, 11b, and 12b show the graphs of analog reading versus time for 3 different participants that used both leg during driving in the naturalistic driving test. These participants used their left feet to press the brake pedal and right feet for the accelerator pedal. However, there are slightly difference between all of them. Based on the data, the behavior of participant 6 and 17 are similar, the analog reading for the accelerator pedal and brake pedal are almost in the same trend except during braking. When the accelerator pedal is pressed, the brake pedal is also pressed.

However, for participant 10, the behavior for this participant is almost same with other participants who used only one leg during driving, but there are still significant forces applied on the brake pedal during accelerating unlike for one-legged behavior, there are no forces at all applied on the brake pedal during accelerating. It is because participants with one-legged behavior only use one feet at one time which means, there will be only one pedal with forces at a time. Thus, it can be said that participants with two-legged behavior cannot be predicted since there are variety of driving patterns.

4 Conclusion

In conclusion, this research reveals that there are two types of driving behavior, including one-legged and two-legged driving behavior. It can be obtained that drivers who drive using both of their feet are quite dangerous because the brake lights will always turn on due to the force applied on the brake pedal. Drivers with two-legged driving behavior always place their foot on the brake pedal even when accelerating, hence it is dangerous for other drivers because of the brake lights are always on and could be a distraction for them.

It can also be observed the driver's leg behavior based on the force that they applied on the car pedals during driving. In this research, the sources of foot placement errors and factors which contributing to the wrong pedal placement among Malaysian drivers are found. Several factors identified which influence the pedal error including interruption, confusion and surprised. Moreover, the factors that contribute to road accidents, such as driving under influence, changing lane dangerously, dangerous driving and not paying attention while driving also are obtained in this research. All of the factors are strongly agreed to become the main road accident factors.

Acknowledgements The authors would like to express their gratitude and special acknowledgements to ASEAN NCAP for the ASEAN NCAP Collaborative Holistic Research (ANCHOR) research grant, which funded this project. Also, to our collaborators from Universiti Teknikal Malaysia Melaka (UTeM), and Malaysian Institute of Road Safety Research (MIROS) for the continuous support to conduct this project.

References

1. JKJR (2019) Buku Statistik Keselamatan Jalan Raya
2. Noh NC (2021) 223 kemalangan akibat fizikal jalan raya. <https://www.bharian.com.my/berita/kes/2021/01/773051/223-kemalangan-akibat-fizikal-jalan-raya>. Accessed 02 Aug 2021
3. Bernama (2016) Penggunaan telefon bimbit antara punca utama kemalangan jalan raya | Astro Awani. <https://www.astroawani.com/berita-malaysia/penggunaan-telefon-bimbit-antara-punca-utama-kemalangan-jalan-raya-109199>. Accessed 02 Aug 2021
4. Ibrahim MF (2021) 6 kesalahan utama pengguna jalan raya. *Harian Metro* (2018). <https://www.hmetro.com.my/utama/2018/03/322201/6-kesalahan-utama-pengguna-jalan-raya>. Accessed 02 Aug 2021
5. Farid A (2020) Kemalangan Di Jalan Raya: 5 Punca Ia Terjadi Di Malaysia! Hello Doktor. <https://hellodoktor.com/kesihatan/fakta-menarik/kemalangan-di-jalan-raya/>. Accessed 02 Aug 2021
6. Wu J, Yang J, Yoshitake M (2014) Pedal errors among younger and older individuals during different pedal operating conditions. *Hum Factors* 56(4):621–630. <https://doi.org/10.1177/0018720813487200>
7. Schmidt RA, Young DE (2010) Cars gone wild: the major contributor to unintended acceleration in automobiles is pedal error. *Front Psychol* 1:1–4. <http://doi.org/10.3389/fpsyg.2010.00209>
8. Jonas R, Crump C, Brinkerhoff R, Krake A, Watson H, Young D (2018) Variability in circumstances underlying pedal errors: an investigation using the national motor vehicle crash causation survey. *SAE Technical Papers*, pp 1–8. <http://doi.org/10.4271/2018-01-0493>
9. Padmanaban J, Fitzgerald M, Marsh J (2013) Pedal misapplication: crash characteristics and contributing factors. *SAE Int J Passeng Cars Mech Syst* 6(2):601–607. <http://doi.org/10.4271/2013-01-0446>
10. Nilsson R (2002) Evaluation of a combined brake-accelerator pedal. *Accid Anal Prev* 34(2):175–183. [https://doi.org/10.1016/S0001-4575\(01\)00011-2](https://doi.org/10.1016/S0001-4575(01)00011-2)
11. Wu Y, Boyle LN, McGehee D, Roe CA, Ebe K, Foley J (2017) Foot placement during error and pedal applications in naturalistic driving. *Accid Anal Prev* 99:102–109. <https://doi.org/10.1016/j.aap.2016.10.019>
12. Consiglio W, Driscoll P, Witte M, Berg WP (2003) Effect of cellular telephone conversations and other potential interference on reaction time in a braking response. *Accid Anal Prev* 35(4):495–500. [https://doi.org/10.1016/S0001-4575\(02\)00027-1](https://doi.org/10.1016/S0001-4575(02)00027-1)
13. Karali S, Gyi DE, Mansfield NJ (2017) Driving a better driving experience: a questionnaire survey of older compared with younger drivers. *Ergonomics* 60(4):533–540. <https://doi.org/10.1080/00140139.2016.1182648>
14. Deng TM, Fu J, Shao YM, Peng J, Xu J (2019) Pedal operation characteristics and driving workload on slopes of mountainous road based on naturalistic driving tests. *Saf Sci* 119:40–49. <http://doi.org/10.1016/j.ssci.2018.10.011>
15. Jammes Y, Behr M, Llari M, Bonicel S, Weber JP, Berdah S (2017) Emergency braking is affected by the use of cruise control. *Traffic Inj Prev* 18(6):636–641. <https://doi.org/10.1080/15389588.2016.1274978>
16. Mcgehee DV, Mazzae EN, Baldwin GHS (1998) Driver reaction time in crash avoidance research: validation of a driving simulator study on a test track
17. Horiue M, Tomonori O, Okiyama H, Tanaka Y, Tsuji T (2012) A study on design factors of gas pedal operation. *SAE Int J Passeng Cars Mech Syst* 5(1), 30–35. <http://doi.org/10.4271/2012-01-0073>
18. Tran C, Doshi A, Trivedi MM (2012) Investigating pedal errors and multi-modal effects: driving testbed development and experimental analysis. In: *IEEE international conference on intelligent transportation systems proceedings, ITSC*, pp 1137–1142. <http://doi.org/10.1109/ITSC.2012.6338908>
19. Yuda E, Yoshida Y, Ueda N, Kaneko I, Miura Y, Hayano J (2020) Effects of aging on foot pedal responses to visual stimuli. *J Physiol Anthropol* 39(1):3. <https://doi.org/10.1186/s40101-020-0213-2>

20. Groeger JA, Murphy G (2020) Driver performance under simulated and actual driving conditions: validity and orthogonality. *Accid Anal Prev* 143:105593. <http://doi.org/10.1016/j.aap.2020.105593>
21. Sharpe SS, Brinkerhoff R, Crump C, Young D (2017) Accelerator-to-brake pedal transition movements during on-road stopping in an older population. *SAE Technical Papers*, vol 2017. <http://doi.org/10.4271/2017-01-1396>
22. Barnard Y, Utesch F, van Nes N, Eenink R, Baumann M (2016) The study design of UDRIVE: the naturalistic driving study across Europe for cars, trucks and scooters. *Eur Transp Res Rev* 8(2). <http://doi.org/10.1007/s12544-016-0202-z>

Copper Coated Electrode by Fused Deposition Modelling (FDM) Process



Nicolas Ng Yang Zu, Reazul Haq Abdul Haq , Mohd Fahrul Hassan ,
Mohd Nasrull Abdol Rahman , Said Ahmad , and Haslina Abdullah 

Abstract Electrode manufacturing significantly affects the machining cost and time of the Electrical Discharge Machine (EDM). Therefore, many researchers investigated the metallization of 3D-printed electrodes for EDM as an alternative method to improve electrode manufacturing throughout the years. This study aims to investigate the metallization by Aluminum-carbon (Al-C) paste. Furthermore, the copper deposition of the metalized electrode was examined for different acidic bath concentrations and sample immersion duration. This particular electrode can be used in Electrical Discharge Machine (EDM). The electrode was fabricated by a Fused Deposition Machine (FDM). The material used to fabricate the electrode was Polyethylene Terephthalate Glycol (PETG). Aluminum-carbon (Al-C) paste is used for surface preparation as the first metallization step. This metallization method is environmentally friendly as electroless metallization eliminates the etching process. The samples have dipped 5 wt% of copper sulfate CuSO_4 and 15 wt% of sulfuric acid H_2SO_4 for 24, 72 and 120 h for the copper deposition process. After the metallization, the characteristics of each sample were evaluated by scanning electron microscope (SEM), electrical performance measurement and microscopic testing. The average resistance for 24, 72 and 120 h were 1.0 Ω , 0.7 Ω , and 0.23 Ω respectively. The standard deviation was calculated for 24, 72 and 120 h, which were 0.5, 0.35 and 0.12 respectively. For the SEM observation, the presence of Cu on 24 h was not distinctly visible and the deposited Cu on the samples was 28.58%. For 72 h, the Energy Dispersive X-ray for the sample corresponds with 42.20% of Cu. Meanwhile, the growth of Cu deposition was visible for 120 h, where the Cu deposition was 80.85%. The microscopic testing for the thickness of Cu coated on the samples was measured. The average thickness for 24, 72 and 120 h were $8.6^{+1.51}_{-1.96}$ μm , $108^{+13.19}_{-13.82}$ μm and $150^{+10.82}_{-33.43}$ μm respectively. Based on the results provided from all the tests, the 120 h sample has

N. N. Y. Zu · R. H. A. Haq (✉) · M. F. Hassan · M. N. A. Rahman · S. Ahmad · H. Abdullah
Faculty of Mechanical and Manufacturing Engineering, Universiti Tun Hussein Onn Malaysia,
86400 Batu Pahat, Johor, Malaysia
e-mail: reazul@uthm.edu.my

R. H. A. Haq
Precision Manufacturing Research Center, UTHM, 86400 Batu Pahat, Johor, Malaysia

better Cu deposition than 24 h and 72 h. From the results, the longer the samples dipped in the acidic bath, the more the Cu deposition occurred.

Keywords FDM · EDM · Electrode · PETG · Metallization

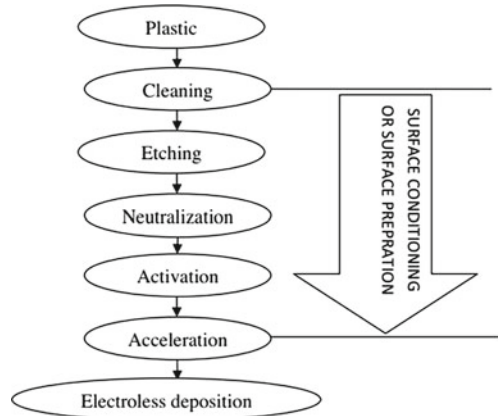
1 Introduction

Electrical discharge machining (EDM), in other words, is known as spark machining, spark eroding, die sinking, wire burning or in some cases, wire erosion is a method of metal fabrication by which electrical discharges (sparks) are used to obtain the desired form [1]. A series of rapidly repeated current discharges between two electrodes, separated by a dielectric liquid and subject to an electrical voltage, remove material from the workpiece. The tool-electrode, or simply the tool or electrode, is one of the electrodes, while the other is called the workpiece-electrode, or piece of work. The method depends on not making physical contact with the tool and workpiece. The white layer has been named this resolidified/recast layer. It includes numerous pock-marks, globules, cracks and micro-cracks, whose thickness and density depend on the conditions of the method. In addition to the molten workpiece surface, during the EDM process, electrode wear occurs, resulting in a shortage of machining precision in the workpiece geometry. Various aspects of the EDM process have been thoroughly investigated like types of EDM machines (Wire cut/Die-sinking), tooling, control circuits, the performance of the process under certain process circumstances, online machine control, etc. Studies on developing analytical process models for die-sinking EDM processes are critical in the current context [2].

Common electrode materials used for electrical discharge machining (EDM) are graphite and copper alloys due to their properties such as high melting temperature and excellent electrical and thermal conductivity. Electrodes produced from special powders using powder metallurgy technology have been used in recent years to modify EDM surfaces to improve wear and corrosion resistance. However, electrodes are usually produced at high temperatures and pressures, so manufacturing is costly. Metallization is a procedure in which, by offering a conductive coating on it a non—conductive substance such as plastic is made conductive. The mechanical properties of plastics were significantly improved after metallization [3].

Different types of plastics such as Polythene, Teflon, Polyethylene Terephthalate Glycol (PETG), Polylactic Acid (PLA), and acrylonitrile butadiene styrene (ABS), etc. can be metalized with different metals like copper (Cu), zinc (Zn), nickel (Ni), gold (Au), chromium (Cr) and silver (Ag), etc. Cu has been widely studied for metallization, having high-quality electric conductivity and being remarkably inexpensive. Many plastics have been plated with Cu. Among these, electroless plating finds the most extensive usage in the metallization of plastic due to its simplicity and inexpensiveness. In this way, a thin metallic layer formed on oxidation-reduction processes on the activated plastic surface without the aid of an electrical potential. Therefore,

Fig. 1 Procedure for electroless metallization of plastics [2]



this study aims is to investigate the metallization of 3D-printed electrodes for EDM as an alternative method to improve electrode manufacturing

Figure 1 Illustrates the procedure for electroless metallization of plastics are described below [4, 5].

Deposition occurs spontaneously on any surface in the electroless technique without additional electricity and processing abilities. However, it is more challenging to regulate the operation for film thickness and uniformity. In addition, a step-by-step process that involves a long term of chemical solutions that are complicated to deposition needs to be applied. Some of these chemicals are environmentally harmful and expensive. Several researchers have suggested removing several routes or using less expensive and friendlier chemicals to address these limitations [6].

For part manufacture, fused deposition modeling (FDM) is used. FDM is one of the processes of rapid prototyping (RP) that produces the component directly from the computer-aided design (CAD) model of the part on the layer-wise deposition principle. This method uses heated thermoplastic filaments, which are extruded from the tip of a nozzle in a prescribed manner, unlike other RP processes, which require a variety of lasers, powders and resins. Elsewhere in the literature, the details of this process were provided [7].

2 Materials and Methods

For this research, the material selected is Polyethylene Terephthalate Glycol (PETG). PETG was used in the form of a filament diameter of 1.75 mm. Next, the samples were fabricated by an FDM. The sample size is 15 mm in height and 9.7 mm in diameter. Metallization was the following step after the fabrication of the samples. In metallization, aluminum-carbon paste has been used for surface conditioning in the electroless process. After the surface conditioning, those samples are dipped in

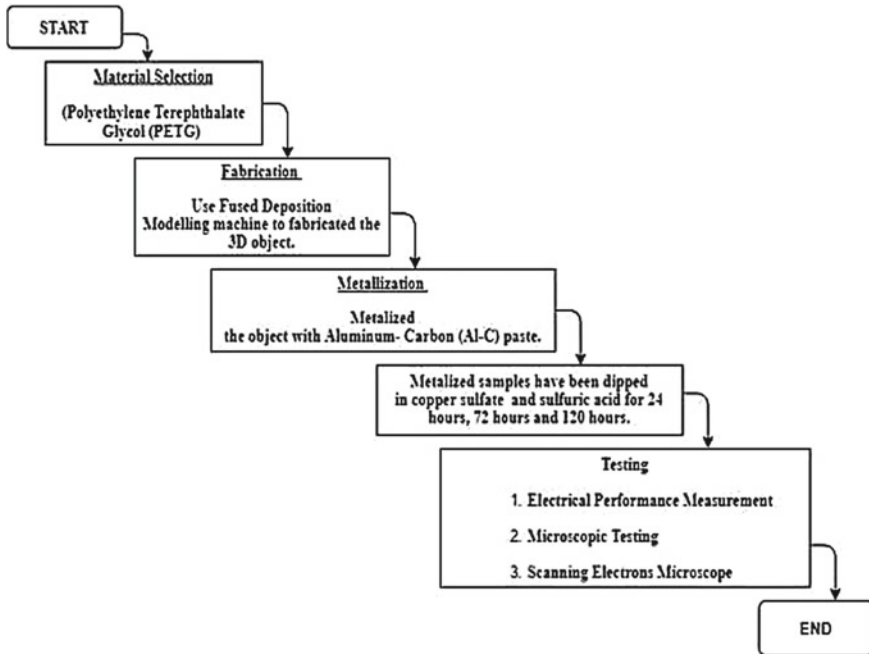


Fig. 2 Flowchart for electroless metallization of plastics

the acid bath for 24, 72, and 120 h, consisting of 5 wt% of copper sulfate CuSO_4 and 15 wt% of sulfuric acid H_2SO_4 . Once the samples are removed from the acid bath, they are tested with three tests to evaluate the copper coating performance on the samples. The three tests conducted were Electrical Performance Measurement, Scanning Electron Microscopy (SEM) and Microscopic Testing. Figure 2 shows the flowchart for electroless metallization of plastics.

2.1 Materials

For this research, the material which been selected is Polyethylene Terephthalate Glycol (PETG). Polyethylene terephthalate glycol, commonly known as PETG, is a thermoplastic polyester that provides significant chemical resistance, durability and excellent formability. As for fabricating the sample, PETG was used in an FDM filament with a diameter of 1.75 mm.

2.2 Fabrication

In this research, the present work deals with the CAD model, conversation STL files, and PETG plastic EDM electrode fabrication via Fused Deposition Modeling (FDM). For this project, Raise 3D V2 Plus machine has been used to fabricate the samples. This machine is one of the FDM machines used to print 3D objects. The sample has been fabricated in a cylindrical shape with 15 mm in height and 9.7 mm in diameter.

2.3 Metallization

In metallization, aluminum-carbon paste has been used for surface conditioning in the electroless process. After surface conditioning, those samples are dipped in the acid bath for 24, 72, and 120 h, consisting of 5 wt% of copper sulfate CuSO_4 and 15 wt% of sulfuric acid H_2SO_4 . The copper deposition on the samples is then tested after the metallization process.

2.4 Chemical Treatment Route

The weight of chemicals was measured with weight balance. First, the various constituents such as Al powder, C powder, enamel paint and distilled water were taken separately and in a weight ratio of 40:36:3:21 which were 10 g of aluminum powder, 0.75 g of carbon powder, 9 g of enamel paint and 5.25 g of distilled water. All the constituents were mixed in a 500 ml beaker with a glass rod. The mixture was continuously stirred with a magnetic stirrer for nearly an hour until it formed like paste. The paste was then carefully applied on PETG samples with a small fine brush. All of the pasted PETG parts were allowed to dry without moisture on the surface for the entire night at room temperature. The dried samples were scoured with 320-grit sandpaper to expose the aluminum over the surfaces. Then rinsed the samples were thorough with water and dried in an oven for pre-heat for 45 min in 45. After surface conditioning, those samples were dipped in the acid bath for 24, 72 and 120 h. The Cu deposited PETG samples were taken out after the re-respective time duration and then rinsed with water and dried in an oven at 45 for 45 min. After the samples were taken out from the oven, the samples were tested for electrical performance measurement. Then the samples were cut in half using a linear precision saw machine to observe the thickness of Cu deposition.

2.5 *Electrical Performance Measurement*

A digital multi-meter (VC830L) was used to measure the resistance of the metallized PETG parts at different points on the surface. The average resistance (R) value and the standard deviation (σ) have been calculated. The deposition process yields the lower average resistance value and a lower standard deviation among all of the listed methods where R_i is measured resistance value at the i th point, and the total number of points are n . Among all of the methods described, the deposition technique that provides the lowest average resistance value and the lowest standard deviation has been considered better.

2.6 *Surface characterization Scanning Electron Microscope (SEM)*

Scanning Electron Microscope (SEM), Hitachi SU-1510, was used to examine the appearance and elemental composition of the copper deposited on the PETG surfaces. This equipment was also used to analyze the altered surface layer, including determining the atomic elements in the layers by Energy Dispersive X-Ray analysis (EDAX).

Microscope

Microscopic testing was performed to analyze the material's microstructural features under magnification. A material's quality defines how well it will perform in a specific application. These properties are based on the structure of the material. Microscopic was used to measure the thickness of the copper-coated layer on the samples. An Eclipse LV150NL was used to measure the deposited copper layer on the PETG samples.

3 Results and Discussion

In this study, several testing was conducted such as scanning electron microscope (SEM), electrical performance measurement and microscopic testing to examine the mechanical properties of the samples coated with copper through metallization. After that, the testing results were compared with different duration samples, 24, 72 and 120 h.

3.1 Electrical Performance Measurement

The digital multi-meter (VC830L) measures the resistance of the metallized PETG parts at different points on the surface. The resistance was measured at three different points on the sample's surface. The average resistance (\bar{R}) value together with the standard deviation (σ) has been calculated. The results of the reading and calculation have stated in Table 1.

The resistance for 24 h was 0.9 Ω , 1.1 Ω and 1.0 Ω . The average resistance for 24 h is 1.0 Ω . There was a minor change in the 72 h sample compared to 24 h sample. The average resistance for 72 h is 0.7 Ω meanwhile, the resistance values from the three different points was 0.6 Ω , 0.7 Ω and 0.8 Ω . For the 120 days sample, the readings were drastically different from the other two samples. The average resistance (\bar{R}) is 0.23 Ω and the resistance value were 0.2 Ω , 0.3 Ω and 0.2 Ω . The standard deviation (σ) was calculated by the formula given. The standard deviation for 24, 72, and 120 h was 0.5, 0.35, and 0.12.

The conductivity of each sample can understand the growth and distribution of the copper on the samples. The more the hour samples were dipped in the acidic bath, the more the copper deposition happens on the samples. The excellent conductivity of resistance was obtained at 120 h. The resistance reading was taken at three different points to ensure the copper deposition was uniform. The readings were quite close and some of the reading was the same. So, the copper deposition was uniform in the samples.

Copper sulfate CuSO_4 and sulfuric acid H_2SO_4 baths were fit for creating conductive Cu layers on the PETG part to replace the conductive plastic surface with a non—conductive because of the large availability of hydrogen [8]. Copper ions are found to be highly stable on sulfuric acid because of the large availability of hydrogen. Furthermore, in sulfuric acid, rapid dissociation of the solution facilitates the production of copper ions. After a high number of ions have been produced, the resistance of the electrolytic solution to copper ion is transferred to the plastic substrate diminishes [2]. By the electrical performance measurement, it was observed that the conductivity and size of Cu crystals vary from point to point on the sample surface, which improves with an increase in deposition time. The 24 h deposition sample has a maximum resistance value at room temperature. In comparison, the 120 h deposition sample has a minimum resistance value.

Table 1 Results of average resistance and standard deviation

Deposition time (h)	Average resistance (\bar{R})	Standard deviation (σ)
24	1.0	0.5
72	0.7	0.35
120	0.23	0.12

3.2 Scanning Electron Microscope (SEM)

The copper deposition for 24 h was not visible because the growth of the copper all over the sample is visible except few places which been circled in the image Fig. 3a. The microcavities demonstrate uniformity and the size of the copper was not ideal. However, increasing the deposition time can increase the copper deposition. However, the EDS spectra are shown in Fig. 3b show that the copper peak is present and some other elements. The composition of Cu among these elements is 28.58 wt%. The copper peak's presence and the copper peak's height determine the appearance of copper with weight percentage.

Meanwhile, Figure 4a shows the image of SEM after being dipped in the acid for 72 h. There was some improvement compared to 24 hours sample. The growth and the copper deposition uniformity are more apparent than the 24 h. The SEM image of the sample has a few Cu particles dispersed in the part which have been circled in the image. The EDS spectra for the sample correspond with 42.20 wt% of copper. This shows that the growth of the copper on the 72 h sample has almost two times more than the 24 h sample. As shown in Fig. 4b, the EDS spectra indicate a medium copper peak at 1 keV and a small copper peak at 8 keV and 9 keV, indicating 100 % copper at the point where the spectra are taken.

Figure 5a presents the image of SEM for the sample deposited for 120 h. As can be seen in the SEM image, the white spots indicate the copper deposition. There was a rapid growth of copper on the sample compared to 24 and 72 h samples. The SEM image of the sample has a few copper particles dispersed in the part which been circled in the image. The copper deposition on the samples is 80.85 wt% of copper found from the EDS spectra in Fig. 5b. The growth of copper deposition is visible. As shown, the EDS spectra indicate a slight copper peak at 1 keV and a minor copper

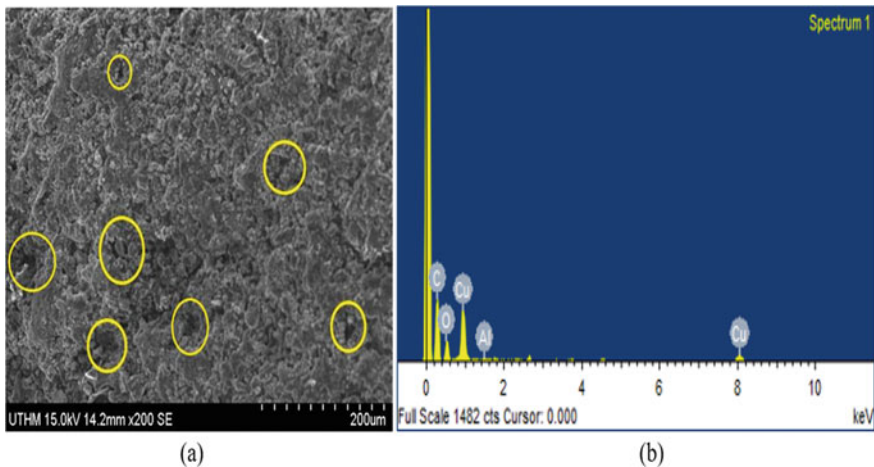


Fig. 3 a SEM image and b EDS image of 24 h sample

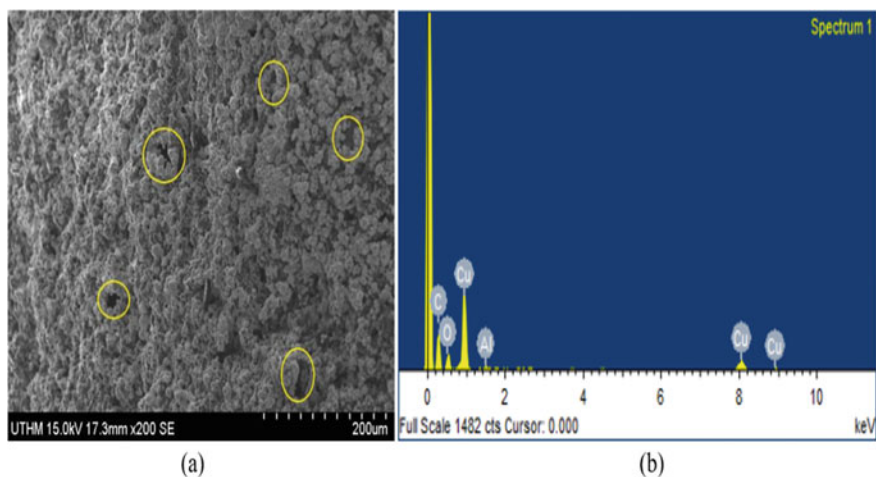


Fig. 4 a SEM image and b EDS image of 72 h sample

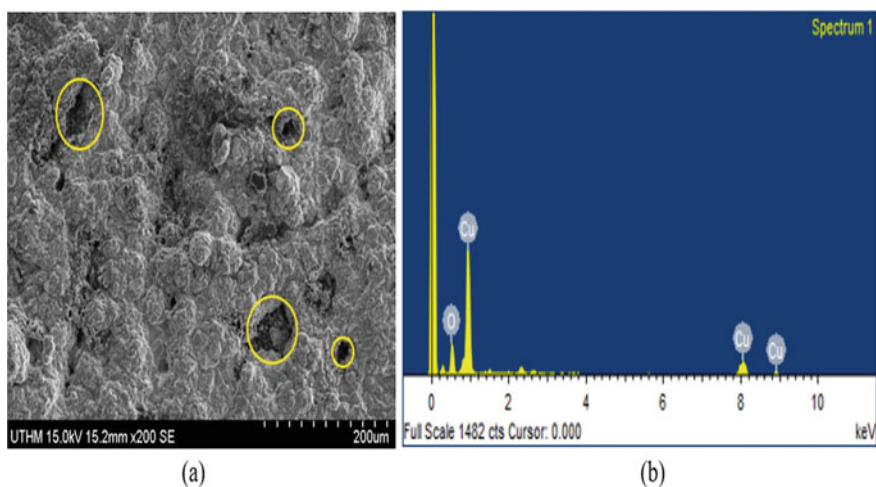


Fig. 5 a SEM image and b EDS image of 120 h sample

peak at 8 keV and 9 keV, indicating 100 % wt% copper at the point where the spectra were taken.

The result obtained was 88.83 wt% Cu for the sample dipped in the H_2SO_4 baths based on previous research. Even the metallization route was chromic acid. Meanwhile, the result obtained for 120 h in this experiment was 80.85 wt% [9]. The Cu crystal particles are also clearly viewed in the SEM image as the 120 h sample for this experiment. Copper deposition by using copper sulfate is highly soluble in sulphuric acid solution. Due to that, the copper deposition was increased when the

time deposition increased [4, 9]. As the deposition time gradually increases, the size of Cu crystals increases. The formation of large uniform Cu crystals on samples metallic shining was observed when the deposition time was longer [10].

3.3 Microscopic Testing

When the time duration of copper deposition increases, the copper's thickness also increases. Figure 6 shows the image of the thickness of the copper for 24 h. The average thickness for 24 h sample is $8.6^{+1.51}_{-1.96}$ μm . The thickness for 72 h is approximately average is $108^{+13.39}_{-13.82}$ μm over the sample after increasing the time to 48 h compared to the previous sample. The image of the copper thickness for 72 h is shown in Fig. 7. The thickness average for 120 h is $150^{+10.82}_{-33.43}$ μm . The image of the thickness

Fig. 6 The thickness of the Cu layer on 24 h sample

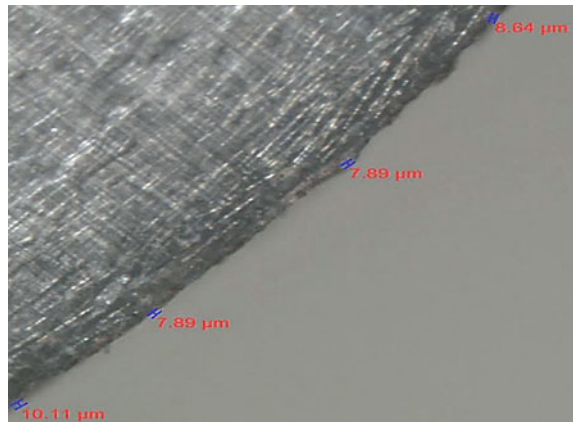


Fig. 7 The thickness of the Cu layer on 72 h sample

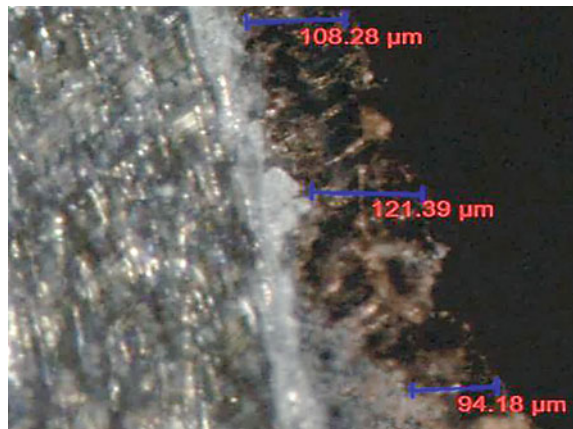
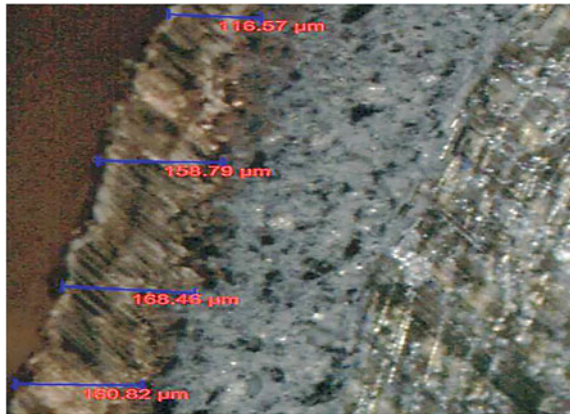


Fig. 8 The thickness of the Cu layer on 120 h sample



of 120 h sample taken from the microscope is shown in Fig. 8. By comparing all the sample thicknesses based on the time duration increase for copper deposition, the thickness of the copper increased rapidly.

The copper deposition thickness is directly proportional to the duration of copper deposition. This happens due to reducing the concentration of acidic bath and it slows down the reaction. Thus, the concentration of acidic baths decreases. This was observed in fading of blue color in the copper sulfate CuSO_4 and sulfuric acid H_2SO_4 solution. When the concentration of the acidic bath decreases the copper ions in the solution decrease thus, the copper deposition has been slow [6, 10].

The growth of the copper is adequate to the time duration. Thus, the uniformity of copper distribution is not satisfactory. The copper gets deposited only at the site where the aluminum and carbon are exposed more during the surface preparation. The dried samples were scrubbed with sandpaper to expose the aluminum and carbon over the surface during the experiment. However, some micro surfaces were unreachable to expose to the copper during the scoured. So, the uniformity of copper deposition on the surface is not satisfactory but can be improved by electroplating. Increasing the deposition time can increase the copper deposition on the samples [11].

4 Conclusion

The metallization of PETG parts has been studied by evaluating the performance of the samples with a scanning electron microscope (SEM), electrical performance measurement and microscopic testing. A better Cu deposition was observed on the 120 h sample. By comparing the resistance of the sample, the slightest electrical resistance was measured on the 120 h sample. The growth and distribution of the Cu of the sample were better compared to the other two samples, where the resistance was more significant than 120 h sample. The more the hour samples were dipped in the acidic bath, the more the copper deposition happens on the samples.

Furthermore, the SEM images validate that the 120 h sample has better copper deposition. The Cu deposition for 120 h sample is visible compared to 24 and 72 h samples. The copper deposition on the samples is 80.85% of copper found from the EDS spectra.

Additionally, the microscopic testing proved that 120 h has better Cu deposition. The average thickness of Cu deposition on the samples was $150_{-33.43}^{+10.82}$ μm . By comparing all the sample thicknesses based on the time duration increase for Cu deposition, the thickness of the copper increased rapidly. Based on the results provided from all the tests, the 120 h sample has better Cu deposition than 24 h and 72 h. From the results, the longer the samples dipped in the acidic bath, the more the Cu deposition occurred.

Acknowledgements The authors would like to acknowledge Universiti Tun Hussein Onn Malaysia (UTHM) and Postgraduate Research Grant (GPPS), Vot H643 for financial support.

References

1. Jha B, Ram K, Rao M (2011) An overview of technology and research in electrode design and manufacturing in sinking electrical discharge machining. *J Eng Sci Technol Rev* 4
2. Saxena P, Metkar R (2019) Development of electrical discharge machining (EDM) electrode using fused deposition modeling (FDM). In: 3D printing and additive manufacturing technologies, pp 257–268
3. Eqbal A, Eqbal MI, Sood AK (2019) An investigation on the feasibility of fused deposition modelling process in EDM electrode manufacturing. *CIRP J Manuf Sci Technol* 26:10–25
4. Teixeira L, Santini M (2005) Surface conditioning of ABS for metallization without the use of chromium baths. *J Mater Process Technol* 170:37–41
5. Luan B, Yeung M, Wells W, Liu X (2000) Chemical surface preparation for metallization of stereolithography polymers. *Appl Surf Sci* 156(1):26–38
6. Eqbal A, Sood AK (2014) Metallization on FDM parts using the chemical deposition technique. *Coatings* 4:574–586
7. Sood AK, Ohdar RK, Mahapatra SS (2009) Improving dimensional accuracy of fused deposition modelling processed part using grey Taguchi method. *Mater Des* 30(10):4243–4252
8. Sahoo SK, Sahu AK, Mahapatra SS (2017) Environmental friendly electroless copper metallization on FDM build ABS parts. *Int J Plast Technol* 21(2):297–312
9. Ono S, Naitoh K, Osaka T (1999) Initial propagation stage of direct copper plating on non-conducting substrates. *Electrochim Acta* 44(21):3697–3705
10. Hsu C, Chen D-Y, Lai M, Tzou G (2008) EDM electrode manufacturing using RP combining electroless plating with electroforming. *Int J Adv Manuf Technol* 38:915–924
11. Wu X, Sha W (2008) Surface morphology of electroless copper deposits using different reducing agents. *Synth React Inorg Met-Org* 292–296

FTIR Analysis of Plant-Based Cellulose as Adsorbents for Water Remediation



Arjun Asogan, Norazlianie Sazali, Wan Norharyati Wan Salleh, Haziqatulhanis Ibrahim, and Rishen Nair Krishnan

Abstract Finding an effective, green adsorbent for removal of heavy metals is one of the main problems in water purification field. Cellulose has gain tremendous attention for its variability of purposes including heavy metal removal via adsorption. As a preliminary material study, Fourier Transform Infrared Spectroscopy (FTIR) would be a good step in analyzing the removal potential of an adsorbent. In this study, cellulose-based adsorbent extracted from Pandan leaves was subjected to acid hydrolysis after being pre-treated with alkali and bleaching treatment. The output material was then analyzed in this research using FTIR. The result showed that some components were removed after the treatments and the material has potential for future development as adsorbent for heavy metal removal due to presence of carboxyl group in the backbone.

Keywords Cellulose · Green technology · Adsorbent

1 Introduction

Water pollution is a serious environmental issue, and the accumulation of chemical compounds in water sources exceeds the World Health Organization's (WHO) and Environmental Protection Agency's (EPA) established thresholds (EPA). Heavy metals are among the most common pollutants in aquatic climates, and chronic exposure adds to human health issues. Anthropogenic processes, such as mining, industry, and the use of metals and metal-containing compounds for residential and agricultural reasons, are the major sources of water pollution [1]. Membranes and filters

A. Asogan · N. Sazali (✉) · H. Ibrahim · R. N. Krishnan
Centre of Excellence for Advanced Research in Fluid Flow (CARIFF), Universiti Malaysia
Pahang, 26600 Pekan, Pahang, Malaysia
e-mail: azlianie@ump.edu.my

W. N. W. Salleh
Advanced Membrane Technology Research Centre (AMTEC), School of Chemical and Energy,
Faculty of Engineering, Universiti Teknologi Malaysia, Johor Darul Takzim, 81310 Skudai,
Malaysia

© The Author(s), under exclusive license to Springer Nature Singapore Pte Ltd. 2023
N. H. Johari et al. (eds.), *Proceedings of the 2nd Energy Security and Chemical
Engineering Congress*, Lecture Notes in Mechanical Engineering,
https://doi.org/10.1007/978-981-19-4425-3_9

can be used to differentiate chemical species by allowing certain organisms to enter while blocking others. The microstructure and chemistry of a membrane's substance determine its selectivity. Membranes with well-defined pores for size exclusion and tailored surface chemistry can be designed to selectively adsorb certain solutes [2]. Cellulose can be obtained from almost all plants, including Pandan leaves. Pandan leaves is not a seasonal plant and can be obtained easily in Malaysia. Using a plant that are available in abundance would be a cost-effective method if it turns out as a good adsorbent.

Heavy metal species in water are very hazardous pollutants that can arise from both natural and anthropogenic sources. Heavy metals could form anionic and cationic species in water in a variety of ways. Identification of the dominating species and adjustment of the sorbent material's surface chemistry to improve uptake ability, partitioning coefficient, and selectivity are usually required for effective heavy metal species uptake. The pH approach is a critical parameter that can affect absorption and selectivity significantly [2]. Heavy metal pollution is a major issue nowadays, having a negative effect on the environment, ecology, and humans. It poses a risk of contaminating the food supply. As a result, professionals from all around the world have concentrated their efforts on finding a solution to this urgent problem. Materials having a range of structural component between 1 and 100 nm are known as nanomaterials. Mechanical, electrical, optical, magnetic, adsorption, and high reactivity characteristics differ considerably from typical materials due to the nanoscale dimension of the nanomaterial. Utilizing nanomaterials in water treatment has gotten a lot of attention recently. Nanoparticles have been characterized as components having major implications for usage in modern water treatment systems, in order to improve and raise the effectiveness of water purification and to expand the availability of water by using sustainable and non-conventional sources. Recent advancements in this field provide potential for the next decade's water resource networks to be developed.

In this study, FTIR analysis of nanocellulose from Pandan leaves was done in order to assess the possibility of the material as an efficient adsorbent for pollutant removal. Nanotechnology enables low-cost, high-performance, and less dependent water treatment procedures for huge infrastructures as an alternative to conventional centralized frameworks. Aside from their persistence, one of the most significant benefits of employing nanoparticles for water treatment is that they may be utilised as a point-of-use technology, as opposed to traditional water treatment technologies that are intended for use in a centralized treatment facility. Nanomaterials have several benefits, including large specific surface areas, quick dispersion, high reactivity, and the ability to absorb a variety of chemical compounds, heavy metals, and microbes. Unlike typical chemical disinfectants, hazardous disinfection by-products are unlikely to develop since they are not efficient oxidants [3].

1.1 Heavy Metal in Wastewater

In normal circumstances, the human body can manage small amounts of metals without creating severe health problems. Water pollution with heavy metals, on the other hand, has become a serious issue across the world. According to Fu and Wang [4], metals having an atomic weight of 63.5–200.6 and a specific gravity greater than 5.0 are classified as heavy metals. Water quality is threatened by both human industrial activity and trash dumped directly into water streams. Another researcher disclosed that just 1% of continental freshwater is accessible for daily use, and with global population increase, contaminant-free water shortages will eventually become the next worldwide issue [5]. The presence of hazardous contaminants in water puts the environment and all living species, especially marine life, in jeopardy. Unlike organic contaminants, heavy metals are not biodegradable and can cause serious health problems in people and animals.

2 Adsorption

Adsorption is the accumulation of a liquid solute or adsorbate on an adsorbent surface [6]. The two forms of adsorption are physical adsorption (physisorption) and chemical adsorption (chemisorption). To discriminate between the two types of adsorptions, the attraction between the sorbent surface and the adsorbate was assessed. Chemisorption is characterised by strong chemical bonds between molecules, whereas physisorption is characterised by natural contact between molecules and mild van der Waals forces. Adsorbents for metal removal have been explored using a variety of materials, including oxide-based adsorbent, carbon nanotubes, and graphene-based adsorbent [7]. Cellulosic-based adsorbent, on the other hand, has piqued the interest of academics all over the world due to its abundance and low cost, and has been proposed as a low-cost adsorbent [8, 9].

Metal binding was achieved by interactions with surface functional groups in polysaccharides such as cellulose, chitin, and alginate. The low cost, high specific surface area, simple handling, and affinity for adsorption against a wide spectrum of pollutants have prompted interest in the development of cellulose-based adsorbents for water remediation [10]. A variety of adsorbents have been used to remove toxic contaminants, and its processes were studied in numbers of research and reviews. To remove pollutants from water and wastewater, low-cost adsorbents such as biomass-based activated carbon, agricultural waste peels, and industrial residues were used. There was also comparison of those natural adsorbents and commercial activated carbon in terms of efficiency. Other than cellulose, chitosan is regarded as one of largely studied adsorptive materials. The inclusion of amino and hydroxyl groups in the molecules aids several possible adsorption interactions between chitosan and pollutants (dyes, metals, ions, phenols, pharmaceuticals/drugs, pesticides, herbicides, etc.) [6].

3 Methodology

Pandan leaves was obtained from residential areas and dried in the oven. It was then grinded and undergo alkali treatment using 5 wt% of sodium hydroxide, NaOH solution at 125 °C for 120 min. Bleaching was done using sodium chlorite, NaClO₂ with few drops of nitric acid, HNO₃ under condition of 100 °C for 240 min. Prior and after the bleaching treatment, the product was dialyzed until pH 7. Outcome from the step was a white-colored sample which was later dried in the oven for 24 h. Next, the sample was subjected to acid hydrolysis using ratio cellulose to acid of 5:100 (wt%) for 60 min at optimum reaction temperature of 45 °C and cold distilled water was added at the end to stop the reaction [11]. Suspensions was washed several times and centrifuged for 15 min. One of the analytical techniques that can efficiently detect the functional groups and chemical bonds that were found in adsorbent is FTIR. Thus, the sample was analyzed using the spectrophotometer and elaborated in next section.

4 FTIR Result

All samples have similar absorption bands in their FTIR spectra as observed in Fig. 1, indicating that their chemical compositions are equivalent. Graph below showed typical cellulose composition graph. Characteristics bands of hydroxyl, –OH stretching at 3000–3700 cm⁻¹, 2915 cm⁻¹ for stretching of C = C–H and symmetric bending of methyl group, CH₂ was observed at 1425 cm⁻¹. Other than that, at 1150 cm⁻¹ is the stretching of C–O of primary –OH and 1040 cm⁻¹ is C–O–C anti-symmetric bridge stretching [12, 13].

The peak at 1613 cm⁻¹ nearly vanished after the raw material was treated with NaOH, and the intensity of the 1519 cm⁻¹ peak was lowered after treated with NaClO₂. This suggests that bleaching treatment removed some components other

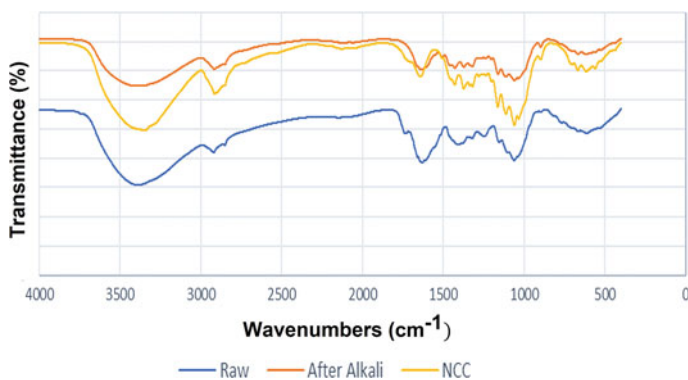


Fig. 1 FTIR result

than cellulose such as lignin and hemicellulose [14]. The pre-treatment serves the purpose of removing any amorphous regions and constituents other than cellulose from the structure, leaving particles with high crystallinity [15].

5 Conclusion

The sample obtained after each treatment were observed using Fourier transform infrared spectroscopy. Typical cellulose composition was generated from the result and for removal of cationic heavy metal, presence of carboxyl group in the sample is anticipated. After the pre-treatment, FTIR graph have showed that there are presence of carboxyl group (negative ion) in the cellulose which indicates its possibility to efficiently remove cationic pollutants (positive ion) from water. Although the efficiency percentage of the adsorbent cannot be determined, it can be concluded that this plant-based material has potential to be adsorbent for heavy metal removal. Furthermore, the crystallinity of adsorbent, surface area and many other parameters need to be studied in order to determine the efficiency of adsorbent derived from Pandan leaves.

Acknowledgements Authors would like to thank Ministry of Higher Education Malaysia and Universiti Malaysia Pahang for funding under grant RDU210314.

References

1. Lingamdinne LP, Koduru JR, Karri RR (2019) A comprehensive review of applications of magnetic graphene oxide based nanocomposites for sustainable water purification. *J Environ Manage* 231:622–634. <https://doi.org/10.1016/j.jenvman.2018.10.063>
2. Voisin H, Bergström L, Liu P, Mathew A (2017) Nanocellulose-based materials for water purification. *Nanomaterials* 7:57. <https://doi.org/10.3390/nano7030057>
3. Pinto M, Ramalho PSF, Moreira NFF, Gonçalves AG, Nunes OC, Pereira MFR, Soares OSGP (2020) Application of magnetic nanoparticles for water purification. *Environ Adv* 2:100010. <https://doi.org/10.1016/j.envadv.2020.100010>
4. Fu F, Wang Q (2011) Removal of heavy metal ions from wastewaters: a review. *J Environ Manage* 92:407–418. <https://doi.org/10.1016/j.jenvman.2010.11.011>
5. Andrews JE, Brimblecombe P, Jickells TD, Liss PS, Reid B (2004) An introduction to environmental chemistry. Blackwell Publishing
6. Singh NB, Nagpal G, Agrawal S, Rachna (2018) Water purification by using adsorbents: a review. *Environ Technol Innov* 11:187–240. <https://doi.org/10.1016/j.eti.2018.05.006>
7. Anjum M, Miandad R, Waqas M, Gehany F, Barakat MA (2016) Remediation of wastewater using various nano-materials. *Arab J Chem*
8. Pyrzynska K (2019) Removal of cadmium from wastewaters with low-cost adsorbents. *J Environ Chem Eng* 7:102795
9. Ulmanu M, Maranon E, Fernandez Y, Castrillon L, Anger I, Dumitriu D (2003) Removal of copper and cadmium ions from diluted aqueous solutions by low cost and waste material adsorbents. *Water Air Soil Pollut* 142:357–373

10. Septevani AA, Rifathin A, Sari AA, Sampora Y, Ariani GN, Sudiyarmanto, Sondari D (2020) Oil palm empty fruit bunch-based nanocellulose as a super-adsorbent for water remediation. *Carbohydr Polym* 229:115433
11. Mohamed MA, Salleh WNW, Jaafar J, Ismail AF, Abd Mutalib M, Mohamad AB, Zain MFM, Awang NA, Mohd Hir ZA (2017) Physicochemical characterization of cellulose nanocrystal and nanoporous self-assembled CNC membrane derived from *Ceiba pentandra*. *Carbohydr Polym* 157:1892–1902
12. Wichaita W, Samart C, Yoosuk B, Kongparakul S (2015) Cellulose graft poly (acrylic acid) and polyacrylamide: grafting efficiency and heavy metal adsorption performance. *Macromol Symp* 354:84–90
13. Gupta M, Gupta H, Kharat DS (2018) Adsorption of Cu(II) by low cost adsorbents and the cost analysis. *Environ Technol Innov* 10:91–101
14. Mohamed MA, Salleh WNW, Jaafar J, Asri SEAM, Ismail AF (2015) Physicochemical properties of “green” nanocrystalline cellulose isolated from recycled newspaper. *RSC Adv* 5:29842–29849. <https://doi.org/10.1039/C4RA17020B>
15. Song K, Zhu X, Zhu W, Li X (2019) Preparation and characterization of cellulose nanocrystal extracted from *Calotropis procera* biomass. *Bioresour Bioprocess* 6:45. <https://doi.org/10.1186/s40643-019-0279-z>

A Study on the Wear Resistance and Lubrication Properties of Mixed Engine Oils



Khairulafizal Sultan Ali, Mohd Nadzeri Omar , Nasrul Hadi Johari , and Mohd Hasnun Arif Hassan 

Abstract Engine oils have traditionally served as the principal lubrication for combustion engines. With so many engine oils on the market, each has its unique set of ingredients and qualities that set it apart from the others. Customers are often influenced by the variety to switch between different types of engine oil. The wear resistance and lubrication properties of a few mixtures of different engine oil brands are investigated in this study. Three brands of engine oil were chosen and mixed in a 1:1 weight ratio. The viscosity, coefficient of friction (COF), and wear scar diameter (WSD) of the mixtures were determined using the Four-ball tribotester and viscosity testing equipment at three testing periods. The results demonstrate that the mixtures act differently than pure oil. Even though the mixing yielded more viscous lubricants, which is preferred, the data reveal that the COF and WSD also increased. The mixing might cause chemical interactions between additives, causing the oil's structure to change. According to this study, using pure oil is superior for extending the life of a combustion engine.

Keywords Four-ball tribotester · Wear scar diameter · Coefficient of friction · Viscosity · Engine oil

1 Introduction

Engine oil serves as a lubricant in the internal combustion engine. The engine oil lubricates the internal engine components, allowing for smooth movement and protecting against the constant interaction between the components [1–3]. The engine oil also acts as a coolant that regulates the temperature within the engine by absorbing the heat emitted [4].

The engine oil comes in a variety of grades to ensure that it performs correctly in a variety of engine situations. The SAE grade is the most often used. The grade is

K. S. Ali · M. N. Omar (✉) · N. H. Johari · M. H. A. Hassan
Faculty of Mechanical and Automotive Engineering Technology, Universiti Malaysia Pahang,
26600 Pekan, Pahang, Malaysia
e-mail: nadzeri@ump.edu.my

represented by numbers such as 10 W-30, 10 W-40, and 5 W-40 which is a measure of the engine oil's suitability for usage in specific temperatures and conditions. The first figure reflects the flow of oil during winter, whereas the second number represents the flow of oil during regular operating conditions.

In general, the selection of suitable engine oil is dictated by the efficiency [5], durability [6], and environmental aspects of the engine [7–9]. Engine oil with lower viscosity can help in minimizing power loss. However, at elevated temperatures, the viscosity of the oil reduces [10], hence the engine oil with a lower viscosity must be able to maintain its properties, especially its load carrying and protecting capacity. The viscosity of the engine oil also contributes to the lubrication regime, wearability, and coefficient of friction (COF). In this case, the Stribeck curve has been commonly used to describe the relationship [11]. Based on the Stribeck curve, the condition in the engine is located in between mixed to hydrodynamic lubrication regimes which the latter is the preferred condition [12]. According to Korcek et al., the hydrodynamic lubrication regime can be achieved through the low viscosity oils, however, the durability of these oils is a major concern [11].

Due to these reasons, additives have been added into engine oils to improve the engine oil performance to ensure the effective [11, 13]. Additives are synthetic chemical ingredients that can increase a variety of engine oil properties. Most engine oil contains 15–30% oil additives right out of the bottle, and aftermarket oil supplements can be utilized to improve oil and engine performance even more. Commercially, manufacturers will emphasize the benefits of the additives, such as better protection, greater distance, environmentally friendly, and longer durability [14–16].

When the amount of engine oil is critically low, lubrication inside the engine is diminished, which can lead to engine failure. In this situation, customers are prone to using any engine oil to raise the amount once again. When using random engine oil, it might be of different grades, types, or brands. When different engine oils are blended, the additives inside the engine oils are also mixed, and a chemical reaction is possible, especially at high temperatures [17, 18]. There is relatively little evidence available in the literature that illustrates the effect of using different engine oils at the same time. In this study, the effect of the mixtures on wear resistance and lubricating qualities is studied. This study only focuses on engine oil mixtures of the same grade and type made by different manufacturers.

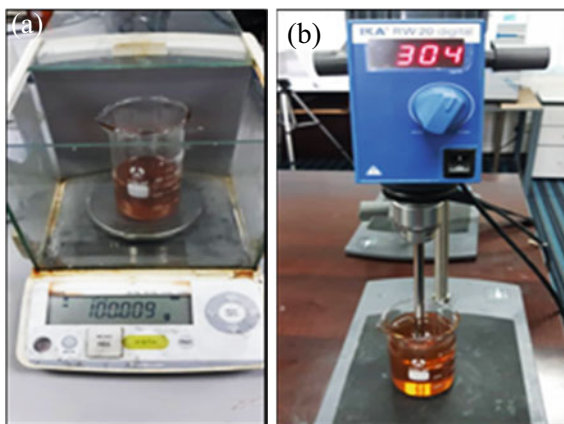
2 Experimental Procedure

2.1 Oil Samples

For this study, three different brands of engine oil were used. The brands chosen were designated by the letters A, B, and C. Each of these oils has the same SAE10W-30 grade and their physical characteristics are as shown in Table 1. The three different brands of engine oil were used to generate three distinct oil samples. The first sample

Table 1 Physical characteristics of the selected engine oils

	Engine oil A	Engine oil B	Engine oil C
SAE viscosity grade	10 W-30		
Viscosity @ 40 °C (cSt)	75.1	69.05	66.9
Viscosity @ 100 °C (cSt)	11.31	10.42	11
Viscosity index	142	137	156
Density @ 15 °C (g/cm ³)	0.878	0.87	0.85
Flash point (°C)	>200	228	238
Pour point (°C)	-36	-43	-42

Fig. 1 **a** The weighting of the engine oil using a digital scale, and **b** the blending setup using the IKA RW20 digital mixing machine

is entirely made up of Brand A. This sample serves as a reference point for pure oil. The second sample comprised Brand A and Brand B, whereas the third sample contained Brand A and Brand C. The second and third samples are now referred to as the AB and AC mixtures, respectively. The mixtures were produced by combining the two oils in a weight-to-weight ratio of 1:1. Each oil was weighted at 100 g on a digital scale and blended using the IKA RW20 mixer machine, as shown in Fig. 1. The rotating speed of the mixing blades was 300 rpm, and the mixture was mixed for 15 s.

2.2 Four-Ball Experiment

The DUCOM TR-30L four-ball testing machine (see Fig. 2a) was utilised as per the ASTM D4172-B standard [19]. The subjected lubricant was filled into the ball pot,

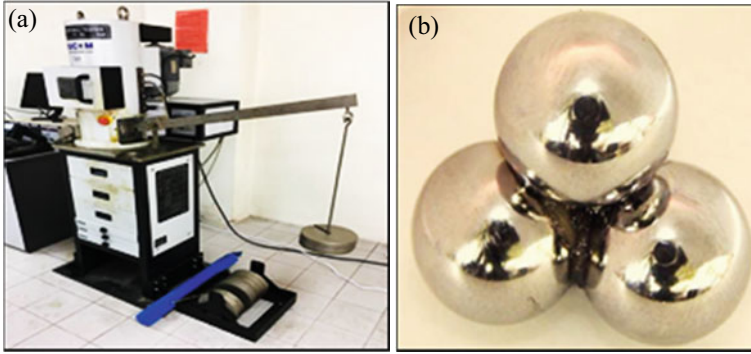


Fig. 2 a The DUCOM four ball tester TR-30L and b steel balls

which contains a rotating steel ball and three securely held steel balls. In the presence of the subjected lubricant, the rotating steel ball will be pressed against the other three steel balls when the machine is operating. The speed (RPM), the load applied (N), temperature ($^{\circ}\text{C}$), and duration of the operation (mins) are used to regulate the running condition. All of these parameters were fixed in this investigation. The speed was set at 1200 rpm, the load was 40 kg, the temperature was 75°C , and the duration was set to 60 min. WINDOCOM 2010 software provides an interface for the analysis and logs of the data.

The steel balls (see Fig. 2b) used in the four-ball testing machine have the following properties: Chrome alloy steel, made from AISI E-52100, 12.7 mm diameter, Extra polish (EP) grade 25, and Rockwell C hardness 64–66. Before each analysis, the steel balls were immersed with acetone to ensure the ball is clean from any dust or debris.

2.3 Coefficient of Friction (COF) Analysis

From the four-ball tester result, all the value of the friction torque is recorded and the friction coefficient, as calculated according to IP-239, is expressed as follows

$$\mu = \frac{F_T \sqrt{6}}{3Wr} \quad (1)$$

where μ is the coefficient of friction, W is the applied load (kg), F_T is the frictional torque (kg.mm) and r is the distance from the centre of the contact surface on the lower balls to the axis of rotation, which was measured to be 3.67 mm.



Fig. 3 The setup of the WSD analysis using the HPM

2.4 *Wear Scar Diameter (WSD) Analysis*

After the four-ball testing, a high-power microscope (HPM) was utilised to measure the Wear Scar Diameter (WSD) on the steel ball as illustrated in Fig. 3. The HPM was set to high resolution to see the entire image. The program used to take the picture of the WSD is called “Isolation lite”.

2.5 *Viscosity Analysis*

The viscosity of all oil samples was determined using the Cole-Parmer Advanced Viscometer testing machine as depicted in Fig. 4. The viscosity of the oil samples was measured at temperatures ranging from 23 to 100 °C. It was accomplished by allowing the machine to operate in a step mode, during which the temperature

Fig. 4 Cole-Parmer advanced viscometer machine (EW-98965-46)

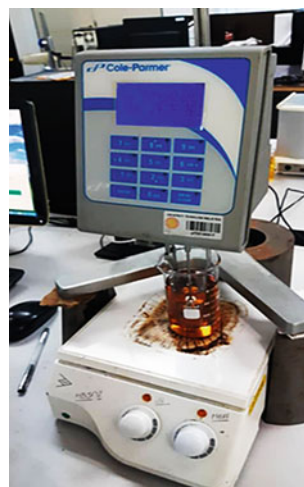


Table 2 The experiment parameters used to determine the viscosity

Experiment settings	Experiment configuration
Experiment type: STEP	Density units: g/cm ³
STEP: 100	Viscosity units: centistokes (cSt)
Duration: 30 min	Temperature units: °C
Time increment: 1 s	

was gradually increased over the period of 30 min. The experiment parameters and configuration are as shown in Table 2.

2.6 Testing Periods

The wear resistance and lubrication properties of all oil samples were examined over three testing periods. The testing periods after mixing are 5 min, 1 week, and 1 month. Between the testing periods, the oil samples were kept undisturbed in glass bottles. However, when the testing period arrived, the samples were returned to the mixing machine for re-blending. The same parameters were used for each re-blending process. The overall process of the experiment is as illustrated in Fig. 5.

3 Results

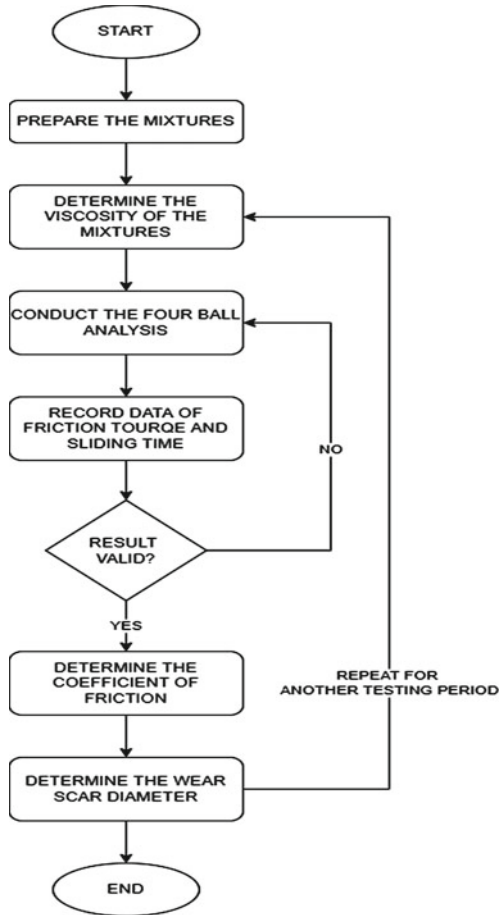
3.1 Wear Scar Diameter (WSD)

The four-ball tribometer experiment yielded the WSD results. Figure 6 depicts the WSD results for all oil samples, whereas Fig. 7 depicts examples of the collected WSDs using the HPM.

In general, the wear tendency rises as the mixture's period increases. The AB mixture obtained the lowest WSD in the first testing period, which was 5 min after mixing, even lower than Brand A alone. It demonstrates that the oil from Brand B has an excellent lubricating performance. The presence of Brand C's oil, on the other hand, raises the WSD for the AC mixture, indicating a poor lubricating process. The second and third testing periods show a similar pattern.

However, when it came to the rate of increment, the AB mixture performed the poorest. In percentage terms, the WSD of the mixture increases by 22% after one week and by 72% after one month of mixing. In comparison, the AC mixture accounted for 8% and 24% of the WSD growth over one week and one month, respectively. According to the findings, Brand C's oil provides better lubrication in terms of duration. Despite this, the WSD for the AB mixture is still lower than that of the AC mixture after 1 month of mixing. However, if a longer mixing period is considered,

Fig. 5 The overall process of the analysis



the WSD for the AB mixture can develop beyond the WSD for the AC mixture based on the increment rate. Taking the first week’s increment rate (22% for the AB mixture and 8% for the AC mixture), the WSD for the AB mixture will be approximately 877.1 μm after eight weeks or two months, while the WSD for the AC mixture will be around 745.7 μm .

It should be emphasised that the tests were carried out on a clean mixture. Between testing periods, the oil samples were left undisturbed. As a result, the findings achieved here were solely the product of the chemical interaction of the oils. Different WSD readings will be recorded in the regular use where the mixture is placed in the combustion engine due to other factors involved such as temperature, working loads, and contaminations [6, 20].

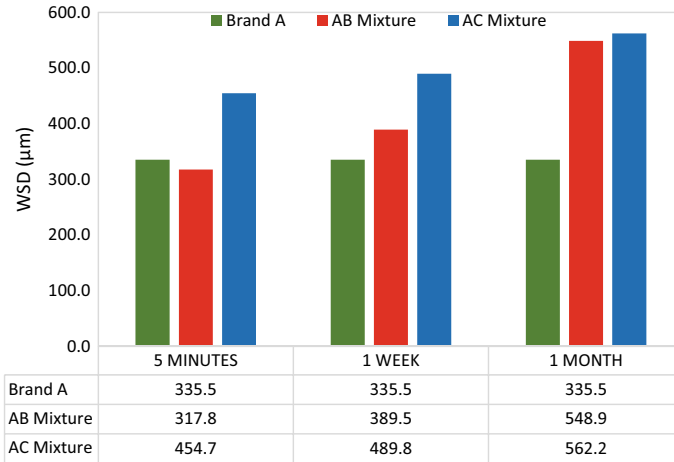


Fig. 6 The mean value of WSD for all oil samples at respective testing period

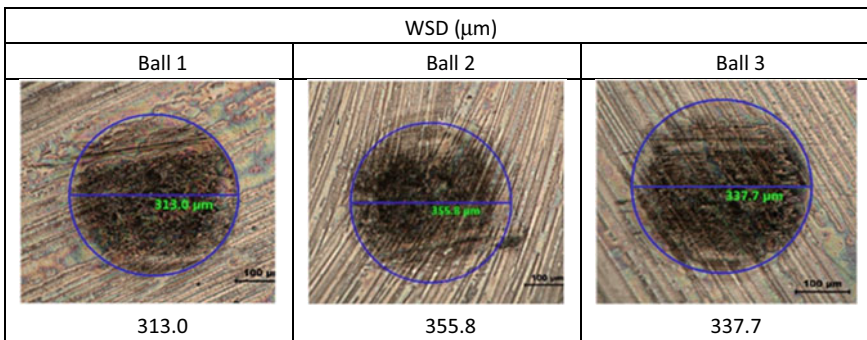


Fig. 7 Samples of WSD image and measurement obtained using the HPM

3.2 Coefficient of Friction (COF)

The COF is one of the factors that contribute to wear development. The COF is a dimensionless parameter that is used to determine friction force for any motion condition. It occurs when two metal surfaces slide against each other, causing friction and pressure. In principle, a high friction value will contribute to a high COF value, which has a high potential to cause damage in mechanical operation.

The COF values for all oil samples during the testing periods are shown in Fig. 8. In general, the COF value measured over time drops [11]. The AB mixture had a higher COF than the AC mixture for all of the testing periods. The most significant difference was seen during the first testing period when the COF for the AB mixture was 0.016 greater. The difference, however, decreases over time until it reaches just 0.0012 at the end of the testing period. Furthermore, the decrement rate of the COF

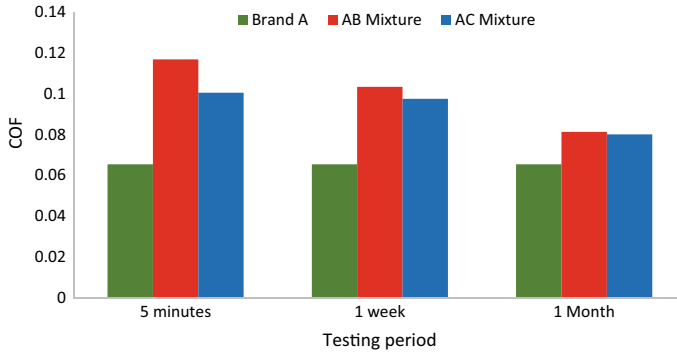


Fig. 8 The COF for all oil samples measured at respective testing period

for the AB mixture is greater than that of the AC mixture over the mixing period. The decrement rate corresponds to the recorded WSD value.

The drop in the COF readings of the oil mixtures, as indicated in Fig. 8, suggests that the mixtures have become more compatible with one another. The less sliding force is required, the lower the COF value.

3.3 Viscosity

Figure 9 depicts the viscosity of all oil samples at each testing period in response to temperature variations. In general, the viscosity of all oil samples decreases as the temperature rises [17]. This situation is evident because the viscosity of the samples is high at the room temperature 23 °C, ranging from 90 to 160 cSt. The viscosity of all oil samples then reduces from one point to the next as the temperature rises. It implies that viscosity and temperature are inversely related which is as found in Syahrullail et al. [21]. Figure 9a indicates that the AB mixture has the highest viscosity value of 160 cSt at 23 °C, whereas the AC mixture has the lowest viscosity, even lower than Brand A alone, which is 90 cSt at the same temperature. The trend continued until 80 °C when the AB mixture had a lower viscosity than Brand A alone. Figure 9a shows that the presence of Brand B's oil increases the mixture's viscosity, but the existence of Brand C's oil decreases the mixture's viscosity.

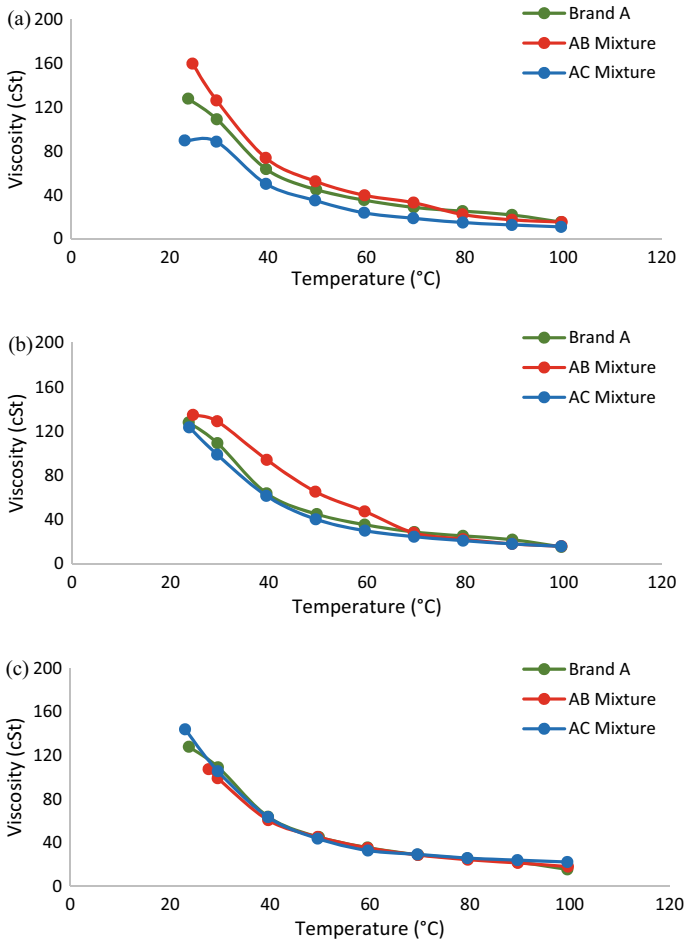


Fig. 9 The relationship between the viscosity of the oil samples and temperature at respective testing period, **a** 5 min, **b** One week, and **c** One month

4 Discussion

The effects of mixing different brands of engine oil on the characteristics of WSD, COF, and viscosity were investigated in this study. These three features were discovered with respect to the mixing period. The research revealed that the WSD is proportional to the mixing period. The longer the mixing duration, the greater the WSD for all oil samples. The COF, on the other hand, was inversely related to the mixing time, with a smaller COF reported at a longer mixing period. Meanwhile, the viscosity-mixing period relationship differs for each oil sample. The viscosity of the AB mixture decreased with time, but the viscosity of the AC mixture increased with mixing time.

Engine oil is used to lubricate the moving parts of an automobile engine. The viscosity of the engine oil is crucial in the formation of the so-called lubrication film at the surface of the moving components. A greater viscosity often results in a thicker lubricating film, which provides better protection between the components [22]. It was demonstrated (as shown in Fig. 6) that the AB mixture, which has the highest viscosity, had a smaller WSD than the AC mixture.

Furthermore, a thicker lubricating film should provide a lower COF, implying that a smaller force is required for the components to move between one another [23]. The friction between the components is low in this situation, which minimizes the tendency for damage. Despite its increased viscosity, the AB mixture scored the greatest COF in the first testing period, as shown in Fig. 8. This anomaly might be caused by the unsettled composition in which the engine oils of Brand A and Brand B have not yet been thoroughly integrated. Instead of friction on a single lubricant, the four-ball must move across lubricants with varied characteristics, demanding a higher COF. This notion is corroborated by the findings of the second testing period, in which the COF value of the AB mixture decreased drastically, suggesting that the oils had thoroughly mixed. Also, the findings are consistent with those of Ezzat [24], Durak et al. [25] and Heredia-Cancino et al. [17] who found that the link between friction and wear is not necessarily straightforward.

On the other hand, few works have been reported that link the amount of antioxidant additive in engine oil to the size of WSD. According to Farhanah [26], a high level of antioxidant additive correlates to a smaller WSD. It is related to the additive's capacity to produce a protective film on the surface of the metal body. Moreover, Gangopadhyay underlined the need for antioxidation additives in avoiding oil oxidation, which can contribute to greater wear [22]. While according to Rudnick [27], the antioxidant additive not only delays oxidation but also helps to stabilise and optimise lubrication performance. They stressed the need of maximising oxidation stability to minimise oil oxidation, which can increase friction and wear. This might explain the rapid increase in WSD for AB mixtures observed in this investigation. The combination of Brand A and Brand B oils induces chemical reactions that disrupt the condition and stability of the antioxidant additive, causing the mixture to oxidise [17, 18]. As a result, even though the viscosity is high, the WSD of the mixture increases.

The mixing of different brands of engine oil, on the other hand, only impacted the relationship of viscosity over temperatures at the beginning of the mixing period. After a month, the relationship for all mixtures is equal, as illustrated in Fig. 9c. In reality, the effect may be reduced sooner owing to engine workload, which allows the different oils to be thoroughly mixed. However, Fig. 9c signifies that the viscosity of the mixtures at room temperature varies. As a consequence, it will have an impact on the engine's protection and performance when it is started for the first time of the day.

5 Conclusion

The results of this investigation indicate that the AB mixture outperforms the AC mixture in terms of WSD and viscosity. The AB mixture was able to develop a more viscous lubricant, resulting in greater component protection. However, the AC mixture has a lower COF and provides greater long-term protection. Despite the benefits, as compared to pure oil, pure oil performs better in the WSD and COF. It is generally known that various additives exist in each engine oil; when these additives are combined, the chemical reaction that happens may destroy the efficiency of the additives and, to a certain extent, may damage the engine. This research only looks at a small portion of the problem, namely the influence on WSD, COF, and viscosity under constant speed and load. Further research on the products of the chemical process, as well as their characteristics at different speeds and loads, may give more insight into the influence of mixing.

Acknowledgements The authors gratefully acknowledge the financial support of Faculty of Mechanical and Automotive Engineering Technology (FTKMA), Universiti Malaysia Pahang.

References

1. Tung SC, McMillan ML (2004) Automotive tribology overview of current advances and challenges for the future. *Tribol Int* 37(7):517–536
2. Souza de Carvalho MJ, Rudolf Seidl P, Pereira Belchior CR, Ricardo Sodr  J (2010) Lubricant viscosity and viscosity improver additive effects on diesel fuel economy. *Tribol Int* 43(12):2298–2302
3. Quinchia LA, Delgado MA, Reddyhoff T, Gallegos C, Spikes HA (2014) Tribological studies of potential vegetable oil-based lubricants containing environmentally friendly viscosity modifiers. *Tribol Int* 69:110–117
4. Mujahid A, Dickert FL (2012) Monitoring automotive oil degradation: analytical tools and onboard sensing technologies. *Anal Bioanal Chem* 404(4):1197–1209
5. Kaleli H, Demirtaş S, Uysal V, Karnis I, Stylianakis MM, Anastasiadis SH, Kim D-E (2021) Tribological performance investigation of a commercial engine oil incorporating reduced graphene oxide as additive. *Nanomaterials* 11(2):386
6. Soleimani M, Sophocleous M, Glanc M, Atkinson J, Wang L, Wood RJK, Taylor RI (2013) Engine oil acidity detection using solid state ion selective electrodes. *Tribol Int* 65:48–56
7. Kumar A, Deval P, Shrinet ES, Ghosh SK (2020) Investigation on tribological properties of used engine oil with graphene. *Proc Inst Mech Eng Part J J Eng Tribol* 235(7):1420–1429
8. Yunus R, Rasheed HS, Zulkifli NWM (2020) Wear and friction behavior of semi synthetic engine oil blended with palm oil/TMP ester and nano glass powder additive. *Jurnal Tribologi* 26:16–36
9. Mushtaq Z, Hanief M (2021) Enhancing the tribological characteristics of Jatropha oil using graphene nanoflakes. *J Tribol* 28:129–143
10. Khairuldean AK, Ing TC, Che Kob MS, Budianto A, Bambang S, Baharin TK, Ariyono S, Syahrullail S (2012) Extreme pressure properties investigation of palm olein using four ball tribotester. *AIP Conf Proc* 1440:920–927
11. Korcek S, Sorab J, Johnson MD, Jensen RK (2000) Automotive lubricants for the next millennium. *Ind Lubr Tribol* 52(5):209–220

12. Kapoor A, Tung SC, Schwartz SE, Priest M, Dwyer-Joyce RS (2000) Automotive tribology. In: Modern tribology handbook, vol 2, no 32. CRC Press, pp 1187–1213
13. Vardhaman BSA, Amarnath M, Ramkumar J, Mondal K (2020) Enhanced tribological performances of zinc oxide/mwcnts hybrid nanomaterials as the effective lubricant additive in engine oil. *Mater Chem Phys* 253:123447
14. Inoue K, Tominaga E, Akiyama K, Ashida T (1995) Effects of lubricant composition on fuel efficiency in modern engines. *SAE Tech Pap Ser* 45–53
15. Meng Y, Xu J, Jin Z, Prakash B, Hu Y (2020) A review of recent advances in tribology. *Friction* 8(2):221–300
16. Song H, Chen J, Liu Z, Ji L, Li H, Ling G, Chen J (2018) Toward low friction in high vacuum by designing textured a-c/il duplex lubricating film. *Vacuum* 148:11–17
17. Heredia-Cancino JA, Ramezani M, Álvarez-Ramos ME (2018) Effect of degradation on tribological performance of engine lubricants at elevated temperatures. *Tribol Int* 124:230–237
18. Dörr N, Brenner J, Ristić A, Ronai B, Besser C, Pejaković V, Frauscher M (2019) Correlation between engine oil degradation, tribochemistry, and tribological behavior with focus on ZDDP deterioration. *Tribol Lett* 67(2):62
19. Chouhan M, Thakur L, Sindhu D, Patel MK (2020) An investigation on the optimization of anti-wear performance of nano-Fe₃O₄ based ferro-magnetic lubricant. *J Tribol* 25:119–135
20. Hu E, Hu X, Liu T, Fang L, Dearn KD, Xu H (2013) The role of soot particles in the tribological behavior of engine lubricating oils. *Wear* 304(1–2):152–161
21. Syahrullail S, Wira JY, Wan Nik WB, Fawwaz WN (2013) Friction characteristics of rbd palm olein using four-ball tribotester. *Appl Mech Mater* 315(936–940):936
22. Gangopadhyay AK, Carter RO, Simko S, Gao H, Bjornen KK, Black ED (2007) Valvetrain friction and wear performance with fresh and used low-phosphorous engine oils. *Tribol Trans* 50(3):350–360
23. Kovalchenko A, Ajayi O, Erdemir A, Fenske G, Etsion I (2005) The effect of laser surface texturing on transitions in lubrication regimes during unidirectional sliding contact. *Tribol Int* 38(3):219–225
24. Ezzat FMH (1993) The friction and wear of fresh and used engine oils during reciprocating sliding. *Wear* 169(2):167–172
25. Durak E, Kurbanoğlu C, Fatih Tunay R (2006) Experimental study of effects of oil additives into coefficient of friction in journal bearings at different temperatures. *Ind Lubr Tribol* 58(6):288–294
26. Farhanah AN, Bahak MZ (2015) Engine oil wear resistance. *J Tribol* 4:10–20
27. Rudnick LR (2017) Lubricant additives: chemistry and applications. CRC Press, Taylor & Francis Group

Effect of Hot Cylinder Materials on Gamma-Type Stirling Engine Performance Using Solar Dish Concentrator



Purbo Suwandono , Gigih Priyandono , Kushendarsyah Saptaji ,
and Akhmad Rizal Fanani

Abstract The characteristics of Indonesia's tropical climate by getting good sunlight throughout the year can be used as alternative and renewable energy. Stirling engine in general is a type of combustion motor that applies the principle of external combustion because the working system is done on the outside of the engine. The origins of the Stirling engine were discovered by a British scientist named Dr. Robert Stirling. This research using Parabolic Dish type powered by solar energy as a heat source. The Stirling engine is heated using solar energy from the Parabolic Dish. Hot cylinder as a displacer cover is varied by using different materials, namely stainless steel, copper, and glass. The results showed that hot cylinder material using glass gets the highest RPM of 131 RPM and indicated engine power of 0.0712 Watts.

Keywords Stirling engine · Solar dish concentrator · Performance · Hot cylinder · Materials · Stainless steel · Copper · Glass · Displacer

1 Introduction

Indonesia is a country that has tropical climate characteristics that lie below the equator and through the east monsoon with the direction of gusts from parts of the Australian continent to the Asian continent, so that the Indonesian region experiences a dry season and gets good sunlight throughout the year with potential around 4.8 KWh/m^2 [1]. Stirling engine in general is a type of combustion motor that applies the principle of external combustion because the working system is done on the outside of the engine. The origins of the Stirling engine were discovered by a British scientist named Dr. Robert Stirling in 1816 [2]. Engines of this type apply the system regenerating in a closed cycle, where there is a working fluid that undergoes a process

P. Suwandono (✉) · G. Priyandono · A. R. Fanani
Universitas Widyagama, Kota Malang, Indonesia
e-mail: purbo@widyagama.ac.id

K. Saptaji
Sampoerna University, Jakarta, Indonesia

of compression and expansion in a separate reservoir then distributed to move the power piston reciprocating [3]. Stirling engine is defined as a type of engine with a thermal regeneration system using closed cycles. The cycle is closed because the working fluid is permanently trapped in the system. Regeneration is interpreted by the use of heat exchangers internally, which can increase the efficiency of the machine [4]. Stirling engines are also referred to as engines with external combustion or external combustion [5]. A Stirling engine is a heat exchanger that operates on a closed cycle and is designed with the aim of converting the resulting heat energy into mechanical or motion energy. Stirling engine is an engine that utilizes heat energy that comes from outside its working cylinder. Various sources of heat can be used in operating Stirling engines such as heat derived from sunlight radiation, heating elements, and external combustion, but with a note there must be a significant temperature difference between the two cylinders in order to move the engine [6, 7]. In practice, the Stirling cycle that occurs is different from the theoretical cycle in which there are two phases including constant temperature and volume. In analyzing the thermodynamic elements present in the Stirling engine system, several theories are used. One of them was presented by Schmidt, so this theory came to be known as Schmidt Theory [8].

Parabolic Dish is a CSP Solar Power Concentrating System with a type of parabola that uses a concave-shaped mirror to concentrate sunlight onto the receiver located at the focal point of the mirror. Concentrated solar energy is absorbed by the receiver to heat the fluid to 750 °C [9]. The Parabolic Dish uses highly polished mirrors that are composed by parabolic and can reflect 90% of the light that hits it to direct and concentrate sunlight to the heat receiver in this case the Stirling engine. To get the solar heat energy that is greater and centralized at one point requires a concave-shaped solar concentrator coated with glass on the inside. Then the heat energy generated, is changed in the form of mechanical energy to operate the generator that will later generate electricity.

From research related to the development of Stirling engines as power plants have been widely done, it is known that Stirling engines with gamma type have the highest efficiency at low operating temperatures. This is because the Stirling gamma type engine has a heat exchanger and cold exchanger area that is greater than the size of the piston so that the volume of the gas chamber to expand is relatively greater and the process of mechanical power transfer by gas becomes more efficient. Efficiency can be further improved if there is a significant temperature change between hot cylinder (displacer) and cold cylinder. Can cinar [10] has been concerned about the effect of variations in displacer material on low temperature different Stirling engines. The energy source of the study came from LPG. Two types of displacers have been studied using aluminum and MDF (Medium density fiberboard). The highest power is obtained using MDF type displacers with a power of 3.06 Watts. Where displacer uses aluminum emits power of 2.59 Watts. Higher torque was obtained at low speeds because of the increase of the cyclic heating and cooling periods. Many other studies have been about material variations in displacers but little research on material variations in displacer cylinders / hot cylinders.

The study will examine the influence of several specimens of material used on Stirling engine hot cylinders using concentrated solar energy. The material used in

this study has different properties so that the rate of heat transfer will also change which results in different Stirling engine efficiency. The types of materials that will be used include copper, stainless steel, and glass. Each of these materials has a different heat conductivity, so it is interesting to research which materials are able to improve the performance of the gamma type Stirling engine.

2 Stirling Engine

Parabola reflector made dish type with aluminum plate base material formed concave with a diameter of 1.2 m, then coated with a square-shaped mirrored glass with the size of each mirror box 1 cm² glued using sealant fluid. The experimental apparatus can be seen at Fig. 1 which generally consists of a Stirling engine and a parabolic solar reflector.

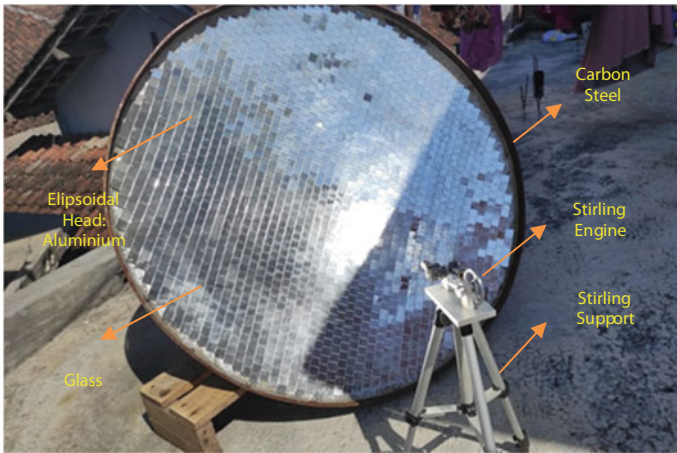


Fig. 1 Dish-type parabolic reflector

Table 1 Dish-type parabolic reflector spesification

No	Part	Material	Description							
1	Elipsoidal head	Aluminium	Plate	2.3	t	x	1000	x	1000	L
2	Stiffener	Carbon steel	Flat Bar	50	t	x	6	x	3078	L
3	Mirror	Glass	Mirror	3.2	t	x	20	x	20	L
<i>Support</i>										
1	Stirling support	Stainless steel								
2	Parabolic support	Aluminium	Dia. 1.2 m							

Table 1 describes the specifications of the material used to make dish-type parabolic reflectors.

The Stirling gamma-type engine works by utilizing alternative energy in the form of solar thermal radiation reflected by dish-type reflector parabolic to the end of the hot cylinder [11]. The selection of gamma-type Stirling engines is used because this type of engine has a heat exchanger and cold exchanger area that is greater than the size of the piston, so the volume of gas chambers to expand is relatively greater and the process of transferring mechanical power by gas becomes more efficient [12]. Focal point calculations are needed to obtain the optimal distance of the reflector parabola in reflecting solar radiation [13]. The focal point value used according to the design is 0.57 m. The closer or farther the placement of the reflector parabola to the Stirling engine by ignoring the focal point calculation, the radiation temperature at the end of the hot cylinder received by the gamma type stirling machine tends to be lower because the heat is not focused on a single point and tends to spread in all directions. The heat energy received by the Stirling engine hot cylinder is then converted into motion energy through a closed regeneration system, where the working fluid in the system will undergo a process of compression and expansion in a convection-separated reservoir. This process causes changes in temperature, pressure difference, and volume which are then distributed to move the power piston. The resulting motion is translationally converted into rotational motion on the flywheel. The resulting motion energy is measured to get the result of the rotation speed in rpm and torque units and the calculation of the efficiency of each type of hot cylinder material produced. In this study, the use of three types of materials including copper, stainless steel, and glass with different conductivity was used to obtain research results related to the effect of conductivity that occurred in the hot cylinder of Stirling engines.

Stirling engine modeling using solidworks software Fig. 2. Explain the design of Stirling engine and Table 2 explain about the materials used to make Stirling engines. The machining process is done with a system that makes it easy to replace hot cylinders. The machining process uses a lathe and a milling machine.

The Stirling engine consists of a heater from solar dish concentrator, an expansion chamber, a regenerator, a cooler fin and a compression chamber. The fluid used is air. To be able to plotting P-V diagram can be done the calculation process using Schmidt's formula [14]. Schmidt's formula can also calculate the power of the Stirling engine. V_{SE} —Swept Volume Expansion, V_{SC} —Swept Volume Compression, dx —Phase Angle between expansion and compression piston, V_E —The expansion momental volume and V_C —The compression momental volume, V_{DC} —Dead Volume of Compression Space, V_{DE} —Dead Volume of Expansion Space and V —Total Momental Volume [15].

$$V_E = \frac{V_{SE}}{2}(1 - \cos x) + V_{DE} \quad (1)$$

$$V_C = \frac{V_{SE}}{2}(1 + \cos x) + \frac{V_{SC}}{2}[1 - \cos(x - dx)] + V_{DC} \quad (2)$$

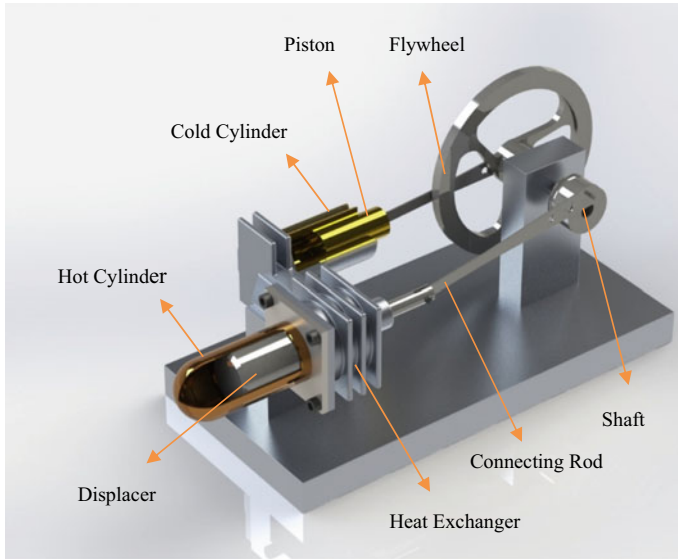


Fig. 2 Gamma-Type stirling engine

Table 2 Gamma-Type stirling engine specification

No.	Part	Material	Description							
1	Base frame	Aluminium	Plate	10	t	x	80	x	140	L
2	Support frame	Aluminium	Plate	10	t	x	25	x	30	L
3	Support frame	Aluminium	Plate	10	t	x	25	x	40	L
4	Hot cylinder	Cooper	Pipe	OD	15	mm		x	45	L
5	Hot cylinder	Stainless steel	Pipe	OD	15	mm		x	45	L
6	Hot cylinder	Glass	Pipe	OD	15	mm		x	45	L
7	Displacer	Stainless steel	Round bar	Dia	13	mm		x	25	L
8	Heat exchanger	Aluminium	Plate	2	t	x	20	x	20	L
9	Cold cylinder	Aluminium	Pipe	OD	12	mm		x	40	L
10	Piston	Brass	Round bar	Dia	8	mm		x	12	L
11	Connecting rod	Stainless steel	Plate	2	t	x	5	x	40	L
12	Shaft	Stainless steel	Round Bar	Dia	6	mm		x	20	L
13	Flywheel	Stainless steel	Plate	4	t	x	60	x	60	L
14	Bolt	Stainless steel	Bolt	M6					40	L

$$V = V_E + V_R + V_C \quad (3)$$

P —The Engine Pressure, P_{mean} —The mean Pressure, P_{min} —The minimum pressure, P_{max} —The maximum pressure, can be calculated using equation:

$$P = \frac{P_{\text{mean}}\sqrt{1-c^2}}{1-c\cos(x-a)} = \frac{P_{\text{min}}(1+c)}{1-c\cos(x-a)} = \frac{P_{\text{max}}(1-c)}{1-c\cos(x-a)} \quad (4)$$

$t = \frac{T_C}{T_E}$ —Temperature ratio, $v = \frac{V_{SC}}{V_{SE}}$ —Swept volume ratio, $X_{DE} = \frac{V_{DE}}{V_{SE}}$ —Dead volume expansion ratio, $X_{DC} = \frac{V_{DC}}{V_{SE}}$ —Dead volume compression ratio, $X_R = \frac{V_R}{V_{SE}}$ —Dead volume regenerator ratio, T_C —Compression gas temperature, T_E —Expansion gas Temperature, T_R —Regenerator gas temperature.

$$a = \tan^{-1} \frac{v \sin dx}{t + \cos dx - 1} \quad (5)$$

$$S = t + 2tX_{DE} + \frac{4tV_R}{1+t} + v + 2X_{DC} + 1 \quad (6)$$

$$B = \sqrt{t^2 + 2(t-1)v\cos dx + v^2 - 2t + 1} \quad (7)$$

$$c = \frac{B}{S} \quad (8)$$

W_E (Joule)—indicated energy in the expansion space, W_C (Joule)—indicated energy in the compression space, W_I (Joule)—indicated energy per one cycle of the engine, L_E (Watt)—indicated expansion power, L_C (Watt)—indicated compression power, L_I (Watt)—Indicated engine power, n —revolution per second can be calculated using following equation:

$$W_E = \oint PdV_E = \frac{P_{\text{mean}}V_{SE}\pi c \cdot \sin a}{1 + \sqrt{1-c^2}} \quad (9)$$

$$W_C = \oint PdV_C = -\frac{P_{\text{mean}}V_{SE}\pi c \cdot \sin a}{1 + \sqrt{1-c^2}} \quad (10)$$

$$W_I = W_E + W_C \quad (11)$$

$$L_E = W_E n \quad (12)$$

$$L_C = W_C n \quad (13)$$

$$L_I = W_I n \tag{14}$$

3 Stirling Engine Performance

Table 3 shows the results of data capture that has been done from the three material specimens. Stirling machine performance is recorded to only operate for one work with a different duration range. Referring to the ΔT temperature difference between temperature expansion stroke (hot cylinder) and compression stroke (cold cylinder) shows that the cause of Stirling engine stops working because the temperature difference has increased insignificantly and even tends to decrease even though the intensity of solar radiation received is getting greater. The decrease in temperature difference was influenced by cold cylinder conditions whose temperature was increasing. It should be in this part that the temperature is kept constant in colder conditions so that there can be a greater temperature difference. Indications of a lack of cooling fins cause the rate of heat transfer from the hot cylinder to the cold cylinder tends to occur on the outside of the engine surface by conduction.

Using the above equation can be plotted the P-V cycle for Stirling engines. Figure 3 shows that the P-V diagram for the materials using glass as hot cylinder. From the P-V cycle it can be seen that the highest pressure is at a phase angle of 20° of 118 kPa. The smallest pressure is at a phase angle of 200° of 86.6 kPa. The difference between maximum pressure and minimal pressure is quite low, this causes the performance of the Stirling engine to decrease. Stirling engine performance can be improved by increasing the difference in hot cylinder temperature with cold cylinder.

From Table 4 it was found that hot cylinders using glass have the most indicated expansion power compared to other materials in the study. Thermal conductivity of the material affects indicated energy per one cycle of the engine and indicated expansion power. The smaller the thermal conductivity of the material will increase indicated expansion power, this is because the heat from sunlight quickly propagates into the cold cylinder, so that the ΔT temperature difference between temperature expansion stroke (hot cylinder) and compression stroke (cold cylinder) is getting smaller. This phenomenon is because glass material has an influence in storing heat

Table 3 Experimental result

No.	Material	Thermal conductivity (W/m. C)	Solar intensity (W/m ²)	Temperature (°C)		ΔT	RPM
				Hot	Cold		
1	Copper	379.0	194.8	175	60	115	106
2	Stainless Steel	16.0	185.3	155	52	103	124
3	Glass	0.78	184.9	132	44	88	131

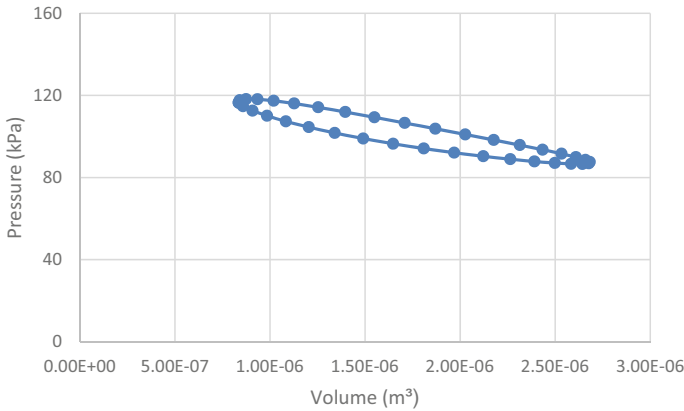


Fig. 3 P-V cycle Stirling engine using glass material as hot cylinder

Table 4 Comparison performance using different material as hot cylinder

No.	Material	W _I (Joule)	L _I (Watt)
1	Copper	0.0048	0.0576
2	Stainless steel	0.0043	0.0663
3	Glass	0.0039	0.0712

better in the hot cylinder area so that the rate of heat transfer that occurs is not quickly propagated by conduction on the outside of the Stirling engine, but tends to take place convectionally on the inside of the Stirling engine in accordance with the principle of work where the working fluid will be compressed or expanded in a separate reservoir then distributed to move the piston in a reciprocating movement.

Yaseen [16] stated that the selection of materials for displacer cylinders or in this study hot cylinder must have characteristics that are thermally insulated, low thermal conductivity and have a light weight. This is in accordance with the results of research that the material that has the lowest heat conductivity, namely glass has the higher rotation, indicated energy and indicated power higher than stainless steel and copper.

4 Conclusions

Gamma-type Stirling machines can convert solar energy into mechanical energy by using dish-type reflectors parabolic concentrated towards the end of the hot cylinder. The heat energy received by the Stirling engine hot cylinder is then converted into motion energy through a closed regeneration system, where the working fluid present in the system is compressed or expanded in a convection-separated reservoir. In this study, the material variation is carried out on the hot cylinder or displacer cylinder,

where the materials used are stainless steel, copper and glass. The result of the study was that glass material got the highest rotation of 131 RPM while for stainless steel 124 RPM and copper 106 RPM. The effect of thermal conductivity on Stirling engine hot cylinder materials using concentrated solar energy showed that the use of glass material with a heat conductivity of 0.78 W/m °C resulted in the highest indicated expansion power 0.0712 W. This is because the glass material is able to store heat better in the hot cylinder area so that the rate of heat transfer that occurs does not quickly propagate by conduction on the outside of the Stirling engine, but tends to take place convection on the inside of the Stirling engine.

References

1. Nasional TSJDE (2019) Indonesia energy out look 2019. *J Chem Inf Model* 53(9):1689–1699
2. Shufat SA, Kurt E, Cinar C, Aksoy F, Hançerlioğulları A, Solmaz H (2019) Exploration of a stirling engine and generator combination for air and helium media. *Appl Therm Eng* 150(April):738–749
3. Borowik B, Borowik B, Kurytnik IP (2015) The application of microcontrollers diagnostic system for evaluation of Stirling engine. *Adv Intell Syst Comput* 317:19–30
4. Getie MZ, Lanzetta F, Bégot S, Admassu BT, Hassen AA (2020) Reversed regenerative Stirling cycle machine for refrigeration application: a review. *Int J Refrig* 118:173–187
5. Caetano BC, Lara IF, Borges MU, Sandoval OR, Valle RM (2019) A novel methodology on beta-type Stirling engine simulation using CFD. *Energy Convers Manag* 184(November):510–520
6. Cardozo E, Malmquist A (2019) Performance comparison between the use of wood and sugarcane bagasse pellets in a Stirling engine micro-CHP system. *Appl Therm Eng* 159(February):113945
7. Hasanpour Omam S (2021) Exhaust waste energy recovery using Otto-ATEG-Stirling engine combined cycle, vol. 183. Elsevier Ltd
8. Dehelean NM, Dehelean LM, Perju D (2010) New trends in mechanism science. *New Trends Mech Sci* 613–623
9. Backes JG, D'Amico A, Pauliks N, Guarino S, Traverso M, Lo Brano V (2021) Life cycle sustainability assessment of a dish-stirling concentrating solar power plant in the Mediterranean area. *Sustain Energy Technol Assessments* 47(July):101444
10. Çinar C, Aksoy F, Erol D (2012) The effect of displacer material on the performance of a low temperature differential Stirling engine. *Int J Energy Res* 36(8):911–917
11. Nazemzadegan MR, Kasaeian A, Toghiani S, Ahmadi MH, Saidur R, Ming T (2020) Multi-objective optimization in a finite time thermodynamic method for dish-Stirling by branch and bound method and MOPSO algorithm. *Front Energy* 14(3):649–665
12. Khanjanpour MH, Rahnama M, Javadi AA, Akrami M, Tavakolpour-Saleh AR, Iranmanesh M (2021) An experimental study of a gamma-type MTD Stirling engine. *Case Stud Therm Eng* 24(October 2019):100871
13. Shboul B et al (2021) Design and Techno-economic assessment of a new hybrid system of a solar dish Stirling engine instegrated with a horizontal axis wind turbine for microgrid power generation. *Energy Convers Manag* 245:114587
14. Hans-detlev K (2019) Energy and thermal management, air-conditioning, and waste heat utilization. *Energy Therm Manag Air-Conditioning, Waste Heat Util* 30–39
15. Hirata K (1997) Schmidt theory for Stirling engines. Stirling Engine home page. Disponível em, pp 1–9
16. Mahmood YH (2020) Fabrication of Stirling engine and study its characteristics. *Tikrit J Pure Sci* 23(September)

The Analysis of Risk Factor Repetitive Motion in Manufacturing Activities Based on Ergonomics



Nur Ezzatul Balqis Binti Mohd Zahari, Norazlianie Sazali, Zawati Harun, and Norsuhailizah Sazali

Abstract The research of ergonomics in the glove manufacturing company was done in the production line. The workers performed most of the processes manually. Consequently, they were exposed to Musculoskeletal Disorders (MSDs) risk factors such as repetitive motion and awkward postures while working. In this case study, the Rapid Upper Limb Assessment (RULA) was used to determine the worker's risk level of MSDs. It was based on a working assessment of video records and photos by the workers. The final RULA score found that the former changing process indicates the high risk of MSDs, investigating, and implementing change required. Besides, the final RULA score of glove rework scores a five. The score indicates a medium risk of MSDs, need further investigation, and change soon. Meanwhile, the glove packing process scored four which indicates a low risk of MSDs and changes might be needed. Other than, the Body Discomfort Survey was answered by the workers ($n = 18$), and the mean MSDs impact scores from the survey concluded that workers felt discomfort the most in the former changing (53,264.75), followed by glove rework (12,419.67), and glove packing (6313.33) process. The DELMIA software was then used to evaluate the improved body postures. The analysis provided the limitations of angular movement of body parts, allowing the manikin to bend at a minimum angle to fit the task while also reducing the final RULA score to an acceptable score.

Keywords Musculoskeletal disorders (MSDs) · Rapid upper limb assessment (RULA) · Body discomfort survey

N. E. B. B. M. Zahari · N. Sazali (✉)
Centre of Excellence for Advanced Research in Fluid Flow (CARIFF), Universiti Malaysia
Pahang, 26600 Pekan, Pahang, Malaysia
e-mail: azlianie@ump.edu.my

Z. Harun · N. Sazali
Advanced Materials and Manufacturing Centre (AMMC), Faculty of Mechanical and
Manufacturing Engineering, Universiti Tun Hussein Onn, 86400 Batu Pahat, Johor, Malaysia

© The Author(s), under exclusive license to Springer Nature Singapore Pte Ltd. 2023
N. H. Johari et al. (eds.), *Proceedings of the 2nd Energy Security and Chemical
Engineering Congress*, Lecture Notes in Mechanical Engineering,
https://doi.org/10.1007/978-981-19-4425-3_12

119

1 Introduction

The study of Ergonomics is between the working environment and the workers. Other than that, the potential ergonomic risk factors around their workplace are crucial for the workers to concern and realize as the consequences are fatal, such as death and disability. The purpose of ergonomics is to minimize effort and limitations while using the product and ensure the design compliments the ability as well as strengthens the consumer. The most significant aspect of Ergonomics is injury prevention since it is scientifically looking for the least painful and least tiring manner to utilize muscles while working. Ergonomics then seeks to increase productivity by making work easier and faster to achieve. Repetitive motion, static posture, heavy lifting, forceful exercise, and exposure to excessive vibration are all examples of possible ergonomic risk factors [1].

According to the Canadian Centre for Occupational Health and Safety, musculoskeletal diseases (MSDs) are a set of painful conditions of muscles, tendons, and nerves. Thus, Bursitis, Epicondylitis, Tendinitis, Carpal tunnel syndrome, and Tenosynovitis are some of the MSDs that can gradually develop with constant excessive exertion [2]. MSDs can affect your quality of life in the short and long term if they are not resolved. Aside from that, conforming to The International Ergonomics Association defines ergonomics into three categories which are physical, cognitive, and organizational [3]. Therefore, physical ergonomics analyzes human anatomical, anthropometric, physiological, and biomechanical functions related to physical activity. To design industrial and consumer products is the principle of physical ergonomics. As for cognitive, it is related to perception, memory, reasoning, and motor response [4]. The interaction may affect humans with systems of other elements. For example, involving several facets such as stress and workload with computer interaction. The concerned of organization economics is the optimization of socio technical systems, as well as crew resources management, communication, work design, work system, working time design, teamwork, participatory design, community ergonomics, cooperative work, new work, programs, virtual organizations, telework, and quality management [5].

2 Literature Review

In the workplace, the terms ergonomics and human factors are frequently used interchangeably. Workplaces have often been designed to effectively transfer items or service machinery. People who integrate at work have gotten less attention because they appear to be so adaptive. By that, since the number of injuries caused by repetitive motion, excessive force, and awkward postures has increased, ergonomics has become a key issue in workplace safety. Based on analysis and research, employing an ergonomic method to lower the amount of pain, musculoskeletal problem risk level, and optimize productivity [6]. The ergonomic approach to certain human interaction

with the workplace and the assigned activities, ensure that machines or tools meet the needs of workers, and improve the performance of work together with deliver an approach understanding the behavior of workers when conducting risk assessments. For entirety, ergonomic approach goals are to reduce work related injury and illness and improve productivity and satisfaction among the workers in the workplace [7].

In the year of 1999, almost 1 million people took time out of work to treat and recover from work-related musculoskeletal pain or impaired function in the lower back or upper extremities. Besides, work-related musculoskeletal disorders (WMSDs) in the manufacturing industry are the crucial causes of sick leaves [8]. In fact, the cause of work-related musculoskeletal disorders is numerous but misunderstood. Biomechanical factors including repetitive motion, strenuous exercises, extreme joint postures, and psychosocial factors determine the most important part in work-related musculoskeletal disorders [9].

The main risk factor of work-related musculoskeletal disorders in two categories which are physical and psychosocial. Thus, pursuant to the (Global Burden of Disease Study 2012). The leading cause of physical disability worldwide is considered as low back pain. Estimated 540 million people are affected, it happens in similar proportions in all societies, interrupts quality of life and work efficiency, and is the most probable cause for medical consultation. Even so, work-related musculoskeletal disorders (WMSDs) can be prevented because ergonomics helps reduce muscle fatigue, increase productivity, and minimizes the possibility and severity of work-related MSDs.

2.1 Rapid Upper Limb Assessment (RULA)

The RULA method was designed to allow the analysis of the requirements on the upper limbs of the worker for the purpose of the risk screening of developing MSDs. This is caused by tasks with rising expenses on the upper body and relatively low demands upon the lower part provides an objective measure of the risks of MSDs. Many ergonomists around the world have used the RULA method. RULA method of use will be observed by positions of individual body segments, the greater the deviation from the neutral position, the higher the score for each body part. The postural loading throughout the body with extra attention to the neck, trunk, and upper limbs and assesses biomechanically is a screening tool of RULA.

The research that used the RULA method [10]. The study was identifying the risk level of injury to musculoskeletal disorders (MSDs) during the production process at PT. Indiana Paint. From the result, 30 awkward postures are identified, 12 working postures (40%) are at high risk, 11 working postures (36.7%) are at medium risk, and 7 working postures (23.3%) are at low risk. As well based on research data, some crucial concerns related to awkward postures on the part of workers, such as incorrect lifting techniques and working methods, manual handling of heavy drums, and a variety of working position heights.

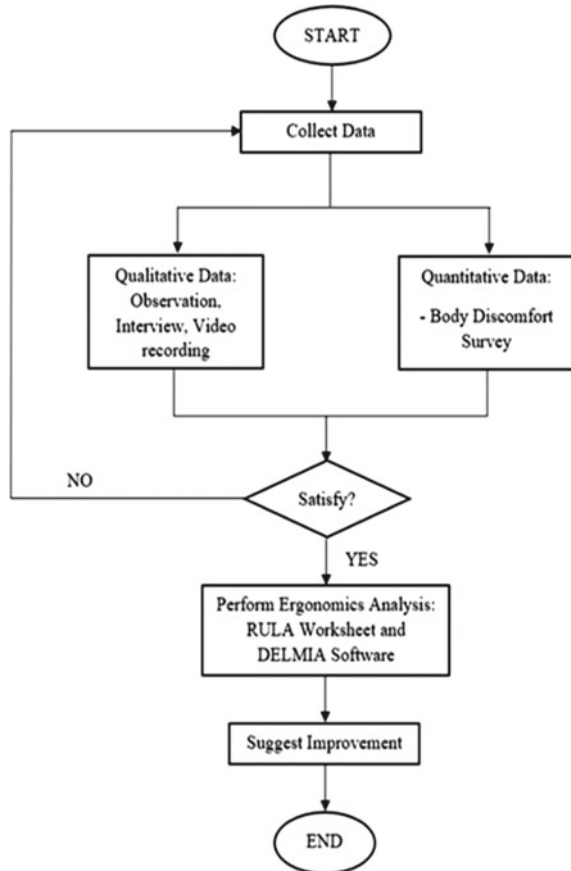
3 Methodology

The industry’s Environmental, Health, and Safety (EHS) department has performed an initial Ergonomics Risk Assessment (ERA) for their workers. Subsequently, they discovered that advanced ERA could be used in the former changing, glove rework and glove packing. The researcher prefers RULA because the workers are concerned with sedentary work as well as to minimize the risk of MSD.

3.1 Research Flowchart

Referring to the flowchart in Fig. 1, this study starts from collecting qualitative data and quantitative data that are related to the research. The qualitative data must include observation, interview and recording while quantitative data using body discomfort survey

Fig. 1 Research flowchart



survey. After that, followed by doing analysis using RULA Worksheet and DELMIA software to determine postural scoring and conduct ergonomic design. Lastly, suggest the improvement for the company to improve to meet the scores in DELMIA software while also lowering the level of MSDs.

4 Results and Discussion

In the quantitative data type, the Body Discomfort Survey was used. Eighteen random workers answered the survey in the former changing, glove rework and glove packing. Moreover, age and work experiences of the workers does not affect the Musculoskeletal Disorders (MSDs) impact scores for any process in this study. Besides, the MSDs effect score may be derived from the survey using formula Total Weighted Frequency x Total Weighted Severity x Total Weighted Productivity. Furthermore, based on the mean MSDs effect scores, it was determined that workers mostly uncomfortable in the former changing (53,264.75), followed by glove rework (12,419.67) and glove packing (6313.33). There is no range for good or bad, but it can be concluded that the highest number of mean MSDs impact score means that it has higher impact on the workers in the process.

Other than that, the analysis was conducted using RULA worksheet. The RULA scores resulting in the former changing process received the final score of seven from the evaluations, indicating that the worker is at a high risk of MSDs and that they need to investigate and implement change as soon as possible. Consequently, the upper arm position obtains the highest score in the former changing process. Following, the RULA score result in the glove rework process received the final score of five from the evaluations, indicating that the worker is at a medium risk of MSDs and changing of body posture is required. The upper arm and wrist position received the highest score for this process, followed by the other body parts. Besides, the glove packing process received a score of four, indicating that the worker is at a low risk of MSD and that a change in body position may be required. The wrist position received the highest score for this process.

Moreover, the DELMIA software is used to evaluate the body posture following improvement. As stated in Fig. 2, DELMIA software is used to analyze body posture once it has improved. The final RULA for the former changing process and glove rework process is reduced into three, as well as the glove packing process is reduced into two and this value indicates acceptable worker body posture.

5 Conclusion

Overall, the study achieves the study objectives. The study started with a Body Discomfort Survey to determine the level of discomfort reported by workers. According to the results, the former changing process has the highest mean MSDs




PROCESS	FORMER CHANGING	GLOVE REWORK	GLOVE REWORK
PICTURE			
UPPER ARM	1	2	1
FOREARM	2	2	1
WRIST	3	2	1
WRIST TWIST	1	1	1
POSTURE A	3	3	1
MUSCLE	0	1	1
FORCE/LOAD	0	0	0
WRIST & ARM	3	4	2
NECK	1	1	1
TRUNK	1	1	1
LEG	1	1	1
POSTURE B	1	1	1
NECK, TRUNK & LEG	1	2	2
FINAL SCORE	3	3	2

Fig. 2 Result of DELMIA score

effect score (53,264.75), followed by the glove rework process (12,419.67) and glove packing process (6313.33). Afterwards, an RULA worksheet is used to analyse the worker’s body position while performing manual work. The research showed that the former changing process obtained a final RULA score of seven. This score indicates that the process is at a high risk of MSDs and that a change in body posture is required. Moreover, the final RULA score of glove rework obtained a five that indicates it was at a medium risk-level of MSDs. Meanwhile, the glove process obtained a four, indicating a low risk of MSDs.

Acknowledgements Authors would like to thank Ministry of Higher Education Malaysia and Universiti Malaysia Pahang for funding under grant RDU210314.

References

1. Glance H (2019) Risk factors. pp 1–9
2. Brown G (2008) Occupational hygiene, 3rd edn., pp 26–46
3. Middlesworth M (2021) Ergonomics 101: the definition, domains, and applications of ergonomics. <https://ergo-plus.com/ergonomics-definition-domains-applications>. Accessed 7 July 2021
4. Reilly T (2013) Ergonomics in sport and physical activity, 1st edn. Human Kinetics
5. Kramer A. An overview of organizational ergonomics. <http://old.askergoworks.com/news/20/An-Overview-of-Organizational-Ergonomics.aspx>. Last accessed 4 July 2021
6. Owen B (2000) AORN J 72(6):1031–1033
7. United States Department of Labor homepage. <https://www.osha.gov/ergonomics>. Last accessed 4 July 2021
8. Liang D, Sun GZ, Wu S (2016) The ergonomics analysis in the process of reversed loader cylinder virtual assembly based on CATIA and DELMIA. In: International conference on electronic, information and computer engineering, vol 44
9. Korhan O., Ahmed Memon A (2019) Introductory chapter: work-related musculoskeletal disorders. Work-related Musculoskeletal Disorders (2019)
10. Restuputri D, Eriko, Masudin I (2019) IOP Conference series: materials science and engineering, vol 598

The Development of Quick Response Manufacturing in Supply Chains Activities Based on Product Planning Control



Siti Nursuhailah Md Suhaidin, Norazlianie Sazali,
and Wan Norharyati Wan Salleh

Abstract The research of Quick Response Manufacturing (QRM) in the production supply chain activities of an organization are based on product planning control. A supply chain with a poor flow for instance in the company's logistics could cause the performance of the company. Inadequate preparation will result in mediocre quality, a loss of productivity and inefficiency. The objective of this thesis is to enhance the critical supply chain of a selected production line in the company by analyzing the existing data. From there, a simulation using software which is WITNESS, is conducted. The output from the simulation will be used in determining methods or solutions to enhance the supply chain related issues. The methods or solutions will be resulting in better efficiency, quality, and productivity. The data collected from the improvement will then be compared to the existing data to gauge whether the improvement contributes to the increase in efficiency and productivity of the selected line. The results from the simulation appear positive feedback, with an average of 85% of the busy time on the proposed layout simulation compared to 66% on the current layout. Even though the differences are minor, they can be critical during peak hours. Finally, the result obtained between the current layout and improved layout proves that the implementation of Quick Response Manufacturing (QRM) can increase the productivity of Dunham Bush company at Kajang, Selangor.

Keywords Quick response manufacturing (QRM) · WITNESS software · Supply chain

S. N. M. Suhaidin · N. Sazali (✉)
Centre of Excellence for Advanced Research in Fluid Flow (CARIFF), Universiti Malaysia
Pahang, 26600 Pekan, Pahang, Malaysia
e-mail: azlianie@ump.edu.my

W. N. W. Salleh
Advanced Membrane Technology Research Centre (AMTEC), School of Chemical and Energy,
Faculty of Engineering, Universiti Teknologi Malaysia, 81310 Skudai, Johor Bahru, Johor,
Malaysia

© The Author(s), under exclusive license to Springer Nature Singapore Pte Ltd. 2023
N. H. Johari et al. (eds.), *Proceedings of the 2nd Energy Security and Chemical
Engineering Congress*, Lecture Notes in Mechanical Engineering,
https://doi.org/10.1007/978-981-19-4425-3_13

127

1 Introduction

Quick Response Manufacturing (QRM) framework was chosen for this project because it is conceptually close to Responsive Manufacturing. QRM is designed to work with high-mix, low-volume production systems with highly changeable demand and highly tailored orders [1]. Paired-Cell Overlapping Loops of Cards with Authorization (POLCA) is a hybrid push–pull of the Production Material Flow Control (PMFC) system that was built as part of the QRM for the strategy [2]. The POLCA mechanism is used to monitor material flow in the QRM system. POLCA's uniqueness and constant work-in-progress (CONWIP) for managing work in process (WIP) in such a complex setting are shown why one would be an advantage over the other regarding to lead time, work in process, and throughput (TP) [1, 3].

QRM aims to minimize lead times in a company's manufacturing supply chain [4, 5]. QRM is described as the process of rapidly designing and manufacturing products in response to customer needs. Internally, it means shortening all job lead times, increasing performance, decreasing costs, and improving response times. With inventory replenishment methods like the Toyota Kanban System (TKS), this is usually difficult to accomplish. Since existing companies such as Toyota Motor Corporation have embraced the Kanban method to take their manufacturing strategy to the next level [6]. The Kanban framework has increased its manufacturing quality and versatility in response to customer needs. The Kanban method is a pull system approach to replenishing parts that have been consumed by customers. It authorizes output at a predetermined rate and a predetermined period [6].

Other than that, QRM has the potential to help in the improvement of lean manufacturing projects, especially in the case of high-variety and low-volume goods. Nonetheless, empirical research is needed to understand better this approach's impact and contribution, especially its synergistic effect with lean manufacturing [7]. Suri believes that focusing solely on lead time is the best practice for many businesses or markets. These businesses are defined by a broad range of products manufactured in a single manufacturing system, customers that demand highly customized goods, and demand that is extremely unpredictable.

There are two types of companies that often conduct QRM. The first type of business creates highly engineered products in small groupings. Another form of business that can profit from QRM does not need to engineer each item but has a large number of them with wildly fluctuating needs. QRM guarantees that everyone in the organization comprehends and participates in the procedure. Furthermore, both management and staff ought to be knowledgeable about the company's production processes, particularly those that have an impact on lead times. Nonetheless, manufacturing procedures do not necessarily specify lead times. The sourcing of raw materials, which is a back-office element, will cause a lead time, and a portion of the QRM strategy will be to reduce lead times for non-manufacturing processes. As a result, the QRM will address every aspect of procurement, transportation, finance, and human resource management. As a company introduces QRM, it must be able to achieve a 95% decrease in lead times, a 30% drop in the price of the final product,

a 60% improvement in on-time delivery reliability, and an 80% or more reduction in scrap and rework. The QRM will assist in improving the critical supply chain.

2 Methodology

This study starts by collecting data that are related to the research. The data that need to observe and record is the time taken for a forklift to go from the inventory area to the designated workstations on the selected production line, as well as the distance the forklift travelled. Following a review of the company’s issue, this study will conclude that a more thorough data collection is required if the data provided by the company is insufficient for an analysis to be performed using the WITNESS software. The software’s performance may be used to improve the company’s competitiveness, and the problem they discovered can be minimised. The simulation’s outcome will assist in the investigation of the company’s problem. Lastly, observe the result and compare the data to the existing configuration of the selected production line using the findings based on the outcome. The comparison of data will provide a clearer picture of what is being suggested and whether it is appropriate for the organization to incorporate in the future or to do additional research to boost results.

3 Results and Discussion

Figure 1 shows the flow for the company in the WITNESS software after entering the data that were collected during the observation. Figure 1 shows three sections in the inventory area which is the unpacking line, transportation and local part. These three

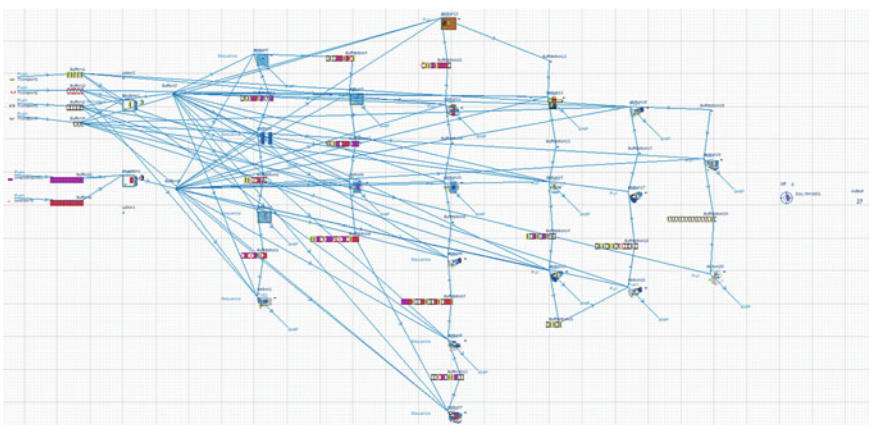


Fig. 1 Current layout with element flow in Dunham Bush company as shown in WITNESS software



Fig. 2 Percentage of performance on the current layout of production department

sections serve as feedback for a production line of 20 workstations that is continuous and interdependent. If there is a problem at one or more of the workstations, the company’s output of the product cannot reach their target for each day. The output quantity that the company gets for current data is only 27 units.

As shown in Fig. 2, there is only three colours appearing on the graph after running the simulation using witness software which is a percentage of idle for yellow colour, percentage of busy for green colour and percentage of blocked for purple colour. From the Fig. 2, there is more idle time at station ten (Brazing Sections), than at station eleven which is one of the Electrical sections, due to the longer takt time. Due to the meeting point of the Brazing and Electrical Sections, these two stations are considered vital, and if one of the stations takes a longer takt time, a blockage will result. Based on these findings, the takt time, distance travelled, and time spent from the inventory area to this vital station should be examined and, if possible, lowered to achieve a good outcome.

According to the Fig. 2, the alterations in the Brazing Section not only increased the average percentage of busy time, but also generated a blockage at station seven which is 6.3%. The obstruction occurs as a result of a mismatch between the workstation’s takt time and the distance travelled by the forklift from the inventory section to the designated workstation. After running the witness simulation with current data, the value for the Electrical Section maintains 100% busy time on each workstation. This value means that was exceeding the *QRM* goal of 80% busy time.

For the improvement, some changes have been done by rearranging the placement of the previous inventory area and adding another inventory area at a vacant area in the company. Furthermore, an additional forklift is suggested to alleviate the blockage that formed in a few workstations as a result of the increased inventory space. Figure 3 shows that there are two parts for inventory, an interface from WITNESS software, which will deliver on a valued route that has been set. On the left side at the bottom inventory should be routed to Brazing Section, while for the

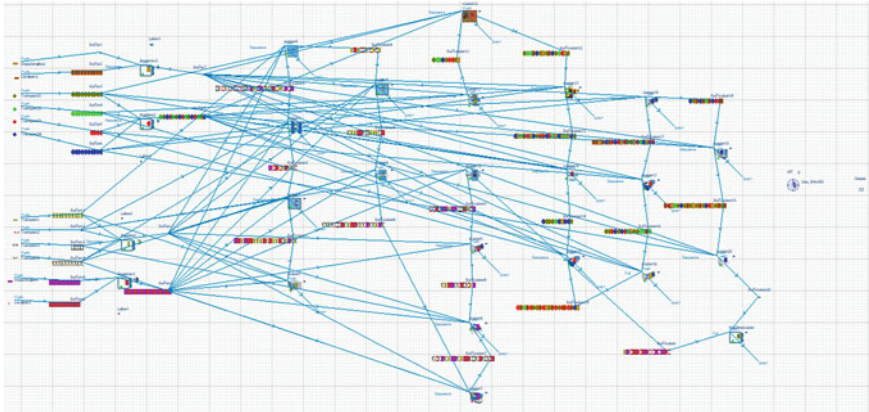


Fig. 3 Proposed improved layout for production department using WITNESS software

upper on the left side inventory should be routed to Electrical Section. This action is being taken to improve the workstation’s efficiency and establish a better traffic flow for all inventory delivered through the workstation, even during peak periods. The output quantity increased from 27 to 32 units after the improvement.

The result is given in Fig. 4, which shows that the workstations in the Brazing Section and Electrical Section, which total are 20 workstations, have produced a positive output when compared to the prior result. However, in this graph, there is the same color that appears in the current graph which is a percentage of idle for yellow color, percentage of busy for green color and percentage of blocked for purple color. These colors appear according to the process that takes place while producing the product. Following a review of the current situation and certain adjustments, the

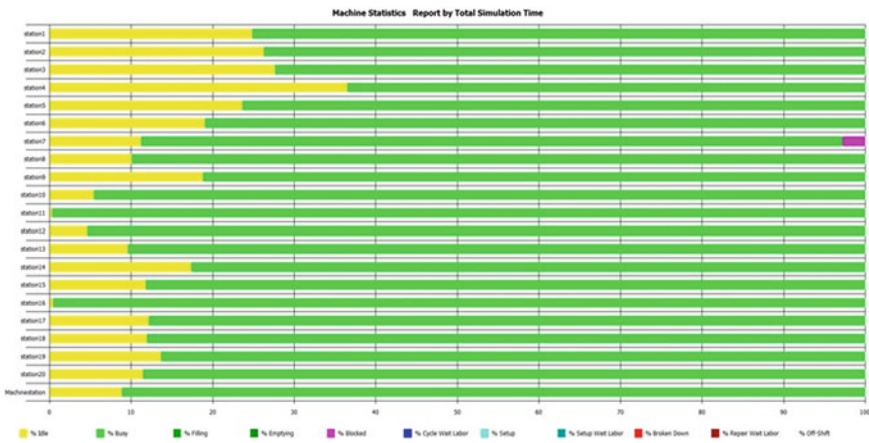


Fig. 4 Percentage of performance on the improved layout in production department

QRM's goal of achieving a busy time of between 80 and 90% has been achieved in terms of the average percentage of line output, which is 85%. At 0.13% across all workstations, the blockage appears to be minor.

4 Conclusion

As a result, the study is successful in achieving its goals. The research began with observational data to identify the issue that arose in the company. According to the results, the graph demonstrates a slight improvement and a setback on idle time, busy time, and blockage when the same strategy is used for improvement. When comparing the current layout of line production to the improved layout of line production, the percentage of idle time shows a significant increase in the Brazing Section. This is because of a blockage that occurred at station seven in the top inventory portion. Besides, the impact of Quick Response Manufacturing on supply chain activities has a positive feedback loop. The average percentage of busy time has increased from 65.72% in the current layout to 85% in the improved layout. When implementing QRM in Dunham Bush company's production line, a thorough analysis of the workflow is needed to prevent any unwanted incidents in the future.

Acknowledgements Authors would like to thank Ministry of Higher Education Malaysia and Universiti Malaysia Pahang for funding under grant RDU210314.

References

1. Bong CS, Chong KE, How WC (2018) Job shop material control based on the principles of quick response manufacturing. *J Adv Manuf Technol* 12(1):15–30 (special issue 2)
2. Viana DD (2015) Integrated production planning and control model for engineer to order prefabricated building systems
3. Frazee T, Standridge C (2016) CONWIP versus POLCA: A comparative analysis in a high-mix, low-volume (HMLV) manufacturing environment with batch processing. *J Ind Eng Manage* 9(2):432–449
4. Sugawara E, Nikaido H (2014) Analysis of POLCA and GPOLCA material control strategies. *Antimicrob Agents Chemother* 58(12):7250–7257
5. Godinho FM, Marchesini AG, Riezebos J, Vandaele N, Ganga GMD (2017) The extent of knowledge of quick response manufacturing principles: an exploratory transnational study. *Int J Prod Res* 55(17):4891–4911
6. Adnan AN, Jaffar A, Yusoff NB, Halim NHBA (2013) Implementation of just in time production through Kanban system. *Ind Eng Lett* 3(6):11–20
7. Gomez PFJ, Filho MG (2017) Complementing lean with quick response manufacturing. *Int J Adv Manuf Technol* 90(5–8):1897–1910

Rheological Characteristics and Optimization of Novel TiO₂-POE Nanolubricant Using Response Surface Method (RSM) for Air Conditioning System Compressor Application



Agus Nugroho , Rizalman Mamat, Zhang Bo, Wan Azmi Wan Hamzah, Mohd Fairusham Ghazali, and Talal Yusaf

Abstract This study aims to determine the viscosity characteristics of TiO₂-Polyolester (POE) nanolubricant and optimize it for heat transfer applications in compressor air conditioning systems. A magnetic stirrer was used to mix TiO₂ and POE lubricant for 30 min. The nanolubricant was then ultrasonicated with a probe for 120 min to stabilize the TiO₂-POE nanolubricant. There were seven different types of samples examined in this study, with concentrations of 0, 0.05, 0.15, 0.25, 0.35, 0.45, and 0.85 vol%. Rotational Rheolab QC was used to quantify viscosity from 30 to 90 °C. The viscosity of nanolubricant augmented as the proportion of nanolubricant increased. In contrast, when the test temperature rises, the viscosity drops. The greatest viscosity rise was 56.657% at 0.85 vol% at 80 °C, while the lowest viscosity increase was 0.029% at 0.05% at 30 °C. Based on the Response Surface Approach, optimization using the Multivariable Functions Optimization (MBFO) method with the Central Composite Design (CCD) type. The uncertainty analysis was also performed in this study. The most optimum dynamic viscosity is 34.8098 mPa s. At a temperature of 60 °C, this condition was achieved in samples with a concentration of 0.45 vol%.

Keywords Central composite design (CCD) · Response surface methodology (RSM) · Newtonian · Viscosity · TiO₂-polyolester (POE) nanolubricant

A. Nugroho (✉) · R. Mamat · Z. Bo
School of Mechanical Engineering, Ningxia University, Yinchuan, China
e-mail: ir.agusnug@gmail.com

A. Nugroho · R. Mamat · W. A. Wan Hamzah
College of Engineering, Universiti Malaysia Pahang, Gambang, Malaysia

R. Mamat · W. A. Wan Hamzah · M. F. Ghazali
Centre for Research in Advanced Fluid & Processes, Universiti Malaysia Pahang, Lebuhraya Tun Razak, 26300 Gambang, Kuantan, Pahang, Malaysia

T. Yusaf
School of Engineering and Technology, Central Queensland University, Rockhampton, Australia

Nomenclature

min	Minute
h	Hour
g	Gram
vol%	Volume %
TiO ₂	Titanium dioxide
POE	Polyolester
PAG	Polyalkylene glycol
UV Vis	Ultra violet visible
T	Temperature (°C)
BMFO	Multivariable functions optimization
CCD	Central composite design
RSM	Responses surface method
TEM	Transmission electron microscopy
ANOVA	Analysis of variance

Greek symbols

ϕ	Volume concentration (%)
ρ	Density (kg/m ³)
μ	Dynamic viscosity (mPa s)

Subscripts

<i>L</i>	Lubricant
<i>P</i>	Nanoparticle
<i>nf</i>	Nanofluid
<i>bf</i>	Base fluid

1 Introduction

Friction and wear have long been recognized as the primary causes of damage to a moving component [1–3]. As a result, lubricants are developed to reduce friction and wear and tear on any two metal surfaces that come into contact. Conventional lubricants cannot provide optimal protection to the two metal contacts because their surfaces are not as smooth as they appear to our eyes. The roughness of the two metal contact surfaces make it possible for the two parts to be the source of friction and wear

without even realizing it at the atomic level [4–6]. This phenomenon has inspired researchers to make lubricants that can overcome atomic-scale roughness, preventing friction and wear more effectively. Compared to conventional lubricants, evidence from the previous study shows that nanolubricant provides significant protection in preventing wear and lowering friction in the refrigeration system compressor [7–9]. Nanolubricant claims to be able to give atomic-level lubrication that traditional lubricants cannot give such protection [10–12].

Sharif et al. [13] adopted a two-step strategy to produce Al_2O_3 /polyalkylene glycol (PAG) 46 nanolubricant in vehicle air conditioning compressors. The nanolubricant's viscosity increased considerably at concentrations of 0.3 vol% and higher. Later, Zawawi et al. [14] adopted a two-step approach to produce Al_2O_3 - TiO_2 /PAG46, with two concentrations of 0.02 and 0.1 vol%. The most significant increase in viscosity was 20.50% in the sample with a concentration of 0.1 vol%. Babarinde et al. [15] using a graphene-mineral oil nanolubricant in the refrigeration system escalate system performance. The findings show that the ideal concentration of graphene nanolubricant for 50 and 60 g charge is 0.02 vol%. In the meantime, the optimal refrigerant charge of 70 g graphene nanolubricant is between 0.06 and 0.07 vol%. The maximum value is used to determine optimization, which is based on experimental outcomes.

Lingamdinne et al. [16] used a form of CCD based on the RSM to establish the optimal adsorption process of the new adsorbent iron-oxide-immobilized graphene-gadolinium oxide (Fe-GO-Gd) nanocomposite adsorption. The highest desirability criteria are used to carry out optimization. Furthermore, Fazeli et al. [17] used the response surface method (RSM) to optimize the heat transmission and flow behavior of an MWCNT-CuO hybrid nanofluid at a concentration of 0.1 wt% in a plate heat exchanger application.

In this assessment, a novel TiO_2 -POE nanolubricant was synthesized, and its properties and optimization were examined. A detailed experimental technique was conducted to investigate the fundamental rheological behavior. Using the Multivariable Functions Optimization (MBFO) approach with the CCD based on RSM, the interaction impacts of various process parameters on dynamic viscosity were thoroughly examined. An analysis of variance (ANOVA) analysis was used to examine and statistically confirm the relationship of dynamic viscosity on two independent process factors (volume concentration and temperature). The process optimization is conducted by using RSM with utmost desirability to determine the best conditions of independent variables that can yield in optimum dynamic viscosity.

2 Experimental Methodology

2.1 Nanolubricant Preparation

Sigma Aldrich of the United States supplied TiO₂ nanopowder with typical size of 21 nm and a cleanliness of 99.5% for Transmission Electron Microscopy (TEM). SUNISO, a Belgian company, manufactures special electric compressor lubricants for air conditioning system compressors. Several previous researchers have advocated a two-step approach for the synthesis of this nanolubricant. The magnetic stirring and ultrasonication processes can be changed according to the need to manufacture the best nanolubricant product using this method easily.

Formula 1 was used to calculate the proportion of TiO₂ nanopowder in POE compressor lubricant, as done by Nugroho et al. [18] in earlier studies.

$$\phi = \frac{m_p/\rho_p}{m_p/\rho_p + m_l/\rho_l} \times 100\% \quad (1)$$

The preparation of nanolubricant begins by weighing the two materials, which are then blended for 30 min without being heated using magnetic stirring. This procedure aims to generate a homogeneous nanoemulsion of TiO₂ nanopowder with POE lubricant. Furthermore, the ultrasonication of the nanolubricant formulated for 120 min was used to prevent the formation of nanopowder augmentation in the lubricant as suggested by Nabil et al. [19]. Agglomeration phenomenon will occur due to the addition of nanopowder to this nanolubricant, which will encourage sedimentation. The presence of sedimentation will make the nanolubricant unstable [20, 21]. Figure 1 illustrates the process of forming a nanolubricant using a two-step method.

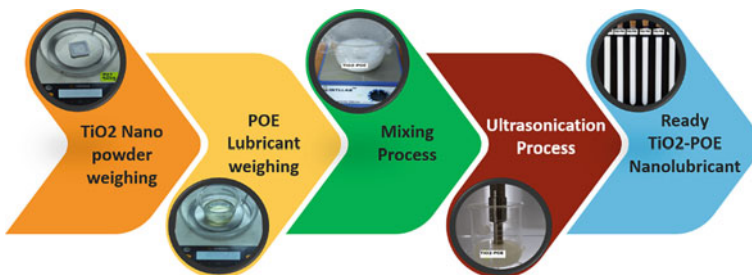


Fig. 1 Two-steps approach for nanolubricant preparation

2.2 Viscosity Measurement

The RheolabQC Rotational Rheometer instrument from Anton Paar, which refers to ISO 3219, was used to test viscosity in this investigation as suggested by Azima et al. [22]. RheolabQC was chosen because of its ability to combine high performance with ease of usage. Single point measurements, melting point determinations on flow curves, and analyses of complex viscosity features can all be done swiftly with Rheolab QC reported by previous researchers [23, 24]. The concept of this viscosity measurement is to deposit TiO₂-POE nanolubricant in a 21 ml tube and rotate the tube from a motionless position to 1000 rpm. The measurement refers to DIN EN ISO 3219 standard. Each sample was measured three periods, with the middling value selected for further assessment. The TiO₂-POE nanolubricant was examined at temperatures ranging from 30 to 90 °C.

2.3 Uncertainty Analysis

The use of formula 2 is used to determine the uncertainty analysis as suggested by Zawawi et al. [25]. The number of dynamic viscosity measurements on each sample at all measurement temperatures determines the standard deviation. The number of samples is defined by the number of executed measurements taken on each sample at each temperature, which is three. As a result, the determination of uncertainty analysis ii involves the use of 147 data sets.

$$\sigma = \frac{\text{standard deviation of sample range}}{\sqrt{\text{number of the sample}}} \quad (2)$$

2.4 Optimization

A CCD based on the response surface method is adopted in the optimization as suggested by previous researchers [26, 27]. The volume concentration and temperature of TiO₂-POE nanolubricant are used as multivariable in this optimization study. These two factors will result in a dynamic viscosity response, which will be investigated to discover the optimum dynamic viscosity value. The optimum criteria in this study's topic will be elaborated in more detail in the following sub-section. This optimization model used Multivariable Functions Optimization (BMFO). In BMFO, the first optimization results are adopted for re-optimization to discover the most optimum level of TiO₂-POE viscosity. As a result, the optimization outcomes obtained are unbiased and detailed in the following sub-section.

3 Results and Discussion

3.1 The Impact of Volume Fraction on Dynamic Viscosity Analysis

The viscosity of a lubricant is an indicator of its resistance to flow. In basic form, viscosity is a measurement of a fluid's thickness or resistance to substances passing through it. Figure 2 depicts the influence of TiO₂-POE nanolubricant volume concentration on dynamic viscosity. Figure 2 shows that the dynamic viscosity value of TiO₂-POE nanolubricant increases in response to escalation in the volume concentration of TiO₂-POE nanolubricant. On the graph, it can also be seen that while dynamic viscosity increases insignificantly, it increases significantly at the concentration volume of 0.85%. At a proportion volume of 0.05% and a temperature of 90 °C, the lowest dynamic viscosity value of TiO₂-POE nanolubricant is 11,947 mPa s, while the most significant dynamic viscosity value is 130,148 mPa s at a volume of 0.85% and a temperature of 30 °C. The dynamic viscosity value of POE lubricants was increased by 0.029–56.657%.

Figure 3 depicts the escalation in dynamic viscosity as a dependent of the volume concentration of TiO₂-POE nanolubricant. According to the graph, there is a trend of increasing dynamic viscosity linearly with the increasing TiO₂-POE nanolubricant concentration. At 80 °C, the increment in concentration volume increased by 56.657% at 0.85 vol%. The sample with 0.05% volume concentration at 30 °C has the lowest dynamic viscosity escalation by 0.029% only.

The chart depicts that dynamic viscosity of the nanolubricant increased with proportion. The Van der Waals effect amid molecules in nanolubricant are one of the possible physical structure triggering an increase in dynamic viscosity reported by Saedodin et al. [28]. Later, Ali et al. [29] stated in another study that increasing exchanges between nanopowder and oil molecules can promote to an increase in viscosity. Higher friction and viscosity result from greater particle internal collision; on the other hand, lower viscosity results from less internal collision.

Fig. 2 The link between the volume of concentration and changes in dynamic viscosity

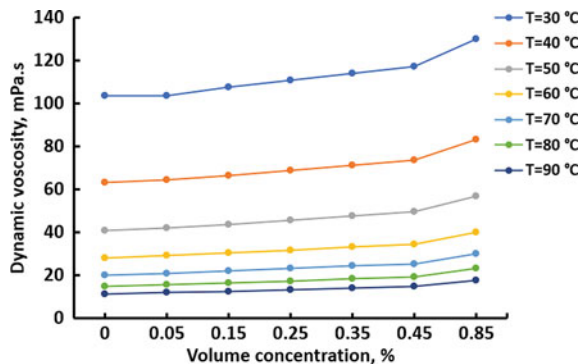
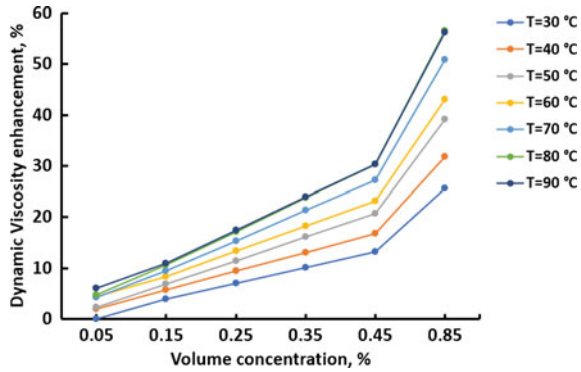


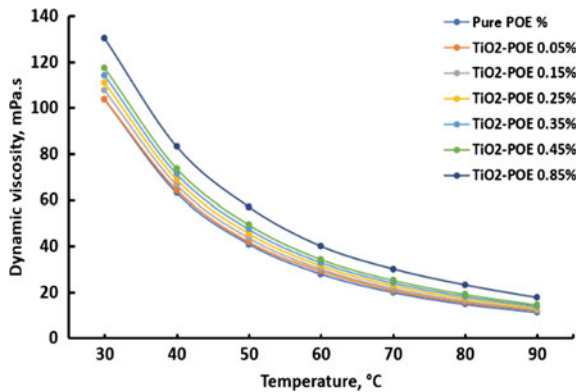
Fig. 3 The correlation between the volume of concentration and the increase in dynamic viscosity



3.2 The Impact of Temperature on Dynamic Viscosity Analysis

Figure 4 depicts the influence of temperature on the dynamic viscosity of TiO₂-POE nanolubricant. According to Fig. 4 all samples exhibit the same trend, namely a decrease in dynamic viscosity with increasing temperature. The pattern of decreasing dynamic viscosity is consistent with that observed in pure POE lubricants, as reported by Kedzierski [30]. This is due to the fact that as the temperature increases, the energy level of the liquid molecules rises, as does the distance between the molecules. This reduces the intermolecular attraction between them, bringing down the viscosity. The cohesive force inclines to decline, resulting in an upsurge in the rate of molecular exchange between fluid layers, increasing the interaction between layers. As the temperature rises, so does the kinetic energy or heat, and the molecules become more dynamically moving. The atomic bonding power is reduced, and thus if we continue to heat the nanolubricant, the kinetic energy will drain the atomic bonding inside the nanolubricant and then potentially cause the molecules to escape and become vapor. This phenomenon leads to the viscosity decline [31].

Fig. 4 The relationship between temperature and changes in dynamic viscosity



3.3 Optimization Using Response Surface Method (RSM)

Table 1 displays the results of the Quadratic model’s analysis of variance (ANOVA). The model’s F-value is 117.67, which is substantially greater than 0.0001. This value indicates that the model in this variant analysis is a significant one. Other conditions were also confirmed with a *p*-value is lower than 0.0001 as reported by Thriveni and Mahanthesh [32]. The significance of each component was also determined using the *F*-value and *p*-value. A *p*-value of less than 0.05 indicates a significant model condition. The larger the degree of the *F*-value and the lower the *p*-value, the more noteworthy the relevant coefficient term is. In this scenario, the A-volume concentration and B-temperature model terms were significant, with F values of 222.04 and 227.40, respectively, for each model. The dynamic viscosity of TiO₂-POE nanolubricant is significantly affected by volume concentration and temperature, as shown in Table 2. The correlation coefficient of regression (R²) of 0.9849, which corresponds precisely with the adjusted R² of 0.9766, confirms this

Table 1 Output ANOVA from model quadratic

Sources	Sum of squares	df	Mean square	F-value	p-value	Remark
Model	1995.90	5	399.18	117.67	<0.0001	Significant
A. Volume concentration	753.26	1	753.26	222.04	<0.0001	
B. Temperature	771.46	1	771.46	227.40	<0.0001	
AB	1.77	1	1.77	0.5214	0.4886	
A ²	408.78	1	408.78	120.50	<0.0001	
B ²	4.04	1	4.04	1.19	0.3034	
Residual	30.53	9	3.39			
Lack of fit	30.53	3	10.18			
Pure error	0.0000	6	0.0000			
Car total	2026.44	14				
Model	1995.90	5	399.18	117.67	<0.0001	Significant

Table 2 Coefficient of regression

Parameters	Value
Standard deviation	1.84
Mean	30.52
CV %	6.03
R-squared	0.9849
Adjusted R ²	0.9766
Prediction R ²	0.8660
Adequate precision	38.7271

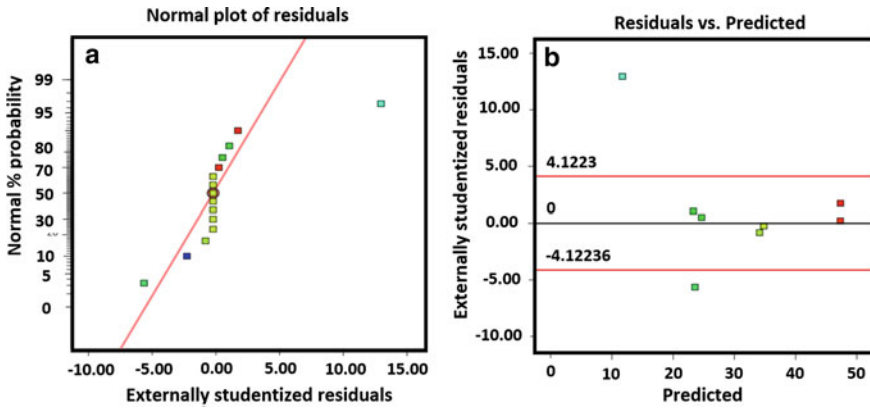


Fig. 5 TiO₂-POE nanolubricant viscosity diagram

result. The results of this model have a high level of consistency, ensuring that they are accurate and reliable. The adjusted R^2 of 0.9766 is in reasonable agreement with the predicted R^2 of 0.8660. The difference of less than 0.2 in this circumstance. Because the value is more than 4, adequate precision of 38.7271 is desirable.

Concerning temperature and volume fraction variables, Fig. 5a displays the ratio of normal probability to studentized residuals of TiO₂-POE nanolubricant. The proximity of data to a line can be used to examine the design model’s suitability. The ratio of internally studentized residuals to predicted is shown in Fig. 5b.

The data values are acceptable under the characteristics defined by the red line. Following that is indicated the ratio of studentized residuals to statistics quantity. The results are within the specified range, indicating that the designed model performed satisfactorily despite the lack of a procedure as reported by [33] Esfe et al. The viscosity increases in all portions of Fig. 5 by following the color gradient from blue to red, from 11.947 mPa s to 130.148 mPa s. The experimental and predicted points are clustered along the normality line in Fig. 5a, confirming the analytical system’s consistency. On the other hand, residues are dispersed randomly across the baseline, with no evident tendency, as seen in Fig. 5b.

The proximity of the predicted and present work findings values is confirmed in Fig. 6. As a result, based on all three plots, it is reasonable to conclude that the quadratic equation is sufficiently reliable to establish a relationship between the examined conditions and the variables considered in the dynamic viscosity of TiO₂-POE nanolubricant.

Figure 7a depicts the output contour of BMFO TiO₂-POE nanolubricant utilizing CCD in the volume concentration range of 0.35–0.55%. The color gradient from blue to red depicts changes in the samples’ dynamic viscosity. The most optimum point in this study is point 7 in the middle. It is the meeting point of the sample with a concentration of 0.45 vol%, which is 34.8098 mPa s at a temperature of 60 °C. Figure 7b depicts a three-dimensional diagram showing viscosity’s optimum in-range favorability as a temperature and volume fraction function.

Fig. 6 Correlation between predictions and present work findings

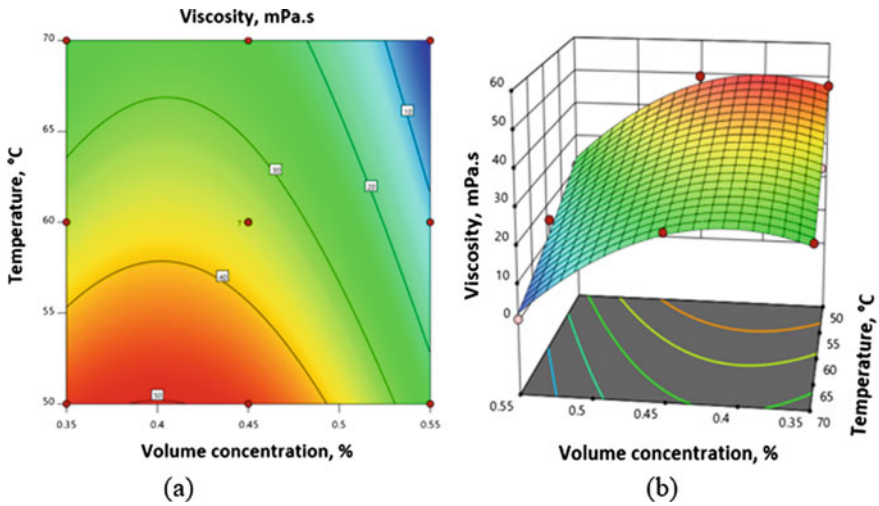
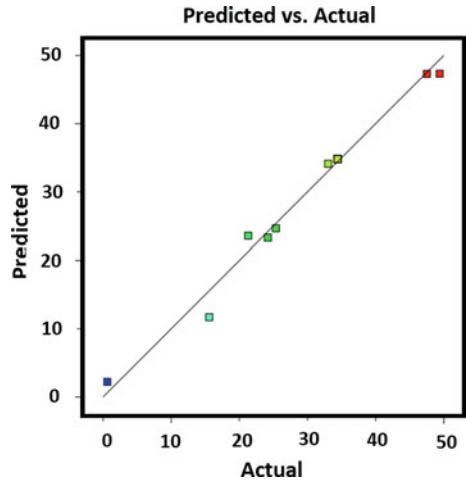


Fig. 7 Dynamic viscosity of TiO₂-POE nanolubricant **a** 2D and **b** 3D contour plotting

The color gradient and curve of the graph surface show changes in the dynamic viscosity of the samples [34]. The blue color in the lower position denotes the lowest dynamic viscosity value, while the red color on the upper surface denotes the most significant level of the dynamic viscosity sample. Quadratic analysis with polynomial models generated the curved surface shape. This model has a high level of agreement and is used to optimize TiO₂-POE nanolubricant.

Fig. 8 Optimization solution for TiO₂-POE nanolubricant

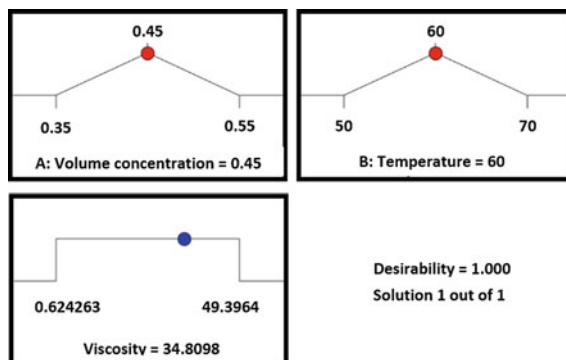


Table 3 Summary of uncertainty measurement of dynamic viscosity

No	Thermo-physical properties	Measured value		Equipment accuracy	Uncertainties, u (%)	
		Min	Max		Min	Max
1	Viscosity (mPa.s)	11.891	120.148	0.01	0.017	0.021

3.4 Optimization Solution

The dynamic viscosity value that is considered the most optimum based on the output of the optimization process of TiO₂-POE nanolubricant samples is 34.8098 mPa.s with desirability of 1000. At a temperature of 60 °C, this condition can be accomplished by applying TiO₂-POE nanolubricant at a concentration of 0.45 vol% as depicted in Fig. 8.

3.5 Uncertainty Analysis

The findings of dynamic viscosity measurements are compared to the accuracy of the methods used to determine the level of uncertainty analysis. As a result, Table 3 provides a summary of the uncertainty analysis.

As a result, based on the uncertainty value, the dynamic viscosity value can be claimed to be in the range of $0.017 \leq \mu \leq 0.021$ mPa s.

4 Conclusion

In this study, a novel TiO₂-POE nanolubricant was synthesized for its rheological characteristic and its optimization. TiO₂-POE nanolubricants' dynamic viscosity was

elevated by 0.029–56.657%. A linear escalation in dynamic viscosity as the TiO₂-POE nanolubricant concentration increases. At 0.85 vol% and 80 °C, the rise in concentration volume was 56.657%. At 30 °C, the sample with a volume concentration of 0.05% had the smallest dynamic viscosity escalation of only 0.029%. The characteristic rheological condition was optimized using the RSM with a central composite design (CCD) type by adopting the Multivariable Functions Optimization (MBFO) method. The correlation effects analysis depicted that the dynamic viscosity is straightly proportional to the volume concentration and temperature test. The ANOVA test identified a quadratic model that strongly reflects the interplay of individual independent variables on response prediction and resulted in a high coefficient of determination viscosity. According to the RSM model, the optimum desirability of 1.000 can be attained at 34.8098 mPa.s. The optimal conditions of volume proportion and temperature of 0.45 vol% and 60 °C, respectively. As a result, the maximum amount of TiO₂-POE nanolubricant that should be used in an air conditioning system is 0.45 vol%.

Acknowledgements This study was supported by the Helan Mountain Scholarship program from Ningxia University, China. The authors like to extend their appreciation to Universiti Malaysia Pahang (UMP) for funding provided by the dedicated internal fund RDU190336 and the FRGS award RDU 1901112.

Conflicts of Interest

The authors declare no conflict of interest.

References

1. Duan C, He R, Li S, Shao M, Yang R, Tao L et al (2019) Exploring the friction and wear behaviors of Ag-Mo hybrid modified thermosetting polyimide composites at high temperature. *Friction* 8(5):893–904. <https://doi.org/10.1007/s40544-019-0306-2>
2. Meng Y, Xu J, Jin Z, Prakash B, Hu Y (2020) A review of recent advances in tribology. *Friction* 8(2):221–300. <https://doi.org/10.1007/s40544-020-0367-2>
3. Zhang Y, Li P, Ji L, Liu X, Wan H, Chen L et al (2020) Tribological properties of MoS₂ coating for ultra-long wear-life and low coefficient of friction combined with additive g-C₃N₄ in air. *Friction* 9(4):789–801. <https://doi.org/10.1007/s40544-020-0374-3>
4. Biswas OF, Sen A, Kibria G, Doloi B, Bhattacharyya B (2020) Parametric analysis on surface roughness of micro-channel by fiber laser milling on zirconia (ZrO₂). *Advances in materials and manufacturing engineering. Lecture notes in mechanical engineering*. pp 91–7
5. Mijušković G, Cica D (2021) Investigation, modeling, and optimization of surface roughness in micro-milling of graphite electrodes. *Int J Adv Manuf Technol* 117(1–2):579–590. <https://doi.org/10.1007/s00170-021-07762-4>
6. Wang Z, Fan Z, Chen X, Kang Y, Cheng J, Chen W (2021) Modeling and experimental analysis of roughness effect on ultrasonic nondestructive evaluation of micro-crack. *Chinese J Mech Eng* 34(1). <https://doi.org/10.1186/s10033-021-00637-5>
7. Marcucci Pico DF, da Silva LRR, Hernandez Mendoza OS, Bandarra Filho EP (2020) Experimental study on thermal and tribological performance of diamond nanolubricants applied to a refrigeration system using R32. *Int J Heat Mass Transfer* 152:119493. <https://doi.org/10.1016/j.ijheatmasstransfer.2020.119493>

8. Sai Pinni K, Katarkar AS, Bhaumik S (2020) A review on the heat transfer characteristics of nanomaterials suspended with refrigerants in refrigeration systems. *Mater Today: Proc.* <https://doi.org/10.1016/j.matpr.2020.11.389>
9. Senthilkumar A, Anderson A (2020) Experimental investigation of SiO₂ nanolubricants for R410A vapour compression refrigeration system. *Mater Today Proc.* <https://doi.org/10.1016/j.matpr.2020.09.659>
10. Sanukrishna SS, Vishnu S, Krishnakumar TS, Jose PM (2018) Effect of oxide nanoparticles on the thermal, rheological and tribological behaviours of refrigerant compressor oil: an experimental investigation. *Int J Refrig* 90:32–45. <https://doi.org/10.1016/j.ijrefrig.2018.04.006>
11. Rajendhran N, Palanisamy S, Shyma AP, Venkatachalam R (2018) Enhancing the thermophysical and tribological performance of gear oil using Ni-promoted ultrathin MoS₂ nanocomposites. *Tribol Int* 124(February):156–168. <https://doi.org/10.1016/j.triboint.2018.03.030>
12. Zin V, Agresti F, Barison S, Littl L, Fedele L, Meneghetti M et al (2018) Effect of external magnetic field on tribological properties of goethite (α-FeOOH) based nanofluids. *Tribol Int* 127:341–350. <https://doi.org/10.1016/j.triboint.2018.06.023>
13. Sharif MZ, Azmi WH, Redhwan AAM, Mamat R (2016) Investigation of thermal conductivity and viscosity of Al₂O₃/PAG nanolubricant for application in automotive air conditioning system. *Int J Refrig* 70:93–102. <https://doi.org/10.1016/j.ijrefrig.2016.06.025>
14. Zawawi NNM, Azmi WH, Redhwan AAM, Sharif MZ, Samykano M (2018) Experimental investigation on thermo-physical properties of metal oxide composite nanolubricants. *Int J Refrig* 89:11–21. <https://doi.org/10.1016/j.ijrefrig.2018.01.015>
15. Babarinde TO, Akinlabi SA, Madyira DM, Ekundayo FM (2020) Enhancing the energy efficiency of vapour compression refrigerator system using R600a with graphene nanolubricant. *Energy Rep* 6:1–10. <https://doi.org/10.1016/j.egy.2019.11.031>
16. Lingamdinne LP, Choi JS, Choi YL, Chang YY, Yang JK, Karri RR et al (2020) Process modeling and optimization of an iron oxide immobilized graphene oxide gadolinium nanocomposite for arsenic adsorption. *J Mol Liq.* 299:112261. <https://doi.org/10.1016/j.molliq.2019.112261>
17. Fazeli I, Sarmasti Emami MR, Rashidi A (2021) Investigation and optimization of the behavior of heat transfer and flow of MWCNT-CuO hybrid nanofluid in a brazed plate heat exchanger using response surface methodology. *Int Commun Heat Mass Transfer.* 122:105175. <https://doi.org/10.1016/j.icheatmasstransfer.2021.105175>
18. Nugroho A, Bo Z, Mamat R, Azmi WH, Najafi G, Khoirunnisa F (2021) Extensive examination of sonication duration impact on stability of Al₂O₃-Polyol ester nanolubricant. *Int Commun Heat Mass Transfer* 126:105418. <https://doi.org/10.1016/j.icheatmasstransfer.2021.105418>
19. Nabil MF, Azmi WH, Hamid KA, Mamat R (2018) Experimental investigation of heat transfer and friction factor of TiO₂-SiO₂ nanofluids in water: ethylene glycol mixture. *Int J Heat Mass Transf* 124:1361–1369. <https://doi.org/10.1016/j.ijheatmasstransfer.2018.04.143>
20. Ali MKA, Xianjun H (2020) Colloidal stability mechanism of copper nanomaterials modified by ionic liquid dispersed in polyalphaolefin oil as green nanolubricants. *J Colloid Interface Sci* 578:24–36. <https://doi.org/10.1016/j.jcis.2020.05.092>
21. Xian HW, Sidik NAC, Saidur R (2020) Impact of different surfactants and ultrasonication time on the stability and thermophysical properties of hybrid nanofluids. *Int Commun Heat Mass Transfer* 110. <https://doi.org/10.1016/j.icheatmasstransfer.2019.104389>
22. Azima M, Başaran Bundur Z (2020) Bio-derived rheology modifying agents for cement-based materials. *Rheology and processing of construction materials. RILEM Bookseries*, pp 79–86
23. Ekstrand EM, Svensson BH, Safaric L, Bjorn A (2020) Viscosity dynamics and the production of extracellular polymeric substances and soluble microbial products during anaerobic digestion of pulp and paper mill wastewater sludges. *Bioprocess Biosyst Eng* 43(2):283–291. <https://doi.org/10.1007/s00449-019-02224-4>
24. Jeong J, Chuta E, Ramézani H, Guillot S (2019) Rheological properties for fresh cement paste from colloidal suspension to the three-element Kelvin-Voigt model. *Rheol Acta* 59(1):47–61. <https://doi.org/10.1007/s00397-019-01171-x>

25. Zawawi N, Azmi W, Redhwan A, Sharif M, Sharma KJijor (2017) Thermo-physical properties of $\text{Al}_2\text{O}_3\text{-SiO}_2\text{/PAG}$ composite nanolubricant for refrigeration system, vol 80, pp 1–10
26. Mahapatra APK, Saraswat R, Botre M, Paul B, Prasad N (2020) Application of response surface methodology (RSM) in statistical optimization and pharmaceutical characterization of a patient compliance effervescent tablet formulation of an antiepileptic drug levetiracetam. *Future J Pharm Sci* 6(1). <https://doi.org/10.1186/s43094-020-00096-0>
27. Singh Y, Singh J, Sharma S, Aggarwal V, Pruncu CI (2021) Multi-objective optimization of Kerf-taper and surface-roughness quality characteristics for cutting-operation on coir and carbon fibre reinforced epoxy hybrid polymeric composites during CO_2 -pulsed laser-cutting using RSM. *Lasers Manuf Mater Process* 8(2):157–182. <https://doi.org/10.1007/s40516-021-00142-6>
28. Saedodin S, Kashefi MH, Bahrami Z (2019) Experimental study on the rheological behavior of nanolubricant-containing MCM-41 nanoparticles with viscosity measurement. *J Therm Anal Calorim* 137(5):1499–1511. <https://doi.org/10.1007/s10973-019-08074-2>
29. Ali MKA, Hou X, Abdelkareem MAA (2019) Anti-wear properties evaluation of frictional sliding interfaces in automobile engines lubricated by copper/graphene nanolubricants. *Friction* 8(5):905–916. <https://doi.org/10.1007/s40544-019-0308-0>
30. Kedzierski MA (2013) Viscosity and density of aluminum oxide nanolubricant. *Int J Refrig* 36(4):1333–1340. <https://doi.org/10.1016/j.ijrefrig.2013.02.017>
31. Ali A, Ilyas SU, Garg S, Alsaady M, Maqsood K, Nasir R et al (2020) Dynamic viscosity of Titania nanotubes dispersions in ethylene glycol/water-based nanofluids: experimental evaluation and predictions from empirical correlation and artificial neural network. *Int Commun Heat Mass Transfer* 118(September):104882. <https://doi.org/10.1016/j.icheatmasstransfer.2020.104882>
32. Thriveni K, Mahanthes B (2021) Significance of variable fluid properties on hybrid nanoliquid flow in a micro-annulus with quadratic convection and quadratic thermal radiation: response surface methodology. *Int Commun Heat Mass Transfer* 124:105264. <https://doi.org/10.1016/j.icheatmasstransfer.2021.105264>
33. Hemmat Esfe M, Goodarzi M, Reiszadeh M, Afrand M (2019) Evaluation of MWCNTs-ZnO/5W50 nanolubricant by design of an artificial neural network for predicting viscosity and its optimization. *J Mol Liq* 277:921–931. <https://doi.org/10.1016/j.molliq.2018.08.047>
34. Pinto F, de Barros DPC, Reis C, Fonseca LP (2019) Optimization of nanostructured lipid carriers loaded with retinoids by central composite design. *J Molecular Liq*. 293. <https://doi.org/10.1016/j.molliq.2019.111468>

A Comprehensive Investigation of Low Proportion TiO₂-POE Nanolubricant Stability for Residential Air Conditioning System Application



Agus Nugroho , Rizalman Mamat, Zhang Bo, Wan Azmi Wan Hamzah, Talal Yusaf, Mohd Fairusham Ghazali, and Fitri Khoerunnisa

Abstract The paper aims to expound on the comprehensive experimental investigation of the stability of TiO₂-Polyolester (POE) nanolubricant. A magnetic stirrer was used to disperse TiO₂ nanopowder into POE lubricant for 30 min. The six samples were then subjected to various ultrasonication treatments lasting 40-, 60-, 80-, 100-, and 120-min. Stability analysis was performed in three stages: visual observation, Ultra Violet (UV) visible spectrophotometric analysis, and measurement of the absolute zeta potential. The results showed that sample without ultrasonication treatment had substantial agglomeration as compared to other samples. The absorbance ratio of the sample without ultrasonication treatment is 0.33. The absorbance ratio value escalated as the duration of the ultrasonication treatment on the sample increases. After ultrasonication treatment for 40–120 min, the absorbance ratio increased by 34–117%. The samples treated with 120 min of ultrasonication showed the highest level of stability, as evidenced by the high absorbance ratio and zeta potential values of 0.95 and –80.48 mV, respectively. As a result, the findings suggests that TiO₂-POE with ultrasonication treatment for 120 min could generate the excellent stability compared to other samples in this experiment.

A. Nugroho (✉) · R. Mamat · Z. Bo
School of Mechanical Engineering, Ningxia University, Yinchuan, China
e-mail: ir.agusnug@gmail.com

A. Nugroho · R. Mamat · W. A. Wan Hamzah
College of Engineering, Universiti Malaysia Pahang, 26600 Pekan, Pahang, Malaysia

T. Yusaf
School of Engineering and Technology, Central Queensland University, Rockhampton 4702,
Australia

M. F. Ghazali
Centre for Research in Advanced Fluid & Processes, Universiti Malaysia Pahang, Lebuhraya Tun
Razak, 26300 Gambang, Kuantan, Pahang, Malaysia

F. Khoerunnisa
Department of Chemistry, Indonesia University of Education, Bandung, Indonesia

Keywords TiO₂-POE nanolubricant stability · Interlude ultrasonication · UV visible spectrophotometry · Zeta potential

Abbreviations

min	Minute
abs	Absorbance
OFAT	One factor at a time
Std. Dev	Standard deviation
POE	Polyolester
Anova	Analysis of variance
UV	Ultraviolet
A	Initial Absorbance
A _o	Final Absorbance
A _r	Absorbance Ratio

Greek symbols

ζ	Absolute zeta potential (mV)
Ø	Concentration
P	Density

Subscripts

<i>l</i>	Refers to lubricant
<i>p</i>	Refers to nanoparticle

1 Introduction

Choi and Eastman [1] pioneered the use of nanofluids for heat transfer applications. Several researchers then developed nanolubricants, a novel subclass of nanofluids based on lubricants. Numerous investigations have discovered that nanolubricants can significantly increase heat transfer in heat transfer equipment. Nanolubricants can be used in air conditioning system equipment, engine lubricants, vacuum pump cooling lubricants, and vehicle air conditioning systems. In the majority of these systems, the first step toward increasing the heat transmission rate is to increase

the thermal conductivity of the poor lubricant. The inclusion of nanoparticles to the lubricant improves heat conductivity due to the nanoparticles' uniform dispersion in a colloid.

Zawawi et al. reported that dispersing $\text{Al}_2\text{O}_3\text{-SiO}_2$ to Polyalkylene Glycol (PAG 46) can increase the thermal conductivity of nanolubricant by 2.41% at 0.1 vol%. A two-step approach was used to make the $\text{Al}_2\text{O}_3\text{-SiO}_2/\text{PAG 46}$ nanolubricant. An ultrasonic bath is utilized for 2 h to prevent nanolubricant aggregation and sedimentation.

Furthermore, Kedzierski [2] reported a 12% escalation in heat transmission by adding CuO to POE synthetic lubricants at a mass concentration of 2%. CuO was combined with magnetic stirring and ultrasonically treated for 24 h to synthesize stable nanolubricants. The light scattering approach was employed to determine the stability of the nanolubricant. Later, Adelekan et al. [3] reported that adding TiO_2 in a domestic refrigerator can elevate the coefficient of performance (COP) by 12%, hitting a maximum of 2.8 at a 40 g of refrigerant charge. Compared to mineral oil/LPG refrigerants, this enhancement in COP is attributable to amplify in the heat transmission rate in the refrigeration system, which stimulates an increase in cooling capacity.

In terms of stability, Li et al. [4] reported that ultrasonication treatment for 60 min can improve the stability of $\text{Al}_2\text{O}_3\text{-ethylene glycol}$ nanofluids. The ultrasonication treatment that lasted more than 60 min did not lead to a significant increase in the stability of the nanofluids. Dhanola and Garg [5] reported that $\text{Al}_2\text{O}_3\text{-SiO}_2/\text{PAG 46}$ nanolubricant can be adopted in automotive air conditioners at a concentration of less than 0.1%. After 30 days storages, the zeta potential of the elements 1:2, 1:3, and 1:4 dropped by 41%, 20%, and 55%, respectively. Mahbulul et al. [6] reported that longer sonication effectively reduces nanoparticle sedimentation, resulting in more excellent nanofluid stability. Lin et al. [7] reported that a 60-min ultrasonication treatment improved the stability of $\text{TiO}_2\text{-NM56}$ nanolubricant for air conditioning systems. Chen et al. [8] discovered the effects of mixing time and sonication period on the thermal conductivity and stability of an aqua $\text{Al}_2\text{O}_3/\text{paraffin}$ mixture. The results show that the best sonication time is 3 h 15 min.

This study utilized visual observation for 30 days, UV visible spectrophotometry, and absolute zeta potential to evaluate the effectiveness of sonication period on the stability of the six $\text{TiO}_2\text{-POE}$ nanolubricants samples. The results of the experimental evaluation were then used to discover the appropriate sample. According to the findings, the duration of sonication has a significant effect on the stability of $\text{TiO}_2\text{-POE}$ nanolubricant. The absorbance ratio has escalated as the period of the ultrasonic treatment on the samples increased. Zeta potential measurement then performed to verify the $\text{TiO}_2\text{-POE}$ nanolubricant's stability.

2 Experimental Method

2.1 Nanolubricant Preparation

The nanoparticles are mixed in a POE lubricant to synthesize a nanolubricant. POE lubricants are supplied by a Belgian multinational firm under the SUNISO brand. The primary nature of POE lubricant is listed in Table 1. Sigma-Aldrich in Saint Louis, Missouri, USA, manufactured TiO₂ nanopowder form with a typical particle size of 21 nm and a purity of 99.5% for this purpose. Table 2 summarizes the fundamental properties of TiO₂ nanoparticles. TiO₂-POE nanolubricant was synthesized using two-steps approach as suggested by Zawawi et al. [9]. The initial stage employs magnetic stirring to disperse TiO₂ nanoparticles into POE lubricant without warmer. The nanolubricant was sonicated using an ultrasonic homogenizer UP400S produced by Hielscher Germany. An ultrasonic homogenizer's objective is to supply more energy than a conventional ultrasonic bath as reported by Modarres-Gheisari et al. [10]. The findings will result in an increase in the homogeneity of the nanolubricant while decreasing the sonication period. The use of an ultrasonic homogenizer is particularly successful at preventing the agglomeration and sedimentation of nanolubricants as reported by previous researchers [11–14]. Additionally, Sofiah et al. [15]

Table 1 POE lubricant's physical and thermal properties

Properties	Value
Absolute viscosity at 40 °C	70.1 mPa.s
Absolute viscosity at 100 °C	9.1 mPa.s
Density at 15 °C	0.960 g/cm ³
Viscosity Index	105
Flash point	252 °C

Table 2 TiO₂ nanopowder's physical and thermal properties

Properties	Metric
Morphology	Spherical shape
Molar mass	79.87 g/mol
Average diameter	21 nm
Representative color	White
Melting point	1843 °C
Dielectric constant (1 MHz)	85
Thermal conductivity at 25 °C	11.7 Wm/K
Density	4 g/cm ³
Dielectric strength	4 kV/mm
Dielectric strength	4 kV/mm



Fig. 1 Graphical process of TiO₂-POE nanolubricants preparation using a two-step method

and Sujith et al. [16] proposed characterizing the geometry and morphology of dry TiO₂ nanopowder using a Transmission Electron Microscopy (TEM).

The ultrasonic with probe device's parameters are 400 W, 24 kHz, 50% amplitude, and 0.5 cycles. Six samples were used in this investigation, all of which had the same 0.02 vol% concentration volume. A 30-min stirring with various sonication treatments was done on the samples for 0, 40, 60, 80, 100, and 120 min. Each sample will be discussed in further depth in the results and discussion. The method of TiO₂-POE nanolubricant synthesis is depicted in Fig. 1.

The synthesis of nanolubricant is separated into four stages. The first phase involves calculating the required lubricant and nanoparticle mass. Equation 1 is used to determine the volume fraction ratio of nanoparticles to lubricants [12].

$$\varnothing = \frac{m_p / \rho_p}{m_p / \rho_p + m_l / \rho_l} \times 100\% \quad (1)$$

where the nanoparticle volume fraction % is symbolized by \varnothing ; the TiO₂ nanopowder's mass is noted as m_p ; the lubricant's mass is m_l ; density of TiO₂ nanopowder is ρ_n ; and POE lubricant's density is symbolized by ρ_l .

The two-step nanolubricant preparation procedure is depicted in Fig. 1. Second, after weighing, the nanoparticles are blended using a magnetic stirrer in the lubricant. Following that, the formed nanolubricant is subjected to a designated time of ultrasonication. Unlike other types of nanofluids, TiO₂-POE nanolubricants were synthesized by an intermittent ultrasonication method. This interlude ultrasonication technique is a progressive procedure in which the ultrasonication process is repeated every 40-min with a 15-min break in between. The 15-min time period is meant to achieve complete immersion of the POE lubricant in the nanoparticles. Fourth once, they are ready, the samples were stored in an experimental tube for further visual analysis. As observed by Al-Ansari et al. [17] this immersion increases the wettability of the nanoparticles, resulting in a more essential contact between the TiO₂ nanoparticle molecules and the lubricant. Additionally, a 15-min pause allowed the nanolubricant to cool gradually, preventing damage to the interaction between the TiO₂ nanoparticles and the lubricant, as illustrated in Fig. 2.

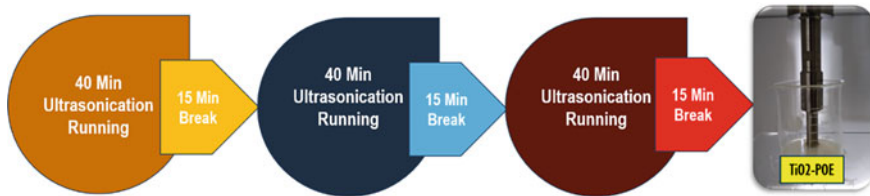


Fig. 2 Graphical process of interlude ultrasonication method

2.2 TiO_2 -POE Nanolubricant Stability Analysis

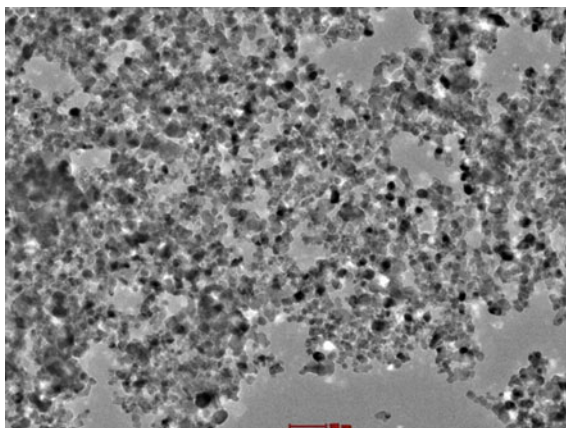
The stability of the TiO_2 -POE nanolubricant was determined using a direct visual approach, an absorbance value was measured by a spectrophotometer, and the absolute value of the zeta potential. These three evaluations are interconnected, as established by previous researchers. Visual inspection is used to detect sedimentation and aggregation of the generated nanolubricant [18]. UV vis will be utilized to authenticate the visual inspection's findings. The absorbance ratio of the nanolubricant was examined on the first day after it was synthesized. The absorbance ratio was determined for a period of 30 days. The results of the absolute zeta potential analysis will verify the results analysis of the highest absorbance ratio values as reported by Redhwan et al. [19]. The zeta potential on the day 30th was measured only on the nanolubricant with the highest absorbance ratio value as suggested by Sharif et al. [20].

3 Result and Discussion

3.1 TiO_2 Nanoparticle Characterization

The Tecnai™ Spirit TWIN Transmission Electron Microscopy (TEM) was employed in this investigation. The TEM was used to characterize TiO_2 -POE nanolubricants and to examine the morphology of TiO_2 dispersed in the POE lubricant in ambient temperature state. The TEM results of the TiO_2 -POE nanolubricant characterization at a concentration of 0.02 vol% are shown in Fig. 3. The crystal structure and microstructure differences between the materials were further investigated using TEM analysis on a concentration selected for TEM investigation. The TEM film reveals a porous and spherical structure of nanopowder. The image demonstrates a distinct lattice fringe, which confirms the nanostructure's strong crystallinity. The image exhibits concentric circles caused by the nanostructure's polycrystallinity. Because the grain boundaries of each crystal grain are oriented in several directions rather than just one, TiO_2 nanopowder is a polycrystalline material [21–23]. The

Fig. 3 TiO₂ nanoparticles morphology in 14,500 magnifications



TEM image reveals that the grain sizes of TiO₂ nanopowder are on average 21.0 nm, which is consistent with the manufacturer's claimed size.

3.2 TiO₂-POE Nanolubricant Visual Analysis

Visual inspection is the initial stage in determining the stability of the TiO₂-POE nanolubricant. Figure 4 depicts the results of 30 days of observations. The first visible observations were made on the first day of nanolubricant synthesis, and the last visible observations were made on the 30th. Figure 4a illustrates the nanolubricant synthesized in the observation tube. Six nanolubricant tubes depict nanolubricant samples that were ultrasonicated for 0, 40, 60, 80, 100, and 120 min using the interlude method, as stated in the methodology. The nanoparticles in the POE lubricant were consistently dispersed in all nanolubricant samples. At this point, there was no

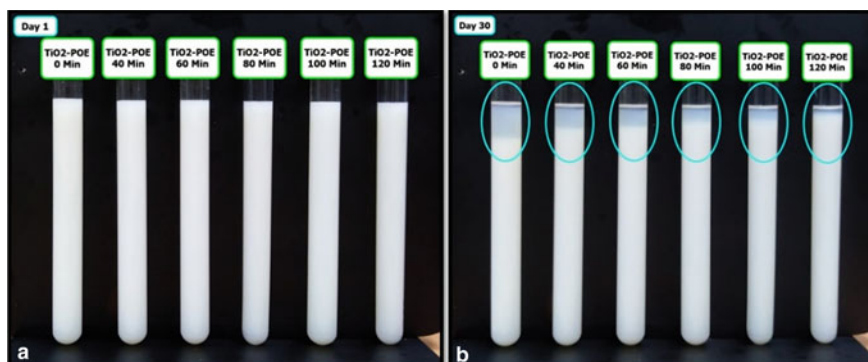


Fig. 4 TiO₂-POE nanolubricant visual observation comparison **a** day 1 and **b** day 30

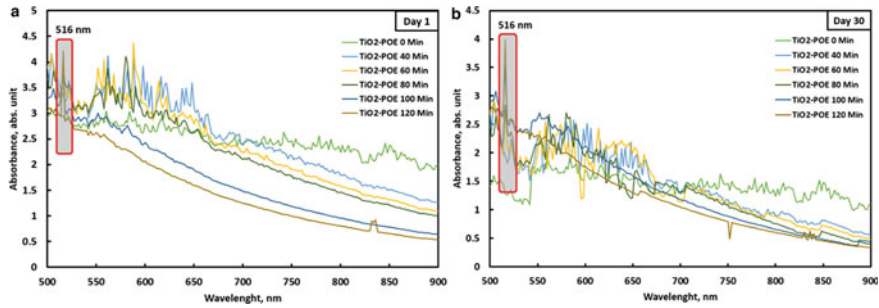


Fig. 5 TiO₂-POE nanolubricant absorbance value comparison **a** day 1 and **b** day 30 from all samples

evidence of agglomeration or sedimentation in any of the samples. This occurrence demonstrates that each sample has generated a stable nanolubricant.

Figure 4b depicts the findings on day 30 after the nanolubricant had been in the monitoring tube for 30 days. The nanolubricant samples that were not ultrasonicated experienced severe damage, as evidenced by sedimentation in the observation tube (shown in the figure by the turquoise ellipse). This phenomenon indicates that the nanolubricant agglomerates significantly. The agglomeration in nanolubricant will promote in sedimentation. This phenomenon is affected by two major causal variables. The first aspect is the van der Waals forces, which drive amplification between nanoparticle molecules [24]. The second aspect is the nanopowder's density, which is superior to lubricants, causing the nanoparticles to always fall to the bottom of the tube due to gravity effect. The augmentation of nanoparticles will accelerate the sedimentation process in the nanolubricant sample as reported by previous researchers [25] As a result, for unstable nanolubricants, the sedimentation and agglomeration rates will be higher if the nanolubricant is stored in a storage monitoring tube for a longer period of time.

According to observations on day 30, agglomeration and sedimentation had occurred in all samples. However, each sample has a different level of agglomeration and sedimentation than the others. The increment in ultrasonication treatment was able to reduce the visibility of agglomeration and sedimentation in the sample, as seen visually. This phenomenon is clearly visible in Fig. 5's turquoise ellipse (b).

3.3 TiO₂-POE Nanolubricant Absorbance Ratio Analysis by Means of UV Visible Spectrophotometry

Absorbance measures the amount of light that a sample can absorb in a cell cuvette. The absorbance of the nanolubricant sample is directly related to its density. Principally, the light source releases a predetermined amount of UV light across the sample. The sample absorbs light in the cell cuvette, and the results of the light

absorption measurement using absorbance units are displayed on the screen. This is how absorbance is measured using UV visible spectrophotometry [26]. To ensure the precision of measuring absorbance values, sample handling with cuvette cells is essential. Measurements are taken correctly only twice for each sample. First, at the first day just after sample have been prepared and then second, after all samples are stored for 30 days.

A 3 ml sample of TiO₂-POE nanolubricant was inserted in each quartz cuvette cell for this experiment as suggested by Kalmár et al. [27]. In addition, the cuvette cell sample is inserted into the UV visible spectrophotometry slot, which has a measuring range of 500–900 nm. When comparing the absorbance measurement findings from day 1 to day 30, it can be seen that all samples have a declining trend, as formerly done by Huo et al. [28]. The sample comparison point was determined at 516 nm since it yielded a substantial absorbance level and merited to be compared as a determination of the absorbance ratio on the first and 30th days. This condition was applied to all samples to ensure that they were all compared at the same point.

Figure 5 illustrates the absorbance measurement results for all tests performed on days 1 and 30. Using UV visible spectrophotometry, both images show that UV light successfully absorbed the nanoparticles in the nanolubricant sample. The findings of the scanning spectrum from 500 to 900 nm demonstrate this phenomenon. Several fluctuating spectrum peaks may be seen in the two plots. The addition of nanoparticles to the nanolubricant is depicted by the peak of the spectrum. The addition of nanoparticles to the nanolubricant sample enhances agglomeration formation [29]. Figure 5a, b show that nanoparticle augmentation is becoming more predominant in all samples. This is evidenced by the increasing number of spectral peaks.

Sample TiO₂-POE 0 min on Fig. 5a shows an untreated sample. The graphic illustrates that there are considerable spectral fluctuations in almost every region of the graph. Particularly for TiO₂-POE 0 min sample on Fig. 5b depicts a similar scenario that occurred on day 30. This event demonstrates that nanoparticles are augmented in almost every region of the nanolubricant along the cuvette cell. As a result, this condition can be justified by the fact that the nanoparticles in the POE lubricant are not properly dispersed, as determined by UV visual examination.

Furthermore, based on this finding, the absorbance ratio value can be adopted to quantify the stability level of TiO₂-POE nanolubricant, as proposed by Khedher et al. [30]. The absorbance ratio (\bar{A}_r) is calculated by comparing the initial absorbance (A) to the final absorbance (A₀) produced by Eq. 2.

$$\bar{A}_r = \frac{A}{A_0} \quad (2)$$

Figure 6 depicts a comparison of absorbance values in sample 1. Sample 1's nanolubricant was synthesized using only a magnetic stirrer for 30 min, with no ultrasonication treatment. Figure 6a illustrates that, despite the fact that the nanolubricant was freshly generated, many nanoparticle augmentations can be clearly seen from 500 to 900 nm. Figure 6b shows increased spectral fluctuations across all regions, as well as a decrease in spectral height because nanoparticle augmentation

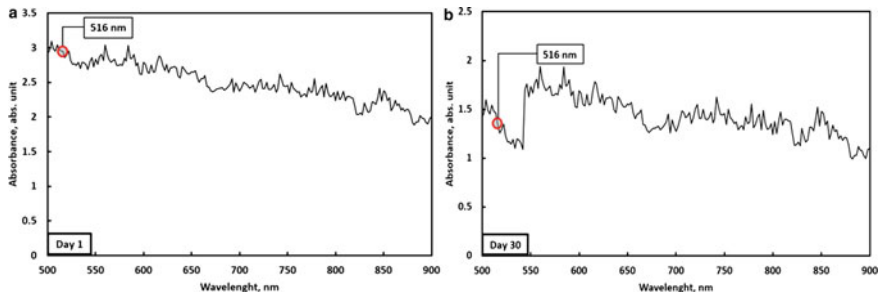


Fig. 6 TiO₂-POE nanolubricant absorbance value comparison as dependent of ultrasonication period of 0 min between **a** day 1 and **b** day 30

occurs throughout the lubricant region. This sample has an absorbance ratio of 0.25. Figure 7 illustrates a comparison of the sample's absorbance value after a 40-min ultrasonication treatment. On day 1 and 30, the amount of fluctuating spectrum in the graph decreases. The absorbance ratio was increased by 34% after a 40-min ultrasonic treatment to 0.58 absorbance unit.

The nanoparticles' The Van der Waals force is applied the TiO₂ nanoparticles to clump together. The Van der Waals force is applied by the dipoles of the TiO₂ nanoparticle molecules in this nanolubricant. The dipole is formed by the electron dispersion in the molecule. Molecules with a high concentration level become negative dipoles, attracting molecules with a low concentration level, such as positive dipoles and uncharged dipoles. This procedure is currently being carried out in the nanolubricant region, which includes the nanoparticles. When numerous nanoparticle molecules fuse together, the Van der Waals effect results in an agglomeration as recorded by Tiwari et al. [31].

Figure 8 illustrates the comparison of the absorbance value of the sample TiO₂-POE nanolubricant with ultrasonication treatment for 60 min. Figure 8a shows a relatively steady spectrum in the wavelength range of 660–900 nm, then high spectrum fluctuations begin to occur in the region of 500–650. This condition demonstrates that there is an augmentation of nanoparticles so that UV rays can be up to greater.

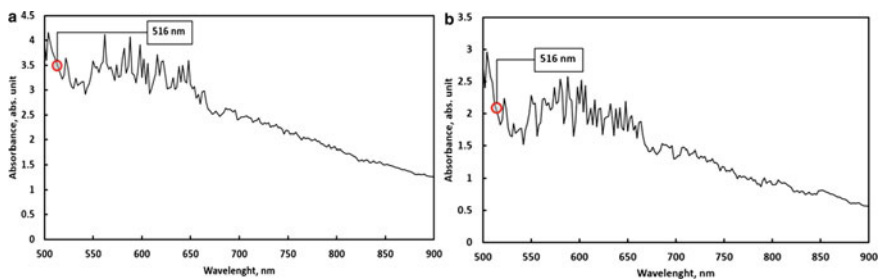


Fig. 7 TiO₂-POE nanolubricant absorbance value comparison as dependent of ultrasonication period of 40 min between **a** day 1 and **b** day 30

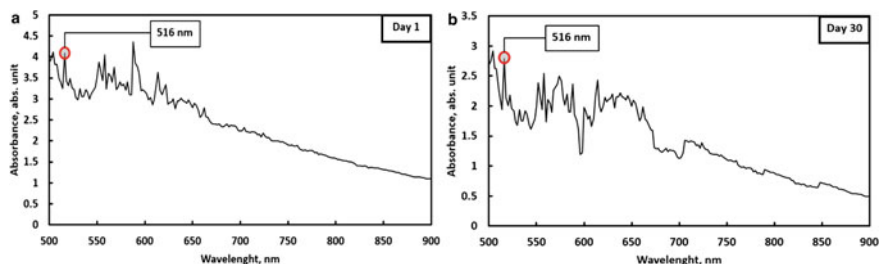


Fig. 8 TiO₂-POE nanolubricant absorbance value comparison as dependent of ultrasonication period of 60 min between **a** day 1 and **b** day 30

This is also validated by raising the absorbance value. In Fig. 8b there is a general decline in the absorbance value. Significant spectrum fluctuations occurred in the 500–700 nm area. This reveals that the augmentation of nanoparticles increases so that they become aggregation and sedimentation. This criterion verifies the prior visual judgment and is displayed in Fig. 5. The ultrasonication treatment for 60 min on the TiO₂-POE nanolubricant sample was able to produce an absorbance value of 4.09 on the first day and an absorbance value of 2.79 on the 30th day.

Figure 9 depicts a comparison of the absorbance value of the TiO₂-POE nanolubricant sample after 80 min of ultrasonication treatment. Figure 9a depicts a more stable spectrum than Fig. 8a, including in the wavelength range of 600–900 nm, before high spectrum fluctuations appear in the range of 500–590 nm. This case shows that nanoparticles have been augmented, allowing UV rays to penetrate deeper [32]. Increasing the absorbance value also confirms this. The absorbance value decreases overall in Fig. 8b. Significant fluctuations in the spectrum occurred in the 500–700 nm range. The ultrasonication treatment on the TiO₂-POE nanolubricant sample for 60 min generated an absorbance value of 3.81 on the first day and declined to 2.84 on the 30th day.

Figure 10 displays a comparison of the absorbance value of the TiO₂-POE nanolubricant sample after 100 min of ultrasonication treatment. In contrast to the previous

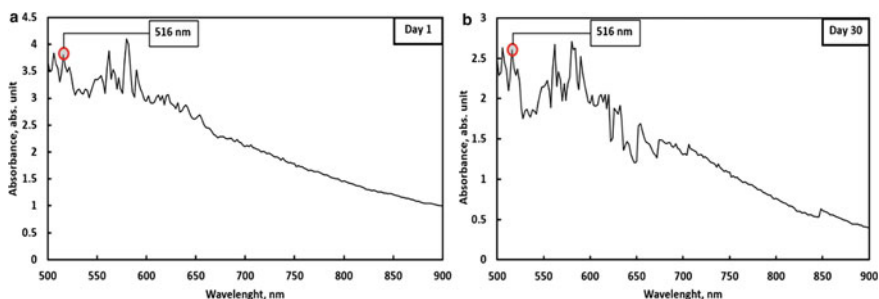


Fig. 9 TiO₂-POE nanolubricant absorbance value comparison as dependent of ultrasonication period of 80 min between **a** day 1 and **b** day 30

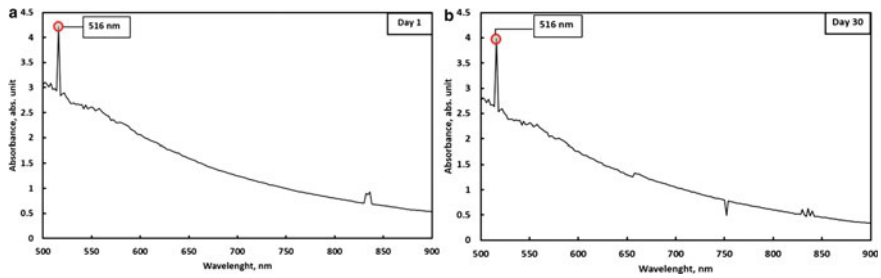


Fig. 10 TiO₂-POE nanolubricant absorbance value comparison as dependent of ultrasonication period of 100 min between **a** day 1 and **b** day 30

visual profile, the spectrum in Fig. 10a is substantially steadier than in Fig. 9a. The graph increased smoothly and practically without a noticeable shift in the spectrum in the 575–900 nm range. This circumstance is justified by the fact that the nanoparticles are well dispersed in the POE lubricant. UV light from spectrophotometry can be well absorbed as reported by Munkhbayar et al. [33]. However, there is a little spectrum variation in the 500–575 nm band. Figure 10b shows that there is no overall significant change in all region, although there is an increase in spectrum fluctuation in the 500–575 nm range. This demonstrates an increase in the augmentation of nanoparticles in this range, resulting in agglomeration and sedimentation. Figure 5b depicts this sedimentation event. However, in general, this sample performs far better than the prior sample. The ultrasonication treatment for 100 min on the TiO₂-POE nanolubricant sample yielded an absorbance value of 3.82 on the first day and diminished to 3.52 on the 30th day.

Figure 11 depicts a comparison of the absorbance value of the sample TiO₂-POE nanolubricant after 120 min of ultrasonication treatment. In contrast to the previous graphic profile, the spectrum in Fig. 11a is substantially steadier than in Fig. 10a. The graph increases continuously and practically without notable spectrum shifts between 550 and 900 nm. Although there are modest oscillations at 870–875 nm,

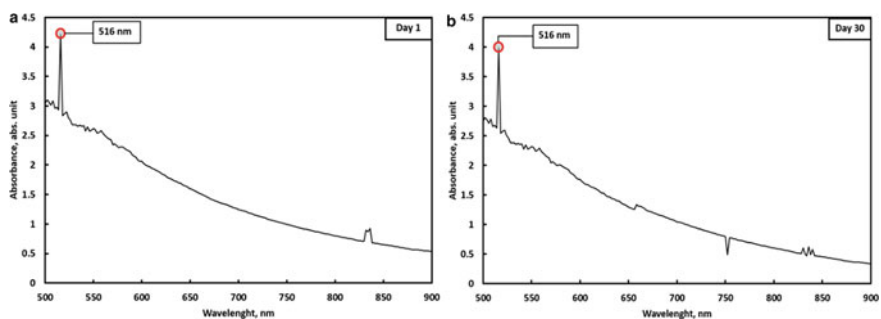
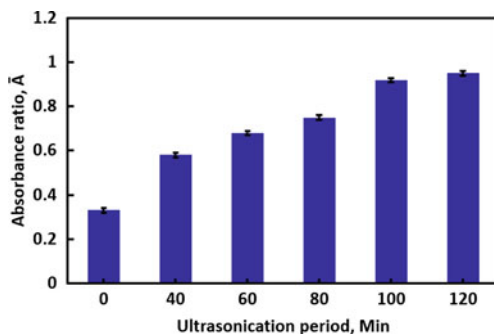


Fig. 11 TiO₂-POE nanolubricant absorbance value comparison as dependent of ultrasonication period of 120 min between **a** day 1 and **b** day 30

Fig. 12 TiO₂-POE nanolubricant absorbance ratio as a dependent of ultrasonication duration

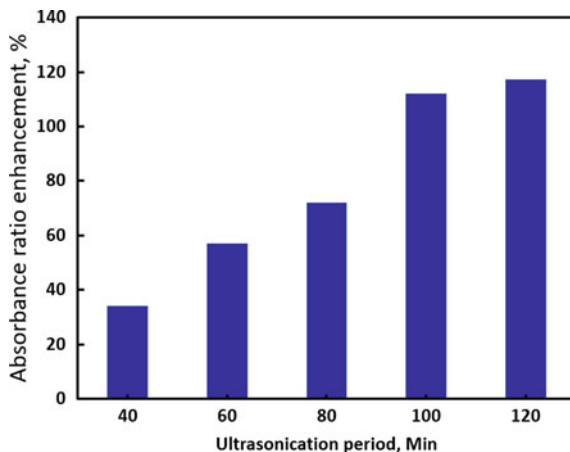


this does not have a substantial impact on the overall performance of this sample stability.

Furthermore, this circumstance is justified by the fact that the nanoparticles are well disseminated in the POE lubricant. There are small spectral changes between 500 and 550 nm. Figure 11b shows that there is no overall significant change in all region, although there is an increase in spectrum variations in the 500–550 nm range. This demonstrates an increase in the augmentation of nanoparticles in this range, resulting in agglomeration and sedimentation [34]. Figure 5b depicts this sedimentation event. There was no significant drop in absorbance in this sample, although there was a substantial rise. The ultrasonication treatment for 120 min on the TiO₂-POE nanolubricant sample resulted in an absorbance value of 4.21 on the first day and 3.98 on the 30th day. This sample has the greatest absorbance value and ratio, which can be justified. As a result, when compared to other samples, the sample with 120-min of ultrasonication treatment is the most stable. The absorbance ratio of the sample was increased by 117%, or 0.95, after 120 min of ultrasonication treatment as shown in Fig. 13.

As shown in Fig. 12, the duration of the nanolubricant's sonication treatment causes an increase in the absorbance ratio. The absorbance ratio value for the greatest sonication duration, 120-min, was 0.95, whereas the absorbance ratio value for the shortest sonication period, 100-min, was 0.92. Because the increase in absorbance ratio is minor, ultrasonication treatment of the TiO₂-POE sample for more than 120-min is not required. This graph illustrates how sonication can contribute in the prevention of agglomeration and sedimentation in nanolubricants as experimented by Xian et al. [35]. As a result, by ultrasonication of the nanolubricant for an appropriate amount of time, the nanolubricant's stability can be increased [36]. The best ultrasonication duration in this investigation for achieving the highest level of stability for TiO₂-POE nanolubricant was 120-min.

Fig. 13 TiO₂-POE nanolubricant absorbance ratio enhancement as dependent of ultrasonication period in various samples



3.4 TiO₂-POE Nanolubricant Zeta Potential Analysis

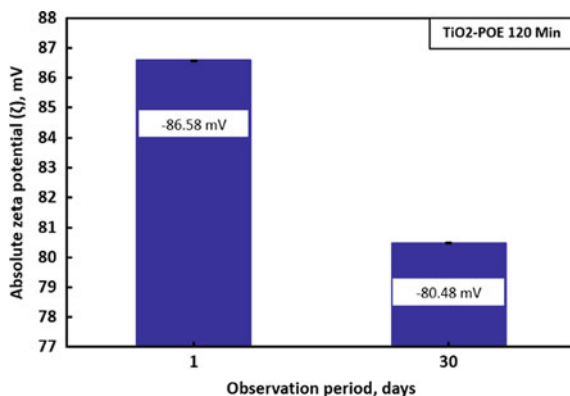
The purpose of the zeta potential assessment on TiO₂-POE nanolubricant is to determine the sample's stability. The zeta potential is a significant degree of the stability of the nanolubricant dispersion because it determines the potential variance amongst the dispersing medium and the steady fluid layer associated to the dispersed particles. The absolute value of the TiO₂-POE sample's zeta potential following a 120-min ultrasonication treatment is shown in Fig. 13. The absolute zeta potential value was -80.48 mV on day 1 and -80.48 mV on day 30. The absolute zeta potential value declines as sample storage duration rises, according to the graph. The consequent decrease in the absolute value of the zeta potential, on the other hand, is quite minor. Nanofluids with an absolute zeta potential of -80.48 mV are outstanding nanofluids with great stability since they are in the -60 to -100 mV range as stated by Mahbubul et al. [6]. The negative absolute zeta potential of TiO₂-POE nanolubricant as shown in Fig. 14 reflects the surface charge of TiO₂ nanopowder [37]).

4 Conclusion

Based on a comprehensive experimental evaluation of TiO₂-POE samples, several key points can be drawn:

To examine the stability of TiO₂-POE in an experimental context, visual inspection, UV Visible spectrophotometry, and zeta potential were adopted. The results of these three methodologies all confirm one another. When compared to the other samples, Sample 6 exhibits the least amount of sedimentation after 30 days. This conclusion is supported by the fact that, when compared to the other samples, sample 6 had the greatest absorbance ratio of 0.95. On days 1 and 30, absolute zeta potential

Fig. 14 TiO₂-POE nanolubricant absolute zeta potential from sample 6



values of -86.58 and -80.48 mV were utilized to validate the absorbance ratio results in this sample. This observation qualifies the TiO₂-POE nanolubricant in sample 6 as a nanolubricant with an outstanding level of stability since it has an absolute value of zeta potential in the range of 60–100 mV. As a result of the findings of the nanolubricant's stability in this study, TiO₂-POE with ultrasonication treatment for 120-min is an excellent candidate for use in residential air conditioning systems.

Future experimental may be needed by changing the ultrasonication setting to achieve the similar TiO₂-POE nanolubricant's stability to using a shorter ultrasonication period.

Acknowledgements Ningxia University in China provided funding for this research through the Helan Mountain Scholarship program. The authors would like to express their gratitude to UMP for providing money through the specialized internal fund RDU190336 and the FRGS award RDU 1901112.

Conflicts of Interest

The authors declare no conflict of interest.

References

1. Choi SU, Eastman JA (1995) Enhancing thermal conductivity of fluids with nanoparticles. Argonne National Lab., IL, USA
2. Kedzierski MA (2012) Viscosity and density of CuO nanolubricant 35:1997–2002
3. Adelekan DS, Ohunakin OS, Babarinde TO, Odunfa MK, Leramo RO, Oyedepo SO, Badejo DC (2017) Experimental performance of LPG refrigerant charges with varied concentration of TiO₂ nano-lubricants in a domestic refrigerator. *Case Studies Thermal Eng* 9:55–61
4. Li L, Zhai Y, Jin Y, Wang J, Wang H, Ma M (2020) Stability, thermal performance and artificial neural network modeling of viscosity and thermal conductivity of Al₂O₃-ethylene glycol nanofluids. *Powder Technol* 363:360–368
5. Dhanola A, Garg HC (2020) Experimental analysis on stability and rheological behaviour of TiO₂/canola oil nanolubricants. *Mater Today Proceedings* 28:1285–1289

6. Mahbulul IM, Elcioglu EB, Amalina MA, Saidur R (2019) Stability, thermophysical properties and performance assessment of alumina–water nanofluid with emphasis on ultrasonication and storage period. *Powder Technol* 345:668–675
7. Lin L, Peng H, Chang Z, Ding G (2017) Experimental investigation on TiO₂ nanoparticle migration from refrigerant–oil mixture to lubricating oil during refrigerant dryout. *Int J Refrig* 77:75–86
8. Chen Z, Shahsavari A, Al-rashed AAAA, Afrand M (2020) The impact of sonication and stirring durations on the thermal conductivity of alumina-liquid paraffin nanofluid: an experimental assessment. *Powder Technol* 360:1134–1142
9. Zawawi NNM, Azmi WH, Redhwan AAM, Sharif MZ, Sharma KV (2017) Thermo-physical properties of Al₂O₃-SiO₂/PAG composite nanolubricant for refrigeration system. *Int J Refrig* 80:1–10
10. Modarres-Gheisari SMM, Gavagsaz-Ghoachani R, Malaki M, Safarpour P, Zandi M (2019) Ultrasonic nano-emulsification—a review. *Ultrason Sonochem* 52:88–105
11. Khedkar RS, Shrivastava N, Sonawane SS, Wasewar KL (2016) Experimental investigations and theoretical determination of thermal conductivity and viscosity of TiO₂-ethylene glycol nanofluid. *Int Commun Heat Mass Transfer* 73:54–61
12. Mahbulul IM, Shahrul IM, Khaleduzzaman SS, Saidur R, Amalina MA, Turgut A (2015) Experimental investigation on effect of ultrasonication duration on colloidal dispersion and thermophysical properties of alumina–water nanofluid. *Int J Heat Mass Transf* 88:73–81
13. Ghadimi A, Metselaar IH (2013) The influence of surfactant and ultrasonic processing on improvement of stability, thermal conductivity and viscosity of titania nanofluid. *Exp Thermal Fluid Sci* 51:1–9
14. Caneba GT, Dutta C, Agrawal V, Rao M (2010) Novel ultrasonic dispersion of carbon nanotubes. *J Miner Mater Charact Eng* 9(3):165–181
15. Sofiah AGN, Samykano M, Shahabuddin S, Kadirgama K, Pandey AK (2020) An experimental study on characterization and properties of eco-friendly nanolubricant containing polyaniline (PANI) nanotubes blended in RBD palm olein oil. *J Therm Anal Calorim*
16. Sujith SV, Solanki AK, Mulik RS (2019) Experimental evaluation on rheological behavior of Al₂O₃-pure coconut oil nanofluids. *J Mol Liq* 286:110905
17. Al-Anssari S, Arif M, Wang S, Barifcani A, Lebedev M, Iglauer S (2018) Wettability of nanofluid-modified oil-wet calcite at reservoir conditions. *Fuel* 211:405–414
18. Zhang T, Zou Q, Cheng Z, Chen Z, Liu Y, Jiang Z (2021) Effect of particle concentration on the stability of water-based SiO₂ nanofluid. *Powder Technol* 379:457–465
19. Redhwan AAM, Azmi WH, Sharif MZ, Mamat R, Samykano M, Najafi G (2018) Performance improvement in mobile air conditioning system using Al₂O₃/PAG nanolubricant. *J Therm Anal Calorim* 135:1299–1310
20. Sharif M, Azmi W, Redhwan A, Mamat R (2016) Investigation of thermal conductivity and viscosity of Al₂O₃/PAG nanolubricant for application in automotive air conditioning system. *Int J Refrig* 70:93–102
21. Jiang W, Cheng X, Cai H, Ali T, Zhang J (2018) The response of yttrium aluminum garnet (YAG) grains and grain boundaries to nanoindentation. *J Mater Sci* 53:16198–16206
22. Pandey A, Dalal S, Dutta S, Dixit A (2021) Structural characterization of polycrystalline thin films by X-ray diffraction techniques. *J Mater Sci Mater Electron* 32:1341–1368
23. Wang J, Ding W, Zhu Y, Xu W, Yang C (2017) Fracture mechanism of polycrystalline cubic boron nitride abrasive grains during single-grain grinding of Ti-6Al-4V titanium alloy. *Int J Adv Manuf Technol* 94:281–291
24. Sarsam WS, Amiri A, Shanbedi M, Kazi SN, Badarudin A, Yarmand H, Bashirnezhad K, Zaharinie T (2017) Synthesis, stability, and thermophysical properties of aqueous colloidal dispersions of multi-walled carbon nanotubes treated with beta-alanine. *Int Commun Heat Mass Transfer* 89:7–17
25. Ilyas SU, Ridha S, Abdul Kareem FA (2020) Dispersion stability and surface tension of SDS-stabilized saline nanofluids with graphene nanoplatelets. *Colloids Surf A* 592:124584–124584

26. Nugroho A, Bo Z, Mamat R, Azmi WH, Najafi G, Khoirunnisa F (2021) Extensive examination of sonication duration impact on stability of Al₂O₃-Polyol ester nanolubricant. *Int Commun Heat Mass Transfer* 126:105418
27. Kalmár J, Lente G, Fábrián I (2016) Kinetics and mechanism of the adsorption of methylene blue from aqueous solution on the surface of a quartz cuvette by on-line UV-Vis spectrophotometry. *Dyes Pigm* 127:170-178
28. Huo M, Wu H, Xie H, Zhao J, Su G, Jia F, Li Z, Lin F, Li S, Zhang H, Jiang Z (2020) Understanding the role of water-based nanolubricants in micro flexible rolling of aluminium. *Tribol Int* 151:106378-106378
29. Du M, Tang GH (2015) Optical property of nanofluids with particle agglomeration. *Sol Energy* 122:864-872
30. Khdher AM, Sidik NAC, Hamzah WAW, Mamat R (2016) An experimental determination of thermal conductivity and electrical conductivity of bio glycol based Al₂O₃ nanofluids and development of new correlation. *Int Commun Heat Mass Transfer* 73:75-83
31. Tiwari AK, Pandya NS, Said Z, Chhatbar SH, Al-Turki YA, Patel AR (2021) 3S (Sonication, surfactant, stability) impact on the viscosity of hybrid nanofluid with different base fluids: an experimental study. *J Mol Liq* 329:115455-115455
32. Rahman N, Sameen S, Kashif M (2019) Application of Box-Behnken design and desirability function in the optimization of spectrophotometric method for the quantification of WADA banned drug: acetazolamide. *J Mol Liq* 274:270-277
33. Munkhbayar B, Bat-Erdene M, Sarangerel D, Ochirkhuyag B (2013) Effect of the collision medium size on thermal performance of silver nanoparticles based aqueous nanofluids. *Compos B Eng* 54:383-390
34. Fazeli I, Sarmasti Emami MR, Rashidi A (2021) Investigation and optimization of the behavior of heat transfer and flow of MWCNT-CuO hybrid nanofluid in a brazed plate heat exchanger using response surface methodology. *Int Commun Heat Mass Transfer* 122:105175-105175
35. Xian HW, Sidik NAC, Saidur R (2020) Impact of different surfactants and ultrasonication time on the stability and thermophysical properties of hybrid nanofluids. *Int Commun Heat Mass Transfer* 110
36. Demirkır Ç, Ertürk H (2020) Rheological and thermal characterization of graphene-water nanofluids: hysteresis phenomenon. *Int J Heat Mass Transfer* 149
37. Liao DL, Wu GS, Liao BQ (2009) Zeta potential of shape-controlled TiO₂ nanoparticles with surfactants. *Colloids Surf, A* 348:270-275

OFAT Adoption on FAI_2O_3 -POE Nanolubricant Absorbance Ratio Optimization Based on Spectrophotometric Method



Agus Nugroho, Rizalman Mamat, Zhang Bo, Wan Azmi Wan Hamzah, Mohd Fairusham Ghazali, and Talal Yusaf

Abstract The UV visible spectrophotometry technique is one of the methods for determining a nanolubricant's stability standard. The absorbance level of a nanolubricant is determined by spectrophotometry. This method measures how well the nanolubricant absorbs UV rays from a light source. In this study, one factor at a time (OFAT) based on surface response was adopted to determine the effect of wavelength selection on the absorbance ratio of FAI_2O_3 -POE nanolubricant. The FAI_2O_3 -POE sample was prepared using a two-steps approach. The sample was ultrasonicated for 100 min using a homogenizer. UV visible spectrophotometry analysis was performed on day 1 and 15 to determine the absorbance ratio. Sixteen runs were performed using a quadratic design to acquire experimental data were fitted. The ANOVA analysis discovered that the experimental statistics were well suited to the polynomial model, with an R^2 value of 0.9951 and a model F-value of 1316.47. The findings suggest that the optimum wavelength is 375 nm with an absorbance value of 0.935473 and a desirability level of 1.0.

Keywords ANOVA · OFAT · FAI_2O_3 -POE nanolubricant · UV visible spectrophotometry

A. Nugroho (✉) · R. Mamat · Z. Bo
School of Mechanical Engineering, Ningxia University, Yinchuan, China
e-mail: ir.agusnug@gmail.com

A. Nugroho · R. Mamat · W. A. Wan Hamzah
College of Engineering, Universiti Malaysia Pahang, Pekan, Pahang, Malaysia

R. Mamat · W. A. Wan Hamzah · M. F. Ghazali
Centre for Research in Advanced Fluid & Processes, Universiti Malaysia Pahang, Lebuhraya Tun Razak, 26300 Gambang, Kuantan, Pahang, Malaysia

T. Yusaf
School of Engineering and Technology, Central Queensland University, Rockhampton, Australia

Abbreviations

min	Minute
abs	Absorbance
MO	Mineral oil
OFAT	One factor at a time
Std. Dev	Standard deviation
POE	Polyolester
Anova	Analysis of variance
UV	Ultraviolet
A	Initial Absorbance
A_o	Final Absorbance
A_r	Absorbance Ratio
FAI ₂ O ₃	Functionalized Al ₂ O ₃

Greek symbols

ζ	Absolute zeta potential, mV
\emptyset	Concentration
P	Density

Subscripts

<i>l</i>	Refers to lubricant
<i>p</i>	Refers to nanoparticle

1 Introduction

The biggest challenge with any colloidal suspension known as a nanolubricant, whether water-based or oil-based, is its stability [1–3]. Several researchers are working to increase the nanolubricant's stability on a regular basis so that the nanolubricant used in the system can offer superior heat transfer [4–6]. A nanolubricant's stability level can be determined using the UV visible spectrophotometry approach. UV rays are emitted throughout the nanolubricant area, and the nanoparticles scattered in the lubricant absorb them [7]. Absorbance refers to a nanolubricant's capacity to absorb UV light. On the first and second days, the absorbance of the nanolubricant sample was measured.

Marcucci Pico et al. [8] prepared diamond-POE nanolubricant using two-steps approach for use in air conditioning systems. The spectrophotometric technique was used to determine the stability of the nanolubricant. The samples were tested in the 190–1100 nm region to evaluate the level of UV absorption by the nanolubricant. The sample was placed in a polystyrene cuvette and measured at a wavelength of 400–700 nm. Sedimentation was seen in the sample after it had been stored for one week. Sharif et al. [9] prepared SiO_2 /PAG nanolubricants for automobile air conditioning systems. The spectrophotometric method, which measures the UV rays emitted into a sample of SiO_2 /PAG nanolubricants, is used to determine the level of stability of SiO_2 /PAG nanolubricants. The optimal absorbance ratio is determined by comparing the absorbance values displayed at the spectral wavelength of 313 nm. Later, while Rajendran et al. [10] reported that spectrophotometry approach is a very effective method for assessing the stability of nanolubricants based on the ratio of the nanolubricant spectrum peaks. The stability of the Ni-MoS₂-gear nanolubricant was determined by comparing spectral peaks in the 300–600 nm region using a spectrophotometer. This technique is claimed to be the best for determining the optimal absorbance of an experimental sample. Mello et al. [11] reported using a spectrophotometer to compare the spectral peaks of Cu-polyalphaolefin (PAO) absorbance values in the region of 200–1100 nm to measure stability. There is a significant spectral fluctuation in the range of 200–400 nm. Therefore, this region considers the most optimum region to analyze. The data show that the sample with the Toluene dispersant has the highest spectral.

There is a strong relation between wavelength selection and the absorbance ratio to estimate nanolubricant's stability. Based on the spectrophotometric wavelength determination on the absorbance ratio, this study revealed the optimum absorbance ratio. The most optimal absorbance ratio was determined by measuring one element at a time using response surface methods. Based on the quadratic design of OFAT, the data reveal that spectrophotometric wavelength determination has a substantial impact on the absorbance ratio of TiO_2 -POE nanolubricant. The most ideal wavelength is determined using several OFAT-proposed solution conditions and the highest desirability with maximum absorbance.

2 Experimental Method

2.1 Nanolubricant Preparation

To synthesize a nanolubricant, the nanoparticles are combined with a POE lubricant. POE lubricants are manufactured by SUNISO, a Belgian multinational corporation. For this purpose, Sigma-Aldrich in Saint Louis, Missouri, USA, produced TiO_2 nanopowder with a typical particle size of 21 nm and a purity of 99.5%. Hielscher Germany's UP400S ultrasonic homogenizer was used to sonicate the nanolubricant. The goal of an ultrasonic homogenizer is to provide more energy than a traditional

ultrasonic bath. The discoveries will improve the nanolubricant's homogeneity while reducing the sonication time [12]. The use of an ultrasonic homogenizer is very effective in preventing nanolubricant agglomeration and sedimentation [13–15]. The ultrasonic device has the following specifications: 400 W, 24 kHz, 50% amplitude, and 0.5 cycles. In this study, six samples were used, all of which had the same 0.02 vol % concentration volume. After a 30-min stirring period, the nanolubricant was ultrasonicated for 100 min.

2.2 UV Visible Spectrophotometry Analysis

The UV visible spectrophotometry approach was used to predict the stability of the FAI_2O_3 -POE nanolubricant [16]. Spectrophotometry spectrums from days 1 to 15 were studied. The absorbance ratio was calculated over a 15-day period. The absorbance ratio will forecast nanolubricant stability by looking at the maximum absorbance ratio values.

2.3 Optimization

This study employs the OFAT strategy, with only one element to be investigated using Design Expert 7.16's statistical calculation of the response surface method (Stat-Ease Inc., Minneapolis, MN, USA) [17–19]. The developed model was statistically investigated using the analysis of variance (ANOVA) method. The superiority of the fit of the polynomial model equivalence was evaluated using the R^2 and adjusted R^2 coefficients. As proposed by earlier studies, the F-test and p -values were employed to validate the numerical and coefficient of determination significance [18–20].

Furthermore, the maximum absorbance value, the shortest wavelength spectrum, and the highest attractiveness value were used to determine the optimization condition. Based on the OFAT suggestion and the actual peak spectral, this proposed solution will be selected [21].

3 Result and Discussion

3.1 TiO_2 -POE Nanolubricant Absorbance Ratio Analysis Using UV Visible Spectrophotometry

Figure 1 shows a comparison of the absorbance values of FAI_2O_3 -POE nanolubricant at a concentration of 0.02 vol % after 100 min of ultrasonication. The two photos show each of the five spectral positions optimized with OFAT. The absorbance result

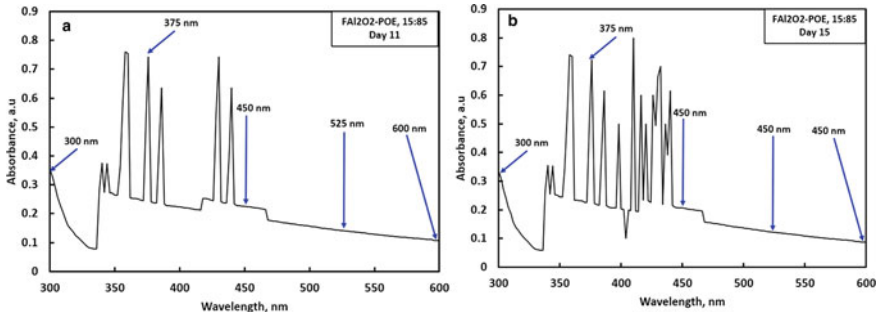


Fig. 1 FA12O3-POE nanolubricant absorbance comparison **a** day 1 and, **b** day 15 from the assessed sample

Table 1 Independent variable on FA12O3-POE OFAT study

Factor	Name	Units	Type	Low actual	High actual	Low coded	High coded	Mean	Std. dev
A	Wavelength	nm	Numeric	300.00	600.00	-1.000	1.000	450.000	79.550

on the first day after the sample was made is shown in Fig. 1a, and the absorbance result after 15 days of storage is shown in Fig. 1b. The difference between the two is the fluctuation in the value spectrum of each absorbance value calculated by Design-Expert software at many places. Table 1 lists the independent variables in the OFAT optimization, Table 2 lists the response parameters, and Table 3 lists the optimization process’ experimental data.

Furthermore, the absorbance ratio value can be used to determine the stability degree of FA12O3-POE nanolubricant based on this discovery, as proposed by Redhwan et al. [22]. The absorbance ratio (\bar{A}_r) is calculated by comparing the baseline absorbance (A) to the final absorbance (A₀) calculated by Eq. 1.

$$\bar{A}_r = \frac{A}{A_0} \tag{1}$$

3.2 Analysis of Variant (ANOVA)

The results of the ANOVA for the response surface quadratic model investigation are summarized in Table 4. The statistical results based on the ANOVA are presented in Table 4. The model is significant since it has a *p*-value of 0.0001, an F-value of 1316.47, and a 0.05 *p*-value. F-values and *p*-values were used to establish the importance of each component. The more significant the relevant coefficient terms are, the higher the degree of the F value and the lower the *p*-value. In this case, models

Table 2 Response parameters on FAI2O3-POE OFAT study

Response	Name	Units	Type	Analysis	Min.	Max.	Mean	Std. dev	Model
Y1	Absorbance ratio	–	ratio	Polynomial	0.813084	0.9382	0.90255	0.037893	Quadratic

Table 3 Experiment result for optimization

No	Run	Wavelength	Absorbance ratio
1	7	300	0.943820225
2	12	300	0.943820225
3	11	375	0.931487297
4	16	525	0.880537581
5	13	600	0.813084112
6	4	600	0.813084112
7	6	450	0.911504425
8	5	450	0.911504425
9	9	450	0.911504425
10	14	450	0.911504425
11	15	450	0.911504425
12	3	450	0.911504425
13	8	450	0.911504425
14	1	450	0.911504425
15	10	450	0.911504425
16	2	450	0.911504425

Table 4 ANOVA response summary

Source	Sum of squares	df	Mean square	F value	p-value	Remark
Model	0.021	2	0.011	1316.47	<0.0001	Significant
A-Wavelength	0.018	1	0.018	2247.79	<0.0001	
A ²	3.135E-003	1	3.135E-003	385.15	<0.0001	
Residual	1.058E-004	13	8.140E-006			
Lack of fit	1.058E-004	2	5.291E-005			
Pure error	0.000	11	0.000			
Car total	0.022	15				

A-wavelength and A², with F values of 2247.79 and 385.15, respectively, are equally significant [23].

This finding is supported by a coefficient of determination (R²) of 0.9951, which agrees well with an adjusted R² of 0.9943. The results of this model are exact and consistent because it has a high replication rate [24, 25]. A shallow pure error value of 0.000 is indicative of this condition. In this study, the coefficient of determination has a substantial value, showing that the absorbance ratio assessment is positively influenced by wave-length determination as shown in Table 5.

The adequacy of the regression model was determined using residuals and residuals vs predicted plots, as shown in Fig. 2a and b. The current work findings and

Table 5 Coefficient of determination

Parameters	Value
Standard deviation	2.853E-003
Mean	0.90
CV %	0.32
Press	1.596E-004
R-squared	0.9951
Adjusted R ²	0.9943
Prediction R ²	0.9926
Adequate precision	103.229

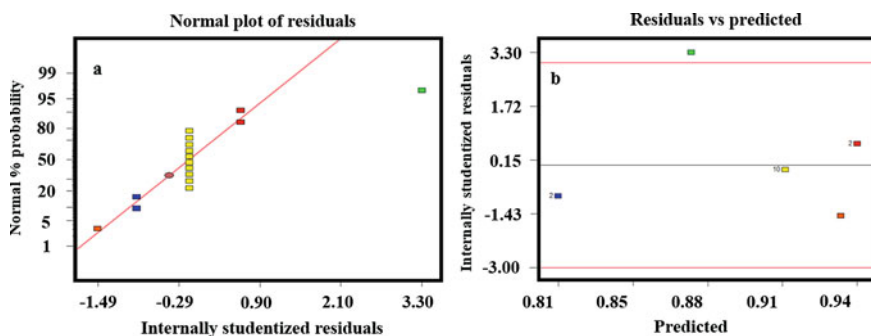
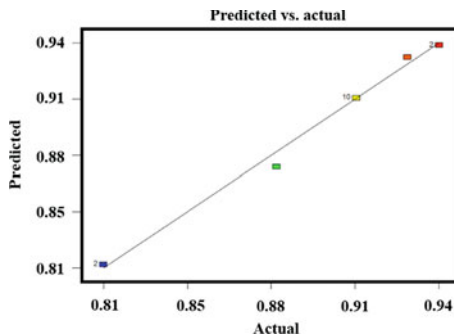


Fig. 2 a Normal plot of residuals; b correlation amid residuals and predicted the plot of present work findings

estimated points are clustered along the normality graph, as shown in Fig. 2a, demonstrating the analytical system’s consistency. The residue, on the other hand, are randomly spread throughout the reference line with no discernable pattern, as seen in Fig. 2. Figure 3 confirms that the anticipated value is close to the actual value.

Fig. 3 Correlation amid predicted and the actual plot of present work findings



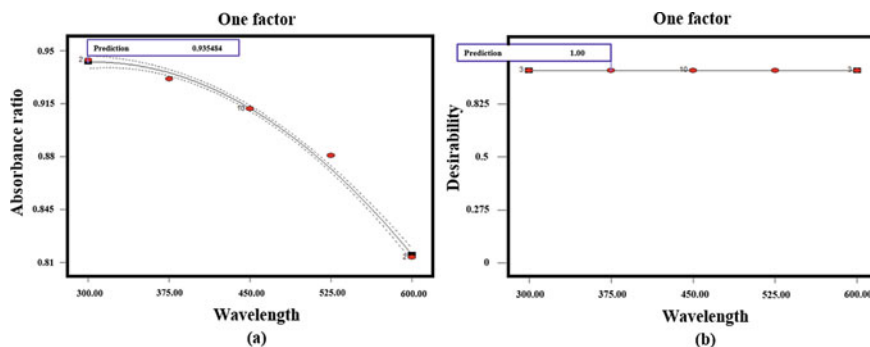


Fig. 4 A plot of **a** absorbance ratio as the dependent of wavelength determination and, **b** wavelength criteria based on the desirability of OFAT optimization

Based on the graphs, the quadratic model can be justified in establishing a satisfactory correlation between the researched limits and the variable [26–28]. The variable, wavelength determination, influenced the change in absorbance ratio.

3.3 OFAT Optimization Solution

The relationship between the absorbance ratio and wavelength is depicted in Fig. 4a. The shorter the wavelength, the higher the absorbance ratio, as indicated in the graph. 600 nm has the lowest absorption, while 300 nm has the greatest. The highest desirability value determines the appropriate wavelength in Fig. 4b. Table 6 lists OFAT's 32 solution conditions in numerical order.

As a result, the maximum desirability value, 1.0, is found in various wavelength range as shown in Table 6. The solution number two is the selected one as shown in bold in Table 6. However, according to this analysis criteria, the best wavelength determination value is 360 nm, with an absorbance ratio of 0.935473, as shown in Fig. 5. The selected optimum wavelength has good agreement with the actual spectral as shown in Fig. 1. This result is in line with what has been described in the literature [28–30].

4 Conclusion

Based on the findings, it is plausible to conclude that in UV visible spectrophotometry studies, the absorbance value increases as the wavelength level decreases. The ANOVA results suggest that the quadratic model's response is a reliable model for explaining the importance of the positive relationship between wavelength determination and optimum absorbance ratio outcomes. The regression coefficient R^2

Table 6 Solution condition proposed by OFAT

Number	Wavelength	Absorbance ratio	Desirability
1	450	0.911867845	1
2	360	0.935473	1
3	525	0.87811478	1
4	600	0.813386962	1
5	375	0.929064496	1
6	568.32	0.845431512	1
7	352.08	0.933227467	1
8	546.06	0.863688479	1
9	325.89	0.938267641	1
10	357.54	0.932231955	1
11	329.97	0.937439454	1
12	417.42	0.920525095	1
13	570.81	0.84318093	1
14	423.93	0.918988308	1
15	494.28	0.894866159	1
16	435.63	0.916001407	1
17	478.95	0.901590504	1
18	523.32	0.879156194	1
19	387.48	0.926740057	1
20	592.74	0.821406532	1
21	465.3	0.90679629	1
22	488.31	0.897602577	1
23	430.44	0.917364542	1
24	320.1	0.939480592	1
25	303.6	0.943234764	1
26	342.42	0.935021699	1
27	491.19	0.896301867	1
28	507.33	0.888321431	1
29	396.24	0.925037381	1
30	459.75	0.90872333	1
31	471.78	0.904410824	1
32	526.77	0.877000761	1

0.9951 validates this synthesis, which is supported by a substantial F test result of 2154.24. The adjusted R^2 value of 0.9943 matches the R^2 value very well. The maximum absorbance value with the highest high desire approaching the value 1 is used to determine the ideal wavelength. As a result, OFAT analysis proposes that the optimum wavelength in the UV visible spectrophotometry FAI_2O_3 -POE study



Fig. 5 Ramps plotting of optimum absorbance ratio as the dependent of wavelength determination

be found in the region of 360 nm with an absorbance value of 0.935473 and desirability level of 1.0. Future studies are needed to conduct analysis tests on other concentration.

Acknowledgements Ningxia University in China provided funding for this research through the Helan Mountain Scholarship program. The authors would like to express their gratitude to UMP for providing money through the specialized internal fund RDU190336 and the FRGS award RDU 1901112.

Conflicts of Interest

The authors declare no conflict of interest.

References

1. Walvekar R, Zairin DA, Khalid M, Jagadish P, Mubarak NM, Tcsm G (2021) Stability, thermo-physical and electrical properties of naphthenic/POME blended transformer oil nanofluids. *Therm Sci Eng Prog* 23:100878
2. Choudhary S, Sachdeva A, Kumar P (2020) Investigation of the stability of MgO nanofluid and its effect on the thermal performance of flat plate solar collector. *Renewable Energy* 147:1801–1814
3. Sharaf OZ, Rizk N, Munro CJ, Joshi CP, Waheed W, Abu-Nada E, Alazzam A, Martin MN (2021) Thermal stability and plasmonic photothermal conversion of surface-modified solar nanofluids: comparing prolonged and cyclic thermal treatments. *Energy Convers Manage* 244:114463
4. Pandya NS, Shah H, Molana M, Tiwari AK (2020) Heat transfer enhancement with nanofluids in plate heat exchangers: a comprehensive review. *Eur J Mech B Fluids* 81:173–190
5. Amjadian M, Safarzadeh H, Bahiraei M, Nazari S, Jaber B (2020) Heat transfer characteristics of impinging jet on a hot surface with constant heat flux using Cu_2O -water nanofluid: an experimental study. *Int Commun Heat Mass Transf* 112
6. Saeed M, Kim M-H (2018) Heat transfer enhancement using nanofluids (Al_2O_3 - H_2O) in mini-channel heatsinks. *Int J Heat Mass Transf* 120:671–682
7. Nugroho A, Bo Z, Mamat R, Azmi WH, Najafi G, Khoirunnisa F (2021) Extensive examination of sonication duration impact on stability of Al_2O_3 -polyol ester nanolubricant. *Int Commun Heat Mass Transf* 126:105418
8. Marcucci Pico DF, da Silva LRR, Hernandez Mendoza OS, Bandarra Filho EP (2020) Experimental study on thermal and tribological performance of diamond nanolubricants applied to a refrigeration system using R32. *Int J Heat and Mass Transf* 152:119493–119493

9. Sharif MZ, Azmi WH, Redhwan AAM, Mamat R, Najafi G (2019) Energy saving in automotive air conditioning system performance using SiO₂/PAG nanolubricants. *J Therm Anal Calorim* 135:1285–1297
10. Rajendhran N, Palanisamy S, Shyma AP, Venkatachalam R (2018) Enhancing the thermophysical and tribological performance of gear oil using Ni-promoted ultrathin MoS₂ nanocomposites. *Tribol Int* 124:156–168
11. Mello VS, Faria EA, Alves SM, Scandian C (2020) Enhancing CuO nanolubricant performance using dispersing agents. *Tribol Int* 150:106338–106338
12. Modarres-Gheisari SMM, Gavagsaz-Ghoachani R, Malaki M, Safarpour P, Zandi M (2019) Ultrasonic nano-emulsification—a review. *Ultrason Sonochem* 52:88–105
13. Mahbulul IM, Shahrul IM, Khaleduzzaman SS, Saidur R, Amalina MA, Turgut A (2015) Experimental investigation on effect of ultrasonication duration on colloidal dispersion and thermophysical properties of alumina–water nanofluid. *Int J Heat Mass Transf* 88:73–81
14. Ghafurian MM, Akbari Z, Niazmand H, Mehrkakh R, Wongwises S, Mahian O (2020) Effect of sonication time on the evaporation rate of seawater containing a nanocomposite. *Ultrason Sonochem* 61:104817–104817
15. Graves JE, Latvytė E, Greenwood A, Emekwuru NG (2019) Ultrasonic preparation, stability and thermal conductivity of a capped copper-methanol nanofluid. *Ultrason Sonochem* 55:25–31
16. Rahman N, Sameen S, Kashif M (2019) Application of Box-Behnken design and desirability function in the optimization of spectrophotometric method for the quantification of WADA banned drug: acetazolamide. *J Mol Liq* 274:270–277
17. Kumar V, Kumar A, Chhabra D, Shukla P (2019) Improved biobleaching of mixed hardwood pulp and process optimization using novel GA-ANN and GA-ANFIS hybrid statistical tools. *Bioresour Technol* 271:274–282
18. Yahaya YA, Don MM (2014) Flavonoid production by *T. lactinea*: screening of culture conditions via OFAT and optimization using response surface methodology (RSM). *J Korean Soc Appl Biol Chem* 57:749–757
19. Saha SP, Mazumdar D (2019) Optimization of process parameter for alpha-amylase produced by *Bacillus cereus* amy3 using one factor at a time (OFAT) and central composite rotatable (CCRD) design based response surface methodology (RSM). *Biocatal Agric Biotechnol* 19
20. Mazaheri H, Ghaedi M, Asfaram A, Hajati S (2016) Performance of CuS nanoparticle loaded on activated carbon in the adsorption of methylene blue and bromophenol blue dyes in binary aqueous solutions: using ultrasound power and optimization by central composite design. *J Mol Liq* 219:667–676
21. Lingamdinne LP, Koduru JR, Chang YY, Karri RR (2018) Process optimization and adsorption modeling of Pb(II) on nickel ferrite-reduced graphene oxide nano-composite. *J Mol Liq* 250:202–211
22. Redhwan A, Azmi W, Sharif M, Mamat R, Zawawi NNM (2017) Comparative study of thermophysical properties of SiO₂ and Al₂O₃ nanoparticles dispersed in PAG lubricant. 116:823–832
23. Said Z, Sundar LS, Rezk H, Nassef AM, Ali HM, Sheikholeslami M (2021) Optimizing density, dynamic viscosity, thermal conductivity and specific heat of a hybrid nanofluid obtained experimentally via ANFIS-based model and modern optimization. *J Mol Liq* 321
24. Bhan M, Satija S, Garg C, Dureja H, Garg M (2017) Optimization of ionic liquid-based microwave assisted extraction of a diterpenoid lactone-andrographolide from *Andrographis paniculata* by response surface methodology. *J Mol Liq* 229:161–166
25. Thriveni K, Mahanthesh B (2021) Significance of variable fluid properties on hybrid nanoliquid flow in a micro-annulus with quadratic convection and quadratic thermal radiation: response surface methodology. *Int Commun Heat Mass Transfer* 124:105264–105264
26. Fazeli I, Sarmasti Emami MR, Rashidi A (2021) Investigation and optimization of the behavior of heat transfer and flow of MWCNT-CuO hybrid nanofluid in a brazed plate heat exchanger using response surface methodology. *Int Commun Heat Mass Transfer* 122:105175–105175
27. Leili M, Shirmohammadi Khorram N, Godini K, Azarian G, Moussavi R, Peykoshian A (2020) Application of central composite design (CCD) for optimization of cephalixin antibiotic removal using electro-oxidation process. *J Mol Liq* 313:113556–113556

28. Agarwal S, Tyagi I, Gupta VK, Dastkhon M, Ghaedi M, Yousefi F, Asfaram A (2016) Ultrasound-assisted adsorption of sunset yellow CFC dye onto Cu doped ZnS nanoparticles loaded on activated carbon using response surface methodology based on central composite design. *J Mol Liq* 219:332–340
29. Kousha M, Tavakoli S, Daneshvar E, Vazirzadeh A, Bhatnagar A (2015) Central composite design optimization of acid blue 25 dye biosorption using shrimp shell biomass. *J Mol Liq* 207:266–273
30. Salehnezhad L, Heydari A, Fattahi M (2019) Experimental investigation and rheological behaviors of water-based drilling mud contained starch-ZnO nanofluids through response surface methodology. *J Mol Liq* 276:417–430

Surface Modification for Dispersion Stability of Novel FAI_2O_3 -POE Nanolubricant Using Functional SiO_2



Agus Nugroho, Rizalman Mamat, Zhang Bo, Wan Azmi Wan Hamzah, Mohd Fairusham Ghazali, and Talal Yusaf

Abstract The presence of a hydroxyl group on the surface of Al_2O_3 is responsible for the low level of stability of Al_2O_3 -based nanolubricant. This paper aims to illustrate how the SiO_2 functionalization approach can be used to modify the surface of Al_2O_3 nanoparticles. The effects of four different functionalization treatments on Al_2O_3 on the dispersion stability of FAI_2O_3 -Polyolester (POE) nanolubricant were found to be significant. There are four samples with SiO_2 : Al_2O_3 ratios of 15:85, 30:60, 45:55, and 50:50%, respectively. Each sample was mechanically stirred for 120 min for adsorption process. Then, each sample received a sub-inter critical annealing treatment at 120 °C in the furnace for 180 min, after which the samples were chilled using the gradual cooling approach to avoid thermal shock on the FAI_2O_3 nanoparticle surface. Newly synthesized FAI_2O_3 was dispersed in POE lubricant for 30 min with a magnetic stirrer and then ultrasonicated for 100 min to prevent agglomeration. On day 1 and day 15, dispersing stability was examined using the UV visible spectrophotometry method to verify the wettability of FAI_2O_3 nanoparticles enhancement. The results reveal that increasing the SiO_2 ratio in the functionalization process enhances the dispersion stability of FAI_2O_3 -POE nanolubricant. The findings suggest that FAI_2O_3 -POE sample with a 50:50 ratio has the best dispersion stability, as shown by the highest absorbance ratio value of 0.945.

Keywords Alumina surface modification · Functionalized Al_2O_3 · FAI_2O_3 · Nanolubricant dispersion stability · FAI_2O_3 -POE nanolubricant

A. Nugroho (✉) · R. Mamat · Z. Bo
School of Mechanical Engineering, Ningxia University, Yinchuan, China
e-mail: ir.agusnug@gmail.com

A. Nugroho · R. Mamat · W. A. Wan Hamzah
College of Engineering, Universiti Malaysia Pahang, Pekan, Pahang, Malaysia

R. Mamat · W. A. Wan Hamzah · M. F. Ghazali
Centre for Research in Advanced Fluid & Processes, Universiti Malaysia Pahang, Lebuhraya Tun Razak, 26300 Gambang, Kuantan, Pahang, Malaysia

T. Yusaf
School of Engineering and Technology, Central Queensland University, Rockhampton, Australia

Abbreviations

H	Hour
min	Minute
abs	Absorbance
POE	Polyolester
UV	Ultraviolet
A	Initial Absorbance
A_o	Final Absorbance
\bar{A}_r	Absorbance Ratio
TEM	Transmission Electron Microscopy

Greek symbols

\emptyset	Concentration
ρ	Density

Subscripts

l	Refers to lubricant
p	Refers to nanoparticle

1 Introduction

Nanolubricant, a sub-class of nanofluid, is an advanced lubricant when it is compared to conventional lubricants [1–3]. It is said to have significantly improved heat-transfer and tribology characteristics [4, 5]. However, the essential criterion for any nanolubricant is its stability, nanolubricants will not be able to work optimally without proper stability. Only when the nanoparticles are adequately dispersed in a lubricant can the nanolubricant be stable.

Aluminum oxide (Al_2O_3) is a sort of nanoparticle that is frequently employed by researchers as a nano solid material in the formation of nanolubricants [6–8]. Al_2O_3 was chosen because it possesses unique properties such as hardness, chemical stability, electrical insulation, high thermal conductivity, and low density when compared to metal-based nanoparticles. Al_2O_3 has a lot of potential as a nano solid material for making nanolubricants as a replacement for conventional lubricants because of this basic character.

However, considering Al_2O_3 is a metal oxide-based nano solid material, it contains a hydroxyl group on the surface [9–11]. Al_2O_3 has hydrophilic characteristics due to the presence of hydroxyl groups on its surface, making it difficult to disperse well in oil-based fluids. The poor stability level of Al_2O_3 -based nanolubricant is affected by this behavior. As a result, several active efforts are required to change the surface of Al_2O_3 from hydrophilic to hydrophobic in order to improve the dispersion stability of Al_2O_3 -based nanolubricant.

Rahimi et al. [12] employed amine as a functional material in order to change the surface of the MWCNT. The MWCNT's surface character is changed from hydrophobic to hydrophilic through surface modification. The findings suggest that the dispersion of amine-MWCNT increased when water was used as the host fluid. The optimum concentration of amine addition in MWCNT is 0.05 wt%. Motokuro et al. [13] adopted the functionalization approach of cationic indium species and tertiary amine groups to modify the surface of $\text{SiO}_2\text{-Al}_2\text{O}_3$. Ion exchange and silane coupling reactions are used to carry out the functionalization process. Later, Yang et al. [14] adopted silane coupling agents on Al_2O_3 by adding γ Methacryloxy propyl tri-methoxy silane, γ Glycidoxy propyl triethoxy silane, γ Mercapto propyl tri-methoxy silane, and γ Amino propyl triethoxy silane to adjust the surface of Al_2O_3 . The findings reveal that a carbolic nanolayer forms on the Al_2O_3 surface. Wang et al. [15] modified the surface of Al_2O_3 and CaCO_3 at ambient temperature without heating using chloroform as a solvent and fatty acid as a fatty acid. The hydrophobic character of Al_2O_3 and CaCO_3 can be activated by the presence of these two modifiers.

There is a significant influence between the functional material (SiO_2) and the functionalized material (Al_2O_3). This paper aims to elaborate the surface modification process of Al_2O_3 using the SiO_2 functionalization method. This method allows SiO_2 as a functional material to patch to the Al_2O_3 surface and form a nanolayer without damaging the surface of each nanoparticle through adsorption process. The SiO_2 adsorption process using ethanol 95% as solvent agent on Al_2O_3 affects the surface properties of Al_2O_3 . Changes in the surface properties of Al_2O_3 were identified by increasing the dispersion stability of the $\text{FAl}_2\text{O}_3\text{-POE}$ nanolubricant experimentally. The results of increasing the dispersion stability of $\text{FAl}_2\text{O}_3\text{-POE}$ nanolubricant were verified by proving the value of the absorbance ratio using a spectrophotometer.

2 Experiment

2.1 Materials

The physical parameters of the Al_2O_3 and SiO_2 nanoparticles employed in this experiment are listed in Table 1. Figure 1a and b show the respective structures that are similar to Al_2O_3 and SiO_3 (b). The lubricant used in this experiment was an electric

Table 1 Physical properties of Al₂O₃ and SiO₂ nanoparticle

Nanoparticle	Size (nm)	Morphology	Density (g/cm ³)	Thermal conductivity (W/m.K)	Melting point (°C)	Color	Refractive index
Al ₂ O ₃	13	Spherical	3.9	35	2020	White	1.768
SiO ₂	21	Spherical	2.65	1.3	1830	White	1.458

Fig. 1 Compound structure of **a** Al₂O₃ and, **b** SiO₂**Table 2** Physical properties of POE lubricant

Properties	Value
Absolute viscosity at 40 °C	70.1 cSt
Absolute viscosity at 100 °C	9 cSt
Density at 27 °C	0.9601 g/cm ³
Flash point	252 °C
Color	Clear

Table 3 Physical properties of ethanol 95%

Name	Molecular weight	State	Vapor density	Boiling point (°C)	Melting point (°C)	Color	Evaporation rate
Ethanol, 95%	46.07	Liquid	1.59	78.5	-114.1	Colorless	3.3

compressor lubricant for an air conditioning system that was provided from Belgium and was of the type Polyolester (POE). Table 2 summarizes the typical characteristics of this lubricant. The mechanical stirring process of nanoparticles uses 95% ethanol as solvent. Properties of 95% ethanol indexed in Table 3.

2.2 Functionalized Al₂O₃ Synthesis Procedure

Mechanical stirrer method was adopted to synthesize functionalized Al₂O₃ (FAl₂O₃) in this study. Al₂O₃ and SiO₂ nanoparticles were dispersed in ethanol 95% using a magnetic stirrer for 30 min separately in the same proportion. Al₂O₃ and SiO₂ nanoparticles were mixed for 120 min without being heated continuously using a magnetic stirrer for adsorption process for adsorption process of SiO₂ to Al₂O₃. The adsorption process of SiO₂ on Al₂O₃ will adjust its polarity. The use of 95% ethanol

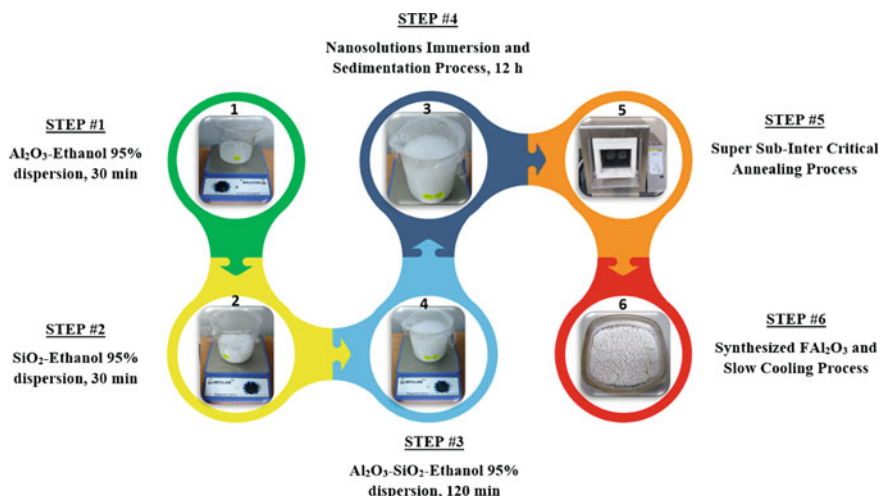


Fig. 2 Functionalization procedure of Al_2O_3 using SiO_2

as a solvent will boost the adsorption process without giving significant negative impact to both nanoparticles character [16–18].

In addition, the solution is left in the beaker for 12 h to provide the two nanoparticles with an immersion time effect, which improves their wettability. After that, the solution is heated in a furnace using the super sub-inter critical annealing process [19]. The pre-heat treatment process includes room temperature to the heat treatment temperature of $120\text{ }^\circ\text{C}$ is 15 min, 180 min to hold the heat treatment temperature at $120\text{ }^\circ\text{C}$, and 30 min to cool down to room temperature. The heat treatment process in this state aims to dry the new synthesized FAI_2O_3 and reduce the hydroxyl group surrounding the Al_2O_3 and SiO_2 because these two compounds are oxide-based nanoparticle. The gradual cooling technique is intended to protect the functionalized Al_2O_3 nanoparticle surface from thermal shock [20–22]. Figure 2. depicts the functionalization method adopted in this study. The same process was used to synthesize FAI_2O_3 in the following ratios: 15–85, 30–70, 45–65, and 50–50%.

2.3 FAI_2O_3 -POE Nanolubricant Preparation and Characterization

A two-step approach was used to prepare the production of FAI_2O_3 -POE nanolubricant, which included dispersing FAI_2O_3 into POE lubricant for 30 min using a magnetic stirrer without heating. After that, the sample was ultrasonicated for 100 min to prevent agglomeration and sedimentation. The ultrasonication employed is Hielscher Germany's UP400S ultrasonic type. With a cycle of 0.5, the ultrasonication device is set at 50% amplitude. In this experiment, four samples were used,

each with a different proportion of FAI_2O_3 and a concentration of 0.02 vol%. The morphology of FAI_2O_3 dispersed in POE lubricant was studied using Transmission Electron Microscopy (TEM).

For FAI_2O_3 -POE nanolubricant preparation. This experiment used four different ratios of Al_2O_3 : SiO_2 , namely 15:85, 30:70, 45:55, and 50:50 vol%, respectively. Calculation of the concentration volume using Eq. 1. Where \emptyset is volume fraction %; the TiO_2 nanopowder's mass is noted as m_p ; the lubricant's mass is m_l ; density of TiO_2 nanopowder is ρ_n ; and POE lubricant's density is ρ_l .

$$\emptyset = \frac{m_p / \rho_p}{m_p / \rho_p + m_l / \rho_l} \times 100\% \quad (1)$$

2.4 UV Visible Spectrophotometry

The UV visible spectrophotometry method works by absorbing UV light by the FAI_2O_3 -POE nanolubricant compound, which then generates a distinct spectrum. From time to time, the amount of absorbance value of nanolubricant is determined by this varied spectrum.

The level of dispersion stability of the FAI_2O_3 -POE nanolubricant was used to determine the indicator of increased wettability of FAI_2O_3 at POE. On each sample, the dispersion stability can be assessed using UV visible spectrophotometry. Furthermore, measuring the absorbance of FAI_2O_3 -POE molecules on days 1 and 15 is used to determine the absorbance ratio. Figure 3 depicts a schematic of the principle of measuring the absorbance of FAI_2O_3 -POE nanolubricant compounds.

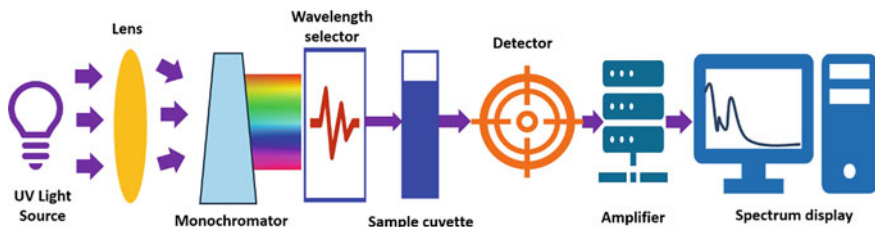


Fig. 3 Schematic UV visible spectrophotometry principle

3 Result and Discussion

3.1 FAI_2O_3 Characterization

Figure 4 shows a TEM picture of an FAI_2O_3 sample that was ultrasonically treated for 120 min at varied composition ratios. TEM images of sample FAI_2O_3 -POE nanolubricant with Al_2O_3 : SiO_2 ratios of 15:85, 30:70, 45:55, and 50:50 is shown in Fig. 4a, b, c and d. Al_2O_3 and SiO_2 are homogeneously combined into a new nanoparticle unit, as shown in the diagram. As depicted in the TEM image, SiO_2 physically surrounds Al_2O_3 and induces the formation of a new grain unit.

In this study, the TecnaiTM Spirit TWIN Transmission Electron Microscope (TEM) was used as suggested by previous researchers [23–25]. Under ambient temperature conditions, TEM was utilized to characterize FAI_2O_3 -POE nanolubricants and examine the morphology of FAI_2O_3 dispersed in POE lubricants. TEM analysis was used to explore differences in crystal structure and microstructure between materials at the concentrations chosen for TEM examination. The porous and spherical structure of the nanopowder is seen in the TEM images. The image displays prominent

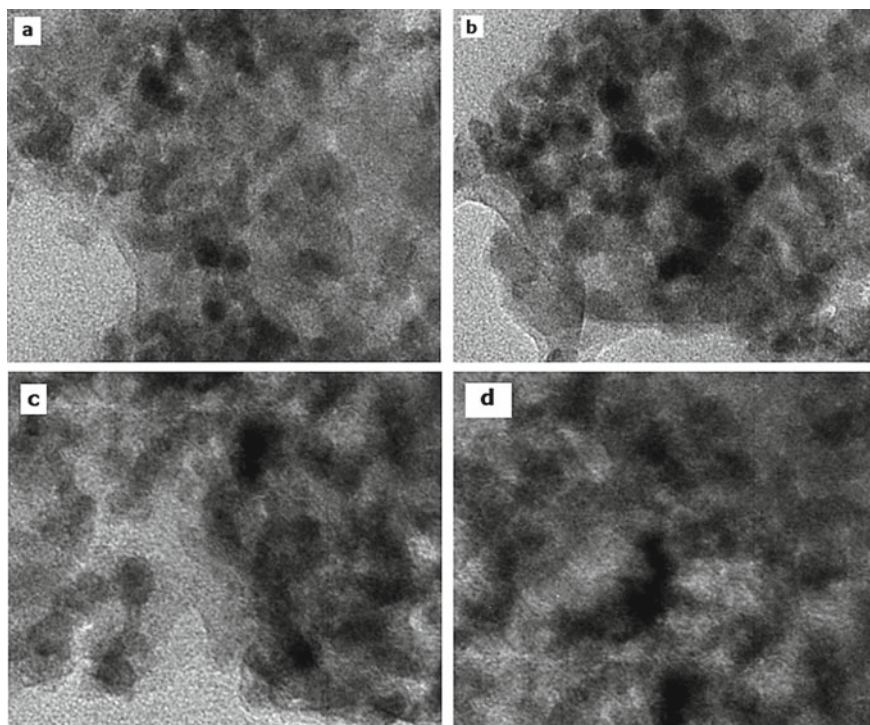


Fig. 4 TEM image of FAI_2O_3 -POE nanolubricant with **a** 15:85, **b** 30:70, **c** 45:55, and **d** 50:50 Al_2O_3 and SiO_2 ratio

lattice edges, confirming the spherical nanostructure's remarkable crystallinity. The polycrystallinity of the nanostructures of the two nanoparticles causes concentric circles in the crystal structure of $\text{FAI}_2\text{O}_3\text{-POE}$, as seen in the picture. The FAI_2O_3 nanopowder is a polycrystal-line material because the grain boundaries of each crystal grain are orientated in several directions rather than just one.

3.2 $\text{FAI}_2\text{O}_3\text{-POE}$ Absorbance Ratio Analysis

The absorbance samples of the $\text{FAI}_2\text{O}_3\text{-POE}$ nanolubricant were measured on day 1 and day 15. Figure 5 displays the findings of an $\text{FAI}_2\text{O}_3\text{-POE}$ absorbance sample with a 15:85 ratio. There are a number of fluctuating spectra in the two images. In Fig. 5a spectrum fluctuations mostly occur at a wavelength of 430–290 nm. This demonstrates the high level of UV ray absorption by the sample in this area when emitted by the spectrophotometer. UV light absorption is significant in this region, indicating that there are numerous nanoparticle agglomerations. The sample measurement on day 15 shows the similar trend, with the number of spectrum changes increasing as reported by previous researchers [26–28]. Spectral variations still have the dominant position at a wavelength of 430–290 nm.

An increase in the amount of nanoparticle agglomeration in the nanolubricant induced a considerable increase in the number of spectrum peaks in the sample measurement on day 15. Sedimentation on the nanolubricant in the form of nanolayers can absorb significantly more UV light [29]. As a result, the display depicts the increased absorption of UV radiation as an increase in the number of variations in the spectrum peak.

The ratio of the peaks of the absorbance spectrum in each sample is used to determine the absorbance ratio. Spectral peaks at 292 nm were chosen and compared on absorbance measurements taken on day 1 and day 15 to determine the absorbance ratio [30, 31]. In comparison to a number of other peaks, the wavelength of 292 nm is the highest.

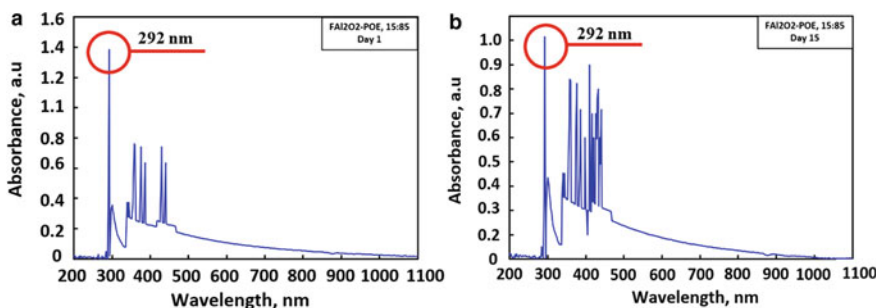


Fig. 5 Absorbance value of $\text{FAI}_2\text{O}_3\text{-POE}$ with ratio 15:85 on **a** day 1 and, **b** day 15

Absorbance studies on FAI_2O_3 -POE nanolubricant samples with a functionalization ratio of $\text{SiO}_2:\text{Al}_2\text{O}_3$, 30:70 is shown in Fig. 6. The spectrum peak of 292 nm was chosen as the wavelength peak that was compared on both day 1 and day 15 absorbance ratio tests. The number of fluctuations in the spectral peak in Fig. 6a is less than that in Fig. 6b. This behavior suggests that the FAI_2O_3 nanoparticles in the POE are well dispersed, with minor aggregation in the nanolubricant area that receives UV light from the spectrophotometer. In Fig. 6b, on the other hand, agglomeration begins to develop, resulting in a large rise in the number of spectra. On day 1, the absorbance of this sample was 2386 nm, but by day 15, it had dropped to 1816 nm. The absorbance value of the second sample on day 15 is higher than the first sample's absorbance value of 0.916 nm as depicted in Fig. 7.

The FAI_2O_3 -POE sample, which has a functionalization ratio of $\text{SiO}_2:\text{Al}_2\text{O}_3$ of 45:55, shows fewer spectrum variations than the two prior samples. A considerable value is seen at a wavelength of 292 nm, thus the absorbance value in that area is appropriate for comparison with the absorbance values in the next measurement. The FAI_2O_3 -POE nanolubricant in this sample can be justified as having a more stable dispersion than the two previous samples. The phenomenon of dispersion stability is evidenced by the slight increase in fluctuations in the spectral peaks and the low level of decrease in the spectral peaks at 292 nm. This demonstrates that functionalization

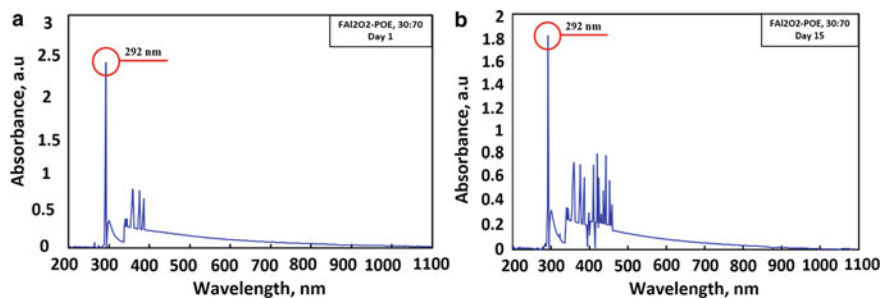


Fig. 6 Absorbance value of FAI_2O_3 -POE with ratio 30:70 on **a** day 1 and, **b** day 15

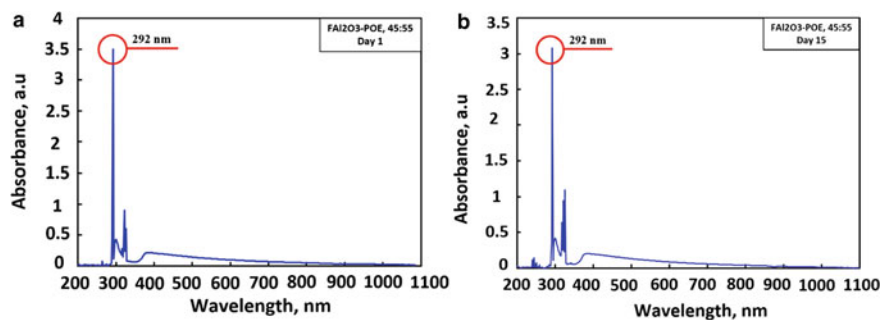


Fig. 7 Absorbance value of FAI_2O_3 -POE with ratio 45:55 on **a** day 1 and, **b** day 15

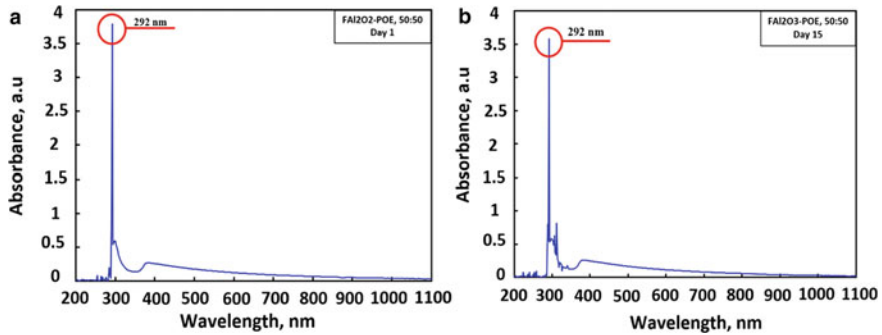


Fig. 8 Absorbance value of FAI_2O_3 -POE with ratio 50:50 on **a** day 1 and, **b** day 15

at a level of 45:55 can offer a significantly improved surface coating effect on Al_2O_3 . This Al_2O_3 surface coating effect modifies the character of the surface of Al_2O_3 nanoparticles, promoting higher wettability of the nanoparticles' surface to oil [32].

This increase in nanoparticle surface wetness promotes higher bonding of oil molecules with Al_2O_3 molecules, allowing nanoparticle agglomeration to last longer [33–35]. On day 1, the absorbance value in the third sample was 3499, and on day 15, the absorbance value was 3079, resulting in an absorbance ratio of 0.879.

The fourth sample has a SiO_2 : Al_2O_3 ratio of 50:50, which means that the proportions of each are equal. The absorbance spectrum value in Fig. 8a is noticeably smoother than the prior sample. In the 400–1100 nm wavelength region, there is essentially no significant variation. The spectrum has a decreasing pattern that is nearly identical to the previous sample, and the graph peaks at a wavelength of 292 nm, with a value of 3793 absorbance units. Then, on day 15, the absorbance value dropped to 3583. Based on these two absorbance values, the drop in absorbance is relatively small, resulting in a high absorbance ratio value of 0.945.

Figure 8b shows that there is a small amount of nanoparticle aggregation in the nanolubricant due to the low number of spectrum variations. The nanoparticles in the POE lubricant were well dispersed despite the nanolubricant having been kept for 15 days. This phenomenon can be highlighted by the fact that the adsorption process of functionalization of SiO_2 with the method shown in Fig. 2 has resulted in a major change in character on the surface of Al_2O_3 [36]. SiO_2 nanoparticles have formed a layer on the surface of Al_2O_3 that increased its wettability properties [37–39]. FAI_2O_3 's wettability increment effect strengthens the bond between Al_2O_3 molecules in solid materials and POE molecules in liquid materials. FAI_2O_3 's with higher wettability nature is proven experimentally by its high absorbance ratio, which means it has the best dispersion stability of all the samples due to SiO_2 adsorption as reported by Metin et al. [40]. Figure 9 shows the recapitulation of the absorbance ratio for all samples using FAI_2O_3 nanoparticles in various ratio.

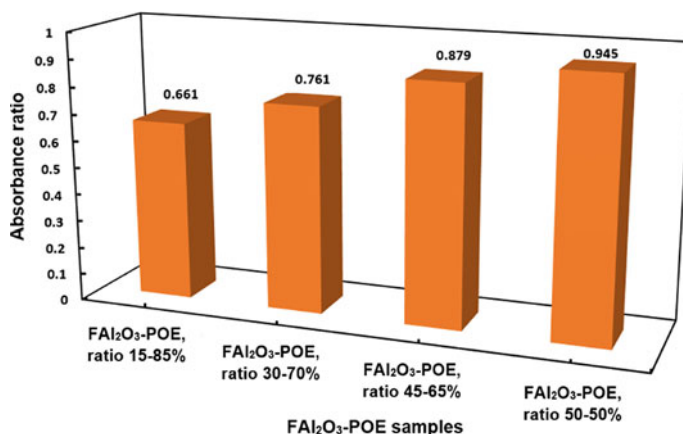


Fig. 9 Absorbance ratio of FAI₂O₃-POE nanolubricant using various FAI₂O₃ ratio

4 Conclusion

The surface of Al₂O₃ is adjusted using a functionalization approach in this paper. Since of its silicon concentration, SiO₂ was chosen as a functional solid material because it can induce a wettability effect enhancement on the surface of Al₂O₃. The adsorption method in this functionalization treatment was able to activate the Al₂O₃ surface's wettability properties. The hydroxyl group on the surface of both nanoparticles was adjusted during the functionalization process. TEM study demonstrated that SiO₂ physically surrounds Al₂O₃ and forms a new grain unit. Experimental results of FAI₂O₃ dispersion into POE lubricants have validated this synthesis. The experimental results demonstrate that as the proportion of SiO₂ as functional material increases, the stability of FAI₂O₃-POE dispersion increases. The fifth sample FAI₂O₃-POE, which has a SiO₂:Al₂O₃ ratio of 50:50, has the greatest absorbance ratio, which is 0.945. As a result, the FAI₂O₃-POE sample with a SiO₂:Al₂O₃ ratio of 50:50 can be justified as the sample with the best dispersion stability. The use of SiO₂ as a modifier material on Al₂O₃ to improve the dispersion stability of FAI₂O₃-POE nanolubricant was shown to be effective. This approach has been shown to be effective in changing the surface polarity character of Al₂O₃. In comparison to other typical methods such as silane, amine coupling agents, and chemical surfactant, this approach is also more economical to support industrialization of nanolubricant production.

Acknowledgements This study was supported by the Helan Mountain Scholarship program from Ningxia University, China. The authors like to extend their appreciation to Universiti Malaysia Pahang (UMP) for funding provided by the dedicated internal fund RDU190336 and the FRGS award RDU 1901112.

Conflicts of Interest The authors declare no conflict of interest.

References

1. Adelekan DS, Ohunakin OS, Oladeinde MH, Jatinder G, Atiba OE, Nkiko MO, Atayero AA (2021) Performance of a domestic refrigerator in varying ambient temperatures, concentrations of TiO₂ nanolubricants and R600a refrigerant charges. *Heliyon* 7:e06156
2. Yogesh J, Dinesh Z, Sandeep J (2021) Performance investigation of vapor compression refrigeration system using R134a and R600a refrigerants and Al₂O₃ nanoparticle based suspension. *Mater Today Proc* 44:1511–1519
3. Choi TJ, Kim DJ, Jang SP, Park S, Ko S (2021) Effect of polyolester oil-based multiwalled carbon-nanotube nanolubricant on the coefficient of performance of refrigeration systems. *Appl Therm Eng* 192
4. Keklikcioglu O, Ozceyhan V (2022) Heat transfer augmentation in a tube with conical wire coils using a mixture of ethylene glycol/water as a fluid. *Int J Therm Sci* 171:107204
5. Rashidi M, Sedaghat A, Misbah B, Sabati M, Vaidyan K (2021) Experimental study on energy saving and friction reduction of Al₂O₃-WBM nanofluids in a high-speed Taylor-Couette flow system. *Tribol Int* 154:106728
6. Saranya S, Al-Mdallal QM (2021) Computational study on nanoparticle shape effects of Al₂O₃-silicon oil nanofluid flow over a radially stretching rotating disk. *Case Stud Therm Eng* 25:100943
7. Bharadwaj G, Sharma A, Rawat M, Singhal P (2020) Analysis of energy storage system by using aluminum oxide nanofluid (Al₂O₃) with paraffin wax. *Mater Today Proc*
8. Anish W, Sunil J, Sadasivuni KK (2020) Viscosity of Al₂O₃-water nanofluids. *Mater Today Proc* 21:681–683
9. Huang L, Yang Z, Zhang Z, Jin L, Yang W, He Y, Ren L, Wang H (2020) Enhanced surface hydroxyl groups by using hydrogen peroxide on hollow tubular alumina for removing fluoride. *Microporous Mesoporous Mater* 297:110051
10. Poli E, Ouk T-S, Barrière G, Lévêque G, Sol V, Denes E (2019) Does low hydroxyl group surface density explain less bacterial adhesion on porous alumina? *Orthop Traumatol Surg Res* 105:473–477
11. Digne M, Sautet P, Raybaud P, Euzen P, Toulhoat H (2002) Hydroxyl groups on γ -alumina surfaces: a DFT study. *J Catal* 211:1–5
12. Rahimi K, Riahi S, Abbasi M (2020) Effect of host fluid and hydrophilicity of multi-walled carbon nanotubes on stability and CO₂ absorption of amine-based and water-based nanofluids. *J Environ Chem Eng* 8
13. Motokura K, Ito Y, Noda H, Miyaji A, Yamaguchi S, Baba T (2014) Surface functionalization for synergistic catalysis: silica-alumina-supported cationic indium and organic base for cyanoethoxycarbonylation. *ChemPlusChem* 79:1053–1058
14. Yang Y-C, Jeong S-B, Kim B-G, Yoon P-R (2009) Examination of dispersive properties of alumina treated with silane coupling agents, by using inverse gas chromatography. *Powder Technol* 191:117–121
15. Wang Y, Eli W, Zhang L, Gao H, Liu Y, Li P (2010) A new method for surface modification of nano-CaCO₃ and nano-Al₂O₃ at room temperature. *Adv Powder Technol* 21:203–205
16. Kim B-J, Cha S-H, Kong K, Ji W, Park HW, Park Y-B (2018) Synergistic interfacial reinforcement of carbon fiber/polyamide 6 composites using carbon-nanotube-modified silane coating on ZnO-nanorod-grown carbon fiber. *Compos Sci Technol* 165:362–372
17. Cao L, Sinha TK, Tao L, Li H, Zong C, Kim JK (2019) Synergistic reinforcement of silanized silica-graphene oxide hybrid in natural rubber for tire-tread fabrication: a latex based facile approach. *Compos B Eng* 161:667–676
18. Xie Y, Wang X, Hou L, Wang X, Zhang Y, Zhu C, Hu Z, He M (2021) Graphene covalently functionalized by cross-linking reaction of bifunctional pillar organic molecule for high capacitance. *J Energy Storage* 38:102530
19. Kapoor I, Lan Y, Rijkenberg A, West G, Li Z, Janik V (2020) Correlative analysis of interaction between recrystallization and precipitation during sub-critical annealing of cold-rolled low-carbon V and Ti–V bearing microalloyed steels. *Mater Sci Eng A* 785:139381

20. Li B, Yan Y, Jin X, Geng Y, Wang S, Cao M, He X, Li N, Zhuang Y (2021) Microstructure and mechanical and thermal shock properties of hierarchically porous ceramics. *Ceram Int* 47:24887–24894
21. Lutpi HA, Mohamad H, Abdullah TK, Ismail H (2021) Effect of ZnO on the structural, physio-mechanical properties and thermal shock resistance of Li₂O–Al₂O₃–SiO₂ glass-ceramics. *Ceram Int*
22. Tian Z, Lu J, Feng X, Wang J (2021) Effect of grain size and orientation degree on thermal shock resistance of BN-matrix textured ceramics under cyclic thermal shock. *J Eur Ceram Soc* 41:441–446
23. Tiwari AK, Pandya NS, Said Z, Chhatbar SH, Al-Turki YA, Patel AR (2021) 3S (Sonication, surfactant, stability) impact on the viscosity of hybrid nanofluid with different base fluids: an experimental study. *J Mol Liq* 329:115455
24. Clauser AL, Giulian R, McClure ZD, Sarfo KO, Ophus C, Ciston J, Árnadóttir L, Santala MK (2020) Orientation and morphology of Pt nanoparticles in γ -alumina processed via ion implantation and thermal annealing. *Scripta Mater* 188:44–49
25. Zawawi N, Azmi W, Redhwan A, Sharif M, Sharma KV (2017) Thermo-physical properties of Al₂O₃-SiO₂/PAG composite nanolubricant for refrigeration system. 80:1–10
26. Zhang T, Zou Q, Cheng Z, Chen Z, Liu Y, Jiang Z (2021) Effect of particle concentration on the stability of water-based SiO₂ nanofluid. *Powder Technol* 379:457–465
27. Sofiah AGN, Samykanom M, Shahabuddin S, Kadirgama K, Pandey AK (2020) An experimental study on characterization and properties of eco-friendly nanolubricant containing polyaniline (PANI) nanotubes blended in RBD palm olein oil. *J Therm Anal Calorim*
28. Cagua K, Murshed SMS, Pabón E, Buitrago R (2020) Dispersion and thermal conductivity of TiO₂/water nanofluid. *J Therm Anal Calorim* 140:109–114
29. Baek S, Shin D, Kim G, Lee A, Noh J, Choi B, Huh S, Jeong H, Sung Y (2021) Influence of amphoteric and anionic surfactants on stability, surface tension, and thermal conductivity of Al₂O₃/water nanofluids. *Case Stud Therm Eng* 25:100995
30. Sharif M, Azmi W, Redhwan A, Mamat R, Yusof T (2017) Performance analysis of SiO₂/PAG nanolubricant in automotive air conditioning system. *Int J Refrig* 75:204–216
31. Nugroho A, Bo Z, Mamat R, Azmi WH, Najafi G, Khoirunnisa F (2021) Extensive examination of sonication duration impact on stability of Al₂O₃-polyol ester nanolubricant. *Int Commun Heat Mass Transfer* 126:105418
32. Fratoddi I (2017) Hydrophobic and hydrophilic Au and Ag nanoparticles. Breakthroughs and perspectives. *Nanomaterials (Basel)* 8
33. Gbadamosi AO, Junin R, Manan MA, Agi A, Oseh JO, Usman J (2019) Effect of aluminium oxide nanoparticles on oilfield polyacrylamide: rheology, interfacial tension, wettability and oil displacement studies. *J Mol Liq* 296:111863
34. Motokawa T, Makino M, Yamamoto K, Takase H, Nagano S, Enomoto-Rogers Y, Iwata T, Kawaguchi T, Sakaguchi M (2017) Chemical surface modification of aluminum oxide nanoparticles with graft copolymer of aluminum oxide and poly(isobutyl vinyl ether) mechanochemically synthesized in vacuum at low temperature. *Adv Powder Technol* 28:266–279
35. Agustin AR, Tamura K (2021) Surface modification of TiO₂ nanoparticles with terephthalic acid in supercritical carbon dioxide. *J Supercrit Fluids* 174:105245
36. Desmet C, Valsesia A, Oddo A, Ceccone G, Spampinato V, Rossi F, Colpo P (2017) Characterisation of nanomaterial hydrophobicity using engineered surfaces. *J Nanopart Res* 19:117
37. Zhao L, Du Z, Tai X, Ma Y (2021) One-step facile fabrication of hydrophobic SiO₂ coated super-hydrophobic/super-oleophilic mesh via an improved Stöber method to efficient oil/water separation. *Colloids Surf A* 623:126404

38. Sefhra PJ, Baraneedharan P, Sivakumar M, Thangadurai TD, Nehru K (2018) CuO/SiO₂ modified amine functionalized reduced graphene oxide with enhanced photocatalytic and electrochemical properties. *SN Appl Sci* 1:73
39. Klippel N, Jung G, Kickelbick G (2021) Hybrid inorganic-organic fluorescent silica nanoparticles—influence of dye binding modes on dye leaching. *J Sol-Gel Sci Technol*
40. Metin CO, Baran JR Jr, Nguyen QP (2012) Adsorption of surface functionalized silica nanoparticles onto mineral surfaces and decane/water interface. *J Nanopart Res* 14:1246

Absorbance Ratio Optimization as a Function of TiO₂-POE Nanolubricant Spectrophotometric Wavelength Using the Quadratic Design on One Factor at a Time



Agus Nugroho, Rizalman Mamat, Zhang Bo, Wan Azmi Wan Hamzah,
Talal Yusaf, Mohd Fairusham Ghazali, and Fitri Khoerunnisa

Abstract Errors in the UV visible spectrophotometry analysis' selection of spectral peaks can lead to errors in the nanolubricant stability analysis. Despite the fact that the spectral peak results are compared at the same peak, it is critical to identify the correct spectral to avoid errors in the nanolubricant stability analysis results. In this study, one factor at a time (OFAT) based on surface response was adopted to determine the effect of wavelength selection on the absorbance ratio of TiO₂-POE nanolubricant. The TiO₂-POE sample was prepared using a two-steps approach. The sample was ultrasonicated for 100 min using a homogenizer. UV visible spectrophotometry analysis was performed on day 1 and 15 to determine the absorbance ratio. Sixteen runs were performed using a quadratic design to acquire experimental data were fitted. The ANOVA analysis discovered that the experimental statistics were well suited to the polynomial model, with an R² value of 0.9970 and a model F-value of 2154.24. The findings suggest that the optimum wavelength is 500 nm with an absorbance value of 0.901239 and a desirability level of 1.0.

Keywords ANOVA · OFAT · TiO₂-POE nanolubricant · UV visible spectrophotometry

A. Nugroho (✉) · R. Mamat · Z. Bo
School of Mechanical Engineering, Ningxia University, Yinchuan, China
e-mail: ir.agusnug@gmail.com

A. Nugroho · R. Mamat · W. A. Wan Hamzah
College of Engineering, Universiti Malaysia Pahang, Gambang, Pahang, Malaysia

T. Yusaf
School of Engineering and Technology, Central Queensland University, Rockhampton, Australia

M. F. Ghazali
Centre for Research in Advanced Fluid & Processes, Universiti Malaysia Pahang, Lebuhraya Tun Razak, 26300 Gambang, Kuantan, Pahang, Malaysia

F. Khoerunnisa
Department of Chemistry, Indonesia University of Education, Bandung, Indonesia

Abbreviations

min	Minute
abs	Absorbance
MO	Mineral oil
OFAT	One factor at a time
Std. Dev	Standard deviation
POE	Polyolester
Anova	Analysis of variance
UV	Ultraviolet
A	Initial absorbance
A_o	Final absorbance
A_r	Absorbance ratio

Greek Symbols

ζ	Absolute zeta potential (mV)
\emptyset	Concentration
P	Density

Subscripts

<i>l</i>	Refers to lubricant
<i>p</i>	Refers to nanoparticle

1 Introduction

The main issue with any colloid, whether water-based or oil-based, known as a nanolubricant, is its stability [1–4]. Several researchers continue to improve the stability of nanolubricant regularly so that the nanolubricant applied to the system can provide maximum heat transfer performance [4–6] and tribological effects [7–9]. The UV visible spectrophotometry technique can determine the stability level of a nanolubricant. UV rays are emitted throughout the nanolubricant area to be absorbed by the nanoparticles dispersed in the lubricant [10]. Absorbance is the ability of a nanolubricant to absorb UV light. The absorbance of the nanolubricant sample was assessed on the first and the predetermined day.

Sharif et al. [11] prepared SiO₂/PAG nanolubricants for automobile air conditioning systems. The spectrophotometric method, which measures the UV rays emitted into a sample of SiO₂/PAG nanolubricants, is used to determine the level of stability of SiO₂/PAG nanolubricants. The optimal absorbance ratio is determined by comparing the absorbance values displayed at the spectral wavelength of 313 nm. Later, Zawawi et al. [12] created Al₂O₃-SiO₂/PAG hybrid nanolubricants at a concentration of 0.1%. Before applying the nanolubricant to the vehicle's air conditioning system, stability must be determined to ensure that the nanolubricant can provide optimal performance. The UV visible spectrophotometry method was used to predict the stability level of Al₂O₃-SiO₂/PAG nanolubricant. On day 1 and day 30, observations and spectrophotometry spectrum analysis were performed at 315 nm wavelength on day 1 and day 30.

Meanwhile, Rahman et al. [13] optimized the spectrophotometric function of the N-bromosuccinimide colloid using the surface response method. The absorbance at 513 nm was used to monitor the oxidation of methyl orange by unreacted N-bromosuccinimide. The absorbance was drafted versus the acetazolamide proportion resulting in a linear contour, and the correlative regression model was generated. This technique is claimed to be the best for determining the optimal absorbance of an experimental sample. Jatinder et al. [14] created a TiO₂-mineral oil (MO) nanolubricant using a two-step approach for domestic refrigerators. The samples were prepared at concentrations of 0, 0.2, 0.4, and 0.6 g/L. The stability of TiO₂-MO nanolubricant was determined using UV-visible spectrophotometry. Finally, observations and analyses were carried out at the peak of the 290 nm spectrum. This area is the most optimum point.

This study aims to discover the optimum absorbance ratio based on the spectrophotometric wavelength selection on the absorbance ratio of TiO₂-POE nanolubricant statistically by means of one factor at a time. One factor at a time based on response surface methodology was performed to measure the most optimum absorbance ratio of TiO₂-POE nanolubricant based on the quadratic design. It is essential to validate that the spectral peak determination based on experimental results of UV visible spectrophotometric readings is consistent with the statistical method. The findings of the study can be used to determine the wavelength spectrum determination over the next UV visible spectrometry nanolubricant analysis to prevent any bias result.

2 Experimental Method

2.1 Nanolubricant Preparation

The nanoparticles are mixed in a POE lubricant to synthesize a nanolubricant as suggested by Redhwan et al. [15]. POE lubricants are supplied by a Belgian multinational firm under the SUNISO brand. Sigma-Aldrich in Saint Louis, Missouri, USA, manufactured TiO₂ nanopowder form with a typical particle magnitude of 21 nm

and a cleanliness of 99.5% for this purpose. The nanolubricant was sonicated using an ultrasonic homogenizer UP400S produced by Hielscher Germany. An ultrasonic homogenizer's objective is to supply more energy than a conventional ultrasonic bath. The findings will increase the homogeneity of the nanolubricant while decreasing the sonication period [16]. The adoption of an ultrasonic homogenizer is particularly successful at preventing the agglomeration and sedimentation of nanolubricants. The ultrasonic device's parameters are 400 W, 24 kHz, 50% amplitude, and 0.5 cycles. Six samples were used in this investigation, all of which had the same 0.02 vol% concentration volume. A 30-min stirring was applied, and then the nanolubricant was subjected to ultrasonication for 100-min.

2.2 UV Visible Spectrophotometry Analysis

The stability of the TiO₂-POE nanolubricant was predicted by adopting the UV visible spectrophotometry method. Spectrophotometry spectrums were analyzed from day 1 and day 15. The absorbance ratio was determined for 15 days. The absorbance ratio will predict the nanolubricant stability through the highest absorbance ratio values, as reported by Redhwan et al. [17].

2.3 Optimization

The OFAT approach is used in this study, with only one factor to be studied based on the statistical calculation of the response surface method with Design Expert 7.16 (Stat-Ease Inc., Minneapolis, MN, USA). The analysis of variance (ANOVA) approach was used to examine the generated model statistically. The R² and adjusted R² coefficients were used to examine the superiority of the fit of the polynomial model equivalency. The F-test and p-values were used to validate the significance of the numerical and coefficient of determination, respectively, as suggested by the previous researchers [18–20].

Furthermore, the optimization condition was determined based on the highest absorbance value, the shortest wavelength spectrum, and the highest desirability value.

3 Result and Discussion

3.1 TiO₂-POE Nanolubricant Absorbance Ratio Analysis Using UV Visible Spectrophotometry

Figure 1 depicts a comparison of the absorbance values of TiO₂-POE nanolubricant with a concentration of 0.02 vol% after 30 min of mixing and 100 min of ultrasonication. Each of the five spectral locations optimized with OFAT is depicted in the two images. Figure 1a shows the absorbance result on the first day after the sample was made, whereas Fig. 1b shows the absorbance result after 15 days of storage. The difference between the two is the variation in the value spectrum of each absorbance value at several points determined by Design-Expert software. Table 1 summarizes the independent variables involved in the OFAT optimization, Table 2 shows the response parameters, and Table 3 shows the experimental data for the optimization process.

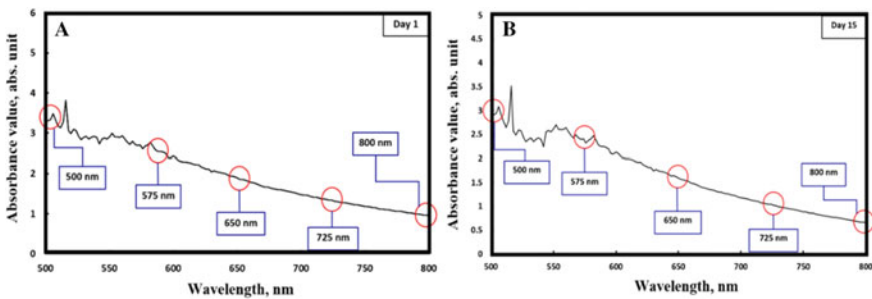


Fig. 1 TiO₂-POE nanolubricant absorbance comparison **a** day 1 and **b** day 15 from the assessed sample

Table 1 Independent variable involved OFAT study

Factor	Name	Units	Type	Low actual	High actual	Low coded	High coded	Mean	Std. dev
A	Wavelength	nm	Numeric	500.00	800.00	-1.000	1.000	650.000	79.550

Table 2 Response parameters involved OFAT study

Response	Name	Units	Type	Analysis	Min	Max	Mean	Std. dev	Model
Y1	Absorbance ratio	nm	ratio	Polynomial	0.75	0.9	0.815	0.0419524	Quadratic

Table 3 Experiment result for optimization

No	Run	Wavelength	Absorbance ratio
1	7	500	0.9
2	16	500	0.9
3	2	575	0.86
4	15	725	0.78
5	11	800	0.75
6	3	800	0.75
7	9	650	0.81
8	8	650	0.81
9	4	650	0.81
10	5	650	0.81
11	13	650	0.81
12	6	650	0.81
13	12	650	0.81
14	14	650	0.81
15	1	650	0.81
16	10	650	0.81

Furthermore, as proposed by Zawawi et al. [21], the absorbance ratio value can be used to assess the stability level of TiO₂-POE nanolubricant based on this discovery. By comparing the baseline absorbance (A) to the final absorbance (A_o) given by Eq. 1, the absorbance ratio (\bar{A}_r) is estimated.

$$\bar{A}_r = \frac{A}{A_0} \quad (1)$$

3.2 Analysis of Variant (ANOVA)

Table 4 summarizes the results of the ANOVA for the response surface quadratic model study. Table 4 presents the statistical results based on the ANOVA. The model is significant because it has a *p*-value of 0.0001, less than 0.05, and an *F*-value of 2154.24. The significance of each component was also determined using *F*-values and *p*-values [22–24]. The bigger the degree of the *F* value and the lower the *p*-value, the more significant the relevant coefficient terms are [25–27]. Models A-wavelength and A², with *F* values of 4205.08 and 103.40, respectively, are similarly significant in this scenario.

The coefficient of determination (R²) of 0.9970, which has a good agreement with the adjusted R² of 0.9965, supports this conclusion. This model has a high replication

Table 4 ANOVA response summary

Source	Sum of squares	df	Mean square	F value	p-value	Remark
Model	0.026	2	0.013	2154.24	<0.0001	Significant
A-wavelength	0.026	1	0.026	4205.08	<0.0001	
A ²	6.317E-004	1	6.317E-004	103.40	<0.0001	
Residual	7.942E-005	13	6.109E-006			
Lack of fit	7.942E-005	2	3.971E-005			
Pure error	0.000	11	0.000			
Car total	0.026	15				

Table 5 Coefficient of determination

Parameters	Value
Standard deviation	2.472E-003
Mean	0.82
CV %	0.30
Press	1.085E-004
R-squared	0.9970
Adjusted R ²	0.9965
Prediction R ²	0.9959
Adequate precision	141.192

rate, ensuring that the results are precise and consistent. This condition is indicated by a shallow pure error value of 0.000. The coefficient of determination indicates a significant value in this investigation, indicating that wavelength determination positively influences the absorbance ratio assessment [22, 28, 29] as shown in Table 5.

The regression model's appropriateness was determined using residuals and residuals versus predicted plots as depicted in Fig. 2a, b. The present work findings and estimated points are clustered along with the normalcy graph as shown in Fig. 2(a), confirming the analytical system's consistency [30, 31]. As illustrated in Fig. 2, the residual, on the other hand, are scattered uncertainly through the reference line with no discernible pattern. Figure 3 approves the predicted value's closeness to the actual value. Based on the graphs, it can be justified that the quadratic model is satisfactorily reliable to establish the relationship between the investigated boundaries and the variable. The variable influenced the change in absorbance ratio, namely wavelength determination.

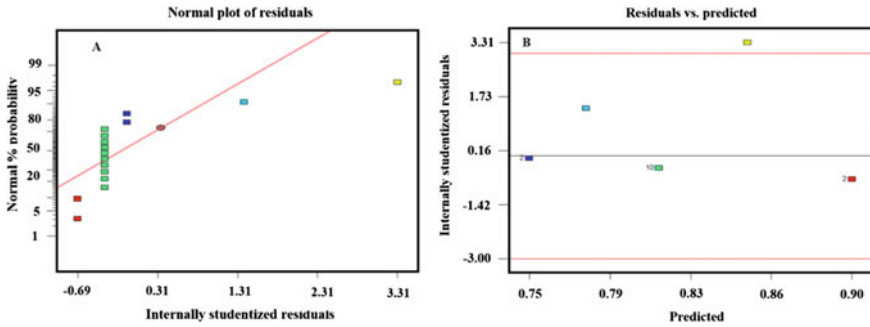


Fig. 2 a Normal plot of residuals; b correlation amid residuals and predicted the plot of present work findings

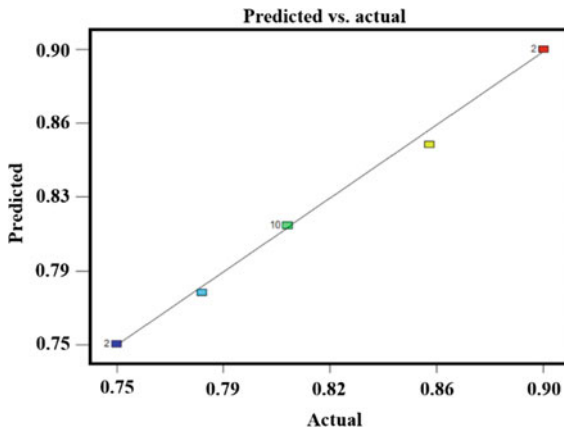


Fig. 3 Correlation amid predicted and the actual plot of present work findings

3.3 OFAT Optimization Solution

Figure 4a depicts the relationship between absorbance ratio and wavelength. As shown in the graph, there is a trend that the shorter the wavelength, the higher the absorbance ratio. The wavelength with the lowest absorbance is 800 nm, while the wavelength with the highest absorbance is 500 nm. In Fig. 5b, the optimal wavelength is determined by the highest desirability value. As a result, the graph shows that the highest desirability value, 1.0, is in the 500 nm range. This investigation reveals that the best wavelength determination value is in the 500 nm range, with an absorbance ratio of 0.901239, as shown in Fig. 5. This finding is consistent with what has been published in the literature [32–34].

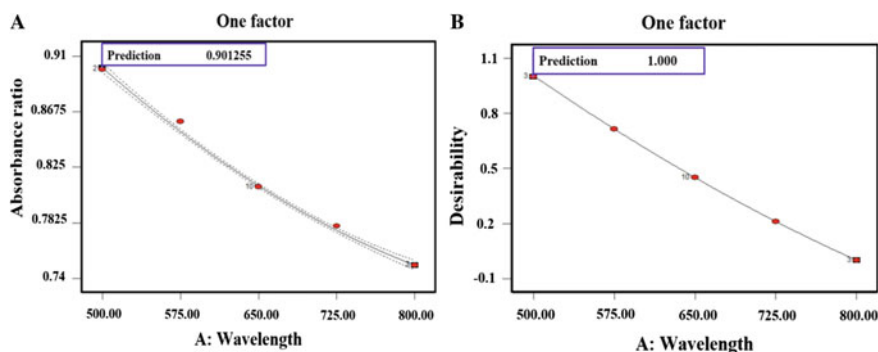


Fig. 4 A plot of **a** absorbance ratio as the dependent of wavelength determination and **b** wavelength criteria based on the desirability of OFAT optimization

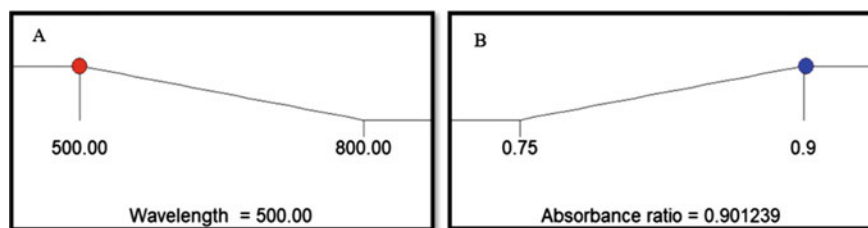


Fig. 5 Ramps plotting of optimum absorbance ratio as the dependent of wavelength determination

4 Conclusion

The prepared TiO₂-POE nanolubricant sample was analyzed experimentally using UV visible spectrophotometry. Based on the findings, it is reasonable to conclude that there is an increasing absorbance value with decreasing wavelength level in UV visible spectrophotometry measurements. The results of the ANOVA analysis show that the response of the quadratic model is a reliable model for explaining the significance of the positive effect between the wavelength determination and the optimum absorbance ratio results. This synthesis is backed by a significant F test result of 2154.24 and validated by the regression coefficient R^2 0.9970. The adjusted R^2 value of 0.9965 agrees well with the R^2 value. The optimum wavelength is determined based on the maximum absorbance value with the highest high desirability approaching the value 1. As a result, OFAT analysis suggests that the optimum wavelength be determined in the UV visible spectrophotometry TiO₂-POE analysis in the range of 500 nm with an absorbance value of 0.901239 and desirability level 1.0. Future studies are needed to conduct analysis tests on other types of nanolubricants.

Acknowledgements Ningxia University in China provided funding for this research through the Helan Mountain Scholarship program. The authors would like to express their gratitude to UMP

for providing money through the specialized internal fund RDU190336 and the FRGS award RDU 1901112.

Conflicts of Interest The authors declare no conflict of interest.

References

1. Graves JE, Latvytė E, Greenwood A, Emekwuru NG (2019) Ultrasonic preparation, stability and thermal conductivity of a capped copper-methanol nanofluid. *Ultrason Sonochem* 55:25–31
2. Kumar RS, Sharma TJC (2018) Stability and rheological properties of nanofluids stabilized by SiO₂ nanoparticles and SiO₂-TiO₂ nanocomposites for oilfield applications. *Colloids and Surfaces A: Physicochem Eng Aspects* 539:171–183
3. Sarsam WS, Amiri A, Shanbedi M, Kazi SN, Badarudin A, Yarmand H, Bashirnezhad K, Zaharinie T (2017) Synthesis, stability, and thermophysical properties of aqueous colloidal dispersions of multi-walled carbon nanotubes treated with beta-alanine. *Int Commun Heat Mass Transfer* 89:7–17
4. Asadi A, Asadi M, Siahmargoi M, Asadi T, Andarati MG (2017) The effect of surfactant and sonication time on the stability and thermal conductivity of water-based nanofluid containing Mg (OH) 2 nanoparticles: An experimental investigation. *Int J Heat Mass Transf* 108:191–198
5. Mukherjee S, Chakrabarty S, Mishra PC, Chaudhuri P (2020) Transient heat transfer characteristics and process intensification with Al₂O₃-water and TiO₂-water nanofluids: An experimental investigation. *Chemical Eng Processing Process Intensification* 150:107887
6. Munkhbayar B, Bat-Erdene M, Sarangerel D, Ochirkhuyag B (2013) Effect of the collision medium size on thermal performance of silver nanoparticles based aqueous nanofluids. *Compos B Eng* 54:383–390
7. Gao T, Li C, Zhang Y, Yang M, Jia D, Jin T, Hou Y, Li R (2019) Dispersing mechanism and tribological performance of vegetable oil-based CNT nanofluids with different surfactants. *Tribol Int* 131:51–63
8. Rajendhran N, Palanisamy S, Shyma AP, Venkatachalam R (2018) Enhancing the thermophysical and tribological performance of gear oil using Ni-promoted ultrathin MoS₂ nanocomposites. *Tribol Int* 124:156–168
9. Liu X, Xu N, Li W, Zhang M, Chen L, Lou W, Wang X (2017) Exploring the effect of nanoparticle size on the tribological properties of SiO₂/polyalkylene glycol nanofluid under different lubrication conditions. *Tribol Int* 109:467–472
10. Kalmár J, Lente G, Fábíán I (2016) Kinetics and mechanism of the adsorption of methylene blue from aqueous solution on the surface of a quartz cuvette by on-line UV–Vis spectrophotometry. *Dyes Pigment* 127:170–178
11. Sharif MZ, Azmi WH, Redhwan AAM, Mamat R, Najafi G (2019) Energy saving in automotive air conditioning system performance using SiO₂/PAG nanolubricants. *J Therm Anal Calorim* 135:1285–1297
12. Zawawi NNM, Azmi WH, Sharif MZ, Najafi G (2018) Experimental investigation on stability and thermo-physical properties of Al₂O₃-SiO₂/PAG nanolubricants with different nanoparticle ratios. *J Therm Anal Calorim* 135:1243–1255
13. Rahman N, Sameen S, Kashif M (2019) Application of Box-Behnken design and desirability function in the optimization of spectrophotometric method for the quantification of WADA banned drug: acetazolamide. *J Mol Liq* 274:270–277
14. Jatinder G, Ohunakin OS, Adelekan DS, Atiba OE, Daniel AB, Singh J, Atayero AA (2019) Performance of a domestic refrigerator using selected hydrocarbon working fluids and TiO₂-MO nanolubricant. *Appl Therm Eng* 160

15. Redhwan AAM, Azmi WH, Sharif MZ, Mamat R, Samykano M, Najafi G (2018) Performance improvement in mobile air conditioning system using Al₂O₃/PAG nanolubricant. *J Therm Anal Calorim* 135:1299–1310
16. Modarres-Gheisari SMM, Gavagsaz-Ghoachani R, Malaki M, Safarpour P, Zandi M (2019) Ultrasonic nano-emulsification—a review. *Ultrason Sonochem* 52:88–105
17. Redhwan A, Azmi W, Sharif M, Mamat R, Zawawi NJATE (2017) Comparative study of thermo-physical properties of SiO₂ and Al₂O₃ nanoparticles dispersed in PAG lubricant 116:823–832
18. Saha SP, Mazumdar D (2019) Optimization of process parameter for alpha-amylase produced by *Bacillus cereus* amy3 using one factor at a time (OFAT) and central composite rotatable (CCRD) design based response surface methodology (RSM). *Biocatal Agr Biotechnol* 19
19. Mazaheri H, Ghaedi M, Asfaram A, Hajati S (2016) Performance of CuS nanoparticle loaded on activated carbon in the adsorption of methylene blue and bromophenol blue dyes in binary aqueous solutions: using ultrasound power and optimization by central composite design. *J Mol Liq* 219:667–676
20. Yahaya YA, Don MM (2014) Flavonoid production by *T. lactinea*: screening of culture conditions via OFAT and optimization using response surface methodology (RSM). *J Korean Soc Appl Biol Chem* 57:749–757
21. Zawawi NNM, Azmi WH, Redhwan AAM, Sharif MZ, Sharma KV (2017) Thermo-physical properties of Al₂O₃-SiO₂/PAG composite nanolubricant for refrigeration system. *Int J Refrig* 80:1–10
22. Chananipoor A, Azizi Z, Raei B, Tahmasebi N (2020) Optimization of the thermal performance of nano-encapsulated phase change material slurry in double pipe heat exchanger: design of experiments using response surface methodology (RSM). *J Build Eng* 34
23. Bayuo J, Abukari MA, Pelig-Ba KB (2020) Optimization using central composite design (CCD) of response surface methodology (RSM) for biosorption of hexavalent chromium from aqueous media. *Appl Water Sci* 10
24. Mahapatra APK, Saraswat R, Botre M, Paul B, Prasad N (2020) Application of response surface methodology (RSM) in statistical optimization and pharmaceutical characterization of a patient compliance effervescent tablet formulation of an antiepileptic drug levetiracetam. *Future J Pharm Sci* 6
25. Fazel I, Sarmasti Emami MR, Rashidi A (2021) Investigation and optimization of the behavior of heat transfer and flow of MWCNT-CuO hybrid nanofluid in a brazed plate heat exchanger using response surface methodology. *Int Commun Heat Mass Transfer* 122:105175–105175
26. Roshdi S, Kasiri N (2021) Coupling VOF interfacial mass transfer model with RSM approach in LLE systems: developing the new correlations for mass transfer, aspect ratio and terminal velocity. *Int Commun Heat Mass Transfer* 123:105216–105216
27. Dehghani MH, Karri RR, Yeganeh ZT, Mahvi AH, Nourmoradi H, Salari M, Zarei A, Sillanpää M (2020) Statistical modelling of endocrine disrupting compounds adsorption onto activated carbon prepared from wood using CCD-RSM and DE hybrid evolutionary optimization framework: comparison of linear vs non-linear isotherm and kinetic parameters. *J Mol Liq* 302:112526–112526
28. Ali Rothan Y, Ali FF, Issakhov A, Selim MM, Li Z (2021) Optimization analysis of hydrogen production using ammonia decomposition. *J Mol Liquids* 335
29. Altun A, Şara ON, Şimşek B (2021) A comprehensive statistical approach for determining the effect of two non-ionic surfactants on thermal conductivity and density of Al₂O₃-water-based nanofluids. *Colloids Surf A* 626:127099
30. Hemmat Esfe M, Goodarzi M, Reiszadeh M, Afrand M (2019) Evaluation of MWCNTs-ZnO/SW50 nanolubricant by design of an artificial neural network for predicting viscosity and its optimization. *J Mol Liq* 277:921–931
31. Mohammed A, Alshibani A, Alshamrani O, Hassanain M (2021) A regression-based model for estimating the energy consumption of school facilities in Saudi Arabia. *Energy Build* 237:110809–110809

32. Ahmed SA, Abdella MAA, El-Sherbiny GM, Ibrahim AM, El-Shamy AR, Atalla SMM (2019) Application of one-factor-at-a-time and statistical designs to enhance α -amylase production by a newly isolate *Bacillus subtilis* strain-MK1. *Biocatal Agr Biotechnol* 22
33. Keshvardoostchokami M, Majidi M, Zamani A, Liu B (2021) Adsorption of phenol on environmentally friendly Fe_3O_4 /chitosan/zeolitic imidazolate framework-8 nanocomposite: optimization by experimental design methodology. *J Mol Liq* 323:115064–115064
34. Mohd Sharif NSA, Thor ES, Zainol N, Jamaluddin MF (2017) Optimization of ferulic acid production from banana stem waste using central composite design. *Environ Progress Sustain Energy* 36:1217–1223

Multiscale Modelling of 3-Dimensional Brain Tissue Using Ideal Capillary Model



Abbas Shabudin, Mohd Jamil Mohamed Mokhtarudin, Stephen Payne, Wan Naimah Wan Ab Naim, and Nik Abdullah Nik Mohamed

Abstract This project aims to investigate the effects of capillary size and shape toward the brain tissue poroelastic properties model using asymptotic expansion homogenization (AEH). Applying AEH to the existing poroelastic governing equations (GE) results in a new GE consists of 6 macroscale equations and 4 microscale cell problems. The cell problems are solved on a microstructure geometry of brain tissue with capillary embedded to obtain effective parametric tensors, namely the capillary and interstitial hydraulic conductivity (\mathbf{K} and \mathbf{G}), capillary and interstitial homogenous Biot's coefficient (α_c and α_t), Young's modulus (E) and Poisson's ratio (ν). By varying the tortuosity, the percentage difference of \mathbf{K} is 97.98%, shows that it is highly affected by tortuosity. The percentage difference of \mathbf{G} is 0.25% implying that tortuosity insignificantly affecting \mathbf{G} . Meanwhile, α_c and α_t decreases and increases with tortuosity, respectively. The percentage difference of E and ν are 0.14% and 0.03% respectively, implying that both parameters does not affected by tortuosity. Besides, \mathbf{K} is exponentially increases with the increase of radius. On the other hand, \mathbf{G} decreases as the radius increases. Meanwhile α_c and α_t increases and decreases, respectively as radius increases. The percentage differences of E and ν are 18.26% and 14.55% respectively, suggesting that they are significantly affected by the radius. In conclusion, capillary shape and size have significant impact on the simulation of human brain. Thus, both characteristics should be precisely emphasized in the development of the geometry so that accurate parameters can be obtained to solve macroscale equations in future.

Keywords Ischaemic stroke · Asymptotic expansion homogenization · Macroscale equations · Microscale cell problems · Ideal capillary model

A. Shabudin (✉) · M. J. M. Mokhtarudin
College of Engineering, Universiti Malaysia Pahang, Gambang, Malaysia
e-mail: abbasshabudin@gmail.com

S. Payne
Institute of Applied Mechanics, National Taiwan University, Taipei, Taiwan

W. N. W. A. Naim · N. A. N. Mohamed
Faculty of Mechanical and Automotive Engineering Technology, Universiti Malaysia Pahang, Pekan, Pahang, Malaysia

1 Introduction

Stroke is described as a damage to the brain tissues due to the abnormalities in the blood supply to the brain, which gradually leads to brain tissue damage and death [1]. It is ranked as one of top five leading causes of death and also a major cause of permanent disability in the world [2]. Based on the report by World Stroke Organization, one in six people will have stroke in their lifetime, and more than 13.7 million suffer stroke every year resulting in 5.8 million people die [3]. In Malaysia, stroke is the third leading cause of mortality, which comprised about 9.8% of total death [4], causes a significant economic burden to the country [5]. The Global Burden of Disease Report (2016) projects stroke to be the second leading cause of mortality by 2040 [6].

With the latest advancement in medical technology, various treatments have been proposed to treat stroke. However, there are issues regarding the effectiveness of applying these treatments to patients. For example, apart from the thrombolytic recombinant tissue plasminogen activator (rtPA), there is no effective drugs that can be given to patients soon after stroke onset to minimize the subsequent neurological problems [7]. About 50 drugs have reached clinical trials but failed due to their toxicity and lack of demonstrable efficacy. In fact, even rtPA can only be used to treat selected patients and not without risk. These problems are mainly due to lack of understanding of the formation and recovery process of ischaemic stroke during treatment [8].

In order to understand the mechanism of ischaemic stroke formation, several animal studies have been performed [9]. Rodent stroke models have been widely used in ischaemic stroke research due to their advantages, including low cost, logistical ease, and simple ethical standards [10]. However, stroke models using small animals have significant differences from humans in term of physiological and pathophysiological characteristic [11]. Alternatively, large animals were proposed to be used since they are analogous to humans in genetic background, behavioral characteristics, concurrent complications, risk factors for cerebrovascular diseases and anatomical structure of brain tissues and blood vessels [12]. However, large animal models also have many disadvantages such as high maintenance costs, with lacking of physiological information, involving complicated ethical issues, and stroke models are also relatively more difficult to prepare [13]. Therefore, mathematical models are usually developed as an alternative solution to test hypotheses related to a particular biological processes in ischaemic stroke.

There are many mathematical models that have been developed to simulate different parts of the brain covering a wide range of length scales [14–18]. For example, Payne developed models of the whole brain [14], whereas Su et al. created artificial capillary networks that mimic statistical data obtained from human statistical data obtained from human cerebral tissue sample [15]. On the other hand, Cloutier et al. [16] and Orłowski et al. [17] focus on modelling the biochemistry of cell metabolism. Meanwhile, Mokhtarudin et al. has developed a brain model to study the formation of brain oedema after ischaemic stroke reperfusion treatment

[18]. In their model, the brain is assumed as a homogenized structure where the blood pressure is constant throughout the brain, while the shape and size of brain capillaries are assumed to be similar all over the brain. However, in actual brain, there are complex network distribution of brain capillaries with positive skewness distribution [19].

Histogram of the experimental data has been converted into a discrete form of capillary distribution by Su et al. in order to do a direct comparison with simulation models, which reported that the vessel length histogram reflects a left-shifted distribution [15]. Since the brain capillaries have a skewed distribution instead of homogeneous as assumed in the existing model, hence the assumptions in Mokhtarudin et al. should be reconsidered to allow for a complete modelling of ischaemic stroke effect.

However, human brain consists of large number of microvessels or capillaries (about tens of billions), which makes any modeling approach with an explicit architectural representation to the scale of capillaries difficult [20]. The main limitation is that the computational cost of the simulations grows quickly with the number of microvessels. According to Linninger et al., the most advanced computations available nowadays have reached a volume of about 30 mm³ or equivalent to 25,000 vessels, which is far lower than what would be required for a complete brain simulation [21]. With normal simulation computer, simulation of the complex brain capillary networks will be considerably costly and time consuming, unless some modifications are performed to simplify the model. In order to overcome this limitation, a modification on the existing model is introduced to include complex brain capillary networks using multiscale modelling technique. One example of multiscale modelling technique is asymptotic expansion homogenization (AEH). AEH is a technique used to separate a complex governing model into two different scales; the homogenized brain and capillary distribution, which are governed by macroscale equations and microscale cell problems respectively. Microscale cell problems need to be solved first in order to obtain certain characteristic parameters that will be used in solving the macroscale governing model.

Thus, this projects aims to investigate the effects of capillary size and shape toward the brain tissue poroelastic model using AEH technique in describing the brain mechanical and fluid transport properties. Two sets of simulations will be performed using this idealized geometry, (1) varying the tortuosity or twistedness shape of the capillary, (2) varying the radius or size of the capillary.

2 Mathematical Model

This section will describe in brief the homogenized governing equations and the respective cell problems used for the investigation of the effect of the capillary morphology in the brain tissue.

2.1 Governing Equation and Asymptotic Expansion Homogenization

Consider a volume $\Omega \subset \mathbb{R}^3$ such that $\Omega = \Omega_t \cup \Omega_c$, where Ω_t and Ω_c represent the poroelastic tissue and fluid compartment in the capillary respectively. The interface between the two compartments can be defined as $\Gamma = \partial\Omega_t \cap \partial\Omega_c$. Figure 1a shows an example of capillary distribution within a brain tissue, captured using micro-angiogram, while Fig. 1b shows a 2D illustration of brain tissue that consists of poroelastic tissue interstitial and capillary. The brain tissue is governed by poroelastic equations, which consists of stress balance, the Darcy’s Law, and mass conservation equations. Meanwhile, the blood flow in the capillary is governed by the Navier-Stokes equations.

To allow for the application of the AEH method, the scale separation between the intercapillary distance and the tissue length must be large. Assumed that the typical pore scale, r is much smaller than the distance between two adjacent microvessels, d , while d is in turn much smaller than the average size of the domain L . Thus, $r \ll d \ll L$. This can be illustrated in Fig. 2. A small parameter ϵ satisfying:

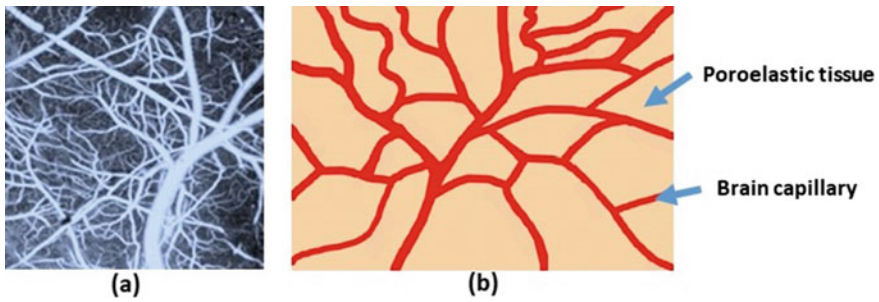


Fig. 1 a Capillary distribution within brain tissue, captured using micro-angiogram, b 2D illustration of brain capillary distribution

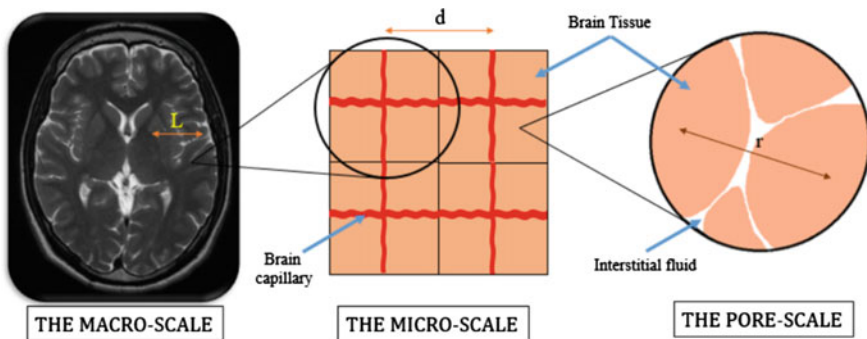


Fig. 2 Multiple scale of brain tissue; the macroscale, the microscale and the pore scale

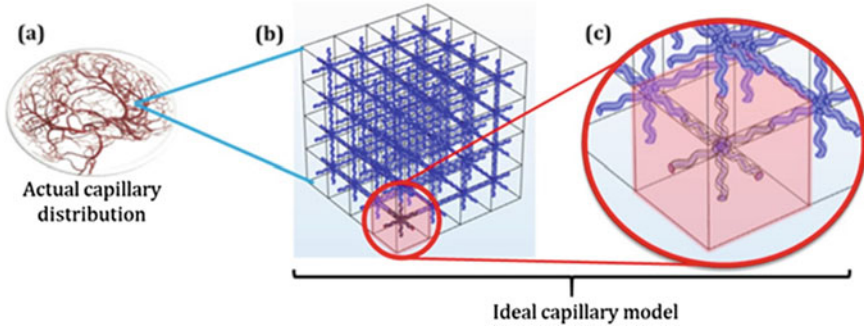


Fig. 3 Representation of actual capillary distribution with an ideal capillary model

$$\epsilon = \frac{d}{L} \ll 1 \tag{1}$$

Which means that the sharp scale separation between L and d (or macroscale and microscale) enables the application of the AEH technique. Further, two independent spatial variables y and x are defined, such that:

$$x = \epsilon y \tag{2}$$

each corresponds for the macroscale and microscale space coordinates.

Applying AEH results in 6 new governing equations, which consists of 6 homogenized macroscale equations, in which the parameters can be determined by solving 4 microscale cell problems on a periodic microstructure. Figure 3 shows the representation of the brain and capillary to an idealized periodic microstructure of brain tissue.

Instead of solving the blood flow and brain mechanics on the whole brain, which could be time consuming and costly, the AEH technique enables the simulation to be done by part; (1) firstly, the microscale cell problems will be solved on one repeating unit of the ideal brain tissue with capillary embedded microstructure geometry; and then, (2) the results obtained will be used to calculate the parametric tensors, which will be used to solve the homogenized macroscale equations on a whole brain geometry. By applying this technique, we can significantly reduce the computational cost and time of the simulation. The subsequent sections will describe the macroscale and microscale equations obtained from the AEH technique.

2.2 Homogenized Macroscale Governing Equations

Homogenizing the poroelastic and Navier-Stokes coupled equations results in a set of homogenized macroscale equations analogous to the double Darcy poroelastic equations. More specifically, referring to the equations (153)–(157) in [22]. In general, these equations are made of a stress balance equation and two Darcy's equations, one for each fluid compartment. Nevertheless, the study here will present several assumptions to simplify the homogenized governing equations proposed by [22], which specifically used to solve brain tissue swelling problem. Firstly, the brain tissue swelling can be assumed as a quasi-steady process because its development is of the order of hours and days. Secondly, the brain tissue, blood and interstitial fluid are assumed to be incompressible, thus the Biot's coefficients are assumed to equal 1.

Applying the aforementioned assumptions, the stress balance equation is given as:

$$\nabla_x \cdot \sigma_H = 0 \quad (3)$$

where σ_H is the effective stress given by:

$$\sigma_H = \bar{C} : \nabla_x \mathbf{u} - \alpha_c P_c - \alpha_t P_t \quad (4)$$

Here \mathbf{u} , P_c , and P_t represent the tissue displacement, capillary fluid pressure, and interstitial fluid pressure field respectively. The effective stress σ_H is the sum of the tissue stress and stress contributions from the fluid pressures in the capillary and interstitial fluid. The terms \bar{C} , α_c , and α_t represent the effective elasticity tensor and the effective Biot's coefficient tensors for capillary and interstitial fluid respectively. These tensors are further defined as:

$$\bar{C} = \langle (C\mathbf{L}C + C) \rangle_t \quad (5)$$

$$\alpha_c = (\phi_c \mathbf{I} - \langle C : \mathbf{Q} \rangle_t) \quad (6)$$

$$\alpha_t = (\langle C : \mathbf{Q} \rangle_t + \phi_t \mathbf{I}) \quad (7)$$

where \mathbf{I} is the identity tensor, while ϕ_c and ϕ_t are the volume fractions for the capillary and interstitial compartments respectively. Further, the tensors \mathbf{L} and \mathbf{Q} are to be calculated from the microscale cell problems.

The fluid pressure distributions are defined using mass balance equations as:

$$\frac{1}{M_c} \dot{P}_c = -\nabla_x \cdot \langle \mathbf{w}_c \rangle_c - \alpha_c : \nabla_x \dot{\mathbf{u}} + \frac{1}{M_c} \dot{P}_t + \frac{|\Gamma|}{|\Omega|} \bar{L}_p \Phi \quad (8)$$

$$\frac{1}{M_t} \dot{P}_t = -\nabla_x \cdot \langle \mathbf{w}_t \rangle_t - \alpha_t : \nabla_x \dot{\mathbf{u}} + \frac{1}{M_c} \dot{P}_c - \frac{|\Gamma|}{|\Omega|} \bar{L}_p \Phi \quad (9)$$

where $\frac{1}{M_c}$ and $\frac{1}{M_t}$ are the effective capillary and interstitial fluid relative compressibility respectively. Meanwhile, $|\Gamma|$, $|\Omega|$, and \bar{L}_p are the total area of the interface Γ , the volume of the microstructural geometry, and the hydraulic conductivity through capillary walls. Lastly, the term Φ represents the fluid transfer between the two fluid compartments depending on the pressure difference, given by:

$$\Phi = P_c - P_t \quad (10)$$

The average relative velocities $\langle \mathbf{w}_c \rangle_c$ and $\langle \mathbf{w}_t \rangle_t$ over respective fluid compartments are related with their respective pressure fields through Darcy's law:

$$\langle \mathbf{w}_c \rangle_c = -\mathbf{K} \nabla_x P_c \quad (11)$$

$$\langle \mathbf{w}_t \rangle_t = -\bar{k} \mathbf{G} \nabla_x P_t \quad (12)$$

Here the terms \mathbf{K} and $\bar{k} \mathbf{G}$ are the effective hydraulic conductivity for the capillary and interstitial, respectively with \bar{k} is the brain interstitial hydraulic conductivity. The tensors \mathbf{K} and \mathbf{G} are also to be determined by solving the microscale cell problems.

2.3 Microscale Cell Problems

The tensors presents in the homogenized macroscale equations described above must be calculated beforehand using the microscale cell equations solved on a brain tissue microstructure. The microscale cell problems are described in the following sections.

Laplace Cell Problem. The interstitial fluid conductivity tensor \mathbf{G} can be calculated by averaging the following over the interstitial space volume:

$$\mathbf{G} = \phi_t \mathbf{I} - \left\langle (\nabla_y P_t)^T \right\rangle_t \quad (13)$$

where the auxiliary interstitial fluid pressure P_t can be determined by solving the following Laplace's cell equations on the microstructural geometry:

$$\nabla_y^2 P_t = 0 \text{ in } \Omega_t \quad (14)$$

$$(\nabla_y P_t) n = n \text{ on } \Gamma \quad (15)$$

$$\langle P_t \rangle_t = 0 \text{ in } \Omega_t \quad (16)$$

This is supplemented by periodicity conditions.

Stoke's Cell Problem. The effective blood conductivity tensor \mathbf{K} can be calculated by averaging the auxiliary velocity \mathbf{W} over the capillary volume:

$$\mathbf{K} = \langle \mathbf{W} \rangle_c \quad (17)$$

where the auxiliary velocity \mathbf{W} and capillary pressure P_c must be first calculated by solving the following Stokes' cell equations on the microstructural geometry:

$$\nabla_y^2 \mathbf{W}^T - \nabla_y P_c + \mathbf{I} = 0 \text{ in } \Omega_c \quad (18)$$

$$\nabla_y \cdot \mathbf{W}^T = 0 \text{ in } \Omega_c \quad (19)$$

$$\mathbf{W}^T = 0 \text{ on } \Gamma \quad (20)$$

$$\langle P_c \rangle_c = 0 \text{ in } \Omega_c \quad (21)$$

This equation is supplemented by periodicity conditions on the microstructural geometry and \mathbf{I} represents the identity tensor.

One-elastic Cell Problem. Tensor \mathbf{Q} can be calculated using formula as following:

$$\mathbf{Q} = \langle \nabla_y \mathbf{a} \rangle \quad (22)$$

where auxiliary vector, \mathbf{a} can be calculated by solving the one-elastic cell equations on microstructural geometry:

$$\nabla_y \cdot (C \nabla_y \mathbf{a}) = 0 \text{ in } \Omega_t \quad (23)$$

$$(C \nabla_y \mathbf{a})n = -n \text{ on } \Gamma \quad (24)$$

$$\langle \mathbf{a} \rangle_t = 0 \quad (25)$$

where n is normal vector to Γ , and $C = C(E, \nu)$ is the elasticity moduli, which can be represented by Young's modulus and Poisson's ratio, of the porous solid compartment.

Six-elastic Cell Problem. Tensor \mathbf{L} is a fourth rank tensor, defined as:

$$\mathbf{L} = \langle \nabla_{\mathbf{y}} A \rangle \tag{26}$$

where third rank tensor, A can be calculated by solving the six-elastic cell equations, in component form, are described as:

$$\frac{\partial}{\partial y_j} \cdot \left(\mathbb{C} \frac{\partial A_{kmn}}{\partial y_l} \right) = 0 \text{ in } \Omega_t \tag{27}$$

$$\mathbb{C} \frac{\partial A_{kmn}}{\partial y_l} n_j = -\delta_{im} \delta_{jn} n_j \text{ on } \Gamma \tag{28}$$

$$\langle A \rangle_t = 0 \tag{29}$$

2.4 Varying Capillary Tortuosity and Radius

In order to investigate the effect of capillary tortuosity towards parameter \mathbf{G} , \mathbf{K} , \mathbf{Q} and \mathbf{L} , the simulation is repeated by making the capillary more twisted or more bending. Figure 4 shows 4 samples of tortuosity variation used, where the twisted shape of the capillary is governed by the function, $f(s) = A \sin(2\pi\omega s/l)$. ω and A represents the frequency and amplitude of twisted shape respectively. The straight capillary in Fig. 4a represents the lowest tortuosity, whereas Fig. 4d represents the highest tortuosity with ω and A equal 3 and 1 respectively. The high tortuosity capillary can be used later to represent the ischaemic stroke since the blood flow within the capillary is relatively slow compared to the normal or straight capillary.

Another set of simulation is done to investigate the effect capillary size or radius towards the parameter. Figure 5 shows 3 samples of radius variation used in the simulation, where (a) represents the smallest radius, 0.02 and (c) represents the biggest radius used, 0.8. For this part, the small capillary radius can be used later to represent the constriction of the capillary due to thrombus formation at the capillary

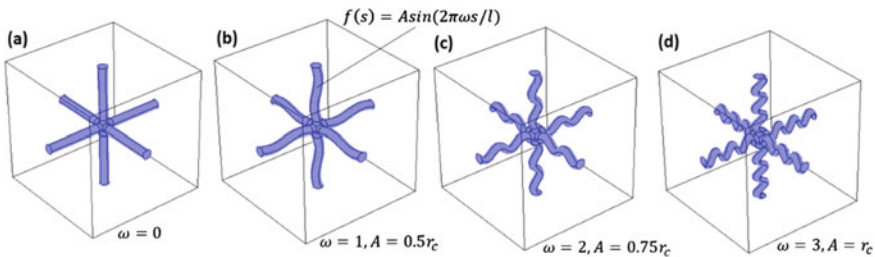


Fig. 4 A few examples of capillary tortuosity variation used for the simulation; **a** represents the lowest tortuosity and, **d** represents the highest tortuosity

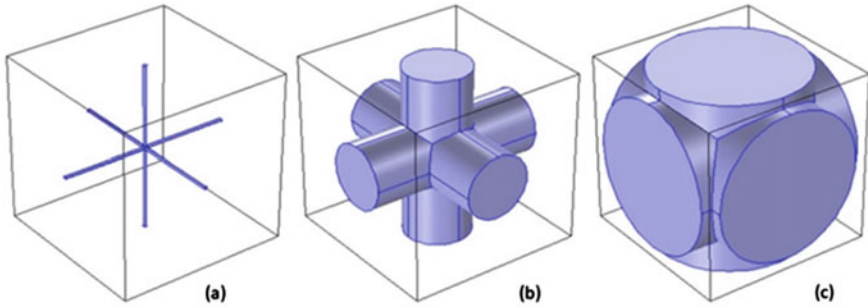


Fig. 5 Examples of capillary radius variation used for the simulation

wall. Besides, it can also be used to represent the secondary stroke formation due to capillary compression during vasogenic oedema.

3 Results and Discussion

Figures 6 and 7 show the example of the simulation results obtained when solving the four cell problems for the straight capillary case. The results then can be used to calculate the parameters **G**, **K**, **Q** and **L** using the Eqs. (13)–(29).

3.1 Capillary Hydraulic Conductivity, **K**

Hydraulic conductivity is a property that describes the ability of fluid moves through a porous media [23]. It can be seen in Fig. 8a that the value of **K** decreases as the tortuosity of the capillary increases.

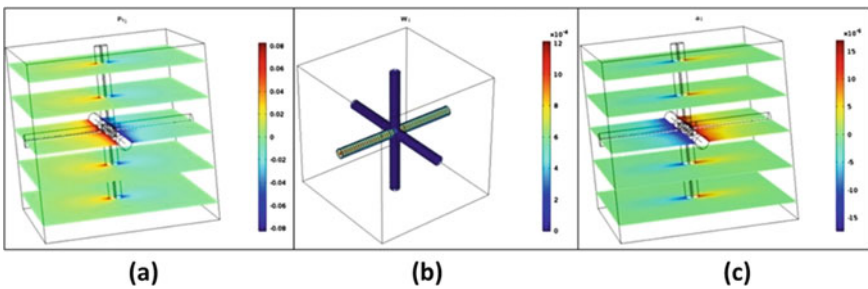


Fig. 6 Example of simulation results of the cell problems to obtain the parameters, **a G**, **b K** and, **c Q**

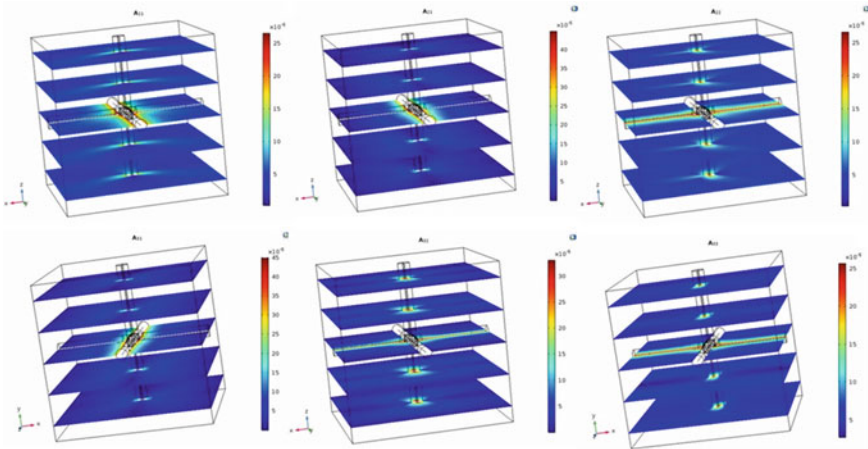


Fig. 7 Example of simulation results of the cell problems to obtain parameter L

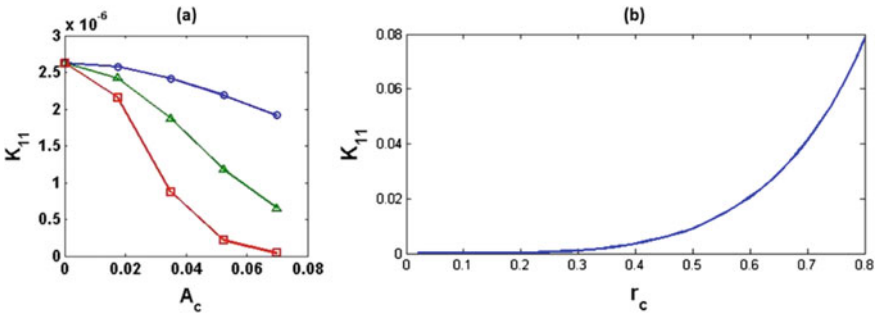


Fig. 8 Graph of parameter K against **a** capillary tortuosity and, **b** capillary size

It is reported that hydraulic conductivity is dependent on factors such as soil structure, particle size distribution, roughness, tortuosity, shape and degree of inter-connection of fluid conducting pores. In the study of hydraulic conductivity of soil, it is used as a measure of the ease with which water moves through soil, where the higher the hydraulic conductivity, the greater the flow rate [24]. From the simulation results obtained, it can be said that the high tortuosity shape has reduced the ease of fluid flow within the capillary, thus reducing the hydraulic conductivity of the capillary. The percentage difference between ω_1 and ω_3 is very large, which is about 97.98%. Therefore, it can be concluded that the hydraulic conductivity is highly affected by the tortuosity of the brain capillary.

The effect of capillary size (or radius) variation against K can be seen in Fig. 8b, where it is exponentially increased with the radius. An increase in radius or diameter means there is less blood contacting the vessel wall, thus lowering the friction and resistance subsequently, increases the flow. The influence of capillary lumen radius on

resistance is really significant because a slight change in radius causes a huge change in resistance. This is because resistance is inversely proportional to the radius of the blood capillary to the fourth power ($R \propto 1/r^4$).

3.2 Interstitial Hydraulic Conductivity, G

The interstitial hydraulic conductivity, G describes the ease of fluid moves through pore spaces or fractures and is highly dependent on the interstitial volume. Effects of capillary tortuosity towards G can be seen in Fig. 9a, where the value of G increase as the tortuosity increases.

As we can see in Table 1, as the capillary tortuosity increases, volume of the interstitial space is also increases. Therefore, the fluid flow within the interstitial space will also increases, resulting in higher conductivity as shown in Fig. 9a. However, the percentage difference of parameter G between ω_1 and ω_3 is only about 0.25%, implying that the tortuosity is insignificantly affecting G.

Meanwhile, G value decreases as the capillary radius increases as shown in Fig. 9b. Capillary with bigger radius has a bigger vascular volume with smaller interstitial space assuming the volume of the cube is constant.

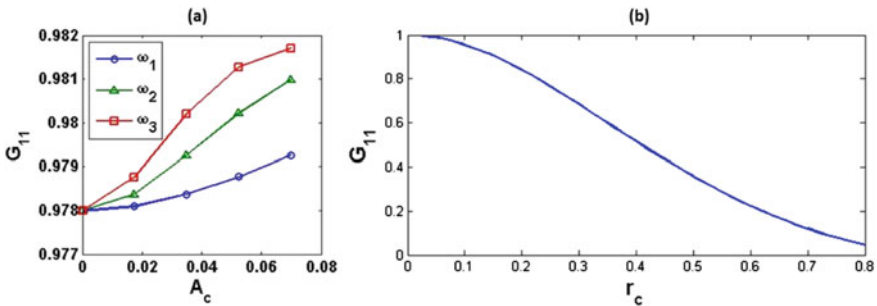


Fig. 9 Graph of parameter G against a capillary tortuosity and, b capillary size

Table 1 Interstitial and capillary volume variation for each capillary tortuosity setting

Amplitude, A	Frequency, ω	Interstitial volume	Capillary volume
0	0	6.148	0.082
0	1	6.148	0.082
0	2	6.148	0.082
0	3	6.148	0.082
0.018	0	6.148	0.082
0.018	1	6.149	0.081
0.018	2	6.150	0.080
0.018	3	6.151	0.079
0.035	0	6.148	0.082
0.035	1	6.150	0.080
0.035	2	6.153	0.077
0.035	3	6.157	0.073
0.053	0	6.148	0.082
0.053	1	6.151	0.079
0.053	2	6.157	0.073
0.053	3	6.162	0.068
0.070	0	6.148	0.082
0.070	1	6.153	0.077
0.070	2	6.160	0.070
0.07	3	6.165	0.065

3.3 Parameter Q

Parameter Q alone has no physical meaning. However, calculating the homogenous Biot's coefficient of interstitial and capillary, α_c and α_t require parameter Q . Biot's coefficient measures the ratio of the fluid volume squeezed out to the volume change of the poroelastic medium if the medium is compressed while allowing the water to escape [25]. Thus, it is dependent on the volume of the poroelastic medium and the capillary.

In Fig. 10a, as the capillary tortuosity increases, α_c decreases for all frequencies, ω_1 – ω_3 . This is because of the reduction of the capillary volume when capillary tortuosity increases as shown in Table 1. Meanwhile, Fig. 10b shows the value of α_t increases with capillary tortuosity. As previously explained, volume of poroelastic tissue and interstitial space increase with tortuosity, thus more volume of fluid can be squeezed out of the medium resulting in higher α_t .

For radius variation, the changes of α_c and α_t against capillary radius are shown in Fig. 11. As radius increases, α_c also increases which again related to capillary volume increment and more fluid can be squeezed out. Instead, α_t decreases as radius increases. Since the cubic volume of the capillary model is constant, the increment of

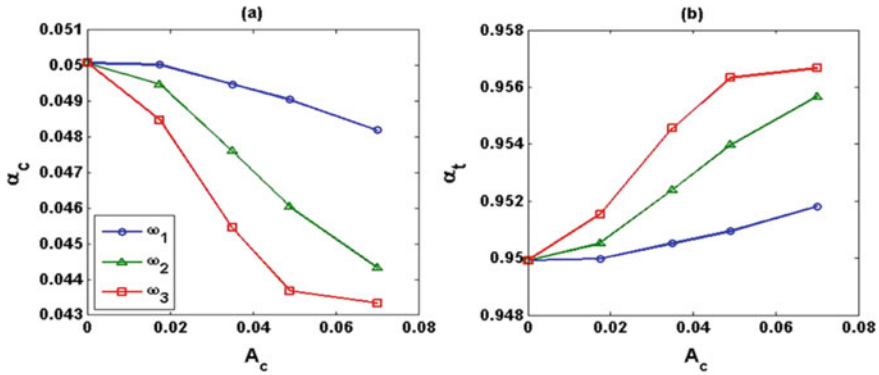


Fig. 10 Graph of a α_c and, b α_t against capillary tortuosity

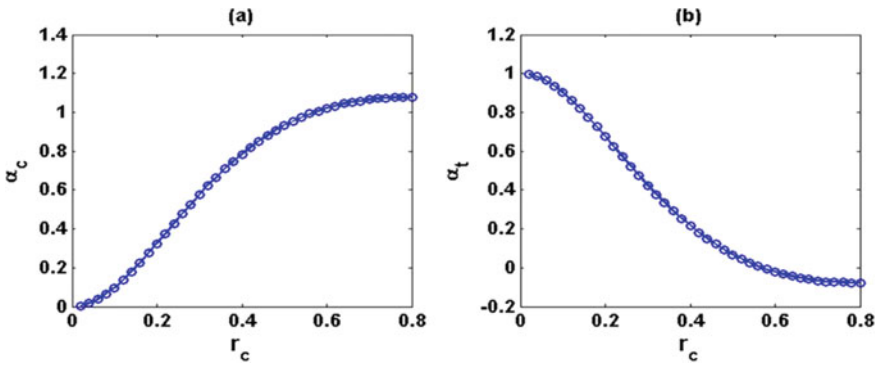


Fig. 11 Graph of a α_c and, b α_t against capillary radius

capillary volume results in the reduction of the interstitial space volume. As a result, less fluid can be squeezed out of the medium and thus, lower α_t .

3.4 Parameter L

Parameter **L** alone does not have a clear physical meaning. However, **L** can be used to calculate the homogenized Young’s modulus and Poisson’s ratio using Eqs. (4–7).

Figure 12 shows both E and ν variations with the capillary tortuosity. Here, the variations are 0.14% and 0.03% respectively. Since the percentage is small, the capillary tortuosity does not significantly affecting E and ν .

Different trends can be seen on E and ν when the capillary radius is varied as shown in Fig. 13. The value of E and ν decrease until radius about 0.4. After that, the E and ν values increase as radius increases. The percentage changes of E and ν are

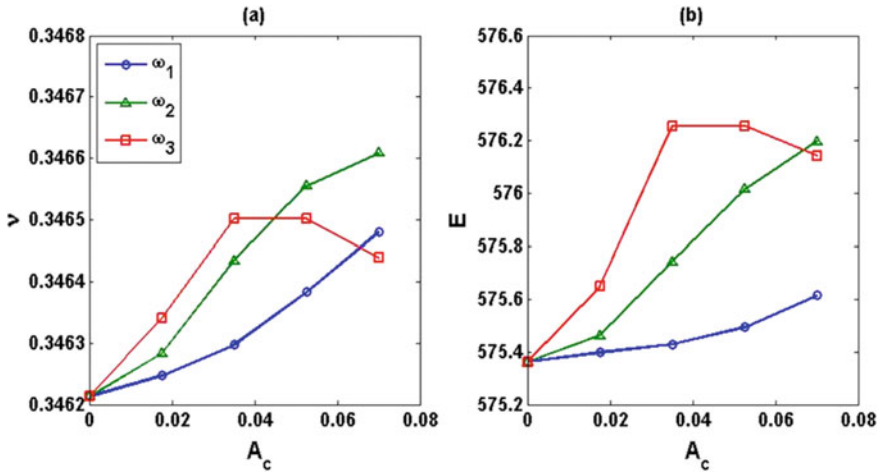


Fig. 12 Graph of **a** v and, **b** E against capillary tortuosity

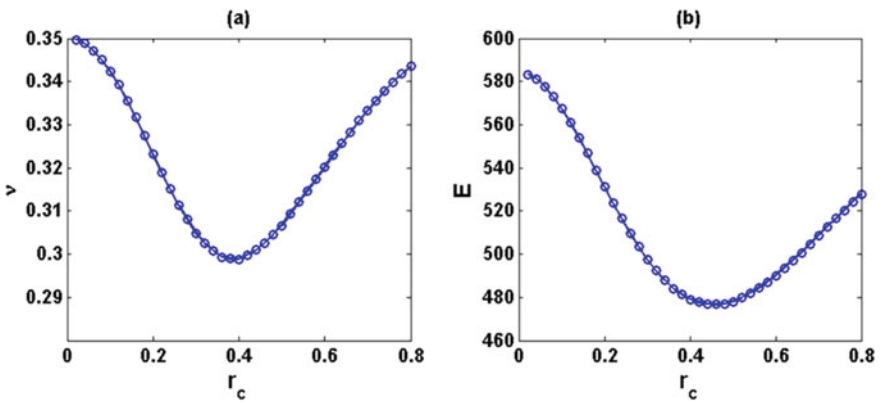


Fig. 13 Graph of **a** v and, **b** E against capillary radius

18.26% and 14.55% respectively. It can be concluded that E and v are significantly affected by radius variation.

4 Conclusions

By applying the AEH technique, the existing governing equations are changes into new governing equations consist of macroscale equations and microscale cell problems representing cerebral tissue and capillary. In this report, 4 microscale cell problems are solved in ideal capillary model to obtain the important parameters, namely

the capillary and interstitial hydraulic conductivity (\mathbf{K} and \mathbf{G}), capillary and interstitial homogenous Biot's coefficient (α_c and α_t), Young's modulus (E) and Poisson's ratio (ν). Tortuosity and radius variations are then applied to the ideal capillary model in order to investigate the effects of shape and sizes of the capillary towards the parameters. As a result, \mathbf{K} is significantly affected by both tortuosity and radius, \mathbf{G} , E and ν are only affected by the radius, while α_c and α_t are affected by both tortuosity and radius. In conclusion, capillary shape and size have significant impact on the simulation of human brain, especially for ischaemic stroke study. Both characteristics should be precisely emphasized in the development of the geometry so that accurate parameters can be obtained to solve macroscale equations in a bigger brain geometry.

Acknowledgements This research is supported by the Fundamental Research Grant Scheme from the Ministry of Higher Education of Malaysia (FRGS/1/2018/TK03/UMP/02/15) and the International Publication Grant from Universiti Malaysia Pahang (RDU203302).

References

1. Kanyal N (2015) The science of ischemic stroke: pathophysiology and pharmacological treatment. *Int J Pharma Res Rev* 4(10):65–84
2. Katan M, Luft A (2018) Global burden of stroke. *Semin Neurol*
3. Phipps MS, Cronin CA (2020) Management of acute ischemic stroke. *BMJ* 368
4. WHO World Health Ranking (2018) (Malaysia: Stroke). [Cited 2020 10 July]. Available from: <https://www.worldlifeexpectancy.com/malaysia-stroke>
5. Evaluation I.f.H.M.a. (2017) Statistics data. [Cited 2020 10 July]. Available from: <http://www.healthdata.org/malaysia>
6. Foreman KJ et al (2018) Forecasting life expectancy, years of life lost, and all-cause and cause-specific mortality for 250 causes of death: reference and alternative scenarios for 2016–40 for 195 countries and territories. *Lancet* 392(10159):2052–2090
7. Kim JS (2019) tPA helpers in the treatment of acute ischemic stroke: are they ready for clinical use? *J Stroke* 21(2):160
8. Byrne H (1999) Using mathematics to study solid tumour growth. In: *Proceedings of the 9th general meetings of European women in mathematics*. Hindawi Publishing, New York
9. McCabe C et al (2018) Animal models of ischaemic stroke and characterisation of the ischaemic penumbra. *Neuropharmacology* 134:169–177
10. Mhairi MI (1992) New models of focal cerebral ischaemia. *Br J Clin Pharmacol* 34(4):302–308
11. Howells DW et al (2010) Different strokes for different folks: the rich diversity of animal models of focal cerebral ischemia. *J Cereb Blood Flow Metab* 30(8):1412–1431
12. Cook DJ, Tymianski M (2011) Translating promising preclinical neuroprotective therapies to human stroke trials. *Expert Rev Cardiovasc Ther* 9(4):433–449
13. Cai B, Wang N (2016) Large animal stroke models vs. rodent stroke models, pros and cons, and combination? In: *Brain edema XVI*. Springer, pp 77–81
14. Payne S (2006) A model of the interaction between autoregulation and neural activation in the brain. *Math Biosci* 204(2):260–281
15. SU SW, Catherall M, Payne S (2012) The influence of network structure on the transport of blood in the human cerebral microvasculature. *Microcirculation* 19(2):175–187
16. Cloutier M et al (2009) An integrative dynamic model of brain energy metabolism using in vivo neurochemical measurements. *J Comput Neurosci* 27(3):391

17. Orlowski P et al (2011) Modelling of pH dynamics in brain cells after stroke. *Interface Focus* 1(3):408–416
18. Mokhtarudin MM, Payne S (2015) Mathematical model of the effect of ischemia–reperfusion on brain capillary collapse and tissue swelling. *Math Biosci* 263:111–120
19. Cassot F et al (2006) A novel three-dimensional computer-assisted method for a quantitative study of microvascular networks of the human cerebral cortex. *Microcirculation* 13(1):1–18
20. Peyrounette M et al (2018) Multiscale modelling of blood flow in cerebral microcirculation: details at capillary scale control accuracy at the level of the cortex. *PLoS ONE* 13(1):e0189474
21. Linninger A et al (2013) Cerebral microcirculation and oxygen tension in the human secondary cortex. *Ann Biomed Eng* 41(11):2264–2284
22. Penta R, Merodio J (2017) Homogenized modeling for vascularized poroelastic materials. *Meccanica* 52(14):3321–3343
23. Ray LA, Heys JJ (2019) Fluid flow and mass transport in brain tissue. *Fluids* 4(4):196
24. Papadopol C (2005) Determination of soil hydraulic conductivity in nurseries and plantations. *Tree planters' notes*
25. Biot MA (1941) General theory of three-dimensional consolidation. *J Appl Phys* 12(2):155–164

Tribological Performance Effect of SiO₂ and TiO₂ Nanoparticles as Lubricating Oil Additives



M. F. Ismail  and Wan Azmi Wan Hamzah 

Abstract Friction is one of major concern in mechanical movement while the lubricant is one of solution to counter it. The additive of nanoparticles in lubricant may improve its tribological performance. The current study focusses on the effect of SiO₂ and TiO₂ nanoparticles as additive in PVE lubricant. The new solution namely nanolubricant was prepared at three different concentrations. The nanolubricants were characterized using TEM and its stability was evaluated up to 30 days. Four-ball method was used to determine the effect of nanoparticle concentration on coefficient of friction (COF) and wear scar diameter (WSD). The results reveal that nanoparticle additive provide better COF at low volume concentration. The COF for nanolubricant at volume concentration less than 0.010% for TiO₂ and less than 0.005% for SiO₂ attained lower than pure PVE lubricant. The results for WSD also were in agreement with the trend of COF. Therefore, the nanolubricant has potential to provide better friction coefficient performance for lubrication application.

Keywords Nanolubricant · Tribology · Coefficient of friction · Wear scar diameter · Four-ball test

M. F. Ismail · W. A. Wan Hamzah (✉)
Department of Mechanical Engineering, College of Engineering, Universiti Malaysia Pahang,
Lebuhraya Tun Razak, 26300 Gambang, Kuantan, Pahang, Malaysia
e-mail: [wanazmi2010@gmail.com](mailto:wamazmi2010@gmail.com)

M. F. Ismail
e-mail: mfarid@utem.edu.my

W. A. Wan Hamzah
Centre of Excellence for Advanced Research in Fluid Flow, Lebuhraya Tun Razak, 26300
Gambang, Kuantan, Pahang, Malaysia

M. F. Ismail
Faculty of Mechanical and Manufacturing Engineering Technology, Universiti Teknikal Malaysia
Melaka, Hang Tuah Jaya, 75150 Durian Tunggal, Melaka, Malaysia

1 Introduction

Sustainable development is the new focus of the whole society in this modern era. Energy efficiency on machine and devices always be the main topic circulate among engineers and researcher to have better environment for the next generation. The improvement on machine components and mechanism pairs may lead to increase devices performance thus increase its energy efficiency. Therefore, lubrication was introduced in the mechanical motion to improve its tribological performance.

The goal of tribological study is to reduce friction and wear. The study to fine better lubricant for mechanism are always in focus in the recent study. The introduction of nanoparticle additive in lubricant oil opens a new chapter in research and development since decades ago [1]. Starting from the nanofluids, the idea already expands to nanolubricants, nanopaints and other application that taking advantage of nanosized material for better performance [2]. In tribological aspect, nanolubricants had shown positive impact on several application including engine, compressor, and heat transfer equipments [3–5].

The material used as nano-additive shows positive advancement from time to time. Each of this material has its own advantages in such application. For instance, ZnO nanoparticles was used as additive in mineral oils that intent to be used in domestic refrigeration systems. ZnO nanoparticles successfully reduce the friction coefficient that leads to a significant reduction in friction coefficient inside the compressor [5]. A refrigeration system with R-32 refrigerant also being applied with diamond nanoparticles that dispersed in polyol ester (POE) lubricant for compressor lubrication. The results show a reduction in friction up to 4% and wear reduces to 30% compared to lubricant without nanoparticles [6].

For a relatively new lubricant like polyvinyl ether (PVE), studies related to nanoparticles dispersion is limited in literatures. Even the PVE lubricant has the same compatibility with POE lubricant, its advantages in several property make it favorable lubricant for low global impact refrigerant. PVE lubricant does not hydrolyze thus hydrolysis is not required. It can greatly improve capillary tube blockage and eliminate the use of filter dryer. PVE lubricant also has flexible polymer properties thus the viscosity and miscibility can be optimally modified [7].

The physical properties of PVE lubricant with CuO nanoparticles had been conducted by Motozawa et al. [8]. However, the studies only focus on thermal conductivity, viscosity and dielectric properties. The tribological studies on PVE with nanoparticles additive had not been investigate yet. In this paper, the tribological property was investigated by using SiO₂ and TiO₂ nanoparticles as additive in PVE lubricant. The tribological property of nanolubricant will be compared with pure PVE lubricant to identify the changes in its tribology performance.

2 Methodology

2.1 Preparation of Nanolubricants

The base lubricant used in the current study is a type of poly vinyl ether (PVE). The PVE lubricant was commercially used as a compressor lubricant especially for refrigeration system. It has good compatibility with hydrofluorocarbon (HFC) refrigerant which has low global warming potential (GWP) level than other synthetic refrigerants. The physical properties of PVE lubricant for the current study is shown in Table 1. The SiO₂ and TiO₂ nanoparticles were procured from HWNANO (Hongwu International Group Ltd and DKNANO (Beijing Deke Daojin Science and Technology Co., Ltd.), respectively. Both nanoparticles have high level purity more than 99.9%. Table 2 summarized the material properties of the nanoparticles.

The preparation of nanolubricants was undertaken in a control laboratory with good ventilation system under room temperature. The personnel that conduct the preparation was equipped with proper personal protective equipment (PPE) for safety precautions. Nanolubricants were prepared with two-step method and widely being used by previous researchers [9–11]. Glass beakers were used to fill the pure lubricant that measured using measuring cylinder. A four-decimal accuracy weight balance was used to measure the quantity of nanoparticles required for each concentration presented in Eq. (1).

$$\phi = \frac{m_p / \rho_p}{m_p / \rho_p + m_L / \rho_L} \times 100\% \tag{1}$$

Table 1 Properties of PVE lubricant base

Property	PVE FVC68D
Dynamic Viscosity, mm ² /s @ 40 °C	68.1
Dynamic Viscosity, mm ² /s @ 100 °C	8.04
Pour Point, °C	−37.5
Flash point, °C	204
Density, kg/m ³ @ 15 °C	936.9

Table 2 Material properties of TiO₂ and SiO₂ nanoparticles

Property	Unit	TiO ₂	SiO ₂
Molecular mass	g/mol	79.87	60.08
Density	Kg/m ³	4230	2220
Average particle diameter	nm	50	30
Specific heat	J/kg·K	692	745

where ϕ is the volume concentration in percent, m_p and m_L are the masses of the nanoparticles and lubricant, respectively; and ρ_p and ρ_L are the density of the nanoparticles and density of lubricant, respectively. The nanolubricants were prepared in three different concentrations: 0.005, 0.010 and 0.030%. A magnetic stirrer was used to mix the nanoparticles with lubricant for 30 min. The stirring process breaks the solid particle agglomerations into smaller size using mechanical agitation method. After that, the homogenizing process took place using ultrasonic bath. The sonication process was done using FB15051 by Fisherbrand with 200 W power and 50 MHz frequency. After the homogenizing process completed, 15 ml samples were poured into test tube for visual stability inspection and the balance of nanolubricants were used in tribological test.

2.2 Tribological Test

The tribological performance of the nanolubricants were investigated using four-ball method. The test was conducted using Koehler Four-Ball Tribo Tester. The present nanolubricants are intentionally to be used as compressor lubricant in vapour compression refrigeration system. The four-ball method is the best to mocking the mechanical movement in rotary compressor. The test was carried out according to ASTM D4172 standard. The balls are used steel chromium type with G20 standard that conforms to ISO 3290. The Fig. 1 depicted the tribology machine of the current study. Three balls were kept in the sample handler and tighten. Lubricant sample is filled the space until all three balls are submerged. The fourth ball is located inside the machine that will touch the three bottom balls during the experiment. Load was added on the load handle until it reached up to 40 kg. A heater was used to maintain the sample temperature at 75 °C. The rotational motion of the top ball will generate the torque forces on sample handler. The data logger collects the output from the



Fig. 1 Four-ball tribo tester

motion and calculates the coefficient of friction (COF). Each test running up to 3600 s and the average of COF is considered in the analysis.

3 Results and Discussion

3.1 Nanolubricant Characterization and Stability

The nanolubricants was characterized using transmission electron microscopy (TEM). Figure 2 shows TEM images for TiO₂ and SiO₂ nanoparticles dispersed in PVE lubricant. The images were captured with high resolution of up to 100,000. The nanoparticles are observed in well dispersion with some portion of agglomeration. The size of nanoparticles for TiO₂ and SiO₂ are identified as 30 and 50 nm, respectively and within the range of manufacturer data.

The stability of nanolubricants were evaluated by visual inspection. Under steady condition, the photo of nanolubricants were captured on daily basis from the first day until 30 days of preparation. The results in Fig. 3 show that the nanolubricants has good stability up to 30 days after preparation. Some sedimentation appeared at

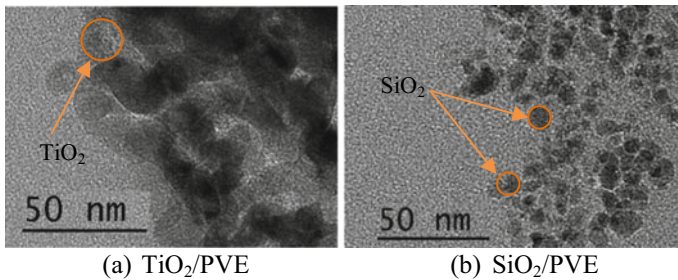


Fig. 2 TEM images of nanoparticles in PVE lubricants

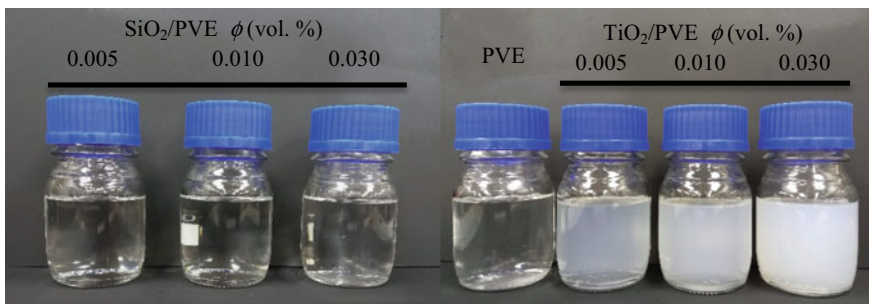


Fig. 3 Pure PVE lubricant and nanolubricants at different concentrations

the bottom of the test tube, but the sedimentation happened due to the gravitational effect only.

3.2 Tribological Performance of Nanolubricants

Effect of nanoparticles to coefficient of friction

The coefficient of friction (COF) is the common parameter to determine the frictional property of any lubricant. The COF can be interpreted as in Eq. (2) and influenced by the frictional torque T_f (kg·cm) and the load applied on the contact surfaces, W (kg).

$$CoF = 2.23004 \frac{T_f}{W} \tag{2}$$

The COF of nanolubricants are compared relatively with the COF of pure lubricant to identify the tribology performance improvement due to additive of nanoparticles in lubricant. Figure 4 shows the COF of all samples from 1000 to 3600 s. Low COF is always recommended for the application in refrigeration system. The COF for pure PVE lubricant was identified at 0.11. The nanolubricants at low volume concentration has lower COF than pure PVE lubricant however performed greater COF than PVE at high volume concentration. The nanolubricants at low volume concentration of less than 0.01% shows better COF than higher volume concentration.

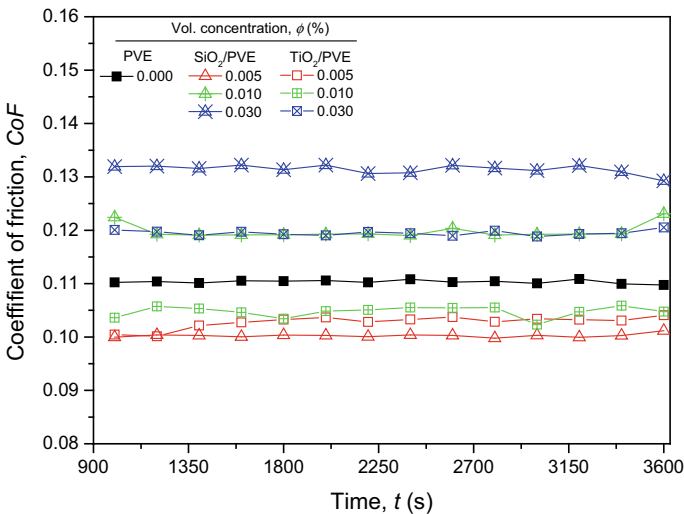


Fig. 4 Coefficient of friction for SiO₂/PVE and TiO₂/PVE nanolubricants in comparison with pure PVE lubricant

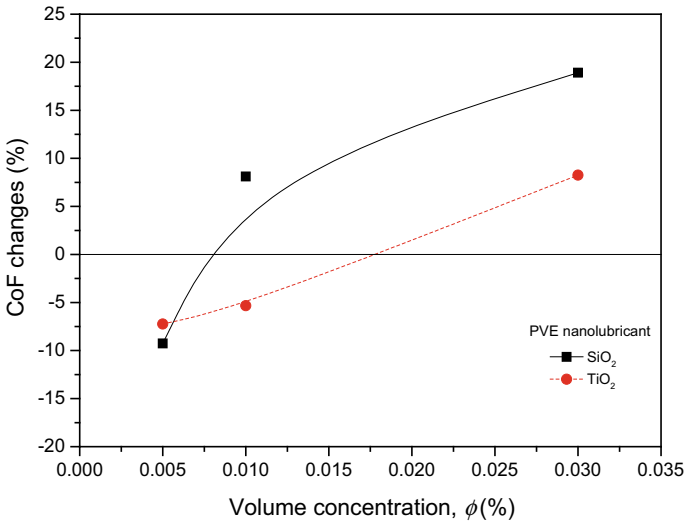


Fig. 5 The changes of CoF by the increment of volume concentrations

The CoF changes of nanolubricants is presented in Fig. 5. The figure shows the CoF changes relative to pure PVE lubricant in percentage. It is clearly shown that the CoF was increased with volume concentration. The negative sign of CoF represents the CoF of nanolubricant is lower than pure PVE and vice versa. For SiO₂/PVE nanolubricants, the CoF increased significantly from volume concentration of 0.005–0.01%. However, the increment slope slightly decreases when the concentration reaches 0.03%. The TiO₂/PVE nanolubricant shows a linear increment in CoF by the increment of concentration. Interestingly, the CoF for nanolubricants at volume concentration less than 0.01% is lower than pure PVE lubricant hence performed with better tribology properties.

Effect of nanoparticles to wear scar diameter

The rotational motion created by the top ball in tribological test may produces dent mark on the contact surface of the three bottom balls. Diameter size of the dent mark on spherical shape ball can be measured quantitatively. The wear scar diameter (WSD) can be used to determine the weight loss from the balls during the test. The weight loss during the experiment, W_{loss} can be determined using Eqs. (3)–(5).

$$W_{loss} = W_{int} - W_{final} \tag{3}$$

$$W_{final} = \frac{1}{3}\pi h^2(3R - h) \tag{4}$$

$$h = R - \sqrt{R^2 - r^2} \tag{5}$$

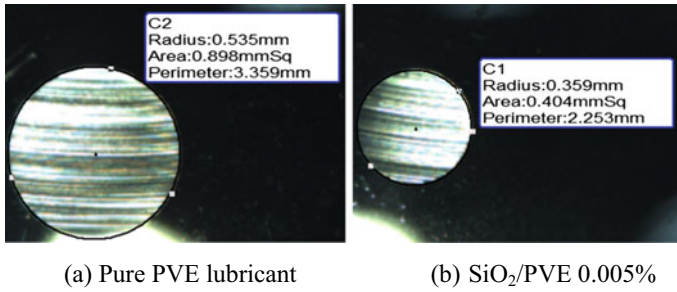


Fig. 6 Comparison of wear scar diameter of pure PVE lubricant and nanolubricant

where W_{int} (g) is the initial weight of ball before the experiment; W_{final} (g) is the final ball weight after the experiment; R is the radius of ball which is 6.35 mm and r is the radius of wear scar in mm. Figure 6 depicted the example of wear scar images. The diameter was measured using integrated software with microscope and attached to the tribology machine. The WSD for pure PVE lubricant is higher than the SiO_2/PVE nanolubricant at 0.005% concentration. The trend for WSD is in agreement with the COF variation. Higher COF will create bigger size of WSD.

The decrement and increment of COF nanolubricants and relatively to pure PVE is represented the effect of nanoparticles additive in the base PVE lubricant. The small volume concentration of nanoparticles in lubricant contributes to better frictional between the surfaces. However, more nanoparticles may provide reverse effect to the frictional property. It also creates bigger size of WSD on the surface of the ball. The SiO_2 and TiO_2 nanoparticles is small enough to provide rolling and mending effect on the surface and generated by frictional between balls. The even distribution of nanoparticles in the lubricant increases the lubricant ability to reduce friction. However, high number of nanoparticles may create abrasive effect on the contact surface. The nanoparticles itself creates resistance between each other and the surface in contact with it. Therefore, the friction force between balls increases and may lead to high COF and more wear scar.

4 Conclusions

The current study applied SiO_2 and TiO_2 nanoparticles as additive in PVE lubricant to investigate their effect on the tribological performance. The preparation of nanolubricant is considered the two-step method. The stability of nanolubricants is observed in excellent condition where the nanolubricants are well dispersed for up to 30 days. The tribological test revealed that the increment of nanoparticle concentration increased the COF. The COF of nanolubricants is lower than pure PVE lubricant at lower volume concentration. However, the COF was increased at high volume concentration. The trend for WSD is in agreement with the COF variation. Higher

COF will create bigger size of WSD. The TiO₂/PVE nanolubricant performed with better tribological performance up to 0.010% volume concentration while SiO₂/PVE nanolubricant attained improvement for COF at 0.005% volume concentration only. As a conclusion, the SiO₂ and TiO₂ nanolubricants provide enhancement in tribological performance especially at low volume concentration and recommended for application in refrigeration system.

Acknowledgements The authors are grateful to the Universiti Malaysia Pahang for financial supports given under RDU213302 and additional financial support under Postgraduate Research grant PGRS2003202. The authors also thank the research team from Centre for Research in Advanced Fluid and Processes (Pusat Bendalir) and Advanced Automotive Liquids Laboratory (AALL), who provided insight and expertise that greatly assisted in the present research work.

References

1. Wang H, Wang YM (2012) Tribological Performance of AlN nanoparticles as lubricating oil additive. *Adv Res Mater Eng Architectural Eng Informatization* 366:238–242
2. Azmi WH, Sharif MZ, Yusof TM, Mamat R, Redhwan AAM (2017) Potential of nanorefrigerant and nanolubricant on energy saving in refrigeration system—a review. *Renew Sustain Energy Rev* 69:415–428
3. Karthick M, Karuppiah SK, Kanthan V (2020) Performance investigation and exergy analysis of vapor compression refrigeration system operated using r600a refrigerant and nanoadditive compressor oil. *Therm Sci* 24(5A):2977–2989
4. Kotia A, Rajkhowa P, Rao GS, Ghosh SK (2018) Thermophysical and tribological properties of nanolubricants: a review. *Heat Mass Transf* 54(11):3493–3508
5. Kumar R, Singh DK, Chander S (2020) An experimental approach to study thermal and tribology behavior of LPG refrigerant and MO lubricant appended with ZnO nanoparticles in domestic refrigeration cycle. *Heat Mass Transf* 56(7):2303–2311
6. Marcucci Pico DF, da Silva LRR, Hernandez Mendoza OS, Bandarra Filho EP (2020) Experimental study on thermal and tribological performance of diamond nanolubricants applied to a refrigeration system using R32. *Int J Heat Mass Transf* 152:119493
7. Idemitsu Kosan CL (2020) Characteristics of Daphne hermetic oil. <https://www.idemitsu.com/business/lube/pve/daphne.html>. Accessed 1 Jan (2020)
8. Motozawa M, Makida N, Fukuta M (2018) Experimental study on physical properties of CuO—PVE Nano-oil and its mixture with refrigerant. *Int Compressor Eng Conf. Purdue*
9. Redhwan AAM, Azmi WH, Sharif MZ, Mamat R, Samykano M, Najafi G (2019) Performance improvement in mobile air conditioning system using Al₂O₃/PAG nanolubricant. *J Therm Anal Calorim* 135(2):1299–1310
10. Sanukrishna SS, Jose Prakash M (2018) Experimental studies on thermal and rheological behaviour of TiO₂-PAG nanolubricant for refrigeration system. *Int J Refrig* 86:356–372
11. Zawawi NNM, Azmi WH, Sharif MZ, Najafi G (2019) Experimental investigation on stability and thermo-physical properties of Al₂O₃-SiO₂/PAG nanolubricants with different nanoparticle ratios. *J Therm Anal Calorim* 135(2):1243–1255

Comparison of Thermal Efficiency and Heat Transfer Rate on the Fluidized-Bed Combustor Using Oil Palm Fuel



Muhammad Faisal, Erdiwansyah , Muhtadin, Mahidin, Asri Gani, Mahyuddin, Rizalman Mamat, Mohd Fairusham Ghazali, and Bukhari Manshoor

Abstract Waste in oil palm biomass is one of the renewable energy sources that can be converted into energy. The availability of oil palm biomass which is a renewable energy source is currently very adequate. This research will specifically analyze the differences in the level of thermal efficiency and heat transfer rates of two different types of biomasses. In addition, this comparative analysis was also carried out when testing the modification of the perforated plate with the standard plate or without modification. The combustion test was carried out in a fluidized-bed combustor (FBC) combustion chamber with data measurements using a Digital Thermometer brand Hot-Temp HT-306. Palm oil solid waste biomass such as palm kernel shells and oil palm fronds were used as testing fuel in this study. The results show that the average level of thermal efficiency for palm kernel shell (PKS) and oil palm midrib (OPM) fuels, when tested with a modified hollow plate, is 33.59% and 28.31%, respectively. Meanwhile, the results of the average thermal efficiency at the time of testing the standard plate were 19.77% PKS and 28.29% OPM. The results of the heat transfer rate test for standard plates with PKS fuel are 7363.53 W/m², which is lower than after modification, which is 7762.38 W/m². Meanwhile, the results of combustion using OPM fuel were higher when testing the standard plate at

M. Faisal · Muhtadin · Mahyuddin

Department of Mechanical Engineering, Universitas Abulyatama Aceh, Besar, Aceh 23372, Indonesia

Erdiwansyah (✉)

Faculty of Engineering, Universitas Serambi Mekkah, Banda, Aceh 23245, Indonesia

e-mail: erdi.wansyah@yahoo.co.id

Mahidin · A. Gani

Department of Chemical Engineering, Universitas Syiah Kuala, Banda, Aceh 23111, Indonesia

R. Mamat · M. F. Ghazali

Centre for Research in Advanced Fluid & Processes, Universiti Malaysia Pahang, Lebuhraya Tun Razak, 26300 Gambang, Kuantan, Pahang, Malaysia

B. Manshoor

Faculty of Mechanical and Manufacturing Engineering, University Tun Hussein Onn Malaysia, 86400 Parit Raja, Batu Pahat, Johor, Malaysia

© The Author(s), under exclusive license to Springer Nature Singapore Pte Ltd. 2023

233

N. H. Johari et al. (eds.), *Proceedings of the 2nd Energy Security and Chemical*

Engineering Congress, Lecture Notes in Mechanical Engineering,

https://doi.org/10.1007/978-981-19-4425-3_21

7289.84 W/m² compared to 7162.81 W/m² when testing with a modified perforated plate. Overall, testing with the application of modified perforated plates can increase the thermal efficiency and heat transfer rate in the FBC chamber.

Keywords Efficiency thermal · Heat transfer rate · Oil palm fuel · FBC · Combustion

1 Introduction

Palm oil biomass solid waste is one of the abundant renewable energy sources and can be converted into energy, especially biomass power plants. The availability of abundant renewable energy sources in Indonesia in general and in Aceh Province, in particular, has been conveyed and reported in publications [1–3]. Renewable energy technologies that can convert into energy have also been widely discussed in several publications [4–11]. The utilization of renewable sources into energy can help to reduce dependence on fossil energy which has been depleting in recent years.

Studies on investigating three types of palm oil processing to support technological advancements and renewable energy transitions in the African palm oil industry have also recently been discussed [12]. This is done to overcome the emission of carbon dioxide (CO₂) and nitrous oxide (N₂O) which are more commonly found in smallholder factories than in large-scale factories with a ratio of 47 and 73%. A study of the results of about 100 researchers has been published since the period 2000–2019 in various scientific journals. The research submitted is generally about the technology of producing renewable energy from palm oil biomass waste. This is done to contribute to achieving a sustainable energy supply [13]. Research findings from several researchers conclude that globally there are around 270.0 million tons of biomass sourced from palm oil mill waste every year. This amount is equivalent to an energy substitute of 189 million tons of coal. Thus, this amount is estimated to reduce around 420 million tons of carbon emissions. Meanwhile, the availability of renewable energy sources for solid waste biomass in Aceh Province is currently also very adequate if it is utilized and converted into energy [14, 15].

The application of perforated plates to analyze the NO_x emission characteristics of premix micro-combustion systems has also been applied by [16]. The detailed chemical-kinetic mechanism for ammonia-oxygen combustion in the developed micro-combustion chamber was modeled through three-dimensional (3D) computation. The effect of diffusion can result in a considerable decrease in the atomic N/O ratio, mainly due to the reduction and increase of O₂ and H₂O. In addition, less N₂ can cause the rate of NO formation to be reduced. Exploration in the combustion chamber by making the hole size and position of the single perforated plate has been discussed [17]. Based on the results of the research conducted, it shows that the flame speed initially increases and then decreases as the hole size increases. The design of the perforated plate by varying the initial conditions in the combustion chamber with constant volume has also been discussed [18]. The size of the hole and the

porosity of the flame to the shock wave propagation can affect the intensity of the shock wave and the pressure oscillation in the combustion chamber. The application of perforated plates in the combustion chamber for certain purposes has been widely carried out and published by previous researchers [19–23]. However, of the many studies conducted on the application of perforated plates, only a few were found to use pure palm oil biomass as fuel. Thus, energy conversion from palm oil biomass solid waste sources has a great opportunity to be investigated further. This is because the availability of fuel from existing palm oil mill sources is quite promising.

Perforated plate modification which is applied in this research is specifically to analyze the level of thermal efficiency and heat transfer rate. The results obtained from this test were compared with the test results using standard plates. The combustion testing process is carried out in the FBC combustion chamber using palm oil biomass such as PKS and OPM. Furthermore, the purpose of this perforated plate modification is to optimize combustion so that the injected fuel can be burned all with excess air supply of the modified plate. Measurement data were taken at four different points in the FBC combustion chamber. In particular, this study aims to compare the combustion performance when using standard and modified plates, especially for thermal efficiency, combustion temperature, and heat transfer.

2 Experimental Setup and Material

The oil palm biomass combustion chamber used in this study is a fluidized-bed combustor (FBC) with the application of a standard plate and a modified perforated plate. Experimental setup diagram to analyze the results of thermal efficiency, heat

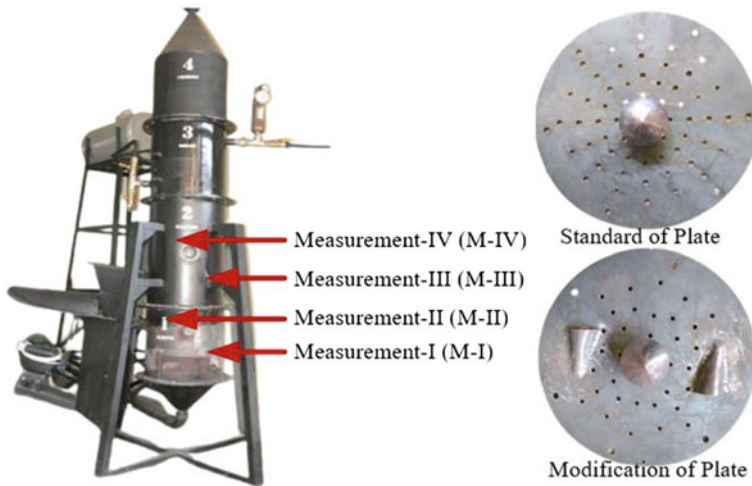


Fig. 1 Experimental setup



Fig. 2 Type of fuel and thermometer

transfer rate, and combustion temperature as presented in Fig. 1. The combustion test on each plate was tested using two types of fuel with four different data measurement points. The application of the modification of the perforated plate aims to compare the test results with the standard plate. This experimental diagram is one of the modifications of previous research [24].

The fuel material used in this research is a solid waste of oil palm biomass such as palm kernel shell (PKS) and oil palm midrib (OPM). The process of making this biomass from start to use takes ± 25 days. Each fuel is tested on a different plate to determine the optimal combustion rate. While the measurement tool to obtain data from the combustion process uses a thermometer with a maximum temperature range of 1300 °C. The fuel material and measurement tools used in this test are as shown in Fig. 2.

In a combustion test, the computation of thermal efficiency is a critical variable. Its goal is to determine the fuel’s efficiency of combustion. Thermodynamic efficiency can be calculated using (Eq. 1) [25]. In addition, the heat transfer calculation tries to determine how efficient the combustion furnaces generated in this study are. In this test, the heat transfer was calculated using (Eq. 2) [25].

$$\eta_{th} = \frac{ma C_p \Delta T}{mb LHV_{fuel}} \tag{1}$$

where

- η_{th} efficiency thermal
- ma liters of water
- C_p calorific value
- ΔT last value–first value

mb fuel weight
 LHV_{fuel} lower heating value

$$q = \frac{M1 - M5}{\frac{1}{hoAo} + \frac{\ln(\frac{ro1}{ri1})}{k1} + \frac{\ln(\frac{ro2}{ri2})}{k2} + \frac{\ln \frac{ro3}{ri3}}{k1} + \frac{1}{hiAi}} \quad (2)$$

where

q Convection heat rate
 $M1$ Temperature Fluid
 $M5$ Temperature wall
 $ro1$ The outer radius of the cylinder
 $ri1$ Radius in cylinder
 $ro2$ The outer radius of insulation
 $ri2$ The outer radius in isolation
 $ro3$ The cylinder outer radius
 $ri3$ Radius in the cylinder
 $k1$ Thermal conductivity of the plate
 $k2$ Insulating conductivity
 ho Convection heat transfer coefficient
 Ao Outer cross-sectional area
 hi The coefficient in the wall
 Ai Inner cross-sectional area

3 Result and Discussion

The combustion process carried out in this test uses a stand-alone plate module with a modified perforated plate. The test was carried out in the FBC combustion chamber using palm oil biomass fuel (PKS and OPM) which was tested on each plate. The modification of the perforated plate applied in this study specifically aims to provide an adequate supply of air into the combustion chamber. Measurement and data collection of the results of each test using a Digital Thermometer brand HotTemp HT-306 at four different points.

Based on the results of measurements carried out, it shows that the level of thermal efficiency recorded on the standard plate is lower than at the time after the modification. The average value of thermal efficiency recorded at the time of the application of the modified perforated plate reached 33.59% PKS and OPM 30.31%. Meanwhile, the average value of thermal efficiency when testing was carried out on standard plates was 19.77% PKS and 28.29% OPM, as shown in Fig. 3. The most significant increase occurred in the PKS fuel when the plate was modified from the previous one without modification. This increase in efficiency level is due to sufficient air supply into the combustion chamber when plate modifications are applied.

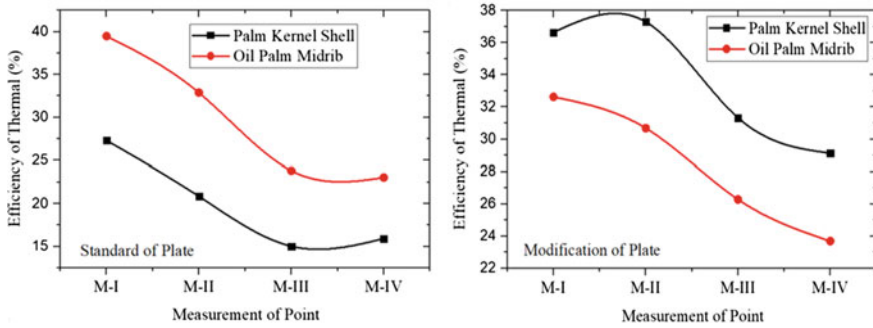


Fig. 3 Comparison of efficiency thermal for different fuel and measurement point

Furthermore, the results of data analysis from the palm oil palm biomass burning process and OPM which were tested on standard plates showed different temperature trends between the two. The level of combustion temperature indicated by the combustion of PKS is slightly higher at M-1 875 °C, M-II 935 °C, M-III 775 °C, and M-IV 723 °C. Meanwhile, the combustion temperatures recorded from the combustion of OPM respectively reached MI 934 °C, M-II 866 °C, M-III 763 °C, and M-IV 716 °C as shown in Fig. 4. The measurement results at the MI point show that the OPM temperature is higher than the temperature from PKS. Meanwhile, at the M-II, M-III, and M-IV measurement points, the combustion temperature of the PKS is higher than the OPM combustion temperature. However, the temperature trend resulting from OPM combustion is more optimal than the PKS combustion temperature trend which shows up and down or is not optimal. The results of the burning of oil palm biomass which were tested in the FBC combustion chamber have also been carried out by [24]. The highest temperature level obtained from their research reached 910 °C. Meanwhile, the highest temperature recorded during this study was 935 °C. However, the combustion temperature analysis carried out in their study compared the combustion temperature based on the weight of the biomass-based on the amount of airflow rate. The results obtained from this study were carried out on

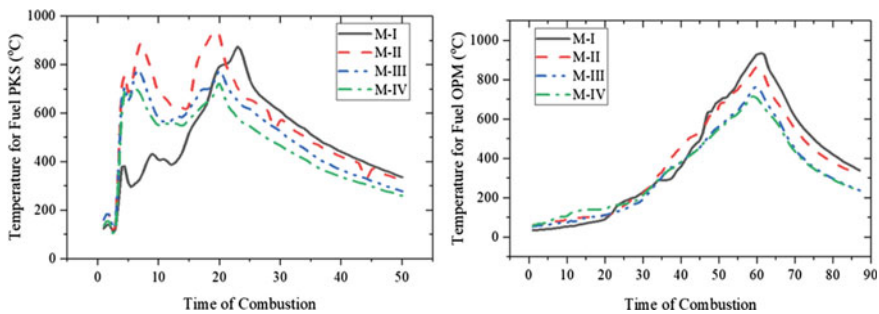


Fig. 4 Comparison of temperature for different fuel at standard plate

a standard plate in the FBC combustion chamber using two types of fuel PKS and OPM.

The results of the analysis of the displacement rate tested on the standard plate module and after the modification showed different results. The rate of heat transfer from the combustion of PKS fuel shows a higher yield after modification of the plate compared to the standard plate. The average value of the heat transfer rate from PKS fuel has a plate modification of 7762.38 W/m² compared to the standard plate of 7363.52 W/m² as shown in Fig. 5. While the average value of the heat transfer rate of OPM fuel showed a decrease when plate modification was done compared to the standard plate. The average value of heat transfer rate OPM fuel at the time of modification was 7162.81 W/m² compared to 7289.84 W/m² when using standard plates. However, the overall heat transfer rate when applying the modified perforated plate was slightly better than when applying the standard plate. This is because the modification of the perforated plate placed in the FBC combustion chamber can supply more air so that the fuel can be burned completely and nothing is left. Analysis of the rate of heat transfer with a modification of the four-way perforated plate has also been carried out previously by [26]. The results of the heat transfer rate obtained by the application of the modified four air supply perforated plate are slightly higher than the modified two air supply plates applied in this study.

The results of the combustion temperature measurement when applying the modification of the hollow plate show that it is more optimal than when using the standard plate in Fig. 4. The combustion temperature level of PKS fuel for each measurement point is M-I 948 °C, M-II 847 °C, M-III 971 °C, and M-IV 699 °C. While the combustion temperatures recorded during the combustion process with OPM fuel are M-I 884 °C, M-II 874 °C, M-III 764 °C, and M-IV 707 °C as shown in Fig. 6. Trends in combustion temperature of PKS fuel and The OPM which was tested during the modification of the perforated plate showed more optimal results than when using the standard plate. This shows that the modifications made in this study are the latest because the air entering the FBC combustion chamber through the modified plate can work optimally. The injected fuel can burn completely and nothing is left because enough air can raise the fuel so it is not saturated. Research on the modification of

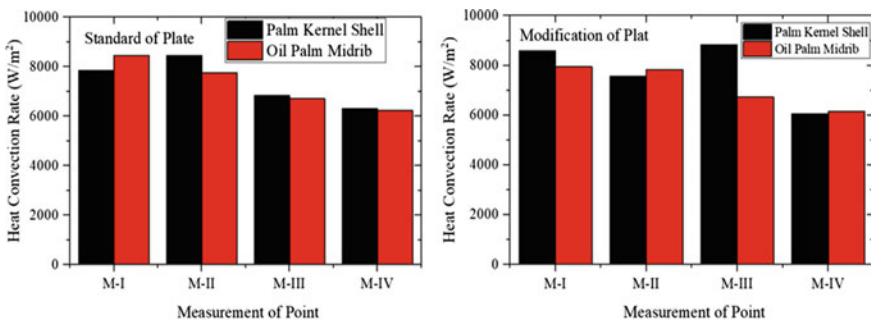


Fig. 5 Comparison of heat transfer rate for different fuel and measurement point

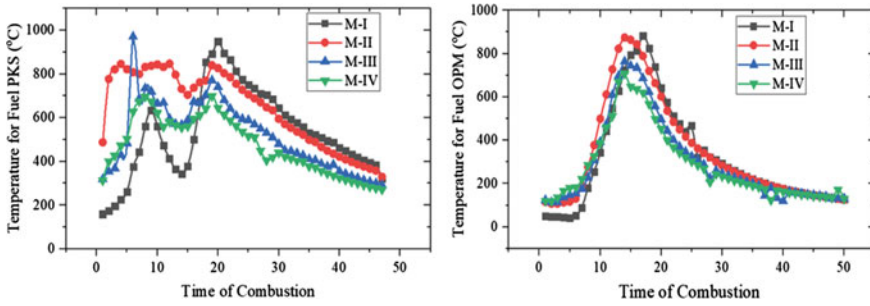


Fig. 6 Comparison of temperature for different fuel at modification perforated plate

the four-perforated air supply plate has also been carried out by [26, 27]. Where the combustion temperature tested from the study as a whole showed optimal results.

Based on the results of the tests carried out in this study as a whole, shows that the thermal efficiency of the application of the modified perforated plate is higher than when testing the standard plate. The heat transfer rate recorded from the modified perforated plate test shows that it is slightly more optimal than the standard plate. Meanwhile, the combustion temperature obtained from the testing process using a modified perforated plate is also more optimal than the standard plate. OPM fuel shows a trend of maximum combustion temperature compared to PKS fuel. The air that enters the FBC combustion chamber is more or enough when the perforated plate is modified by adding two main air suppliers.

4 Conclusion

This research was conducted to analyze the thermal efficiency and heat transfer rate through the modification of the perforated plate by comparing it with the standard plate test. Based on the results of the analysis of the results of the combustion test in the FBC combustion chamber using PKS and OPM fuel, several conclusions can be drawn as follows:

1. The level of thermal efficiency at the time of testing by applying the modification of the perforated plate showed an average result of 33.59% PKS and 28.31% OPM, respectively. Meanwhile, the average results obtained when testing using standard plates were 19.77% PKS and 28.29% OPM.
2. The heat transfer rate for PKS fuel tested with the modification of the perforated plate shows a higher average value of 7762.38 W/m² compared to 7363.52 W/m² at the time of testing with the standard plate.
3. The combustion temperature recorded during the test with the modified hollow plate was also higher than the test on the standard plate.
4. The perforated plate modification applied in this study can increase thermal efficiency, heat transfer rate, and combustion temperature.

Acknowledgements This work was supported by the Universitas Syiah Kuala, Kementerian Pendidikan, Kebudayaan, Riset dan Teknologi with the contract number of 166/UN11/SPK/PNBP/2021.

Conflict of Interest The authors declare that they have no known competing financial interests or personal relationships that could have appeared to influence the work reported in this paper.

References

1. Erdiwansyah E, Mahidin M, Husin H, Nasaruddin N, Khairil K, Zaki M, Jalaluddin J (2021) Investigation of availability, demand, targets, and development of renewable energy in 2017–2050: a case study in Indonesia. *Int J Coal Sci Technol* 1–17
2. Erdiwansyah MR, Sani, MSM, Sudhakar K (2019) Renewable energy in southeast Asia: policies and recommendations. *Sci Total Environ*. <https://doi.org/10.1016/j.scitotenv.2019.03.273>
3. Erdiwansyah M, Mamat R, Sani MSM, Khoerunnisa F, Kadarohman A (2019) Target and demand for renewable energy across 10 ASEAN countries by 2040. *Electr J* 32:106670 (2019). <https://doi.org/10.1016/J.TEJ.2019.106670>
4. Erdiwansyah M, Husin H, Nasaruddin, Zaki M, Muhibbuddin (2021) A critical review of the integration of renewable energy sources with various technologies. *Prot Control Mod Power Syst* 6:3. <https://doi.org/10.1186/s41601-021-00181-3>
5. Salame C-T, Aillerie M, Papageorgas P, Perilhon C, Haider A, Vokas G, Shaban A, Jabur A (2019) Preface: technologies and materials for renewable energy, environment and sustainability. *Energy Procedia* 157:1. <https://doi.org/10.1016/j.egypro.2018.11.156>
6. Shan S, Genç SY, Kamran HW, Dinca G (2021) Role of green technology innovation and renewable energy in carbon neutrality: a sustainable investigation from Turkey. *J Environ Manage* 294:113004. <https://doi.org/10.1016/j.jenvman.2021.113004>
7. Suman A (2021) Role of renewable energy technologies in climate change adaptation and mitigation: a brief review from Nepal. *Renew Sustain Energy Rev* 151:111524. <https://doi.org/10.1016/j.rser.2021.111524>
8. Masukujjaman M, Alam SS, Siwar C, Halim SA (2021) Purchase intention of renewable energy technology in rural areas in Bangladesh: Empirical evidence. *Renew Energy* 170:639–651. <https://doi.org/10.1016/j.renene.2021.01.125>
9. Oryani B, Koo Y, Rezanisa S, Shafiee A (2021) Barriers to renewable energy technologies penetration: perspective in Iran. *Renew Energy* 174:971–983. <https://doi.org/10.1016/j.renene.2021.04.052>
10. Pina EA, Lozano MA, Serra LM (2021) Assessing the influence of legal constraints on the integration of renewable energy technologies in polygeneration systems for buildings. *Renew Sustain Energy Rev* 149:111382. <https://doi.org/10.1016/j.rser.2021.111382>
11. Chen C, Hu Y, Karuppiah M, Kumar PM (2021) Artificial intelligence on economic evaluation of energy efficiency and renewable energy technologies. *Sustain Energy Technol Assessments* 47:101358. <https://doi.org/10.1016/j.seta.2021.101358>
12. Anyaoha KE, Zhang L (2021) Renewable energy for environmental protection: Life cycle inventory of Nigeria's palm oil production. *Resour Conserv Recycl* 174:105797. <https://doi.org/10.1016/j.resconrec.2021.105797>
13. Shahidul MI, Malcolm ML, Begum S, Hashmi MSJ, Islam MS, Eugene JJ (2020) Renewable energy production from environmental hazardous palm oil mill waste materials: a review
14. Mahidin S, Erdiwansyah, Hamdani, Hisbullah, Hayati AP, Zhafran M, Sidiq MA, Rinaldi A, Fitriya B, Tarisma R, Bindar Y (2020) Analysis of power from palm oil solid waste for biomass power plants: a case study in Aceh Province. *Chemosphere* 126714. <https://doi.org/10.1016/j.chemosphere.2020.126714>

15. Mahidin M, Erdiwansyah E, Husin H, Hisbullah H, Hayati AP, Zhafran M, Sidiq MA, Rinaldi A, Fitria B, Tarisma R (2020) Utilization of oil palm biomass as a renewable and sustainable energy source in Aceh Province. *J Adv Res Fluid Mech Therm Sci* 67:97–108
16. Cai T, Becker SM, Cao F, Wang B, Tang A, Fu J, Han L, Sun Y, Zhao D (2021) NOx emission performance assessment on a perforated plate-implemented premixed ammonia-oxygen micro-combustion system. *Chem Eng J* 417:128033. <https://doi.org/10.1016/j.cej.2020.128033>
17. Wei H, Li, K, Zhao J, Zhou L (2020) Experimental investigation on the propagation of flow and flame in a confined combustion chamber equipped with a single-hole perforated plate. *Int J Hydrogen Energy* 45:32589–32597. <https://doi.org/10.1016/j.ijhydene.2020.08.285>
18. Zhou L, Gao D, Zhao J, Wei H, Zhang X, Xu Z, Chen R (2018) Turbulent flame propagation with pressure oscillation in the end gas region of confined combustion chamber equipped with different perforated plates. *Combust Flame* 191:453–467. <https://doi.org/10.1016/j.combustflame.2018.01.023>
19. Wei H, Zhao J, Zhou L (2019) The mechanism of flame propagation affected by flow/shock wave in a confined combustion chamber equipped with a perforated plate. *Int J Hydrogen Energy* 44:7675–7683. <https://doi.org/10.1016/j.ijhydene.2019.01.217>
20. Oh S, Shin Y, Kim Y (2016) Stabilization effects of perforated plates on the combustion instability in a lean premixed combustor. *Appl Therm Eng* 107:508–515. <https://doi.org/10.1016/j.applthermaleng.2016.06.143>
21. Wei H, Gao D, Zhou L, Feng D, Chen R (2017) Different combustion modes caused by flame-shock interactions in a confined chamber with a perforated plate. *Combust Flame* 178:277–285. <https://doi.org/10.1016/j.combustflame.2017.01.011>
22. Ng HD, Chao J, Ju Y, Lee JHS (2008) Combustion regimes subsequent to the reflection of a detonation from a perforated plate. *Commun Nonlinear Sci Numer Simul* 13:243–247. <https://doi.org/10.1016/j.cnsns.2006.03.018>
23. Noiray N, Durox D, Schuller T, Candel S (2007) Passive control of combustion instabilities involving premixed flames anchored on perforated plates. *Proc Combust Inst* 31:1283–1290. <https://doi.org/10.1016/j.proci.2006.07.096>
24. Hani MR, Mahidin M, Husin H, Khairil K, Hamdani H, Erdiwansyah E, Hisbullah H, Faisal M, Mahyudin M, Muhtadin M (2020) Experimental studies on combustion characteristics of oil palm biomass in fluidized-bed: a heat energy alternative. *J Adv Res Fluid Mech Therm Sci* 68:9–28
25. Holman JP (1988) *Perpindahan Kalor* (terjemahan E. Jasfi). Jakarta Penerbit Erlangga. (Buku Asli 1986)
26. Erdiwansyah M, Husin H, Nasaruddin, Muhtadin, Faisal M, Gani A, Usman, Mamat R (2021) Combustion efficiency in a fluidized-bed combustor with a modified perforated plate for air distribution
27. Erdiwansyah M, Husin H, Faisal M, Muhtadin Gani A, Sardjono RE, Mamat R (2021) The modification of the perforated plate in the fluidized-bed combustor to analyze heat convection rate and temperature. *J Combust* 2021:4084162. <https://doi.org/10.1155/2021/4084162>

Performance Optimization of Low Proportion Biodiesel Blend on Marine Diesel Engine Using Response Surface Method



C. W. Mohd Noor, Rizalman Mamat, Mohd Fairusham Ghazali,
S. M. Rosdi, Husni Husin, and Bukhari Manshoor

Abstract Biodiesel is an alternative source of non-fossil fuels for diesel engines and can be used without the need for engine modifications. The effects of employing low proportions of palm biodiesel blends on marine diesel engine performance are investigated in this study. Response surface methodology (RSM) model had been employed to determine the optimal operating conditions of marine diesel engine with respect to palm biodiesel blend, engine load and speed. The ANOVA analysis was selected to verify the adequacy of the model. The use of palm biodiesel blends has lowered the CO emissions while increasing BSFC and NO_x emissions marginally. The results of statistically goodness of fit (R^2) and the goodness of prediction (Adjusted R^2) for all response parameters were above 90%. This value indicates that the developed model is able to predict the data with high accuracy. This study revealed that the optimum condition of fuel was determined as 5% palm biodiesel and 95% of petroleum diesel which operated at 1500 rpm speed and 36.97% engine loading with 78% of RSM desirability. The RSM model was tremendously helpful in structuring the experiment and lowering the amount of time required by reducing the number of experiments to be conducted.

C. W. Mohd Noor (✉)

Faculty of Ocean Engineering Technology and Informatics, Universiti Malaysia Terengganu,
21030 Kuala, Terengganu, Malaysia
e-mail: che.wan@umt.edu.my

R. Mamat · M. F. Ghazali

Centre for Research in Advanced Fluid & Processes, Universiti Malaysia Pahang, Lebuhraya Tun Razak, 26300 Gambang, Kuantan, Pahang, Malaysia

S. M. Rosdi

Politeknik Sultan Mizan Zainal Abidin, 23000 Dungun, Terengganu, Malaysia

H. Husin

Department of Chemical Engineering, Universitas Syiah Kuala, Banda Aceh 23111, Indonesia

B. Manshoor

Faculty of Mechanical and Manufacturing Engineering, University Tun Hussein Onn Malaysia,
86400 Parit Raja, Batu Pahat, Johor, Malaysia

Keywords Engine performance · Optimization · Response surface methodology · Marine diesel engine

1 Introduction

Marine diesel engines used in the shipping industry are similar to compression-ignition engines found in land vehicles, but they are bulkier, bigger, have more complex systems, and operate more efficiently [1]. The main source of power for sea transportation is marine engines. Marine engine emissions, on the other hand, are one of the most significant sources of air pollution, posing a significant threat to the environment [2]. Carbon monoxide, carbon dioxides, sulphur oxides, nitrogen oxides, and particulate matter are the most significant seaborne emissions produced by the combustion of marine fuel oil. Marine vessels contribute approximately 14–31, 4–9, and 3–6% of global nitrogen oxides, sulphur oxides, and carbon dioxides emissions, respectively [3, 4].

Growing energy demand, high volatility crude oil prices, diminishing oil supplies, and carbon emissions issues associated with the use of carbon fuels have captivated the research community in the development of alternative fuels [5, 6]. As a consequence, biodiesel obtained from plant oil has gained popularity as a possible alternative for petroleum diesel fuel. Its key benefits are that it is recyclable, sustainable energy, sulphur-free, and does not emit harmful noxious gases [7]. Biodiesel can be produced from various plant sources such as palm oil, peanuts, soybeans, sunflower, animal fats and used oils [8–11]. Palm biodiesel was chosen for the current study due to the abundance of resources available locally. The planted area of palm oil trees has grown year after year [12].

Several studies have looked into the effects of palm biodiesel and its blends on the performance and emissions of diesel engines. Most of them reported that palm biodiesel leads to an increase in BSFC and NO_x when compared to baseline petroleum diesel fuel. Instead they found palm biodiesel gave a reduction in brake power, CO , CO_2 and HC emission. The summary of their research and findings are listed in Table 1.

Despite previous research on the effects of biodiesel use in compression ignition engines, the optimum condition of an independent parameter involved in the process must also be investigated. The response surface method (RSM) was identified as one of useful method for optimization solution in many types of industrial problems. Previously, the RSM was used to analyse non-linear engineering problems by modelling and optimising the response surface, which is influenced by experiment factors [21]. RSM is a set of mathematical and statistical techniques for developing empirical models. This method was pioneered by K. B. Wilson and G. E. P. Box in 1951 [22]. The application of RSM to design optimization aims to lower the expensive cost of current analysis methods such as computational fluid dynamic (CFD) and finite element analysis. The main advantage of RSM is required less time consuming for design of experiment (DOE) and optimization process. Many researchers have

Table 1 Summary of palm biodiesel research findings

Authors [Ref]	Power	BSFC	CO	CO ₂	NO _x	HC
Monirul et al. [13]	↓ (9.31–12.93%)	↑ (7.96–10.15%)	–	–	–	–
Rizwanul et al. [14]	↓ (1.02%)	↑ (4.71%)	↓ (29.9%)	–	↑ (16.9%)	↓ (30.8%)
Rashed et al. [15]	↓ (6.92–8.75%)	↑ (5.42–8.39%)	↓ (22.93–32.65%)	–	↑ (6.91–18.56%)	–
Ali et al. [16]	↓ (2.6%)	↑ (3.02%)	–	–	–	–
Senthilkumar et al. [17]	↓ (5%)	–	↓ (46%)	↓ (1%)	–	↓ (73%)
Yasin et al. [18]	–	↑ (13.8%)	↓ (2.5%)	↓	↑	↓
Chong et al. [19]	–	↑ (10%)	±Unchanged	–	±Unchanged	±Unchanged
Juoperi & Ollus [20]	–	–	↓	–	↑	↓

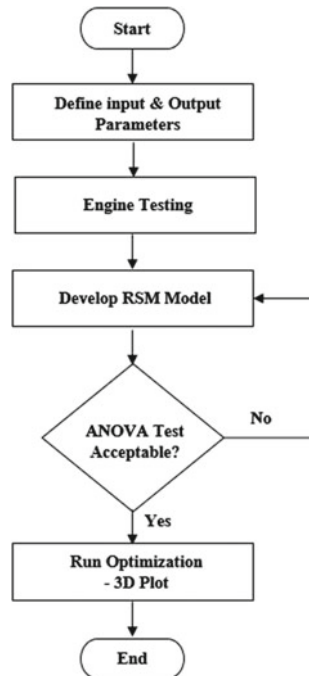
used RSM to optimise engine parameters such as fuel blend ratio, combustion injection timing, fuel injection pressure, and cylinder compression ratio in order to obtain optimum engine performance characteristics [21–29].

A review of the literature found most of the findings involved the use of automotive engines; while research on marine engines powered by biodiesel fuel is still limited and considered new. The authors are therefore highly interested in investigating the impact of palm biodiesel blends and their optimization on the performance and exhaust emissions of marine diesel engines. The first portion of the research examines at how input parameters including palm biodiesel blend percentage, engine loads, and speeds affect brake power, BSFC, CO, and NO_x emissions. Meanwhile, the second step involves determining the optimal input parameter values that result in the best marine engine performance. The RSM technique was used for these goals.

2 Research Methodology

In achieving the objectives of this study, several steps have been carried out as shown in Fig. 1. The first step is to determine the input and output parameters that need to be determined in the experiment, where biodiesel blend percentage, engine loads, and speeds have been identified as input parameters while the engine brake power,

Fig. 1 Flowchart of marine diesel engine optimization study



BSFC, CO, and NO_x emissions are the output. The number of test series and engine operating condition were also determined during design of experiment process. All these parameters were measured during a full engine test in the laboratory. Next, the development of the RSM model was performed by using experimental data as data input. This model will undergo an analysis of variance (ANOVA) test where the p-value must be less than 0.05. The accepted model has been applied to the optimization process using a desirability approach by giving different priorities to some specific outputs.

The engine tests were carried out using a medium-speed, four-stroke, six-cylinder direct injection marine diesel engine. The engine arrangement and engine specifications are shown in Fig. 2 and Table 2, respectively. An engine brake power and torque were measured using a 250-kW eddy-current dynamometer model SAJ SE-250. The engine’s exhaust stream was channelled to an exhaust gas analyser for emission measurement as illustrated in Fig. 3. REO-DCA data acquisition unit as shown in Fig. 4 was used to collect all of the required data from the engine sensors.

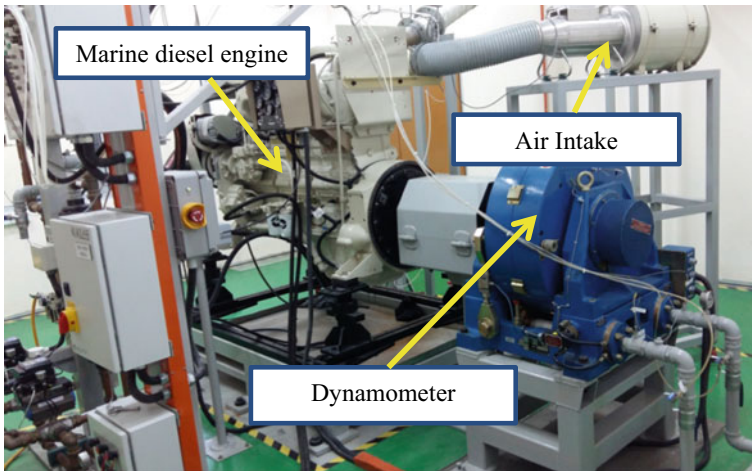


Fig. 2 The test rig for marine diesel engine

Table 2 Engine specification

Description	Specifications
Brand	Cummins-NT855
Displacement volume	14 L
Engine type	4 stroke-Inline-6 cylinders
Bore × stroke	139 mm × 152 mm
Compression ratio	14.5:1
Max. power & torque	201 kW & 1068 Nm
Cooling system	Water-cooled

Fig. 3 KANE gas analyser



Fig. 4 Data acquisition unit



Low blend biodiesel fuel B0, B5, B10, and B15 which contain 5, 10 and 15% of palm biodiesel were used in the experiments. The fuel samples were made by combining pure diesel (B0) and certified palm oil biodiesel obtained from a local supplier. The tests were performed in a steady-state condition with a constant engine load and at various engine speeds ranging from 800 to 1600 rpm speed.

3 Response Surface Methodology Model

The purpose of RSM is to utilise a series of designed test data to obtain optimal response output. RSM method employs statistical approaches to construct an equation that connects output response (Y) and the input variables (x) as shown in Eq. (1).

$$Y = f'(x)\beta + \varepsilon \tag{1}$$

Table 3 Input parameters factor

Variables	Symbols	Levels		
		Lower	Mean	Upper
Fuel blend (%)	Blend	5	10	15
Engine Load (%)	Load	10	30	50
Engine speed (rpm)	Speed	800	1200	1600

where, $f(x)$ is a vector function of p elements composed of powers and cross-products of powers of x_1, x_2, \dots, x_k up to a certain degree signified by $d (>1)$, β is a vector of p unknown constant coefficients, and ε represents the noise observed in the response y . The surface expressed by $f(x_1, x_2, \dots, x_k)$ is known as response surface. In RSM, two important models are commonly used: the first-degree (Eq. 2) and second-degree (Eq. 3) models:

$$y = \beta_0 + \sum_{i=1}^k \beta_i x_i + \varepsilon \tag{2}$$

$$y = \beta_0 + \sum_{i=1}^k \beta_i x_i + \sum_{i=1}^k \beta_{ii} x_i^2 + \sum_{i < j}^k \beta_{ij} x_i x_j + \varepsilon \tag{3}$$

where y denotes the response, x_i denotes the factor values, terms $\beta_0, \beta_i, \beta_{ii}$ and β_{ij} denotes the coefficients of the regression equation, and ε is the experimental uncertainty or error [30].

ANOVA studies were selected to assess the significant relationship between input and output parameters. The quality and strength of the developed model is also evaluated based on the statistics of goodness of fit (R^2) and goodness of prediction (Adjusted R^2). The input parameter to the model was categorized into three levels as listed in Table 3. In determining the number of experiments, the Central Composite Design (CCD) method was used because it has the ability to predict first-order and second-order equations model quickly.

4 Results and Discussion

4.1 ANOVA Analysis

The RSM model developed in this study is used to investigate the effect of a low proportion palm biodiesel blends on marine engine performance parameters and to optimise the engine operating conditions. The ANOVA analysis, which provides statistical information about the p-value, was applied to validate the model's

adequacy. All models show statistically significant, with all p-values less than 0.05. A p-value of less than 0.05 indicates that the factors have a significant influence at the 95 percent confidence level [31]. According to the statistics of goodness of fit (R^2) and goodness of prediction (Adjusted R^2), the model fits the data quite well. The modified R^2 value accounts for the number of predictors in the model, while the R^2 value represents the total variability of the individual answer after considering the significant components. All response parameters had R^2 and adjusted R^2 values above 90%, indicating that the model was capable of accurately predicting the data. In this investigation, the RSM model was able to predict response parameters such as brake power, BSFC, CO, and NO_x emission, as well as establish significant relationships between input components and responses.

4.2 Brake Power

Figure 5 depicts the 3D interaction plot of engine brake power running on low blend of palm biodiesel. As seen in the plot, raising the proportion of biodiesel in diesel fuel has no effect on the engine's braking power. The results reveal that no significant changes in observed engine brake power exist across all fuel blends evaluated. The value of brake power is only directly proportional to the value of the given load. For all biodiesel blends tested, the highest brake power was found to be 78.0 kW at 50% engine load. This suggests that low blend of biodiesel can be utilised in marine engines without sacrificing power of the engine. Equations (4) show the predicted equation based on the actual factors that acquired from the experimental data by applying two factor interaction model analyses.

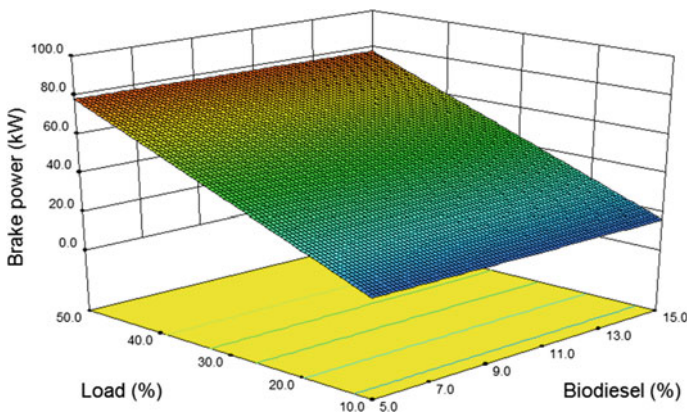


Fig. 5 The interactive effect of biodiesel on engine brake power

$$\begin{aligned} \text{Power} = & -2.19250 + 0.094000 * \text{Blend} + 0.048250 * \text{Load} \\ & + 2.18125\text{E-}003 * \text{Speed} - 1.00000\text{E-}003 * \text{Blend} * \text{Load} \\ & - 7.50000\text{E-}005 * \text{Blend} * \text{Speed} + 1.00313\text{E-}003 * \text{Load} * \text{Speed} \quad (4) \end{aligned}$$

4.3 Brake Specific Fuel Consumption

Brake specific fuel consumption (BSFC) increased as the percentage of biodiesel in blends increased as illustrated in Fig. 6. Previous research stated that it is necessary to compensate for biodiesel’s loss of heating value, the blend with a higher biodiesel percentage consumed more by the engine [32]. As a result, when using biodiesel blends, the volume of fuel delivered into the cylinder for a given energy input should always be increased. It was noticed that maximum BSFC was 906.4 and 712.1 g/kW.hr for 15% and 5% biodiesel respectively at 10% loading condition. The increase in BSFC with the biodiesel mixture was consistent with previous research [13–16]. In all fuels tested, BSFC was shown to decrease as engine loads increased. One probable explanation for this tendency is that the rise in the rate of demand fuel for engine combustion is lower than the increase amount in engine power since heat losses at higher loads are substantially reduces. Equations (5) present the predicted model of BSFC as fitted based on RSM method.

$$\begin{aligned} \text{BSFC} = & 1690.56021 + 61.72774 * \text{Blend} - 59.20433 * \text{Load} \\ & - 0.62242 * \text{Speed} - 0.54725 * \text{Blend} * \text{Load} \end{aligned}$$

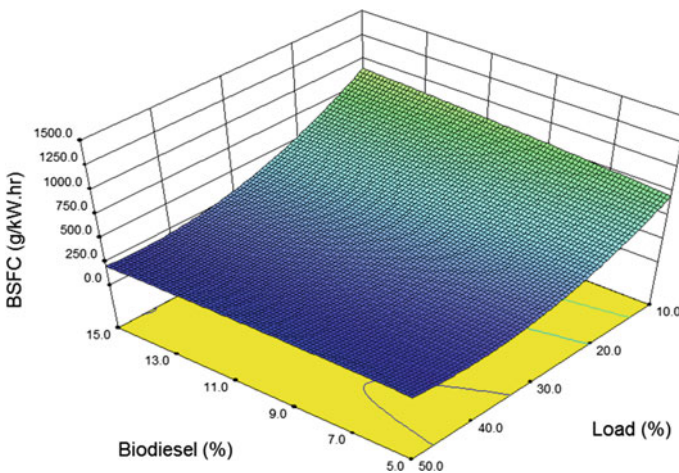


Fig. 6 The interactive effect of biodiesel on BSFC

$$\begin{aligned}
 & - 0.016263 * \text{Blend} * \text{Speed} + 9.77738\text{E-}003 * \text{Load} * \text{Speed} \\
 & - 0.58540 * \text{Blend}^2 \\
 & + 0.58337 * \text{Load}^2 + 9.18164\text{E-}005 * \text{Speed}^2
 \end{aligned} \tag{5}$$

4.4 CO Emissions

CO is a by-product of incomplete fuel combustion. Figure 7 depicts the impact of palm biodiesel blends on CO levels as a function of engine loads. The amount of palm biodiesel in blends is found to reduce CO emissions. A similar pattern was discovered in [14, 15, 17, 18]. This is most likely due to biodiesel’s higher oxygen content, which encourages complete combustion and so lowers CO emissions. The amount of CO emitted was unaffected by loading circumstances. The lowest CO emission is seen at 30 percent engine load, indicating that full combustion occurs at that moment. Equation (6) presents a prediction response surface model for CO emissions.

$$\begin{aligned}
 \text{CO} = & 0.10044 + 1.72598\text{E-}003 * \text{Blend} - 1.66544\text{E-}003 * \text{Load} \\
 & - 9.99816\text{E-}005 * \text{Speed} + 1.25000\text{E-}005 * \text{Blend} * \text{Load} \\
 & + 6.25000\text{E-}007 * \text{Blend} * \text{Speed} \\
 & - 4.68750\text{E-}007 * \text{Load} * \text{Speed} - 1.72549\text{E-}004 * \text{Blend}^2 \\
 & + 3.92157\text{E-}005 * \text{Load}^2 + 3.55392\text{E-}008 * \text{Speed}^2
 \end{aligned} \tag{6}$$

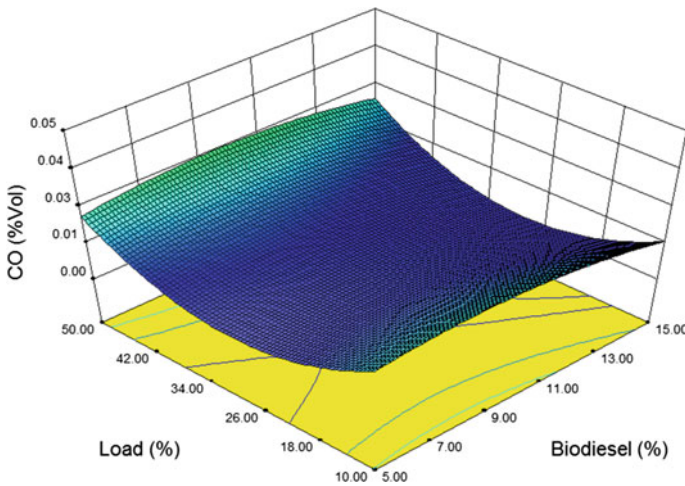


Fig. 7 The interactive effect of biodiesel on CO emission

4.5 NO_x Emissions

NO_x pollutants are emitted during the engine combustion process when oxygen and nitrogen gases are reacting at high temperatures in engine cylinders [33]. The Zeldovich mechanism governs the generation of NO_x, and it is largely dependent on temperature and oxygen availability [35]. The interaction effect of biodiesel proportion and engine loads on NO_x emissions is shown in Fig. 8. When there was a higher percentage of biodiesel in the blend, NO_x emissions show an increment pattern, especially under low loading conditions. Biodiesels have a larger oxygen content [34–36], thus it's obvious that the extra oxygen will interact with nitrogen gases from the air intake, and generate in more NO_x emission. According to Fattah et al. [37], the amount of palm methyl ester (FAME) in a blend increases NO_x. Equation (7) shows the predicted model of NO_x that was derived from RSM model.

$$\begin{aligned}
 \text{NO}_x = & -76.08176 + 2.53359 * \text{Blend} + 7.95236 * \text{Load} \\
 & + 0.10676 * \text{Speed} - 0.052500 * \text{Blend} * \text{Load} + 2.62500\text{E-}004 \\
 & * \text{Blend} * \text{Speed} - 4.42969\text{E-}003 * \text{Load} * \text{Speed} \\
 & - 0.018529 * \text{Blend}^2 + 0.10122 * \text{Load}^2 - 1.93015\text{E-}005 * \text{Speed}^2 \quad (7)
 \end{aligned}$$

4.6 Optimization Results

An optimization process is any kind of process that systematically comes up with solutions that are better than the solution used before. Optimization is one of the most important processes in the design of multiple input data. The goal of this study

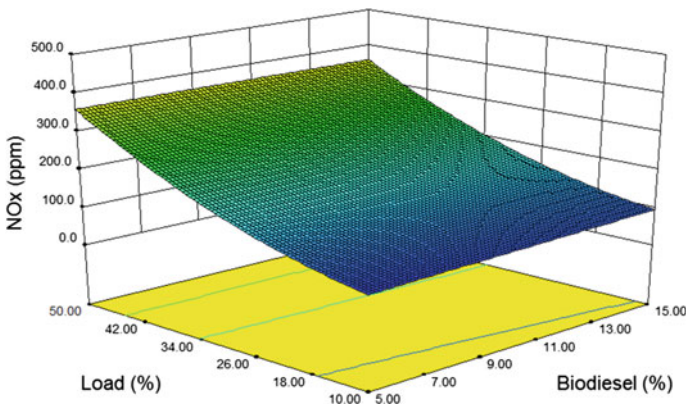


Fig. 8 The interactive effect of biodiesel on NO_x emission

Table 4 Optimization solutions and desirability of responses parameters

No	Blend (%)	Load (%)	Speed (RPM)	Power (kW)	BSFC (g/kW.hr)	CO (%Vol)	NO _x (ppm)	RSM Desirability
1	5.00	36.97	1500	58.2	185.1	0.01	231.8	0.78
2	5.00	37.43	1500	58.9	183.4	0.01	235.8	0.78
3	5.00	36.41	1500	57.3	187.6	0.01	227.1	0.78
4	12.44	38.77	1500	60.6	223.5	0.01	251.7	0.75
5	15.00	38.84	1500	60.5	223.2	0.01	253.3	0.75

was to discover the optimal conditions for factor level (biodiesel % and engine load) on marine diesel engine performance and emission characteristics. More than one response, such as brake power, BSFC, CO, and NO_x, was used to determine the process's suitability. Because there is a trade-off between response characteristics, it is critical to optimise the load, engine speed and percentage of biodiesel in diesel fuel with the purpose of optimising those parameters. The RSM approach in this study used the CCD procedure with the goal of achieving a high desirability solution. According to previous findings, in circumstances where a non-sequential batch response surface experiment is required, the CCD provides a particularly efficient design [31].

In achieving various objective functions, the desirability approach has been used by setting priority levels for different response parameters where the least important value is marked as (+) while the most important value is marked as (+ + + + +). The highest desirability output value is considered to be the optimal solution of the model. Different optimal solutions were obtained using a desirability-based method, as shown in Table 4. The ideal condition was determined to be 78 percent desirability, which was achieved at the following operating parameters: 1500 rpm engine speed, 36.97 percent engine load, and 5% biodiesel percentage. The brake power, BSFC, CO, and NO_x values at this optimum position were found to be 58.2 kW, 185.1 g/kW.hr, 0.01% volume and 231.8 ppm, respectively. Figure 9 shows plot for global desirability as a function of load and proportion of biodiesel in the blend fuel.

5 Conclusions

Response surface methodology (RSM) based design of experiments were used in this work to create and conduct statistical analysis to find the parameters that have the greatest impact on the performance and emissions of a marine diesel engine. The RSM's desirability approach was used to discover the best settings for improving performance and emission characteristics. The following are the most noticeable findings from this research:

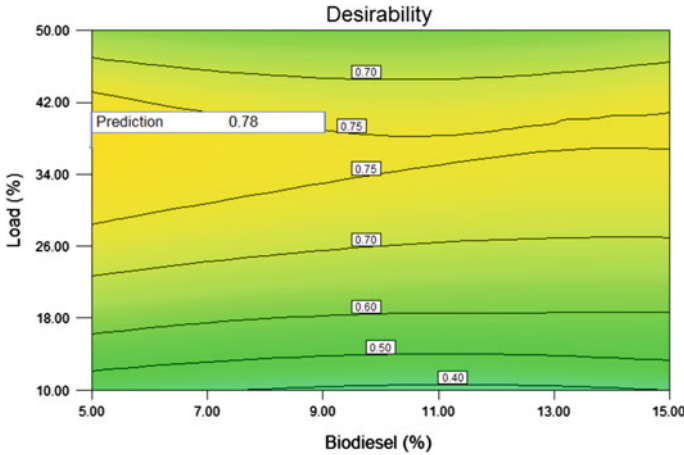


Fig. 9 Desirability condition as a function of load and biodiesel proportion

- (i) The optimum blend ratio of fuel was determined as 5% palm biodiesel and 95% of petroleum diesel operated at 1500 rpm speed and 36.95% engine loading. This condition resulted in 78% RSM desirability.
- (ii) The use of palm biodiesel blends has no significant effect on engine brake power, however it can reduce CO gas emissions while marginally increasing BSFC and NO_x emissions.
- (iii) The use of RSM can improve the engine performance to the optimum condition. The mathematical models produce in this study can be used to forecast factor levels that haven't been tested.
- (iv) All of the response parameters' goodness of fit (R^2) and goodness of prediction (Adjusted R^2) were above 90%, indicating that the model fits the data remarkably well.
- (v) The RSM-based experiment design was extremely beneficial in terms of designing the experiment and reducing the time necessary by reducing the number of tests to be run. It also included statistically validated models for each of the responses.

Acknowledgements The financial support of Universiti Malaysia Pahang, Malaysia through grant RDU172204, RDU1703147, RDU1703314, PGRS160359, PGRS160303, PGRS1903166, and PGRS190341 is greatly acknowledged.

References

1. Palocz-Andresen M (2013) Decreasing fuel consumption and exhaust gas emissions in transportation. Marine diesel engines marine. Springer, Berlin Heidelberg, pp 159–172

2. Wang C, Corbett JJ, Firestone J (2008) Improving spatial representation of global ship emissions inventories. *Environ Sci Technol* 42:193–199
3. Eyring V, Köhler HW, Aardenne J van, Lauer A (2005) Emissions from international shipping: 1. The last 50 years. *J Geophys Res* 110:D17305
4. Corbett JJ, Wang C, Winebrake JJ, Green E (2007) Allocation and forecasting of global ship emissions. Clean Air Task Force, Boston, MA, USA
5. Ashraful AM, Masjuki HH, Kalam MA, Rizwanul Fattah IM, Imtenan S, Shahir SA, Mobarak HM (2014) Production and comparison of fuel properties, engine performance, and emission characteristics of biodiesel from various non-edible vegetable oils: a review. *Energy Convers Manag* 80:202–228
6. López I, Pinzi S, Leiva-candia D, Dorado P (2015) Multiple response optimizations to reduce exhaust emissions and fuel consumption of a diesel engine fuelled with olive pomace oil methyl ester/diesel fuel blends. *Energy* 1–7
7. Demirbas A (2009) Progress and recent trends in biodiesel fuels. *Energy Convers Manag* 50:14–34
8. Knothe G, Van GJH, Krahl J (2005) The biodiesel handbook. AOCS Press, Champaign, Illinois
9. Jahiril MI, Brown RJ, Senadeera W, O'Hara IM, Ristovski ZD (2013) The use of artificial neural networks for identifying sustainable biodiesel feedstocks. *Energies* 6:3764–3806
10. Ng J-HH, Ng HK, Gan S (2012) Development of emissions predictor equations for a light-duty diesel engine using biodiesel fuel properties. *Fuel* 95:544–552
11. Wan Nor Maawa WG, Rizalman M, Masjuki HH, Najafi G (2015) Effects of biodiesel from different feedstocks on engine performance and emissions: a review. *Renew Sustain Energy Rev* 51:585–602
12. Malaysian Palm Oil Board (2016) Overview of the Malaysian Oil Palm Industry. Kuala Lumpur
13. Monirul IM, Masjuki HH, Kalam MA, Mosarof MH, Zulkifli NWM, Teoh YH, How HG (2016) Assessment of performance, emission and combustion characteristics of palm, Jatropha and Calophyllum inophyllum biodiesel blends. *Fuel* 181:985–995
14. Rizwanul Fattah IM, Masjuki HH, Kalam MA, Mofijur M, Abedin MJ (2014) Effect of antioxidant on the performance and emission characteristics of a diesel engine fueled with palm biodiesel blends. *Energy Convers Manag* 79:265–272
15. Rashed MM, Kalam MA, Masjuki HH, Mofijur M, Rasul MG, Zulkifli NWM (2016) Performance and emission characteristics of a diesel engine fueled with palm, jatropha, and moringa oil methyl ester. *Ind Crops Prod* 79:70–76
16. Ali OM, Mamat R, Abdullah NR, Adam A (2016) Analysis of blended fuel properties and engine performance with palm biodiesel-diesel blended fuel. *Renew Energy* 86:59–67
17. Senthilkumar S, Sivakumar G, Manoharan S (2015) Investigation of palm methyl-ester biodiesel with additive on performance and emission characteristics of a diesel engine under 8-mode testing cycle. *Alexandria Eng J* 54:423–428
18. Yasin MHM, Paruka P, Mamat R, Yusop AF, Najafi G, Alias A (2015) Effect of low proportion palm biodiesel blend on performance, combustion and emission characteristics of a diesel engine. *Energy Procedia* 75:92–98
19. Chong CT, Ng JH, Ahmad S, Rajoo S (2015) Oxygenated palm biodiesel: Ignition, combustion and emissions quantification in a light-duty diesel engine. *Energy Convers Manag* 101:317–325
20. Juoperi K, Ollus R (2008) Alternative fuels for medium-speed diesel engines. *WÄRTSILÄ Tech J* 1:24–28
21. Ileri E, Karaoglan AD, Atmanli A (2013) Response surface methodology based prediction of engine performance and exhaust emissions of a diesel engine fuelled with canola oil methyl ester. *J Renew Sustain Energy* 5:1–19
22. Najafi G, Ghobadian B, Yusaf T, Safieddin Ardebili SM, Mamat R (2015) Optimization of performance and exhaust emission parameters of a SI (spark ignition) engine with gasoline-ethanol blended fuels using response surface methodology. *Energy* 90:1815–1829
23. Ali O, Mamat R, Najafi G, Yusaf T, Safieddin Ardebili S (2015) Optimization of biodiesel-diesel blended fuel properties and engine performance with ether additive using statistical analysis and response surface methods. *Energies* 8:14136–14150

24. Atmanli A, Yüksel B, Ileri E, Karaoglan AD (2015) Response surface methodology based optimization of diesel—n-butanol—cotton oil ternary blend ratios to improve engine performance and exhaust emission characteristics. *Energy Convers Manag* 90:383–394
25. Ganapathy T, Gakkhar RP, Murugesan K (2011) Optimization of performance parameters of diesel engine with *Jatropha* biodiesel using response surface methodology. *Int J Sustain Energy* 30:37–41
26. Hirkude JB, Padalkar AS (2014) Performance optimization of CI engine fuelled with waste fried oil methyl ester-diesel blend using response surface methodology. *Fuel* 119:266–273
27. Khoobbakht G, Najafi G, Karimi M (2016) Optimization of operating factors and blended levels of diesel, biodiesel and ethanol fuels to minimize exhaust emissions of diesel engine using response surface methodology. *Appl Therm Eng* 99:1006–1017
28. Kumar BR, Saravanan S, Rana D, Nagendran A (2016) Combined effect of injection timing and exhaust gas recirculation (EGR) on performance and emissions of a DI diesel engine fuelled with next- generation advanced biofuel—diesel blends using response surface methodology. *Energy Convers Manag* 123:470–486
29. Pandian M, Sivapirakasam SP, Udayakumar M (2011) Investigation on the effect of injection system parameters on performance and emission characteristics of a twin cylinder compression ignition direct injection engine fuelled with pongamia biodiesel-diesel blend using response surface methodology. *Appl Energy* 88:2663–2676
30. Montgomery DC (2013) *Design and analysis of experiments*. Wiley, Eighth
31. Myers RH, Montgomery DC, Anderson-Cook CM (2009) *Response surface methodology: process and product optimization using designed experiments*. Wiley, Third Edit
32. Shojaefard MH, Etghani MM, Akbari M, Khalkhali A, Ghobadian B (2012) Artificial neural networks based prediction of performance and exhaust emissions in direct injection engine using castor oil biodiesel-diesel blends. *J Renew Sustain Energy* 4:063130–063219
33. Can Ö (2014) Combustion characteristics, performance and exhaust emissions of a diesel engine fuelled with a waste cooking oil biodiesel mixture. *Energy Convers Manag* 87:676–686
34. Roskilly AP, Nanda SK, Wang YD, Chirkowski J (2008) The performance and the gaseous emissions of two small marine craft diesel engines fuelled with biodiesel. *Appl Therm Eng* 28:872–880
35. Öztürk E (2015) Performance, emissions, combustion and injection characteristics of a diesel engine fuelled with canola oil–hazelnut soapstock biodiesel mixture. *Fuel Process Technol* 129:183–191
36. Palash SM, Kalam MA, Masjuki HH, Masum BM, Rizwanul Fattah IM, Mofijur M (2013) Impacts of biodiesel combustion on NOx emissions and their reduction approaches. *Renew Sustain Energy Rev* 23:473–490
37. Rizwanul Fattah IM, Masjuki HH, Liaquat AM, Ramli R, Kalam MA, Riazuddin VN (2013) Impact of various biodiesel fuels obtained from edible and non-edible oils on engine exhaust gas and noise emissions. *Renew Sustain Energy Rev* 18:552–567

Performance Investigation of R32 and R410a Refrigerants with Different Compressor Lubricants



M. F. Ismail  and Wan Azmi Wan Hamzah 

Abstract The present study aims to investigate the effect of changing air conditioning refrigerants and compressor lubricants on system performance. Two types of refrigerants namely R410a and R32 paired with two different lubricants were investigated. A test rig consists of residential air conditioning with a thermal control room was developed in the present study. The initial refrigerant charge was varied to determine the optimum charge for each refrigerant-lubricant mixture. The results reveal that the optimum charge for R32 is 350 g that represents only 70% of the refrigerant amount for R410a. R32 performs better than R410a for both lubricants mixture. The R32-POE combination shows the best performance with 14% improvement from the baseline data. R32 performs better in the air conditioning originally design for R410 refrigerant and has a good prospect to replace R410a as a more environmentally friendly refrigerant.

Keywords Residential air conditioning · R32 refrigerant · R410a refrigerant · PVE lubricant · COP

M. F. Ismail · W. A. Wan Hamzah (✉)
Department of Mechanical Engineering, College of Engineering, Universiti Malaysia Pahang,
Lebuhraya Tun Razak, 26300 Gambang, Kuantan, Pahang, Malaysia
e-mail: [wanazmi2010@gmail.com](mailto:wamazmi2010@gmail.com)

M. F. Ismail
e-mail: mfarid@utem.edu.my

W. A. Wan Hamzah
Centre of Excellence for Advanced Research in Fluid Flow, Lebuhraya Tun Razak, 26300
Gambang, Kuantan, Pahang, Malaysia

M. F. Ismail
Faculty of Mechanical and Manufacturing Engineering Technology, Universiti Teknikal Malaysia
Melaka, Hang Tuah Jaya, 75150 Durian Tunggal, Melaka, Malaysia

1 Introduction

Difluoromethane (R32) is not a new refrigerant in vapor compression refrigeration systems (VCRS). Today, this hydrofluorocarbon (HFC) type refrigerant is commonly used in refrigeration and air conditioning system. The R32 has been named as a favorable candidate to replace R410a as a refrigerant for residential air conditioning (RAC) system [1]. Being a single substance material is one of the advantages of R32 compared to R410a [2]. Even it has a few more advantages than R410a, its flammability level makes R32 less favorable to replace R22 as a refrigerant in RAC for the past decades ago [3]. However, the idea to replace R410a with R32 was initiated again due to the demand of replacing commercial refrigerant to lower global warming impact (GWP) [4]. The GWP for R410a and R32 refrigerant are 2077 and 675, respectively. Therefore, the GWP for R32 is much lower than R410a [5]. In fact, 50% of R410a composition is R32 while the other half is R125. In addition, R410a and R32 refrigerants contain same component of mixture almost similar characteristics hence the replacement process much easier than other refrigerants.

Application of R32 in a new RAC shall be not a big deal for the manufacturer. However, replacement of a new refrigerant into the existing operational of RAC system is slightly a challenge. One major issue is to define optimum amount of R32 to replace R410a. R32 has lower density than R410a, thus dropping it into the system that was initially built for R410a shall be at less volume [6]. Therefore, the determination of the optimum refrigerant amount that provides the best performance is crucial. The method to determine the RAC performance is already being developed and used by the previous researcher. The performance of RAC is influenced by various factors. One of them is the type of compressor lubricants in the system.

The RAC system with R410a commonly being paired with polyol ester (POE) lubricant. The POE is a synthetic-based lubricant that is soluble in HFC refrigerant. A relatively new lubricant named polyvinyl ether (PVE) is also soluble with HFC [7]. By comparing PVE with POE, the new lubricant has better characteristics that should be considered such as anti-hydro, flexible polymer properties, favorable resistivity, and features as an effective extreme pressure agent [8]. Due to those advantages, the replacement of compressor lubricant from POE to PVE shall be investigated. The effect of lubricant changing on the performance of RAC shall be determined. Therefore, the objective of this paper is to investigate the performance of the RAC system operated with two different refrigerants (R410a, R32) in combination with POE and PVE lubricants.

2 Methodology

2.1 Experimental Setup

The RAC test rig together with the thermal control room (TCR) is developed according to ISO 5151:2010 [9]. An existing split unit RAC with cooling capacity of 9000 Btu/h was installed back-to-back on a customized RAC hanger. The RAC system was installed according to the manufacturer’s recommendation in the Service Manual provided by Gree Electric Appliances, Inc of Zhuhai. Proper tools and PPE were used to conduct the installation process including electrical wiring connection, refrigerant piping with insulation, and condensate water piping. The schematic diagram of the present experimental setup is shown in Fig. 1. The refrigeration system was equipped with a rolling piston rotary compressor originally operated with R410a and Polyol ester (POE) lubricant. The evaporator and condenser are made with an aluminum finned-copper tube type heat exchanger with a diameter of 5 and 7 mm, respectively. The exposed copper pipes were insulated properly by a foam insulator.

The TCR is a room consists of two confine spaces namely indoor and outdoor areas and separating by a wall. The indoor area is used for the RAC indoor unit with other measurement instrumentations. The air conditioning outdoor unit is located in the outdoor area together with a thermal controller system. The outer wall is made of 5 mm plywood and insulated with 50 mm polystyrene to avoid any influence of outer

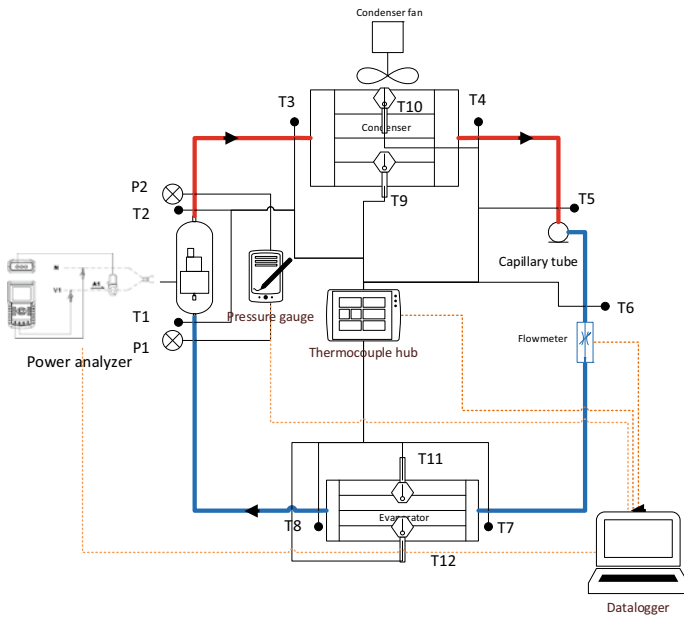


Fig. 1 Schematic diagram of RAC experimental setup

condition to the indoor and outdoor area. The TCR is located inside a laboratory with a controlled temperature between 23 and 25 °C. The indoor and outdoor areas were equipped with an environment control system consisting of fans, temperature and humidity sensors, temperature controllers, and damper for air handling operation and heat recovery. For safety purposes to the equipment and the operator, the firefighting equipment and gas evacuation system were installed in the TCR. The RAC system was operated at the standard test condition with outdoor air temperature of 35 °C while indoor air temperature is 27 °C.

2.2 *Measurement and Experimental Procedure*

The original unit only comes with one pressure valve on the low-pressure side. A modification was done on the outdoor unit to install a new pressure valve for the high-pressure side. The Testo 550 (accuracy of $\pm 0.5\%$) was used to measure pressure before and after the compressor. The temperature was measured at 12 different points as illustrated in Fig. 1. Additional thermocouples were installed in the TCR and at the ambient temperature area. The K-type thermocouples were used with an accuracy of $\pm 0.5\%$. To measure the accurate refrigerant charge in the RAC, a digital refrigerant scale with an accuracy of $\pm 5\%$ was used.

Initially, the TCR was kept at the controlled ambient temperature of 23–25 °C before run the experiment. The measurement devices and data logger were started and recorded continuously along with the experiment run. The RAC was vacuumed, and compressor lubricant was transferred into the system. The refrigerant was charged according to the desired amount before the RAC unit was turned on. The RAC was monitored continuously using a data logger that display real-time data during the experiment [10]. After the desired outdoor and indoor temperature was achieved, the sample data were captured for 10 min with intervals of 2 s.

The experiment undertaken with two types of compressor lubricants (POE and PVE) and two refrigerants (R32 and R410a). Four combinations of refrigerant-lubricant mixture were investigated: (i) POE-R410a mixture, (ii) POE-R32 mixture, (iii) PVE-R410a mixture, and (iv) PVE-R32 mixture. The refrigerant charge for each combination was varied from 200 to 600 g. After each experiment, the refrigerant was recovered using the refrigerant recovery machine, and continued with the lubricant reclamation with the same machine. The properties of lubricants in this study are presented in Table 1.

2.3 *Thermodynamic Analysis*

The experimental data such as pressure and temperature were used to calculate the vapor saturated enthalpy at the compressor suction side (h_1), superheated vapor enthalpy at the compressor discharge (h_2), and the vapor enthalpy for evaporator inlet

Table 1 Properties of compressor lubricants [8, 11]

Property	POE	PVE
Dynamic viscosity, mm ² /s @ 40 °C	66.6	68.1
Dynamic viscosity, mm ² /s @ 100 °C	9.4	8.04
Pour Point, °C	-39	-37.5
Flash point, °C	270	204
Density, kg/m ³ @ 15 °C	977	936.9

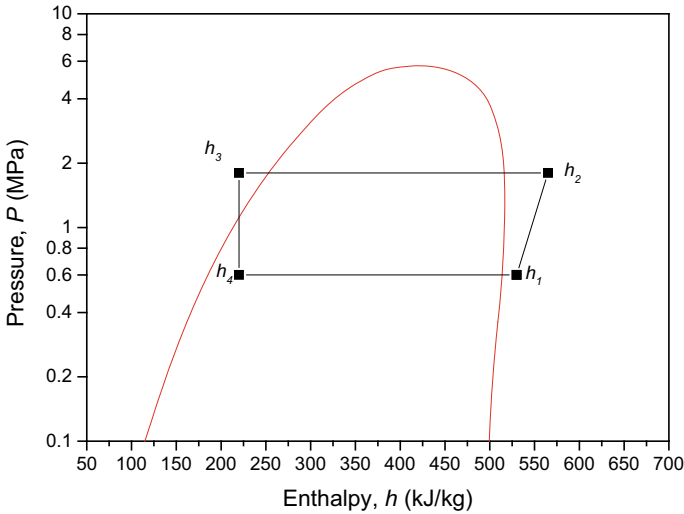


Fig. 2 *P-h* diagram of R32 and R410a for thermodynamic analysis [12]

(*h*₄). A *P-h* diagram for R32 and R410a was used to calculate the ideal condition for VCRS as shown in Fig. 2. The engineering equation solver (EES) was used to calculate the enthalpy for determination of RAC behavior namely compressor work (CW), refrigerant effect (RE), and coefficient of performance (COP) of the ideal VCRS condition. Equations (1)–(3) determine the RE, CW, and COP, respectively.

$$RE = h_1 - h_4 \tag{1}$$

$$CW = h_2 - h_1 \tag{2}$$

$$COP = \frac{RE}{CW} \tag{3}$$

3 Results and Discussion

This section will be discussed the results of the experimental analysis consists of the performance of the compressor, the output at the evaporator, and the overall performance of VCRS. The effect of different refrigerant charges will be discussed to find the optimum charge at the best performance condition.

3.1 Compressor Performance

Compressor work is the amount of work done by the compressor that depends on several factors such as the amount of refrigerant, mass flow rate and refrigerant viscosity. The original combination provided by the manufacturer of the RAC system is R410a-POE with a 520 g optimum refrigerant charge. The low CW is recommended to optimize the performance of VCRS. Figure 3 shows the compressor work at different refrigerant charges for the four refrigerant-lubricant combinations. The similar trend was observed for all four combinations refrigerant-lubricant. The CW was attained high at low refrigerant charge. However, the CW was decreased with the increment of refrigerant charge. At a specific point, the CW suddenly fluctuates to the high value and slowly decreasing with refrigerant charge. The CW spike occurred at 550 g refrigerant charge for the original combination of R410a-POE mixture. Similar condition also observed for the RAC with R410a-PVE combination. In contrast,

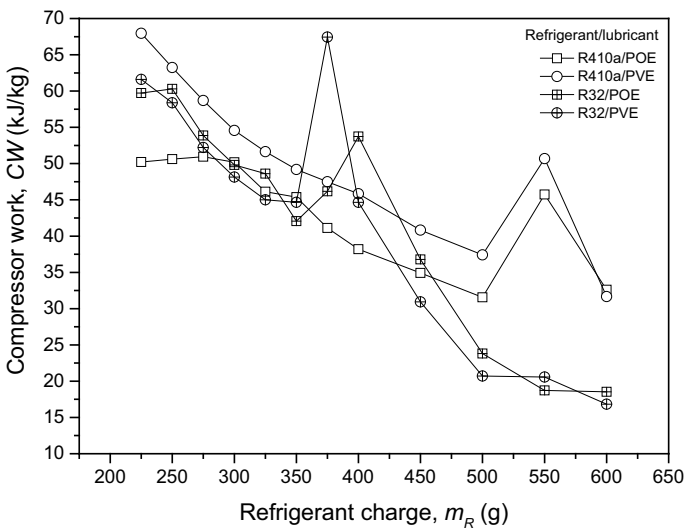


Fig. 3 Comparison of compressor work at different refrigerant-lubricant combinations

the spike for R32-POE and R32-PVE mixtures were happened at 400 g and 375 g refrigerant charges, respectively.

By referring to the amount of refrigerant charge for the original refrigerant-lubricant combination, 520 g is the optimum charge and recommended by the RAC manufacturer for their RAC system. The RAC with R410a-POE mixture showed the lowest value of CW at 500 g. In addition, the mass capacity of refrigerant in the system at 550 g charge already exceeded the optimum point. Therefore, the CW increased after 500 g charge due to overcharge refrigerant. When the refrigerant was charged more than 600 g, the evaporator outlet temperature showed the lowest value compared to other temperature points in VCRS. This condition should not happened because the normal lowest temperature occurred at the outlet of the capillary tube. When the system is overcharged, the evaporation process was incomplete. This is due to the heat transfer medium (in this case refrigerant) is exceeded the optimum amount required to absorb the heat. Consequently, some refrigerant was returned to the compressor in liquid form while some refrigerant was evaporated in the pump-down tank just before entering the compressor. The heat absorbance process was occurred in the compressor with the heat source from the compressor body.

The same trend also appeared for R410a-PVE combination. However, the CW for R410a-PVE is consistent higher than R410a-POE. The effect of lubricant can be seen where POE delivers lower CW hence better lubrication than PVE. In contrast, the CW for R32-PVE is lower than R32-POE. The optimum charge is 350 g and applicable for both R32 combinations. Meanwhile, the maximum CW for R32 refrigerant combination with PVE and POE occurred at 375 and 400 g, respectively. Beyond these points, the overcharge behavior happened on the RAC system. The effect of different lubricants on the CW for R32 refrigerant is almost insignificant with some PVE data is shown higher than POE. However, the majority of the CW for PVE is lower than POE hence performs better compared to POE.

3.2 Cooling Performance

The cooling performance in the current study was evaluated by the refrigerant effect of the VCRS. RE was measured by the enthalpy difference at evaporator inlet and outlet. The comparison of RE for all refrigerant-lubricant combinations is shown in Fig. 4. The RE results showed similar trend at particular refrigerant type and combination with different lubricants. The RE is shown the highest value at the lowest refrigerant charge of 200 g. The RE was decreased with refrigerant charge. At 375 g and 400 g refrigerant charge, the slope of decrement for RE was slowly decreased. There is a slight increment with RE for R410a at 450 g charge. After that, the RE is almost constant. The effect of lubricant appeared on 450 g onwards for R410a where PVE shows better RE than POE. The range of RE for R410a shown between 160 and 200 kJ/kg. Meanwhile, the range of RE for R32 presented between 230 and 270 kJ/kg. The effect of different lubricant on RE for R32 refrigerant is insignificant and the results for RE are almost similar between the two lubricants. The optimum

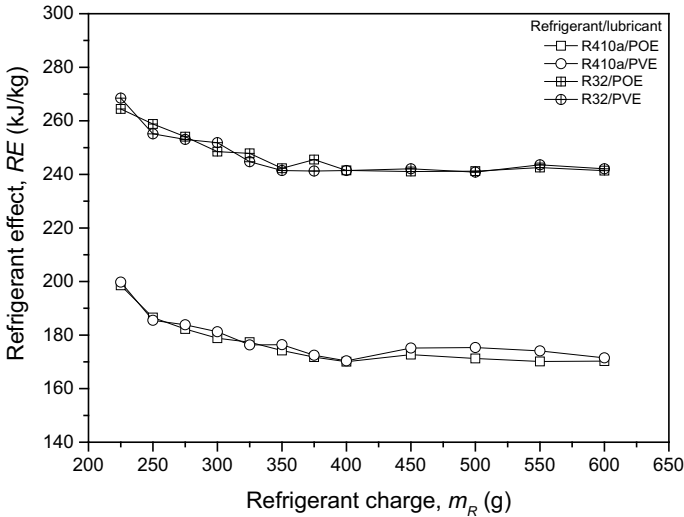


Fig. 4 Comparison of refrigerant effect at the different refrigerant-lubricant combination

refrigerant charge was recommended when the charge started to provide constant RE. Therefore, the optimum charge for R32 is proposed at 350 g charge while R410a is suggested at 400 g according to the RE outcomes.

3.3 Overall System Performance

In this paper, the RAC system performance was translated to the effect of variable parameters on the COP of the system. COP was calculated using Eq. 3 and plotted in Fig. 5. The COP is plotted from the lowest possible refrigerant charge (200 g) until the proposed optimum charge. For the case of R32, the experiment is undertaken until 375 g charge. From the analysis, the COP beyond this charge is not reliable. In general, the COP was increased with the refrigerant charge and reached the maximum at the optimum charge. The COP was decreased after the system overcharge. The R410a-PVE combination showed the lowest COP compared to other combinations. Meanwhile, R32-PVE presented the best performance at the lowest refrigerant charge. Overall, R32 performed better than R410a at all refrigerant charge for both PVE and POE lubricants combination. The effect of lubricant on COP is observed similar to the CW trend. Nevertheless, the POE performs better than PVE at the charge with maximum COP for all combinations.

The overall performance for the refrigerant-lubricant was compared in Fig. 6 with the best COP for each combination. The R410a-POE is the original combination for the RAC system in the present study. Therefore, the COP and refrigerant charge for the other three combinations are calculated and compared relative to R410a-POE.

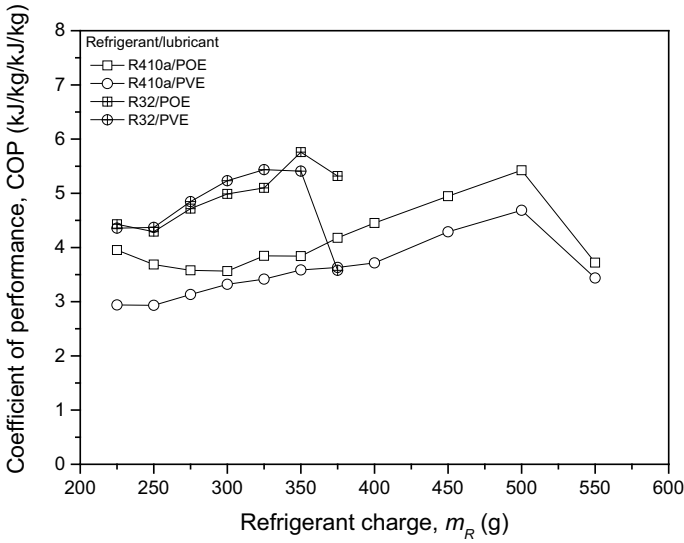


Fig. 5 Coefficient of performance for the different refrigerant-lubricant combination

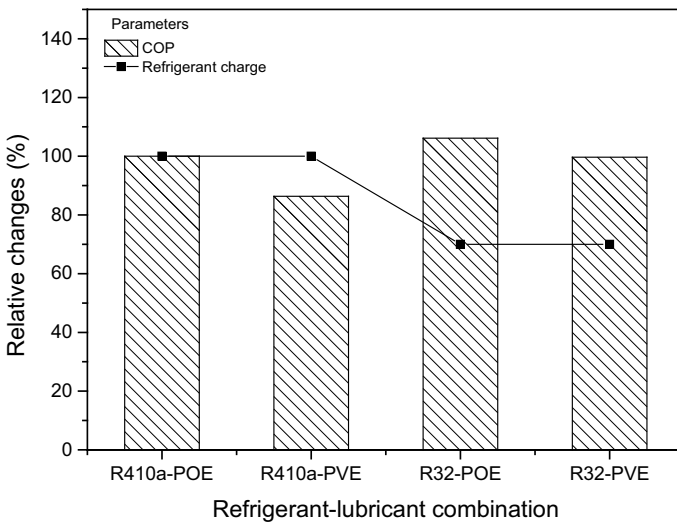


Fig. 6 Relative comparison of parameters at highest COP for all combinations

The COP of R410a-PVE performed with the lowest COP and nearly 14% lower than the original combination. Further, the R32-PVE mixture also showed lower than R410a-POE while the R32-POE attained COP improvement. Interestingly, the two combinations using R32 refrigerant showed reduction of the optimum refrigerant charge. The R32 only required 70% amount of refrigerant compared to R410a to

perform the optimum performance. Even though the POE performed better than PVE, the replacement of refrigerant from R410a to R32 was increased the COP of RAC system. From the present analysis, the POE was increased 6% while PVE up to 13%. The COP increment is due to the higher RE for the RAC system with R32 than R410a refrigerant. In addition, the heat capacity in R32 is also higher than R410a refrigerant. Therefore, R32 can absorb higher amount of heat in a unit of refrigerant than R410a.

4 Conclusions

The current study investigates the performance of R410a and R32 refrigerants with different lubricants. Four refrigerant-lubricant combinations were tested in an existing RAC system. A test rig with TCR was developed to study the performance of RAC system with different refrigerant-lubricant combinations in terms of compressor work (CW), refrigerant effect (RE), and coefficient of performance (COP). The optimum refrigerant charge was determined for R32 refrigerant at 350 g charge and performed at the maximum COP. The best combination performance was observed with R32-POE mixture and increased significantly up to 14% higher than the original refrigerant-lubricant of R410a-POE. The present RAC system with R32 refrigerant only requires 70% amount of refrigerant compared to R410a to perform the optimum performance. As a conclusion, R32 refrigerant is recommended as an alternative refrigerant to replace R410a refrigerant for RAC system and operated with POE lubricant as compressor lubricant.

Acknowledgements The authors are grateful to the Universiti Malaysia Pahang for financial supports given under RDU213302 and additional financial support under Postgraduate Research grant PGRS2003202. The authors also thank the research team from the Centre for Research in Advanced Fluid and Processes (Pusat Bendarir) and Advanced Automotive Liquids Laboratory (AALL), who provided insight and expertise that greatly assisted in the present research work.

References

1. Xu X, Hwang Y, Radermacher R (2013) Performance comparison of R410a and R32 in vapor injection cycles. *Int J Refrig-Rev Int Froid* 36(3):892–903
2. Marcucci Pico DF, da Silva LRR, Hernandez Mendoza OS, Bandarra Filho EP (2020) Experimental study on thermal and tribological performance of diamond nanolubricants applied to a refrigeration system using R32. *Int J Heat Mass Transf* 152:119493
3. Yajima R, Kita K, Taira S, Domyo N (2000) R32 as a solution for energy conservation and low emission
4. Ciconkov R (2018) Refrigerants: there is still no vision for sustainable solutions. *Int J Refrig* 86:441–448
5. Barve A, Cremaschi L (2012) Drop-in performance of low GWP refrigerants in a heat pump system for residential applications

6. Zhu Y, Wu XM, Zhao R (2017) R32 flow boiling in horizontal mini channels: part II flow-pattern based prediction methods for heat transfer and pressure drop. *Int J Heat Mass Transf* 115:1233–1244
7. Jia T, Bi SS, Wu JT, Li PY (2020) Solubilities of difluoromethane (R32) in polyol ester, polyvinyl ether, and polyalkylene glycol base oils at temperatures from 273 K to 351 K. *Int J Refrig* 111:63–70
8. Idemitsu Kosan CL (2020) Characteristics of Daphne hermetic oil. <https://www.idemitsu.com/business/lube/pve/daphne.html>. Accessed 01 Jan 2020
9. International Organization for Standardization I (2010) ISO 5151-2010 Non-ducted air conditioners and heat pumps—testing and rating for performance. International Organization for Standardization (ISO), Switzerland, p
10. Deymi-Dashtebayaz M, Farahnak M, Moraffa M, Ghalami A, Mohammadi N (2018) Experimental evaluation of refrigerant mass charge and ambient air temperature effects on performance of air-conditioning systems. *Heat Mass Transf* 54(3):803–812
11. Hamisa AH, Yusof TM, Azmi WH, Mamat R, Sharif MZ (2020) The stability of TiO₂/POE nanolubricant for automotive air-conditioning system of hybrid electric vehicles. In: IOP conference series: materials science and engineering, 1 ed. Institute of Physics Publishing, p 012050
12. Xu SX, Fan XS, Ma GY (2017) Experimental investigation on heating performance of gas-injected scroll compressor using R32, R1234yf and their 20wt%/80wt% mixture under low ambient temperature. *Int J Refrig-Rev Int Froid* 75:286–292

Micromechanical Modeling of Glass Filled Epoxy Using the Variational Asymptotic Method for Unit Cell Homogenization



Izzuddin Zaman , Nurul Jannah Mohammad, Bukhari Manshoor , and Amir Khalid 

Abstract Essentially, composite materials are formed by combining two or more constituents with different properties to obtain a new material with unique combination of features, thus has potential to provide value-added properties absent in one of the constituents. In this paper, the effects of glass particle size on mechanical properties of epoxy composite materials, such as stress, strain, and Young's modulus and its relationship with the particle volume fraction are investigated by using Finite Element Analysis of Ansys Mechanical APDL. A 2D micromechanics model based on variation asymptotic method for unit cell (VAMUCH) was employed for this study. The research study comprises of two cases: (1) the comparison of different size of glass particle filler from nano to micro size, and (2) the comparison of volume fraction of glass particle ranging from 5 to 25 vol% towards the mechanical properties of epoxy resin. The results of the first case study demonstrated that the stress and strain against gradient displacement is slightly increased for all modelling samples. In fact, the smallest area size particle of 7.85 nm^2 produces the highest value of Young's modulus 3.66 GPa. Similarly, for second case study, it is found that the highest Young's modulus 5.14 GPa was achieved at 10 vol% glass particles, which is about 91% increment compared to unfilled epoxy. Therefore, concludes that as the size of glass particle getting smaller from macro to nano size, and the volume fraction of glass to epoxy is lower, then the Young's modulus of composite increases.

I. Zaman (✉)

Mechanical Failure Prevention and Reliability Research Centre, Universiti Tun Hussein Onn Malaysia, 86400 Batu Pahat, Johor, Malaysia
e-mail: izzuddin@uthm.edu.my

N. J. Mohammad

Mega Label (Malaysia) Sdn. Bhd, Seksyen 34, 40470 Shah Alam, Selangor, Malaysia

B. Manshoor

Faculty of Mechanical and Manufacturing Engineering, University Tun Hussein Onn Malaysia, 86400 Parit Raja, Batu Pahat, Johor, Malaysia

A. Khalid

Faculty of Engineering Technology, Universiti Tun Hussein Onn Malaysia, 86400 Batu Pahat, Johor, Malaysia

Keywords Ansys APDL · Composite · Epoxy · Young's modulus · VAMUCH

1 Introduction

A composite material is made up from two or more different combination of materials to form a new material. The combination of metal with metal, metal with polymer, metal with ceramic, polymer with polymer or polymer with ceramic have capability to form composite material. In fact, from the combination of different material it can improve their physical, chemical and mechanical properties significantly as proven in our previous studies [1–5]. Generally, composite material consists of two major parts known as matrix and reinforcement (filler). Matrix is referred to the non-fiber phase of composite material which is functioning as binder and protector to the filler from any physical or external damages. In other words, matrix usually controls physical properties of the composite. On the other hand, reinforcement is the things that strengthening or encouraging the matrix behaviour. Thus, differences reinforcement used in composite material gives different properties and effects in the composite material in different ways [6, 7].

Epoxy resins known as thermosetting plastic are commonly used in an adhesive, paints, coating, medical implants and electrical devices [8, 9]. Besides, epoxy matrix in reinforcing fibrous composite has also become the most exclusive application in aircraft components, aerospace and wind turbine industries [10]. The reinforcing phase can be any of geometries or materials, and it can be categorized into three types: fibres, particles and flakes. One of the common reinforcements for epoxy is glass particles, which comes from glass materials that is basically contains of non-crystalline silica, sodium oxide, calcium oxide and other components. The different types of glass give different chemical composition based on their raw materials [11]. Recently with the increased knowledge and manufacturing technology, more new materials are fabricated to achieve better performance. Thus, an efficient tool such as finite element analysis (FEA) is required to predict their effective properties.

Finite element analysis or known as numerical analysis technique has been widely used by engineers and scientists to solve physical or non-physical problems [12–14]. In this work, finite element software of Ansys Mechanical APDL was used to model the epoxy composite reinforced glass particle. However, in Ansys, the most common approach in simulations of composite material are layered-shells, layered-solids and stacked solid elements, and none for particle-reinforcement type composite. Therefore, a new interface such as VAMUCH is obliged to be used with Ansys in order to provide better insight of the composite modelling. VAMUCH which acronym for variational asymptotic method for unit cell homogenization has been known as a code for implementing the various micromechanics theories based on the variational asymptotic method. VAMUCH takes a finite element mesh of the unit cell including all the geometry and material details as inputs to compute the effective properties [15, 16]. These properties are needed for the macroscopic analysis to predict the global behaviour of composite.

This paper investigates the effects of glass particle size and its volume fraction on the mechanical properties of epoxy composite using Ansys Mechanical APDL integrated with VAMUCH. The properties of Young’s modulus were determined from the stress and strain curved obtained from the analysis.

2 Methodology

Figure 1 illustrates the methodology flow chart of research study that was carried out in this work. Aforementioned, the simulation software used was Ansys integrated with VAMUCH. The specimen used was a combination of polymer epoxy as the matrix of composite and glass particle as reinforcement, by making appropriate assumptions regarding the kinematics of deformation or the stress conditions between the matrix and reinforcement. Both the mechanical properties of epoxy and glass particle are tabulated in Table 1.

Based on the flow chart, the first case study investigates the effect of size of glass particle which ranging from 0.0785 to 0.75 μm^2 , while the second case investigates the effect of volume fraction of glass particle from 0 to 25 vol%. The epoxy composition is based on the remaining volume fraction of the glass particles used. Figure 2 shows some part of meshing analysis that involved in the first and second case of studies.

Fig. 1 Research flow chart

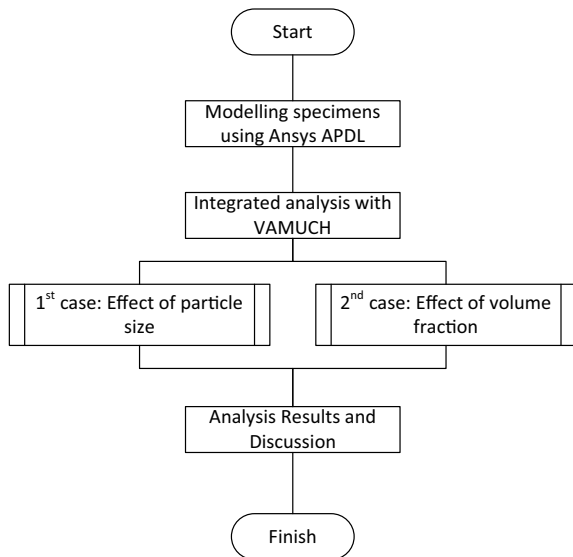


Table 1 Parameters applied for epoxy matrix and glass particle

Properties	Epoxy	Glass	Units
Young's modulus	3.01	76	GPa
Poisson ratio	0.35	0.23	–
Density	1100	2457.6	kg/m ³
Tensile strength	28	40	MPa
Compressive strength	104	50	MPa
Thermal conductivity	0.188	0.74976	W/mK

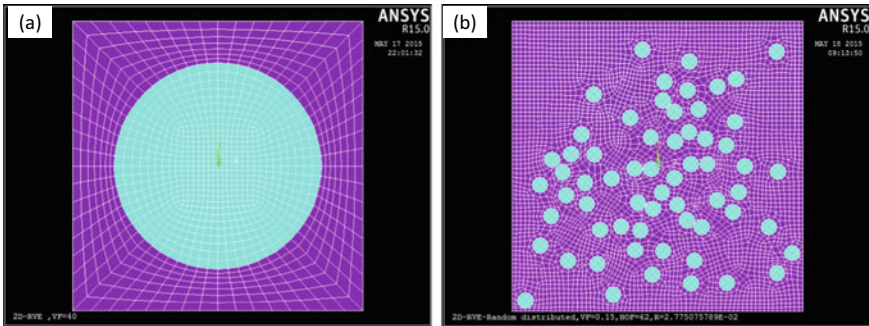


Fig. 2 Meshing model of (a) first case of unit cell, and (b) second case of random unit cell

3 Result and Discussion

3.1 Comparison of Different Size of Glass Particle

In this analysis, there were six different sizes of glass particle filler observed by two-dimensional unit cell. The smallest size of glass particle is in nano size dimension, which is 7.85 nm², and the remaining sizes were in micro dimension of 0.1, 0.2, 0.4 and 0.75 μm². The micromechanical analysis was conducted using Ansys APDL through the Vibrational Asymptotic Method for Unit Cell Homogenization (VAMUCH) to analyse and observe the relationship of the mechanical properties of epoxy composite filled glass such as stress and strain.

For stress and strain analysis, the Von Mises approach was selected to investigate the stress and strain distribution in the unit cell. Figures 3 and 4 show the contour plot of the respective stress and strain distribution obtained by different size of glass particle. Obviously, the glass particle sizes had a noticeable influence on the stress and strain mechanical properties of epoxy composites. It can be seen from Fig. 3 as the size of glass particle increases, the maximum stress (indicated by red colour) of glass particle decreases. It was found that the glass particle's mean stress is getting larger than the epoxy matrix when the size of particle getting smaller. Therefore,

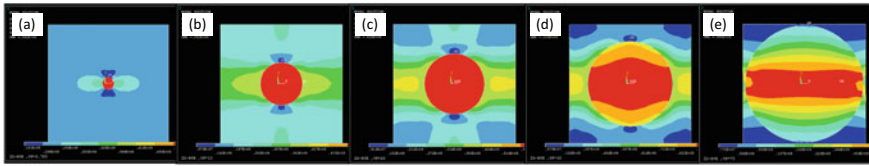


Fig. 3 Von Mises stress plot for (a) 7.85 nm², (b) 0.1 μm², (c) 0.2 μm², (d) 0.4 μm² and (e) 0.75 μm² of glass particle in epoxy composite

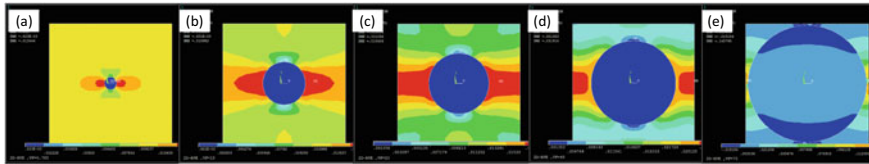


Fig. 4 Von Mises strain plot for (a) 7.85 nm², (b) 0.1 μm², (c) 0.2 μm², (d) 0.4 μm² and (e) 0.75 μm² of glass particle in epoxy composite

indicates that the load transfer to the particle from the matrix increases. This result clearly shows that the smaller size of glass particle can produce stronger material.

A similar trend was observed for Von Mises strain as illustrated in Fig. 4. With the reduction of glass particle size, the Von Mises strain increased and spread uniformly throughout the epoxy matrix. This can be explained by the increase of total contact surface of glass particle with reduction of particle size, thus resulted in large transfer load from the matrix to the particle [7, 17].

Figure 5 shows the relationship between stress and strain obtained by these epoxy composite reinforced glass samples. The highest stress-strain graph is obtained from 7.85 nm² glass particle, while the lowest is from 0.75 μm². Again, this result proved that the nanoparticle size of glass particle produces higher stress compared to micro or macro-particle size. The size of the nano fillers is also expected to play a crucial role on the types of toughening mechanisms operating in filled epoxy-based nanocomposites. From the stress–strain graph, the Young’s modulus of composites can be calculated, and the result is tabulated in Table 2. From this result, it shows that the glass particle with area size of 7.85 nm² displays the superior Young’s modulus value with 36% increment compared to neat epoxy.

3.2 Comparison of Volume Fraction of Glass Particle

Figure 6 illustrates the contour plot of Von Mises stress distribution of different volume fraction of glass particle within the epoxy matrix. As the volume fraction of glass particle increases, the distance and interaction between the particles become

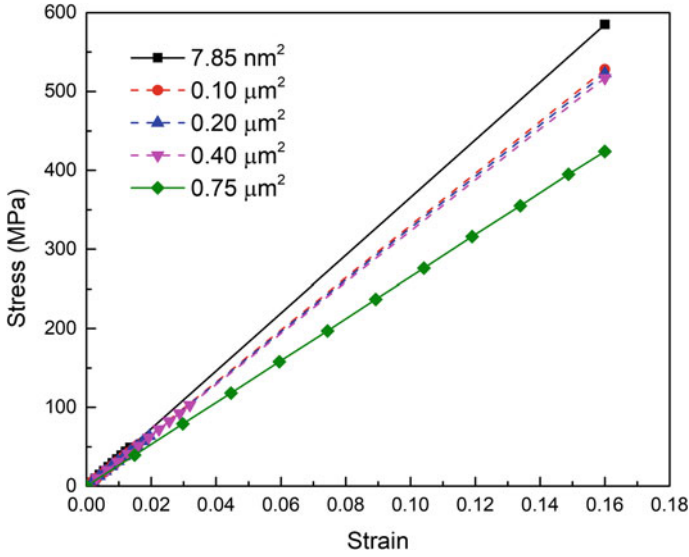


Fig. 5 Effect of glass particle sizes on stress-strain relationship of epoxy composites

Table 2 Young’s modulus of neat epoxy and epoxy filled glass composite with different size of glass particle

Sample	Size of glass particle	Young’s modulus (GPa)
Neat epoxy [18]	–	2.69
Glass particle filled epoxy composite	7.85 nm ²	3.66
	0.1 µm ²	3.30
	0.2 µm ²	3.27
	0.4 µm ²	3.23
	0.75 µm ²	2.65

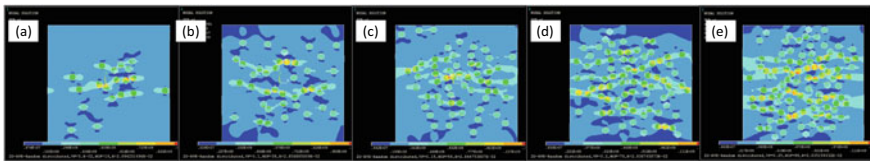


Fig. 6 Von Mises stress plot for (a) 5 vol%, (b) 10 vol%, (c) 15 vol%, (d) 20 vol% and (e) 25 vol% of glass particle in epoxy composite

dense. It demonstrates that the stress concentration become higher (as shown by red and yellow collar), thus effect to the lower stress produced globally in the sample.

Meanwhile, Fig. 7 shows the contour plot of Von Mises strain of glass particle with different volume fraction. Obviously, it shows that the strain region is higher

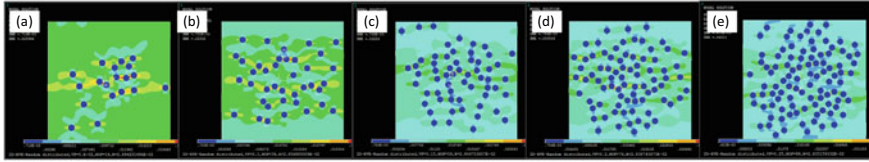


Fig. 7 Von Mises strain plot for (a) 5 vol%, (b) 10 vol%, (c) 15 vol%, (d) 20 vol% and (e) 25 vol% of glass particle in epoxy composite

(indicated by green color) in low volume fraction and start decreasing as the volume fractions increase. This result indicates that when a similar stress value imposed on the sample, the smaller volume fraction of glass particle will display a smaller elongation of epoxy composite.

Figure 8 displays the relationship between stress and strain for different volume fraction of glass particle filled epoxy composites. It can be observed that sample epoxy with 10 vol% glass particle shows the highest stress-strain value compared to other vol%. The Young's modulus results obtained from stress-strain graph of each sample are translated in Table 3. The result clearly shows that the Young's modulus of epoxy increased with the reinforcement glass particle. However, as the glass particle reaches the optimum value at 10 vol%, the Young's modulus starts to decrease until 25 vol%. According to Fu [19], the decrement of Young's modulus after exceeding 10% volume fraction of glass particle filler may be caused by poor

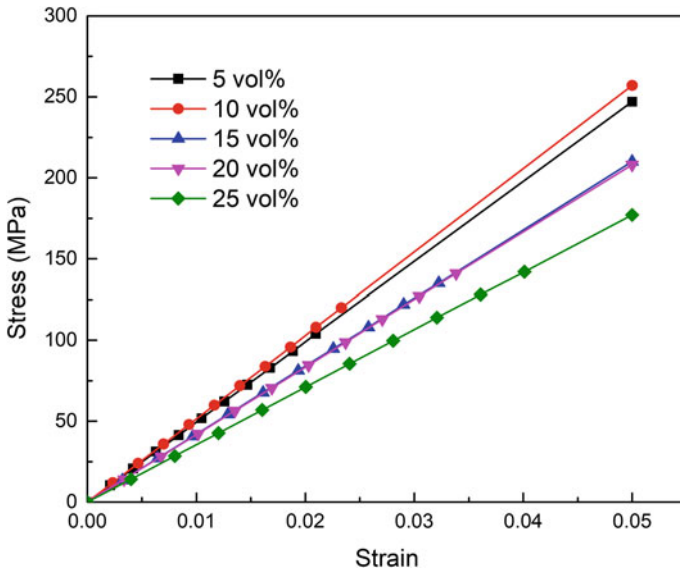


Fig. 8 Effect of volume fraction of glass particle on stress-strain relationship of epoxy composites

Table 3 Young's modulus of neat epoxy and epoxy filled glass composite with different volume fraction of glass particle

Sample	Volume fraction of glass particle (vol%)	Young's modulus (GPa)
Neat epoxy [18]	–	2.69
Glass particle filled epoxy composite	5	4.94
	10	5.14
	15	4.19
	20	4.17
	25	3.54

interfacial bonding between the particle and matrix. This is also agreed well in our previous finding in Refs. [6, 18].

4 Conclusion

In the nutshell, the purpose of this work was to investigate the effect of: (1) glass particle size and (2) its volume fraction on the mechanical properties of Young's modulus of epoxy composite. The research was conducted by using a commercial finite element software namely Ansys Mechanical APDL, integrated with variation asymptotic method for unit cell (VAMUCH). From the first case study, the result indicated the smallest area size of glass particle, 7.85 nm^2 produces the highest Young's modulus of 3.66 GPa. This result proves the fundamental theory of nanoparticle; whereby glass nanoparticle imposed higher Young's modulus than micro- and macro-size particle. On the other hand, for the second case, the highest Young's modulus obtained was at 10 vol% glass particles with 91% increment compared to neat epoxy.

Acknowledgements This research was supported by Ministry of Higher Education (MOHE) through Fundamental Research Grant Scheme (FRGS/1/2020/TK0/UTHM/02/24). We also want to acknowledge the Faculty of Mechanical and Manufacturing Engineering at the Universiti Tun Hussein Onn Malaysia (UTHM) for the use of their lab facilities and support.

References

1. Zaman I, Nor FM, Manshoor B, Khalid A, Araby S (2015) Influence of interface on epoxy/clay nanocomposites: 2. Mechanical and thermal dynamic properties. *Procedia Manuf* 2:23–27
2. Zaman I, Nor FM, Manshoor B, Khalid A, Araby S (2015) Influence of interface on epoxy/clay nanocomposites: 1. Morphology structure. *Procedia Manuf* 2:17–22

3. Karim MAA, Zaman I, Rozlan SAM, Berhanuddin NIC, Manshoor B, Mustapa MS, Khalid A, Chan SW (2017) Structural characterization and mechanical properties of polypropylene reinforced natural fibers. *J Phys Conf Ser* 914(1):012035
4. Berhanuddin NIC, Zaman I, Rozlan SAM, Karim MAA, Manshoor B, Khalid A, Chan SW, Meng Q (2017) Enhancement of mechanical properties of epoxy/graphene nanocomposite. *J Phys Conf Ser* 914(1):012036
5. Che Berhanuddin NI, Mohd Rozlan SA, Zaman I, Mustapa MS, Abdullah MS, Bahrudin IA (2017) Effect of thermal expansion and sonication on mechanical properties and adhesive toughness measurement of polymer/graphene composite. *Mater Sci Forum* 889:14–18
6. Zaman I, Manshoor B, Khalid A, Meng Q, Araby S (2014) Interface modification of clay and graphene platelets reinforced epoxy nanocomposites: a comparative study. *J Mater Sci* 49(17):5856–5865
7. Zaman I, Manshoor B, Khalid A, Araby S (2014) From clay to graphene for polymer nanocomposites—a survey. *J Polym Res* 21(5):429
8. Pascual-Sanchez V, Martin-Martinez JM (2006) Influence of the curing temperature in the mechanical and thermal properties of nanosilica filled epoxy resin coating. *Macromol Symp* 233:137–146
9. Meng Q, Zaman I, Hannam JR, Kapota S, Luong L, Youssf O, Ma J (2011) Improvement of adhesive toughness measurement. *Polym Testing* 30:243–250
10. Garces JM, Moll DJ, Bicerano J, Fibiger R, McLeod DG (2000) Polymeric nanocomposites for automotive applications. *Adv Mater* 12:1835–1839
11. Jones JR (2015) Reprint of: review of bioactive glass: from Hench to hybrids. *Acta Biomater* 23:S53–S82
12. Rozlan SAM, Zaman I, Chan SW, Manshoor B, Khalid A, Sani MSM (2017) Study of a simply-supported beam with attached multiple vibration absorbers by using finite element analysis. *Adv Sci Lett* 23(5):3951–3954
13. Hou TY, Wu X-H (1997) A multiscale finite element method for elliptic problems in composite materials and porous media. *J Comput Phys* 134(1):169–189
14. Salleh MM, Zaman I (2016) Finite element modelling of fixed-fixed end plate attached with vibration absorber. *ARPN J Eng Appl Sci* 11(4):2336–2339
15. Tang T, Yu W (2007) A variational asymptotic micromechanics model for predicting conductivities of composite materials. *J Mech Mater Struct* 2(9):1813–1830
16. Yu W, Tang T (2007) A variational asymptotic micromechanics model for predicting thermoelastic properties of heterogeneous materials. *Int J Solids Struct* 44(22–23):7510–7525
17. Wiacek J, Parafiniuk P, Stasiak M (2017) Effect of particle size ratio and contribution of particle size fractions on micromechanics of uniaxially compressed binary sphere mixtures. *Granular Matter* 19(2):34
18. Zaman I, Le Q, Kuan HC, Kawashima N, Luong L, Gerson A, Ma J (2011) Interface-tuned epoxy/clay nanocomposites. *Polymer* 52:497–504
19. Fu Q, Rahaman MN, Bal BS, Brown RF, Day DE (2008) Mechanical and in vitro performance of 13–93 bioactive glass scaffolds prepared by a polymer foam replication technique. *Acta Biomater* 4(6):1854–1864

Finite Element Analysis of Tuned Mass Damper



Izzuddin Zaman , Bukhari Manshoor , Amir Khalid ,
and Shiau Wei Chan

Abstract The idea of a tuned mass damper emerges due to a common vibration problem existed in mechanical and civil structures applications. Vibration turns out to be a hazard that can reduce the life of the structure, thus tuned mass damper is considered as one of the most practical methods in the engineering branches since it can be used as vibration attenuator. The present paper investigated the design of tuned mass damper (TMD) to reduce the vibration amplitude of a building structure model. In the initial stage, the frequency of the building model and tuned mass damper were determined by using the theoretical equations. This is followed by the finite element modal analysis to determine the natural frequency and mode shape and then compared with the calculation. It was found that the percentage error of natural frequency between the theoretical and the simulation result was less than 15% for building model (without tuned mass damper) and 2% for building model with attached tuned mass damper. The simulation analysis was further carried out by utilizing tuned mass damper to suppress vibration on the building model when subjected to a 10 N force. The results demonstrated that the attachment of TMD on the building model could significantly reduce the vibration amplitude by more than half.

Keywords Natural frequency · Tuned mass damper · Vibration amplitude

I. Zaman (✉)

Mechanical Failure Prevention and Reliability Research Centre, Universiti Tun Hussein Onn Malaysia, 86400 Batu Pahat, Johor, Malaysia
e-mail: izzuddin@uthm.edu.my

B. Manshoor

Faculty of Mechanical and Manufacturing Engineering, Universiti Tun Hussein Onn Malaysia, 86400 Batu Pahat, Johor, Malaysia

A. Khalid

Faculty of Mechanical and Manufacturing Engineering, University Tun Hussein Onn Malaysia, 86400 Parit Raja, Batu Pahat, Johor, Malaysia

S. W. Chan

Faculty of Technology Management and Business, Universiti Tun Hussein Onn Malaysia, 86400 Batu Pahat, Johor, Malaysia

1 Introduction

The mechanical motion that results through the development of unpredictable period of a part or body from its resting function is known as vibration. Vibration can be a supply problem in the early stages of engineering due to its effect which can reduce the operating performance in the machine. Even at low levels, vibration can also cause pain, and while at high levels, it can cause structural failure and uncomfortable sound in the receiver that can eventually lead to disaster and hearing damage [1, 2].

Generally, every mechanical structure will have a tendency to oscillate with large amplitude at a certain frequency. Typically, this frequency is known as the resonance frequency or natural frequency of the structure. At this resonant frequency, even a small periodic driving force can also produce vibrations of large amplitude. When resonance occurs, the structure will begin to vibrate excessively and will eventually cause failure on the structure [3].

Therefore, to reduce vibration, vibration control has to be implemented to lessen the vibration amplitude and keep away from resonance frequency. Vibration handling in mechanical structures is important where vibrations are suppressed [4, 5]. The tuned mass damper (TMD) is one of the most well-known devices because of its simple design concept that is used to regulate the behavior of mechanical structures that subjected to vibration excitation. It is also considered as a passive control which consist of a mass and spring that attached to a structure as a way to lessen the dynamic reaction of the structure [6–8].

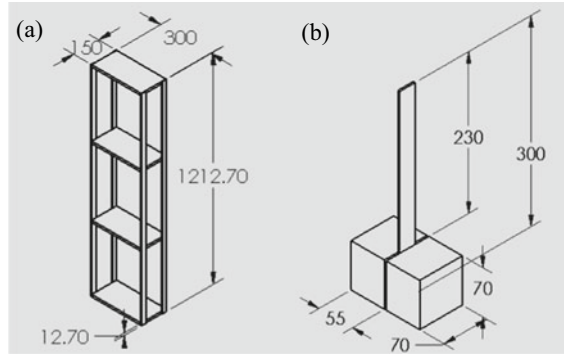
In general, vibration control of structures can be divided into passive, active and semi-active [9], where passive control devices do not require any external electricity source for lowering the structural vibrations, while in active control, it requires external electricity source. The semi-active control also known as hybrid systems require less external energy source in comparison with active control. In these systems, both damping coefficient and structural stiffness vary through applied force [10].

There are several strategies used in dealing with vibration control. A common method of eliminating vibration is by including tuned mass damper into the structural system. In this study, a passive tuned mass damper was selected to be examined in which the amount of reduced vibration of building structure model would be determined through finite element analysis using Ansys Workbench. Prior to this finite element analysis, a theoretical framework on the passive tuned mass damper was developed and its feasibility to reduce vibration was investigated.

2 Design Modelling and Analysis

For design modeling, SolidWorks (CAD) software was selected to draw models of three-story building structure and tuned mass damper before these models were

Fig. 1 a Three-storey building model and **b** Pendulum-type TMD



exported into the Ansys Workbench for simulation analysis. Fig. 1a shows a prototype model of a three-storey building consisting of a rigid floor erected through 4 deformable columns as it reflects the actual structural building.

For vibration control, a pendulum type of tuned mass damper as illustrated in Fig. 1b was designed. The design consists of two mass blocks and a column with a length of 300 mm. The measurement shown in Fig. 1a and b is in mm, and the entire structure is made of aluminium with a density of 2700 kg/m³. Both designs were converted into IGES format before being exported into Ansys Workbench.

In this research, the modal analysis and harmonic analysis were conducted to determine the natural frequency and vibration amplitude of the building model with and without attached tuned mass damper. The detail procedures of these analysis are shown in the following sub-section.

2.1 Modal Analysis in Ansys Workbench

Here, the modal analysis was used to determine the dynamic characteristics such as natural frequency and mode shapes of building model, tuned mass damper and building with attached tuned mass damper. To begin with, the “Modal” from the Analysis System was selected and dragged onto the project schematic. After the IGES format was imported into Ansys Workbench in the Design Modeler window, the material was appointed for each design (refer Fig. 2a) followed by setting the initial condition, such as fixed support (refer Fig. 2b). For meshing part, the hexahedron element was chosen with the element size of 10 mm (refer Fig. 2c).

2.2 Harmonic Analysis in Ansys Workbench

The harmonic analysis was used in extension to modal analysis to determine the response of the three-storey building to excitation at specific frequency. The

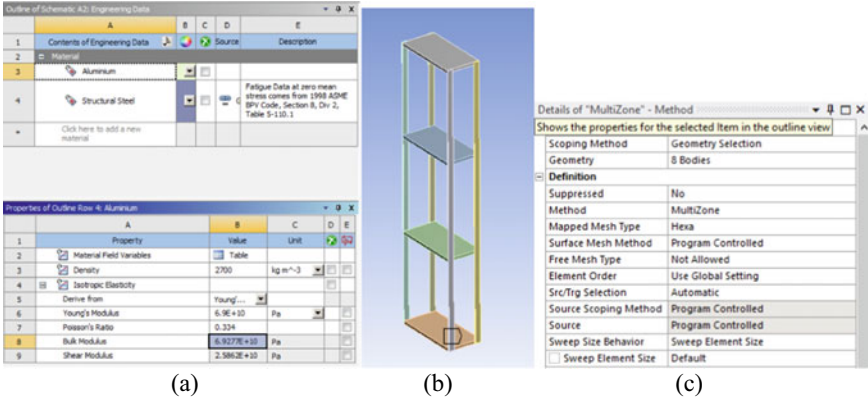
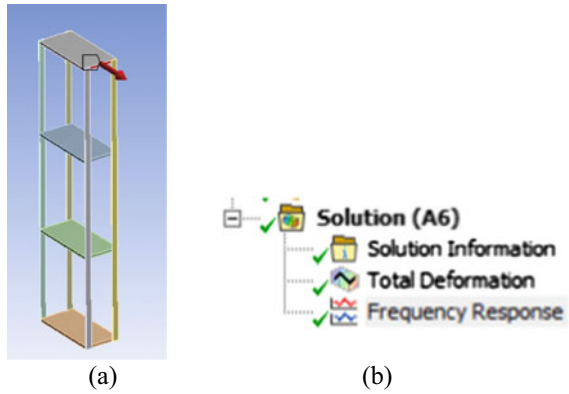


Fig. 2 Procedure running modal analysis in ansys workbench

“Harmonic” from the Analysis System was selected and dragged onto the project schematic, which later used to connect with “Modal”. Similar to modal analysis, initial conditions such as fixed support were set and 10 N force in horizontal direction was added to the above tip of the building model (refer to Fig. 3a). Later, the frequency response was added to analyze the vibration response of the system (refer Fig. 3b).

Fig. 3 Procedure of harmonic analysis in ansys workbench



3 Theoretical Equation

3.1 Three-Storey Building Model

Figure 4 shows a simplified primary mass-spring model of a three-storey building with mass m_1 and elasticity constant k_1 . A harmonic force F_o is exerted on the primary structure. The tuned mass damper is labelled as mass m_2 and stiffness k_2 attached to primary structure the act as the medium to absorb vibration of the structure.

Derivation of equation of motion masses m_1 and m_2 is given as follows [11]:

$$\begin{bmatrix} m_1 & 0 \\ 0 & m_2 \end{bmatrix} \begin{Bmatrix} \ddot{x}_1 \\ \ddot{x}_2 \end{Bmatrix} + \begin{bmatrix} (k_1 + k_2) & -k_2 \\ -k_2 & k_2 \end{bmatrix} \begin{Bmatrix} x_1 \\ x_2 \end{Bmatrix} = \begin{Bmatrix} F_0 \\ 0 \end{Bmatrix} \tag{1}$$

By writing matrix equation in terms of maximum displacement amplitude x for each respective mass to get:

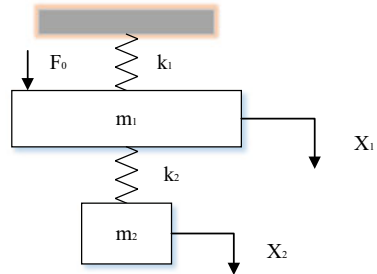
$$\begin{bmatrix} -m_1(\omega_1)^2 + (k_1 + k_2) & -k_2 \\ -k_2 & m_2(\omega_2)^2 + k_2 \end{bmatrix} \begin{Bmatrix} x_1 \sin \omega_1 t \\ x_2 \sin \omega_2 t \end{Bmatrix} = \begin{Bmatrix} F_0 \sin \omega_1 t \\ 0 \end{Bmatrix} \tag{2}$$

where ω_1 and ω_2 is the respective natural frequency of building model and TMD.

$$\omega_1 = \sqrt{\frac{k_1}{m_1}} \tag{3}$$

$$\omega_2 = \sqrt{\frac{k_2}{m_2}} \tag{4}$$

Fig. 4 Simplified mass-spring model of a three-storey building with attached TMD



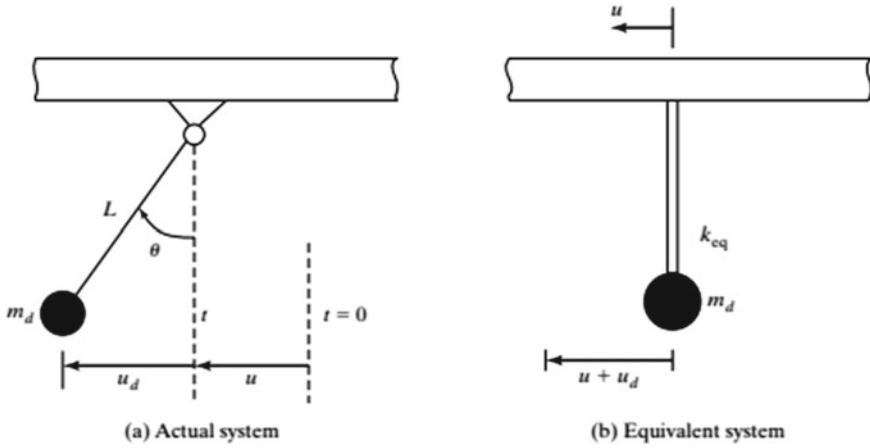


Fig. 5 A simple pendulum tuned mass damper

3.2 Tuned Mass Damper

The equation of motion for the tuned mass damper can be derived from simplified model shown in Fig. 5, where the equation is given in Eq. (5):

$$m_d \ddot{u}_d + \frac{W_d}{L} u_d = -m_d \ddot{u} \tag{5}$$

And it follows that the equivalent shear spring stiffness is:

$$k_{eq} = \frac{W_d}{L} \tag{6}$$

The first natural frequency of the pendulum is related by [12]:

$$\omega_d^2 = \frac{k_{eq}}{m_d} = \frac{g}{L} \tag{7}$$

4 Results and Discussion

4.1 Modal Analysis

A dynamic characteristic such as the first five natural frequency and mode shapes of three-storey building model, TMD and building model with attached TMD was determined using finite element analysis of Ansys Workbench. For theoretical modelling,

only the first natural frequency was determined as been demonstrated in Sect. 3. Table 1 tabulates the results of natural frequencies obtained from these approaches. It shows that these approaches corroborated well, although there is a small discrepancy less than 15% found in the building model. Based on this outcome, it is found that vibration attenuation for the building model can be cancelled by attaching TMD since the resonance frequency of TMD is approximated to the first natural frequency of three-storey building [13].

Meanwhile, the mode shape of the first natural frequency of three-storey building, TMD and building with attached TMD are displayed in Fig. 6. The result shows that all the model having a first buckling mode, where the maximum deformation occurs in the area opposite to fixed support area.

Table 1 Theoretical and simulation natural frequency

Mode	3-storey building		TMD		Building with TMD	
	Theory	Simulation	Theory	Simulation	Theory	Simulation
1	2.60	2.98	3.20	3.24	2.35	2.40
2	–	8.51	–	16.98	–	7.12
3	–	11.97	–	26.96	–	10.64
4	–	18.42	–	33.32	–	13.18
5	–	27.66	–	290.27	–	14.28

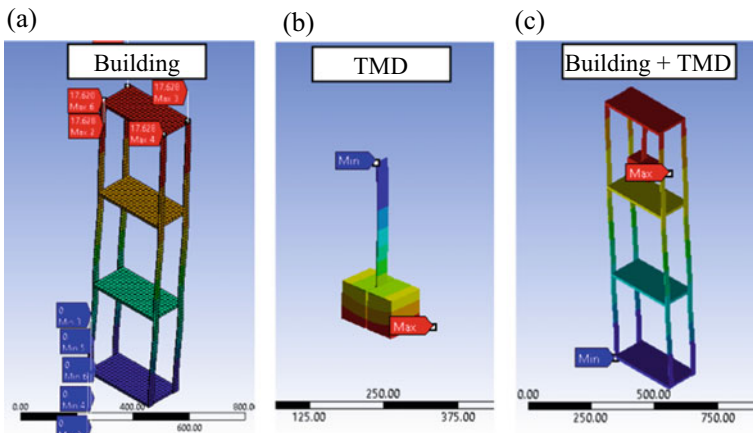


Fig. 6 First mode shape of **a** building, **b** TMD and **c** building with attach TMD models

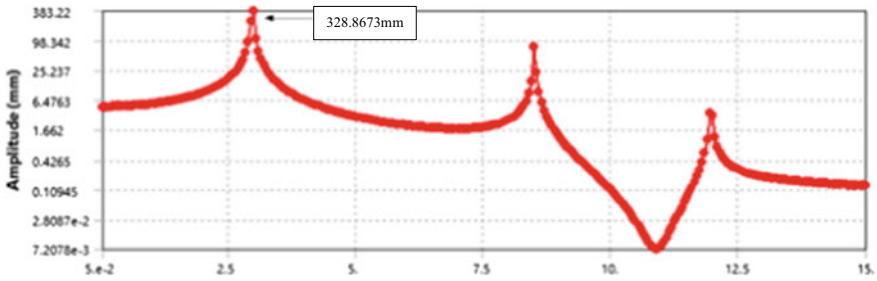


Fig. 7 Frequency response function of three-storey building model

4.2 Harmonic Analysis

The frequency response function (FRF) of a three-storey building as illustrated in Fig. 7 was determined over the frequency range of 0–15 Hz with a step size of 0.1 Hz. Within this range, three frequency modes are observed as proved from modal analysis as shown in Table 1, where the maximum amplitude of vibration ~329 mm occurred at the first natural frequency of 2.98 Hz.

The next stage of analysis incorporates the attachment of TMD on three-storey building. The TMD’s resonance frequency is tuned as closed as possible to the first fundamental frequency of the building model at 2.98 Hz in order to suppress the vibration. Fig. 8 show the result of the frequency response function of three-storey building model with attached TMD. Obviously, the result shows that by attaching TMD onto the building creates four frequency modes over the frequency range of 0–15 Hz. This result correlates well with our previous study which showed that the adding of absorber caused new natural frequency to form on the system [11]. On top of that, the natural frequencies of the new system also reduced slightly as the additional mass of TMD to the system [14, 15]. Table 2 tabulates the percentage vibration reduction of building model with and without attach TMD. It was found that almost 56% vibration reduction achieved at the first frequency mode followed by 47% at

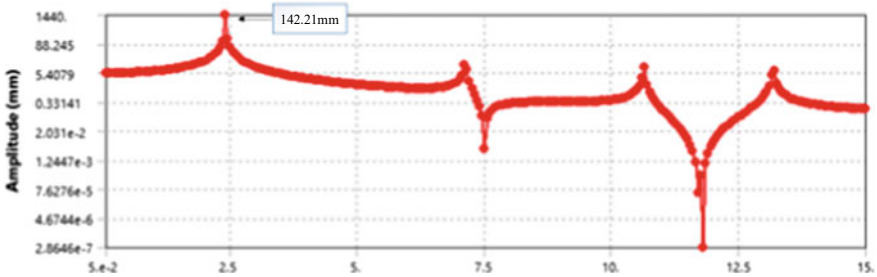


Fig. 8 Frequency response function of three-storey building model with attached TMD

Table 2 Vibration reduction percentage with TMD attachment

Frequency mode	Vibration of building model (mm)	Vibration of building model with attached TMD (mm)	Reduction (%)
1	328.87	142.21	56.8
2	15.00	7.94	47.1

the second frequency mode of building model. The result clearly demonstrated that TMD performs effectively when attached to building model to lessen the vibration.

5 Conclusion

The dynamic characteristic of three-storey building with and without attached tuned mass damper was successfully prepared in this study. The preliminary result of modal analysis from finite element analysis of Ansys showed in agreement with theoretical equation with error less than $\pm 15\%$ for the first natural frequency. From subsequent harmonic analysis, the structural vibration of the three-storey building was found decrease with tuned mass damper attachment from 328.87 to 142.21 mm, which is about $\sim 57\%$ reduction. The study reveals that tuned mass damper attached to a building model proved to be effective approach in vibration suppression.

Acknowledgements This research was supported by Ministry of Higher Education (MOHE) through Fundamental Research Grant Scheme (FRGS/1/2020/TK0/UTHM/02/24). We also want to acknowledge the Faculty of Mechanical and Manufacturing Engineering at the Universiti Tun Hussein Onn Malaysia (UTHM) for the use of their lab facilities and support.

References

1. Qatu MS, Abdelhamid MK, Pang J, Sheng G (2009) Overview of automotive noise and vibration. *Int J Veh Noise Vib* 5:135
2. Griffin M (2004) Minimum health and safety requirements for workers exposed to hand-transmitted vibration and whole-body vibration in the European Union; a review. *Occup Environ Med* 61(5):387–397
3. Zaman I, Khalid A, Manshoor B, Araby S, Ghazali MI (2013) The effects of bolted joints on dynamic response of structures. *IOP Conf Ser: Mater Sci Eng* 50(1):012018
4. Hao KY, Mei LX, Ripin ZM (2011) Tuned vibration absorber for suppression of hand-arm vibration in electric grass trimmer. *Int J Ind Ergon* 41(5):494–508
5. Zahari SN, Sani MSM, Husain NA, Ishak M, Zaman I (2016) Dynamic analysis of friction stir welding joints in dissimilar material plate structure. *J Teknologi* 78(6–9):57–65
6. Zaman I, Tobi ALM, Manshoor B, Khalid A, Amin NAM (2016) New approach of dynamic vibration absorber made from natural fibres composite. *ARPJ Eng Appl Sci* 11(4):2308–2313
7. Salleh MM, Zaman I (2016) Finite element modelling of fixed-fixed end plate attached with vibration absorber. *ARPJ Eng Appl Sci* 11(4):2336–2339

8. Zaman I, Salleh MM, Ismon M, Manshoor B, Khalid A, Sani MSM, Araby S (2014) Vibration attenuation of plate using multiple vibration absorbers. *MATEC Web of Conf* 13:03003
9. Wright RI, Kidner MRF (2004) Vibration absorbers: a review of applications in interior noise control of propeller aircraft. *J Vib Control* 10:1221–1237
10. Koo JH, Ahmadian M, Setareh M, Murray TM (2004) In search of suitable control methods for semi-active tuned vibration absorbers. *J Vib Control* 10:163174
11. Zaman I, Salleh MM, Manshoor B, Khalid A, Ngali MZ, Sani MSM (2015) Theoretical modelling of plate with attached vibration absorber. *Appl Mech Mater* 773–774:33–37
12. Amezcua-Sanchez JP, Dominguez-Gonzalez A, Sedaghati R, de Jesus Romero-Troncoso R, Osornio-Rios RA (2012) Vibration control on smart civil structures: a review. *Mech Adv Mater Struct* 21(1):23–38. <https://doi.org/10.1080/15376494.2012.677103>
13. Zaman I, Salleh MM, Manshoor B, Khalid A, Araby S (2014) The application of multiple vibration neutralizers for vibration control in aircraft. *Appl Mech Mater* 629:191–196
14. Alujević N, Tomac I, Gardonio P (2012) Tuneable vibration absorber using acceleration and displacement feedback. *J Sound Vib* 331(12):2713–2728
15. Zaman I, Salleh MM, Ismon M, Manshoor B, Khalid A, Sani MSM, Araby S (2014) Study of passive vibration absorbers attached on beam structure. *Appl Mech Mater* 660:511–515

Comparison of Frequency Levels in Internal Combustion Engines Using a Gasoline-Methanol Fuel Blend



Erdiwansyah , Husni Husin, Fitri Khoerunnisa, Asri Gani, R. E. Sarjono, Rizalman Mamat, Mohd Fairusham Ghazali, S. M. Rosdi, and Bukhari Manshoor

Abstract Investigations of the frequency and vibration levels of the internal combustion engine have been intensively carried out to minimize and make the driver comfortable. This experiment was mostly done by changing engine materials and also testing various suitable fuels. In the last few decades, the analysis of the frequency of internal combustion engines has been carried out by making mixtures of alcohol fuels and fuel additives. The purpose of this work is specifically to analyze the frequency level comparison in an internal combustion engine using a petroleum-methanol fuel mixture (G95%-M5% and G100). The experiment in this test was tested five times with engine speed (1000 rpm, 15,000, 2000, 2500, and 3000 rpm). The test results show that the mixed fuel can produce a lower combustion frequency. However, the burning speed is slightly slower than that of pure petroleum fuels. While pure petroleum fuel has a burning speed so that the level of vibration frequency produced is slightly high. Overall shows that the fuel mixture applied in this work can reduce the level of vibration frequency in the internal combustion engine.

Erdiwansyah (✉)

Faculty of Engineering, Universitas Serambi Mekkah, Banda Aceh 23245, Indonesia

e-mail: erdi.wansyah@yahoo.co.id

H. Husin · A. Gani

Department of Chemical Engineering, Universitas Syiah Kuala, Banda Aceh 23111, Indonesia

F. Khoerunnisa · R. E. Sarjono

Department of Chemistry, Faculty of Mathematics and Science, Indonesia University of Education, Bandung 40522, Indonesia

R. Mamat · M. F. Ghazali

Centre for Research in Advanced Fluid & Processes, Universiti Malaysia Pahang, Lebuhraya Tun Razak, 26300 Gambang, Kuantan, Pahang, Malaysia

S. M. Rosdi

Politeknik Sultan Mizan Zainal Abidin, 23000 Dungun, Terengganu, Malaysia

B. Manshoor

Faculty of Mechanical and Manufacturing Engineering, University Tun Hussein Onn Malaysia, 86400 Parit Raja, Batu Pahat, Johor, Malaysia

© The Author(s), under exclusive license to Springer Nature Singapore Pte Ltd. 2023

291

N. H. Johari et al. (eds.), *Proceedings of the 2nd Energy Security and Chemical*

Engineering Congress, Lecture Notes in Mechanical Engineering,

https://doi.org/10.1007/978-981-19-4425-3_26

Keywords Lever of frequency · Combustion · Fuel blend · G95-M5 · Gasoline

1 Introduction

Today's increasingly sophisticated technology continues to encourage various companies in the world to create various driver comforts, especially for four-wheeled vehicles or better known as cars. Various ways have been done to reduce the level of vibration frequency while driving. Many ways can be done to reduce the frequency of vibrations in vehicles, such as changing materials to fuel. The process of the fuel mixture used for vehicles has been carried out by previous researchers [1–5]. Research on various combustion experiments applied to internal combustion engines most frequently done before [6–10].

Research to investigate low-frequency vibrations of micro-amplitude has the same effect especially on metal deformation [3, 11]. Investigation of the appropriate vibration amplitude and frequency on the CI machine can lead to the knocking phenomenon as reported by Mridha [12]. An experiment with a single point of time-frequency analysis on the vibration of the LPG-diesel engine block has been carried out [13]. Vibration analysis in machines is one of the most powerful technologies for condition-based maintenance [14]. An investigation into the resistance of the power inside the engine has been reported by Qawqzeh et al. [15]. The characteristics of engine combustion are one of the moving components that can produce noise and vibration in the engine. However, the level of vibration generated depends on parameters such as fuel type, engine load, engine speed, spark time, etc. [16–18].

Methanol fuel has advantages, especially in internal combustion (CI) engines. The advantages of this methanol fuel as the results of the research reported by [19]. Their research makes gasoline-methanol mixture fuel through a manual stirring process and left for 24 h in a closed condition. Methanol-gasoline fuel mixture with a ratio of M5, M10, M15, and M20 which was tested on a small spark ignition (SI) engine has also been carried out [20–22]. The results of the tests carried out show that the performance and emissions of the SI engine are low. This can be done by increasing the methanol ratio in the fuel mixture under all experimental conditions.

Experiments on the internal combustion engine tested in this study are specific to analyze the ratio of the frequency levels when petroleum fuel is mixed with methanol. The fuel mixture used in this test is G95%-M5%. The mixed fuel was tested five times at an engine speed of 1000–3000 rpm with 500 rpm intervals. The specific purpose of this work is to analyze the frequency level in the engine when using a gasoline-methanol mixture at different engine speeds. The results of each subsequent test are compared with pure petroleum.

Table 1 Specifications of Engine

Descriptions engine	
Engine type	Mitsubishi 4G93 SOHC
Compression ratio	9.5:1
Number of cylinders	4 (1st cylinder is instrumented)
Fuel injection type	MCI-Multi (electronically controlled multi-pint) fuel injection
Max power	86 kw @ 5500 rpm
Max torque	161 nm @ 4500 rpm
Bore stroke	81.0 mm × 89.0 mm
Piston displacement	1.834L

2 Experimental Setup and Material

This experiment was tested on Mitsubishi 4G93 SOHC four-cylinder and piston engine 1.834L. The specification of the test machine is shown in Table 1. Vibration pressure on the spark plug using a machine-adjusted sensor then combined amplifier device to analyze the combustion system for pressure measurement on the cylinder with 200 combustion cycles continues until the test is completed. This study used a single zone heat-release method.

The fuel mixture used in this test is gasoline and methanol. The ratio of the fuels in the mixture is gasoline (G95%) and methanol (M5%). The results of the analysis of the applied mixture will be compared with the results of pure gasoline (G100%). The experiment was carried out five times at different speeds (1000, 1500, 2000, 2500, and 3000 rpm). While the schematic diagram used in this work is shown in Fig. 1.

3 Result and Discussion

The tests applied in this work were tested on an internal combustion engine. The petroleum-methanol fuel mixture is prepared with a ratio of gasoline (G95%) and M5% methanol. The experiment was carried out five times for each tested fuel. Tests were carried out at engine speeds of 1000, 1500, 2000, 2500, and 3000 rpm. The results of each test for mixed fuels are analyzed to see the level of vibration frequency in the internal combustion engine. Based on the results of tests carried out at an engine speed of 1000 rpm, it shows that the vibration frequency when using the G95-M5 fuel mixture is lower than pure petroleum. Meanwhile, pure petroleum fuel has a more normal vibration frequency as shown in Fig. 2. This is because petroleum is more flammable. While the mixed fuel burns a little slower, at the end of the combustion the mixed fuel is higher because the combustion has started completely.

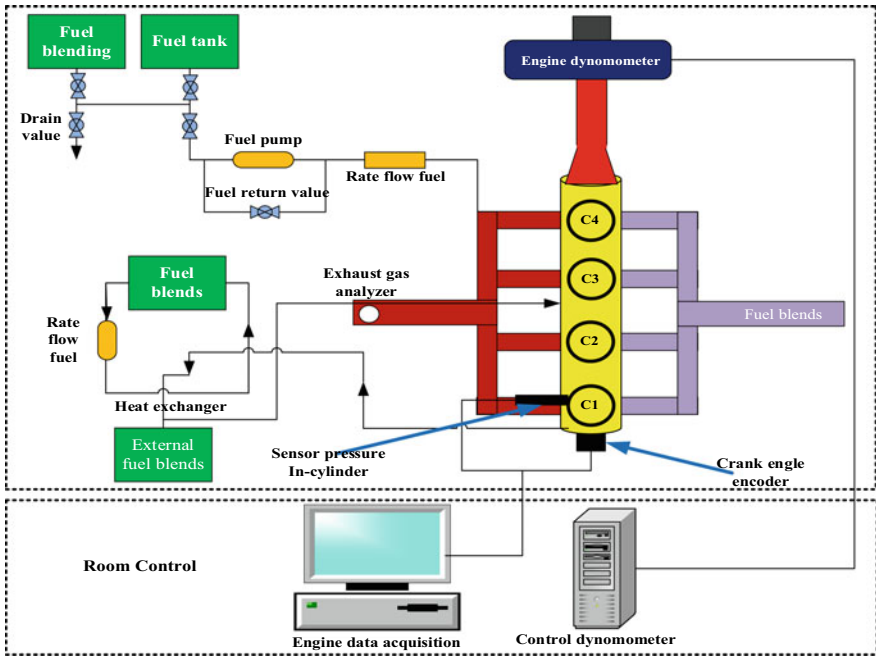


Fig. 1 Diagram schematic for engine SI

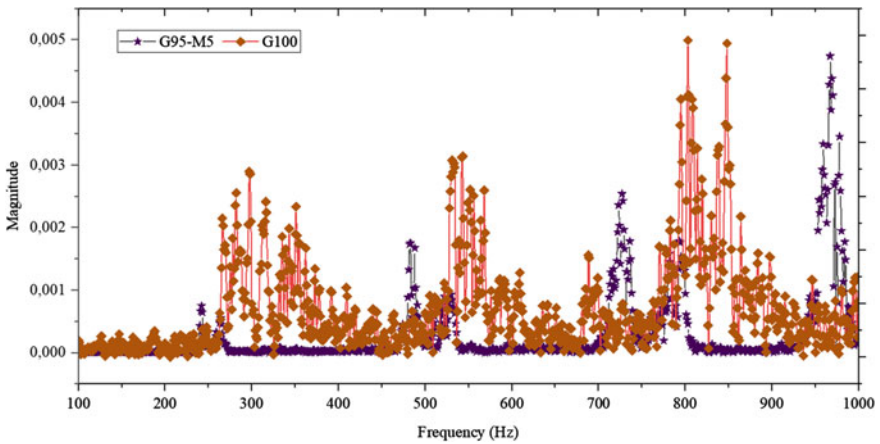


Fig. 2 Lever of frequency for engine speed (1000 rpm)

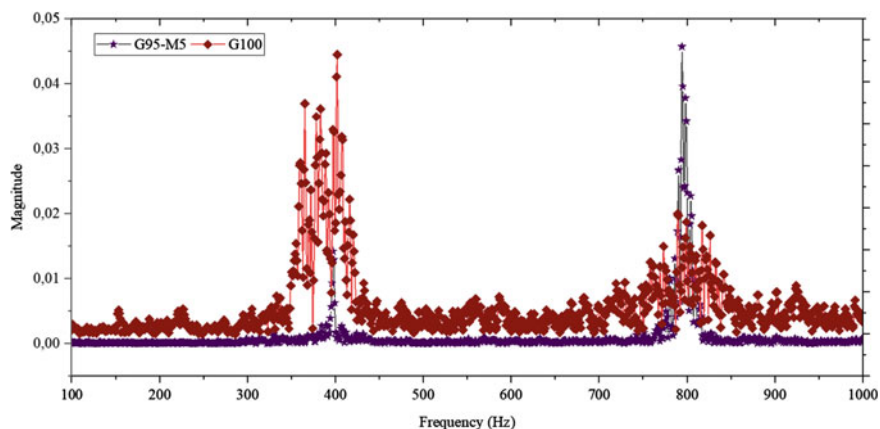


Fig. 3 Lever of frequency for engine speed (1500 rpm)

The results of the analysis carried out at the engine speed of 1500 rpm showed that the overall pure petroleum fuel produced a more normal vibration frequency. However, at the time of 350–430 s of G100 testing, there was a significant increase compared to the G95-M5 mixture. However, at 780–820 s the mixed fuel G95-M5 showed higher results than the G100 shown in Fig. 3. At a speed of 1500 rpm, the vibration frequency from the combustion using a mixed fuel was slightly more normal than when testing at a speed of 1000 rpm.

The test results applied to an engine speed of 2000 rpm show that the G95-M5 fuel mixture has almost the same vibration frequency as the G100 fuel. However, the fuel of the G100 is still better, this can be affected by the firing speed. Meanwhile, the G95-M5 mixture experienced a delay in burning so that the vibration frequency obtained was slightly lower than that of the G100 as shown in Fig. 4. Based on the results obtained, it was shown that the 5% methanol mixture into petroleum was quite good, although the combustion system was slightly slower than G100.

Tests of combustion with pure petroleum fuel at an engine speed of 2500 rpm showed a higher vibration frequency level than when testing at a low engine speed. Meanwhile, the vibration frequency level recorded from the mixed fuel test showed more normal results, but lower than that of pure petroleum fuel as shown in Fig. 5. If you look at the results obtained when using G100 fuel, the peak speed of 2500 is not yet normal. However, for mixed fuels, it has shown maximum results.

The last test carried out in this study was carried out with an engine speed of 3000 rpm for each of the tested fuels. The test results showed that the two types of fuel tested showed the maximum point. Both types of fuel were tested at an engine speed of 3000 rpm and the resulting vibration frequency level has shown normal results. Where it can be concluded that the combustion system with a high engine speed can produce more complete combustion so that the resulting vibration frequency is more optimal as shown in Fig. 6. The highest frequency peaks of the two types of fuel used are obtained at the same second, namely; at the time of 750–820 s.

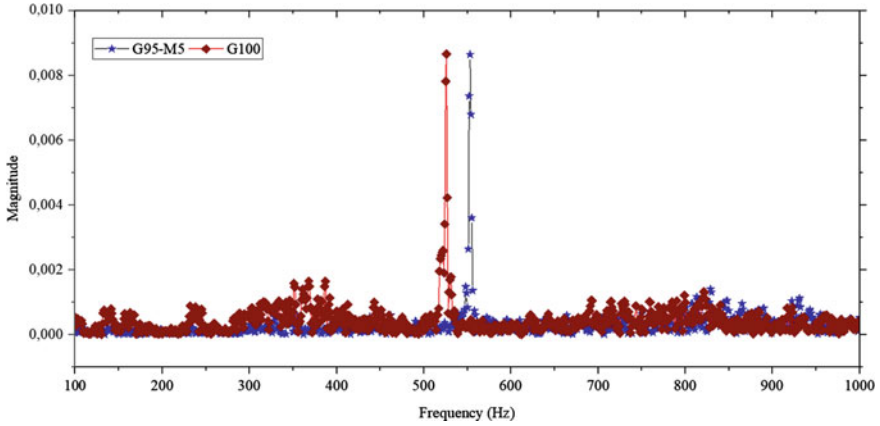


Fig. 4 Lever of frequency for engine speed (2000 rpm)

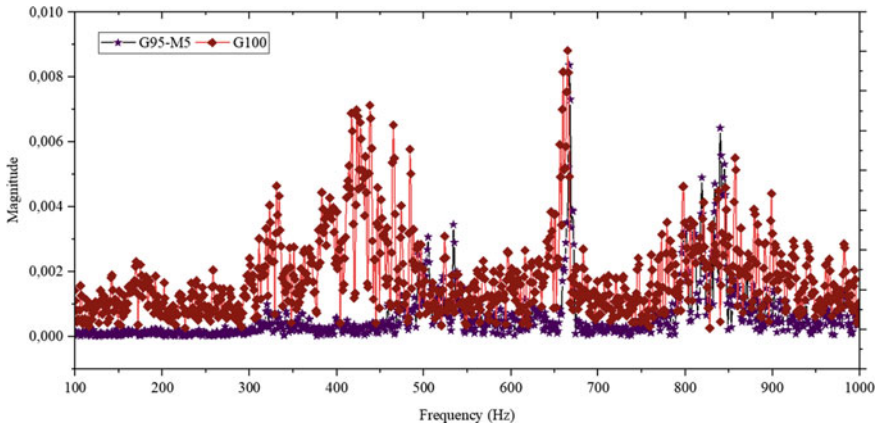


Fig. 5 Lever of frequency for engine speed (2500 rpm)

4 Conclusion

This research was conducted five times for each test fuel. Each fuel that has been primed is tested at different engine speeds and then the results of each test are compared. Based on the results of the experiments that have been carried out, it can be concluded that the high engine speed of the G95-M5 fuel mixture can equal the G100. The vibration frequency level of the G95-M5 mixture test is lower than that of the G100. However, the combustion rate with the mixture is slightly slower than that of pure petroleum.

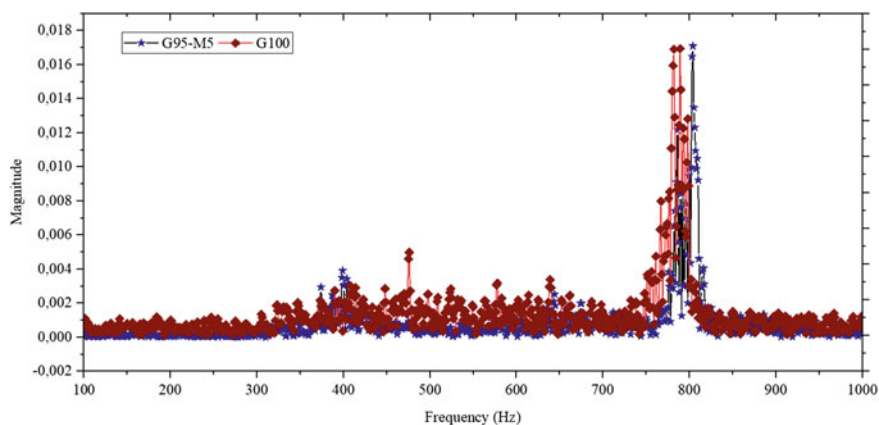


Fig. 6 Lever of frequency for engine speed (3000 rpm)

Acknowledgements The financial support of Universiti Malaysia Pahang—Malaysia through grants RDU172204, RDU1703147, RDU1703314, PGRS160303, PGRS1903166, and PGRS190341 is greatly acknowledged.

Conflict of Interest The authors declare that they have no known competing financial interests or personal relationships that could have appeared to influence the work reported in this paper.

References

1. Miganakallu N, Yang Z, Rogó z R, Kapusta  J, Christensen C, Barros S, Naber J (2020) Effect of water—methanol blends on engine performance at borderline knock conditions in gasoline direct injection engines. *Appl Energy* 264:114750. <https://doi.org/10.1016/j.apenergy.2020.114750>
2. Elfasakhany A (2018) Exhaust emissions and performance of ternary iso-butanol—bio-methanol—gasoline and n-butanol—bio-ethanol—gasoline fuel blends in spark-ignition engines: Assessment and comparison. *Energy* 158:830–844. <https://doi.org/10.1016/j.energy.2018.05.120>
3. Erdiwansyah, Mamat R, Sani MSM, Sudhakar K, Kadarohman A, Sardjono RE (2019) An overview of Higher alcohol and biodiesel as alternative fuels in engines. *Energy Rep* 5:467–479. <https://doi.org/10.1016/j.egy.2019.04.009>
4. Mishra PC, Ishaq RB, Khoshnaw F (2021) Mitigation strategy of carbon dioxide emissions through multiple muffler design exchange and gasoline-methanol blend replacement. *J Clean Prod* 286:125460. <https://doi.org/10.1016/j.jclepro.2020.125460>
5. Elfasakhany A (2016) Performance and emissions of spark-ignition engine using ethanol—methanol—gasoline, n-butanol—iso-butanol—gasoline and iso-butanol—ethanol—gasoline blends: a comparative study. *Eng Sci Technol Int J* 19:2053–2059. <https://doi.org/10.1016/j.jestch.2016.09.009>
6. Szwaja S, Gruca M, Pyrc M (2022) Investigation on ethanol-glycerol blend combustion in the internal combustion sparkignited engine. Engine performance and exhaust emissions. *Fuel Process Technol* 226:107085. <https://doi.org/10.1016/j.fuproc.2021.107085>

7. Shukla A, Vaghasia J, Mistry M (2022) Effect of laser ignition on combustion and performance of internal combustion engine: a review. *Energy Convers Manage X*. 13, 100166 (2022). <https://doi.org/10.1016/j.ecmx.2021.100166>
8. Yu X, Zhu L, Wang Y, Filev D, Yao X (2022) Internal combustion engine calibration using optimization algorithms. *Appl Energy* 305:117894. <https://doi.org/10.1016/j.apenergy.2021.117894>
9. Liu Z, Song J, Kubal J, Susarla N, Knehr KW, Islam E, Nelson P, Ahmed S (2021) Comparing total cost of ownership of battery electric vehicles and internal combustion engine vehicles. *Energy Policy* 158:112564. <https://doi.org/10.1016/j.enpol.2021.112564>
10. Alenezi RA, Erdiwansyah, Mamat R, Norkhizan AM, Najafi G (2020) The effect of fusel-biodiesel blends on the emissions and performance of a single cylinder diesel engine. *Fuel* 279:118438. <https://doi.org/10.1016/j.fuel.2020.118438>
11. Meng D, Ma J, Zhao X, Guo Y, Zhu C, Yu M (2021) Mechanical behavior and material property of low-carbon steel undergoing low-frequency vibration-assisted upsetting. *J Mater Res Technol*. <https://doi.org/10.1016/j.jmrt.2021.12.113>
12. Taghizadeh-Alisaraei A, Mahdavian A (2019) Fault detection of injectors in diesel engines using vibration time-frequency analysis. *Appl Acoust* 143:48–58. <https://doi.org/10.1016/j.apacoust.2018.09.002>
13. Omar FK, Selim MYE, Emam SA (2017) Time and frequency analyses of dual-fuel engine block vibration. *Fuel* 203:884–893. <https://doi.org/10.1016/j.fuel.2017.05.034>
14. Zikri JM, Sani MSM, Yusop AF, Izzudin I, Sapee S (2019) Vibration analysis on palm oil methyl ester biodiesel as a fuel with the additional of butanol. *J Phys Conf Ser* 12012
15. Nithin SK, Hemanth K, Shamanth V (2021) A review on combustion and vibration condition monitoring of IC engine. *Mater Today Proc* 45:65–70. <https://doi.org/10.1016/j.matpr.2020.10.093>
16. Sharma N, Patel C, Tiwari N, Agarwal AK (2019) Experimental investigations of noise and vibration characteristics of gasoline-methanol blend fuelled gasoline direct injection engine and their relationship with combustion characteristics. *Appl Therm Eng* 158:113754 (2019). <https://doi.org/10.1016/j.applthermaleng.2019.113754>
17. Erdiwansyah, Sani MSM, Mamat R, Khoerunnisa F, Rajkumar AR, Razak NFD, Sardjono RE (2018) Vibration analysis of the engine using biofuel blends: a review. *MATEC Web Conf* 225
18. Erdiwansyah, Mamat R, Sani MSM, Khoerunnisa F, Sardjono RE, Ali OM, Ibrahim TK (2018) Effects of diesel-biodiesel blends in diesel engine single cylinder on the emission characteristic. *MATEC Web Conf* 225
19. Waluyo B, Setiyo M, Saifudin, Wardana ING (2021) Fuel performance for stable homogeneous gasoline-methanol-ethanol blends. *Fuel* 294:120565. <https://doi.org/10.1016/j.fuel.2021.120565>
20. Balki MK, Temur M, Erdoğan S, Sarıkaya M, Sayin C (2021) The determination of the best operating parameters for a small SI engine fueled with methanol gasoline blends. *Sustain Mater Technol* 30:e00340. <https://doi.org/10.1016/j.susmat.2021.e00340>
21. Alenezi RA, Norkhizan AM, Mamat R, Erdiwansyah, Najafi G, Mazlan M (2021) Investigating the contribution of carbon nanotubes and diesel-biodiesel blends to emission and combustion characteristics of diesel engine. *Fuel* 285:119046. <https://doi.org/10.1016/j.fuel.2020.119046>
22. Izzudin I, Yusop AF, Sapee S, Hamidi MA, Yusri IM, Mamat R (2020) Experimental studies of single cylinder engine run on diesel-biodiesel-butanol blends. In: *IOP conference series: materials science and engineering*. IOP Publishing, p 12060

Corrosion Performance of Nanopaint for Automotive Application



S. Z. A. Sakinah , Wan Azmi Wan Hamzah , and J. Alias 

Abstract Nanostructured coating that possessed high density of grain boundaries enable excellent physical coverage of the coated surface against corrosion and mechanical problems compared to the larger grain size of particles found in conventional paint. The current study focusses on the effect of SiO_2 and TiO_2 nanoparticles as additive in acrylic automotive paint for corrosion. The new paint namely nanopaints was prepared at three different concentrations. The nanopaint were characterized using Electro-chemical test and the open circuit potential (OCP) is recorded. Electrochemical test in a saltwater solution method also used to determine the potential of nanopaint concentration on automotive surfaces. The results reveal that nanoparticle additive provide better corrosion rate as compared to the original basecoat. The optimum anticorrosion behaviour for both TiO_2 and SiO_2 nanopaints were achieved at weight percentage of 1.5 wt% and 1.0 wt%, respectively. Therefore, the nanopaint has potential to provide better corrosion performance for automotive surface application.

Keywords Nanopaint · Corrosion · Automotive surface · Electro-chemical · Polarization

1 Introduction

Titanium oxide (TiO_2) is a common type of nanomaterial used in coating and corrosion applications. Industrial nanoscale TiO_2 was stored as a dry powder at room

S. Z. A. Sakinah · W. A. Wan Hamzah (✉) · J. Alias
Department of Mechanical Engineering, College of Engineering, Universiti Malaysia Pahang,
Lebuhraya Tun Razak, 26300 Gambang, Kuantan, Pahang, Malaysia
e-mail: wanzmi2010@gmail.com

S. Z. A. Sakinah · W. A. Wan Hamzah
Centre of Excellence for Advanced Research in Fluid Flow, Lebuhraya Tun Razak, 26300
Gambang, Kuantan, Pahang, Malaysia

J. Alias
Faculty of Mechanical and Automotive Engineering Technology, Universiti Malaysia Pahang,
26600 Pekan, Pahang, Malaysia

temperature, and it was reported that the particle has a size range and specific surface area of 6.4–73.8 nm and 54 m²/g, respectively. The distinct and unique chemical and physical characteristics of TiO₂ nanoparticles such as self-cleaning, high abrasive and corrosion resistance, photocatalytic activity, ultra-violet protection, and large refractive index lead to many applications of TiO₂ nanoparticles such as self-cleaning and self-sterilizing construction materials, electrochromic, sensing and photovoltaic. To maximize the dispersion of TiO₂ nanoparticles in an aqueous culture medium, the combination of mechanical dispersion by ultrasonication, electrostatic repulsion by pH adjustment and steric hindrance by addition of humic acid were applied [1].

Silicon dioxide, SiO₂, also known as silicon (IV) oxide or silica, mostly existed as quartz or sand in nature. SiO₂ nanoparticle is a transparent, odourless, crystalline or amorphous solid with a density of 2.65 g m/L. Since the polarity of SiO₂ nanoparticles is zero, it is not a very reactive compound. SiO₂ nanoparticles have been widely applied in the chemical industry such as dyes and paint additives, corrosion inhibitors, anti-adhesives, ceramic and porcelain. Malaki et al. [2] found that the scratch and abrasion resistance of the clear coat had been enhanced and improved by dispersing SiO₂ in the clear coat.

Abaci and Nessark [3] experimented to study the corrosion behaviour of A304 stainless steel by using a coating of conducting polymers polyaniline (PANI) and TiO₂ in an acidic medium. The experiment concluded that the anti-corrosion performance of the substrate increased significantly by using a mixture of PANI and TiO₂ as a composite material. Besides, Shanaghi et al. [4] coated TiO₂ nanoparticles with a range of thickness (300–700 nm) on mild steel via the sol-gel method to study corrosion protection. The experiment result showed that heat treatment at 550 °C will obtain the best coating quality and thickness not more than 561 nm will improve the corrosion resistance of mild steel about 190 times better compared to the raw substrate.

Ammar et al. [5] used host hybrid polymeric matrix (epoxy and polydimethylsiloxane (PDMS)) and reinforcing agents (2–8 wt% of SiO₂ nanoparticles) to fabricate hybrid polymeric based nanocomposite coating systems by using solution intercalation method with the assistance of sonication process. The result from EIS also revealed that the immersion time that shows the best anti-corrosion properties is 30 days and the coating system that with the contents 2 wt% of SiO₂ nanoparticles revealed significant stability over the entire immersion time. In another paper, Kim and Hwang [6] studied the anticorrosion enhancement in silica film with mixing sizes of silica nanoparticles (10–50 nm). Silica films were prepared by the sol-gel dip-coating method followed by the annealing process at 200 °C. Electrochemical characterization concluded that the film with mixed sizes of nanoparticles exhibits lower corrosion current density and delayed loss of film resistance during immersion in an electrolyte solution.

Kamalan Kirubakaran et al. [7] dispersed TiO₂ and SiO₂ nanoparticles to achieve the composite coating by using paste formation and silane treatment method. It was evidenced that nanocomposite (silicone-polyppyrrrole-Interpenetrating Polymer Network (silicone-PPy-IPN) with rutile TiO₂) coating exhibited a very high resistance of 107 Ω cm² after 1 month of immersion in NaCl solution. The main concern

of the current automotive coating is to enhance corrosion performance and create protection against harsh environments. Blistering and fisheyes are the common corrosion or coating defects found in automobiles caused by contaminants. The objective of this paper is to investigate and evaluate the corrosion potential and performance of single TiO_2 and SiO_2 nanopaints for automotive applications.

2 Methodology

2.1 Preparation of Nanopaint

In this study, nanoparticles of silicon oxide (SiO_2) and titanium oxide (TiO_2) nanoparticles were used, and polyester basecoat paint is taken as base fluid. Material properties for TiO_2 and SiO_2 nanoparticles are shown in Table 1. A two-step method is considered in the preparation of the single polyester basecoat nanopaints. As proposed by Das et al. [8] and Ghadimi et al. [9], the two-step method is better for oxide particles, and it provides higher stability thus less agglomeration. Few reasons for the use of polyester basecoat and nanoparticles in the present study, which included (i) they are generally considered as safe material to be handled due to their low toxicity although it is recognized that this may change in future regarding further fundamental research on nanotoxicology; (ii) nanoparticles are chemically more stable than their metallic counterparts; (iii) These nanoparticles exhibit hydrophobic or hydrophilic properties which prone to self-cleaning and dirt repellent, scratch and wear resistance, anti-corrosion, anti-reflection/glass-coating and surface modification; (iv) Polyester basecoat has high tensile strength, chemical and weathering resistance, good process ability and good mechanical properties; (v) Polyester basecoat is widely used in car manufacturing plant in Malaysia.

Sample preparation of single coating is done by dispersing nanoparticles into raw basecoat paint. Since nanoparticles existed in pigments instead of measuring in volume, Eq. (1) was used to calculate the mass fraction or weight concentration of nanopaints. The TiO_2 and SiO_2 nanoparticles at different weight percentage of 0.5, 1.0 and 1.5 wt% are dispersed into 200 ml of raw basecoat paint.

$$\omega = \frac{\omega_{\text{np}}}{\omega_{\text{np}} + \omega_{\text{paint}}} \times 100\% \quad (1)$$

Table 1 Material properties of TiO_2 and SiO_2 nanoparticles

Property	Unit	TiO_2	SiO_2
Molecular mass	g/mol	79.87	60.08
Density	kg/m ³	4230	2220
Average particle diameter	nm	50	30
Specific heat	J/kg·K	692	745

where ω is the weight concentration of the nanopaints, while ω_{np} and ω_{paint} are the weight for nanoparticles and base coat paint, respectively. After the weight of the nanoparticle was calculated, the nanoparticles were then mixed into the raw basecoat paint and stirred using a magnetic stirrer for 20 min. Next, solvent (butyl-acetate) is also added to lower the surface tension (viscosity) of the paint to get the original viscosity of the paint and given by 40 ± 1 cP. The nano paint was prepared in similar viscosity to the base coat paint and required for storage and painting process. Then, the nanopaint is subjected to a sonication process for another 30 min using Fisher Brand Ultrasonic Bath. The sonication process is important to make sure uniform dispersion of the nanoparticles in the paint and reduce the agglomeration of particles.

2.2 Corrosion Resistance

The corrosion resistance performance of the nanopaints was tested using an electrochemical test in a saltwater solution (≈ 3.5 wt% vol NaCl). All corrosion behaviour is the outcome of oxidation and reduction reactions. Corrosion rates or penetration rates were obtained from the potentiodynamic polarization technique, which employs a three-electrode configuration during the electrochemical test [10]. Figure 1 shows the present electrochemical test setup. The three electrodes consisted of reference, counter, and working electrodes. The corrosion rates were determined from the applied potential, E_{corr} and current, I_{corr} (current density). After the potential is scanned to a predetermined current density or potential, the potential scan may be reversed while the current continues to be measured. This type of potentiodynamic scan is referred to as reverse polarization or cyclic polarization. Equation (2) was used to estimate the corrosion rate for each sample.

$$CR = K_1 \frac{I_{corr}}{\rho} EW \quad (2)$$

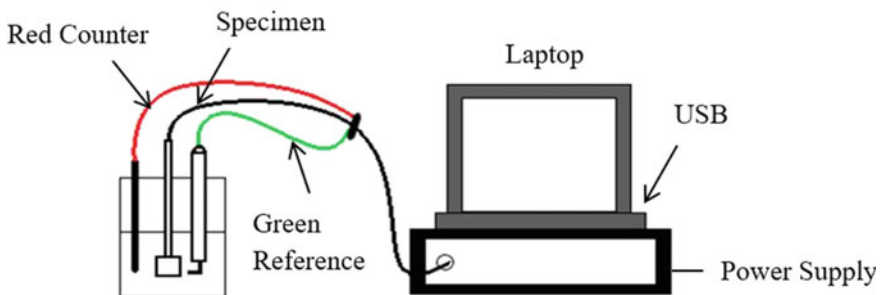


Fig. 1 Electrochemical test set up

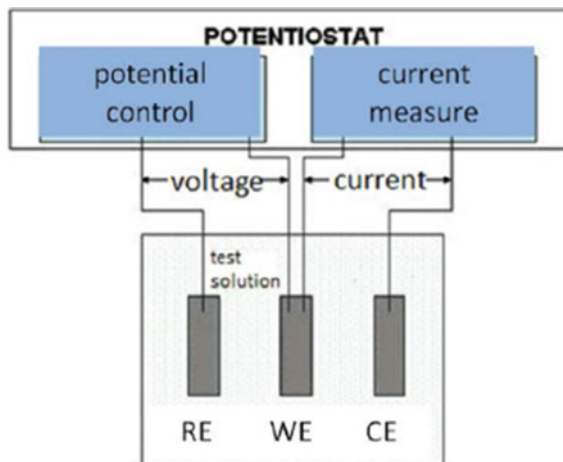
where, CR is penetration rate in mm/year, I_{corr} is corrosion current in $\mu\text{A}/\text{cm}^2$, K_1 is constant value in Faradays's Eq. (3.27×10^{-3} mm g/ $\mu\text{A cm yr}$), ρ is material density in g/cm^3 , and EW is 27.92.

2.3 Polarization Preparation

Polarization is a mechanism that usually results in a change in the potential of an electrode in which the potential of anode become nobler than that of the cathode during electrolysis. It has the effect of reducing the output voltage of batteries and increasing the voltage required for electrolysis cells [11]. The polarization is anodic when the anodic processes on the electrode are accelerated by moving the potential in the positive (noble) direction whereas it is considered to be cathodic when the cathodic processes are accelerated by moving the potential in negative (active) direction. Cathodic polarization, which is the polarization that occur at the cathode, always reduce the corrosion rate for all metals and alloys in any aqueous environment [12]. The term cathodic protection refers to the application of a cathodic polarization to a corroding system. In general, polarization often occurs in three ways which included activation polarization, resistance polarization and concentration polarization [12].

It is helpful in analysing the type of polarization because it provides knowledge to determine the characteristics of a corroding system. For example, any change that raised the diffusion rate of the active species might also increase the rate of corrosion if the corrosion is controlled by concentration polarization. Therefore, in such system, it was estimated that agitating or stirring the liquid could tend to increase the corrosion rate of the metal. However, if the corrosion is controlled by activation polarization, there is no effect on the corrosion rate by stirring or increase the agitation. Figure 2 showed the method of polarization in the present study.

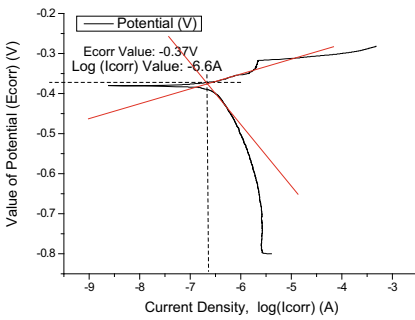
Fig. 2 Polarization method



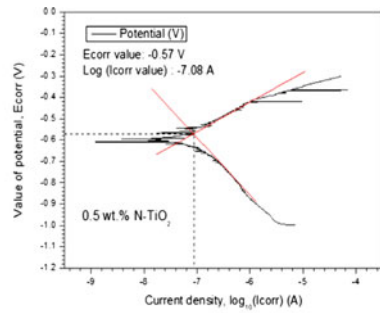
3 Results and Discussion

3.1 Corrosion Potential/ Characteristic

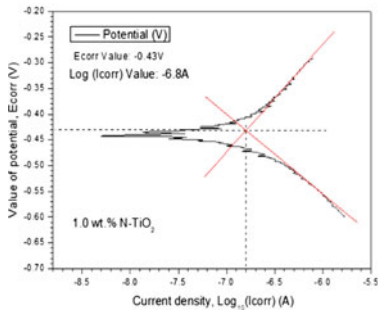
Figure 3 shows the potential, V against current density, A for different weight concentrations of TiO₂ nanoparticles (0 wt%, 0.5 wt%, 1.0 wt% and 1.5 wt%). It was also known as polarization graph with Tafel plotted. The two linear red lines represented oxidation and reduction, respectively. With the linear lines plotted with Tafel anodic and cathodic slopes, the value of potential, E_{corr} and current density, I_{corr} of each sample can be easily defined. It should be noted that the lower the current density of a sample, the greater the anticorrosion behaviour of that sample. It was observed that the value of I_{corr} keep reducing as the concentration of TiO₂ increased. The value of I_{corr} is in descending order as addition of TiO₂ nanoparticles increased: $2.512 \times$



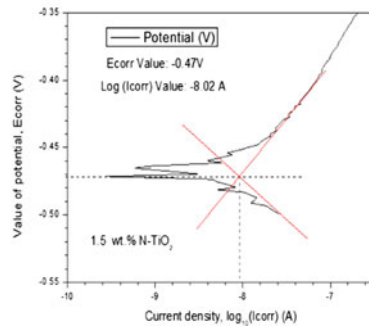
(a) 0.0 wt%



(b) 0.5 wt%



(c) 1.0 wt%



(d) 1.5 wt%

Fig. 3 Potential, E_{corr} (V) against current density, Log₁₀ (I_{corr}) for various concentration of TiO₂ nanopaint

10^{-4} A (0 wt%) $< 1.584 \times 10^{-7}$ A (1.0 wt%) $< 8.318 \times 10^{-8}$ A (0.5 wt%) $< 9.550 \times 10^{-9}$ A (1.5 wt%). This can be concluded that the addition of TiO₂ nanoparticles inside the basecoat will enhance the corrosion performance. The optimum weight percentage of TiO₂ against corrosion was 1.5 wt%.

Figure 4 presents the potential, V against current density, A of different weight concentrations of SiO₂ nanopaint (0, 0.5, 1.0 and 1.5 wt%). A similar trend was observed for SiO₂ nanopaint, whereby the addition of SiO₂ nanoparticles enhanced the paint against corrosion. However, the optimum weight percentage of SiO₂ against the corrosion was achieved at 1.0 wt% and current density was increased back to 1.047×10^{-8} A at 1.5 wt%. However, the addition of SiO₂ nanoparticles within 0 to 1.0 wt% was resulted in descending order of I_{corr} value: 2.512×10^{-4} A (0 wt%) $< 1.585 \times 10^{-8}$ A (0.5 wt%) $< 5.623 \times 10^{-9}$ A (1.0 wt%).

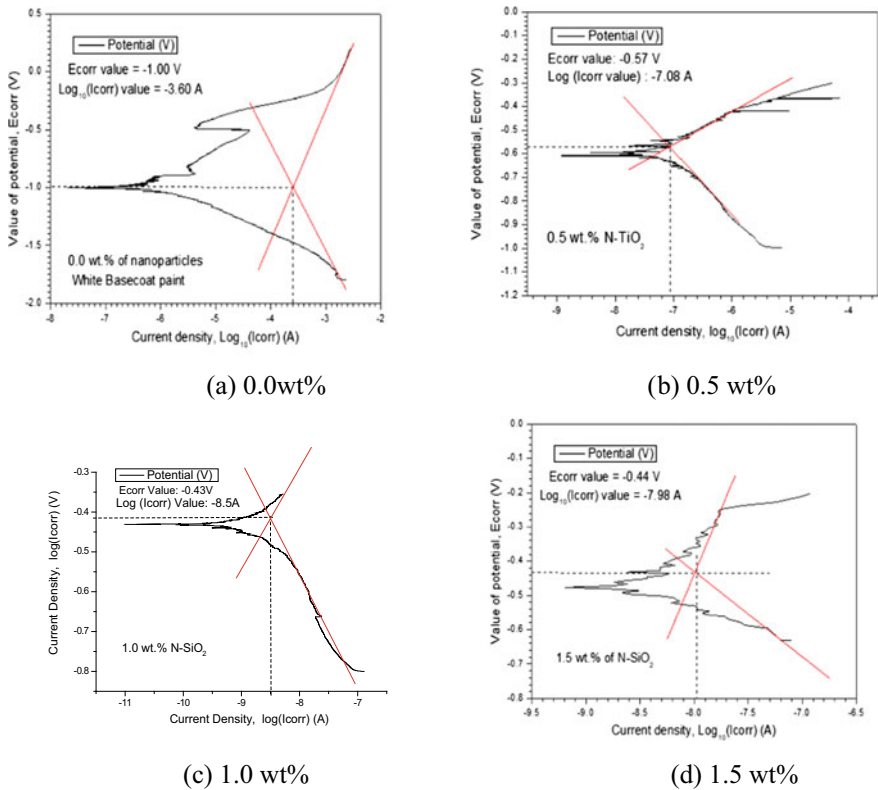


Fig. 4 Potential, E_{corr} (V) against current density, Log₁₀ (I_{corr}) for various concentration of SiO₂ nanopaint

Table 2 The corrosion rate for TiO₂ nanopaint

Weight concentration (wt%)	Corrosion rate (mm/year)
0.0	1.457×10^{-6}
0.5	4.825×10^{-10}
1.0	9.193×10^{-10}
1.5	5.539×10^{-11}

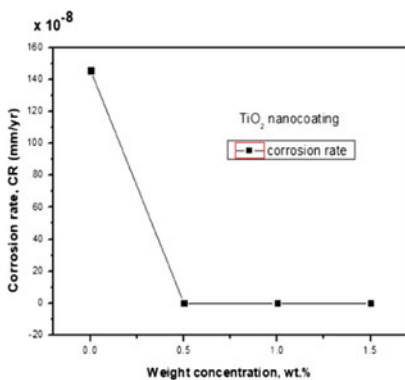
Table 3 The corrosion rate for SiO₂ Nanopaint

Weight concentration (wt%)	Corrosion rate (mm/year)
0.0	1.457×10^{-6}
0.5	9.193×10^{-11}
1.0	3.262×10^{-11}
1.5	6.074×10^{-11}

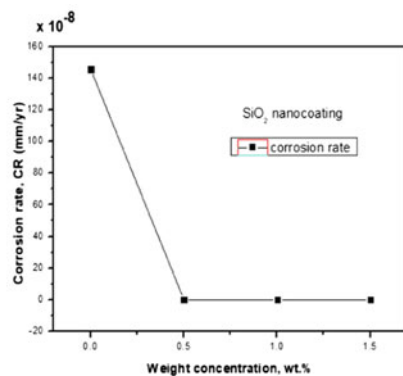
3.2 Corrosion Rate

The result of the corrosion rate for TiO₂ and SiO₂ nanopaints was discussed in this section. The calculated values of corrosion rate for TiO₂ and SiO₂ nanopaints from weight concentration are shown in Tables 2 and 3, respectively by using Eq. (2).

Figure 5 represents the overall corrosion result of TiO₂ and SiO₂ nanopaints for the corrosion rate against weight concentration. It can be obviously observed that the addition of nanoparticles in the paint was improved the anticorrosion properties dramatically. This is due to the porosity of the coating was become less porous and the density of the grains, network and dislocations become higher therefore reduce the corrosion rate and cause the nanocoating possessed the perfect anticorrosion behaviours. However, the optimum anticorrosion behaviour for both TiO₂ and SiO₂



(a) TiO₂ nanopaint



(b) SiO₂ nanopaint

Fig. 5 Corrosion rate against weight concentration of nanopaints

nanopaints were achieved at different weight percentage of 1.5 wt% and 1.0 wt%, respectively. From the figure, the corrosion resistance of nanopaint for both nanoparticles were clearly improved drastically. Nanoparticles acts as additives or fillers when mixed with basecoat paint and it will modify and enhance the paint properties such as microstructures, morphology and corrosion resistance which subsequently improve the corrosion performance of paint.

4 Conclusions

The corrosion performance of TiO₂ and SiO₂ nanopaints for application on automotive surfaces at different weight percentage (0, 0.5, 1.0 and 1.5 wt%) were investigated. Addition of TiO₂ and SiO₂ nanoparticles obviously decreased the corrosion rate dramatically as compared to the original basecoat. However, the corrosion rate unchanged or become higher with concentration of nanopaints. The I_{corr} value was reduced with the concentration of TiO₂ and SiO₂ nanopaints. The optimum weight percentage of TiO₂ and SiO₂ nanopaints were achieved at 1.5 wt% and 1.0 wt%, respectively. Therefore, TiO₂ and SiO₂ nanopaints were recommended for automotive application.

Acknowledgements The authors are grateful to the Universiti Malaysia Pahang for financial supports given under RDU213302 and PGRS1903154. The authors also thank the research team from Centre for Research in Advanced Fluid and Processes (Pusat Bendalir) and Advanced Automotive Liquids Laboratory (AALL), who provided insight and expertise that greatly assisted in the present research work.

References

1. Horst AM, Ji Z, Holden PA (2012) Nanoparticle dispersion in environmentally relevant culture media: a TiO₂ case study and considerations for a general approach. *J Nanopart Res* 14(8). <https://doi.org/10.1007/s11051-012-1014-2>
2. Malaki M, Hashemzadeh Y, Fadaei TA (2018) Abrasion resistance of acrylic polyurethane coatings reinforced by nano-silica. *Prog Org Coat* 125:507–515. <https://doi.org/10.1016/j.porgcoat.2018.07.034>
3. Abaci S, Nessark B (2014) Characterization and corrosion protection properties of composite material (PANI+TiO₂) coatings on Al₂O₃ stainless steel. *J Coat Technol Res* 12(1):107–120. <https://doi.org/10.1007/s11998-014-9611-x>
4. Shanaghi A, Sabour AR, Shahrabi T, Aliofkhaeze M (2009) Corrosion protection of mild steel by applying TiO₂ nanoparticle coating via sol-gel method. *Prot Met Phys Chem Surf* 45(3):305–311. <https://doi.org/10.1134/s2070205109030071>
5. Ammar S, Ramesh K, Ma IAW, Farah Z, Vengadaesvaran B, Ramesh S et al (2017) Studies on SiO₂-hybrid polymeric nanocomposite coatings with superior corrosion protection and hydrophobicity. *Surf Coat Technol* 324:536–545. <https://doi.org/10.1016/j.surfcoat.2017.06.014>

6. Kim H, Hwang T (2012) Corrosion protection enhancement effect by mixed silica nanoparticles of different sizes incorporated in a sol-gel silica film. *J Sol-Gel Sci Technol* 63(3):563–568. <https://doi.org/10.1007/s10971-012-2820-9>
7. Kamalan Kirubakaran AM, Selvaraj M, Maruthan K, Jeyakumar D (2009) Synthesis and characterization of nanosized titanium dioxide and silicon dioxide for corrosion resistance applications. *J Coat Technol Res* 9(2):163–170. <https://doi.org/10.1007/s11998-009-9226-9>
8. Das SK, Putra N, Thiesen P, Roetzel W (2003) Temperature dependence of thermal conductivity enhancement for nanofluids. *J Heat Transfer* 125(4):567–574. <https://doi.org/10.1115/1.1571080>
9. Ghadimi A, Saidur R, Metselaar HSC (2011) A review of nanofluid stability properties and characterization in stationary conditions. *Int J Heat Mass Transf* 54(17):4051–4068. <https://doi.org/10.1016/j.ijheatmasstransfer.2011.04.014>
10. Song H-W, Saraswathy VJM (2006) Analysis of corrosion resistance behavior of inhibitors in concrete using electrochemical techniques. *Int Mater* 12(4):323–329
11. Stern M (1957) Electrochemical polarization: II. ferrous-ferric electrode kinetics on stainless steel. *J Electrochem Soc* 104(9):559
12. Revie RW (2008) *Corrosion and corrosion control: an introduction to corrosion science and engineering*. Wiley

Laser Processing of $\text{La}_{61.4}\text{Al}_{15.9}\text{Ni}_{11.35}\text{Cu}_{11.35}$ Based Functionally Graded Material Bulk Metallic Glass



Qayyum Halim , Nik Abdullah Nik Mohamed,
Mohd Ruzaimi Mat Rejab , Mohd Kamal Kamarulzaman ,
Sakinah Hisham , and A. M. Aizzuddin

Abstract Bulk metallic glass (BMG) based on lanthanum is one of the BMG with exceptional glass-forming ability (GFA). The $\text{La}_{61.4}\text{Al}_{15.9}\text{Ni}_{11.35}\text{Cu}_{11.35}$ bulk metallic glasses were treated to a laser processing test in this experiment. The results showed that the best power, frequency, and speed ranges for laser processing of the $\text{La}_{61.4}\text{Al}_{15.9}\text{Ni}_{11.35}\text{Cu}_{11.35}$ BMG samples are 40–50 W, 160–240 kHz, and 200–400 mm/s, respectively. As a result, the current work was effective in producing the Lanthanum-based functionally graded material (FGM) BMG. The positive findings on the laser's microstructural or morphology, give a solid foundation for future advancement research on the $\text{La}_{61.4}\text{Al}_{15.9}\text{Ni}_{11.35}\text{Cu}_{11.35}$ BMG.

Keywords La-based BMG · Functionally graded material bulk metallic glass · Laser processing

1 Introduction

Metallic glass (MG) is an advanced engineered material with several crucial processes. The first known successful development of bulk metallic glass (BMG) is from Klement et al. from California Technology Institute in 1950–1960 [1–3]. Ruhl et al. team from the Massachusetts Institute of Technology makes additional BMG findings later [4–6]. The known Metallic Glass (MG) was in the ribbon form

Q. Halim · N. A. N. Mohamed · M. R. M. Rejab · S. Hisham
Faculty of Mechanical and Automotive Engineering Technology, Universiti Malaysia Pahang,
26600 Pekan, Pahang Darul Makmur, Malaysia

M. K. Kamarulzaman (✉)
Advanced Nano Coolant-Lubricant (ANCL) Lab, Automotive Engineering Centre, Universiti
Malaysia Pahang, 26600 Pekan, Pahang Darul Makmur, Malaysia
e-mail: kamalkz@hotmail.com

A. M. Aizzuddin
College of Engineering, Universiti Malaysia Pahang, 26600 Pekan, Pahang Darul Makmur,
Malaysia

and only 1 mm in thickness size. Akihisa Inoue et al. from Tohoku University has made MG samples from different elements (Al, La, Fe, Ni, Cu, Ag and Sn) and lists out their glass-forming ability (GFA) [7, 8]. Later the MG creation method was able to be produced in bulk (more than 1 mm thickness), which uses the copper block to supercool (super-cooling time of $1-10^1$ K/s [9] the molten MG elements. Previous alloy system that is less than three elements system have the super-cooling time of 10^3-10^5 K/s [10]. Lower super-cooling time will reduce the effect of stress from rapid cooling, resulting in fracturing. Other methods are also found in the creation of BMG (Exceeding 1 mm thickness). In the latest trend, Ouyang et al. [10] used the selective laser melting 3D metal printer to produce BMG with better shape complexity. This opens up the possibility for BMG to be used in rapid prototyping parts for practical usage. On the other hand, a Lanthanum based BMG as the chosen sample in this work is an alternative for the lightweight alloy. The base metal is abundant and has an excellent glass-forming ability (GFA) for the BMG.

1.1 Ductilisation Studies on BMG

The common understanding of BMG agrees that the ductility of BMG is lower compared to conventional alloys. Although that is the case, studies on how to enhance BMG ductility is continuing. The author has compiled in Table 1 the ductilisation-related research regarding the BMG alloy systems, processes and Young's modulus values that can be a valuable reference for other BMG ductilisation research [3].

Hence, to describe ductility in a comprehensive method, it is agreeable that more properties information is needed [11]. Information such as shear modulus, bulk modulus, alloy's density, and Poisson's ratio are needed to derive a comprehensive conclusion [12]. Nevertheless, as for benchmarking purposes of BMG ductilisation, Young's modulus (stiffness) is inversely proportional to the actual ductility value of BMG samples [13, 14]. It can be beneficial information when the research of localised ductilisation and characterisation of functionally graded material (FGM) bulk metallic glass (BMG) is initiated.

Table 1 Compilation of data from ductilisation-related research in terms of the BMG alloy systems, processes and Young's modulus, E

BMG alloy system	Process	E (GPa)	Refs.
Pt-Cu-Ni-P	Compression, bending	94.8	[12]
Cu-Zr	Compression	84	[15]
Zr-Al-Ni-Cu-Ti	Cold rolling	82	[16]
Ti-Zr-Cu-Be-V	Tensile, nanoindentation	94.2	[17]
Ti-Zr-Nb-Cu-Be-Sn	Nanoindentation	120.3	[18]
Zr-Ti-Cu-Ni-Al	Imprinting	105	[19]
La-Al-Ni-Cu	Compression, bending	25	[20]

1.2 Localised Ductilisation of the Bulk Metallic Glass (BMG)

Investigation of the re-scanning method to prevent macro-cracks during selective laser melting (SLM) of $\text{Al}_{85}\text{Ni}_5\text{Y}_6\text{Co}_2\text{Fe}_2$ bulk metallic glass composites (BMGC's) had been presented by Li et al. [21]. The crack was caused by residual stress of rapid heating and cooling during SLM. BMGC's possess supercooled liquid regions that can release stress by plastic flow. It was shown that high power initial scan for material melting followed by a lower power re-scan for stress relief was able to prevent cracking. A crack free $\text{Al}_{85}\text{Ni}_5\text{Y}_6\text{Co}_2\text{Fe}_2$ BMGC's was created with gear design. The diameter is ~ 25 mm and height ~ 10 mm [21].

Additive manufacturing can produce bulk metallic glass (BMG) with good design and sizes. The major challenge of creating BMG using additive manufacturing is micro-cracking. It is caused by substantial thermal stress in the process, particularly around the micro-pores. Thus, degrade the mechanical performance of the parts created. Systematic experiments and finite element simulation on Fe-based metallic glass, which is intrinsically brittle was done. $\text{Fe}_{43.7}\text{Co}_{7.3}\text{Cr}_{14.7}\text{Mo}_{12.6}\text{C}_{15.5}\text{B}_{4.3}\text{Y}_{1.9}$ (at.%) have the excellent glass-forming ability (critical cooling rate for glass formation approximately at 80 K/s) and was chosen as the powder material base [22]. Using selective laser melting (SLM) with process optimization to avoid micro-cracks. Cu and CU-Ni alloy powder forming BMG composites were introduced to subdue the development of micro-cracks. Results have shown micro-crack reduction with high-density dislocation formation in the second phase of SLM. The second phase reduces thermal stress with the relaxation of strain energy. Fracture toughness of second phase Fe-based BMG improved to $47 \text{ MPa m}^{1/2}$ compared to first phase Fe-based BMG $2.2 \text{ MPa m}^{1/2}$. The SLM method for BMG development with composites can enhance mechanical properties while maintaining geometries of parts created [22].

Imprinted glass is considered an orthotropic material that possesses heterogeneous microstructures due to imprinting ductilisation. Consequently, the shear band dynamics and mechanical behaviour of the BMG would vary under compression or tensile loadings. Scudino et al. [19] studied the correlation between structural heterogeneities and shear bands morphology of a $\text{Zr}_{52.5}\text{Ti}_5\text{Cu}_{18}\text{Ni}_{14.5}\text{Al}_{10}$ BMG through experimental and computational methods. The effects of loading angle, α , on the tensile behaviour of the BMG samples were analyzed through the tensile tests. The results revealed that both strength and ductility improved when α was increased from 0 to 45° due to the shear band branching and deflection mechanisms [19].

Dong et al. [23] examined the ductility of Zr-based BMG having varied hydrogen content. The plasma-assisted hydrogenation method introduced hydrogen at varied content, and uniaxial compression tests were performed on the BMG rods. The results showed that hydrogen significantly improved the compressive properties, plasticity and ductility of the $\text{Zr}_{55}\text{Cu}_{30}\text{Ni}_5\text{Al}_{10}$ metallic glass.

Table 2 Functionally graded material (FGM) BMG alloy system, process, and aim of the study

BMG alloy system	Process	Aim of the study	Refs.
Zr–Ti–Cu–Ni–Al	Laser additive manufacturing (LAM)	Extending the applications of metallic glass for use as functionally graded	[24]
Zr–Ti–Cu–Ni–Al	Laser direct manufacturing (LDM)	LDM technology to fabricate structural-graded materials	[25]

1.3 Functionally Graded Material (FGM) Bulk Metallic Glass (BMG)

To the best of the author's knowledge, functionally graded material (FGM) bulk metallic glass (BMG) is still an area of research that is scarcely explored. Having stated this, an exploration of the niche area would benefit the future practical application of BMG. In Table 2, using laser additive manufacturing (LAM) and direct laser manufacturing (LDM) [3], the researchers aim to extend the BMG application as part of FGM [24, 25].

The author's research with literature support (Table 2) suggested that the FGM BMG would open up BMG capabilities to allow conventional alloy processes such as machining and joining. Similarly, with localised ductilisation using the laser method, various FGM BMG can be produced depending on usage.

1.4 Joining Process of BMG

The bulk metallic glass research area on the joining method is continuing until today. Admittedly, the maturity of BMG engineering would be to produce the part as cast rather than to join it. Although that is the case, Table 3 compiled various research on the joining of BMG [3]. The studies were done to further the general understanding of BMG on this subject matter. Consequently, this understanding comes from the meta-stability of the BMG that is vastly affected by the high-temperature procedure of joining the BMG [26]. Providing crucial information on annealing of the heat-affected zone (HAZ), joining ability, quality, and strength.

Importantly, by introducing a joining procedure to BMG with applying high temperature surpassing the eutectic point. Coupled it with an annealing process that happens by ambient temperature. Therefore will result in the crystalline reverting process of the BMG, which was subjected to the heat-affected zone (HAZ) [28].

The author has a hypothesis that using the laser processing method, the $\text{La}_{61.4}\text{Al}_{15.9}\text{Ni}_{11.35}\text{Cu}_{11.35}$ metallic glass can be processed to become a graded material. A proper study of graded material towards the $\text{La}_{61.4}\text{Al}_{15.9}\text{Ni}_{11.35}\text{Cu}_{11.35}$ metallic glass has not been done to the best of the author's knowledge. This is an excellent

Table 3 Joining of BMG alloys system, process, and aim of the study

BMG alloy system	Process	Aim of the study	Refs.
Zr–Cu–Ni–Al	Laser welding	Laser welding effect on annealed BMG	[27]
Zr–Cu–Al–Ni	Laser welding	Crystallisation effect of BMG in laser welding	[28]
Zr–Cu–Al–Ni	Friction stir welding (FSW)	FSW joining of BMG to alloy plates	[29]
Zr–Ti–Ni–Cu–Al	Friction stir welding (FSW)	Joining of BMG to aluminium alloy	[30]
Zr–Ti–Ni–Cu–Al, Zr–Cu–Ni–Al	Liquid–solid joining process	Joining two BMG using the solid–liquid process	[31]
Cu–Ni–Zr–Ti	Brazing	Joining BMG to carbon steel	[32]

opportunity to closing the gap of expanding the size and application of the metallic glass, specifically for the $\text{La}_{61.4}\text{Al}_{15.9}\text{Ni}_{11.35}\text{Cu}_{11.35}$ metallic glass [33].

2 Materials and Methods

2.1 Samples Preparation

The $\text{La}_{61.4}\text{Al}_{15.9}\text{Ni}_{11.35}\text{Cu}_{11.35}$ BMG was obtained through an organization provides by Malaysia's Ministry of Science, Technology, and Innovation (MOSTI): 03-01-02-SF0257. To eliminate the thermal history from the prior cutting operation, the $\text{La}_{61.4}\text{Al}_{15.9}\text{Ni}_{11.35}\text{Cu}_{11.35}$ BMG samples were manually surface ground using 240, 320, 400, and lastly 640 grid sandpaper. Additionally, to achieve a flat surface for laser processing, the surface roughness must be reduced.

2.2 Localised Heating Process

A conceptualize method to gain localised ductilisation on the BMG samples can be observed from Fig. 1. BMG area at the heat-affected zone (HAZ) from the suggestive laser heating process will crystallize after annealing. The targeted heat applied to reach the crystalline temperature (T_x) of the Lanthanum based BMG that is 417 K. This is still lower from the melting temperature (T_g) of 446 K, with the different temperature of (ΔT) 29 K. When annealed at ambient room temperature, the localised heating area such as Fig. 1 will make the area ductile, which revert to conventional metallic properties [28, 34].

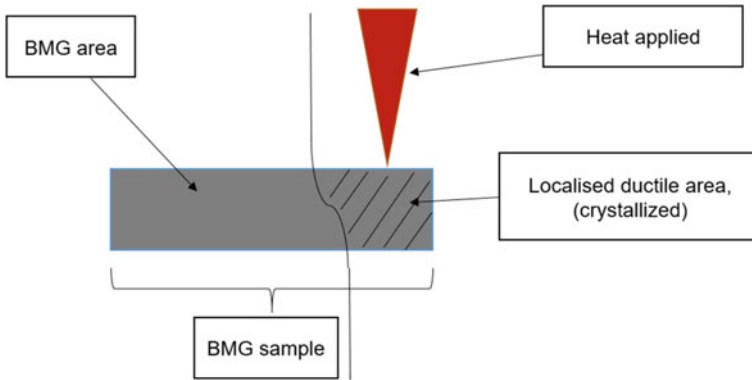


Fig. 1 Illustration of the sample with localised ductilisation

The laser machine of CK-FB3D Laser 3D Fiber Laser Marking Cutting Marking Engraving Machine located Kolej Kemahiran Tinggi MARA Kuantan was used in this study. The machine, laser parameters need to be taken into account, such as pulse or continuous, the thermal conductivity of samples, temperature to heat up, laser speed, laser power, et cetera [27, 35, 36]. Setting up the laser run for the BMG samples is crucial to obtain the best laser parameters to achieve suitable localised heating.

Table 4 shows the compilation of studies on the localised heating of the BMG in terms of the alloys system, process, and aim of the study. These references make the idea generated from the aim of studies, using the laser process to create a localised ductilisation, plausible. By selecting the proper parameter and method of laser process, combined with annealing at ambient temperature, the creation of a localized ductilisation has been proven.

Table 4 Compilation of studies on the localised heating of the BMG in terms of the alloys system, process, and aim of the study

BMG alloy system	Process	Aim of the study	Refs.
Zr–Al–Ni–Cu	Diode laser	Crystallisation effect by laser	[37]
Zr–Ti–Cu–Ni–Be	Single-pulse ablation laser	Explosive boiling of MG superheated by nanosecond pulse laser ablation	[38]
Zr–Ti–Cu–Ni–Be	Nanosecond laser (Yb laser fibre)	Generating micro-scale features on BMG	[35]
Zr–Be–Ti–Cu–Ni	Nanosecond laser	Morphology study of BMG from nanosecond laser	[34]
Zr–Cu–Ni–Al	Laser welding	Characteristics of the weld structure in the heat-affected zone and the fusion zone	[14]

Other methods that are in the back-burner by the author are hot oil quenching of the BMG samples. Another method is conventional controlled localised heating by a blow torch. Both of these localised heating methods are the author’s original ideas.

The localised ductilisation process was done using the CK-FB3D Laser 3D Fiber Laser. The optimum laser parameters to be used on the La-based MG is selected after a thorough comparison from previous works on laser machine MG as compiled in Table 5. The previous researches were found to use the Zr-based and Al-based MG for the samples. While in this study, the author will recreate the laser processing into La-based MG. The following Table 6 shows the CK-FB3D Laser 3D Fiber Laser parameters, which are devised accordingly for this study.

Table 5 The comparison of parameters for BMG laser processing

Laser type	Laser power (W)	Speed (mm/s)	Frequency (kHz)	Material	Refs.
400 W Yb-fibre laser (SLM)	400	–	–	Zr _{59.3} Cu _{28.8} Nb _{1.5} Al _{10.4}	[39]
KrF excimer laser (PLD-IV)	–	–	–	Zr _{47.7} Cu ₃₁ Ni ₉ Al _{12.3}	[40]
Ns-pulsed laser	18	1900	100	Zr _{52.5} Cu _{17.9} Ni _{14.6} Al ₁₀ Ti ₅	[41]
Diode laser	500	300	–	Zr ₅₅ Al ₁₀ Ni ₅ Cu ₃₀	[37]
Fibre laser	200	625	–	Al ₈₅ Ni ₅ Y ₆ Co ₂ Fe ₂	[21]
Nd: YAG laser	–	–	–	Zr _{41.2} Ti _{13.8} Cu _{12.5} Ni _{10.0} Be _{22.5}	[38]
LSF-IIIB laser	4000	200		Zr ₅₅ Cu ₃₀ Al ₁₀ Ni ₅	[42]

Table 6 The default parameter of the CK-FB3D laser machine used in this project

Parameter	
Model	CK-FB3D
Output power	50 W
Depth of engraving (based on material)	<0.3 mm
Operating voltage	AC 220 V 50 Hz 5 A
Laser wavelength	1064 nm
Speed	1000 mm/s
Frequency	30 kHz
Pulse width	0 ns
Laser/on delay	750 μs
Laser/off delay	950 μs
End delay	100 μs
Polygon Tc	30 s

2.3 Characterisation of FGM BMG Samples

Planned functionally graded material (FGM) bulk metallic glass (BMG) samples to be produced will have a part of the samples be crystalline and a part of the samples to be amorphous. Taken into account this fact, the FGM BMG would produce two distinct properties in one sample. One area has high hardness but is inherently brittle, and one area has ductility but is lower in hardness. Characterisation of the ductile portion could be made through the microstructure observation using FESEM. A destructive test is allowable if the quantity of the sample produced was pre-planned. A uniaxial compressive (stress–strain) test, which is set to stop before the failure point to make the test not destructive, can produce a rate of stress–strain relation, which offers information of the FGM BMG behaviour.

2.4 Morphology Around Laser Response of the Lanthanum Based FGM BMG Samples

After the localised ductilisation process of laserising the La-based MG, the laser tracking of the samples was observed under the microscope. The laser parameters were varied by power percentage, frequency (kHz), and speed (mm/s). Overall, 20 laser tracks were observed under the JEOL JSM-7800F high-resolution Field Emission Scanning Electron Microscope (FESEM). With its 300,000 times magnification and fast graphic computation, the observation is suitable for this type of machine. The analysis of the results from the morphology around the laser response can be concluded for the best laser parameter for $\text{La}_{61.4}\text{Al}_{15.9}\text{Ni}_{11.35}\text{Cu}_{11.35}$ FGM BMG.

3 Results and Discussion

The rationale of a functionally graded material bulk metallic glass (FGM BMG) is that both advantageous properties occurring in crystalline and amorphous structures can be applied. An example of FGM BMG is from the research of Windl [43] for military usage, the development of compositionally graded metallic glass $\text{Zr}_{55}\text{Al}_{10}\text{Ni}_5\text{Cu}_{30}$ shows promising results as penetration bullet. Other than that, Yunzhuo et al. research showed how the $\text{Zr}_{50}\text{Ti}_5\text{Cu}_{27}\text{Ni}_{10}\text{Al}_8$ (Zr50) was used to create a gradual variation of crystallinity [24, 25]. This was mainly due to the gradient structural relaxation accumulation induced by the thermal history from laser additive manufacturing (LDM) [24, 25]. As far as the author's knowledge, there are a few or minimal sources of literature point at the FGM from the Lanthanum based BMG. The final Lanthanum, FGM BMG process, is planned to be as Fig. 1, where it is easy to point to which area for ductilisation for the specific application. To achieve this, further experiment and research on the $\text{La}_{61.4}\text{Al}_{15.9}\text{Ni}_{11.35}\text{Cu}_{11.35}$ sample needs to be done to

observe its response. Therefore, in current work, the successful production of the $\text{La}_{61.4}\text{Al}_{15.9}\text{Ni}_{11.35}\text{Cu}_{11.35}$ FGM BMG was a novelty that contributed to BMG knowledge. In current works, the results were promising to show the broad-spectrum laser parameter of the laser tracking process and its results from the FESEM point of view.

3.1 FESEM Results for FGM BMG

The FESEM of FGM BMG laser tracking results were essential for observing the heat-affected zone (HAZ) impact [25]. The different regions of amorphous and crystalline structure in one sample BMG as the laser processing occurred need to be analysed to see the best parameter for the laser tracking experiment [14].

Figure 2 of Wessels et al. [41] work showed the SEM images of the $\text{Zr}_{52.5}\text{Cu}_{17.9}\text{Ni}_{14.6}\text{Al}_{10}\text{Ti}_5$ BMG samples after the samples were applied, the direct laser track was run with various parameters. Wessels et al. [41] showed the explicit representation of the laser tracking in terms of the crystallisation and extreme surface

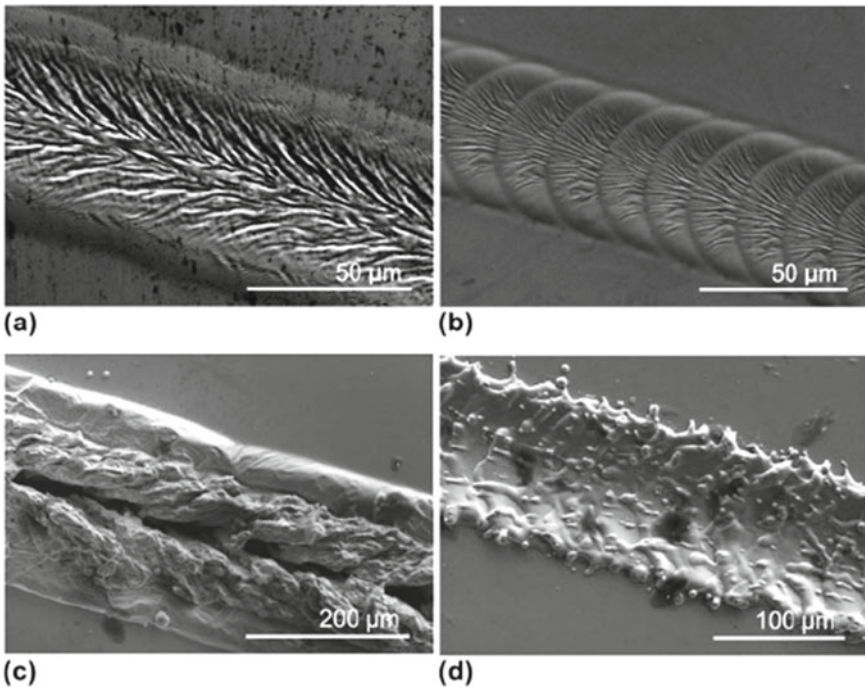


Fig. 2 Grooves engraved into the surface of the BMG by an ns-pulsed laser at **a, b** 100 and 1000 mm/s feed rates, respectively, and 10% power; **c, d** 100 and 1000 mm/s, respectively, and 70% power. In **a, b**, contraction due to crystallisation is indicated by the rippled morphology; in **c, d**, extreme surface damage and redeposition of melted material are seen. *Source* Wessels et al. [41]

damage on the BMG sample. An ns-pulsed laser engraved grooves into the surface of the BMG at (a, b) 100 and 1000 mm/s feed rates, respectively, and 10% power; (c, d) 100 and 1000 mm/s, respectively, and 70% power. The rippling morphology in (a, b) indicates contraction owing to crystallisation; in (c, d), significant surface damage and redeposition of melted material are seen.

In current work, the $\text{La}_{61.4}\text{Al}_{15.9}\text{Ni}_{11.35}\text{Cu}_{11.35}$ FGM BMG was synthesised as in the Wessels et al. [41] works of the laser tracking experiments. The laser can be controlled to be a pulse or continuous. Power penetration can be controlled high and low. Smaller localised heating can be used for the BMG samples. If the parameters are suitable, the percentage of the localised crystalline area on the BMG sample can be increased even further, and the qualitative data is synthesised. Table 5 is the selected compilation of the BMG laser processing parameters.

By compiling several laser processing parameters and analysing the work done by Wessels et al. [41], the laser experiment can be done with a reasonable degree of confidence. To the best of the author's knowledge, the $\text{La}_{61.4}\text{Al}_{15.9}\text{Ni}_{11.35}\text{Cu}_{11.35}$ FGM BMG by laser processing was not published before, and the specific parameters for the laser were also not available. Figures 3, 4 and 5 show the $\text{La}_{61.4}\text{Al}_{15.9}\text{Ni}_{11.35}\text{Cu}_{11.35}$ MG under laser tracking processes via the FESEM observation.

Figure 3 shows FESEM images response towards laser tracking with variations of power (W). A variation from 10 to 100% of power was done to the $\text{La}_{61.4}\text{Al}_{15.9}\text{Ni}_{11.35}\text{Cu}_{11.35}$ BMG. It can be concluded that the crystallisation of $\text{La}_{61.4}\text{Al}_{15.9}\text{Ni}_{11.35}\text{Cu}_{11.35}$ BMG can be completed in the 80, 90, and 100% of the

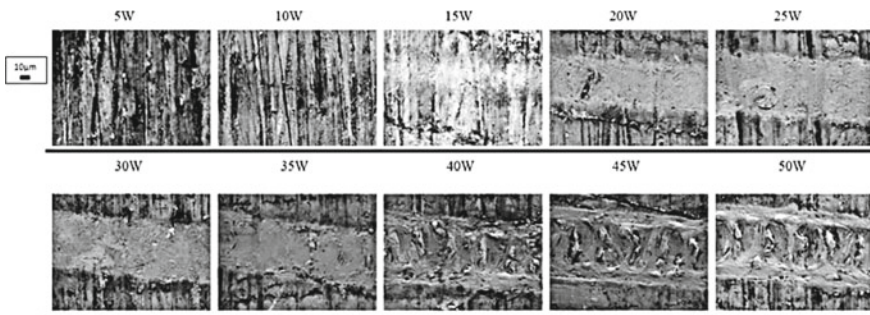


Fig. 3 The morphology of $\text{La}_{62}\text{Al}_{14}\text{Cu}_{12}\text{Ni}_{12}$ BMG samples after laser tracking process. The parameter power (W) was varied from 5 to 50 W with the increment of 5, equivalent to 10–100%

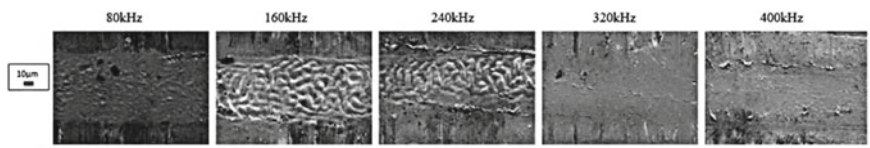


Fig. 4 The morphology of $\text{La}_{61.4}\text{Al}_{15.9}\text{Ni}_{11.35}\text{Cu}_{11.35}$ BMG samples after laser tracking process. The parameter frequency (kHz) was varied from 80 to 400 kHz

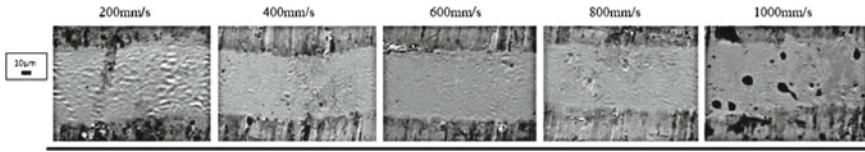


Fig. 5 The morphology of La₆₂Al₁₄Cu₁₂Ni₁₂ BMG samples after laser tracking process. The parameter speed (mm/s) was varied from 200 to 1000 mm/s

power penetration, which are equivalent to 40, 45 and 50 W. This is because the ripple patterns were evident in that region. The 70% power and lower shows no major ripple patterns and can be concluded that the HAZ does not reach the needed temperature to attain a heavy crystalline zone.

Figure 4 shows with the fixed setting of 50% power equal to 25 W, but variations of frequency, the La_{61.4}Al_{15.9}Ni_{11.35}Cu_{11.35} demonstrates heavy ripple pattern creation using 160 and 240 kHz settings. Which translate to 40 and 60% of the frequency intervals. A conclusion of the best crystallisation occurrence with good HAZ happen at 160–240 kHz frequency region.

Figure 5 shows with fixed setting 50% of power equal to 25 W, but variations of speed, the La_{61.4}Al_{15.9}Ni_{11.35}Cu_{11.35} demonstrates substantial ripple pattern creation with 200 and 400 mm/s modes. Which convert to 20 and 40% of the speed intervals. The most acceptable crystallisation existence with decent HAZ happens at 200–400 mm/s speed parameter region. Table 7 lists the optimum parameters for the La_{61.4}Al_{15.9}Ni_{11.35}Cu_{11.35} BMG based on the FESEM observation.

Although the FESEM results were concluded intuitively for the La_{61.4}Al_{15.9}Ni_{11.35}Cu_{11.35} BMG FGM parameters. Equation 1 shows the relation of heat (Q), specific heat (C_p), mass (m), and temperature change (ΔT). The simplified relation of heating from the laser towards the La-based BMG can show the crystallisation occurrence.

Heat and Energy relation.

$$Q = C_p \times m \times \Delta T \tag{1}$$

With 50 W of laser power, Lanthanum specific heat of 0.19 J/g K, the mass of the samples at 0.76 g, the estimated heat changes were at 346 °C (619.15 K). The thermal properties shows the La_{61.4}Al_{15.9}Ni_{11.35}Cu_{11.35} crystalline temperatures of 172.85 °C (446 K). Thus proving that the laser processing method can heat the La-based BMG samples to the crystalline region.

Table 7 The optimum parameters for the laser tracking of La_{61.4}Al_{15.9}Ni_{11.35}Cu_{11.35} bulk metallic glass based on the FESEM observation

Laser power (W)	Frequency (kHz)	Speed (mm/s)
40–50	160–240	200–400

The research towards achieving the finest $\text{La}_{61.4}\text{Al}_{15.9}\text{Ni}_{11.35}\text{Cu}_{11.35}$ BMG FGM needs to be fine-tuned towards the specific application. Placing, gradient, pattern, or the depth of the needed FGM BMG needed to be tuned towards their explicit use. Other than that, the author's work is just the tip of the $\text{La}_{61.4}\text{Al}_{15.9}\text{Ni}_{11.35}\text{Cu}_{11.35}$ FGM BMG research and can be improved further.

4 Conclusion

This research presents the localised heating process of the BMG samples. The explored methods from the literature are the laser processing method. This process has proper proceeding research done on the BMG and is used as the reference. When the localised laser heating process was done, surpassing the eutectic point, coupled with the annealing process of the BMG samples with ambient temperature, the specific area of heating became crystalline, and a graded structure of BMG samples was created. The morphology of the heat-affected zones (HAZ) of $\text{La}_{62}\text{Al}_{14}\text{Cu}_{12}\text{Ni}_{12}$ BMG samples due to the laser processing at various parameters were observed and analysed in terms of the amorphicity and crystallinity. The ripple patterns structure reflected the crystallisation at the HAZ. The results concluded that for laser processing of the $\text{La}_{61.4}\text{Al}_{15.9}\text{Ni}_{11.35}\text{Cu}_{11.35}$ BMG samples' optimum ranges of power, frequency and speed are 40–50 W, 160–240 kHz and 200–400 mm/s, respectively. Thus the Lanthanum based FGM BMG was successfully created by the current work. The promising finding on the microstructural or morphology of the laser processing provides a good understanding for future advancement research on the $\text{La}_{61.4}\text{Al}_{15.9}\text{Ni}_{11.35}\text{Cu}_{11.35}$ BMG.

Acknowledgements The authors are grateful to the Ministry of Education Malaysia: FRGS/1/2017/TK05/UMP/01/1. Ministry of Science, Technology and Innovation (MOSTI), Malaysia SMD, Universiti Malaysia Pahang: 03-01-02-SF0257. The research work is strongly supported by the Advanced Structural Integrity and Vibration Research Group (ASIVR) and Structural Materials and Degradation (SMD) Focus Group, Faculty of Mechanical and Automotive Engineering Technology, University Malaysia Pahang. "Mohd Kamal bin Kamarulzaman" is the recipient of the UMP Post-Doctoral Fellowship in Research.

Declaration of Competing Interest The authors declare that they have no known competing financial interests or personal relationships that could have appeared to influence the work reported in this paper.

References

1. Chen M (2011) A brief overview of bulk metallic glasses. *NPG Asia Mater* 3(9):82–90. <https://doi.org/10.1038/asiamat.2011.30>
2. Ruhl RC (1967) Cooling rates in splat cooling. *Mater Sci Eng* 1(6):313–320. [https://doi.org/10.1016/0025-5416\(67\)90013-4](https://doi.org/10.1016/0025-5416(67)90013-4)

3. Halim Q, Mohamed NAN, Rejab MRM, Naim WNW, Ma Q (2021) Metallic glass properties, processing method and development perspective: a review. *Int J Adv Manuf Technol*. <https://doi.org/10.1007/s00170-020-06515-z>
4. Chen HS, Turnbull D (1969) Formation, stability and structure of palladium-silicon based alloy glasses. *Acta Metall* 17(8):1021–1031. [https://doi.org/10.1016/0001-6160\(69\)90048-0](https://doi.org/10.1016/0001-6160(69)90048-0)
5. Argon AS (1979) Plastic deformation in metallic glasses. *Acta Metall* 27(1):47–58. [https://doi.org/10.1016/0001-6160\(79\)90055-5](https://doi.org/10.1016/0001-6160(79)90055-5)
6. Spaepen F (1977) A microscopic mechanism for steady state inhomogeneous flow in metallic glasses. *Acta Metall* 25(4):407–415. [https://doi.org/10.1016/0001-6160\(77\)90232-2](https://doi.org/10.1016/0001-6160(77)90232-2)
7. Inoue A, Wang XM, Zhang W (2008) Developments and applications of bulk metallic glasses. *Rev Adv Mater Sci* 18(1):1–9
8. Takeuchi A, Yubuta K, Makino A, Inoue A (2009) Evaluation of glass-forming ability of binary metallic glasses with liquidus temperature, crystallographic data from binary phase diagrams and molecular dynamics simulations. *J Alloy Compd* 483(1–2):102–106. <https://doi.org/10.1016/j.jallcom.2008.07.186>
9. Peker A, Johnson WL (1993) A highly processable metallic glass: Zr_{41.2}Ti_{13.8}Cu_{12.5}Ni_{10.0}Be_{22.5}. *Appl Phys Lett* 63(17):2342–2344. <http://doi.org/10.1063/1.110520>
10. Ouyang D, Li N, Xing W, Zhang J, Liu L (2017) 3D printing of crack-free high strength Zr-based bulk metallic glass composite by selective laser melting. *Intermetallics* 90:128–134. <https://doi.org/10.1016/j.intermet.2017.07.010>
11. Halim Q, Mohamed NAN, Rejab MRM, Naim WNW, Ma Q (2021) Metallic glass properties, processing method and development perspective: a review. *Int J Adv Manuf Technol* 112(5):1231–1258. <https://doi.org/10.1007/s00170-020-06515-z>
12. Schroers J, Johnson WL (2004) Ductile bulk metallic glass. *Phys Rev Lett* 93(25):255506. <https://doi.org/10.1103/PhysRevLett.93.255506>
13. Cao JD, Kirkland NT, Laws KJ, Birbilis N, Ferry M (2012) Ca-Mg-Zn bulk metallic glasses as bioresorbable metals. *Acta Biomater* 8(6):2375–2383. <https://doi.org/10.1016/j.actbio.2012.03.009>
14. Pilarczyk W (2018) Structure and properties of Zr-based bulk metallic glasses in As-cast state and after laser welding. *Materials (Basel)* 11(7). <http://doi.org/10.3390/ma11071117>
15. Das J, Tang MB, Kim KB, Theissmann R, Baier F, Wang WH, Eckert J (2005) “Work-hardenable” ductile bulk metallic glass. *Phys Rev Lett* 94(20):205501. <https://doi.org/10.1103/PhysRevLett.94.205501>
16. Rizzi P, Habib A, Castellero A, Battezzati L (2013) Ductility and toughness of cold-rolled metallic glasses. *Intermetallics* 33:38–43. <https://doi.org/10.1016/j.intermet.2012.09.026>
17. Kolodziejska JA, Kozachkov H, Kranjc K, Hunter A, Marquis E, Johnson WL, Flores KM, Hofmann DC (2016) Towards an understanding of tensile deformation in Ti-based bulk metallic glass matrix composites with BCC dendrites. *Sci Rep* 6:22563. <https://doi.org/10.1038/srep22563>
18. Zhai H, Wang H, Liu F (2016) A strategy for designing bulk metallic glass composites with excellent work-hardening and large tensile ductility. *J Alloy Compd* 685:322–330. <https://doi.org/10.1016/j.jallcom.2016.05.290>
19. Scudino S, Bian JJ, Shakur Shahabi H, Soppa D, Sort J, Eckert J, Liu G (2018) Ductile bulk metallic glass by controlling structural heterogeneities. *Sci Rep* 8(1):9174. <https://doi.org/10.1038/s41598-018-27285-5>
20. Ekambaram R, Thamburaja P, Yang H, Li Y, Nikabdullah N (2010) The multi-axial deformation behavior of bulk metallic glasses at high homologous temperatures. *Int J Solids Struct* 47(5):678–690. <https://doi.org/10.1016/j.ijsolstr.2009.11.008>
21. Li XP, Kang CW, Huang H, Sercombe TB (2014) The role of a low-energy-density re-scan in fabricating crack-free Al₈₅Ni₅Y₆Co₂Fe₂ bulk metallic glass composites via selective laser melting. *Mater Des* 63:407–411. <https://doi.org/10.1016/j.matdes.2014.06.022>
22. Li N, Zhang J, Xing W, Ouyang D, Liu L (2018) 3D printing of Fe-based bulk metallic glass composites with combined high strength and fracture toughness. *Mater Des* 143:285–296. <https://doi.org/10.1016/j.matdes.2018.01.061>

23. Dong F, He M, Zhang Y, Wang B, Luo L, Su Y, Yang H, Yuan X (2019) Investigation of shear transformation zone and ductility of Zr-based bulk metallic glass after plasma-assisted hydrogenation. *Mater Sci Eng A* 759:105–111. <https://doi.org/10.1016/j.msea.2019.05.027>
24. Lu Y, Huang Y, Wu J (2018) Laser additive manufacturing of structural-graded bulk metallic glass. *J Alloy Compd* 766:506–510. <https://doi.org/10.1016/j.jallcom.2018.06.259>
25. Lu Y, Huang Y, Wu J, Lu X, Qin Z, Daisenberger D, Chiu Y-L (2018) Graded structure of laser direct manufacturing bulk metallic glass. *Intermetallics* 103:67–71. <https://doi.org/10.1016/j.intermet.2018.10.005>
26. Shin H-S, Jeong Y-J, Choi H-Y, Kato H, Inoue A (2007) Joining of Zr-based bulk metallic glasses using the friction welding method. *J Alloy Compd* 434–435:102–105. <https://doi.org/10.1016/j.jallcom.2006.08.129>
27. Chen B, Shi TL, Li M, Yang F, Yan F, Liao GL (2014) Laser welding of annealed $Zr_{55}Cu_{30}Ni_5Al_{10}$ bulk metallic glass. *Intermetallics* 46:111–117. <https://doi.org/10.1016/j.intermet.2013.11.008>
28. Chen B, Shi T, Li M, Wen C, Liao G (2015) Crystallization of $Zr_{55}Cu_{30}Al_{10}Ni_5$ bulk metallic glass in laser welding: simulation and experiment. *Adv Eng Mater* 17(4):483–490. <https://doi.org/10.1002/adem.201400145>
29. Kumar R, Kumar R, Chattopadhyaya S, Ghosh A, Kumar A (2015) Friction stir welding of BMG's: a review
30. Zhang H, Lu Y, Huang Y, Feng A, Qin Z, Lu X (2015) Joining of $Zr_{51}Ti_5Ni_{10}Cu_{25}Al_9$ BMG to aluminum alloy by friction stir welding. *Vacuum* 120:47–49. <https://doi.org/10.1016/j.vacuum.2015.06.020>
31. Huang Y, Xue P, Guo S, Wu Y, Cheng X, Fan H, Ning Z, Cao F, Xing D, Sun J, Liaw PK (2016) Liquid-solid joining of bulk metallic glasses. *Sci Rep* 6:30674. <https://doi.org/10.1038/srep30674>
32. Kim J, Lee T (2017) Brazing method to join a novel $Cu_{54}Ni_6Zr_{22}Ti_{18}$ bulk metallic glass to carbon steel. *Sci Technol Weld Joining* 22(8):714–718. <https://doi.org/10.1080/13621718.2017.1306155>
33. Halim Q, Nikabdullah N, Rejab MRM, Rashidi M (2020) Fracture response of $La_{61.4}Al_{15.9}Ni_{11.35}Cu_{11.35}$ bulk metallic glass subjected to quasi-static compression loading. *Mater Today Proc* 27:1761–1767. <https://doi.org/10.1016/j.matpr.2020.03.662>
34. Williams E, Lavery N (2017) Laser processing of bulk metallic glass: a review. *J Mater Process Technol* 247:73–91. <https://doi.org/10.1016/j.jmatprotec.2017.03.034>
35. Williams E, Brousseau EB (2016) Nanosecond laser processing of $Zr_{41.2}Ti_{13.8}Cu_{12.5}Ni_{10}Be_{22.5}$ with single pulses. *J Mater Process Technol* 232:34–42. <https://doi.org/10.1016/j.jmatprotec.2016.01.023>
36. Li B, Li ZY, Xiong JG, Xing L, Wang D, Li Y (2006) Laser welding of $Zr_{45}Cu_{48}Al_7$ bulk glassy alloy. *J Alloy Compd* 413(1–2):118–121. <https://doi.org/10.1016/j.jallcom.2005.07.005>
37. Ikutomo R, Tsujikawa M, Hino M, Kimura H, Yubuta K, Inoue A (2013) Crystallisation by laser for Zr based bulk metallic glass. *Int J Cast Met Res* 21(1–4):148–151. <https://doi.org/10.1179/136404608x361855>
38. Jiang MQ, Wei YP, Wilde G, Dai LH (2015) Explosive boiling of a metallic glass superheated by nanosecond pulse laser ablation. *Appl Phys Lett* 106(2). <http://doi.org/10.1063/1.4905928>
39. Best JP, Ast J, Li B, Stolpe M, Busch R, Yang F, Li X, Michler J, Kruczic JJ (2020) Relating fracture toughness to micro-pillar compression response for a laser powder bed additive manufactured bulk metallic glass. *Mater Sci Eng A* 770. <https://doi.org/10.1016/j.msea.2019.138535>
40. Liu WD, Ye LM, Liu KX (2011) Micro-nano scale ripples on metallic glass induced by laser pulse. *J Appl Phys* 109(4):043105–043109. <http://doi.org/10.1063/1.3552914>
41. Wessels V, Grigoryev A, Dold C, Wyen C-F, Roth R, Weingärtner E, Pude F, Wegener K, Löffler JF (2012) Abrasive waterjet machining of three-dimensional structures from bulk metallic glasses and comparison with other techniques. *J Mater Res* 27(8):1187–1192. <https://doi.org/10.1557/jmr.2012.36>

42. Zhang Y, Lin X, Wang L, Wei L, Liu F, Huang W (2015) Microstructural analysis of Zr₅₅Cu₃₀Al₁₀Ni₅ bulk metallic glasses by laser surface remelting and laser solid forming. *Intermetallics* 66:22–30. <https://doi.org/10.1016/j.intermet.2015.06.007>
43. Windl W (2016) Development of compositionally graded metallic glass alloys with desirable properties

Prediction and Optimization of Thermophysical Properties of Hybrid Cellulose Nanocrystal-Copper (II) Oxide Nanolubricant for Tribology Application



Sakinah Hisham , K. Kadirgama , D. Ramasamy , M. Samykano, N. W. Awang, and Mohd Kamal Kamarulzaman 

Abstract Response surface methodology (RSM) was used in conjunction with the miscellaneous design model to identify prediction models for the thermophysical properties of a hybrid cellulose nanocrystal-copper (II) oxide nanolubricant. Minitab 18 statistical analysis software and Response Surface Methodology (RSM) based on Central Composite Design (CCD) were utilised to generate an empirical mathematical model investigating the effect of concentration and temperature. Analysis of variance (ANOVA) is used to validate the significance of the developed empirical mathematical model. Thirteen experiments were conducted to obtain second-order polynomial equations for the desired specific heat capacity, thermal conductivity, and dynamic viscosity, outputs. The predicted values were found to be in reasonable agreement following the investigational finding. In addition, the models could predict more than 80% of the nanolubricant output variations, indicating that the

S. Hisham · K. Kadirgama · N. W. Awang
Faculty of Mechanical and Automotive Engineering Technology, Universiti Malaysia Pahang,
26600 Pekan, Pahang, Malaysia
e-mail: sakinah.hisham0704@gmail.com

K. Kadirgama
e-mail: kumaran@ump.edu.my

N. W. Awang
e-mail: norazmira@psmza.edu.my

S. Hisham · K. Kadirgama · D. Ramasamy · M. K. Kamarulzaman (✉)
Advanced Nano Coolant-Lubricant (ANCL) Lab, Automotive Engineering Centre, Universiti
Malaysia Pahang, 26600 Pekan, Pahang, Malaysia
e-mail: kamalkz@hotmail.com; kamalkz@ump.edu.my

D. Ramasamy
e-mail: deva@ump.edu.my

D. Ramasamy · M. Samykano
College of Engineering, Universiti Malaysia Pahang, 26300 Gambang, Pahang, Malaysia
e-mail: mahendran@ump.edu.my

N. W. Awang
Politeknik Sultan Mizan Zainal Abidin, 23000 Dungun, Terengganu, Malaysia

model is accurate. In the optimization plot, the predicted optimal values for dynamic viscosity, thermal conductivity, and specific heat capacity are 2.3631, 0.1463, and 1.6311, respectively. The relevant parameters are 90 °C and 0.1 for temperature and concentration, respectively. The plotted composite is 0.6531. The findings of the percentage of absolute error (POAE) reveal that the model may precisely predict the optimum experimental parameters.

Keywords Thermophysical properties · Nanocellulose · Copper (II) oxide · Nanolubricant

1 Introduction

The growing necessity for inventing and introducing high-efficiency lubricant and coolant fluids is a result of the evolution of productions in the area of development and optimization of systems reliant on heat transfer [1]. As a result, researchers have expended a great deal of effort in empirical, numerical, and analytical investigations in order to propose improved working fluids for heat transfer systems [2–5]. Friction between moving elements is one of the variables that cause energy damping in numerous sectors, and lubricants are used to reduce this friction. Owing of the importance of lubricants in businesses today, research into their qualities in order to improve efficiency and lower costs is a must.

Response surface methodology (RSM) is the recommended statistical tool for optimising the important parameters of any actual process of manufacturing, which requires the least number of experiments and provides the best condition settings for maximum yield [6]. RSM requires fewer experimental trails than artificial neural networks (ANN) since it develops a mathematical matrix and investigates various factors and their interactions [7]. As a result, multiple RSM-based studies effectively verified experimental data without assuming anything.

Nasirzadehroshenin et al. [8] used ANN and RSM to accurately predict thermal viscosity and conductivity when they synthesised $\text{Al}_2\text{O}_3\text{-TiO}_2$ (10%) nano material in three sizes and distributed them in water to create a hybrid nanofluid at 20–50 °C temperature with volume fraction of 0–0.5%. According to the analysis of variance (ANOVA) table, temperature (A), concentration (B), particle size (C), and the interaction term (AB) had an important influence on the model with a smaller P-value. Peng et al. [9] estimated and optimised the thermal conductivity of CuO/water nanofluid using RSM at 25–40 °C and 0.1–0.4 vol%. According to the authors, the proposed CuO/water nanofluid model could interpolate and extrapolate data with precision lower than 2%. Salehnezhza et al. employed RSM in the water-based drilling fluid application. The authors focused to study the rheological properties of starch-ZnO/water nanofluid. The plastic point, yield point, flow behaviour, and thermal conductivity were explored, and correlations between them were given based on the influence ZnO nanoparticles percentage, starch, and ultrasonication time.

The objective of this study was to use the response surface model (RSM) to develop prediction models for thermophysical properties of nanolubricants such as specific heat capacity, thermal conductivity, and dynamic viscosity, and compare them to the curve fitting method to investigate the effects of primary factors (concentration and temperature) and interaction factors.

2 Methodology

2.1 Regression Modelling

Normally, RSM predicts a low-order polynomial. If the relation between the input and output produce a linear function, then the estimation relation is the simplest first-order model [10]. The output response and input factor can be represented as $x_1, x_2 \dots, x_k$, and y , respectively as following Eq. 1.

$$y = f'(x)\beta + \varepsilon \quad (1)$$

where $x = (x_1, x_2, \dots, x_k)$, $f(x)$ is a vector function of p elements which contains powers of x_1, x_2, \dots, x_k to a maximum specific degree indicated by d (>1). The initial ($d = 1$) degree polynomial is written by following Eq. 2.

$$y = \beta_0 + \sum_{i=1}^k \beta_i x_i + \varepsilon \quad (2)$$

where β_0 is regression coefficient for the intercept, k is number of factors, β_i is regression coefficients of linear parameters, x_i represented factors, and ε is residual (error) of the experiments.

On the other hand, the model should not predict any curvature. If the model predicts curvature, it is essential to apply a higher degree of polynomial such as second-order model. In addition, a simple linear equation (first-order model) unable to explain the interaction between different factors and the quadratic second-order equation with interaction terms is usually implemented in RSM, which is unable to find the critical point. Moreover, the two-level factorial design is applied in the prediction of first-order effects; however, they fail with the presence of supplementary influences, such as the impact of the second order. Therefore, a central point in two-level factorial designs able to be used for analysing curvature. The following level of polynomial model consists of supplementary terms, which explains the interaction amongst the dissimilar experimental variables [11]. Thus, a model for the second-order interaction can be described as in Eq. 3.

$$y = \beta_0 + \sum_{i=1}^k \beta_i x_i + \sum_{1 \leq i \leq j}^k \beta_{ij} x_i x_j + \varepsilon \quad (3)$$

where β_{ij} represents regression coefficients of the interaction parameters.

To discover a critical point (minimum, saddle, or maximum point), it is essential for the polynomial function to include quadratics term in following Eq. 4.

$$y = \beta_0 + \sum_{i=1}^k \beta_i x_i + \sum_{i=1}^k \beta_{ii} x_i^2 + \sum_{1 \leq i \leq j}^k \beta_{ij} x_i x_j + \varepsilon \quad (4)$$

where β_{ii} represents regression coefficients of the quadratic parameter. This model able to estimate the interaction effect among dissimilar input factors and the critical points (minimum, maximum, or saddle point).

After selected an appropriate mathematical model, the predictive capability of the model must be confirmed before it is ready for predicting purpose. Such validation step is to make sure that the model offers a satisfactory estimation to the real system. Among the option to estimate the quality of the fitted model is through the application of analysis of variance (ANOVA). ANOVA is essential to compare the difference owing to the changes in the combination of variable levels with the difference due to random errors inherent to the measurements of the produced responses. Referring to the judgement, it is feasible to analyse the importance of the regression utilized to estimate responses according to the sources of investigational variance. Through ANOVA, the estimation of data set variation is done by evaluating its dispersion. The overall efficiency of a prediction model is commonly described by the coefficient of determination (R^2). The R^2 is the ratio of regression sum of squares (SS_{Reg}) to the total sum of squares (SS_{T}). It determines the total variation of the model or predicted values from the mean. Good prediction efficiency model must have the R^2 value close to 100%. Nevertheless, the prediction efficiency of a model must not be evaluated by R^2 only, as R^2 increases with increase in the number of the model terms, regardless of its statistical significance [12]. The R^2 value must be compared with the adjusted R^2 (R^2_{adjusted}), which consider the number of factors in the experiment. The value of R^2_{adjusted} usually reduces if statistically unimportant parameters are included. Once R^2 and R^2_{adjusted} vary greatly, there is huge potential that non-significant terms have been included in the model. Residual is an essential term in deciding the adequacy of a certain model which represents the gap amongst the actual and predicted value. In addition, the prediction error sum of squares (PRESS) is one more statistic term utilized for evaluating the predictive capability of a model. It is an evaluation of how good the model for the experiment is expected to forecast the response in future testing. The PRESS with small values is desired. The prediction ability of the model for new response is described by $R^2_{\text{predicted}}$ and can be computed from PRESS. Both R^2 and $R^2_{\text{predicted}}$ must be in close agreement with one another [13].

The significance of individual factor and interaction between one another is confirmed using the Fisher test. The bigger the degree of the F-value and together

with the lesser the value of ' $p > F$ ', indicates the corresponding model and each of the coefficients are more significant. If the value of ' $p > F$ ' is lower than 0.05, then the significant of the model is at a 95% confidence interval. Moreover, the significant of the model also can be judged through the lack of fit test. The lack of fit test determines the failure of a model in demonstrating data points in the experimental area by comparing the residual error against the pure error from the duplicated experimental design points (normally the central point in the experimental design) and the lack of fit test must be insignificant. If this ratio is greater than the tabulated F-value, proof of lack of fit is assumed and refinement is required for the model.

2.2 Optimization and Experimental Validation

Response surfaces can be evaluated to determine the minimum or maximum responses, and the equivalent optimum conditions. Using multiple responses, the optimum conditions can be found when all the parameters simultaneously satisfy the desirable criteria [14]. The optimum circumstances can be found using various responses when all the parameters meet the desirable requirements, simultaneously. Furthermore, the optimum condition can be found graphically by superimposing the contour plots of the regression model in an overlay plot. The graphical optimization indicates the area of feasible response values in the factor space and the regions that fit the optimization criteria [15].

The conformation experimental is essential to validate the model's accuracy between the measured experimental data with the predicted value obtained from the regression analysis. Kumar et al. [16] reported that confirmation experiments are not necessary to conduct if the RSM models produce a prediction error of less than 5%. Furthermore, the percentage of absolute error (*POAE*) is used to measure the difference between the measured experimental results with the predicted value obtained from the regression model using Eq. 5.

$$POAE(\%) = \left(\frac{\text{Actual value} - \text{Predicted value}}{\text{Actual value}} \right) \times 100 \quad (5)$$

3 Results and Discussion

In this section, response surface methodology method (RSM) was used in order to determine the prediction models for thermophysical properties of nanolubricant which are specific heat capacity, thermal conductivity, and dynamic viscosity, and compare with the curve fitting method. The RSM is a method of developing and optimising experimental data that is based on statistical and mathematical techniques. This modelling technique is valuable when there are multiple input parameters that

Table 1 Factors at various level

Factors	-1	0	+1
Temperature (continuous)	30	60	90
Concentration (continuous)	0.1	0.5	0.9

interact with one another, and the interaction influences the system's response output. Independent variables are another term for the input parameters. An RSM model reduces the amount of tests needed to understand a system's trends and behaviour [17]. Using Minitab 18, statistical analysis software, an experimental design was created by referring to components with different levels, as indicated in Table 1. Two continuous factors are used in the design of this experiment. As a result, the method of central composite design (CCD) is used to create models which have two continuous variables. There are three levels: centre value (0) high value (+1), and low value (-1). Volume concentration (ϕ) and Temperature (T) are the two continuous variables. Temperature, volume concentration, dynamic viscosity, specific heat capacity, and thermal conductivity were all investigated using a total of 13 experiments. Table 2 summarises the design layout and results of the experiments.

Table 2 Design of experiment with experimental result

Std order	Run order	Temperature (T)	Concentration (ϕ)	Dynamic viscosity (cP)	Thermal conductivity (k)	Specific heat capacity (cp)
1	1	60	0.1	45.59	0.14365	2.99186
2	2	40	0.2	111.60	0.14568	2.26133
3	3	90	0.5	7.20	0.14150	1.66326
4	4	60	0.5	62.39	0.14365	1.76148
5	5	60	0.5	62.39	0.14365	1.76148
6	6	60	0.5	62.39	0.14365	1.76148
7	7	30	0.5	132.00	0.14280	1.13875
8	8	60	0.9	43.19	0.13259	1.34358
9	9	60	0.5	62.39	0.14365	1.76148
10	10	60	0.5	62.39	0.14365	1.76148
11	11	80	0.2	14.40	0.14415	2.38697
12	12	40	0.7	106.79	0.14295	1.19776
13	13	80	0.7	14.40	0.14317	1.31675

3.1 ANOVA Analysis for Thermophysical Properties

The significance and suitability of the constructed model with RSM were determined using the probability (P -value), Fisher's (F -test), and coefficient of variation (R -square) tests [18]. In order to obtain this parameter, the analysis of variance (ANOVA) method was utilised to statistically examine the response model. The variance analysis was performed using the Minitab 18 programme to determine the model's appropriateness and significance. Table 3 shows the derived statistical data for the dynamic viscosity of cellulose nanocrystal-copper (II) oxide (CNC-CuO) nanolubricant. Based on the ANOVA method, a model for determining thermal conductivity is valid if the F value is greater than one and the P -value is less than 0.05. The F -value for the current study is 228.73, indicating the significant of the model. It's worth noting that such a high F -Value has a 0.01 percent chance of being caused by modelling noise. A combination of a low p -value (0.001) with a high F -value implies that the model is capable of accurately predicting thermal conductivity [19]. Furthermore, as shown in Table 3, temperature, values of Prob > F0.05 suggest the model's significance. The square of the statistical deviation between data gained from experiments and those derived using the model is an important parameter, it is known as the coefficient of determination (R^2). Indeed, at R^2 values near to 1, the constructed model and the correlation's predictions are a very good match. Table 4

Table 3 ANOVA result for dynamic viscosity

Source	DF	Adj SS	Adj MS	F-value	P -value
Model	5	17,390.9	3478.2	228.73	0.000
<i>Linear</i>	2	16,319.6	8159.8	536.60	0.000
Temperature (T)	1	16,276.5	16,276.5	1070.36	0.000
Concentration (\emptyset)	1	43.1	43.1	2.84	0.136
<i>Square</i>	2	665.4	332.7	21.88	0.001
T^2	1	122.3	122.3	8.05	0.025
\emptyset^2	1	424.1	424.1	27.89	0.001
<i>2-way interaction</i>	1	12.9	12.9	0.85	0.387
$T\emptyset$	1	12.9	12.9	0.85	0.387
<i>Error</i>	7	106.4	15.2	–	–
Lack-of-fit	3	106.4	35.5	3.244	5.612
Pure error	4	0.0	0.0	–	–
Total	12	–	–	–	–

Table 4 Model summary for dynamic viscosity

S	R-sq	R-sq(adj)	PRESS	R-sq(pred)
3.89956	99.39%	98.96%	774.207	95.58%

Table 5 ANOVA result for thermal conductivity

Source	DF	Adj SS	Adj MS	F-value	P-value
Model	5	0.000096	0.000019	115.59	0.022
<i>Linear</i>	2	0.000072	0.000036	210.44	0.008
Temperature (T)	1	0.000001	0.000001	20.29	0.609
Concentration (\emptyset)	1	0.000071	0.000071	220.60	0.003
<i>Square</i>	2	0.000040	0.000020	45.76	0.033
T ² *	1	0.000000	0.000000	30.08	0.791
\emptyset^2	1	0.000039	0.000039	31.34	0.012
<i>2-way interaction</i>	1	0.000001	0.000001	0.21	0.663
T \emptyset	1	0.000001	0.000001	0.21	0.663
<i>Error</i>	7	0.000024	0.000003	–	–
Lack-of-fit	3	0.000024	0.000008	2.312	3.563
Pure error	4	0.000000	0.000000	–	–
Total	12	–	–	–	–

shows that R-squared (R^2) and R^2 -adj are 99.39% and 98.96%, respectively. As a result, the model accurately represents the data. Notably, adj R^2 indicates R^2 's value while accounting for any biases that may affect it. As a result, the model is more reliable, although R^2 -adj is lower than R^2 . Both results are relatively near to one other in the current experiment, demonstrating the model's accuracy and emphasising the RSM model's suitability for forecasting dynamic viscosity data. The highest adjusted R-squared and R-squared (R^2) values are found in models with a strong capacity to fit the data (R^2 -adj).

Table 5 shows the derived statistical data for the thermal conductivity of CNC–CuO nanolubricant. For thermal conductivity data, the model's F-value was 115.59, indicating that it is significant. It's worth noting that such a high F-Value has a 0.01 percent chance of being caused by modelling noise. A low p -value (0.001) combined with a high F-value implies that the model is capable of accurately predicting thermal conductivity [19]. Moreover, the significance of the model is shown by Prob > F0.05 values. Nonetheless, as shown by Table 6, the model with the highest capability to fit the data had adjusted R-squared (R^2 -adj) and the highest R-squared (R^2) values. The ratio of the model's changes to the total changes is represented by the coefficient of determination, R^2 . As a result, the power of the fitted model representing response variations as a function of the independent variables is greater as R^2 approaches one [20]. Generally, R^2 should be at least 80% for a good fitting model [18]. The governing factors of the model for thermal conductivity in the thermal conductivity

Table 6 Model summary for thermal conductivity

S	R-sq	R-sq(adj)	PRESS	R-sq(pred)
0.0018555	89.97%	85.67%	0.0002069	0.00%

Table 7 ANOVA result for specific heat capacity

Source	DF	Adj SS	Adj MS	F-value	P-value
Model	8	9.4440	1.18050	16.43	0.000
<i>Linear</i>	3	8.6024	2.86746	39.90	0.000
Temperature (T)	1	0.6532	0.65317	9.09	0.008
Concentration (\varnothing)	1	3.9554	3.95542	55.04	0.000
<i>Square</i>	2	0.2685	0.13426	1.87	0.185
T ² *	1	0.0938	0.09377	1.30	0.269
\varnothing^2	1	0.2532	0.25317	3.52	0.078
<i>2-way interaction</i>	3	0.5731	0.19104	2.66	0.081
TC	1	0.0161	0.01614	0.22	0.642
T β	1	0.0010	0.00096	0.01	0.909
$\varnothing\beta$	1	0.5560	0.55601	7.74	0.013
<i>Error</i>	17	1.2216	0.07186	–	–
Lack-of-fit	9	1.2216	0.13573	2.415	1.234
Pure error	8	0.0000	0.00000	–	–
Total	25	10.6656	–	–	–

analysis study are 89.97% and 87.97% for R² (adj), respectively. As a result, the model accurately correlates the experimental results.

ANOVA analysis of specific heat capacity was performed in a similar manner; Table 7 shows the ANOVA result of CNC–CuO nanolubricant. The F-value of the model for the current study was 16.43, indicating that the model is significant. Furthermore, the values of Prob > F0.05 indicate the model’s significance. According to the table, P-values less than 0.05 indicate that the specific heat capacity model is significant. The coefficient of determination (R²), which is the square of the statistical deviation between data gained from experiments and those derived using the model, is an important parameter. Indeed, for R² values near 1, the constructed model and the correlation’s predictions are in close agreement. The adjusted R²-adj (R²-adj) and R² are 85.67% and 89.97%, respectively, as shown in Table 8. Thus, the model fits the data. When any bias is taken into account, Adj R² is comparable to dynamic viscosity and thermal conductivity in that it has a lower value than R². Therefore as outcome, it is lower than R² but more reliable. Both values are very similar to each other in the current work, indicating the model’s accuracy and emphasising the RSM model’s applicability for forecasting specific heat capacity data. RSM has the

Table 8 Model summary for specific heat capacity

S	R-sq	R-sq(adj)	PRESS	R-sq(pred)
0.0786990	98.66%	97.71%	0.311749	90.38%

possibilities to be applied in engineering and thermal science fields, notably in heat and mass transfer applications involving nano-suspensions.

3.2 Independent Variable Influence on Response

The effects of volume concentration and temperature as two independent factors on the nanolubricant's thermophysical properties for dynamic viscosity, specific heat capacity, and thermal conductivity were examined in this study. The P -value is used to identify which model terms are applicable. When the P -value is less than 0.05, Myers and Montgomery [21] conclude that this is an effective response factor. Temperature (T), square of temperature (T^2), and square of concentration (\varnothing^2) are the effective factors in nanolubricant's thermal conductivity, as indicated in Table 3. The effective parameters for thermal conductivity, in contrast to dynamic viscosity, are concentration (\varnothing), and the square of concentration (\varnothing^2). According to Table 7, the effective factors for the response for specific heat capacity are linear T and linear \varnothing . The interaction factor is not essential, according to Tables 3, 5 and 7, thus it can be left out of the model. To put it another way, the insignificant interaction among the independent variables has no influence on the specific heat capacity, thermal conductivity, and dynamic viscosity responses.

3.3 Development of Proposed Regression Model

To create a correlation, a regression analysis was combined with the RSM model results to generate a 2nd order polynomial model that included actual factors like temperature (T) and concentration (\varnothing) as well as their interactions, resulting in a precise prediction of the dynamic viscosity, thermal conductivity, and specific heat capacity of CNC–CuO nanolubricant as a response. The following is the formula that was devised: Eqs. 6, 7 and 8 represent the correlation relationship between the response (dynamic viscosity, thermal conductivity, and specific heat capacity) of CNC–CuO.

$$\text{Dynamic viscosity, } \mu = 219.4 - 3.544T + 70.9\varnothing + 0.00965T^2 - 101.1\varnothing^2 \quad (6)$$

$$\text{Thermal conductivity, } k = 0.14390 - 0.000005T + 0.0144\varnothing - 0.03067\varnothing^2 \quad (7)$$

$$\begin{aligned} \text{Specific heat capacity, } c_p = & 1.439 + 0.05773T - 4.407\varnothing - 0.000439T^2 \\ & + 2.309\varnothing^2 \end{aligned} \quad (8)$$

The dynamic viscosity is denoted by μ , the thermal conductivity is denoted by k , and the nanolubricant's specific heat capacity is denoted by cp . Furthermore, the computed coefficients display the relative importance of the model's individual parameter, whereas the signs show the antagonistic (−) and synergistic (+) influences of response's variables. Concentration \varnothing has a positive effect on the dynamic viscosity of CNC–CuO nanolubricant, as shown in Eq. 6, although Temperature has a negative effect. Furthermore, as a fixed coefficient factor, the factor coefficient for T is smaller than \varnothing , implying that modifying factor T has a smaller impact on the dynamic viscosity of nanolubricant's CNC–CuO than factor \varnothing . The factor \varnothing has a positive effect on the thermal conductivity of nanolubricant's CNC–CuO, while factors T have a negative impact, similar to dynamic viscosity. Furthermore, because the coefficient for factor T is smaller than \varnothing , T is less effective against nanolubricant's CNC–CuO than \varnothing . In contrast to dynamic viscosity and thermal conductivity of nanolubricant's CNC–CuO, factor T has a positive effect on the specific heat capacity, whereas factor \varnothing has a negative impact, according to Eq. 8. Because the factor coefficient \varnothing is smaller than T for specific heat capacity, thus, factor T is less influence for both nanolubricants.

3.4 Comparison Between Predicted and Experimental Model

Figure 1 shows the experimental results of dynamic viscosity are compare to the model's predicted data. As can be seen, the model and experimental results are in good

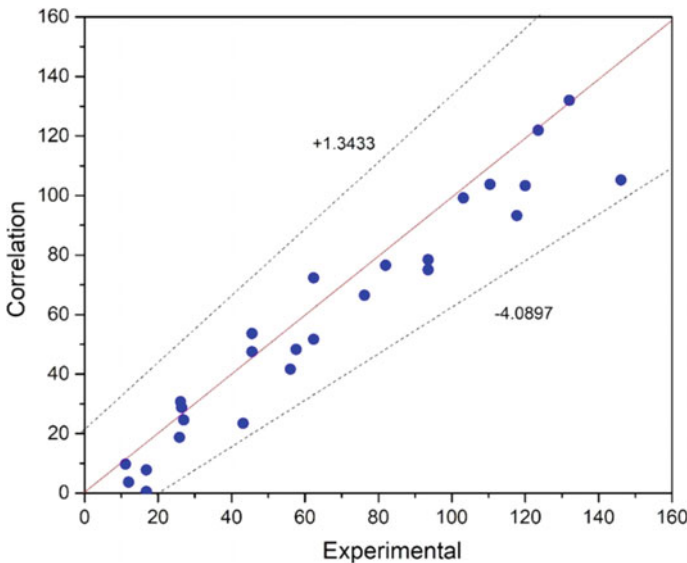


Fig. 1 Comparison between the experimental and correlation of dynamic viscosity

agreement. As a result, the experimental and statistically predicted findings have a significant correlation. Similarly, in Figs. 2 and 3, the experimental results for thermal conductivity and specific heat capacity are compared to the values predicted by the model. As shown in both pictures, the experimental data are accurately predicted by the model. The ineffective terms that have been eliminated from the model are well predicted, and their removal has no negative impact on the model's accuracy.

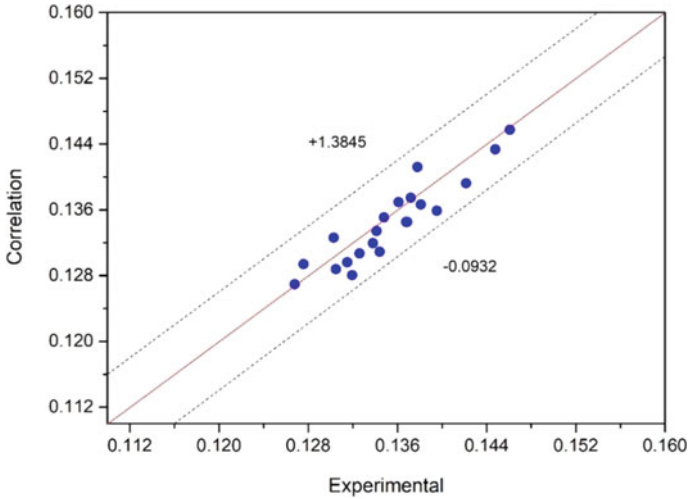


Fig. 2 Comparison between the experimental and correlation of thermal conductivity

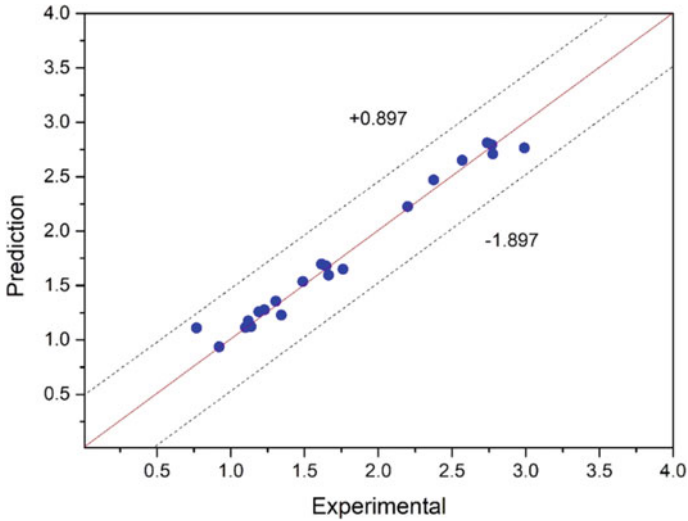


Fig. 3 Comparison between the experimental and correlation of the specific heat capacity

The margin of deviation between the experimental and correlation results for all response was also defined. All three response graphs show the calculated margin of deviation between experimental results and empirical equations at different volume fractions and temperatures. According to the entire figure, the majority of points are located on the bisector or close to it, indicating good accuracy of this equation. In addition, this diagram shows the greatest margin of deviation, which is 1.3433 for dynamic viscosity, 1.3845 for thermal conductivity, and 0.897 for specific heat capacity. This is an acceptable value for an empirical equation. As shown, the forecasted values represent a reasonable compromise with the experimentally obtained values. Furthermore, as explained previously, the majority of the data points are on the 45-degree line, indicating a slight divergence between the predicted and experimental data [22]. As a result, the model produced is reliable.

3.5 Multi-objective Optimization for Thermal and Physical Properties for CNC–CuO

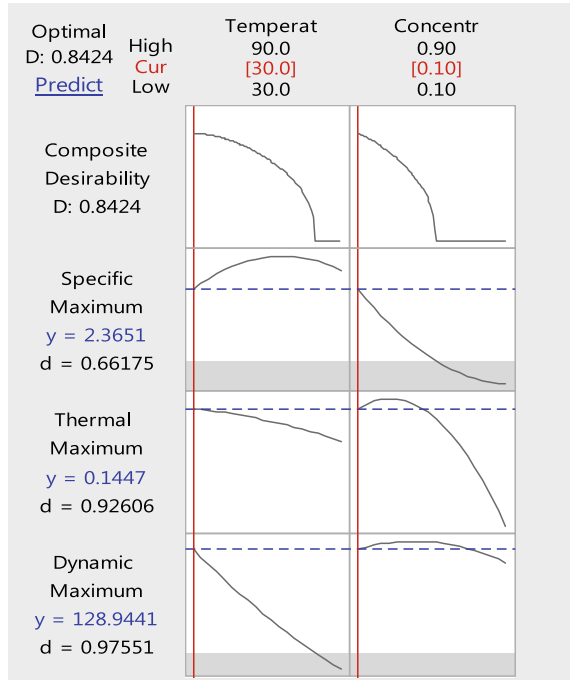
The key benefit of employing response surface methodology (RSM) is that it allows you to control the input parameters to optimise the response [23]. According to the previous section, increasing concentration lead in increases of thermal conductivity, but increasing temperature at a fixed concentration caused increases thermal conductivity at beginning and then remain nearly constant throughout the process. Similarly to thermal conductivity, specific heat capacity increases significantly as temperature rises at a constant concentration. Specific heat capacity, on the other hand, decreases with increasing concentration at a constant temperature. The purpose of this study is to reach the maximum thermal conductivity and specific heat capacity, whereas the goal for dynamic viscosity is to achieve a higher value in order to improve friction and wear. The desirability for the whole process of optimization was calculated to show the feasibility of optimization to examine whether all parameters are within the working range or not. Table 9 shows the optimal condition values for thermophysical properties.

The optimization curve for specific heat capacity and thermal conductivity responses is shown in Fig. 4. The ideal values for specific heat capacity and thermal conductivity are 1.6311 and 0.1463, respectively, as illustrated in the graph. The necessary parameters are 81.51 °C and 0.1 for concentration, temperature, and

Table 9 Optimal condition values for thermophysical properties

Optimum results	Temperature	Concentration	Experimental value	Predicted value	POAE%
μ	90	0.1	2.3631	2.3651	0.08
k	90	0.1	0.14422	0.1463	1.4422
cp	90	0.1	1.52589	1.6311	6.8949

Fig. 4 Optimization plot



nanolubricant type. The composite represented in the plot is 0.6531. An experiment was done utilising the optimum factors to assess specific heat capacity and thermal conductivity in to validate the expected optimization outcomes. Fluid characteristics were tested and compared to the results predicted by the model under optimal conditions. The results, as given in Table 9, imply that the model can accurately predict the optimal experimental conditions.

4 Conclusion

In this research, the Response Surface Methodology (RSM) approach was used to predict the appropriate regression correlation using the regression method and to optimise the thermophysical characteristics of CNC–CuO nanolubricant. The conclusions proposed correlation of the dynamic viscosity, specific heat capacity and thermal conductivity is considered to able to predict the properties as the margin of deviation is closer to the points that are located on the bisector. The plot’s optimum values for dynamic viscosity, thermal conductivity, and specific heat capacity are 2.3631, 0.1463, and 1.6311, respectively. The relevant parameters are 90 °C for concentration and and 0.1 for temperature. In the plot, the composite is 0.6531.

The POAE% findings show that the model is capable of accurately predicting the optimum experimental conditions.

Acknowledgements This work was supported by University Malaysia Pahang [grant number RDU192402]. “Mohd Kamal bin Kamarulzaman” is the recipient of the UMP Post-Doctoral Fellowship in Research.

Credit Authorship Contribution Statement **Sakinah Hisham:** Conceptualization, Methodology, Validation, Formal analysis, Investigation, Data Curation, Writing—Original Draft, Visualization. **K. Kadirgama, D. Ramasamy, M. Samykano:** Conceptualization, Methodology, Validation, Formal analysis, Investigation, Resources, Writing—Review and Editing, Visualization, Supervision. **N. W. Awang:** Conceptualization, Investigation. **Mohd Kamal Kamarulzaman:** Conceptualization.

Declaration of Competing Interest The authors declare that they have no known competing financial interests or personal relationships that could have appeared to influence the work reported in this paper.

References

1. Hisham S, Kadirgama K, Mohammed HA, Kumar A, Ramasamy D, Samykano M, Rahman S (2020) Hybrid nanocellulose-copper (II) oxide as engine oil additives for tribological behavior improvement. *Molecules* 25(13):2975
2. Said Z, Rahman S, Assad MEH, Alami AH (2019) Heat transfer enhancement and life cycle analysis of a shell-and-tube heat exchanger using stable CuO/water nanofluid. *Sustain Energy Technol Assess* 31:306–317
3. Habibi H, Zoghi M, Chitsaz A, Javaherdeh K, Ayazpour M (2019) Thermo-economic performance comparison of two configurations of combined steam and organic Rankine cycle with steam Rankine cycle driven by Al₂O₃-therminol VP-1 based PTSC. *Sol Energy* 180:116–132
4. Mousavi SB, Heyhat MM (2019) Numerical study of heat transfer enhancement from a heated circular cylinder by using nanofluid and transverse oscillation. *J Therm Anal Calorim* 135(2):935–945
5. Mahian O, Kolsi L, Amani M, Estellé P, Ahmadi G, Kleinstreuer C, Marshall JS, Siavashi M, Taylor RA, Niazmand H (2019) Recent advances in modeling and simulation of nanofluid flows-part I: fundamentals and theory. *Phys Rep* 790:1–48
6. Arjmandi H, Amiri P, Pour MS (2020) Geometric optimization of a double pipe heat exchanger with combined vortex generator and twisted tape: a CFD and response surface methodology (RSM) study. *Therm Sci Eng Prog* 18:100514
7. Shankar BR, Rao DN, Rao CS (2012) Experimental investigation on stability of Al₂O₃-water nanofluid using response surface methodology. *Int J Nanosci Nanotechnol* 3(2):149–160
8. Nasirzadehroshenin F, Maddah H, Sakhaeinia H (2020) Experimental and theoretical investigation of thermophysical properties of synthesized hybrid nanofluid developed by modeling approaches. *Arab J Sci Eng* 45(9):7205–7218
9. Peng Y, Khaled U, Al-Rashed AA, Meer R, Goodarzi M, Sarafraz M (2020) Potential application of Response Surface Methodology (RSM) for the prediction and optimization of thermal conductivity of aqueous CuO (II) nanofluid: a statistical approach and experimental validation. *Physica A* 554:124353
10. Kiran B, Pathak K, Kumar R, Deshmukh D (2016) Statistical optimization using central composite design for biomass and lipid productivity of microalga: a step towards enhanced biodiesel production. *Ecol Eng* 92:73–81

11. Kamarulzaman MK, Abdullah A (2020) Multi-objective optimization of diesel engine performances and exhaust emissions characteristics of *Hermetia illucens* larvae oil-diesel fuel blends using response surface methodology. *Energy Sources Part A Recovery Utilization Environ Effects* 1–14
12. Tauler R, Brown SD (2009) *Comprehensive chemometrics: chemical and biochemical data analysis*. Elsevier Science, Amsterdam
13. Myers RH, Montgomery DC, Anderson-Cook CM (2011) *Response surface methodology: process and product optimization using designed experiments*. Wiley, Hoboken
14. Sakinah M, Hassan M, Kadirgama K, Kadirgama G, Ramasamy D, Amirruddin A, Rahman M, Noor M (2018) Optimization on wear performance of anti wear additive added biolubricant. In: *Improved performance of materials*. Springer, Berlin, pp 1–9
15. Ghafari S, Aziz HA, Isa MH, Zinatizadeh AA (2009) Application of response surface methodology (RSM) to optimize coagulation–flocculation treatment of leachate using poly-aluminum chloride (PAC) and alum. *J Hazard Mater* 163(2–3):650–656
16. Kumar BR, Saravanan S, Rana D, Nagendran A (2016) Combined effect of injection timing and exhaust gas recirculation (EGR) on performance and emissions of a DI diesel engine fuelled with next-generation advanced biofuel–diesel blends using response surface methodology. *Energy Convers Manage* 123:470–486
17. Rostamian H, Lotfollahi MN (2019) A novel statistical approach for prediction of thermal conductivity of CO₂ by response surface methodology. *Physica A* 527:121175
18. Esfe MH, Firouzi M, Rostamian H, Afrand M (2018) Prediction and optimization of thermophysical properties of stabilized Al₂O₃/antifreeze nanofluids using response surface methodology. *J Mol Liq* 261:14–20
19. Esfe MH, Rostamian H, Shabani-Samghabadi A, Arani AAA (2017) Application of three-level general factorial design approach for thermal conductivity of MgO/water nanofluids. *Appl Therm Eng* 127:1194–1199
20. Rostamian H, Lotfollahi MN (2016) New functionality for energy parameter of Redlich-Kwong equation of state for density calculation of pure carbon dioxide and ethane in liquid, vapor and supercritical phases. *Periodica Polytech Chem Eng* 60(2):93–97
21. Myers RH, Montgomery DC, Anderson-Cook CM (2016) *Response surface methodology: process and product optimization using designed experiments*. Wiley, Hoboken
22. Peng Y, Khaled U, Alrashed AA, Meer R, Goodarzi M, Sarafriz M (2020) Potential application of Response Surface Methodology (RSM) for the prediction and optimization of thermal conductivity of aqueous CuO (II) nanofluid: a statistical approach and experimental validation. *Phys A Stat Mech Appl* 124353
23. Hemmat Esfe M, Abbasian Arani AA, Esfandeh S (2018) Improving engine oil lubrication in light-duty vehicles by using of dispersing MWCNT and ZnO nanoparticles in 5W50 as viscosity index improvers (VII). *Appl Therm Eng* 143:493–506. <https://doi.org/10.1016/j.applthermaleng.2018.07.034>

Fabrication of Superhydrophobic on Ti6Al4V by Using the Hybrid Process of Nanosecond Laser Texturing



M. H. Zul , M. Ishak , M. H. Aiman , and M. M. Quazi 

Abstract This study aims to investigate the effect of laser parameters on the development of superhydrophobic surfaces by using nanosecond laser texturing with a chemical coating. Ti6Al4V specimens were ultrasonically cleaned before applying silicone oil and laser textured onto the material surface. Nanosecond laser texturing is executed in an argon environment by varying several parameters, such as laser power, laser scan speed, and hatching distance. After that, the textured specimen was again ultrasonically in an acetone bath to clean the surface. Superhydrophobic surfaces are determined by measuring the water contact angle using the sessile drop test method, while the surface profile of the laser textured surface was studied by using a 3D laser scanning confocal microscope. It is found that the use of the laser power above 25 W can produce surfaces with a water contact angle of more than 150° while increasing the laser scanning speed from 50 to 500 mm/s will cause the water contact angle to decrease by 16%.

Keywords Superhydrophobic · Ti6Al4V · Nanosecond laser · Laser texturing · Water contact angle

1 Introduction

Surface characteristics and irregularities associated with a particular pattern, size, shape, density, and arrangement are referred to as micro/nano-texture. Any surface with a micro/nano-texture has functional variation. Hydrophobicity is one of the most significant functions of surface roughness [1]. The hydrophobic surface is determined by the water contact angle (WCA). In general, the hydrophobic surfaces are indicated by a WCA that is larger than 90°, while the WCA higher than 150° is called a superhydrophobic surface (SHS) [2]. Application of hydrophobic surface has gotten more attention in many research with the wide area coverage including aeronautics,

M. H. Zul (✉) · M. Ishak · M. H. Aiman · M. M. Quazi
Faculty of Mechanical and Automotive Engineering Technology, Universiti Malaysia Pahang,
26600 Pekan, Pahang, Malaysia
e-mail: mohdharizanzul@gmail.com

marine, and shipyard, medical, industrial, and agriculture production [1, 3]. SHS has gotten a lot of attention because of its potential application, such as self-cleaning from water repellency [4], anti-corrosion [5], antibacterial adhesion [6], and drag reduction [7].

Laser has brought many benefits and caused the technology to continue to develop so rapidly. The laser processing technology has many advantages, including the simple operational and functionalities to produce efficient and precise process capabilities [1] without involving toxic chemicals, and can be applied to almost all materials [2, 8]. Among the lasers available in the market, nanosecond lasers are preferable and suitable for the industry because of their stability, high efficiency, and low cost compared to ultrafast (femto/pico-second) lasers [1, 8, 9]. Recently, many studies and publications based on the use of nanosecond lasers are focused on the fabrication of SHS. With all the advantages available, this nanosecond laser can produce surfaces with high WCA. However, the use of nanosecond lasers alone does not produce superhydrophobic and the WCA results after laser texturing are hydrophilic [10].

Recently, several publications focused on the fabrication of hydrophobic surfaces by using a laser. SHS can be achieved by several methods, mainly to lower the surface energy. First, change the surface roughness or modify the surface chemical composition (or chemical etching), and last, combine the two methods called the hybrid process [11]. Lu et al. [12] immersed the 316L samples in fluoroalkyl silane (FAS, 1H, 1H, 2H, 2H-perfluorooctyltriethoxysilane) ethanoic solution with a concentration of 1% (v/v) for 10 min after laser texturing can achieve WCA of $160 \pm 5^\circ$. The same solution was used by Shen et al. [13] for the Al 6061 series, laser texturing then followed by heating at 100°C for 2 h resulted in 152° .

The laser texturing and chemical coating followed by low-temperature annealing are required to reduce the surface energy. however, the combination of various methods also needs to be optimized to avoid the implication of the cost and time-consuming being too long. Therefore, this paper aims to investigate the effect of laser parameters such as laser power, laser scanning speed, and geometrical pattern textured on the fabrication of SHS for Ti6Al4V by using the hybrid process of nanosecond laser texturing with silicone oil.

2 Methodology

2.1 Material and Preparation

Titanium alloy (Ti6Al4V) used in this study has been widely applied in many areas, including aeronautics, automotive, marine and shipyard construction, and petroleum refinery because of its excellent corrosion resistance in an aggressive environment. The elements of the Ti6Al4V contain Al, V, C, Fe, O and Ti, and their chemical component (wt%) is 5.5%, 3.5%, 0.08%, 0.4%, 0.2% and allowance, respectively. Ti6Al4V was purchased with the size of 10 mm × 50 mm × 2 mm thick were

Table 1 Properties of Silicone-oil [14]

Property	Unit	Value
Vapor pressure	mmHg	<5 (25 °C) 5 (20 °C)
Viscosity	N.s/m ²	1 (25 °C)
Density	g/mL	0.97 (25 °C)
Vapor density		>1 (vs air)

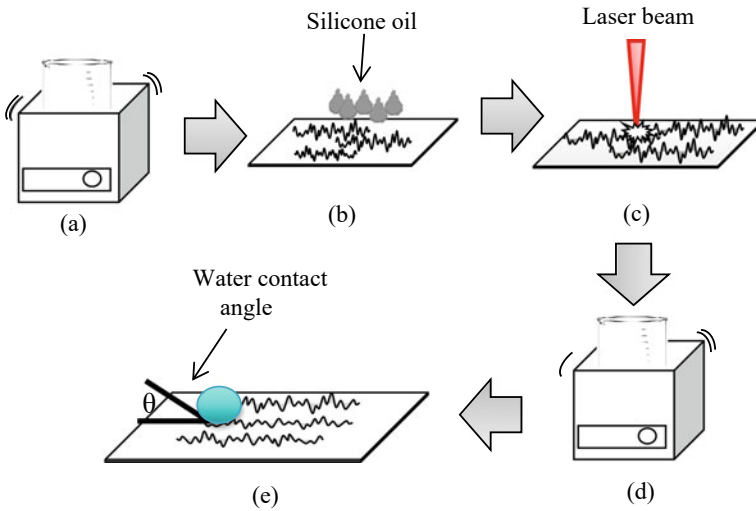


Fig. 1 Preparation process of SHS: **a** clean raw specimen, **b** wetted with silicone oil, **c** laser texturing, **d** ultrasonically to remove excessive oil, and **e** measure water contact angle

ultrasonically cleaned in an acetone bath for 5 min. Then, the surface of the specimen was wetted with silicone oil with a single stroke brush. Table 1 shows the properties of silicone oil. Then, the specimen will undergo laser texturing process. Figure 1 explains the steps in preparing the specimen for laser texturing.

2.2 Laser Surface Texturing

The as-prepared samples were irradiated by using a nanosecond fiber laser system (IPG YLP Q-switch Series, IPG Photonics Corp.) with an average power of 30 W as shown in Fig. 2. The fiber laser modules produce 1064 nm of pulses wavelength with 100 ns duration and pulse energies up to 1 mJ at the frequency range from 2 to 500 kHz. The laser texturing was conducted in argon conditions with a laser beam diameter of ~50 μm during laser processing. The machining parameter specifications

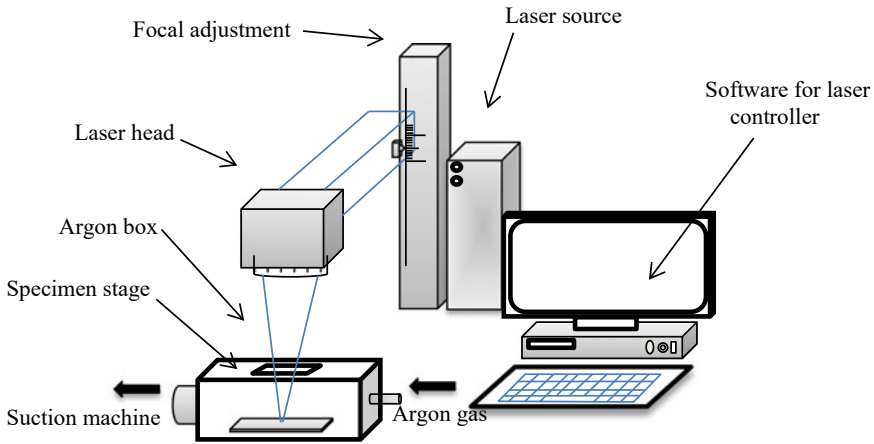


Fig. 2 Laser texturing experimental setup

Table 2 Laser parameters used in the experiments

Laser parameters	Unit	Value
Average power, P	W	16.5–28.5
Frequency, f	kHz	40
Scan speed, v	mm/s	50–500
Hatch distance, H_d	μm	500
Scan run, R	1	
Pattern	Triangular	
Environment	Argon flow at 10 L/min	

are shown in Table 2. The textured specimen will again be ultrasonically cleaned for 1 h in an acetone bath to remove any excess oil and then, dried in ambient air.

The triangular pattern is developed by utilizing all hatches design in laser controller software. Appropriate degree configurations are used to ensure that the triangular pattern is perfect and neat. Surface topography of the laser textured surface was observed using LEXT Olympus OLS5000 3D laser scanning confocal microscope data acquisition application and data analytics application.

2.3 Water Contact Angle Measurement

Contact angle testing was performed on a custom system device at room temperature as shown in Fig. 3. The volume of distilled water droplets deposited on the surfaces was controlled through a 0.5 μL micropipette. Images were captured by a high-resolution telecentric USB microscope (1.6 \times times, adjustable aperture opening).

Fig. 3 Schematic diagram of WCA experimental setup

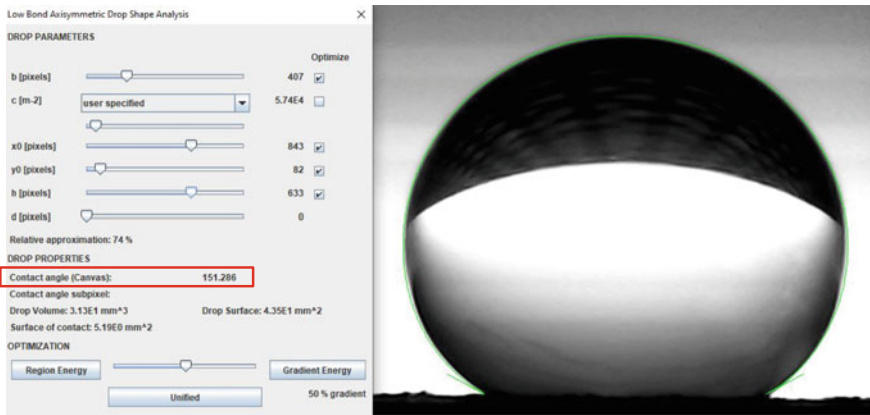
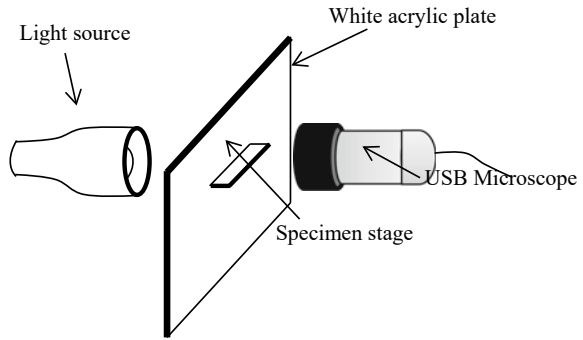


Fig. 4 Image analysis from LBDSA plugin in image J. The result shows in the red box

The light source in the back light offers parallel illumination and increases the image contrast and definition of the object’s edges compared to regular lighting. The deionized water is manually dropped by using a micropipette on specimens. The WCA is measured from the image J software using the Drop Analysis plugin as shown in Fig. 4.

3 Results and Discussion

3.1 Effect of the Laser Power

Laser power is the most significant for surface texturing. According to Samanta et al. [15], further, an increase in laser power intensity will improve the WCA in the fabrication of the hydrophobic surface. SHS was achieved with WCA greater

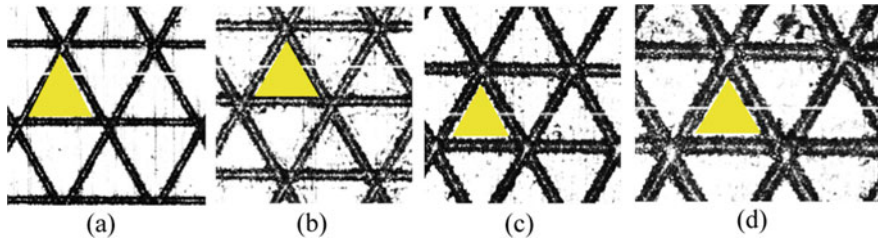


Fig. 5 The laser texture of triangular pattern on Ti6Al4V for **a** 19.5 W, **b** 22.5 W, **c** 25.5 W, and **d** 28.5 W. The triangle with a yellow color inside of each image indicates the “island”

than 150° in all specimens treated with laser power intensities ranging from 0.2 to 18.2 GW/cm². Figure 5 shows the effect of different laser power on the apparent size of the hatching line by 10 × zoom. The increase in laser power causes the hatching line to look rough and wider. This causes the island area to appear smaller.

Further investigation on the textured surface is done by measuring the surface topology on the resulting crater. This study found that increasing the laser power will produce a larger crater size and depth, as shown in Table 3. This is because of laser focus precisely pointing towards the surface of the specimen. The amount of energy applied is high enough to heat the surface.

The more significant effect of laser power on textured surfaces can be seen clearly through the measurement of water contact angle. Figure 7 depicted that with increasing power, the contact angle will also increase. The area of the “island” becomes smaller, which is formed relatively from the hatching line. The size of the channel (hatching line) is described through the Cassie-Baxter model, where the formation of air pockets [10] can cause the SHS.

Table 3 The average surface profile values are based on Fig. 6

Power (W)	r , μm	s , μm	t , μm	u , μm	v , μm ($t + u$)
19.5	34.9	24.5	3.2	7.2	10.6
22.5	77.3	47.1	8.7	12.7	21.4
25.5	90.1	56.5	7.1	18.7	30.9
28.5	100.4	65.3	16.2	23.8	34.9

Fig. 6 The diagram of crater profile in hatching line. The crater profile is measured by r (peak-to-peak), s (crater width), t (upper crater), and u (lower crater)

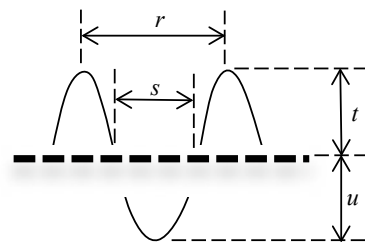
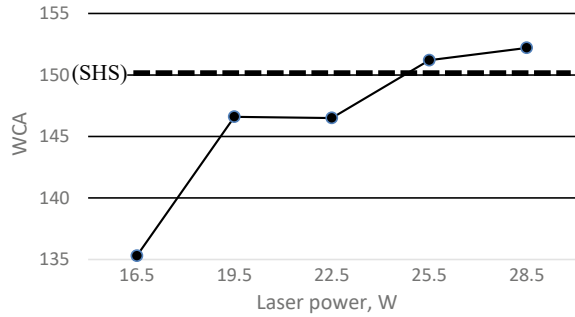


Fig. 7 The effect of laser power on water contact angle



In conclusion, all results show hydrophobic conditions (WCA with $>90^\circ$) while the use of laser power over 25 W can produce SHS (WCA with $>150^\circ$).

3.2 Effect of the Scan Speed

The data on WCA comparisons between this study and references from Tran and Chun [2] are shown in Fig. 8. A similar trend was produced by both studies. A very significant decrease in WCA can also be seen at low scan speeds and gradually stabilizes at speeds of 100 mm/s. The significant difference in WCA value between the study data and the results obtained by Tran and Chun [2] is because of several factors, such as 1. The material used as a specimen (SS316L); 2. The use

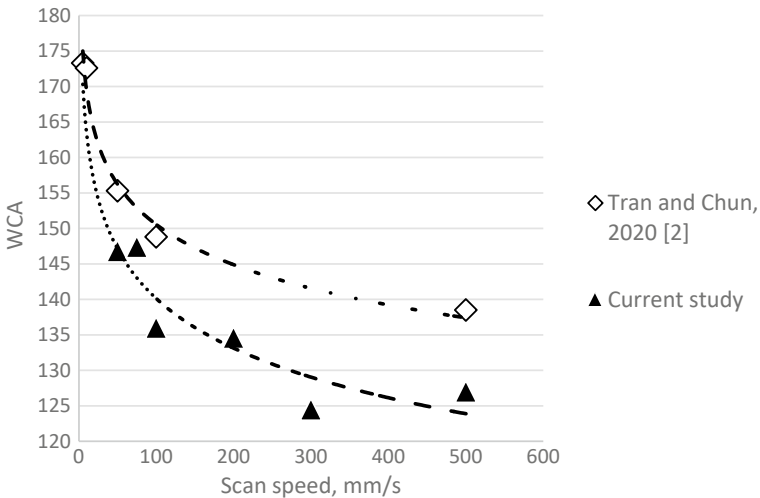


Fig. 8 Comparison of WCA between the current study by using the modified method with literature reference

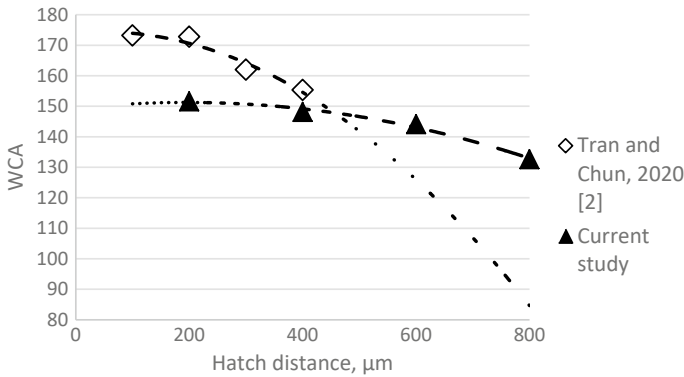


Fig. 9 Comparison of the effect of hatching distance between literature and current study

of chemical coating after laser texturing process, and 3. The specimen is heated by low-temperature annealing (150 °C for 24 h) after chemical coating. However, the methods used for this study were simplified, but the WCA results were still in the hydrophobic range. The effect of the use of low-speed laser scans can produce SHS conditions. Meanwhile, increasing the speed will lower the WCA to 120°. However, these WCA results are still in the hydrophobic state.

3.3 Effect of the Geometrical Pattern

The WCA results in Fig. 9 show the difference between the patterns used by Tran and Chun [2] is grid array, while this study uses a triangular pattern. The results show similarity which is both WCA results is decreased as the hatch distance increased. The study also found that the resulting WCA was almost stable at all hatch distances compared to Tran and Chun [2] where the decrease was very significant.

This result also can confirm the information in 3.1, where the “island” is relatively formed through hatching distance. A large hatching distance will cause the “island” to be smaller, but a small hatching distance will produce a larger “island” size. As a result, the superhydrophobic surface will occur by the effect of the small “island”.

4 Conclusions

The study aims to investigate the effect of laser parameters on the water contact angle of Ti6Al4V by using the hybrid process of nanosecond laser texturing with a chemical coating. The following conclusions were drawn from the study:

- (1) It was deduced that the laser power of ~25 W was the cut-off parameter above which SHS WCA greater than 150° is obtained.
- (2) Lowering the laser scanning speed from 600 to 50 mm/s produced an increase in WCA from 127 to 147° signifying to 16% rise.
- (3) When compared to the grid pattern, the triangle surface pattern provides a range of 130–150° of WCA, signifying stability of the laser texturing parameter range of 800–200 μm.

In a conclusion, the use of a hybrid process to lower the surface energy by wetting the surface with silicone oil and then laser texturing is recommended for the fabrication of SHS on Ti6Al4V. In the future, the laser parameters can be optimized by using various techniques to achieve a water contact angle exceeding 150° for superhydrophobic surfaces.

Acknowledgements The authors are thankful to the Universiti Malaysia Pahang for the financial support given under PDU213002-2 and additional financial support under Postgraduate Research grant PGRS200302. The authors also thank the research team from Joining, Welding, and Laser (JWL) Laboratory, Faculty of Mechanical and Automotive Engineering Technology and the Material Laboratory, Faculty of Manufacturing Engineering Technology for the great support and providing the equipment for laser and surface profilometer.

References

1. Dongre G, Rajurkar A, Raut R, Jangam S (2020) Preparation of super-hydrophobic textures by using nanosecond pulsed laser. *Mater Today Proc*
2. Tran NG, Chun DM (2020) Simple and fast surface modification of nanosecond-pulse laser-textured stainless steel for robust superhydrophobic surfaces. *CIRP Ann* 69:525–528
3. Xiao S, Hao X, Yang Y, Li L, He N, Li H (2019) Feasible fabrication of a wear-resistant hydrophobic surface. *Appl Surf Sci* 463
4. Zhang M, Guo C, Hu J (2020) One-step fabrication of flexible superhydrophobic surfaces to enhance water repellency. *Surf Coat Technol* 400:126155
5. Lian Z, Xu J, Yu Z, Yu P, Yu H (2019) A simple two-step approach for the fabrication of bio-inspired superhydrophobic and anisotropic wetting surfaces having corrosion resistance. *J Alloys Compd* 793:326–335
6. Zhang X, Wang L, Levänen E (2013) Superhydrophobic surfaces for the reduction of bacterial adhesion
7. Xin G, Wu C, Cao H, Liu W, Li B, Huang Y, Rong Y, Zhang G (2020) Superhydrophobic TC4 alloy surface fabricated by laser micro-scanning to reduce adhesion and drag resistance. *Surf Coat Technol* 391:125707
8. Wang Y, Ke C, Wu T, Zhao X, Wang R (2019) Nanosecond laser texturing with hexagonal honeycomb micro-structure on Titanium for improved wettability and optical properties. *Optik* 192:162953
9. Xin G, Wu C, Liu W, Wang M, Huang Y, Rong Y (2021) Fabrication of super-wetting copper foam based on laser ablation for selective and efficient oil-water separation. *Surf Coat Technol* 424
10. Zul MH, Ishak@Muhammad M, Aiman MH, Quazi MM (2021) Influence of laser power in nanosecond laser texturing for a hydrophobic state on SS316L. *J Mech Eng Sci* 15:8592–8600

11. Wang Y, Zhao X, Ke C, Yu J, Wang R (2020) Nanosecond laser fabrication of superhydrophobic Ti6Al4V surfaces assisted with different liquids. *Colloid Interface Sci Commun* 35:100256
12. Lu Y, Guan YC, Li Y, Yang LJ, Wang ML, Wang Y (2020) Nanosecond laser fabrication of superhydrophobic surface on 316L stainless steel and corrosion protection application. *Colloids Surf A Physicochemical and Engineering Aspects* 604
13. Shen H, Liu J, Chen Y, Zhang J, Zhang Z, Guan N, Zhang F, Huang L, Zhao D, Jin Z, Liu X (2020) Investigation on time stability of laser-textured patterned surfaces under different temperatures. *Surf Coat Technol* 400:126225
14. Silicone oil 1,000CST 25°C 63148–62–9. <https://www.sigmaaldrich.com/MY/en/product/aldrich/378399>
15. Samanta A, Wang Q, Shaw SK, Ding H (2019) Nanostructuring of laser textured surface to achieve superhydrophobicity on engineering metal surface. *J Laser Appl* 31:22515

Statistical Approach to the Cellulose Nanocrystal Tribological Behavior on the Piston Liner Contact Using Full Factorial Design (FFD)



N. W. Awang, Sakinah Hisham , D. Ramasamy , K. Kadirgama , and Mohd Kamal Kamarulzaman 

Abstract The primary goal of this research is to investigate the effect of tribo-test parameters on the coefficient of friction (COF) and wear rate of the cylinder liner and piston ring pair. The tribological studies are carried out utilizing a full factorial design (FFD) experimental scheme. Sliding speed, temperature, volume concentration, and applied force were all evaluated as important parameters that determine tribological qualities. The effects of various variables and their interactions on the dependent variables were investigated. The ANOVA analysis demonstrates that the applied load could be the most influential factor affecting the minimum amount of the friction coefficient. The minimum quantity of wear rate indicates that as the sliding speed increases, the wear rate decreases.

Keywords Cellulose nanocrystal (CNC) · Additive · Tribological properties · Piston skirt liner · Engine oil

N. W. Awang

Politeknik Sultan Mizan Zainal Abidin, 23000 Dungun, Terengganu, Malaysia

e-mail: norazmira@psmza.edu.my

N. W. Awang · D. Ramasamy

College of Engineering, Universiti Malaysia Pahang, 26300 Gambang, Pahang, Malaysia

e-mail: deva@ump.edu.my

S. Hisham · K. Kadirgama

Faculty of Mechanical and Automotive Engineering Technology, Universiti Malaysia Pahang, 26600 Pekan, Pahang, Malaysia

e-mail: sakinah.hisham0704@gmail.com

K. Kadirgama

e-mail: kumaran@ump.edu.my

S. Hisham · D. Ramasamy · K. Kadirgama · M. K. Kamarulzaman (✉)

Advanced Nano Coolant-Lubricant (ANCL) Lab, Automotive Engineering Centre, Universiti Malaysia Pahang, 26600 Pekan, Pahang, Malaysia

e-mail: kamalkz@hotmail.com; kamalkz@ump.edu.my

© The Author(s), under exclusive license to Springer Nature Singapore Pte Ltd. 2023

351

N. H. Johari et al. (eds.), *Proceedings of the 2nd Energy Security and Chemical*

Engineering Congress, Lecture Notes in Mechanical Engineering,

https://doi.org/10.1007/978-981-19-4425-3_31

1 Introduction

Lubricant, fuel and engine are closely related to each other. Internal combustion engine performance in terms of frictional power loss, fuel consumption, oil consumption, and hazardous exhaust emissions is closely related to frictional and wear forces between moving engine parts such as piston assemblies, valve rails and bearings. The interaction between the piston assembly and the liner surface is considered to be the most challenging tribological component to examine in an internal combustion engine due to large fluctuations in load, speed, temperature and lubricant availability [1]. In a single piston stroke, the interface of the piston ring with the cylinder wall may experience a boundary, the lubrication of the mixed and full liquid film exerts a great influence on the loss of mechanical friction [2]. Lubrication is the most important factor in reducing wear and friction losses in an internal combustion engine. To reduce the wear and friction of the engine's tribological components, a higher-quality lubricant is being created.

Lubricants are liquids that create a protective layer between two parts, such as bearings and reducers in engines [3]. Lubrication technology is also important for vehicle reliability and longevity, and it has the potential to reduce engine exhaust toxicity. The creation of contemporary lubricants and their right application is critical for national economies, individuals, and the environment, as well as the quest for alternative lubricant sources [4]. According to a literature review, nano lubricants are currently making an appearance in the field of tribology. The idea was to make lubricating oil with polymer, metal, organic, and inorganic nanoparticles. As a result of the combination, many researchers have discovered that nano lubricants have improved and beneficial tribological properties [2, 5–8].

Studies to date have primarily focused on friction characteristics; however, the performance of tribological properties is dependent not only on lubricant properties but also on the sliding conditions of material under the lubricant contact condition [9]. Kapsiz et al. [1] used three process factors, sliding velocity, applied stress, and oil type, to investigate tribological properties between cylinder liner and piston ring pair. They concluded that sliding velocity (68.14%) and weight loss (44.60%) were the primary influences on the friction coefficient and weight loss of CL. For a contact load of 120 N, Ali et al. [2] studied the effect of sliding speed on the friction coefficient and wear rate of the piston ring when using lubricant without nanoparticles (5W-30) and with nanoparticles at various sliding speeds. For both lubricants with and without nanoparticles, they discovered that the formation of a tribo-film on worn surfaces, which functions as a solid lubricant, affects the decrease in friction coefficient and ring wear rate.

Wu et al. [10] reported contradictory behaviour on the trend of the friction coefficient When comparing the lubricating properties and advantages of MoS₂ nanosheets to ZDDP in line contact. For MoS₂ nanosheets, the coefficient of friction varies inexorably with increasing speed, with materials evaluated at high load having a low coefficient of friction. When compared to 1% ZDDP, the friction reduction of MoS₂ in the region of 0.25–1 wt% is only about 10%, while the wear scar width lowers

by around 43% at high load. The average values of friction coefficient were affected by changes in applied load and sliding speed, and while sliding at high speeds, there was no variation in COF [11].

A full factorial screening design (FFD) is used to determine the important components that influence a process. This approach reduces the number of experiments without requiring a large number of them [12]. FFD of experiments involves N^k number of setups for k number of factors each at N level. FFD allows researchers to investigate the effects of numerous variables at the same time while maintaining data collecting quality. FFD can be utilized to start response surface optimization research in the future. The significance of each factor on a particular experimental response, as well as to identify the interaction of important factors influencing the response [13–15]. The effects of operating parameters such as sliding speed, applied load, temperature, and volume concentration on the total additive deposits of Cellulose Nanocrystal (CNC) nanoparticles in engine oil were statistically analyzed in this study using the FFD design approach.

2 Experimental Procedure

2.1 Materials and Lubricant Preparation

The CNC nanoparticles were used in this investigation and dispersed in lubricating engine oil. Mineral oil SAE 40 was used as a baseline lubricant. A magnetic stirrer was used to distribute the nanoparticles in the lubricant at concentrations of 0.1, 0.5, and 0.9 wt% for 30 min. After that, the nano lubricants were agitated for 2 h with an ultrasonic probe to guarantee uniform dispersion and suspension stability. Figure 1 depicts the concentration of the base oil and nanoparticles in a mixture.

The material of tribotest specimens used in this experiment is Aluminum 6061-T6 Flat bar test specimens were initially cut using a band saw to the following

Fig. 1 Sample of nano lubricants with different concentrations

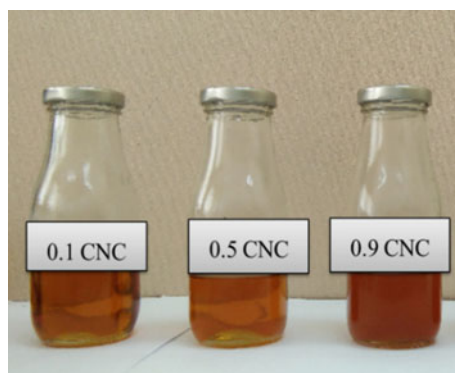


Table 1 Properties of materials

Materials	Properties
CNC nanoparticles	C ₆ H ₁₀ O ₅ , size 75.3 nm
Block specimen Aluminum 6061-T6	Density (g/cm ³): 2.7 Thermal conductivity (W/m-K): 16.7 Modulus of elasticity (GPa): 68.9 Specific heat capacity (J/g °C): 0.896

dimensions: 45.12 mm length × 25.14 mm wide × 6 mm thickness. The surface of the specimens was then thoroughly cleaned of dirt and debris before being exposed to unidirectional polishing with three different grit sizes of abrasive paper: 240, 400, and 1000. Table 1 lists the main properties of the nanoparticles, lubricant and specimen used in the experiment.

2.2 Tribotest

The sliding contact between the engine’s cylinder liner and piston ring was replicated using the equipment. Wear tests were conducted using lubricated sliding conditions and linear movements that mimicked those of a pair of cylindrical piston rings functioning in real life. The wear tribo-tester is schematically depicted in Fig. 2 for determining the friction coefficient at the piston skirt. Before and after the test, all test specimen components were washed and rinsed in acetone and dried with hot air. During the tribology test, the piston ring’s travel distance was adjusted to 33 mm.

The friction coefficient follows the friction equations of Eq. 1.

$$F = \mu_k N \tag{1}$$

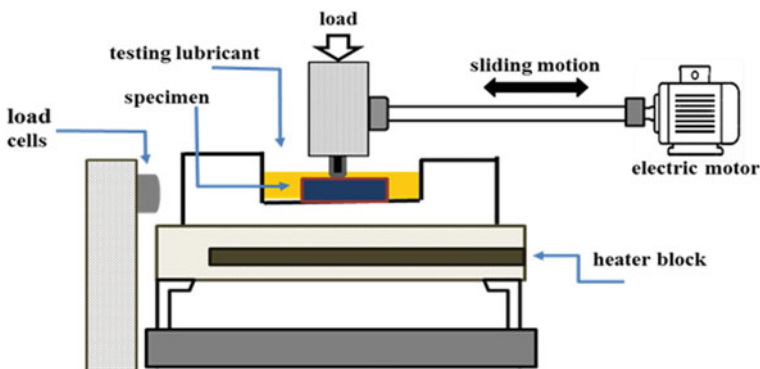


Fig. 2 Schematic diagram of tribological evaluation

Table 2 Factors and levels of 2⁴ FFD scheme

Factors	Coded	Low level (-)	High level (+)
Sliding speed (rpm)	A	200	500
Temperature (°C)	B	30	80

where F is the friction force, μ_k is the kinetic coefficient of friction and N is the normal load, or weight applied. A precision weighing balance with a sensitivity of 0.1 mg was used to assess wear loss. Wear rate (material loss) is calculated using Eq. 2 using a precision weight balance using the following equation in a unit of (mm³/Nm) from the loss of volume in the specimen,

$$W = \frac{\Delta V}{F_n \times S_s} \tag{2}$$

where ΔV is the volume loss (in cm³), F_n is the applied load (N) and S_s is the sliding distance (m). All tests were carried out for each experimental condition, and the COF value was recorded during the testing using a force transducer positioned on the plate to measure the lateral force. The tests were repeated three times to ensure that the readings were consistent, and the average of the three readings was utilised for tribological property statistical analysis.

2.3 Experimentation Scheme

Tribological experiments are conducted in this work using the Full Factorial Design (FFD) experimental scheme to assess the influence of four factors on response. Full two-level factorial designs (2⁴) were performed for these four variables for this objective principally because they are efficient. The level maximum and minimum for each factor are described in Table 2.

Table 3 also shows a total of 20 experiments, including four repetitions for the experimental condition in the middle. Each row of the matrix represents one run under a certain condition, with three repeats required to obtain accurate results. To reduce the systematic bias of uncontrollable factors, the trial sequence was randomized. Design Expert 11 is used to create the data design and statistical analysis.

3 Result and Discussion

3.1 Analysis of Variance

A two-level full factorial design (FFD) was built to identify the significant parameters of reducing friction and wear. The effects of sliding speed, load, temperature, and

Table 3 Experimental scheme and responses

Run	Factor 1	Factor 2	Factor 3	Factor 4	Response 1	Response 2
	A Speed (rpm)	B Temperature (°C)	C Concentration	D Load (N)	COF	Wear rate
1	500	80	0.9	98.1	0.033418	0.488224
2	500	30	0.9	98.1	0.033676	0.487321
3	500	30	0.1	98.1	0.031821	0.507179
4	375	55	0.5	68.67	0.044707	0.341029
5	250	30	0.9	39.24	0.08508	0.418904
6	250	80	0.1	98.1	0.033416	0.405616
7	375	55	0.5	68.67	0.045011	0.342087
8	500	80	0.9	39.24	0.083813	0.564511
9	500	80	0.1	39.24	0.078569	0.494059
10	375	55	0.5	68.67	0.045114	0.328175
11	375	55	0.5	68.67	0.046503	0.334182
12	250	30	0.9	98.1	0.033834	0.406155
13	250	80	0.9	39.24	0.085332	0.463713

concentration of nano-lubricant were screened using 2⁴ full factorial designs. The parameters of this study were screened at the confidence effect level of 95% based on their effect. The calculated regression coefficient and analysis of variance (ANOVA) for the coefficient of friction are shown in Table 4. The experimental and projected values are statistically significant, with R-squared = 0.994, indicating that they are

Table 4 ANOVA of friction coefficient

Source	Sum of squares	df	Mean square	F-value	p-value	(%) contribution PC
Model	0.0098	10	0.0010	1419.62	<0.0001	Significant
A-Speed	0.0000	1	0.0000	25.16	0.0010	7.2
C-Concentration	0.0000	1	0.0000	36.80	0.0003	9.5
D-Load	0.0098	1	0.0098	14,110.55	<0.0001	59.3
AC	5.372E-06	1	5.372E-06	7.75	0.0238	4.8
CD	6.653E-06	1	6.653E-06	9.60	0.0147	5.4
Curvature	0.0005	1	0.0005	1007.85	<0.0001	–
Residual	4.149E-06	8	5.186E-07	–	–	–
Lack of fit	2.237E-06	5	4.47E-07	0.7017	0.6606	Not significant
Error	1.912E-06	3	6.375E-07	–	–	–
Total	0.0103	19	–	–	–	–

DF = degree of freedom; R-sq = 0.994; R-Sq (adj) = 0.987

quite near. Meanwhile, the lack-of-fit of the *P*-value for the COF model was non-significant as it was more than 0.05. The presence of a high F-value in the ANOVA table suggests that the model is significant for the response being assessed. Model terms with a *p*-value less than 0.05 are significant, whereas those with a *p*-value more than 0.1 are irrelevant. The coefficient of friction is affected by the factors speed A, concentration C, load D, AC, and CD in the current study. In addition, the lower the *p*-value, the greater the impact of the factor on the response. The lowest *p*-values encountered are related to the load (D). The percentage contribution “PC%” is frequently a good indication of the relative relevance of each model item. The engine load has a higher contribution influence on the coefficient of friction (59.3%) than volume concentration (9.5%).

The wear rate was calculated using the same procedure as was used to calculate the COF. The wear rate of the nano lubricant is represented in Table 5 by the estimated regression analysis of variance (ANOVA). The regression was statistically significant at a 95% confidence level, according to the results. The model has a high determination coefficient (R-sq = 0.9812), which explained 98.12% of the response variability (Table 5). The F-value of 41.72 infers that the model is statistically significant. The F-value and *p*-value of the lack of a fit test for wear rate were 2.6 and 0.2311, respectively, implying that it was not significant because it was greater than 0.05. In this case, the relevant factors are A, B, C, D, AC, AD, BC, and CD. The most significant factors for wear rate are sliding speed A and load D. Furthermore, it was discovered that sliding speed has a higher contributory influence (14.1%) on wear rate than load (10.7%).

Table 5 ANOVA of wear rate

Source	Sum of squares	df	Mean square	F-value	<i>p</i> -value	(%) contribution PC
Model	0.0351	10	0.0035	41.72	<0.0001	Significant
A-Speed	0.0121	1	0.0121	143.26	<0.0001	14.1
B-Temperature	0.0006	1	0.0006	6.59	0.0333	0.64
C-Concentration	0.0042	1	0.0042	50.35	0.0001	4.9
D-Load	0.0092	1	0.0092	109.08	<0.0001	10.7
AC	0.0033	1	0.0033	39.11	0.0002	3.8
AD	0.0022	1	0.0022	26.08	0.0009	2.6
BC	0.0019	1	0.0019	22.67	0.0014	2.2
CD	0.0015	1	0.0015	17.86	0.0029	1.8
Curvature	0.0499	1	0.0499	593.6	<0.0001	–
Residual	0.0007	8	0.0001	–	–	–
Lack of fit	0.0005	5	0.0001	2.6	0.2311	Not significant
Error	0.0001	3	0.0000	–	–	–
Total	0.0857	19	–	–	–	–

DF = degree of freedom; R-sq = 0.9812; R-Sq (adj) = 0.9577

3.2 Main Effects Analysis on Friction Coefficient and Wear Rate

The individual effects of sliding speed (a), temperature (b), volume concentration (c), and load (d) on the coefficient of friction and wear rate were determined using FFD with four screening factors at two levels. The main effects chart for the friction coefficient are shown in Fig. 3. A line with a steeper slope for long-distance changes indicates a higher main effect compared to the effect produced by less significant elements in this graph [16]. As demonstrated in Fig. 3d, the plot of friction coefficient

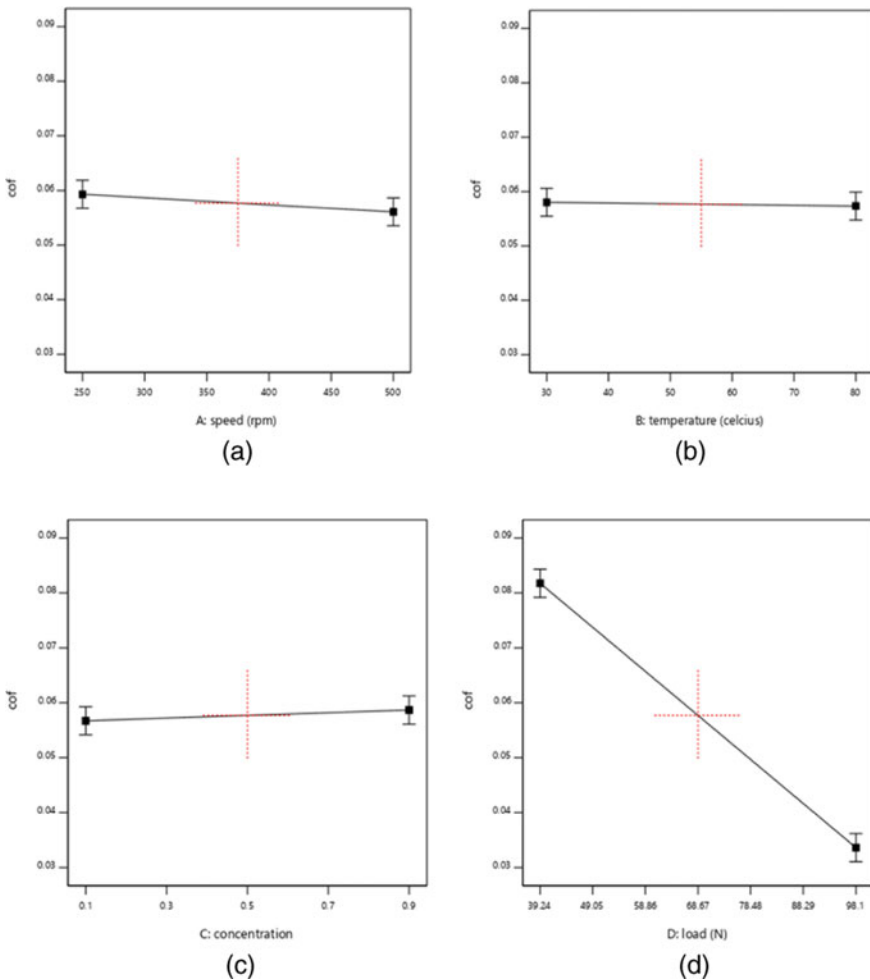


Fig. 3 Main plots of friction coefficient versus **a** sliding speed, **b** temperature, **c** volume concentration and **d** applied load

against applied load demonstrates the most significant effect from a high to a low level. Similar results were obtained by Asnida et al. [17] that indicated that the coefficient of friction decreased as applied load increased. In addition, the speed plot Fig. 3a shows a modest decrease in the coefficient of friction. Overall, the sliding speed led to a decrease in the coefficient of friction. (c) shows the coefficient of friction increased as the fraction of concentration increased. While the temperature in Fig. 3b show less significant compared with another factor.

Figure 4 shows the individual factor of parameters on wear rate. The plot for wear rate against its sliding speed, temperature and volume concentration shows the effect from a low level to a high level and the wear rate decreased as the factors decreased. Figure 4a shows that the wear rate decreases as the sliding speed increases. It is

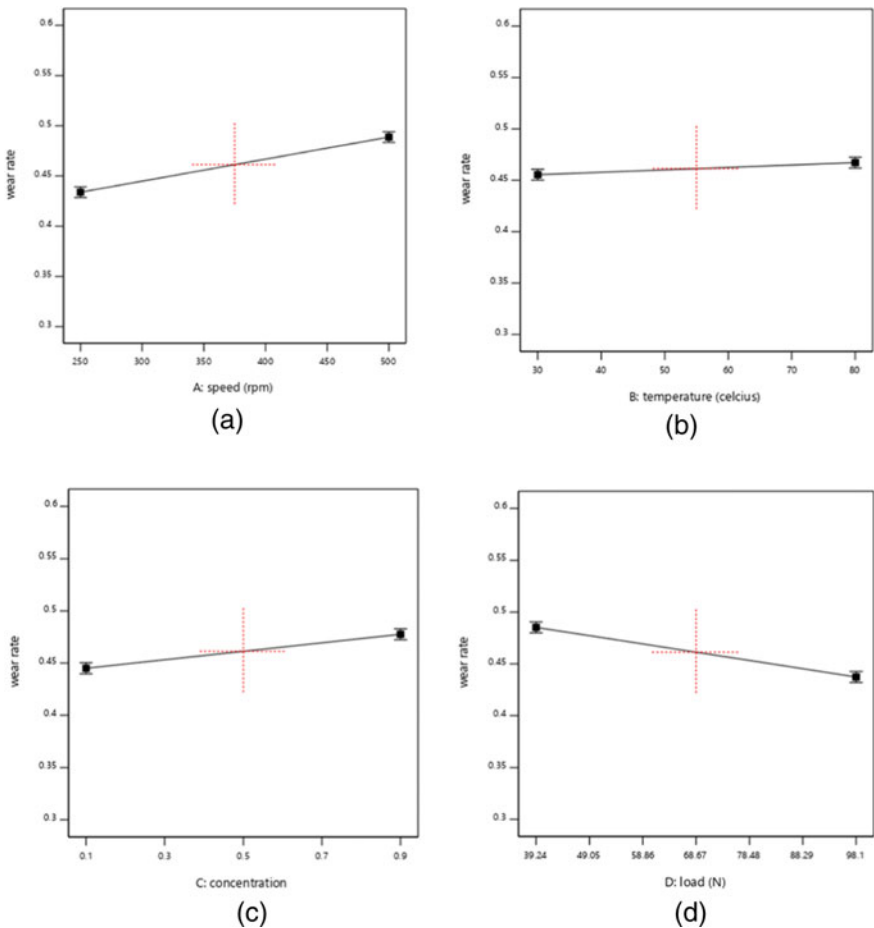


Fig. 4 Main plots of wear rate versus **a** sliding speed, **b** temperature, **c** volume concentration and **d** applied load

feasible to understand how the wear rate is changed by increasing the sliding speed while decreasing the wear rate. The decrease in wear rate was significant with sliding speed [1] and the biggest contribution effect (14.1%) on wear rate compared to other parameters, according to Table 5 and Fig. 4a. The plot of load Fig. 4d shows less slope than sliding speed. Also, Fig. 4b indicates that the temperature effect is very small on the wear rate.

3.3 Interactions Between Factors on Friction Coefficient and Wear Rate

The significant interaction between most affecting the coefficient of friction and wear rate is shown in Figs. 5 and 6. The volume concentration and load interaction in Fig. 5a. It shows that the concentration effect is extremely minor when the load is low but has a large influence when the applied load is high, and the best COF result is obtained with a high load and low concentration. The trend of lubricant with or without CNCs nanoparticles in SAE 40 engine oil is observed to be similar to the findings of COF from previous study by Asnida et al. [17] where the friction coefficient had decreased with an increasing load. Figure 5b shows the interaction between sliding speed and concentration. In comparison to a high concentration, the slope for a low concentration is steeper. The COF is influenced by the concentration of volume, and slightly reduced as the sliding speed increases. The additive film is formed, and resistance at friction gradually decreases, leading to a slight decrease of friction coefficient. Figure 6a shows the interaction between sliding speed with an applied load on the wear rate. The volume concentration and load interaction effects

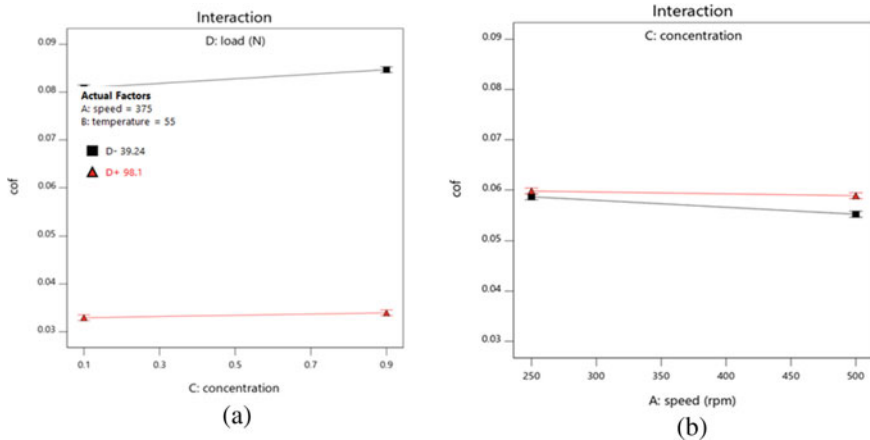


Fig. 5 Interaction plot between factors on the coefficient of friction, a concentration and applied load and b concentration and sliding speed

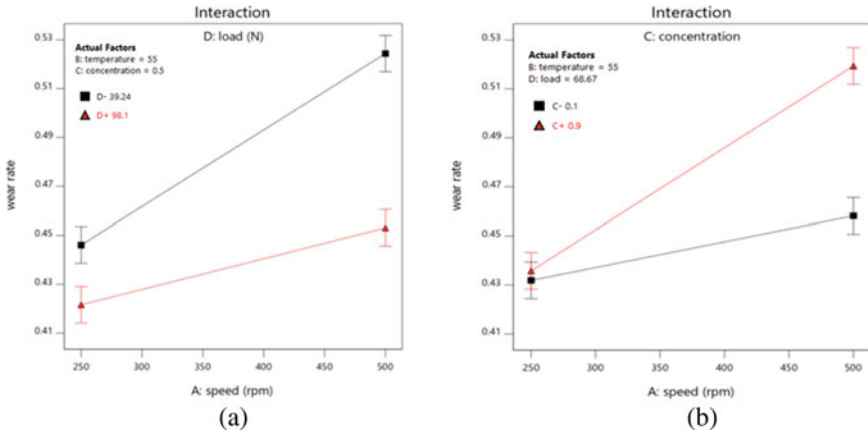


Fig. 6 Interaction plot between factors on the wear rate, **a** sliding speed and applied load and **b** concentration and sliding speed

have the greatest interaction, with the effect of sliding speed being greater when applied load is at 39.24 N. When the data is constrained to a low level of applied load, the volume concentration’s effect is steeper than when the data is restricted to a high level of applied load (D+). However, to find the best result of minimum wear rate was reached with a high applied load level. Figure 6b shows the interaction between sliding speed with volume concentration on wear rate. The slope for high concentration C+ is steeper than lower concentration and gives a significant effect to wear rate.

4 Conclusion

A two-level full factorial design was used to assess the influence of operating parameters on tribological properties. The following are some key conclusions from the experimental study:

- ANOVA analysis reveals that factors speed A, concentration C, load D, AC, and CD are statistically significant to control the friction coefficient and the factors A, B, C, D, AC, AD, BC and CD are physically and statistically significant to influence the wear rate.
- Also, it is observed that the factors load D and sliding speed A, are the predominant factors that influence the friction coefficient and wear rate respectively, of the nano-cellulose. Since they have the highest P (%) value compared to the P (%) value of all the other significant factors.

Acknowledgements This work was supported by University Malaysia Pahang [grant number RDU192402]. “Mohd Kamal bin Kamarulzaman” is the recipient of the UMP Post-Doctoral Fellowship in Research.

Credit Authorship Contribution Statement **N. W. Awang:** Conceptualization, Methodology, Validation, Formal analysis, Investigation, Data Curation, Writing—Original Draft, Visualization. **Sakinah Hisham:** Conceptualization, Investigation. **D. Ramasamy, K. Kadirgama:** Conceptualization, Methodology, Validation, Formal analysis, Investigation, Resources, Writing—Review and Editing, Visualization, Supervision. **Mohd Kamal Kamarulzaman:** Conceptualization.

Declaration of Competing Interest The authors declare that they have no known competing financial interests or personal relationships that could have appeared to influence the work reported in this paper.

References

1. Kapsiz M, Durat M, Ficici F (2011) Friction and wear studies between cylinder liner and piston ring pair using Taguchi design method. *Adv Eng Softw* 42(8):595–603
2. Ali MKA, Xianjun H, Mai L, Qingping C, Turkson RF, Bicheng C (2016) Improving the tribological characteristics of piston ring assembly in automotive engines using Al₂O₃ and TiO₂ nanomaterials as nano-lubricant additives. *Tribol Int* 103:540–554
3. Davim JP (2011) *Tribology for engineers: a practical guide*. Elsevier, Amsterdam
4. Arumugam S, Sriram G (2012) Effect of bio-lubricant and biodiesel-contaminated lubricant on tribological behavior of cylinder liner–piston ring combination. *Tribol Trans* 55(4):438–445
5. Nadooshan AA, Esfe MH, Afrand M (2017) Evaluation of rheological behavior of 10W40 lubricant containing hybrid nano-material by measuring dynamic viscosity. *Physica E* 92:47–54
6. Esfe MH, Saedodin S, Rejvani M, Shahram J (2017) Experimental investigation, model development and sensitivity analysis of rheological behavior of ZnO/10W40 nano-lubricants for automotive applications. *Physica E* 90:194–203
7. Wu H, Zhao J, Xia W, Cheng X, He A, Yun JH, Wang L, Huang H, Jiao S, Huang L (2017) A study of the tribological behaviour of TiO₂ nano-additive water-based lubricants. *Tribol Int* 109:398–408
8. Wu H, Zhao J, Xia W, Cheng X, He A, Yun JH, Wang L, Huang H, Jiao S, Huang L (2017) Analysis of TiO₂ nano-additive water-based lubricants in hot rolling of microalloyed steel. *J Manuf Process* 27:26–36
9. Hisham S, Kadirgama K, Ramasamy D, Noor M, Amirruddin A, Najafi G, Rahman M (2017) Waste cooking oil blended with the engine oil for reduction of friction and wear on piston skirt. *Fuel* 205:247–261
10. Wu H, Wang L, Johnson B, Yang S, Zhang J, Dong G (2018) Investigation on the lubrication advantages of MoS₂ nanosheets compared with ZDDP using block-on-ring tests. *Wear* 394:40–49
11. Kakaš D, Škorić B, Mitrović S, Babić M, Terek P, Miletić A, Vilotić M (2009) Influence of load and sliding speed on friction coefficient of IBAD deposited TiN. *Tribol Ind* 31(3–4):3–10
12. Kasdekar DK, Parashar V (2018) Principal component analysis to optimize the ECM parameters of aluminium alloy. *Mater Today Proc* 5(2):5398–5406
13. Soundararajan R, Ramesh A, Sivasankaran S, Vignesh M (2017) Modeling and analysis of mechanical properties of aluminium alloy (A413) reinforced with boron carbide (B4C) processed through squeeze casting process using artificial neural network model and statistical technique. *Mater Today Proc* 4(2):2008–2030
14. Sunil B, Rajeev V, Jose S (2018) A statistical study on the dry wear and friction characteristics of Al-12.6Si-3Cu-(2–2.6 wt.%)Ni piston alloys. *Mater Today Proc* 5(1):1131–1137

15. Kamarulzaman MK, Abdullah A (2020) Multi-objective optimization of diesel engine performances and exhaust emissions characteristics of *Hermetia illucens* larvae oil-diesel fuel blends using response surface methodology. *Energy Sources Part A Recovery Utilization Environ Effects* 1–14
16. Ridzuan N, Adam F, Yaacob Z (2016) Screening of factor influencing wax deposition using full factorial experimental design. *Pet Sci Technol* 34(1):84–90
17. Asnida M, Hisham S, Awang N, Amirruddin A, Noor M, Kadirgama K, Ramasamy D, Najafi G, Tarlochan F (2018) Copper (II) oxide nanoparticles as additive in engine oil to increase the durability of piston-liner contact. *Fuel* 212:656–667

Covid-19 Embedded with Aerosol Particles Travel Simulation Inside a Mosque



Mohd Rezan Hamji Ajirun, Syifak Izhar Hisham , Mohd Nadzeri Omar , and Nasrul Hadi Johari 

Abstract When an infected person coughs, thousands of micro-size aerosol particles will transmit to the surrounding, especially in a closed space. Mosque is one of the confined areas that Muslims regularly go to pray together. Multiple standards of procedures have been proposed to prevent the virus transmission, however, the cases involving people praying in mosque are still reported. This study aims to simulate the virus transmission in mosque by modelling the aerosol particles generated by the worshipper coughing. A geometry of praying area in mosque was created mimicking the actual praying space. Realistic boundary conditions involving coughing, airflow at the inlet and outlet diffusers were specified. The simulation result confirms that the SARS-COV-2 virus in a closed space praying room is not uniform and it is strongly influenced by the location of the coughing source and the air conditioning layout. The study also recorded *Ma'mums* are at the higher chance to get infected if one of the *Ma'mum* is the COVID-19 carrier due to the nature of normal congregational praying arrangement. The outcomes of this study may help the scientist and the authorities to understand how dramatic COVID-19 virus may spread in the confined praying area, hence, may enforce a better standard of procedure in a mosque.

Keywords COVID-19 · Aerosol particle · Mosque · Indoor space

M. R. H. Ajirun · M. N. Omar · N. H. Johari (✉)
Centre for Advanced Industrial Technology, Universiti Malaysia Pahang, 26600 Pekan, Pahang, Malaysia
e-mail: nhadi@ump.edu.my

Faculty of Mechanical and Automotive Engineering Technology, Universiti Malaysia Pahang, 26600 Pekan, Pahang, Malaysia

S. I. Hisham
Faculty of Computing, Universiti Malaysia Pahang, 26600 Pekan, Pahang, Malaysia

1 Introduction

Coronavirus disease (COVID-19) has become a deadly pandemic that causes millions of deaths and comorbidities, and a severe damage of economic crisis all over the world.

SARS-COV-2 is a unique virus that has the ability to evolve into a new variant with differences of characteristics adaptation and rate of transmission or spread. The Centers for Disease Control and Prevention (CDC) concluded the latest variant, Delta variant (B.1.617.2) that has evolved from the previous variants, namely Gamma variant (P.1) to be much life-threatening as it is airborne, able to spread faster than other variants and thus could cause more severe cases [1, 2].

Infected people can spread the virus from their mouth or nose in a form of micro-size liquid particles during a verbal activities or involuntary act such as coughing. The particles emitted from a larger range of respiratory droplets to a micro-sized aerosol particle has become a nuisance or fatal especially in an indoor space [3, 4]. For the Muslim community in Malaysia, prayers are done 5 times a day in a confined holy place called a mosque. Multiple standards of procedures have been proposed to prevent the virus transmission, however, the cases involving people praying in mosque are still reported [5–7]. To understand the COVID-19 spread in mosque, a complete computational fluid dynamics (CFD) simulation could be useful to predict aerosol particles trajectory in different mosque environment.

Previous studies have explored COVID-19 particles spread using CFD in indoors classroom [8] and on airplane [9]. Abuhegazy et al. [8] modelled a classroom consisting of nine students, an instructor and furniture replicating a realistic classroom scenario. The classroom area was 9×9 m and 3 m height. The distance between each student was set 2.4 m which is greater than the recommended 1.8 m separation distance for COVID-19 mitigation. All students were created in similar dimensions with a cuboid body and head with a rectangular mouth surface. To investigate the virus cross-transmission in the classroom, different particle sizes embedded in the airflow were injected into the system. The overall proportion of particles that fall on the ground, desks, and the source student increases dramatically as particle size increases. The particles deposit quickly in less than a minute in the case of $50 \mu\text{m}$ particles, predominantly on the source student. Gravitational settling and the simplified, rectangular shape of the student modelled are responsible for the significant deposition of $50 \mu\text{m}$ particles on the source student.

Another article on the particles travelling on airplane [9] has determine the effect of reducing capacity of passengers as well as to compare with other intervention methods that is considered as cost-effective, for example sneeze guard (sneeze shield) applied in between passengers. The study also investigates the influence of coughing and speaking in emitting aerosol particles. The CFD results showed the particles do not diffuse over the full cabin space at any given moment. The particles are kept within one or two rows of the index patient at most. This shows that a single patient's presence does not infect the entire cabin.

Most of mosque are also considered a confined area or indoor space. To the authors' knowledge, there are currently no reports investigating the COVID-19 particles transmission in mosque using computational modelling. Hence, this study aims to speculate the aerosol particles travelling inside a mosque using CFD modelling. The outcomes of this study may help the scientist and the authorities to understand how dramatic COVID-19 virus may spread in the confined praying area, hence, may enforce a better standard of procedure in a mosque.

2 Methodology

2.1 Praying Area Model and Mesh Construction

A three-dimensional geometry of a praying area consisting of eight worshippers was created. The model uses a common praying area dimension and a realistic air conditioning (AC). The dimension of the praying area shown in Fig. 1 is $9 \times 9 \text{ m}^2$ and 3 m height. The position of the worshippers is according to normal congregational praying arrangement, with the *Imam* is standing at the front and the others (*Ma'mum*) stand in straight parallel row behind the *Imam*, facing qibla. The distance between *Ma'mums* is 1 meter apart, following the COVID-19 standard of procedure implemented by the government of Malaysia to maintain the social distancing. Both *Imam* and *Ma'mums* are created based on cuboid body with the same dimensions of

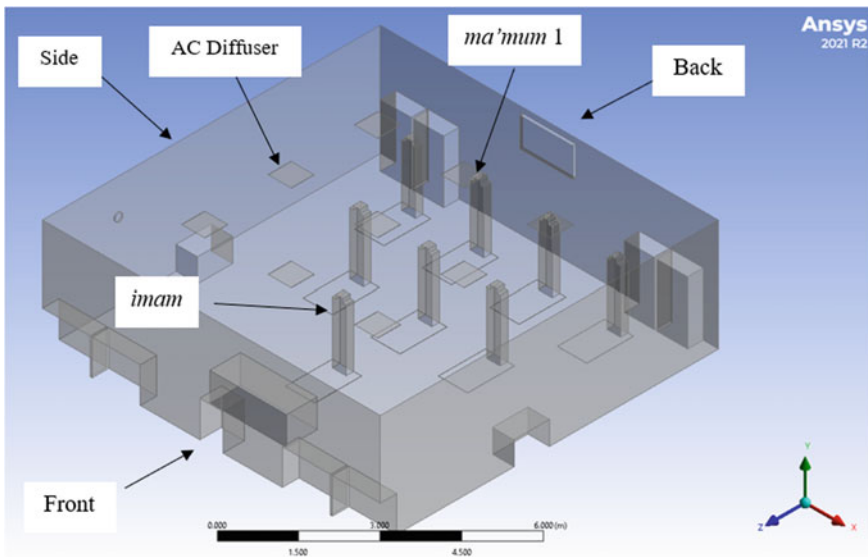


Fig. 1 Three-dimensional (3D) geometry of a typical prayer room in mosque

$1.67 \times 0.36 \times 0.20 \text{ m}^3$ with a rectangular mouth area of $0.06 \times 0.03 \text{ m}^2$. The mouth surface area is dedicated for the air and aerosol particles injected into the praying area. The 3D model also included the prayer mat, tables, chairs and holy Quran shelves. Worshippers are assumed to be exposed to aerosols to see the deposition among them with the influence of AC airflow.

The AC system in the praying area consists of five air supply diffusers and four return diffusers (Fig. 1). All diffusers have similar surface area of 0.294 m^2 , and the vertical air supply from the inlet diffuser is set at 0.395 m/s based on ASHRAE 62.1 [10]. There is no opened window or door in the area considered in the simulations.

The geometry was imported to ANSYS Workbench 2021 for mesh generation. An unstructured tetrahedral mesh is generated, creating an independent mesh with the total 2,145,198 elements (Fig. 2). Local refinement is specified near the surface of the wall and the worshippers to maintain the quality. The gradual transition of the mesh recorded the average quality of 0.828, average skewness of 0.241 and the aspect ration of 1.861.

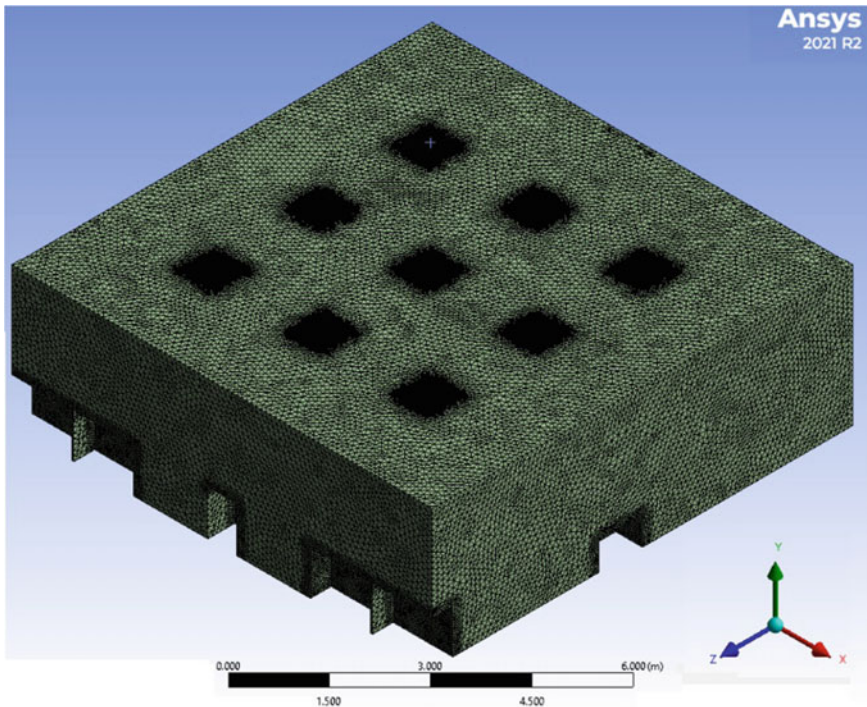


Fig. 2 Isometric view of unstructured mesh model of the prayer room

2.2 Computational Details

The CFD simulations in this study uses ANSYS Fluent 2021 to simulate the airflow and particle transport. The Navier-Stokes equations are solved entirely using the steady state laminar incompressible flow solver. The inlets airflow for the study consists of supply air from AC and from the worshippers' mouth, specifically from the *Imam* and one of the *Ma'mum*. The *Imam* and the *Ma'mum* are assumed to exhaled airflow from their mouths at 0.185 m/s with diameter of 1 μm , based on the range of the particle size of aerosol particles released in exhalation and talking [11]. The aerosol particle is assumed to release together with the airflow at the same velocity normal to the $0.06 \times 0.03 \text{ m}^2$ surface area of the mouth.

The aerosol particle is set according to discrete phase model (DPM) that available in ANSYS FLUENT 2021. Every DPM sources of flow iteration is updated with DPM iteration interval of 10. The maximum number of steps used is 50,000 steps. The SIMPLE algorithm was implemented in ANSYS FLUENT 2021 to solve the pressure-based model where the governing equations were discretized using the second-order discretization scheme.

3 Results and Discussion

3.1 Praying Area Model and Mesh Construction

Figure 3 shows velocity contours and vectors of airflow from the AC diffusers and aerosols emitted from the *Imam* and *Ma'mum* on a cross sectional plane throughout the praying area. The area of flow recirculation occurs throughout the spaces inside of the mosque. A few distinct flow recirculation is recorded around the human models due to pressure difference caused by the wall boundary of the human and the higher airflow velocity. For example, in the inset figure of Fig. 3, large flow recirculation is seen concentrated at the *Imam* with very low velocity. Vortices usually preferred to partially trap aerosol particles to the area and increase the chances of particles deposition on neighboring surfaces [8, 9].

For the purposes of characterizing the dynamics and the fate of exhaled aerosol particles, a single-release impulse source is used. To illustrate particles distribution in the praying area, the 1 μm aerosol particles dispersion to the air are illustrated at different points of in time since the particle release (Fig. 4). For 1 s time frame, both *Imam* (Fig. 4a) and *Ma'mum* (Fig. 4b) begin emitting aerosol particle through coughing with initial Z-velocity of 0.185 ms^{-1} . On the second 10 s-time frame, the particle trajectory from the *Imam* starts to change from Z-axis to Y-axis as if the aerosol particle is moving towards the outlet of return air diffuser. On the other hand, particle trajectory for 10 s-time frame in Fig. 4b shows a slight direction towards Y-axis.

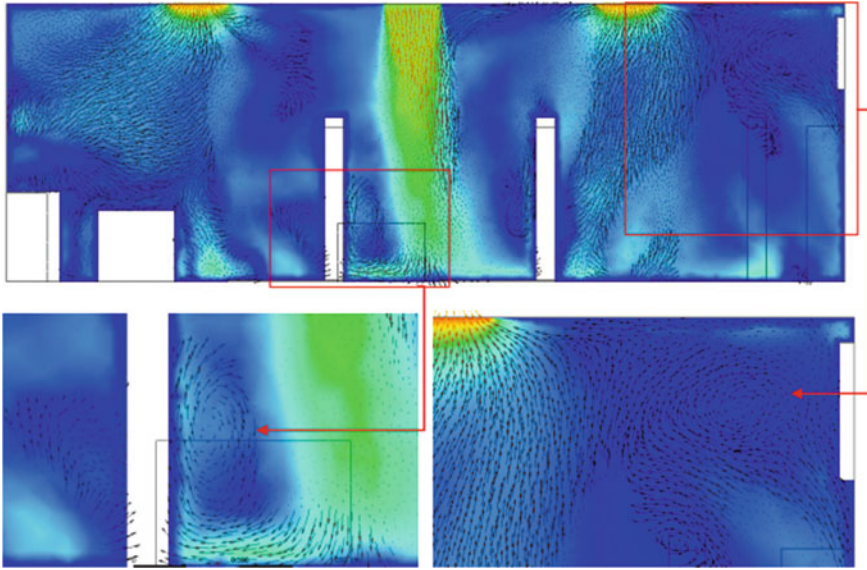


Fig. 3 Airflow velocity contours and vectors on a cross-sectional plane of prayer room. Inset figures show obvious recirculation flow area

Next, in 50 s timeframe, Fig. 4a is having a clear recirculation flow where the particle moves to the opposite downward direction of Y-axis towards the ground of the mosque before eventually flowing back to the earlier upwards Y-axis, whereas particle transmission of Fig. 4b is constantly moving toward the middle of the room and closer to the other *Ma'mum*. It is almost visible to see the occurrence of recirculation flow near the *Ma'mum* in the middle. In 100 s time frame, particle transmission in Fig. 3a shows a pattern of aerosol particles begins to exit the return air diffuser at the most front outlet. However, recirculation flow still takes places governing the trajectory of particle near the middle *Ma'mum* during 100 s in Fig. 4b. Only in 300 s time frame, the particles begin to exit the return air diffuser located at the left side of the mosque for the *Ma'mum* in Fig. 4b. It is also visible some particles transmit to the furniture at the front of the mosque.

It takes approximately 539 s for most of the particles to exit the closed space of the mosque in Fig. 4a. For *Ma'mum* in Fig. 4b, most of the particle exits the mosque approximately 1257 s.

The concentration of particles at the front and at the back areas of the praying room are consistent with the particle trajectory inside a classroom [8]. Particle transmissions behavior emitted in a closed space are depending on the location of the person who coughing. The dispersion of aerosol particle remains close to the location of source and only disperse to nearby entities. Present study recorded almost 90% of the aerosol particles emitted by the *Ma'mum* stays at the worshippers' row and may easily deposit to neighboring worshippers. The particles also stay longer time in spaces before exit at the outlet diffuser compared to the *Imam* source. The similar

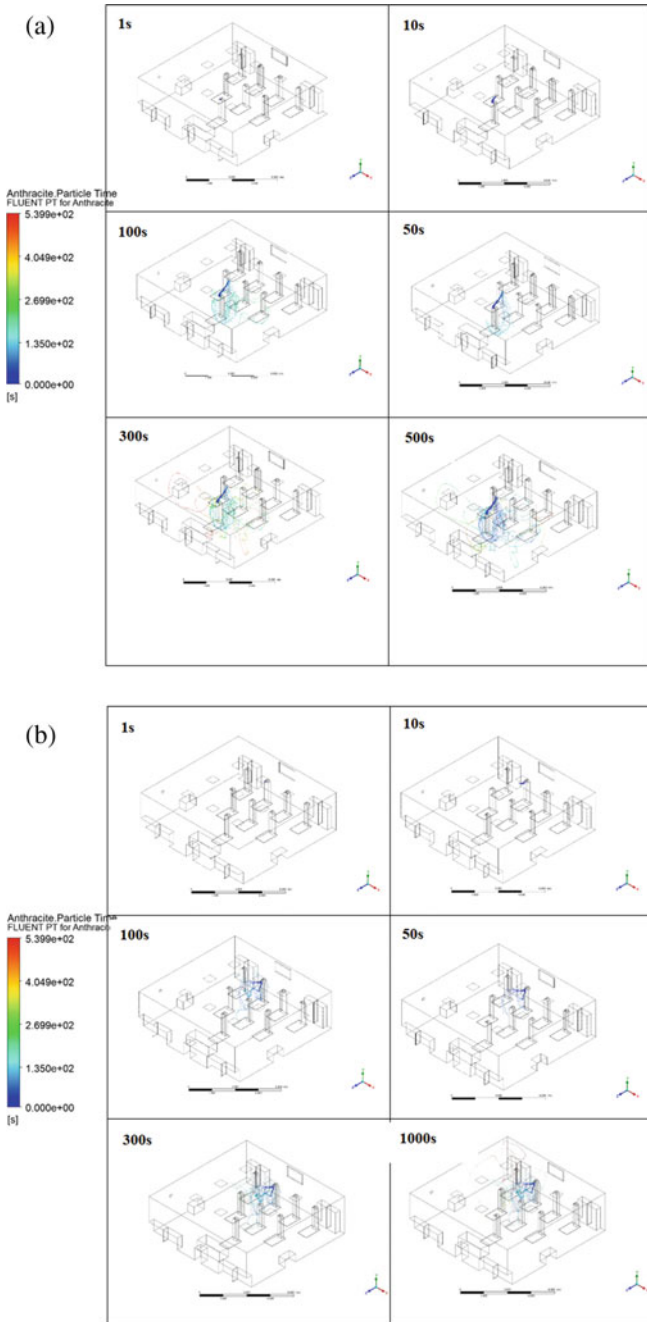


Fig. 4 Velocity streamlines at 6 Point of Time for aerosol particles trajectory emitted by **a** *Imam* and **b** *Ma'mum* in a closed-space praying area

result is recorded by [8] on 100 s time frame, where recirculation of particle occurs around the student located in the middle of the classroom. Moreover, is also stated that most of the aerosol particle is deposited on the source student that is located at the back of the classroom. Generally, the vortices condition would cause the particle to deposit at the recirculated area.

4 Conclusion

The investigation about the aerosol particles generated by coughing of COVID-19 travel simulation specifically for indoor space is crucial to understand the pattern of how the viruses spread in a closed-space for COVID-19 mitigation measures. The extensive computer fluid dynamic simulation cases have been conducted and produced several outcomes to be highlighted:

1. Aerosol distribution in a closed space praying room is not uniform and it is strongly influenced by the location of the coughing source and the air conditioning layout.
2. Particles disperse in the praying area before exit at the outlet diffuser, making high concentration of aerosols at the diffusers.
3. The effect of source location on aerosol transport is significant. Both *Imam* and *Ma'mum* transmitted aerosol mostly to their front area. Only less than 10% of aerosols from the *Imam* transmitted to the *Ma'mum* since the *Imam* is facing the qiblat, the opposite direction to the *Ma'mum*. However, more than 90% aerosols of the *Ma'mum* are well spread to the other worshippers. Therefore, *Ma'mums* are at the higher chance to get infected if one of the *Ma'mum* is the COVID-19 carrier.
4. This preliminary study didn't include windows for open ventilation to be compared with closed space environment. According to previous study by Abuhegazy et al., 2020, opening window could significantly increase particles exit by 38% and would reduce the transmission between the worshippers. Hence, it is recommended to include windows in the future study.

Acknowledgements The authors would like to thank Universiti Malaysia Pahang and research grant RDU200746 for supporting this study.

References

1. Jayaweera M, Perera H, Gunawardana B, Manatunge J (2020) Transmission of COVID-19 virus by droplets and aerosols: a critical review on the unresolved dichotomy. *Environ Res* 188:109819
2. Mittal R, Ni R, Seo J-H (2020) The flow physics of COVID-19. *J Fluid Mech* 894:F2

3. Morawska L et al (2020) How can airborne transmission of COVID-19 indoors be minimised? *Environ Int* 142:105832
4. Anfinrud P, Stadnytskyi V, Bax CE, Bax A (2020) Visualizing speech-generated oral fluid droplets with laser light scattering. *N Engl J Med* 382:2061
5. Suyadi, Nuryana Z, Fauzi FAN (2020) The fiqh of disaster: the mitigation of Covid-19 in the perspective of Islamic education-neuroscience. *Int J Disaster Risk Reduction* 51:101848
6. Hashim JH et al (2021) COVID-19 Epidemic in Malaysia: epidemic progression, challenges, and response. *Front Public Health* 9:560592
7. Tan MM, Musa AF, Su TT (2022) The role of religion in mitigating the COVID-19 pandemic: the Malaysian multi-faith perspectives. *Health Promot Int* 37:1–13
8. Abuhegazy M et al (2020) Numerical investigation of aerosol transport in a classroom with relevance to COVID-19. *Phys Fluids* 32:103311
9. Talaat K et al (2021) Simulation of aerosol transmission on a Boeing 737 airplane with intervention measures for COVID-19 mitigation. *Phys Fluids* 33:033312
10. American Society of Heating, Refrigerating, and Air-Conditioning Engineers, in ASHRAE Standard 62.1-2007 (2007) Ventilation and acceptable indoor air quality, ASHRAE, Inc., Atlanta, GA
11. Wurie F et al (2013) Characteristics of exhaled particle production in healthy volunteers: possible implications for infectious disease transmission. *F1000 Res* 2:14

A Review on Automotive Tires Significant Characteristic Identification for General Consumers



Ahmad Noor Syukri Zainal Abidin, Arief Hakimi Azmi,
Khairil Anwar Abu Kassim, Ahmad Shahir Jamaludin,
and Mohd Nizar Mhd Razali

Abstract A tire serves various types of services and distance over its lifespan. Moreover, for the safety and comfort of vehicle occupants, tire performance is critical. An assessment of literatures on tire-related properties that contribute to better safety performance was conducted in this study. The review elaborates on the most discussed topics from the overall reviewed articles. This study highlights the significant characteristics that be further implemented in tires for specific situations or general consumers. It was determined that tire wear is resulted from several factors. Increasing slip angles cause higher abrasion and temperature on tire surface. Modelling of wear rate can be done realistically with computation. From the review, it is also known that knowledge of tire-pavement and/or ice interactions behavior is improving. Semi-empirical methods in simulation of tire and terrain interactions are a promising candidate for use in multi-body dynamic software (MBS) simulation and vehicle simulations. Thermal aging in rubber tires will result in lower tensile strength. Production of tire wear particles increase 2–3 fold with abrasion from increased slip angles. Carbon black type N220 possess the best tensile, tear, and conductivity qualities. Overall, not much information was able to be obtained with regards to types of tires. Nonetheless research on tire safety performance should be extended so that each of tire component can be continuously improved to enhance tire safety criteria, particularly among the less discussed areas, such as commercial vehicle tires.

Keywords Automotive tire · Significant characteristic · General consumers

A. N. S. Z. Abidin · A. H. Azmi · K. A. A. Kassim
Malaysian Institute of Road Safety Research (MIROS), 43000 Kajang, Selangor, Malaysia
e-mail: ansyukri@miros.gov.my

A. N. S. Z. Abidin · A. S. Jamaludin (✉) · M. N. M. Razali
Faculty of Manufacturing & Mechatronic Engineering Technology, University Malaysia Pahang
(UMP), Pekan Campus, 26600 Pekan, Pahang, Malaysia
e-mail: shahir@ump.edu.my

1 Introduction

A tire is a device that is used to cover the circumference of a wheel. In technical terms, it is a rubber wheel cover reinforced with nylon, fiberglass, or other materials. A tire is pumped full of compressed air. Most land vehicles require rubber tires. For truck, agricultural, industrial, and specialty tires, as well as cycle tires, there are a variety of rubber tires with maximum inflation pressure retention. Tires can attenuate road surface vibrations, protect the wheel from wear and tear, and form a high friction contact between the vehicle and the ground to improve acceleration and handling. Complex interactions between tire, road pavement and other factors could result in degradation of the tire safety performance. Synthesized and natural rubber with varied constituents produce different resilience. Collective revision of past studies concentrating on key elements, that contributes to a better safety standard for future tires is the focus of this study. The literature review covered the most prevalent factors relating to tire safety performance. Even under the most unusual circumstances, understanding the behavior that influences tire performance proves insightful. Commercializing changes to tires for public use using knowledge of interaction between tire and ice for example can vastly prove tire standards in countries that experience changing seasons. When it comes to tire tread materials, wear resistance is unquestionably crucial [1–14]. Besides that, tire manufacturers have also performed research and studies to forecast tire tread wear. However, such research hasn't considered abrasion's history or directional impacts. Rubber's nonlinear behavior, as well as the tire's composite composition, must supply every performance required to properly fit on a vehicle [15–19]. Regulatory reform aiming at decreasing regulatory burden while preserving current tire safety standards is needed. Examining existing regulations to see if ought to be updated to keep up with new technologies should be always kept in mind [20–22].

2 Wear, Tear, and Interactions of Tires

These are the three properties that massively contribute to the performance of a tire. Each research has different focus elements but conclude to the betterment understanding of wear, tear, and friction under different conditions. Predicting the amount of wear in road vehicle tire could be difficult to be done consistently. A multi-variable tribo-system includes the tire-pavement contact. It is plausible to conclude that a better understanding of tribological variables will provide a clearer image of friction and wear phenomena once the pavement surface and rubber tire are linked to transportation safety, fuel consumption, wear rate, noise generation, and other [12].

2.1 Wear of Tire with Controlled and Variable Side Slip Angles

Grosch et al. [3] has concluded that tire wear increases with increasing slip angle, as does tire surface temperature and abrasion pattern intensity; the severity dependency of the relative wear rating of any two types of tires is primarily owing to differences in their temperature and abrasion pattern coefficients. In agricultural tractors it is shown that the longitudinal slip increases as the side slip angle increases, increasing rolling resistance; however, the increase is greater at higher normal loads [15]. When a loaded tire is tested at a small slip angles, the area of slip at the rear of the contact area and the magnitude of this side slide are both low, but when the slip angle increases, the area of slip at the back of the contact area and the magnitude of this side slide rapidly increases. This trend is reflected in the cornering force intensity curves, which show that as the slip angle increases, the overall cornering force also increases [10]. An experimental setup where Pirelli Scorpion Verde All Season 235/55 R19 105 V SUV tire is used for accelerated wearing. Using the Dynamic Tire Test Trailer (DTTT) on a coarse concrete surface, where tread would be noticeably degraded in less than 50 km of effective tire travel [14]. This was made possible by combining longitudinal and lateral braking on a regular basis sweeping slip angle. In addition, it was also found aircraft tire treads at low temperatures, slip angle is a major determinant of tread material wear performance. With increasing slip angle, the distance between protrudes grows [13]. It can be summarized that as the slip angle increases, the tire's total wear increases as well.

2.2 Modelling of Wear Trends

For rubber, an enhanced abrasion model was proposed [8]. It has a strong ability to forecast rubber abrasion, where the pattern or intrinsic abrasion can be observed as a characteristic. The model's most intriguing feature is its capacity to explain a wide range of wear scenarios. Greater sliding direction changes, with the same moving distance and two distinct directions, can create more wear but less abrasion. Furthermore, by altering the sliding velocity properly and fast on a continual basis, the intrinsic abrasion may be determined, resulting in the least amount of material lost. Using meta-models, a new friction model was built that accounts for the friction coefficient's nonlinear dependence on local contact pressure and sliding velocity in the contact surface [11]. The increased contact surface frictional qualities allow for a more accurate calculation of the friction energy dissipation rate and, as a result, the wear rate, resulting in a more realistic geometric configuration change due to wear. Furthermore, incorporating geometry adjustments into the numerical wear analysis also enabled the development of criteria for reduced wear volume and uniform wear distribution at the contact surface. Cho et al. [1] employing a power function wear rate model derived from laboratory research, offered a numerical approach to forecast

tire wear amount. The frictional energy dissipation through the tire footprint on abrasive terrain was calculated, using a 3D patterned tire model's frictional dynamic simulation. Using this, once the outdoor driving and load parameters are set, the suggested approach can predict the tread wear amount in an exceptionally short period of time. As proven by past studies. The modelling of wear rate can realistically replicate real life data without major disadvantages.

2.3 Tire and Pavement/Ice Interactions

Interaction investigations between tire and pavement have been carried out by tire engineers and chemists for many years in isolation. It is quite difficult to develop a tire that can handle the enormous diversity of road layout, pavement, condition, climate, and traffic situations that exist, even in the simplest scenario of straight-ahead braking [6]. The optimization of interaction between tire and road requires compromises to be a solution. To determine if there is a relationship between the tire and pavement categorization indexes, an experimental investigation was carried out. D'Apuzzo et al. [21] determine that using the derived relationship, it was possible to construct a road friction surface categorization that is specific to European tires. From the standpoint of pavement friction, road surfaces may be classified into five categories, and this material about the performance of the road surface can be easily transmitted to consumers. Even with the evolution of automobile and tires safety standards, driving on ice proves unpredictable and a safety hazard. Hence a comprehensive understanding of the behavior of tire on ice is essential. An Advanced Tire-Ice Interface Model (ATIIM) was created to identify the rise in temperature at the contact patch, as well as sections of dry and wet regions in the contact patch [23]. It was discovered that the water film is thickest near the contact patch's trailing edge, where the temperature rise is greatest. Because of the temperature rise at the contact patch, the thin water film acts as a lubricant, reducing the amount of friction available. During temperature changes, different tire-ice behavioral tendencies are found. The development of standard test protocols that consider the various factors that influence the friction coefficient is an urgent need. Bhoopalam and Sandu [24] stated to calculate the friction coefficient at the tire ice interface, state-of-the-art test facilities and procedures that simulate real-world road and weather conditions are necessary to improve vehicle safety.

2.4 Tire-Terrain Interaction Modelling

The problem of off-road vehicle tire-terrain interaction is complex enough that it cannot be solved precisely. Different terrain properties, as well as design and operational parameters, influence the approaches for modelling and assessing wheeled vehicle performance over deformable terrains. The contributions of models to the

progress of soil, tire, soil–tire interaction, experimental analysis, model parameterization, and model validation methodologies are highlighted. The most basic empirical approaches to the most advanced finite element methods are all available. Taheri et al. [25] concluded that empirical models for wheeled vehicles are useful for rudimentary mobility assessments, but they can't be generalized beyond the test data used to build them. To develop a practical framework for dealing with the complicated topic of soil–tire interaction, the physics-based models incorporate methods such as computational physics and numerical analysis. El-Sayegh et al. (2020) presented a new model for the interaction of off-road truck tires and gravelly soil [26]. The simulations and measurements were found to be in good agreement when it came to predicting tire rolling resistance characteristics. The error percentage was shown to be within a reasonable range. Because of their highly discretized structures, these models necessitate a lot of computing power. However, Yang et al. [27] has shown the computational efficiency of some DEM-FEM, which is GPU-based, proves to be a potent tool for modelling the interactions between an off-road tire and granular terrain. The semi-empirical technique, which is well-known in the terra-mechanics community, has been debated and developed in order to include all of an off-road tire's significant features into a single model. The model is tire geometry sensitive and consistently predicts the reaction to varying tire load and inflation pressure [28]. Semi-empirical model techniques, such as high-fidelity formulations and computational tools, were shown to be a feasible alternative capable of forecasting system dynamic behavior and computing important mobility measures for a wide range of off-road wheeled vehicle simulation scenarios [29]. Babulal et al. [30] used algorithms for deformable terrain are numerically implemented 3D system based on semi-empirical formulations. Experimental data is used to validate the simulation results for the normal and shear stress distributions for stiff wheels' oil contact. To get high quality results while minimizing processing effort and model variables, semi-empirical methods combine empirical relationships with analytical approaches. As a result, they're considered promising candidates for use in MBS simulations and vehicle simulations. They concluded the FTire model predicted the most accurate lateral tire behavior for large off-road tires. The model is proven to be able to forecast tire wear and a wide variety of operating conditions. It is, nevertheless, the time-consuming and computationally costly model.

3 Thermal Aging of Rubber in Tires

Rubber is in high demand due to the rubber industries and vehicle industry's rapid development. Rubber ageing, on the other hand, may accelerate the rate of usage and lower the service life. Rubber products will lose their suppleness and harden, making them unsuitable for usage. Thermal aging remains to be one of the biggest components accelerating the decline performance of tires. Zhang et al. [19] shown that the ultimate tensile strength and ultimate strain of vulcanized NR are degraded by thermal ageing. The difference in strength between thermally aged and unaged

rubbers under the same force is negligible. For 4 and 6 weeks, aged styrene butadiene rubber samples were stored in an oven at 80 °C [18]. The tensile strength of the rubber samples after this treatment was significantly lower than before the ageing was also determined. To keep the correct reaction rate in tires, a crucial minimum concentration of oxygen is essential. It is indisputable that the amount of oxygen in the tire cavity reduces as the time spent in the oven increases [16]. The rubber in a tire oxidizes with both the oxygen in the air used to inflate the tire and the oxygen in the air surrounding the tire, which is less well-known. Two-sized radial tires from a well-known manufacturer have been fitted on an Airbus jet. Tread throw failures have occurred on multiple occasions with these tires. Xie et al. [22] determined high temperatures accelerated micro-crack initiation and growth, resulting in increased load and decreased rubber mechanical properties. This eventually resulted in tire failure. Therefore, thermal aged rubber will cause produce dominos effects that will end in the decrease the rigidity of the rubber in the tires. The efficiency and life services of tires will be dramatically reduced.

3.1 Tire Wear Particles (TWPS)

Because many chemicals are utilized in tire manufacture, tire materials are complicated combinations. Fillers, reinforcement agents, processing aids, accelerators and retarders, adhesives, and activators may be added in addition to the rubber itself. The composition of a specific tire is dictated by its use, despite the regular use of general elements. Tire variables (size/width, chemical composition, cumulative mileage), vehicle characteristics (weight, engine power, state of maintenance), and road surface characteristics (material (bitumen/concrete), texture pattern, wetness, temperature) all influence emission factor [4]. With multiple factors in play, only a few should be investigated at a time. Chang et al. [31] concluded abrasive wear is a major wear mechanism that occurs when the tread wear is low and the road roughness is high, making it easier to generate large particles. The wear process is predominantly fatigue wear when the roughness is low or there is water lubrication, which enhances the possibility of small particle production. Furthermore, abrasion from slip angle appears to boost TWP production. PM10 and PM2.5 concentrations were 2–3 times greater in TWPs generated at constant speed with a 4° tire slip angle than in TWPs created under constant speed circumstances alone. Increased slip angles resulted in a lateral frictional force bias, which accelerated tire tread attrition. According to the authors, the creation of these microscopic particles could be explained by the evaporation and condensation of volatile chemicals from the tire material.

3.2 Reinforced Natural Rubber

Rubber is one of the most important materials due to its good mechanical strength, conductivity, and adequate service life when other compounding elements such as fillers are included. Carbon black is a form of reinforcing filler that is used in NR (Natural Rubber) composites to increase mechanical qualities. Azura and Leow (2019) determined carbon black type N220 possessed the best tensile, tear, and conductivity qualities. Before ageing, at 20 phr (part per hundred parts of rubber) filler loading, the optimum tensile characteristics can be seen. However, after an ageing test, the results revealed that 30 phr provides the best tensile qualities. In addition, the best abrasion resistance and thermal stability are found in NR nanocomposites comprising both carbon black N220 and hyper branched polyester modified nano Al_2O_3 [20]. When Al_2O_3 was combined with carbon blacks, the mechanical properties, abrasion resistance, and thermal stability of the nanocomposites were significantly improved. According to preliminary findings from Mané et al. [7], silica-reinforced natural rubber samples with wear resistance equivalent to, if not superior than, carbon black-reinforced natural rubber samples can be made.

4 Conclusion

From the meta-analysis of over 100 articles, a general analysis was conducted by grouping similar points to get the overall trends of the reviewed literature. Only 30 papers were selected for final review and were further elaborated. From Fig. 1, it is

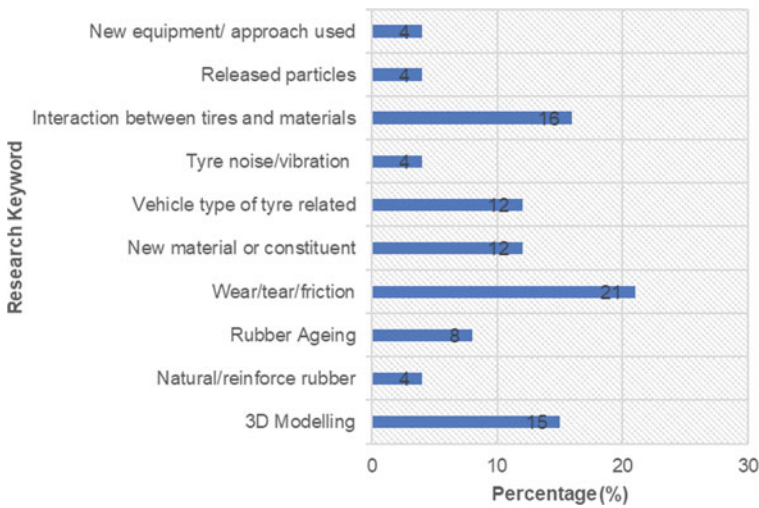


Fig. 1 Reviewed literatures by research keyword

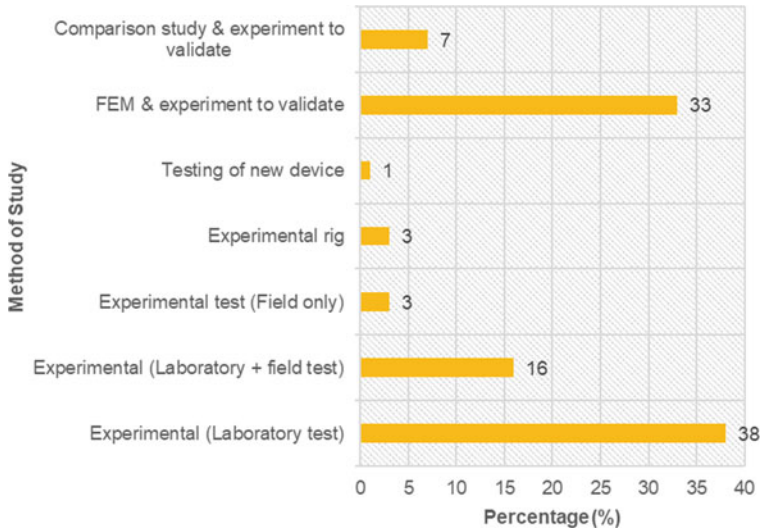


Fig. 2 Reviewed literatures by method of study

shown that from the research keyword grouping for wear, tear and friction of tires have the highest percentage at 21%. The second highest was usage of 3d modelling and FEM, and interaction between tires and pavement. With third being interaction between tires and materials. For methodology employ to validate data, Fig. 2 illustrate the most common method. Laboratory test is first a 38%. Meanwhile usage of FEM software and experiments to validate is placed second. Lastly laboratory and field test come at third. Majority of these topics with the details about the process for the experiments have been further discussed above.

This paper present major findings from the present literature review. Tire safety performance closely impacted by several factors. Wear and tear of tires is mainly resulted from the abrasion of the tire surface from increased slip angle. Generated particles from wear also experience similar trend where slip angle produce 2–3 times more particles. In addition, wear rate can be replicate similar real-world data in software’s using numerical functions and meta models under proper use of parameters. Complex interaction between tires and terrains are better understand using computation simulation improving efficiency and time management. Lower ultimate tensile strength can be when rubber is aged in high temperature. This relates the high-performance tires required for long usage or intense stress in a short period. Last of all, carbon black type N220 provided the best reinforcing properties when in mixture with rubber tires.

Clearly shown, most of the literature reviewed doesn’t specify what type of tires used. Only a few individual papers specify on the type of tires used for example off-road, SUV, and aircraft other than the standard passenger car tires. No paper was found discussing on heavy vehicle tires during the review. Instead using the general term “rubber” does not differentiate on what kind of tires is used in the

automotive industry vehicle wise. Modelling of tire- terrain and pavements interactions are adequate but requires experimental validation. Additionally, few finite element models can produce accurate results to a certain degree in the define parameters. Proper knowledge is essential for the utilization of the models to not intrude its limits. The reviewed literature is placed in specific scenarios. As a result, more research is needed to gain a better grasp of the issues where there are insufficient examinations of elements and criteria.

The development of tires safety performance will always be the subject of future research to ensure continuous improvement in tire safety is obtained. Thus, clear and defined developments that is well documented should be reflected in legislations and standards so that consequently, the communities and industry can enjoy its full benefits.

Acknowledgements The authors would like to express their gratitude to the Malaysian Institute of Road Safety Research (MIROS) and the ASEAN NCAP for guidance and financial assistance through ASEAN NCAP Collaborative Holistic Research (ANCHOR) initiative along with Fundamental Research Scheme (FGRS), RACER/1/2019/TK05/UMP//1 from Malaysia Ministry of Higher Education (MOHE).

References

1. Cho JR, Choi JH, Kim YS (2011) Abrasive wear amount estimate for 3D patterned tire utilizing frictional dynamic rolling analysis. *Tribol Int* 44(7–8):850–858. <https://doi.org/10.1016/J.TRIBOINT.2011.02.007>
2. Chang XD, Huang HB, Jiao RN, Liu JP (2020) Experimental investigation on the characteristics of tire wear particles under different non-vehicle operating parameters. *Tribol Int* 150:106354. <https://doi.org/10.1016/J.TRIBOINT.2020.106354>
3. Grosch KA, Schallamach A (1961) Tyre wear at controlled slip. *Wear* 4(5):356–371. [https://doi.org/10.1016/0043-1648\(61\)90003-5](https://doi.org/10.1016/0043-1648(61)90003-5)
4. Denier van der Gon HAC, Gerlofs-Nijland ME, Gehrig R, Gustafsson M, Janssen N, Harrison RM, Hulskotte J, Johansson C, Jozwicka M, Keuken M, Krijgsheld K, Ntziachristos L, Riediker M, Cassee FR (2012) The policy relevance of wear emissions from road transport, now and in the future—an international workshop report and consensus statement. *J Air Waste Manag Assoc* 63(2):136–149
5. Huang M, Guibert M, Thévenet J, Fayolle C, Chaussée T, Guy L, Vanel L, Loubet J-L, Sotta P (2018) A new test method to simulate low-severity wear conditions experienced by rubber tire materials. *Wear* 410–411:72–82. <https://doi.org/10.1016/J.WEAR.2018.06.004>
6. Holmes T, Lees G, Williams AR (1972) A combined approach to the optimisation of tyre and pavement interaction. *Wear* 20(3):241–276. [https://doi.org/10.1016/0043-1648\(72\)90408-5](https://doi.org/10.1016/0043-1648(72)90408-5)
7. Mané Z, Loubet J-L, Guerret C, Guy L, Sanseau O, Odoni L, Vanel L, Long DR, Sotta P (2013) A new rotary tribometer to study the wear of reinforced rubber materials. *Wear* 306(1–2):149–160. <https://doi.org/10.1016/J.WEAR.2013.07.012>
8. Nguyen VH, Zheng D, Schmerwitz F, Wriggers P (2018) An advanced abrasion model for tire wear. *Wear* 396–397:75–85. <https://doi.org/10.1016/J.WEAR.2017.11.009>
9. Park I, Kim H, Lee S (2018) Characteristics of tire wear particles generated in a laboratory simulation of tire/road contact conditions. *J Aerosol Sci* 124:30–40. <https://doi.org/10.1016/J.JAEROSCI.2018.07.005>

10. Savkoor AR (1966) Some aspects of friction and wear of tyres arising from deformations, slip and stresses at the ground contact. *Wear* 9(1):66–78. [https://doi.org/10.1016/0043-1648\(66\)90015-9](https://doi.org/10.1016/0043-1648(66)90015-9)
11. Serafinska A, Hassoun N, Kaliske M (2016) Numerical optimization of wear performance—utilizing a metamodel based friction law. *Comput Struct* 165:10–23. <https://doi.org/10.1016/J.COMPSTRUC.2015.11.013>
12. Vieira T, Ferreira RP, Kuchiishi AK, Bernucci LLB, Sinatora A (2015) Evaluation of friction mechanisms and wear rates on rubber tire materials by low-cost laboratory tests. *Wear* 328–329:556–562. <https://doi.org/10.1016/J.WEAR.2015.04.001>
13. Wu J, Chen L, Wang Y, Su B, Cui Z, Wang D (2019) Effect of temperature on wear performance of aircraft tire tread rubber. *Polym Testing* 79:106037. <https://doi.org/10.1016/J.POLYMERTESTING.2019.106037>
14. Wright KR, Botha TR, Els PS (2019) Effects of age and wear on the stiffness and friction properties of an SUV tyre. *J Terramech* 84:21–30. <https://doi.org/10.1016/J.JTERRA.2019.04.001>
15. Abdolmaleki H, Jafari A, Tabatabaeifar A, Hajiahmad A, Goli H (2015) Development and evaluation of an in-situ tire testing facility with variable side slip angles. *J Terramech* 59:49–58. <https://doi.org/10.1016/J.JTERRA.2015.03.002>
16. Bauer DR, Baldwin JM, Ellwood KR (2007) Rubber aging in tires. part 2: accelerated oven aging tests. *Polym Degrad Stab* 92(1):110–117. <https://doi.org/10.1016/J.POLYMDEGRADSTAB.2006.08.014>
17. Azura AR, Leow SL (2019) Effect of carbon black loading on mechanical, conductivity and ageing properties of natural rubber composites. *Mater Today Proc* 17:1056–1063. <https://doi.org/10.1016/J.MATPR.2019.06.512>
18. Rodriguez N, Dorogin L, Chew KT, Persson BNJ (2018) Adhesion, friction and viscoelastic properties for non-aged and aged styrene butadiene rubber. *Tribol Int* 121:78–83. <https://doi.org/10.1016/J.TRIBOINT.2018.01.037>
19. Zhang Z, Sun J, Lai Y, Wang Y, Liu X, Shi S, Chen X (2018) Effects of thermal aging on uniaxial ratcheting behavior of vulcanised natural rubber. *Polym Testing* 70:102–110. <https://doi.org/10.1016/J.POLYMERTESTING.2018.06.030>
20. Fu J-F, Yu W-Q, Dong X, Chen L-Y, Jia H-S, Shi L-Y, Zhong Q-D, Deng W (2013) Mechanical and tribological properties of natural rubber reinforced with carbon blacks and Al₂O₃ nanoparticles. *Mater Des* 49:336–346. <https://doi.org/10.1016/J.MATDES.2013.01.033>
21. D'Apuzzo M, Evangelisti A, Nicolosi V (2020) An exploratory step for a general unified approach to labelling of road surface and tyre wet friction. *Accid Anal Prev* 138:105462. <https://doi.org/10.1016/J.AAP.2020.105462>
22. Xie M, Tang H, Yao H (2016) Failure analysis of tire separation in two-sized tires on airbus planes. *Eng Fail Anal* 61:21–27. <https://doi.org/10.1016/J.ENGFAILANAL.2015.07.006>
23. Jimenez E, Sandu C (2019) Towards a real-time pneumatic tire performance prediction using an advanced tire-ice interface model. *J Terramech* 81:43–56. <https://doi.org/10.1016/J.JTERRA.2018.04.004>
24. Bhoopalam AK, Sandu C (2014) Review of the state of the art in experimental studies and mathematical modeling of tire performance on Ice. *J Terramech* 53:19–35. <https://doi.org/10.1016/J.JTERRA.2014.03.007>
25. Taheri S, Sandu C, Taheri S, Pinto E, Gorsich D (2015) A technical survey on terramechanics models for tire–terrain interaction used in modeling and simulation of wheeled vehicles. *J Terramech* 57:1–22. <https://doi.org/10.1016/J.JTERRA.2014.08.003>
26. El-Sayegh Z, El-Gindy M, Johansson I, Öijer F (2020) Development and validation of off-road tire-gravelly soil interaction using advanced computational techniques. *J Terramech* 91:45–51. <https://doi.org/10.1016/j.jterra.2020.05.004>
27. Yang P, Zang M, Zeng H, Guo X (2020) The interactions between an off-road tire and granular terrain: GPU-based DEM-FEM simulation and experimental validation. *Int J Mech Sci* 179:105634. <https://doi.org/10.1016/j.ijmecsci.2020.105634>

28. Senatore C, Sandu C (2011) Off-road tire modeling and the multi-pass effect for vehicle dynamics simulation. *J Terramech* 48(4):265–276. <https://doi.org/10.1016/j.jterra.2011.06.006>
29. Recuero A, Serban R, Peterson B, Sugiyama H, Jayakumar P, Negrut D (2017) A high-fidelity approach for vehicle mobility simulation: Nonlinear finite element tires operating on granular material. *J Terramech* 72:39–54. <https://doi.org/10.1016/J.JTERRA.2017.04.002>
30. Babulal Y, Stallmann MJ, Els PS (2015) Parameterisation and modelling of large off-road tyres for on-road handling analyses. *J Terramech* 61:77–85. <https://doi.org/10.1016/J.JTE RRA.2015.07.001>
31. Chang XD, Huang HB, Jiao RN, Liu JP (2020) Experimental investigation on the characteristics of tire wear particles under different non-vehicle operating parameters. *Tribol Int* 150:106354. <https://doi.org/10.1080/10962247.2012.741055>

Evaluation of Palm Oil Leaves Extracts as a Potential Environment Friendly Corrosion Inhibitor for Metals



Arman Abdullah, Euodia Banius, Azizul Helmi Sofian, and Lum Wai Bin

Abstract Carbon steel were used in various fields as it is economically affordable, environment friendly, highly durable and with high strength. However, carbon steel tends to corrode compared with other superior materials. Corrosion had brought negative effect to economic, health, safety, and also culture. One of the methods use in controlling the internal corrosion is by using the corrosion inhibitor. Inorganic corrosion inhibitor had long been used to suppress corrosion however they are toxic to health and also environment. Therefore, this research had been conducted to evaluate the potential of the corrosion inhibitor from palm oil leaves (POL) extract. The POL extract was extracted using Microwave Assisted Extraction method (MAE). After extraction, POL extract was sent to LC/MSQ-Tof analysis to test for active chemical component present. The presence of active component such as tannin, flavonoid and alkaloid help to inhibit corrosion. Corrosion inhibition testing were conducted by using weight loss method and electrochemical Tafel plot. SEM test show that carbon steel without inhibitor corrodes more than 90% compare with carbon steel coupon contain POL extract as an inhibitor.

Keywords Corrosion inhibitor · Oil palm leaves · Carbon steel · Green inhibitor

1 Introduction

Corrosion is the deterioration of a metal as a result of the chemical reactions between it and the surrounding environment. Among the various methods to avoid or prevent destruction or degradation of metal surface, the corrosion inhibitor is one of the best know methods of corrosion protection [1]. Corrosion inhibitors are chemicals that are added to a chemical stream to prevent corrosion, or lowering the rate of corrosion so that the processing equipment will have a suitable service lifetime [2]. However, there are growing concerns regarding the use of inorganic inhibitors that containing

A. Abdullah (✉) · E. Banius · A. H. Sofian · L. W. Bin
Faculty of Chemical and Process Engineering Technology, Universiti Malaysia Pahang,
Lebuhraya Tun Razak, 26300 Gambang, Kuantan, Pahang, Malaysia
e-mail: armanabdullah@ump.edu.my

© The Author(s), under exclusive license to Springer Nature Singapore Pte Ltd. 2023
N. H. Johari et al. (eds.), *Proceedings of the 2nd Energy Security and Chemical Engineering Congress*, Lecture Notes in Mechanical Engineering,
https://doi.org/10.1007/978-981-19-4425-3_34

387

poisonous compounds such as chromates, phosphates, and heavy metals mainly due to the issue of toxicity and disposal [3]. The use of these inhibitors is now restricted and need to be replaced with natural products [4].

To solve the drawback of toxicity and pollution, the employment of green inhibitors is important consideration. They are cost-effective regarding their abundance in nature and almost composed of non-toxic substances. A lot of plants such as *andropogon paniculata*, and *azadirachta indica* had been tested for their potential for corrosion inhibitor [5, 6].

Previous research has revealed that plant extracts have excellent compounds for suppressing metal electrolyte reactions. Several plant extracts, including *Carica Papaya*, *Rosmarinus*, cashew, mango, *Uncaria gambir*, and *Ficus sycomorus* extracts, had been studied. These plants have sufficient cyclic organic phytochemicals, nitrogen, sulfur, and oxygen atoms, which are responsible for their inhibitory characteristics. Many difficulties exist in the large-scale synthesis of diverse natural plant extracts. The most important of them is the extraction of certain plant extract components having inhibitory properties. Nonetheless, numerous natural plant extracts have been shown to be effective corrosion inhibitors [7–9].

Malaysia is the second largest palm oil producing country and produce 85% of the global palm oil supply. The total palm oil plantation in Malaysia covers 5.85 million hectares in 2018 [10]. These large amounts of oil palm tree generate a lot of waste annually [11]. The leaves and trunks are usually left in the field [12], which may cause various problems if it is not managed properly. Then, utilize the palm oil waste by looking into the new application of the waste as corrosion green inhibitor is a remarkable environmental effort.

This research seeks to evaluate the use of POL extracts for corrosion prevention and control by evaluating its corrosion preventive characteristics of on mild steel in HCl solution. The interaction of palm oil leaves extracts and mild steel in HCl solution become substantial. In industry, hydrochloric acid is the most commonly used acid for pickling, cleaning, and descaling, according to [13], this acid solution is usually utilized in acidification process in the oil and gas industry.

2 Methodology

2.1 Apparatus and Materials

Some of the apparatus and chemical used in this experiment include, carbon steel coupons, emery paper (SIC 800, 600, 400, 100), filter paper, desiccator, blender, microwave extractor, beaker 500 ml, beaker 100 ml, weighing boat, spatula, measuring cylinder, oven, electronic balance, bristle brush, distilled water, dropper, round bottom flask, petri dish, aluminum foil, universal bottle, schott bottle, sieve, hot plate, hydrochloric acid 37% AR grade, methanol AR Grade and acetone AR Grade.

2.2 Sample Collection

The palm oil leaves for this study were collected from Felda Lepar Hilir Dua, Gambang, Pahang. The leaves were freshly cut down from the palm oil tree in the morning. The leaves were collected, and drying process were conducted at UMP, FTKKP laboratory.

2.3 Preparation of Palm Oil Leaves Extract

Palm oil leaves collected were washed and then dried in the oven at 40 °C for a day [14]. The leaves were then grinded into fine powder. The oil palm leaves extraction were obtained using microwave assisted extraction. 25 g of oil palm leaves were mixed with 200 ml of methanol. The mixture was placed into Ethos microwave for extraction process. The temperature of the microwave was set to 40 °C, power at 100 W and total extraction time 82 min. This extraction time include 2 min preheat, 60 min extraction and 20 min for cooling. The mixture was filtered to remove the solid. The filtrate was then evaporated in the rotatory evaporator to remove part of the solution and then further dried in oven at 40 °C until all the methanol were evaporated.

2.4 Phytochemical Screening of Palm Oil Leaves

The palm oil leaves extract were sent to the central lab UMP Pahang to run the LC/MS Q-ToF analysis to determine the chemical component present in the extract. The model used in this analysis was Waters brand of model Vion IMS LCQTOF MS.

2.5 Respond Surface Methodology (RSM)

Carbon steel of size 1 cm × 1 cm × 5 cm will be polished and then coiled with a wire and then covered with resin. Resin was cut to expose a surface area of 1 cm × 1 cm of coupon. The carbon steel coupon was then polished and cleaned before used for potentiostat study. A typical schematic three-electrode set-up was used with carbon steel as working electrode, graphite as counter electrode and Ag/AgCl as reference. The potentiostat study apparatus was set up and let to run. Tafel plot and the corrosion rate was obtained using Gamry interface 1000E. Corrosion rate obtained was key into Design expert 7 for optimization of experiment.

Table 1 Experimental range and coded level of independent variables

Factors	Units	Range and level				
		$-\alpha$	-1	0	$+1$	$+\alpha$
Inhibitor concentration	ppm	32	100	200	300	368
Temperature	°C	26.5	30	35	40	43.5
Acid concentration	M	0.1	0.2	0.3	0.4	0.5

Parameter chosen for study were acid concentration, inhibitor concentration and also temperature. Each independent variable was studied at five different coded levels ($-\alpha$, -1 , 0 , $+1$, $+\alpha$) as shown in Table 1.

2.6 Surface Analysis Test

Carbon steel coupons of size 3.5 cm × 1.5 cm × 0.7 cm was polished with sand paper until all the rust present on the surface were removed. Carbon steel coupon was then degreased with acetone to remove the oil and washed thoroughly with double-distilled water and dried [15]. The clean coupons were dried with clean cloth. One carbon steel was immersed into a beaker with 200 ml of 0.5 M hydrochloric acid and one into a beaker with 200 ml of 0.5 M hydrochloric acid with 300 ppm palm oil leave extract. One was store in desiccator. The carbon steel was taken out after 2 days and sent for scanning electron microscope (SEM) analysis.

3 Results and Discussion

3.1 LC/MS Q-TOF

Figure 1 shows the Base Peak Chromatogram (BPI) plot of blank methanol and also the oil palm leave extract obtained after performing the LC/MS Q-TOF analysis. A lot of constituent were identified present in the oil palm leave extract based on the database of the LC/MS Q-Tof. Some of the major component identified include the Riboflavin (Vitamin B), Santin and 3,5,6-Trihydroxy-3',4',7-trimethoxyflavone which are part of the flavonoid group and also Arecatannin A1 which belong to the tannin group and also Picrasidine which belong to the alkaloid group. Other identified constituents are listed in Table 2.

The LC/MS Q-Tof tested that alkaloid, tannins and flavonoid was present in the oil palm leave extract. The presence of the tannins, flavonoid and alkaloid, with functional group containing nitrogen, oxygen and carbon functional group enhance the process of adsorption on the mild steel and act as corrosion inhibitor [16]. This

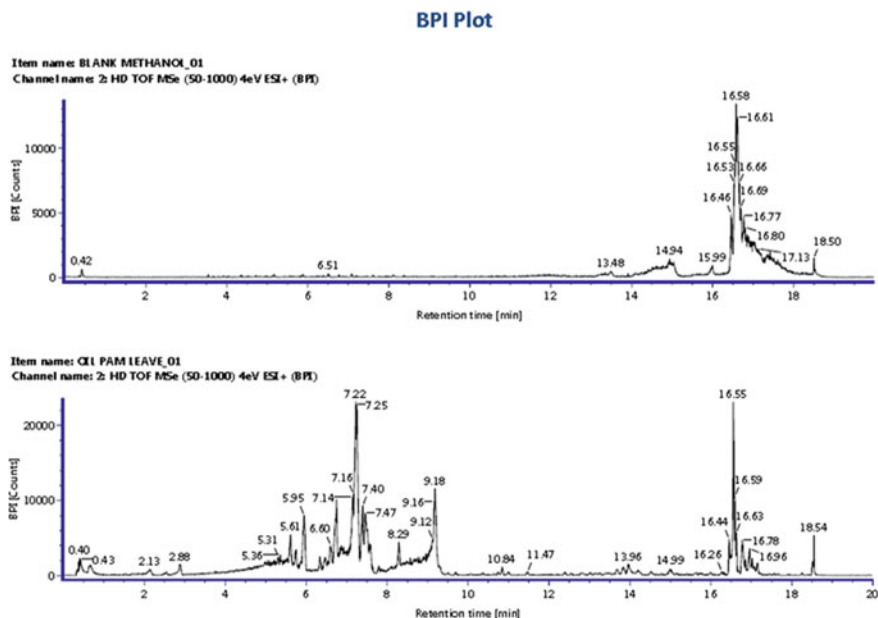


Fig. 1 Base peak chromatogram plot of blank methanol and oil palm leave extract dissolved in methanol

Table 2 Constituents identification in oil palm leaves extract produce by LC/MS Q-ToF

Component name	Formula	Observed fragment ions m/z	Observe retention time (min)	Class
Riboflavin (Vitamin B2)	C ₁₇ H ₂₀ N ₄ O ₆	382.18648, 399.1257, 429.13644	1.8	Flavonoid
Tilianin	C ₂₂ H ₂₂ O ₁₀	295.06004, 325.07079, 469.1134 2.9, 547.14485, 611.16131	6.70	Flavonoid
Senkirkine	C ₁₉ H ₂₈ NO ₆	350.13403, 371.16745, 373.18308, 403.15692	4.48	Alkaloid
Isaindigotidione	C ₂₃ H ₂₂ N ₂ O ₅	295.06003, 379.08146, 397.09180, 547.14559,	7.03	Alkaloid
Arecatannin A1	C ₄₅ H ₃₈ O ₁₈	247.0644, 409.09185, 579.17033, 867.2134	4.13	Tannin

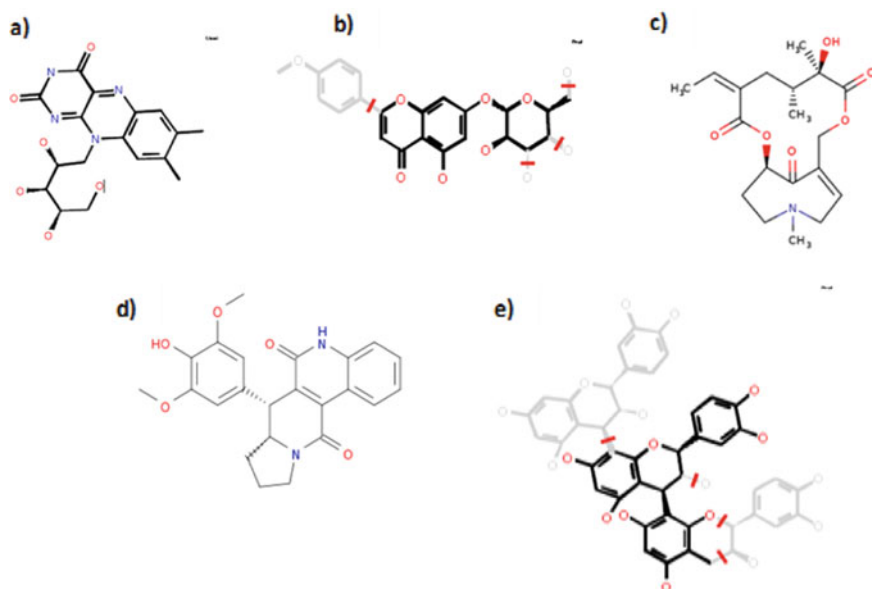


Fig. 2 Active component present in palm oil leave extract. **a** Riboflavin (Vitamin B2), **b** Tilianin, **c** Senkirikine, **d** Isaindigotidione, **e** Arecatannin A1

also corroborates the work of [17–19]. The presence of these compounds has been reported to promote the corrosion inhibition of mild steel in aggressive acid media [20].

Molecules containing nitrogen and acetylenic alcohols are claimed to form a film on the metal surface and can retard the metal dissolution process (an anodic reaction) as well as hydrogen evolution (a cathodic reaction) [21] (Fig. 2).

There are also other studies that found that tannin, flavonoid and alkaloid are good green corrosion inhibitor. Mature leaves of *Combretum bracteosum* were used for the corrosion inhibition of mild steel in H_2SO_4 . Inhibition efficiency increases when the plant extracts concentration increases and tannic acid is proven to be present in the green inhibitor [22].

3.2 Response Surface Methodology

The potentiodynamic polarization curves of the carbon steel in various conditions of temperature, acid and inhibitor concentrations are presented in Fig. 3. The design of experiments and experimental result were reported in Table 3. The corrosion rates obtained were estimated using Tafel extrapolation method. From the experimental result, the lowest corrosion rate recorded was 0.0003471 mm/yr, whereas the highest corrosion rate recorded was 320.3 mm/yr. The predicted quadratic model that relate

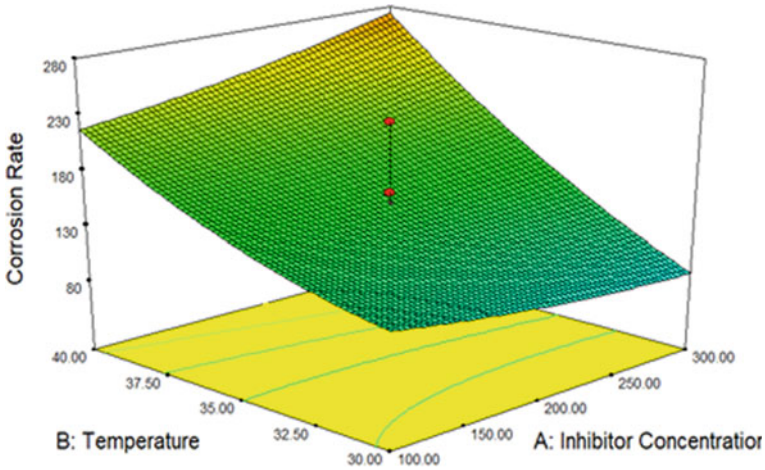


Fig. 3 3-D graph of temperature and inhibitor concentration

corrosion rate with the other entire variable is shown in Eq. 1. It is the final equation in term of coded factor.

$$Corrosion\ rate = 154.09 + 17.09A + 8.18B + 42.41C + 40.32AB - 30.25AC - 11.78BC + 9.03A^2 + 17.85B^2 + 1.8C^2 \quad (1)$$

- A Inhibitor concentration (ppm)
- B Acid Concentration (M)
- C Temperature (°C).

The fitness of the model from the experimental result and predicted values was verified using the value of coefficient of determination (R2). Using Design Expert 7 software, the value of R2 was found to be 0.8218. This R2 value means that approximately 20% of the total variations did not fit the proposed model, whereas 80% out of the total variations fit and was justified by the model. It can also be said that 82.18% of the total variation in the response was justified by the fitted model. The obtained R2 value showed that the model is marginally acceptable and reliable in predicting the response as more than 80% of the variability in the experiment were covered. The R2 obtained is also larger than the minimal R2 of 0.75 for adequate explanation on the variability in the experiments [23].

To further justify the model, ANOVA test was conducted by analysis of the variance. The results of the analysis are presented in Table 4. It was found to be significant as p-value was less than 0.05 and the F-value (5.13) obtained by the software was higher than the F-value of distribution table ($F_{0.05,2,27} = 3.354$) which confirm that the model was significant. The lack of fit obtained also insignificant.

Based on Table 5, a negative “Pred R-Squared” implies that the overall mean is a better predictor of the response than the current model. “Adeq Precision” measures

Table 3 Central composite design of independent variable and corrosion rate obtained

Run	Variable levels			Experimental variables				Corrosion rate (mm/yr)
	Inhibitor concentration	Temperature	Acid concentration	Inhibitor concentration	Temperature	Acid concentration		
1	0	+ α	0	200	43.5	0.3	320.3	
2	0	0	0	200	35	0.3	161.4	
3	+1	+1	-1	300	40	0.2	261.7	
4	-1	+1	+1	100	40	0.4	279.1	
5	0	- α	0	200	26.5	0.3	6.2	
6	-1	-1	-1	100	30	0.2	101.5	
7	-1	-1	-1	100	40	0.2	142.3	
8	0	0	0	200	35	0.3	148.8	
9	+ α	0	0	368	35	0.3	123.1	
10	0	+1	+1	300	40	0.4	319.0	
11	- α	0	0	32	35	0.3	153.5	
12	+1	-1	-1	300	30	0.2	101.2	
13	0	0	- α	200	35	0.13	3.47E4	
14	0	0	0	200	35	0.3	224.5	
15	0	0	+ α	200	35	0.5	235.7	
16	0	0	0	200	35	0.3	141.8	
17	-1	-1	+1	100	30	0.4	177.2	
18	0	0	0	200	35	0.3	138.3	
19	0	0	0	200	35	0.3	123.9	
20	+1	-1	+1	300	30	0.4	164.1	

Table 4 Analysis of variance

Source	Sum of squares	Degree of freedom	Mean square	F-value	P-value	Remark
Model	1.192E+005	9	13,240.37	5.13	0.0088	Significant
A-Inhibitor concentration	655.62	1	655.62	0.25	0.6253	
B-Temperature	71,216.26	1	71,216.26	27.57	0.0004	
C-Acid concentration	38,908.35	1	38,908.35	15.06	0.0031	
Residual	25,834.20	10	2583.42			
Lack of fit	19,516.82	5	3903.36	3.09	0.1206	Not significant
Pure error	6317.37	5	1263.47			

Table 5 ANOVA result for corrosion rate

R-squared	Adj R-squared	Pred R-squared	Adeq precision
0.8218	0.6615	-0.0880	7.549

the signal to noise ratio. A ratio greater than 4 is desirable. The ratio of 7.549 indicates an adequate signal. This model can be used to navigate the design space. The 3D-graphical figures from RSM that represent the interactions between independent variables and corrosion rate are shown in Figs. 3, 4 and 5. Figure 3 illustrates the relationship between corrosion rate with temperature and inhibitor concentration. The

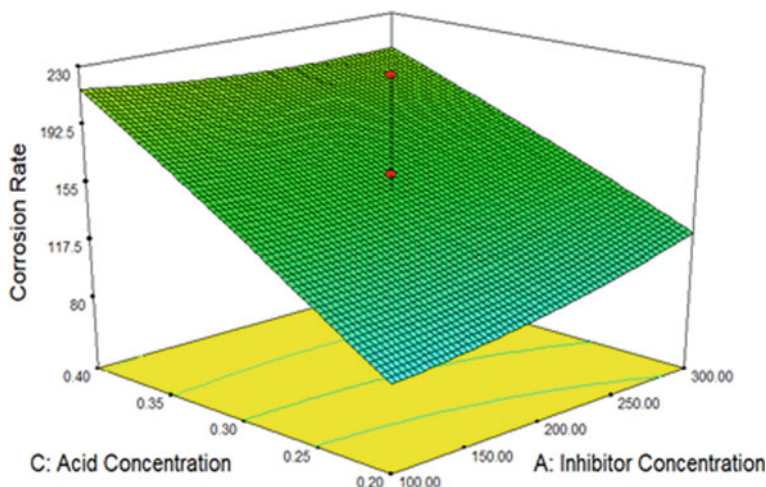


Fig. 4 3-D graph of acid concentration and inhibitor concentration

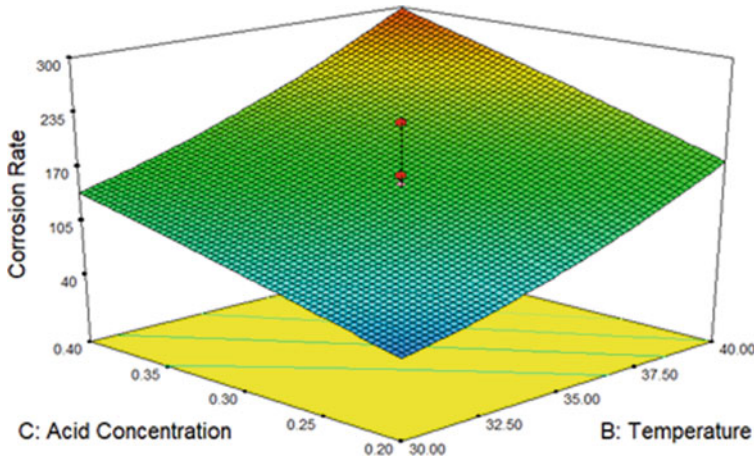


Fig. 5 3-D graph between acid concentration and temperature

response increased with increasing parameters. As temperature increase, the corrosion rate also increases. However, as the corrosion inhibitor increases, the corrosion rate decreases. Temperature also has a steeper slope indicating that the effect of temperature to corrosion rate is higher.

Figure 4 shows the 3-D graph which shows the relationship between acid concentration and inhibitor concentration. Corrosion rate increases as acid concentration increase despite the increase of inhibitor concentration. Acid concentration has a more significant effect compare to inhibitor concentration. Figure 5 shows the 3-D graph which shows the relationship between acid concentration and temperature. The graph shows that as acid concentration and temperature increases, the corrosion rate increases.

3.3 Corrosion Surface Morphology

Figure 6 shows the image of the carbon steel coupon presents under scanning electron microscope (SEM). Figure 6a is the morphology of the polished blank carbon steel coupon. Figure 6b is the carbon steel coupon which had been immersed into 0.5 M hydrochloric acid for two days. Lastly, Fig. 6c is the morphology of carbon steel coupon which had been immersed in 0.5 M hydrochloric acid and 300 ppm oil palm leave extract for two days.

From the images we can see that the blank carbon steel coupon has the smoothest surface. There are only some scratches shown on the carbon steel coupon. The carbon steel coupon immersed in 0.5 M hydrochloric acid show the worst condition. The surface of the carbon steel coupon had become rough and irregular due to corrosion. Corrosion pits had started to form. Carbon steel coupon immersed in 0.5 M

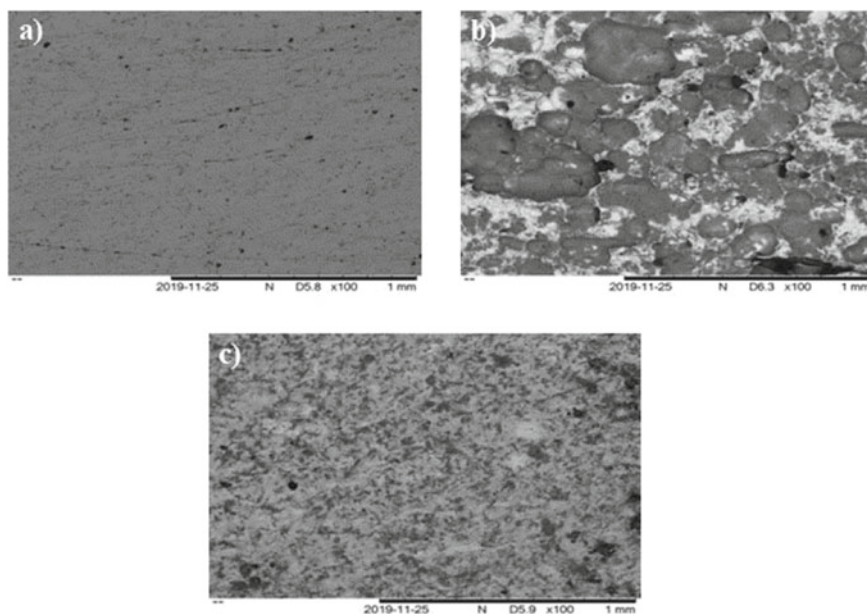


Fig. 6 Morphology of carbon steel coupon at 1 mm (a), morphology of carbon steel coupon at 1 mm after immersing into 0.5 M HCl (b), morphology of carbon steel coupon at 1 mm after immersing into 0.5 M HCl and 300 ppm oil palm leaves inhibitor (c)

hydrochloric acid and 300 ppm oil palm leaves extract was smoother compare to the carbon steel coupon which is only immersed into the acid. It shows that the oil palm leaves extract had successfully act as a corrosion inhibitor. The leaf extract forms a protective thin film as a barrier from the corrosive medium, therefore, reducing the effect of corrosion (the roughening) on the surface of the mild steel. This effect of smoother surface of the metal with the presence of successful corrosion inhibitors was observed in several papers [24].

4 Conclusion and Recommendation

In conclusion, this research was achieving its objectives.

1. Oil palm leaves extract had successfully been extracted using the microwave assisted extraction.
2. LC/MS Q-ToF analysis shows that active component such as tannins, alkaloid and flavonoid is present in the oil palm leaves extract. The presence of these active components with functional group containing nitrogen, oxygen and carbon functional group enhance the process of adsorption on the mild steel and thus act as a corrosion inhibitor.

3. The experimental models had been obtained through a statistical approach, RSM and are able to estimate the corrosion rate as a function of acid concentration, inhibitor concentration and temperature.
4. The morphology study also show that corrosion rate is low when POL extract is presence.

To improve this research, more parameters can be added into the RSM so that we can understand more about how those parameters affect corrosion rate. On the other hand, more analysis can be done to study corrosion and corrosion inhibitor such as the X-ray diffraction analysis, Fourier-transform infrared spectroscopy (FTIR) and wettability test.

Acknowledgements We would like to thank Universiti Malaysia Pahang for the financial assistance through research grants with RDU210350.

References

1. Obot IB, Obi-Egbedi NO, Umoren SA (2009) Antifungal drugs as corrosion inhibitors for aluminium in 0.1 M HCl. *Corros Sci* 51(8):1868–1875
2. William ST (2013) *Handbook of environmental degradation of materials*, 2nd ed. William Andrew Publishing, Norwich, United States
3. Saji VS (2010) A review on recent patent in corrosion inhibitor. *Recent Pat Corros Sci* 2:6–12
4. Haris NIN, Sobri S, Kassim N (2019) Oil palm empty fruit bunch extract as green corrosion inhibitor for mild steel in hydrochloric acid solution: central composite design optimization. *Mater Corros* 70(6):1111–1119
5. Rani BE, Basu BBJ (2012) Green inhibitors for corrosion protection of metals and alloys: an overview. *Int J Corros ID* 380217:15 p
6. Ambrish S, Ebenso EE, Quraisi MA (2012) Corrosion inhibition of carbon steel in HCl solution by some plant extracts. *Int J Corros* 1(1):1–20
7. Ji G, Shukla SK, Dwivedi P, Sundaram S, Prakash R (2011) Inhibitive effect of *Argemone mexicana* plant extract on acid corrosion of mild steel. *Ind Eng Chem Res* 50:11954–11959
8. Kamal C, Sethuraman MG (2012) Caulerpin-A bis-indole alkaloid as a green inhibitor for the corrosion of mild steel in 1 M HCl solution from the marine alga *Caulerpa racemosa*. *Ind Eng Chem Res* 51:10399–10407
9. Yaro AS, Khadom AA, Wael RK (2013) Apricot juice as green corrosion inhibitor of mild steel in phosphoric acid. *Alexandria Eng J* 52:129–135
10. Malaysia Palm Oil Board (2018) Malaysia palm oil industry. Retrieved from http://bepi.mpop.gov.my/images/area/2017/Area_summary
11. Awalludin MF, Sulaiman O, Hashim R, Nadhari WNAW (2015) An overview of the oil palm industry in Malaysia and its waste utilization through thermochemical conversion, specifically via liquefaction. *Renew Sustain Energy Rev* 50(C):1469–1484
12. Wieke P, Andoyo S, Susi S (2018) The effect of pulping process variable and elemental chlorine free bleaching on the quality of oil palm trunk pulp. *J Selulosa* 8(2):85–94
13. Fernando BM, Thais MB, Utsch M, Antonio CMR (2014) Performance of corrosion inhibitors based on n-butylamine in protection of carbon steel in hydrochloric acid solution. *Int Refereed J Eng Sci* 3:38–42
14. Chan CH, Rozita Y, Ngoh GC (2013) Modeling and prediction of extraction profile for microwave-assisted extraction based on absorbed microwave energy. *Food Chem* 140(1–2):147–153

15. Al-Otaibbi MS, Al-Mayouf AM, Khan M, Mousa AA, Al-Mazroa SA, Alkathlan HZ (2012) Corrosion inhibitory action of some plant extracts on the corrosion of mild steel in acidic media. *Arab J Chem* 7(3):340–346
16. Sin HLY, Abdul RA, Gan CY, Saad B, Salleh MI, Umeda M (2017) *Aquilaria subintegra* leaves extracts as sustainable mild steel corrosion inhibitors in HCl. *Measurement* 109:334–345
17. Nwigbo SC, Okafor VN, Okewale AO (2012) Comparative study of *Elaeis guineensis* exudates (palm wine) as a corrosion inhibitor for mild steel in acidic and basic solutions. *Res J Appl Sci Eng Technol* 4(9):1035–1039
18. Prithiba A, Leelavathi S, Rajalakshmi R (2014) Application of natural products as corrosion inhibitors in different steel and media. *Chem Sci Rev Lett* 3:177–187
19. Owate IO, Nwadiuko OC, Dike II, Isu JO, Nnanna LA (2014) Inhibition of mild steel corrosion by *Aspilia africana* in acidic solution. *Am J Mater Sci* 4(3):144–149
20. Umoren SA, Eduok UM, Oguzie EE (2008) Corrosion inhibition of mild steel in 1M H₂SO₄ by polyvinyl pyrrolidone and synergistic iodide additive. *Portugaliae Electrochem Acta* 26(6):533–546
21. Barmatov E, Geddes J, Hughes T, Nagi M (2012) Research on corrosion inhibitors for acid stimulation. In: NACE, C2012-0001573
22. Okafor PC, Uwah IE, Ekerenam OO, Ekpe UJ (2009) *Combretum bracteosum* extracts as eco-friendly corrosion inhibitor for mild steel in acidic medium. *Pigm Resin Technol* 38(4):236–241
23. Wan Omar WNN, Saidina Amin NA (2011) Optimization of heterogeneous biodiesel production from waste cooking palm oil via response surface methodology. *Biomass Bioenergy* 35(3):1329–1338
24. Kıcır N, Tansuğ G, Erbil M, Tüken T (2016) Investigation of ammonium (2,4 dimethylphenyl)-dithiocarbamate as a new, effective corrosion inhibitor for mild steel. *Corros Sci* 105:88–99